सत्यमेव जयते

INDIAN AGRICULTURAL
RESEARCH INSTITUTE, NEW DELHI

I.A.R 1.6.
GIP NLK—H.3 I.A.R.I.—10·5·55—18,000

CANADIAN

JOURNAL OF

RESEARCH

SECTION A

INDEX TO VOLUME 26

Authors

SECTION A

INDEX TO VOLUME 26

Subjects

.

GAS DYNAMIC TREATMENT OF EXOTHERMIC AND ENDOTHERMIC DISCONTINUITIES[1]

BY D. G. SAMARAS

Abstract

Endothermic and exothermic processes in gas dynamic flows taking place in a very narrow zone may be considered as discontinuities. The variation of the static and total head density ratio, pressure ratio, and temperature ratio as well as the angle of deviation, area ratio, and exit normal Mach number have been found as functions of the entry normal Mach number and of heat addition. In addition to these, some other useful quantities such as the area ratio parameter, the difference of the square of velocities, and the normal velocity product have been evaluated. It was found that, in a discontinuity, heat can be added until the exit normal Mach number reaches unity (choking). Depending on the entry normal Mach number, only a limited amount of heat can be added at the discontinuity. An exothermic discontinuity behaves as an expansion when the entry normal Mach number is subsonic, and it is accompanied by a drop in static pressure, density, and total head pressure. An exothermic discontinuity behaves as a compression shock wave when the entry normal Mach number is supersonic, and it is accompanied by an increase in static pressure and density and a decrease in total head pressure. An endothermic discontinuity behaves always as a compression shock wave, and it is accompanied by an increase in static density, pressure, and total head pressure. It is hoped that the results and conclusions found may be useful in a better understanding of many nearly discontinuous phenomena such as flame fronts, condensation and evaporation fronts, and other similar problems.

Notation

The following symbols have been used in the analysis:

A = area,

a = local velocity of sound,

B = heat addition function,

c_p = specific heat under constant pressure,

C^* = critical velocity corresponding to total head conditions,

e = thickness of the flame front,

g = gravitational constant,

H = heat content of the combustible mixture,

J = Joule's equivalent,

M = Mach number,

p = absolute pressure,

R = gas constant,

T = absolute temperature,

V = velocity,

$x = \dfrac{\rho_2}{\rho_1}$ = static density ratio,

$y = \dfrac{V_{2n}}{a_1}$ = ratio of the normal exit velocity to the inlet local velocity of sound,

$z = \dfrac{p_2}{\rho_1 a_1^2}$ = ratio of the exit static pressure to the momentum of the inlet velocity of sound,

γ = isentropic exponent,

δ = angle of deviation,

ν = kinematic viscosity,

ρ = absolute density,

ϕ = angle between the velocity and its normal component,

$\zeta^2 = \dfrac{\gamma - 1}{\gamma + 1} + \dfrac{2\,\gamma}{\gamma + 1} \cdot \dfrac{1}{M^2}$ = auxiliary function of the Mach number used for convenience only.

The following subscripts have been employed:

1, 2 = For the cold and hot sides of the flame front, respectively,

n = For normal,

t = For total head values (except for the velocity and Mach number denoting the tangential component).

1.0 Introduction

1.1.0 GENERAL

Since the combustion process as applied to gas turbines, propulsive ducts, and rockets is of such fundamental importance, the National Research Council of Canada has undertaken a comprehensive experimental and theoretical research program in an attempt to clarify the fundamental laws of combustion.

In the past, very little work has been done regarding the gas dynamic aspects of the combustion process in gas streams.

The first paper (7) of this series dealt with the general problem of heat addition in gas streams in one-dimensional fashion.

This is the second paper, and it deals with the general conditions pertaining in flame fronts.

Generally speaking, a flame front is defined as a thin zone where a rapid chemical reaction (combustion) takes place, accompanied by light emission.

In the case of a premixed gas, the flame zone, for reasons of simplification, called also flame surface, is defined as the surface where the burnt and unburnt gases come into contact.

In natural gas – air mixtures, the luminous zone is marked by the sharp appearance and disappearance of the C-C and C-H bands. When sodium is added to the flame, the sodium D lines appear simultaneously with these bands so that temperature measurements can be effected within the combustion zone.

The fact that the flame is accompanied by light emission is of secondary importance only; one part of the emitted light does not originate in the combustion zone, but from the still hot, just burnt, gases behind it.

The question whether the radiation emitted by a flame front is of thermal or chemical origin is of fundamental importance.

Thermal radiation is defined as that for which the intensity distribution as a function of the wave length depends only on the gas temperature and thus excludes the radiation intrinsic in the nature of the gas and the chemical luminescence (8).

It is apparent then that the radiation of a body must include not only the frequencies corresponding to the temperature radiation but also those excited by other processes. In this particular case, the additional radiation present is that due to luminescence. The energy of this radiation must be supplied from a source other than the heat energy, and, in fact, it is produced from the energy of the chemical reaction. A classical example of chemical luminescence is that of the slow oxidation of phosphorus. The reaction of phenyl magnesium iodide and chloropicrin is accompanied by the emission of green luminescence, and the reaction of formaldehyde with pyrogallol, by an orange-red luminescence (2).

According to Prettre (3), luminescence has been observed during the oxidation of practically all fuels, except hydrogen. The radiation spectrum of flames is a complicated one. It consists of the entire spectrum of solid carbon molecules, radicals of the gaseous substances, and free atoms, as well as the spectrum due to chemical luminescence.

Depending on the temperature at which combustion takes place, different types of flames may appear such as 'cool flames' and normal combustion flames.

Emeleus (3) found that the spectra of 'cool flames' are different from those of normal flames; later from the work of Kontrajew, Chou, and Henri, and Ubbelohde, it was concluded that the 'cool flames' may be attributed to the presence of formaldehyde.

The visibility of the formaldehyde luminescence is attributed to the high momentary concentration of excited formaldehyde, due to the rapid development of the reaction in the peninsula region (short induction period). At these low reaction temperatures the radiation is mostly emitted from the blu: and ultraviolet, and no appreciable amount of thermal radiation is present. However, at higher temperatures, the branching is less intense and the concentrations of intermediate products build up more slowly and finally the luminescence becomes weaker.

In the combustion of ether in air, the 'cool flames' are present between 180° and 270° C. At slightly higher temperatures between 230° and 365° C. a region of 'green flames' appears. In these temperature ranges in the spectrum the C-C bands are most prevalent. The 'green flames' are very different from the bluish 'cool flames' and the white or yellow normal flames.

1.2.0 FLAME STRUCTURE

It is well known that the combustion process is affected by different factors such as heat conduction (transfer of heat energy from the burnt gas to the unburnt), diffusion, especially diffusion of unburnt gas molecules into the combustion zone, and, under certain conditions, diffusion of active particles from the combustion zone into the unburnt gas.

According to the above, the flame front is only a fictitious surface. In reality, a continuous transition from the burnt to the unburnt takes place. This transition is effected in such a thin layer that, in most cases, a discontinuous variation of velocity, pressure, temperature, density, and concentration may be considered.

Little is known regarding the structure of the flame front. Lewis and von Elbe (4), making certain simplifying assumptions, succeeded in finding the order of the temperature distribution, concentration, and thickness of the combustion zone. They assumed that the sum of the chemical and of the heat energy is constant and uniformly distributed over the entire burning zone. This assumption, although not completely justified, results in a great simplification of the problem.

From these calculations, it was found that the thickness of the flame zone is of the order of 1 μ. Fig. 1 shows the experimental results (9) found by Wolfhardt with acetylene and oxygen mixtures as a function of the absolute pressure.
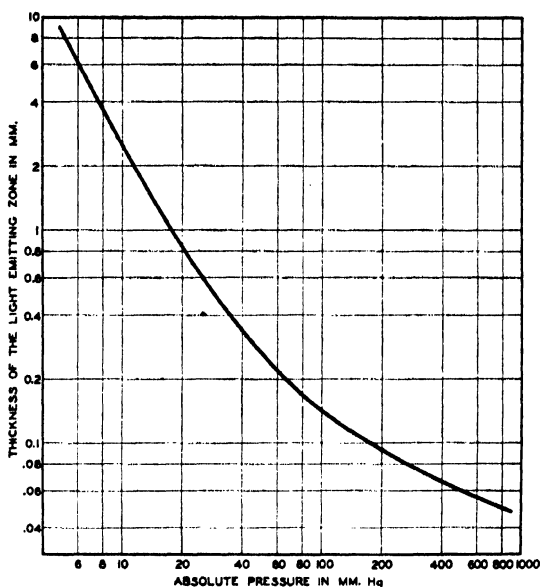
FIG. 1. *Thickness variation of the light emitting zone as a function of the absolute pressure.*

Becker (1, Chap. V) investigated the structure of a shock wave front, taking into consideration the influence of viscosity and heat transmission. His results were put in a more convenient non-dimensional form as follows:

$$\frac{e}{\nu}\sqrt{g\gamma RT_{1t}} = \frac{4}{3}\sqrt{\frac{2}{\gamma (\gamma + 1)}}\, \zeta\, \frac{1 + \zeta}{1 - \zeta}, \tag{1}$$

where

$$\zeta^2 = \frac{\gamma - 1}{\gamma + 1} + \frac{2}{\gamma + 1}\frac{1}{M^2}$$

and were plotted in Fig. 2. This represents the intermediate special case going from the exothermic to endothermic processes.

The flame front is characterized by a very steep temperature gradient which is not so pronounced in a weak shock wave front and it is responsible for the intense radiation and heat conduction.

The flame front forms an angle with the flow lines so that the normal component of the gas velocity equals the burning velocity. Thermal expansion increases the gas velocity as well as the angle of flow lines in such a way that the flow in the stream tube remains constant. It has been observed

(5) that in slow (laminar flow) flames the refraction of a flow line begins well before it enters the luminous combustion zone, indicating a penetration of heat into the unburnt gas. In the case of turbulent flow, a less premature refraction should be expected.
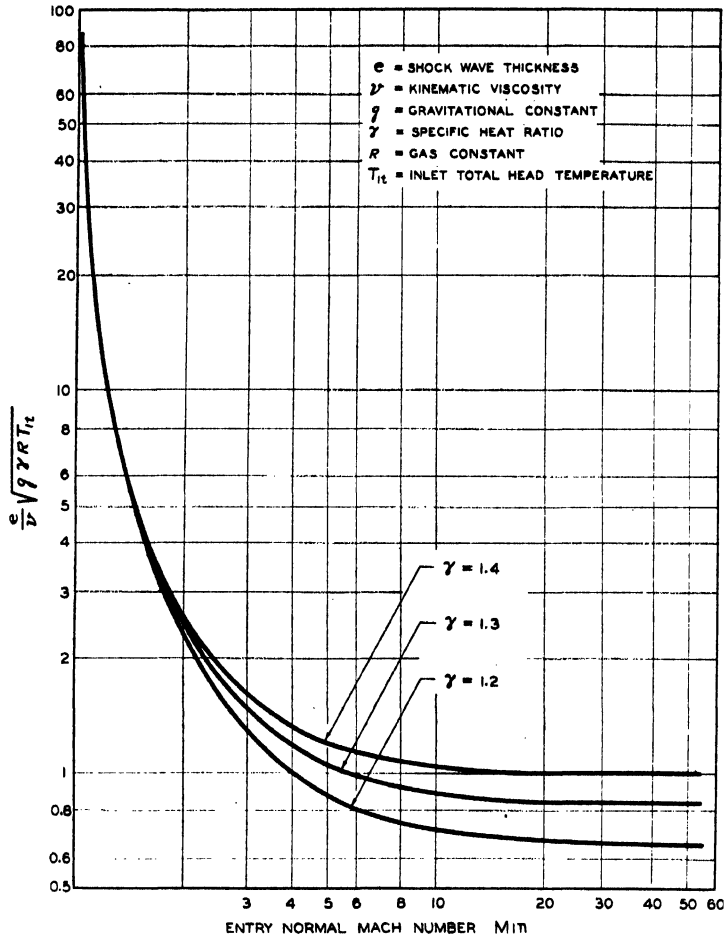
FIG. 2. *Thickness variation of the shock wave front with the entry normal Mach number.*

In a curved flame front a large amount of vorticity is created; this results in an increase of the heat dissipation. To this effect and to the diffusion of active particles may be attributed the increased burning velocity at the tip of the Bunsen burner.

2.0 Assumptions

According to the above discussion, the flame front is assumed as a discontinuity, e.g., zero thickness through which a discontinuous change of state occurs and an increase in entropy takes place.

The influence of viscosity, heat conduction, and radiation are disregarded.

3.0 Range and Scope of Investigation

In the present treatment the endothermic and exothermic reaction fronts have been investigated.

Both subsonic and supersonic flows have been examined, including the normal combustion process as well as detonation.

In addition to the above, similar phenomena, such as condensation and evaporation fronts, are within the scope of the present investigation.

4.1.0 General Equations in the Discontinuity Front

From Fig. 3 the following equations of conservation across the discontinuity front may be written:
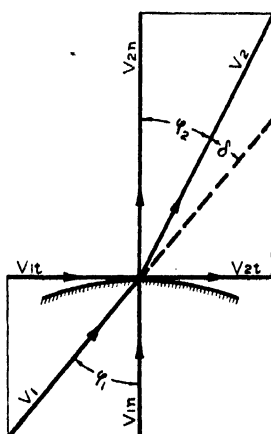
FIG. 3. *Velocity diagram of a discontinuity front element.*

The continuity

$$\rho_1 V_{1n} = \rho_2 V_{2n} \ . \tag{2}$$

The normal component of momentum

$$p_1 + \rho_1 V_{1n}^2 = p_2 + \rho_2 V_{2n}^2 \ . \tag{3}$$

The tangential component of momentum

$$V_{1t} = V_{2t} \ . \tag{4}$$

The energy

$$\frac{\gamma_1}{\gamma_1 - 1} \frac{p_1}{\rho_1} + \frac{V_1^2}{2} + g J H = \frac{\gamma_2}{\gamma_2 - 1} \frac{p_2}{\rho_2} + \frac{V^2}{2} \ . \tag{5}$$

The state equations put in the form of the sound velocity

$$a_1^2 = \gamma_1 \frac{p_1}{\rho_1} \ , \quad a_2^2 = \gamma_2 \frac{p_2}{\rho_2} \ . \tag{6}$$

4.2.0 The Static Density Ratio

By the use of Equations (4) and (6) we can transform Equations (2), (3), and (5) in the following manner:

$$\frac{V_{1n}}{a_1} = \frac{\rho_2}{\rho_1} \frac{V_{2n}}{a_1} , \tag{7}$$

$$\frac{1}{\gamma_1} + \frac{V_{1n}^2}{a_1^2} = \frac{p_2}{\rho_1 a_1^2} + \frac{\rho_2}{\rho_1} \frac{V_{2n}^2}{a_1^2} , \tag{8}$$

$$\frac{1}{\gamma_1 - 1} + \frac{V_{1n}^2}{2a_1^2} + g J \frac{H}{a_1^2} = \frac{\gamma_2}{\gamma_2 - 1} \frac{\rho_1}{\rho_2} \cdot \frac{p_2}{\rho_1 a_1^2} + \frac{V_{2n}^2}{2a_1^2} , \tag{9}$$

and calling

$$x = \frac{\rho_2}{\rho_1} , \quad y = \frac{V_{2n}}{a_1} , \quad z = \frac{p_2}{\rho_1 a_1^2} ,$$

$$M_{1n} = M_1 \cos \phi_1 = \frac{V_{1n}}{a_1} , \quad M_{2n} = M_2 \cos (\phi_1 - \delta) = \frac{V_{2n}}{a_2} ,$$

$$B = g J \frac{H}{a_1^2} = \frac{c_{p_{12}}}{c_{p_1}} \left(\frac{T_{2l}}{T_{1l}} - 1 \right) \left(\frac{1}{\gamma_1 - 1} + \frac{M_1^2}{2} \right) ,$$

we obtain the following equations:

$$xy = M_{1n} \tag{7'}$$

$$\frac{1}{\gamma_1} + M_{1n}^2 = z + x y^2 \tag{8'}$$

$$\frac{1}{\gamma_1 - 1} + \frac{M_{1n}^2}{2} + B = \frac{\gamma_2}{\gamma_2 - 1} \frac{z}{x} + \frac{y^2}{2} . \tag{9'}$$

After some algebraic transformations we finally obtain

$$M_{1n}^2 (1 + \gamma_2) \left(\frac{1}{x} \right)^2 - 2 \gamma_2 \left(\frac{1}{\gamma_1} + M_{1n}^2 \right) \left(\frac{1}{x} \right)$$
$$+ (\gamma_2 - 1) \left[\frac{2}{\gamma_1 - 1} + M_{1n}^2 + 2 B \right] = 0 . \tag{10}$$

The solution of this equation is as follows

$$\frac{\rho_1}{\rho_2} = \frac{1}{x}$$

$$\frac{\left(\dfrac{\gamma_2}{\gamma_1} + \gamma_2 M_{1n}^2 \right) \pm \sqrt{\left(\dfrac{\gamma_2}{\gamma_1} + \gamma_2 M_{1n}^2 \right)^2 - M_{1n}^2 (\gamma_2^2 - 1) \left[\dfrac{2}{\gamma_1 - 1} + M_{1n}^2 + 2 B \right]}}{(\gamma_2 + 1) M_{1n}^2} . \tag{11}$$

The static density curves are asymptotic to two density ratio lines

$$\frac{\rho_1}{\rho_2} = 1.0 \quad \text{and} \quad \frac{\rho_1}{\rho_2} = \frac{\gamma_2 - 1}{\gamma_2 + 1},$$

as is clearly seen from Fig. 4.
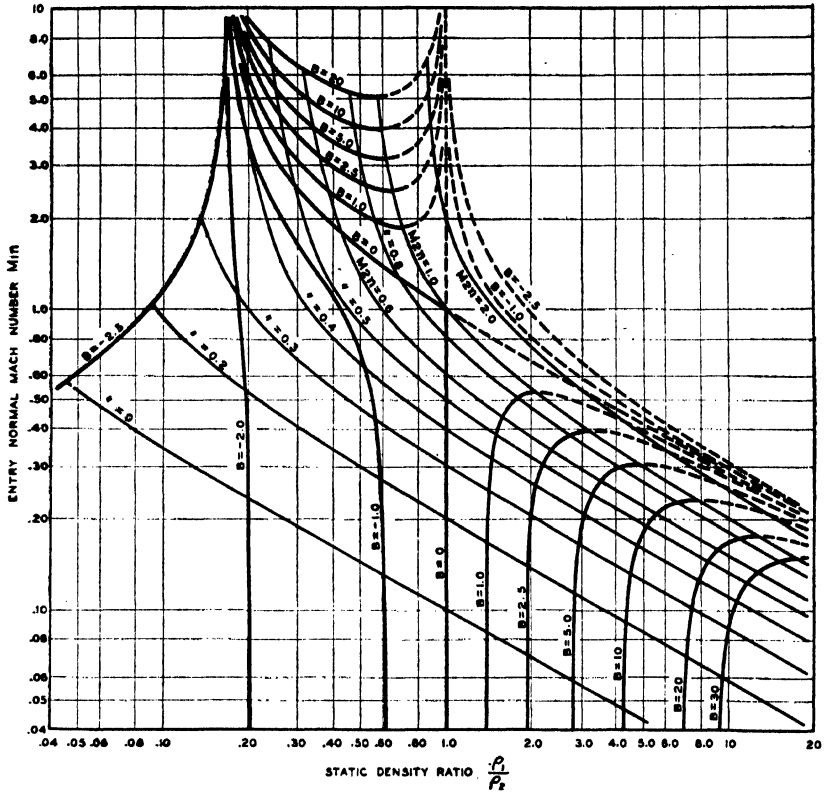
FIG. 4. *Variation of the static density ratio with the entry and exit normal Mach numbers.*

4.3.0 THE STATIC PRESSURE RATIO

The static pressure ratio across the discontinuity front may be found as follows

$$\frac{p_2}{p_1} = \frac{p_2}{\rho_1 a_1^2} \frac{\rho_1 a_1^2}{p_1} = \gamma_1 z , \tag{12}$$

and taking into consideration Equations (7′) and (8′) we obtain finally

$$\frac{p_2}{p_1} = 1 + \gamma_1 M_{1n}^2 \left(1 - \frac{\rho_1}{\rho_2} \right). \tag{13}$$

4.4.0 THE STATIC TEMPERATURE RATIO

This is found to be as follows:

$$\frac{T_2}{T_1} = \frac{R_1}{R_2} \left[1 + \gamma_1 M_{1n}^2 \left(1 - \frac{\rho_1}{\rho_2} \right) \right] \frac{\rho_1}{\rho_2}. \tag{14}$$

4.5.0 THE ANGLE OF DEVIATION

This may be found from the following equation:

$$\frac{tg\,(\phi_1 - \delta)}{tg\,\phi_1} = \frac{\rho_2}{\rho_1} . \tag{15}$$

4.6.0 THE MACH NUMBER RATIO

After a few simple algebraic calculations the normal Mach number ratio is found to be

$$\frac{M_{2n}^2}{M_{1n}^2} = \frac{M_2^2\,\cos^2\,(\phi_1 - \delta)}{M_1^2\,\cos^2\,\phi_1} = \frac{\dfrac{\gamma_1}{\gamma_2}\cdot\dfrac{\rho_1}{\rho_2}}{1 + \gamma_1\,M_{1n}^2\left(1 - \dfrac{\rho_1}{\rho_2}\right)} . \tag{16}$$

4.7.0. THE TOTAL HEAD PRESSURE RATIO

After some simple algebraic transformations the total head pressure ratio was found to be:

$$\frac{p_{2t}}{p_{1t}} = \frac{\left[1 + \gamma_1\,M_{1n}^2\left(1 - \dfrac{\rho_1}{\rho_2}\right)\right]}{\left[1 + \dfrac{\gamma_1 - 1}{2}\,\dfrac{M_{1n}^2}{\cos^2\phi_1}\right]^{\frac{\gamma_1}{\gamma_1 - 1}}}\quad 1 + \frac{\gamma_2 - 1}{2\gamma_2}\left[\frac{\gamma_1\,M_{1n}^2\left(\dfrac{\rho_1}{\rho_2} + \dfrac{\rho_2}{\rho_1}\,tg^2\,\phi_1\right)}{1 + \gamma_1\,M_{1n}^2\left(1 - \dfrac{\rho_1}{\rho_2}\right)}\right] . \tag{17}$$

In the case of a normal front $\phi = 0$ the total head pressure ratio reaches its minimum value.

4.8.0. THE NORMAL VELOCITY RATIO

From Equation (2) it is seen that the normal velocity ratio is as follows:

$$\frac{V_{2n}}{V_{1n}} = \frac{\rho_1}{\rho_2} . \tag{18}$$

4.9.0 THE NORMAL AREA RATIO

From Equations (2), (16), and (18) the area ratio may be found

$$\frac{A_{2n}}{A_{1n}} \cdot \frac{M_2}{M_1} = \sqrt{\frac{\dfrac{\gamma_1}{\gamma_2}\,\dfrac{\rho_1}{\rho_2}}{1 + \gamma_1\,M_{1n}^2\left(1 - \dfrac{\rho_1}{\rho_2}\right)}} . \tag{19}$$

This parameter is plotted against M_{1n} in Fig. 5.
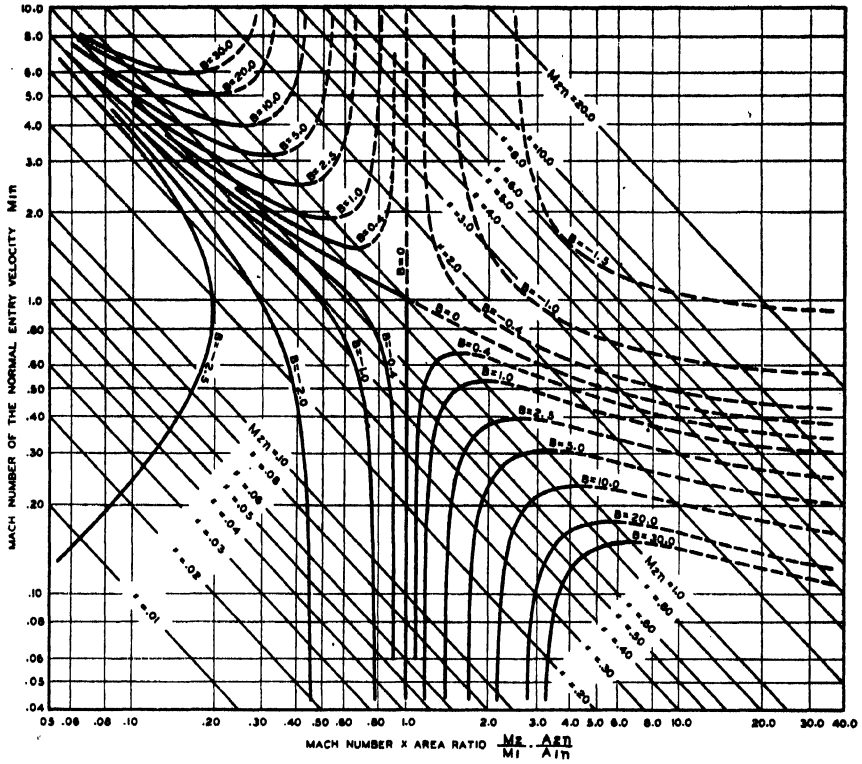
FIG. 5. *Variation of the heat addition parameter with the entry and exit normal Mach numbers in a discontinuity front.*

4.10.0 THE DIFFERENCE OF THE SQUARE OF VELOCITIES

After some simple algebraic calculations, the difference of the square of velocities was found to be:

$$\frac{V_2^2 - V_1^2}{a_1^2} = M_{1n}^2 \left[\left(\frac{\rho_1}{\rho_2} \right)^2 - 1 \right]. \tag{20}$$

4.11.0 THE NORMAL VELOCITY PRODUCT

In the Appendix the product of the normal velocities has been derived and is as follows:

$$\frac{V_{1n} V_{2n}}{C_1^{*2}} = \left(\frac{\gamma_1 + 1}{\gamma_2 + 1} \right) \left\{ \left[\frac{\gamma_2}{\gamma_1} + \frac{\gamma_1 - 1}{2} \frac{M_{1t}^2}{1 + \frac{\gamma_1 - 1}{2} M_1^2} \right] \right. $$

$$\left. - \frac{\frac{\gamma_2}{\gamma_1}}{\frac{\rho_1}{\rho_2} - 1} \left[\left(\frac{T_{2t}}{T_{1t}} - 1 \right) + \frac{\rho_1}{\rho_2} \cdot \frac{\gamma_1 - \gamma_2}{2 \gamma_2} \frac{M_1^2}{1 + \frac{\gamma_1 - 1}{2} M_1^2} \right] \right\} \tag{21}$$

Equation (21) can also be written in another form as follows:

$$
\frac{V_{1n} V_{2n}}{C_1^{*2}} = \left(\frac{\gamma_1 + 1}{\gamma_2 + 1}\right) \left\{ \frac{\gamma_2}{\gamma_1} \left[\frac{\frac{p_1}{p_2} - \frac{T_{2t}}{T_{1t}}}{\frac{\rho_1}{\rho_2} - 1} \right] \right.
$$

$$
+ \frac{\frac{\gamma_1 - 1}{2} M_1^2}{1 + \frac{\gamma_1 - 1}{2} M_1^2} \left[\frac{M_{1t}^2}{M_1^2} - \frac{\rho_1}{\rho_1 - \rho_2} \left(\frac{\gamma_1 - \gamma_2}{\gamma_1(\gamma_1 - 1)} \right) \right] \right\} \tag{22}
$$

5.0 Results and Discussion

Figs. 4 and 5 show the variation of the static density and area ratio parameter with the entry and exit normal Mach numbers for different values of the heat addition function B.

It is seen that the exit normal Mach number has unity as a limiting value. For a given subsonic normal entry Mach number through an exothermic discontinuity, a maximum heat addition function appears, corresponding to unity exit normal Mach number, and the maximum entry normal Mach number decreases with increasing heat addition function.

In a given supersonic normal entry velocity through an exothermic discontinuity, a minimum heat addition function appears, corresponding to unity exit normal Mach number, and the minimum entry normal Mach number increases with increasing heat addition function.

In endothermic discontinuities, no extreme values of the entry normal Mach number appear.

For supersonic normal entry velocities passing through exothermic discontinuities, the resulting exit static density is larger than the entry one and the ratio of the entry to the exit static density decreases with increasing heat addition function; consequently the discontinuity behaves like a compression shock wave. For a subsonic entry normal velocity the reverse is true and an acceleration is realized through the discontinuity. In each case, the static density ratio decreases with increasing entry normal Mach number. When the discontinuity is endothermic the exit static density is always larger than the entry and the static density ratio decreases with increasing heat addition function.

Figs. 6 and 7 show the variation of the entry and exit normal Mach numbers with the minimum total head pressure ratio and the heat addition function.

It is seen that when the flow passes through an exothermic discontinuity, the total head pressure ratio is smaller than unity (loss of momentum) and the reverse is true when it passes through an endothermic discontinuity (Mach number slightly greater than one).

In the endothermic case, a maximum value of the total head pressure ratio $\left(\dfrac{p_{2t}}{p_{1t}}\right)_{min}$ appears at an entry normal Mach number slightly smaller than unity, tending towards unity as the heat addition function tends to zero and accompanied by an increase of the exit normal Mach number. The maximum value of the total head pressure ratio $\left(\dfrac{p_{2t}}{p_{1t}}\right)_{min} = 1.235$. When the flow passes
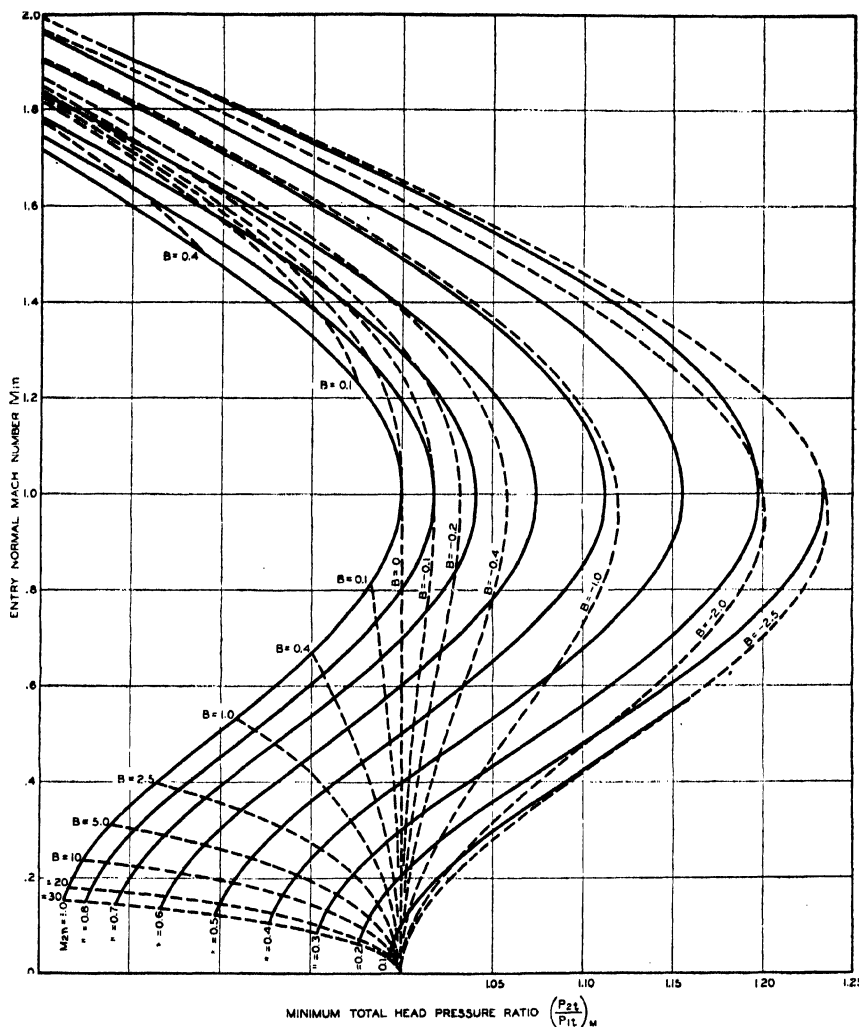
FIG. 6. *Variation of the minimum total head pressure with the entry and exit normal Mach numbers.*

through an exothermic discontinuity and the entry normal Mach number is smaller than unity, the total head pressure ratio is always $\left(\dfrac{p_{2t}}{p_{1t}}\right)_{min} > 0.8$, and increases with an increasing entry normal Mach number and the heat addition function. In the case when the entry normal Mach number is larger than

unity, no lower limit of the total head pressure ratio exists and it decreases with increasing entry normal Mach number and heat addition function B.

From Fig. 7 it is seen that for a given total head pressure ratio $\left(\dfrac{p_{2t}}{p_{1t}}\right)_{min}$ in the exothermic case, a maximum exit normal Mach number appears.
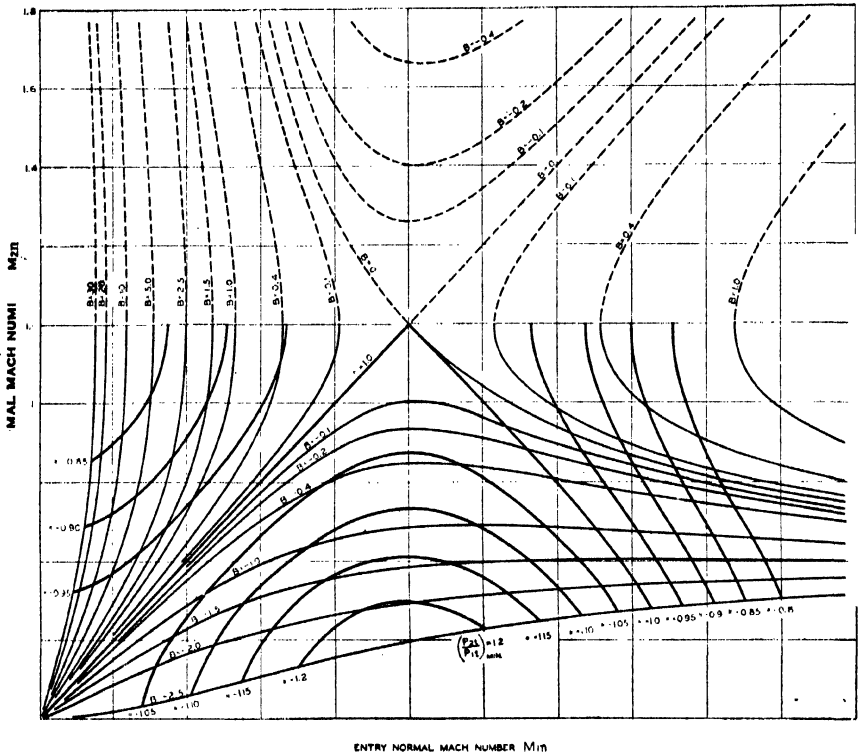
FIG. 7.   *Variation of the exit normal Mach number with the entry normal Mach number.*

In Fig. 8 is shown the variation of the static pressure difference ratio across the discontinuity with the entry and exit normal Mach number and the heat addition function. It is seen that when the entry normal Mach number is smaller than unity, a drop in static pressure occurs on passing through the exothermic discontinuity, and the larger this pressure drop, the larger the entry normal Mach number and the larger the heat addition function.

If the entry normal Mach number is larger than unity, an increase in static pressure occurs and this increase is larger, the larger the entry normal Mach number and the smaller the heat addition function.

Figs. 9, 10, 11, 12, and 13 show the variation of the angle of deviation with the angle of incidence and the entry Mach number for different values of the heat addition function $B = -2.5, -1.0, 0, 2.5,$ and 10, respectively.

It is seen that the maximum (negative) deviation for infinite entry Mach number, $M_1 \rightarrow \infty$, varies little with the heat addition function and is slightly
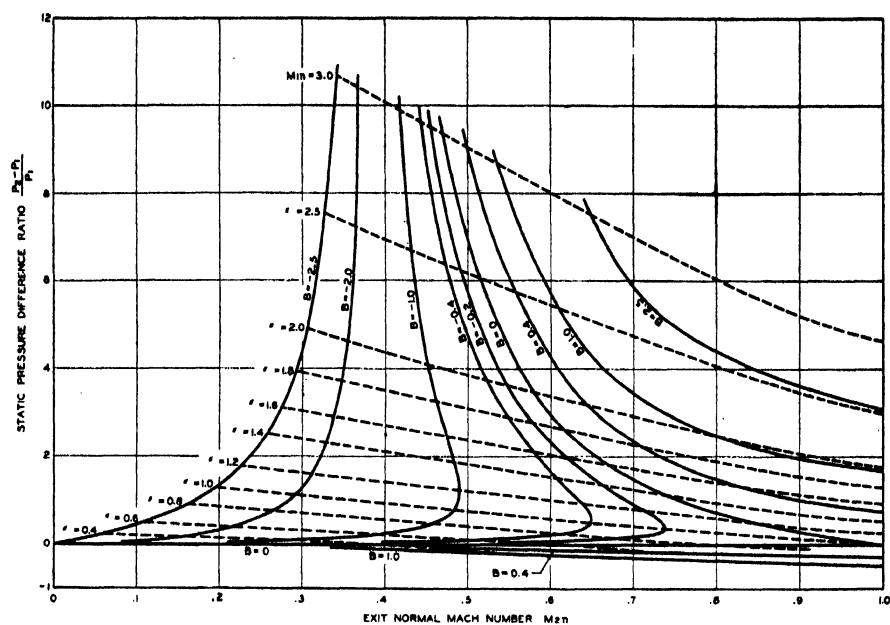
FIG. 8. *Variation of the static pressure difference with the entry and exit normal Mach numbers.*
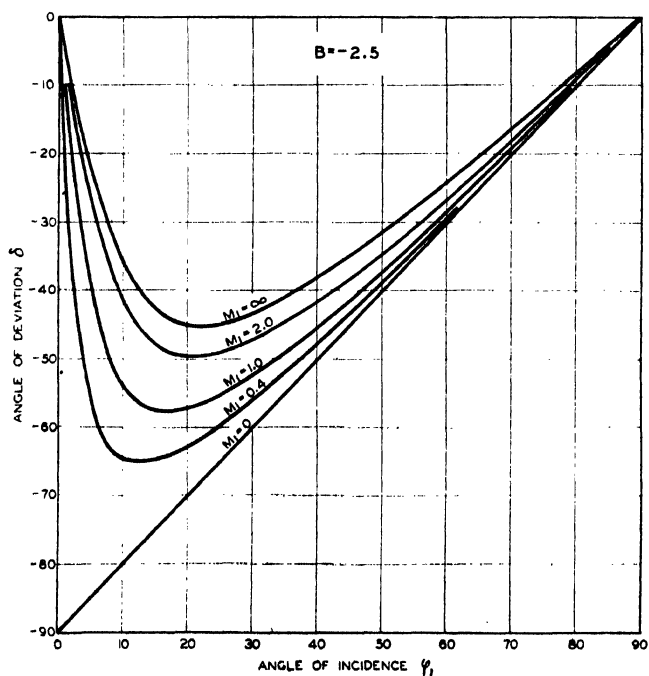
FIG. 9. *Variation of the angle of deviation with the angle of incidence and the entry Mach number.*
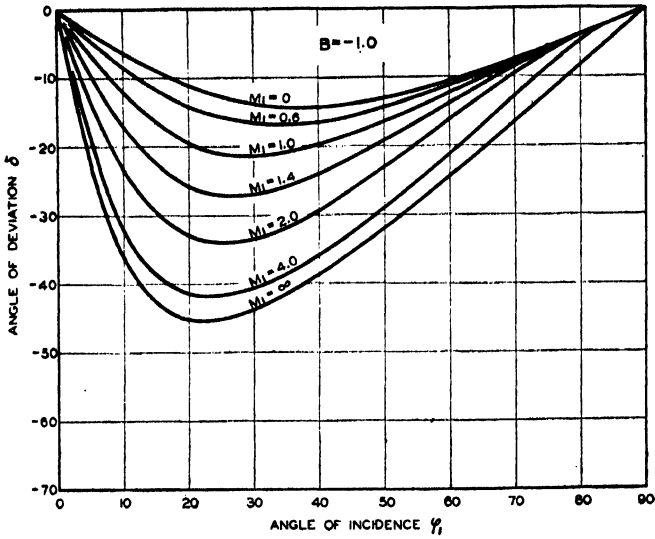
FIG. 10.   *Variation of the angle of deviation with the angle of incidence and the entry Mach number.*
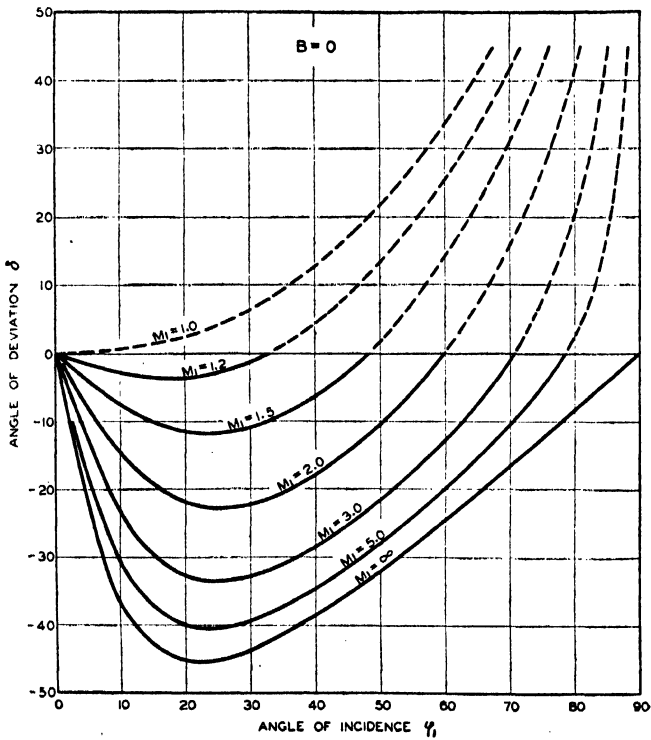
FIG. 11.   *Variation of the angle of deviation with the angle of incidence and the entry Mach number.*

larger than $-45°$. Again the maximum angle of deviation for zero entry Mach number, $M_1 \to 0$, increases with the heat addition parameter from $\delta = -90°, B = 2.5$ to $\delta = 90°, B \to \infty$.

For all endothermic cases, including the isoenergetic, for a given entry Mach number a maximum deviation appears and its value decreases with increasing heat addition function.
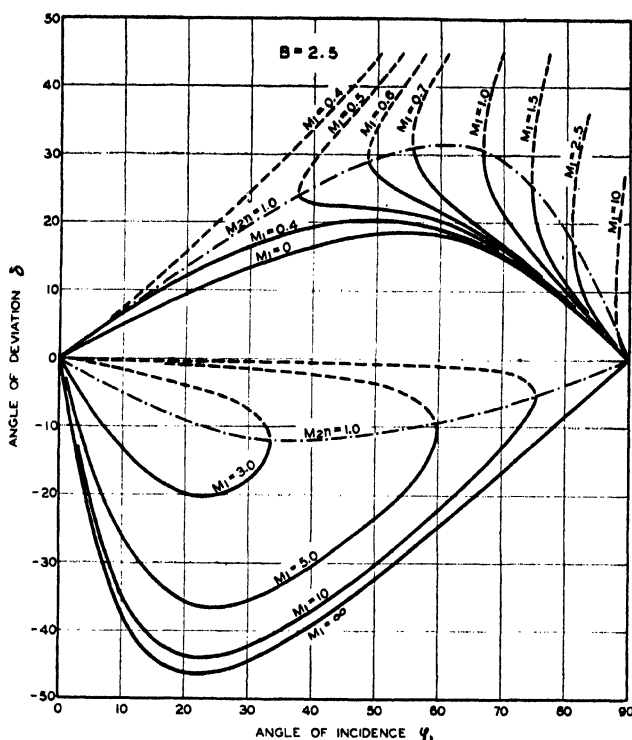
FIG. 12. *Variation of the angle of deviation with the angle of incidence and the entry Mach number.*

In exothermic discontinuities and for low entry Mach numbers (depending on the value of the heat addition parameter), maximum deviation angles appear, until a certain value of the entry Mach number is reached. This is changed into an inflection point and the deviation curve reaches a limiting value when the exit normal Mach number reaches unity. The larger the heat addition function the smaller the M_1 value at which the inflection appears.

For supersonic inlet flows and small angle of incidence the deviation angle is negative, reaching a maximum (negative) value after ending in a limiting line where the exit normal Mach number is unity. Above this angle of incidence no solution exists until another limiting value corresponding to an

exit normal Mach number of unity is reached. Beyond this limiting value a positive angle of deviation appears and its value decreases with increasing angle of incidence.

From the above discussion it may be concluded that, by passing through the discontinuity when the angle of deviation is negative, a compression shock wave occurs, and when the deviation is positive, an expansion occurs.
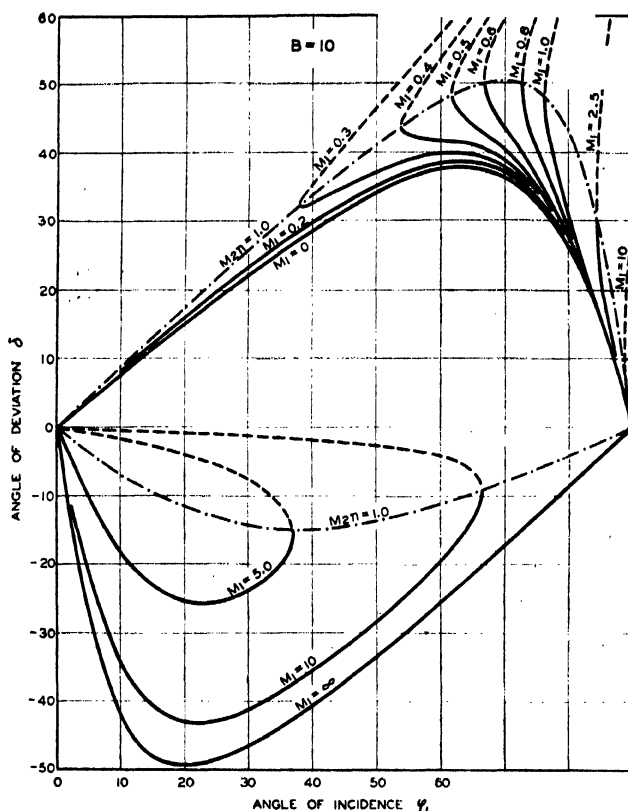
Fig. 13. *Variation of the angle of deviation with the angle of incidence and the entry Mach number.*

The velocity product is not a constant as in the cases examined by L. Prandtl and Th. Meyer (6) but a complicated function of the Mach numbers, densities, and temperatures.

6.0 Conclusions

From the above analysis and discussion, the following conclusions are drawn:

The maximum exit normal Mach number through a discontinuity front is unity.

In an exothermic discontinuity, depending on the value of the heat addition function, a maximum or a minimum value of the entry normal Mach number appears corresponding to the subsonic or supersonic normal flow. In an exothermic discontinuity, when the entry normal Mach number is less than unity, the discontinuity behaves like an expansion and is accompanied by a drop in static pressure, density, and total head pressure. In the reverse case, of a normal Mach number larger than unity, it behaves as a compression shock wave and is accompanied by an increase in static pressure and density and a decrease in total head pressure.

When the flow passes through an endothermic discontinuity, the discontinuity behaves as a compression shock wave, and is accompanied by an increase in static density, pressure, and total head pressure.

References

1. ACKERET, J. *In* Handbuch der Physik. Vol. 7. Julius Springer, Berlin. 1927.
2. AUDUBERT, R. Angew. Chem. 51 : 153. 1938.
3. JOST, W. Explosion and combustion processes in gases. *Translated from the German by* Huber O. Croft. McGraw-Hill Book Co., Inc., New York. 1946.
4. LEWIS, B. and VON ELBE, G. Combustion, flames and explosions of gases. Cambridge Univ. Press, London. 1938.
5. LEWIS, B. and VON ELBE, G. J. Chem. Phys. 11 : 75. 1943.
6. MEYER, T. VDI Forschungsheft, 62 : 31. 1908.
7. SAMARAS, D. G. Can. J. Research, F, 24 : 272. 1946.
8. WERNEBURG, J. Forsch. Gebiete Ingenieurw. 10 : 61. 1939.
9. WOLFHARDT, H. G. Z. tech. Physik, 24 : 206. 1943.

APPENDIX

Derivation of the Normal Velocity Product

The energy equations on either side of the discontinuity front may be written as follows

$$\left.\begin{array}{l}\dfrac{p_1}{\rho_1} = \dfrac{p_{1t}}{\rho_{1t}} - \dfrac{\gamma_1 - 1}{\gamma_1}\dfrac{V_1^2}{2} \\[2mm] \dfrac{p_2}{\rho_2} = \dfrac{p_{2t}}{\rho_{2t}} - \dfrac{\gamma_2 - 1}{\gamma_2}\dfrac{V_2^2}{2} = \dfrac{p_{1t}}{\rho_{1t}} + \left(\dfrac{p_{2t}}{\rho_{2t}} - \dfrac{p_{1t}}{\rho_{1t}}\right) - \dfrac{\gamma_2 - 1}{\gamma_2}\cdot\dfrac{V_2^2}{2}\end{array}\right\} , \quad (23)$$

and after some transformation the following may be obtained

$$p_2 - p_1 = (\rho_2 - \rho_1)\dfrac{p_{1t}}{\rho_{1t}} + \rho_2\left(\dfrac{p_{2t}}{\rho_{2t}} - \dfrac{p_{1t}}{\rho_{1t}}\right) - \dfrac{1}{2}\left(\dfrac{\gamma_2 - 1}{\gamma_2}\rho_2 V_2^2 - \dfrac{\gamma_1 - 1}{\gamma_1}\rho_1 V_1^2\right). \quad (24)$$

By using the momentum Equations (3) and (4) the following is found:

$$p_2 - p_1 = -(\rho_2 - \rho_1)V_t^2 + \rho_1 V_1^2 - \rho_2 V_2^2 , \quad (25)$$

and from Equations (24) and (25)

$$\frac{\gamma_2 + 1}{2\,\gamma_2}(p_2 - p_1) = (\rho_2 - \rho_1)\left[\frac{p_{1t}}{\rho_{1t}} + \frac{\gamma_2 - 1}{2\,\gamma_2}V_t^2\right]$$

$$+ \rho_2\left(\frac{p_{2t}}{\rho_{2t}} - \frac{p_{1t}}{\rho_{1t}}\right) + \frac{\rho_1 V_1^2}{2}\left(\frac{\gamma_1 - 1}{\gamma_1} - \frac{\gamma_2 - 1}{\gamma_2}\right); \qquad (26)$$

but from Equations (3) and (18) the following may be obtained

$$p_2 - p_1 = \rho_1 V_{1n}^2 - \rho_2 V_{2n}^2 = \rho_1^2 V_{1n}^2\left(\frac{1}{\rho_1} - \frac{1}{\rho_2}\right) = \rho_1^2 V_{1n}^2\left(\frac{\rho_2 - \rho_1}{\rho_1\,\rho_2}\right),$$

and finally

$$V_{1n}\,V_{2n} = \frac{p_2 - p_1}{\rho_2 - \rho_1}. \qquad (27)$$

From Equations (26) and (27) the following may be found

$$V_{1n}\,V_{2n} = \frac{2\,\gamma_2}{\gamma_2 + 1}\left\{\left(\frac{p_{1t}}{\rho_{1t}} + \frac{\gamma_2 - 1}{2\,\gamma_2}V_{1t}^2\right) + \frac{\rho_2}{\rho_2 - \rho_1}\left[\left(\frac{p_{2t}}{\rho_{2t}} - \frac{p_{1t}}{\rho_{1t}}\right)\right.\right.$$

$$\left.\left. + \frac{1}{2}\frac{\rho_1}{\rho_2}V_1^2\left(\frac{\gamma_1 - 1}{\gamma_1} - \frac{\gamma_2 - 1}{\gamma_2}\right)\right]\right\}. \qquad (28)$$

The critical velocity corresponding to total head conditions is given by:

$$C_1^{*2} = \frac{2\,\gamma_1}{\gamma_1 + 1}\cdot\frac{p_{1t}}{\rho_{1t}} = \frac{2\,\gamma_1}{\gamma_1 + 1}\,g\,RT_{1t}, \qquad (29)$$

and substituting into Equation (28) after some simple transformations, we finally obtain:

$$\frac{V_{1n}V_{2n}}{C_1^{*2}} = \left(\frac{\gamma_1 + 1}{\gamma_2 + 1}\right)\left\{\left[\frac{\gamma_2}{\gamma_1} + \frac{\gamma_1 - 1}{2}\frac{M_{1t}^2}{1 + \frac{\gamma_1 - 1}{2}M_1^2}\right]\right.$$

$$\left. - \frac{\frac{\gamma_2}{\gamma_1}}{\frac{\rho_1}{\rho_2} - 1}\left[\left(\frac{T_{2t}}{T_{1t}} - 1\right) + \frac{\rho_1}{\rho_2}\frac{\gamma_1 - \gamma_2}{2\,\gamma_2}\frac{M_1^2}{1 + \frac{\gamma_1 - 1}{2}M_1^2}\right]\right\}, \qquad (21)$$

and by rearranging this equation after some transformation we finally obtain:

$$\frac{V_{1n}V_{2n}}{C_1^{*2}} = \left(\frac{\gamma_1 + 1}{\gamma_2 + 1}\right) \cdot \left\{\frac{\gamma_2}{\gamma_1}\left(\frac{\frac{\rho_1}{\rho_2} - \frac{T_{2t}}{T_{1t}}}{\frac{\rho_1}{\rho_2} - 1}\right)\right.$$

$$\left. + \frac{\frac{\gamma_1 - 1}{2}M_1^2}{1 + \frac{\gamma_1 - 1}{2}M_1^2}\left[\frac{M_{1t}^2}{M_1^2} - \frac{\rho_1}{\rho_1 - \rho_2}\left(\frac{\gamma_1 - \gamma_2}{\gamma_1(\gamma_1 - 1)}\right)\right]\right\} \qquad (22)$$

A NOTE ON AN OMNI-DIRECTIONAL ARRAY OF STACKED V-ANTENNAS[1]

By T. P. Pepper

Abstract

An omni-directional antenna array, which might find use in the frequency-modulation broadcast field, is described.

An omni-directional antenna-array, which might find use in the frequency-modulation broadcast field, was developed during the war by the National Research Council of Canada, as an omni-directional radar beacon for the Royal Canadian Air Force (see photograph). Five simple V-antennas, each consisting of two mutually perpendicular end-fed half-wave dipoles, were stacked at half-wave spacing to give the required gain. Each V-element was fed from a double coaxial transmission line, which in turn was center-fed from balanced BA4 (RG22/U) cable.

The two dipoles of each V were mounted, one on each side of the double coaxial feed, and set to make an angle of approximately 45° with the center line through the feed, giving a total of approximately 90° between dipoles. The position of the dipoles was interchanged for alternate V's, to give the required phasing.

A reasonably circular pattern, and a power gain quite comparable with other five-bay stacks proposed for frequency-modulation broadcast purposes, was obtained. At the same time, matching problems proved to be very much simpler than for stacks of some of the so-called loop antennas.

The entire array was weatherproofed, and found simple enough for mounting on a wooden frame.

PLATE I
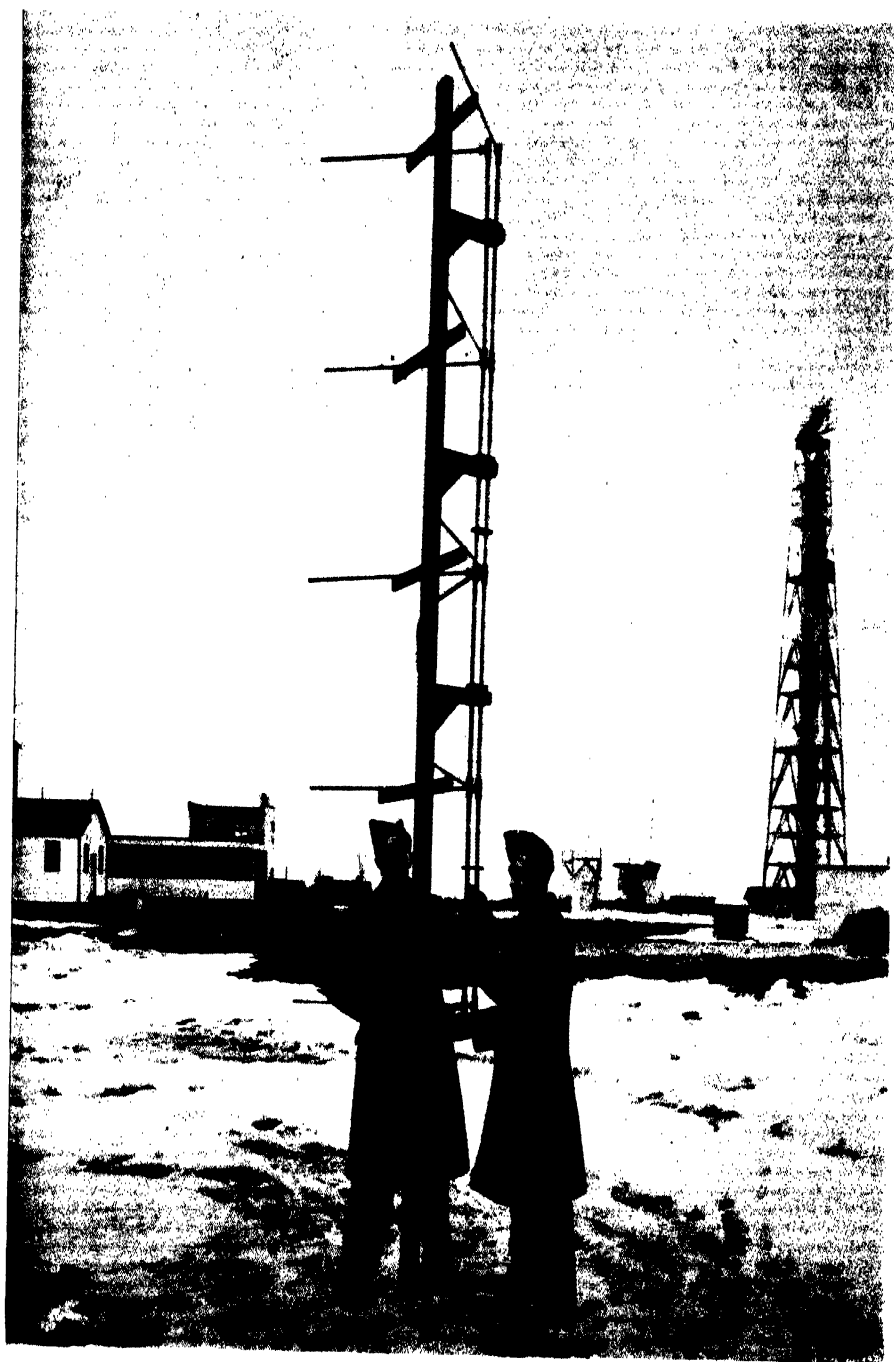
The experimental model of a stacked V-antenna.

APPROXIMATE MEASUREMENT OF COLOR TEMPERATURE WITH A BARRIER-LAYER PHOTOCELL[1]

By W. E. KNOWLES MIDDLETON AND A. R. RAMSEY[2]

Abstract

An objective method of measuring color temperature is described, using apparatus found in nearly every photometric laboratory.

Introduction

The measurement of color temperature by direct visual comparison with a standard is one of the more exacting photometric measurements. It is not surprising, therefore, that photoelectric methods have been devised (6, 10) that are capable of very high accuracy if carefully applied. Their general principle involves simultaneous or successive measurements of the radiation from the test source by two receivers of different spectral sensitivity, as for example two photocells with different cathode surfaces, or one photocell with two interchangeable filters.

No novelty in principle is claimed for the present note, the purpose of which is to direct attention to the fact that objective measurements of color temperature can be made with equipment that is in regular use in many photometric laboratories, and to report an investigation into the errors of such measurements.

Equipment

On the North American continent, it is becoming almost standard practice to perform routine photometry by means of a barrier-layer cell and a so-called 'zero-resistance' circuit (1, 7). The cell is, of course, fitted with a filter that corrects its spectral sensitivity to that of the normal eye (2) with a sufficient degree of accuracy for the purpose in hand. The zero-resistance circuit gives adequate linearity for most purposes, and, if a cell with a reasonably low drift can be selected, a precision nearly equal to that of visual photometry can be attained, with an immense saving of time. The circuit used in the present work is essentially the same as that of Projector, Laufer, and Douglas (7), with the addition of a galvanometer reversing key along the lines described by Wenner (9), which effectively doubles the sensitivity of the galvanometer. This key (K_4 in Fig. 1), incidentally, consists of two S.P.D.T. 'Micro-switches' mounted side by side and operated by a common button, giving a very quick make and break. No thermoelectric effects due to this key have been detected with the portable galvanometer used.

The slide wire is of the Kohlrausch type, as generally used in such circuits, and can be read to the nearest 1/10,000 of its length with great ease. The entire equipment, in fact, is equivalent to that found in many industrial photometric laboratories, with the addition of a suitably diaphragmed holder for the barrier-layer cell, and two filters. It is best to use the entire sensitive surface of the cell, using the diaphragms merely to screen off stray light.
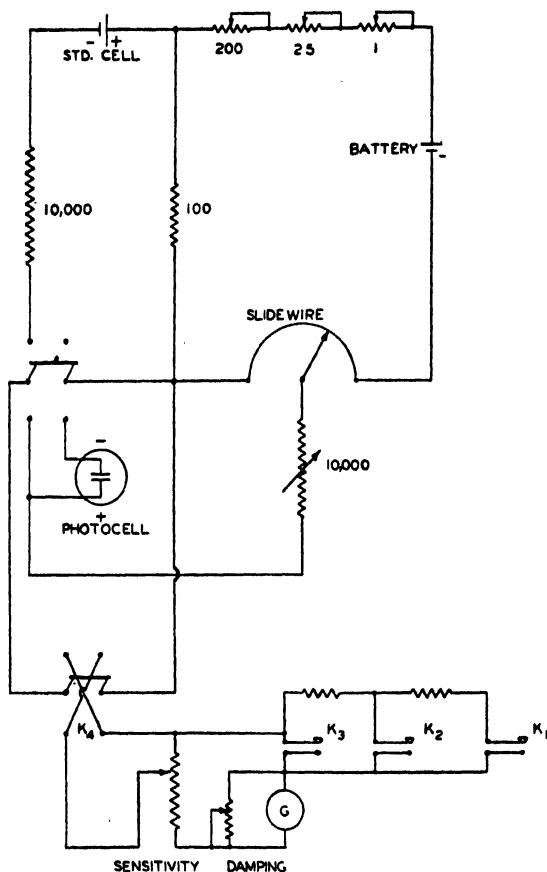
FIG. 1. 'Zero-resistance' circuit used.

Cell and Filters

The cell used in our experiments is The General Electric Co. light-sensitive cell, supplied with a green filter by the makers. The combination has a spectral sensitivity very similar to the normal I.C.I. luminosity curve, though small variations occur from cell to cell. In Fig. 2 are plotted the relative spectral sensitivity of the cell used (full line) and the normal luminosity curve (dashed line). For the present purpose an exact correspondence is not at all necessary.

The spectral transmittance of the pair of red and blue filters used was measured on an automatic recording spectrophotometer and is shown in Fig. 3. These filters were chosen from among a large number of available types, on the following general principles.
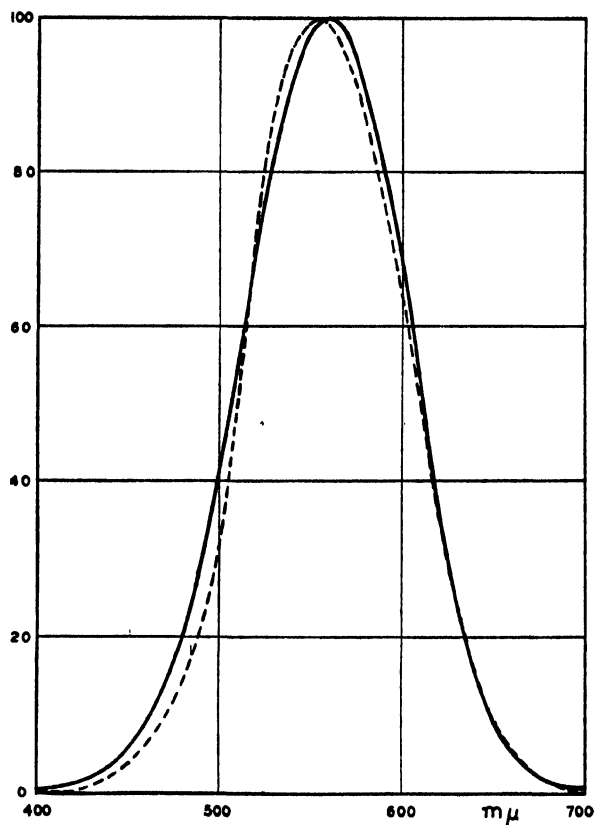
FIG. 2. *Spectral sensitivity of barrier-layer cell with green filter (full line) compared with the spectral luminosity function for the 'normal' I.C.I. observer (dashed line).*
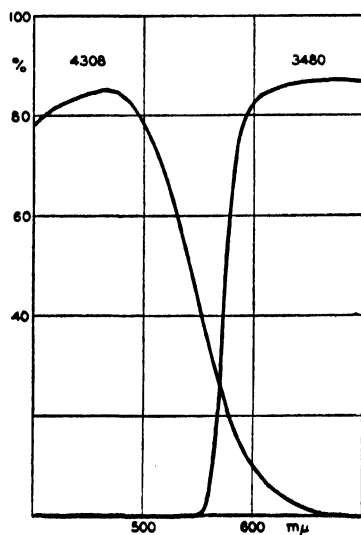
FIG. 3. *Spectral transmittance of red filter (Corning 3480, 5.36 mm. thick) and of blue filter (Corning 4308, 5.11 mm. thick).*

(1) They should divide the entire visible spectrum fairly evenly between them.

(2) Their transmittance should have as regular a slope as possible.
No doubt many other pairs of filters would have been equally suitable.

Calibration

Because of the difficulty of measuring accurately the spectral sensitivity of the photocell, it is better to calibrate the apparatus by the use of a color temperature substandard, a lamp for which the relation between voltage and color temperature is known. Such lamps are usually calibrated in the range 2000° to 2850° K. Light approximately equivalent to sources of higher temperature can be obtained by the use of blue filters (3, 4) with the color temperature substandard.

With the lamp and the photocell in positions that will give a convenient illumination, say about 20 l. ft.$^{-2}$, readings are taken with the filters in position in the order red, blue, red, blue, red. The mean of the two readings with the blue filter I_b, is divided by the mean of the three readings with the red, I_r, and the resulting ratio, R, is adopted as an index of the color temperature of the source. This procedure is repeated with the source set to give light of various color temperatures within the desired range. The result of such a calibration is shown in Fig. 4. The points obtained by means of a blue glass
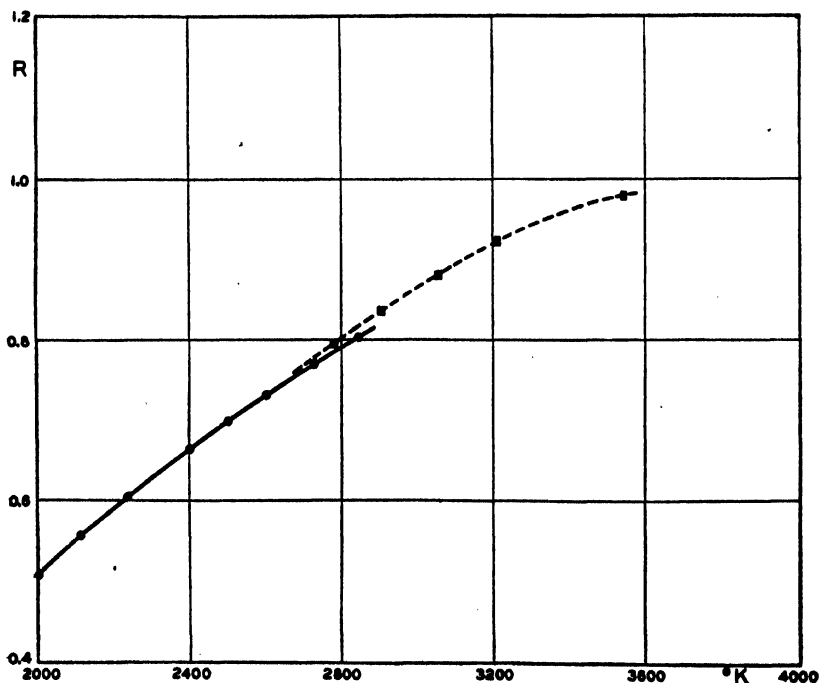
FIG. 4. *Relation between color temperature T and ratio R. The points indicated by squares refer to 'color temperatures' obtained by means of a blue photometric filter.*

filter (NBS 15430) lie on a curve nearly parallel to the curve obtained for the unfiltered tungsten lamp. If it is decided to adopt the scale of color temperatures furnished by the combination of lamp and filter, there is no reason why the method should not be used if it is calibrated with the particular combination employed.*

Users of the 'zero-resistance' circuit will recognize that there is a limited range of illuminations within which it is both linear and sensitive. In taking the measurements at low values of color temperature, when little illumination is available from the substandard, a certain amount of sensitivity will have to be sacrificed because of the comparatively low slide wire readings; but above about 2250° K., where readings of several hundred divisions can easily be obtained, the precision of a single measurement of R, made as above, is at least ± 0.002, corresponding to about $\pm 8°$ K. This assumes that the lamp voltage is regulated sufficiently well, as is usual in photometric laboratories. It is, however, advisable to operate within a 3 to 1 range of illumination if such precision is desired; if a tolerance of 20° K. is permissible, a range of 10 to 1 in illumination can be used. But since the apparatus also serves to measure the illumination, and the lamp is usually mounted on a movable carriage, it is just as easy to adopt a standard value of illumination and work near it.

The measurement is not very sensitive to changes in the temperature of the filters. Experiments in a cold chamber at about 0° C. showed an overestimation of about 20° K. at 2850° K., when a calibration made at 25° C. was used. This overestimation decreased to almost zero at 2500° K. It may be concluded that the effect is less than one degree in color temperature per degree Centigrade, and thus unimportant in the ordinary laboratory, unless the filters are exposed to strong illumination and warmed up in this way.

For routine checks it is adequate to take only three readings, red, blue, and red. With only ordinary care a measurement of this sort should be reliable to within $\pm 15°$ K. if the illumination does not differ by a factor of more than 3 from that used in the calibration.

Limitations of the Method

The most obvious limitation of the method is that it demands that the illumination be kept constant while three readings (or possibly only two) are made. This limits the method to the photometric laboratory, for which it was obviously designed. A recent German patent (8) describes a method of overcoming this difficulty by the use of two barrier-layer photocells, but some experiments by the authors lead them to doubt whether this method would be sufficiently accurate for laboratory purposes.

* *The 'color temperatures' corresponding to these points were obtained by the method of Judd (5).*

The second and not so obvious limitation of the method is that it will assign a color temperature to any illumination that is presented to it, even if this is of a color to which it is highly inappropriate to apply the idea of color temperature. This limitation applies to all objective methods. The user will have to decide for himself, for example, whether the color temperature of fluorescent lamps should be measured in this way. The fundamental method, direct visual comparison in a photometric field, makes it very evident whether a given illumination lies on the Planckian locus.

The authors have not found the 'drift' of the barrier-layer cell at all serious when working with an illumination of about 20 to 30 l. ft.$^{-2}$ Any drift that occurs after the first minute or so has a negligible effect on the color temperature measurement. The situation is different where an illumination of 200 l. ft.$^{-2}$ is .n question; here the effect of drift is at least as great as all the other errors together, and such high values of illumination should not be employed in these measurements.

References

1. BARBROW, L. E.   J. Research Natl. Bur. Standards, 25 : 703.   1940.
2. COMM. INT. DE L'ECLAIRAGE.   Proc. of 8th session, pp. 19-29.   Cambridge.   1931. *Quoted by* Judd, D. B.   J. Optical Soc. Am. 23 : 359.   1933.
3. DAVIS, R. and GIBSON, K. S.   U.S. Dept. of Commerce, Bur. Standards, Misc. Pub. No. 114.   U.S. Govt. Printing Office, Washington.   1931.
4. ESTEY, R. S.   J. Optical Soc. Am. 26 : 293.   1936.
5. JUDD, D. B.   J. Optical Soc. Am. 26 : 421.   1936.
6. PRESTON, J. S.   Proc. Phys. Soc. London, 47 : 1012.   1935.
7. PROJECTOR, T. H., LAUFER, M. K., and DOUGLAS, C. A.   Rev. Sci. Instruments, 15 : 107.   1944.
8. THEISSING, H.   German Patent No. 744,719.   Sept. 12, 1940.
9. WENNER, F.   J. Research Natl. Bur. Standards, 22 : 425.   1939.
10. WINCH, G. T.   J. Sci. Instruments, 6 : 374.   1929.

PERMEABILITY STUDIES

III. SURFACE AREA MEASUREMENTS OF CARBON BLACKS[1]

By J. C. ARNELL AND G. O. HENNEBERRY

Abstract

The modified Kozeny equation has been found to be satisfactory for the measurement of the specific surfaces of carbon blacks having average particle diameters ranging from 0.01 to 0.1 μ to within $\pm 10\%$. Comparative data were obtained from electron microscope counting and from low temperature nitrogen adsorption isotherms. The three methods examined gave results that were in satisfactory agreement, except when the carbon black was porous, and then the adsorption value was extremely large.

Introduction

In two preceding papers (2, 3), a method has been described for the measurement of the specific surface of fine powders by permeability methods. This method depends on the use of a modified Kozeny equation which may be written as:

$$G = \frac{A h \epsilon \alpha \rho_1}{L S_v (1 - \epsilon)} \left[\frac{\epsilon \rho_{Hg} g \bar{P}}{k_0 \eta S_v (1 - \epsilon)} + \delta \times \frac{8}{3} \sqrt{\frac{2 R_0 T}{\pi M}} \right] , \qquad (1)$$

where G = rate of gas flow in cubic centimeters per second,

A = cross-sectional area of the bed in square centimeters,

h = pressure head in centimeters of mercury,

ϵ = volume of pore space per unit volume (porosity),

α = fraction effective void area,

ρ_1 = ρ/p = density of the gas at unit pressure,

L = length of the bed in centimeters,

S_v = specific surface of the powder in square centimeters per cubic centimeter,

ρ_{Hg} = density of mercury in grams per cubic centimeter,

g = acceleration due to gravity,

$\bar{P}$ = $(p_1 + p_2)/2$ = mean pressure in centimeters of mercury,

k_0 = shape factor, approximately equal to $5\alpha/\epsilon$,

η = viscosity of the gas in poises,

δ = variable factor, having a value of approximately 0.9,

R_0 = gas constant,

T = absolute temperature, and

M = molecular weight of the gas.

This equation has been tested against the data obtained from the flow of air through beds of finely ground quartz and inorganic pigment powders and found to give satisfactory results.

In this paper, the method has been extended to a series of carbon black samples, and the resulting specific surfaces have been compared with those obtained from electron microscopy and low temperature nitrogen adsorption.

Apparatus and Technique

The first permeability measurements on the carbon blacks were made with the apparatus that has been described previously (3), but the low rate of flow of air through the packed beds rendered this apparatus impractical and a new apparatus was designed.

A schematic drawing of the new apparatus is shown in Fig. 1. The Lucite tube containing the packed bed of powder, C, was connected into the apparatus by means of rubber pressure tubing, and a pressure differential across the bed
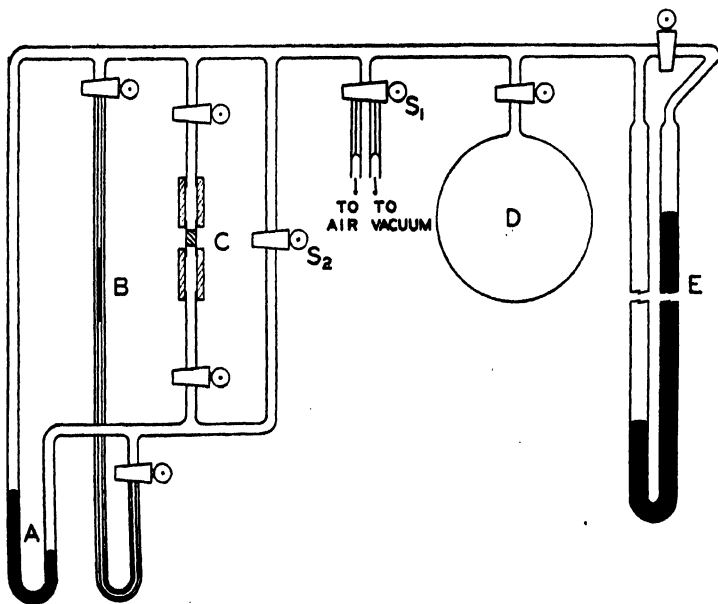
FIG. 1. *Diagram of permeability apparatus.*

was maintained by means of a falling bead of mercury in the capillary tube, B, of uniform bore. The short manometer, A, provided a means of measuring the pressure head across the bed, while the large manometer, E, was used to measure the absolute pressure in the apparatus. The five liter bulb, D, was introduced as a surge volume to compensate for the fact that a larger volume of gas left the bed than entered it, and, without a large surge volume, the flow of gas through the bed resulted in an absolute pressure increase in the apparatus.

The technique of measuring permeabilities was as follows. With the packed tube in position, stopcock S_2 was closed and stopcock S_1 was opened to vacuum. As the system was evacuated, a pressure differential was built up across the bed and finally the mercury bead was drawn up the capillary tube. When the

mercury bead was near the top of the capillary tube, stopcock S_1 was closed and the measurement of the rate of flow could be made. The mercury bead was allowed to fall about 7 cm. to establish equilibrium conditions, and then the time of fall of the bead for each centimeter was recorded over a distance of at least 20 cm. In general, the elapsed time taken by the mercury bead to fall 20 cm. was used in the flow calculations. On completion of a run, stop-cock S_2 was opened and the pressures in the apparatus equalized. If the same operation were repeated, a second run could be made at a lower mean pressure.

From a knowledge of the cross-sectional area of the capillary tube, B, and the pressures in the system, the mass flow at the fixed pressure head could be calculated by means of the equation:

$$G = \frac{A_0 \rho_1 P_1 d}{t} , \qquad (2)$$

where A_0 = cross-sectional area of the capillary tube in centimeters,
$\quad P_1$ = pressure on high pressure side of bed in centimeters of mercury,
$\quad d$ = length of fall of mercury bead in centimeters, and
$\quad t$ = time necessary for bead to fall d cm., in seconds.

It was found necessary to follow the fall of the mercury bead over a considerable distance, because the movement of the bead was somewhat erratic. This was thought to be due to surface forces between the mercury and the glass, even though the glass had been thoroughly cleaned in hot acid and the mercury acid-washed and distilled before the apparatus was assembled. This nonuniformity of fall of the mercury bead appeared to be generally nullified over a distance of 10 cm., and the time of fall over two consecutive 10 cm. lengths usually agreed to within several seconds.

In the apparatus used for these experiments, the capillary tube had a cross-sectional area of 0.0547 sq. cm. and the mercury bead was 5.0 cm. long.

Theoretical

With all powders previously studied, the relation between the mass flow and the mean pressure could be expressed by the equation:

$$G = \frac{Ah}{L} (B\bar{P} + C) , \qquad (3)$$

where B = slope of the line resulting from a G vs. $\bar{P}$ plot, and
$\quad C$ = corresponding intercept.

In the paper immediately preceding this one, it was pointed out that the specific surface of a powder could be calculated from the intercept value by using only the second half of Equation (1), or by writing:—

$$S_v = \frac{8}{3} \sqrt{\frac{2R_0 T}{\pi M}} \frac{\delta \epsilon \alpha \rho_1}{C(1 - \epsilon)} , \qquad (4)$$

where δ is taken as 0.9.

The majority of the carbon blacks studied had average particle sizes that were about an order of magnitude smaller than those of the finest powders

previously studied, and, when the mass flow through a carbon black was
measured at different mean pressures, it was generally found that the mass
flow remained constant to within the experimental error.   At first it was
thought that this was an indication that pure Knudsen flow was occurring
through the beds, but subsequently several beds of larger blacks with high
porosities were found to give flows of the type expressed by Equation (3) with
very small values for the slope.   Calculations of the Adzumi pore radii (1)
were made for those beds that had a finite slope, when plotted according to
Equation (3), and the values of the radii fell in the region of 2–5 $\times$ 10^{-6} cm.

The Knudsen semiempirical equation for the flow of gas through a capillary
tube (8, p. 296) was examined for the flow through a capillary having a radius
of 5 $\times$ 10^{-6} cm. and a length of 1 cm.   This equation takes the form:

$$T = \frac{G}{h\rho_1} = \frac{\pi R^4 \bar{P}}{8\eta L} + \frac{1 + c_1 \bar{P}}{1 + c_2 \bar{P}} \frac{4}{3} \sqrt{\frac{2\pi R_0 T}{M}} \frac{R^3}{L} , \qquad (5)$$

where $c_1 = 2.00 \frac{\rho_1}{\eta} R$, $c_2 = 2.47 \frac{\rho_1}{\eta} R$, and R = radius of the capillary in
centimeters.

The resultant curve is shown in Fig. 2, and it is interesting to note that the
minimum occurs at a pressure of just over 30 cm. of mercury and that in the
pressure range of the experiments described here (10 to 65 cm. of mercury),
the total variation is only 2%.   It therefore seemed reasonable to assume
that the region of the flow of air through the beds of carbon black was near
the minimum in the Knudsen curve and to take an average value through
this region for calculating the values of the specific surface.   This average
value was found to be equivalent to giving δ a value of 0.96 in Equation (4).

All the values of the specific surface to be given in the experimental section of
this paper have been calculated by means of Equation (4) and where the G vs. $\bar{P}$
plot of the data for any bed was found to have a slope, δ was taken as 0.9 and
when the mass flow, G, appeared to be constant, δ was given the value of 0.96.
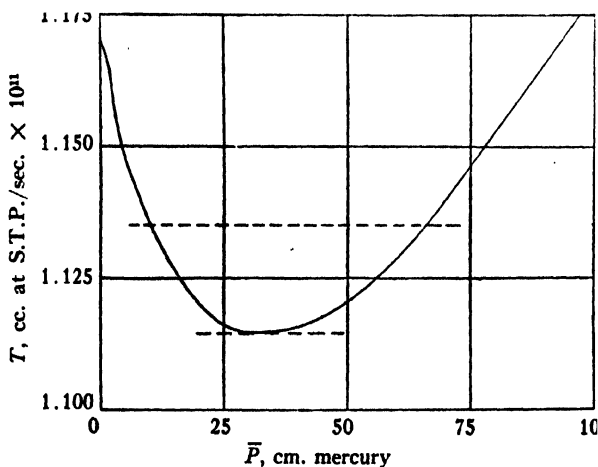
FIG. 2.   *Plot of Knudsen equation for a fine capillary.*

Experimental Results

A series of 12 commercial carbon blacks were chosen as representative of the different methods of manufacture. The specific surface was determined using at least three beds of each black, and the mass flow was generally measured at seven mean pressures ranging from 15 cm. of mercury to 70 cm. of mercury.

The runs were all made at room temperature and the porosities of the beds were calculated using densities calculated by X-ray diffraction.

In order to check the method, the surface areas of the carbon blacks were also calculated from particle counts made from electron microscope photographs by means of the equation:

$$S_v = K \frac{\Sigma nd^2}{\Sigma nd^3}, \tag{6}$$

where K is a shape factor, which was taken as 6.1, since all the blacks appeared spherical (for perfect spheres, $K = 6.0$). Low temperature nitrogen adsorption isotherms were also determined and the surface areas were then calculated by means of the Brunauer, Emmett, and Teller equation (4) and also by the Harkins and Jura equation (6).

The experimental results are all listed in Table I, together with pertinent data pertaining to each black.

TABLE I

SURFACE AREAS OF CARBON BLACKS BY PERMEABILITY, ELECTRON MICROSCOPE, AND ADSORPTION METHODS

Black	Type*	Porosity	Surface area, m.²/cc.				
			Permeability	Electron microscope	N₂ adsorption		Butane** adsorption
					BET	H & J	
Thermax	MT	—	—	13.6	14.5	15.8	19
Kosmos 20	SRF	0.554 0.568 0.579	43⎫ 43⎬ 42 41⎭	47	41	52	29
Kosmos 40	HMF	0.584 0.634 0.638	67⎫ 59⎬ 65 69⎭	72	78	82	45
Shawinigan 100% Comp.	CF	0.729 0.762 0.791	67⎫ 82⎬ 74 72⎭	78	94	—	85
Statex B	FT	0.601 0.610 0.619 0.636 0.645	97⎫ 99⎪ 103⎬ 99 98⎪ 96⎭	72	99	87	80
Statex A	CF	0.603 0.639 0.656	98⎫ 100⎬ 100 103⎭	86	136	152	78

TABLE I—*Concluded*

Surface Areas of Carbon Blacks by Permeability, Electron Microscope, and Adsorption
Methods—*Concluded*

Black	Type*	Porosity	Surface area, m.²/cc.					
			Permeability	Electron microscope	N₂ adsorption		Butane** adsorption
					BET	H & J	
Kosmobile 77	EPC	0.638 0.670 0.672 0.673 0.674 0.675 0.715 0.721	155 150 155 131 131 155 93 70 } 146	161	193	202	80
Dixie densed HM	MPC	0.696 0.704 0.716	164 144 141 } 150	165	228	269	94
Kosmobile S	HPC	0.653 0.666 0.673 0.692 0.707 0.718	178 197 171 126 71 45 } 182	162	277	304	105
Spheron 9	EPC	0.676 0.696 0.696	189 180 182 } 184	144	223	225	80
Voltex	CC	0.707 0.717 0.765	344 328 306 } 326	220	—	1320	281
Neo Spectra Mk. II	Ink Black	0.823 0.825 0.828	435 418 430 } 428	259	1410	1960	—

*This refers to the type of process by which each black was made, and further details can be
found in the manufacturer's literature.

**Data taken from Table 18, page 90, Developments and Status of Carbon Black by Isaac
Drogie. United Carbon Company, Inc., Maryland, U.S.A., 1945.

Discussion

A comparison between these independent methods of measuring the specific
surfaces of a number of carbon blacks is provided by Table I. It is of interest
to examine these methods critically and to consider the relative merits of each.

Electron Microscope

From a cursory consideration, the electron microscope appears to provide
the most direct method of evaluating the specific surface of a fine powder.
There are, however, a number of indeterminate factors which reduce the
accuracy of the method considerably and which also apply, in general, to
similar measurements with larger particles using the optical microscope.

The method, which is based on Equation (6), is a statistical one and consequently requires that the diameters of a large number of particles be measured. This is particularly important if there is a large spread between the diameters of the smallest and the largest particles. In general, a group of between 5 and 10 electron microscope photographs will have enough sufficiently dispersed particles to permit the measurement of several hundred diameters. These are not always sufficient data to ensure a good statistical average, as the following example indicates. In a preceding paper (2), a sample of finely ground quartz powder was studied and the diameters of 335 quartz particles were measured on electron microscope photographs. Two of these particles were found to be at least twice as large as any other particle in the group and about 30 times as large as the particles in the most probable size range. The specific surface of this sample of quartz was found to be 6×10^4 sq. cm. per cc. and, if the two large particles were discarded, the value of the specific surface was approximately doubled. While this is an extreme case, it seems to illustrate the care necessary in using microscopic methods for powders having a wide range of particle sizes.

The shape factor in Equation (6) is another indeterminate source of error, as it involves the surface-volume ratio of the particles. As long as the particles are nearly spherical, as was the case with the carbon blacks being considered here, a value can be assigned for the shape factor, which has no greater an error than 2 to 3%. As the shape of the particles diverges from that of a sphere, the error in the assigned value of the shape factor increases until it may reach 20 to 30% in the case of needlelike particles.

With many powders it is very difficult to get a good dispersion of the particles, and agglomerates are always present in the field of vision. When the powder being examined has a wide range of particle sizes, it is often very difficult to decide between an individual large particle and an agglomeration of small particles. In the case of the carbon blacks, it was felt that some of the large particles may have been discarded for this reason and the values of the specific surface, in consequence, may be slightly high.

Another source of error, that applies in the main to particles of the size of the finest carbon blacks, is the difficulty of enlarging the particles to a size that permits fairly accurate counting. The carbon blacks were all enlarged photographically at around 17,000 diameters and the negatives were then examined under a visual enlarger, which raised the magnification to about $125,000\times$. Even at this power, a fine black was composed of particles with an average apparent diameter of about 2 mm. For example, the Neo Spectra Mk. II carbon black had the following particle distribution:

Less than 0.01	0.01–0.02	0.02–0.03	0.03–0.04μ	Total
3	65	64	5	137

These particles were too small to be subdivided into any more classes and it is apparent that slight errors in the measuring scale, which was based on the final viewing magnification, could markedly change the distribution, and, in consequence, the specific surface.

Adsorption

The adsorption method measures any internal surface that is open to the adsorbate, in addition to the external surface of the particles. This results in a value of the surface area of a porous material higher than the values of the specific surface determined by methods based on the determination of external surface alone, as is the case with the microscopic and the permeability methods. There is no way of telling a priori when a powder consists of porous particles and consequently, if only the external surface is desired, the adsorption method is not reliable. The results in Table I suggest that the majority of the carbon blacks studied are either slightly porous or have roughened surfaces, and the last two blacks in the table are quite obviously very porous, with large internal surfaces.

There are two theories that may be applied to a low temperature nitrogen isotherm in order to calculate the surface area of the adsorbent. The first of these is the Brunauer–Emmett–Teller (BET) method (4), which is valid for a sigmoid isotherm and provides a means of estimating the volume adsorbed in a monolayer and of calculating the surface area, if an area is assigned to an adsorbed molecule. The method probably has an error of at least 10%, and, as Gregg (5) has pointed out in an excellent discussion of the method, the error may run as high as 50% if the isotherm is not a sigmoid (BET Type II) isotherm. The surface area may also be calculated from the semiempirical isotherm equation of Harkins and Jura (6), which appears to fit a greater number of isotherm shapes than the BET equation. With the carbon blacks there was one case (Shawinigan) where the Harkins and Jura plot was too curved for a calculation to be made and the isotherms of the Voltex and the Neo Spectra resembled the Langmuir type, and consequently the BET equation failed to give a straight line plot, but, in general, the specific surfaces of the carbon blacks calculated using the two equations were in fair agreement. Zettlemoyer and Walker (11) also report satisfactory agreement for the surface areas of a number of samples of active magnesia calculated using the two equations. When the two equations lead to surface area values that show reasonable agreement, the average value of the surface probably is correct within 10%.

The butane adsorption values of the surface area listed in Table I are included only as a matter of interest. These values are average figures that have been quoted in the manufacturer's literature and are only intended to give the order of magnitude of the surface. When it is considered that

surface areas calculated from butane adsorption isotherms are generally considerably smaller than those calculated from nitrogen adsorption isotherms, the carbon black samples used for this study appear, in general, to have been fairly representative.

Permeability

A modification of the Kozeny equation for the calculation of the surface area of a powder from gas-permeability measurements has been proposed by Rigden (9, 10) and discussed further by Lea and Nurse (7). This modification is similar to that proposed by one of the authors (2, 3) except for one significant point. Rigden has used the assumption that the fraction void area is equal to the fraction void volume ϵ. This is theoretically true. However, in the case of packed powders, where the dimensions of the individual channels through the bed are varying continually, it has been considered unlikely that the effective void area would approach the theoretical one and, in consequence, a term defined as the fraction effective cross-sectional area, α, has been used instead of the theoretical fraction void area, ϵ, in the derivation of Equation (1). The use of α has been discussed at some length in the preceding papers of this series and an empirical relation between α and ϵ has been used for all specific surface calculations to date. This relation is:

$$\log \alpha = 1.41\epsilon - 1.40. \tag{7}$$

In general, Equation (1) and the Rigden equation should give values of the specific surface that lie within the experimental error of the method.

There are several indeterminate factors that introduce errors into the permeability method. One of these is the difficulty of ensuring that a bed is homogeneous and uniformly packed. Compaction of the bed in increments appears to be the recommended method. However, Lea and Nurse (7) have shown that beds compacted in one stroke give specific surfaces that are not more than 3% lower than an increment-packed bed. This suggests that a well packed bed is reasonably homogeneous.

Lea and Nurse also point out that there is a general decrease in the specific surface values with increasing porosity using the Rigden equation. The use of Equation (1), involving α, appears to eliminate this fall-off over the intermediate porosity range, although it is still present at the higher porosities. This fall-off at the high porosities may be partially due to the fact that high porosity beds are less likely to be homogeneous and the particles tend to bridge, forming an occasional large channel. Such a channel would act as a major conduit and prevent many of the smaller channels from playing their part, with a resultant apparent decrease in calculated specific surface. Rigden (10) also reports a fall-off in the value of the specific surface, calculated for the same bed, with decreasing mean pressure, which is an effect that has never been observed by the authors.

With soft materials there is always the possibility of deforming the particles and creating appreciable areas of contact between particles. As this deformation would be a function of compacting pressure and would appear as a decrease in specific surface, it may be assumed to be absent as long as the calculated specific surface does not increase with increasing porosity.

Conclusions

It would appear that each of the methods examined is probably subject to an error of about 10%, when applied to such small particles. Other methods, such as sedimentation, could not be applied owing to the fineness of the carbon blacks. The permeability method is considered to be the most satisfactory of the methods examined, as it provides a relatively quick estimate of the external surface of very fine powders, and in the final analysis has about the same accuracy as the other methods, which are more time-consuming and require fairly elaborate apparatus.

Acknowledgment

References

1. ADZUMI, H. Bull. Chem. Soc. Japan, 12 : 304. 1937.
2. ARNELL, J. C. Can. J. Research, A, 24 : 103. 1946.
3. ARNELL, J. C. Can. J. Research, A, 25 : 191. 1947.
4. BRUNAUER, S., EMMETT, P. H., and TELLER, E. J. Am. Chem. Soc. 60 : 309. 1938.
5. GREGG, S. J. Trans. Inst. Chem. Engrs. (London), and J. Soc. Chem. Ind. (London), Road and Bldg. Materials Group. Symposium on particle size measurement. Pp. 27-33. Advance Copy, Feb. 4, 1947.
6. HARKINS, W. D. and JURA, G. J. Am. Chem. Soc. 66 : 1366. 1944.
7. LEA, F. M. and NURSE, R. W. Trans. Inst. Chem. Engrs. (London), and Soc. Chem. Ind. (London), Road and Bldg. Materials Groups. Symposium on particle size measurement. Pp. 34-43. Advance Copy Feb. 4, 1947.
8. LOEB, L. B. The kinetic theory of gases. 2nd ed. McGraw-Hill Book Co., Inc., New York & London. 1934.
9. RIGDEN, P. J. Nature, 157 : 268. 1946.
10. RIGDEN, P. J. J. Soc. Chem. Ind. 66 : 130. 1947.
11. ZETTLEMOYER, A. C. and Walker, W. C. Ind. Eng. Chem. 39 : 69. 1947.

THE EFFECT OF VARIATIONS IN THE GENERAL COMPOSITION OF SAMPLES IN SPECTROGRAPHIC ANALYSIS[1]

By G. O. Langstroth and D. Andrychuk[2]

Abstract

Variations that occur in intensity ratios belonging to pairs of elements on the addition of various extraneous substances to standard samples have been studied using a common type of condensed spark discharge. The extent of the variations depended on the test elements chosen, the nature of the added substance, the line pair investigated, and on whether or not the standard samples were buffered. The variations bore no apparent relation to the relative ionization potentials or atomic weights of the test elements, nor to any physical property of the added substances. In general, they were smaller for the line pairs having the most nearly equal excitation potentials. Usually, but not always, they were smaller for buffered than for unbuffered samples. Illumination of the electrodes with ultraviolet light, though resulting in steadier operation of the discharge, or alterations of the capacity in the sparking circuit did not reduce the variations materially. Operation of the discharge at constant current coupled with the use of a buffer however did reduce the variations considerably for the instances studied.

It has been commonly recognized that changes in the general composition of samples introduced into an arc or spark source may cause variations in the relative intensities with which spectral lines of two elements under test are radiated, even though the elements are always present in constant amounts. This effect has an important bearing on the accuracy of spectrographic analyses of samples varying considerably in composition. A study (4) of intensity ratio changes in the radiation from a condensed spark when various substances were added to samples containing magnesium, lead, and cadmium provided no obvious clue to the factors responsible for the variations. An extension of this study, involving a much greater range of data, provides the basis for the present article.

Apparatus and Procedure

The condensed spark discharge was produced by a circuit consisting of a 0.014 μf. condenser, a 30 μh. inductance, a thermocouple ammeter, and a spark gap in series. The condenser was connected across the secondary of a transformer (full rating, 20 kv.) whose primary voltage was controlled by an autotransformer. The electrodes, of the point and movable plane type (1), were copper. The plane electrode on which the sample was dried was 1.2 cm. by 1.0 cm. in area, and an electrode separation of 3.1 mm. was used throughout the work.

Spectra were photographed with a medium quartz spectrograph, using a slit width of 45 μ. An image of the discharge was formed on the collimating lens by a quartz condensing lens at the slit, so that light from all regions of the discharge contributed to the intensity of spectral lines. A standard

exposure of 60 sec. was used; this was made feasible by means of a moving wire screen weakener (2) before the source. For one sample containing a complex salt, determination of intensity ratios of lines of the two anion constituents was made with an antimony weakener (3) covering about half the spectrograph slit, in order that strong lines in the weakened section of the photograph might be comparable in density to fainter lines in the unweakened section.

The plane electrode was loaded by delivering 0.050 cc. of the desired liquid sample to it with a special pipette calibrated to 2%, and drying under low pressure. As a general practice, more electrodes were prepared than were needed, and those with uniform dried deposits were selected for sparking. During an exposure the plane electrode was moved so that the spark traversed a zigzag pattern over it, continually striking to a fresh surface of the deposit. For a large part of the work the spark was operated at the minimum breakdown voltage, the primary voltage being adjusted until the discharge was just on the point of stopping; for some special experiments to be mentioned later other conditions were employed.

The standard samples whose general composition was varied by the addition of extraneous substances consisted of eight solutions each containing three test elements (Table I). Constituents (e.g., silver in Sample 1) that would

TABLE I

COMPOSITION OF THE STANDARD SAMPLES

Sample	Salt		Salt		Salt	
	Kind	Conc., mgm./cc.	Kind	Conc., mgm./cc.	Kind	Conc., mgm./cc.
1	$AgNO_3$	0.194	$SnCl_2 . 6H_2O$	0.94	$MgCl_2 . 6H_2O$	1.05
2	$AgNO_3$	0.194	$SnCl_2 . 6H_2O$	0.94	$PbNO_3$	2.00
3	$MnCl_2 . 4H_2O$	1.50	$NiCl . 6H_2O$	1.00	$MgCl_2 . 6H_2O$	1.05
4	$NiCl . 6H_2O$	1.00	$SnCl_2 . 6H_2O$	0.94	$MgCl_2 . 6H_2O$	1.05
5	$BaCl_2 . 2H_2O$	8.00	$SnCl_2 . 6H_2O$	0.94	$CdCl_2 . 2H_2O$	4.00
6	$SrCl_2 . 6H_2O$	12.0	$AlCl_3 . 6H_2O$	1.00	$MgCl_2 . 6H_2O$	1.05
7	$SrCl_2 . 6H_2O$	10.0	$NiCl . 6H_2O$	3.00	$ZnCl_2$	1.60
8	$KAl(SO_4)_2 . 12H_2O$	4.00	$MgSO_4 . 7H_2O$	4.00	—	—

have been precipitated if made up with the other two were prepared in separate solutions and loaded on the electrodes separately. The test elements were chosen with consideration for ionization potential, atomic weight, and possession of suitable spectral lines (Tables III and IV). The concentrations required to yield comparable intensities for the selected lines were found by trial.

Each of the standard samples 1 to 7 was divided into five portions, of which one was left unaltered and each of the others had a different extraneous material added. The added materials, their concentrations, and the minimum ionization potentials associated with them, are given in Table II. Sample 8 was treated in a similar way but the added materials were different. Duplicate

TABLE II

EXTRANEOUS SUBSTANCES ADDED TO THE STANDARD SAMPLES

To Samples 1 to 7			To Sample 8		
Substance	Conc., mgm./cc.	Min. atomic ion. pot., ev.	Substance	Conc., mgm./cc.	Min. atomic ion. pot., ev.
KCl	6.00	4.32 (K)	CdSO₄	12.0	8.96 (Cd)
NH_4Cl	1.00	13.0 (Cl)	$(NH_4)_2SO_4$	30.0₀	10.3 (S)
LiCl	3.60	5.36 (Li)	Na_2SO_4	15.0	15.12 (Na)
H_3BO_3	10.3	8.26 (B)	$ZnSO_4$	15.0	9.36 (Zn)

TABLE III

IONIZATION POTENTIAL, V_i, AND ATOMIC WEIGHT, M, OF THE TEST ELEMENTS

Element	V_i, ev.	M	Element	V_i, ev.	M
K	4.32	39	Mn	7.41	55
Ba	5.19	137	Ag	7.54	108
Sr	5.67	87	Mg	7.61	24
Al	5.96	27	Ni	7.61	59
Sn	7.30	118	Cd	8.96	112
Pb	7.38	207	Zn	9.36	65

spectra for all portions of a standard sample were photographed on a single plate, along with a calibration spectrum taken with a rotating step-sector and a brass arc operated under constant conditions. A knowledge of the relative intensities of lines of the calibration spectrum was unnecessary, since information on the changes in intensity ratios only was required and each plate contained a complete set of data for a sample. The intensities of selected lines of the test elements (in arbitrary units, not necessarily the same for each) were determined in the usual way with a microphotometer (5). Typical line ratios studied are given in Table IV along with data on their relative excitation potentials.

The experiments outlined above were repeated in exactly the same way with the added feature that each of the standard samples was 'buffered' with 50 mgm. per cc. of potassium acetate. For the unbuffered samples the load of salts on the electrode ranged from 9.1×10^{-7} gm. per mm.² for Sample 1 with no addition, to 104×10^{-7} gm. per mm.² for Sample 7 with boric acid added; for the buffered samples it varied from 217×10^{-7} to 269×10^{-7} gm.

per mm.[2] for the same instances. In these experiments, the amount of extraneous material added was not varied. Only in one instance (addition of boric acid to unbuffered Sample 4) was any attempt made to investigate the effect of changing the amount of the added extraneous substance.

It was noted during the experiments outlined above that, when the spark was operated at minimum breakdown voltage, additions of extraneous material caused changes in the spark circuit current. A subsidiary experiment was

TABLE IV

Typical line pairs, the symbols used to refer to them, and the ratio of their excitation potentials, V/V'

Element Pair	Symbol A		Symbol B		Symbol C		Symbol D	
	λ/λ'	V/V'	λ/λ'	V/V'	λ/λ'	V/V'	λ/λ'	V/V'
Ag/Sn	3383/3262	0.75	3281/3262	0.78	3383/3175	0.85	3281/3175	0.87
Ag/Pb	3383/2614	0.64	3281/2614	0.66	3383/2833	0.84	3281/2833	0.86
Sn/Pb	3175/2614	0.75	3262/2614	0.85	3175/2833	0.99	3175/3640	0.99
Ag/Mg	3383/3838	0.62	3281/3838	0.64	3383/2852	0.84	3281/2852	0.87
Sn/Mg	3175/3838	0.73	3262/3838	0.82	3175/2852	1.00	3262/2852	1.12
Ni/Sn	3525/3262	0.73	3515/3262	0.75	3525/3175	0.82	3415/3175	0.85
Ni/Mg	3515/3838	0.61	3415/3838	0.62	3515/2852	0.83	3415/2852	0.84
Ni/Mn	3415/2610		3515/2610		3515/4033*	1.18	3415/4033*	1.19
Mn/Mg	4033*/2852	0.71	2632/2852		—	—	—	—
Sr/Al	4832/3092	1.09	4812/3082	1.10	4742/3961	1.40	4722/3944	1.40
Sr/Mg	4832/3838	0.74	4742/3838	0.74	4722/2852	1.01	4812/2852	1.02
Al/Mg	3961/3838	0.53	3082/3838	0.68	3944/2852	0.72	3092/2852	0.93
Ni/Sr	3525/4742	0.81	3515/4812	0.84	3415/4742	0.84	3493/4832	0.85
Ni/Zn	3525/3345	0.46	3515/3345	0.47	3415/3345	0.47	3493/3345	0.47
Sr/Zn	4832/3345	0.56	4742/3345	0.57	—	—	—	—
Cd/Sn	4679/2840	1.33	4679/3175	1.48	3404/3175	1.70	3404/2863	1.70
Ba/Sn	3501/2840	0.74	4903/3175	0.97	4903/2863	0.97	4823/3175	1.00
Cd/Ba	4679/4283	1.47	4679/4903	1.51	4679/3501	1.78	3403/3501	2.09
K/Al	4047/3082	0.76	4047/3961	0.98	—	—	—	—

* *A blend of 4033 and 4034 Å.*

therefore performed with Sample 4 plus lithium chloride, in which intensity ratios were determined at different currents as obtained by adjustment of the transformer primary voltage and read from the thermocouple ammeter. Variations with current were observed for some ratios but not for others. For example, with a buffered sample the nickel–magnesium ratios C and D (Table IV) decreased by about 16% on increasing the current from 1.3 to 1.8 amp., and by about 25% on increasing it to 2.2 amp.; on the other hand the ratios A and B remained effectively unchanged. With an unbuffered sample the former ratios decreased by about 14% on increasing the current from 1.5 to 2.0 amp. and the latter ratios remained essentially constant. Accordingly, the main experiments with Samples 1 and 2, with and without the buffer, were repeated, the spark being operated at constant current rather than minimum breakdown voltage.

It was further noted during the experiments that some of the added materials caused changes in the minimum breakdown voltage. Accordingly, the main experiments on unbuffered Sample 1 were repeated with the additional feature that the plane electrode immediately under the point was illuminated with intense ultraviolet light (the image of an iron arc, run at 4.0 amp. and 34 cm. distant, was formed on the electrode by an $f : 4$ quartz combination). This arrangement reduced the breakdown voltage and resulted in a steadier operation of the spark. A further complete set of data for Sample 1 was obtained under this condition with the capacity in the spark circuit increased from 0.014 to 0.026 μf.

Results

The results for the main experiments with the spark operated at minimum breakdown voltage are given in Fig. 1 for Samples 1 to 7. The symbols A,
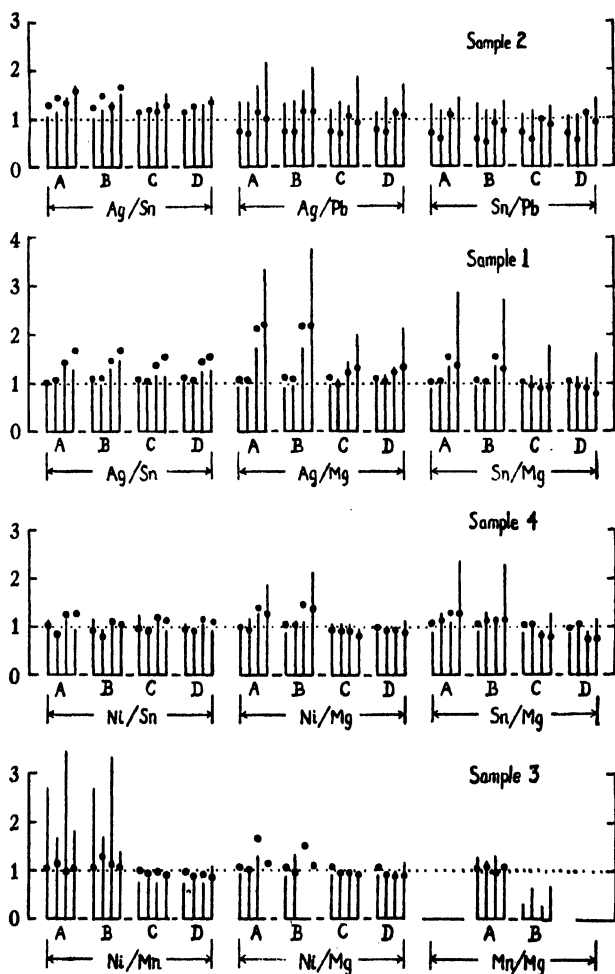
FIG. 1. *Variations in intensity ratios caused by addition of extraneous materials to the samples, as obtained with the spark operated at minimum breakdown voltage. The manner of presentation is described in the text.*

B, *C*, and *D* refer to the various line pairs (Table IV), which are given in order of increasing excitation potential ratio from left to right for each pair of elements. The vertical lines, whose length represents the intensity ratio obtained on addition of an extraneous substance divided by that obtained for the unaltered sample, are plotted in groups of four for each line pair; the members
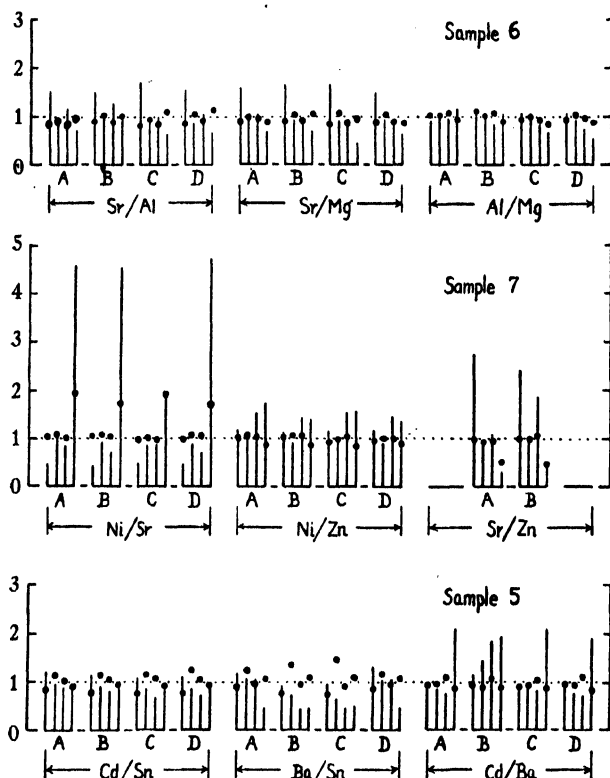
FIG. 1 (continued). *Variations in intensity ratios caused by addition of extraneous materials to the samples, as obtained with the spark operated at minimum breakdown voltage. The manner of presentation is described in the text.*

of each group from left to right refer respectively to additions of potassium chloride, ammonium chloride, lithium chloride, and boric acid. The solid dots denote the corresponding values obtained when the samples were buffered with potassium acetate (they are referred to the intensity ratio for the unaltered buffered sample). If the addition of an extraneous substance had no effect on intensity ratios the ends of the vertical lines and the dots would have ordinate values of unity. The plotted values are averages of nine sets of data for Sample 1, four sets for Samples 2, 3, and 4, and two sets for Samples 5, 6, and 7. Results for the same element pair obtained with different samples are given separately (e.g., silver–tin in Samples 1 and 2) since the composition of the load on the electrode differed.

The effectiveness of various amounts of added boric acid in changing the intensity ratios for unbuffered Sample 4 is indicated in Fig. 2.   In general, boric acid was found to be more effective than the other added substances in changing intensity ratios.

Boric acid concentration, mgm. per cc.
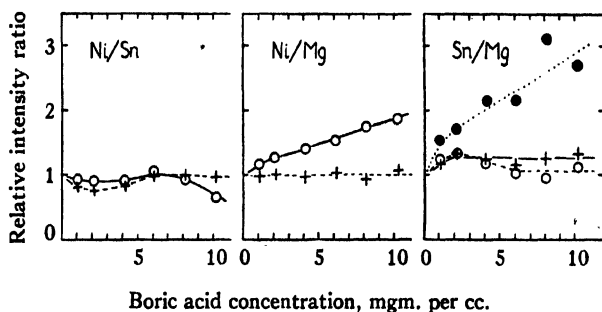
FIG. 2.   *Changes in intensity ratios caused by the addition of various amounts of boric acid to unbuffered Sample 4.   The symbols refer to the following line pairs: Ni/Sn,* ○ *3525/2863,* +*3415/3262; Ni/Mg,* ○ *3515/3838 (A),* + *3415/2852 (D); Sn/Mg,* ● *3175/3838 (A),* + *3175/2852 (C),* ○ *3262/2852 (D).*

Average results obtained for unbuffered Sample 8 with the spark operated at minimum breakdown voltage are shown in Fig. 3.   The method of presentation is similar to that of Fig. 1.   The numbers of each group of four solid lines
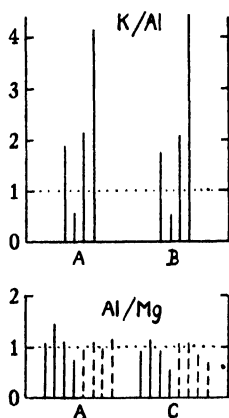
FIG. 3.   *Variations in intensity ratios on the addition of extraneous material to unbuffered Sample 8, which contained a complex salt (potassium aluminium sulphate.)*

refer from left to right to values of the intensity ratios (relative to that for the unaltered sample) obtained on addition of zinc sulphate, sodium sulphate, cadmium sulphate, and ammonium sulphate respectively.   The dashed lines refer to the values for additions of potassium chloride, ammonium chloride, lithium chloride, and boric acid to unbuffered Sample 6, and have been transferred from Fig. 1 for comparison.

A comparison of the average results obtained with various modifications of the sparking procedure is given in Fig. 4. The method of presentation is similar to that of Fig. 1, with results obtained by each modification of the procedure denoted by a special type of line.
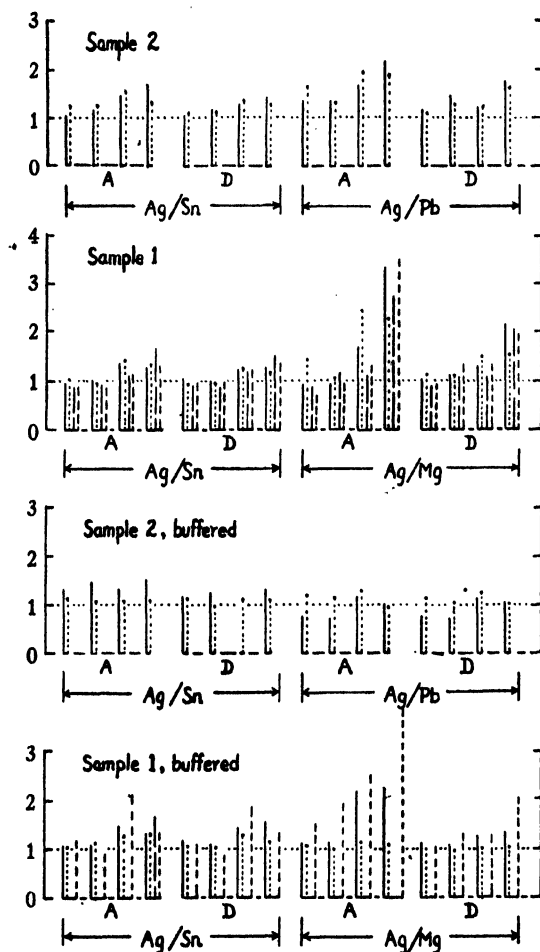
FIG. 4. *A comparison of the variations in intensity ratios caused by addition of extraneous materials, as obtained by various modifications of the procedure. The solid lines refer to values obtained with the spark operated at minimum breakdown voltage and have been transferred from Fig. 1 for comparison; the dotted lines denote values obtained with constant spark current, the broken lines those obtained with ultraviolet illumination on the electrode, and the dashed lines those obtained with increased capacity and ultraviolet illumination.*

Discussion

Examination of Fig. 1 shows that extremely large variations may be caused in intensity ratios by changes in the general composition of samples. It is evident that the magnitude of the variation depended on the line pair and element pair under consideration, on the nature of the substance added to the sample, and on whether or not the sample contained a buffer substance.

Furthermore, it appears probable from the results given in Fig. 2 that for some line pairs the size of the variation depends strongly on the amount of the extraneous substance added, but for others it does not. These findings are in agreement with earlier results (4).

The data of Fig. 3 indicate that large intensity ratio variations are caused by added substances even when the test elements of a pair are in combination in a complex salt and so at least must have the same distribution over the electrode surface and be equally subject to the impinging spark discharge. The aluminium/magnesium data of Fig. 3 show that additions of zinc, sodium, cadmium, or ammonium sulphates produced variations comparable to those caused by additions of potassium, ammonium, or lithium chlorides or boric acid.

The data of Fig. 4 indicate that illumination of the electrode with ultra-violet light, although producing a steadier discharge, did little to reduce silver/tin or silver/magnesium intensity ratio variations caused by the addition of extraneous material; this was true also when the capacity of the spark circuit was approximately doubled.

Operation of the spark at constant current rather than minimum breakdown voltage appears to offer some advantage, since with buffered samples it led to considerably reduced intensity ratio variations for silver/tin, silver/lead, and silver/magnesium (Fig. 4). With unbuffered samples, however, the variations were similar to those obtained under minimum breakdown voltage operation.

The remainder of the discussion deals with an analysis of the data of the main experiments on Samples 1 to 7 with minimum breakdown voltage operation. The element pairs nickel/tin, silver/lead, tin/lead, silver/tin, nickel/manganese, strontium/aluminium, nickel/magnesium, silver/magnesium and tin/magnesium form a series having nearly constant ionization potential ratios (ranging from 0.96 to 1.04), but atomic weight ratios graded from 0.50 to 4.90. The average variations in intensity ratio, considering line pairs A and D and all added extraneous substances, were compared for the members of this series in the attempt to find some trend involving the atomic weight ratio. No significant trend was evident. For example, for an atomic weight ratio of 0.50 (nickel/tin) the average variation with unbuffered samples was 8%, but for a ratio of 0.52 (silver/lead) it was 51%; for ratios of 0.91 (silver/tin) and 4.9 (tin/magnesium) the average variations were 22% and 31% respectively.

A similar comparison was made of the average variations for the series aluminium/magnesium, nickel/zinc, nickel/manganese, silver/tin and cadmium/tin. This series has a roughly constant atomic weight ratio (ranging from 0.91 to 1.08) but ionization potential ratios graded from 0.70 to 1.23. No trend relating the size of the average variation and the ionization potential ratio was evident. For example, with a ratio of 0.70 (aluminium/magnesium) the average variation was 14%, with a ratio of 1.04 (silver/tin) it was 21%, and with a ratio of 1.23 (cadmium/tin) it was 14% for unbuffered samples.

Furthermore, element pairs having ionization potential and atomic weight ratios close to unity were associated with average variations as large as those for pairs having both ratios quite different from unity. The average variations for silver/tin, barium/tin, and cadmium/barium were 22, 22, and 29% respectively with unbuffered samples.

The effectiveness of added substances in producing intensity ratio variations could not be related to any of their physical properties. The average variation, considering line pairs, A, B, C, and D and all element pairs in unbuffered Samples 1 to 7, was progressively greater for added substances in the order ammonium chloride, potassium chloride, lithium chloride, and boric acid. Some element pairs provided exceptions. For example, with nickel/tin the order was ammonium chloride, boric acid, lithium chloride, and potassium chloride, while with nickel/manganese it was boric acid, ammonium chloride, potassium chloride, and lithium chloride. On the average the order with buffered samples was potassium chloride, ammonium chloride, lithium chloride, and boric acid, but some element pairs provided exceptions. With silver/lead the order was boric acid, lithium chloride, potassium chloride, and ammonium chloride, and with barium/tin it was lithium chloride, boric acid, potassium chloride, and ammonium chloride.

In general, the intensity ratio variations caused by addition of extraneous material were less for buffered than for unbuffered samples. On the average, they were about 40% less with potassium chloride as the addition, 42% less with lithium chloride, and 57% with boric acid, but with ammonium chloride additions there was little difference. Some element pairs provided exceptions, e.g., the variations for silver/tin were greater with buffered samples. It was noted, however, that reproducibility was higher with buffered samples.

The average variation for line pairs having the most widely different excitation potentials was from 40 to 50% greater than that for pairs having the most nearly equal excitation potentials, all element pairs and additions being taken into account. Considering the various additions separately, it was 63% greater on the addition of boric acid, 53% greater on addition of lithium chloride, and 26% greater on addition of ammonium chloride to unbuffered samples; and 58, 100, and 17% greater on the addition of these substances to buffered samples. It was about the same for both types of line pairs with additions of potassium chloride. There were very few individual instances in which smaller variations were found for the line pairs having the most widely different excitation potentials. They were found for strontium/nickel on the addition of potassium chloride, for strontium/nickel and aluminium/magnesium on addition of lithium chloride, for aluminium/magnesium on addition of boric acid, and for zinc/nickel on addition of ammonium chloride, all with unbuffered samples.

In the light of these results it seems important that application of spectrographic methods to the analysis of samples that may vary considerably in general composition be preceded by a somewhat extensive investigation of the variability of determinations with the type of material under consideration.

The data provide no clue for the choice of a suitable internal standard element since the variability of intensity ratios does not seem to depend in any systematic way on the ionization potential or atomic weight ratio of an element pair. There is evidence that in general some advantage is to be gained by choosing lines with nearly the same excitation potential, but this feature in itself does not ensure stability (see the results for line pairs *C* of tin/magnesium, *C* of strontium/magnesium, and *D* of tin/lead, which have excitation potential ratios of 1.00, 1.01, and 0.99 respectively). For the most part, the use of a buffer substance appears desirable, but in certain instances it may lead to less rather than more stability. In some instances at least the use of a buffer and operation of the spark at constant current offers considerable advantage.

References

1. FOSTER, J. S., LANGSTROTH, G. O., and McRAE, D. R. Proc. Roy. Soc. London, A, 153 : 141. 1935.
2. HARRISON, G. R. J. Optical Soc. Am. 18 : 492. 1929.
3. LANGSTROTH, G. O. and McRAE, D. R. Can. J. Research, A, 15 : 154. 1937.
4. LANGSTROTH, G. O. and NEWBOUND, K. B. Can. J. Research, A, 20 : 39. 1942.
5. LANGSTROTH, G. O., NEWBOUND, K. B., and BROWN, W. W. Can. J. Research, A, 19 : 103. 1941.

THE THERMAL CONDUCTIVITY OF NAPALM*-GASOLINE GELS[1]

By G. O. Langstroth and F. Zeiler

Abstract

A slightly modified form of the rapid and simple method suggested by Hutchinson for the measurement of the thermal conductivity of liquids has been found to suffer from convection effects with samples of low viscosity, except with conductivity tubes of very small diameter. For more viscous liquids such as glycerol it was found to be adequate under all conditions studied. The method has been applied in the determination of the conductivity of Napalm–gasoline gels. For temperatures T between $-50°$ and $50°$ C., and Napalm concentrations C between 0 and 10%, the conductivity k in cal. sec.$^{-1}$ cm.$^{-1}$ per degree C. is described to better than 1% by the relation, $k \times 10^5 = 29.7 - 0.068\ T + 0.11\ C$. The temperature coefficient of resistance of the unaged tungsten filaments used in the tubes differed considerably from the value given by the International Critical Tables for aged' tungsten filaments. For temperatures T_0 between $-50°$ and $50°$ C., the coefficient α_0 per degree C. is given to better than 1% by the relation, $\alpha_0 \times 10^5 = 427 - 1.89\ T_0 + 0.0088\ T_0^2 - 0.000021\ T_0^3$.

A method for measuring the thermal conductivity of liquids, similar to that used commonly in the past for measurements on gases, has been suggested by Hutchinson (6), who has given some data in support of its reliability. The method has marked advantages in speed and simplicity over the more accurate procedure developed by Bates and his coworkers (1, 2, 3, 4). This article describes an application of the method in the determination of the conductivity of Napalm–gasoline gels over a wide range of temperature and Napalm concentration. In addition, evidence is presented that the method as slightly modified by us yields spuriously high values with liquids of low viscosity because of the occurrence of convection, except with conductivity tubes of small diameter.

Apparatus and Procedure

The conductivity tubes (Fig. 1) differed from that described by Hutchinson (6) in the use of a more rugged filament (diameter of the spiral 0.020 as compared to 0.008 cm.), and the position of one of the side arms. These modifications were required by the necessity for filling the tubes with a jelly-like substance. The spiral filament, F, was taken from an unused 40 w. incandescent lamp and had a resistance of about 25 ohms at 25° C. It was spot-welded to No. 18 tungsten leads which were sealed into selected Pyrex tubing with the filament under slight tension and as nearly as possible coincident with the tube axis. External wires were coated with a resistant lacquer. For investigating the validity of the method a series of nine tubes

with internal diameters ranging from 1.270 to 0.330 cm. was used. The length of the filament spiral was from 4.138 to 4.238 cm., and the other dimensions were as indicated in the scale drawing of Fig. 1. The external diameter of the Pyrex tube for the series ranged from 1.505 to 0.546 cm. Tubes were filled to a level about 1 cm. above the upper filament weld, either by suction or with the aid of a small syringe. Care was necessary with the more viscous gel samples to avoid the inclusion of air bubbles or breakage of the filament.
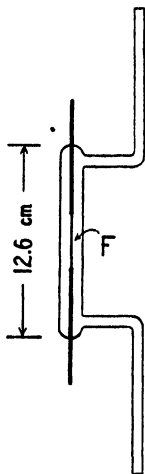
FIG. 1.

The tube, with both arms stoppered, was inserted vertically in a constant temperature bath. An 8 liter water bath with a special mercury thermostat control was used for work above 0° C. Temperature variations were less than 0.001° C. as indicated by series of readings with a Beckmann differential thermometer. Bath temperature was read from a 0.1° mercury thermometer that had been calibrated against a certified standard. For work below 0° C., a covered, carefully insulated 3 liter alcohol bath was used. A heating coil (dissipation about 15 w.), activated by a toluene thermostat control, worked against a cooling device. This device consisted of a 6.5 cm. diameter metal cylinder containing a 4.5 cm. diameter cylinder, both filled with solid carbon dioxide in acetone; the cooling effect was controlled by varying the depth of insertion of either in the bath. Temperature variations were less than 0.01° C. as indicated by a 0.1° C. pentane thermometer used to measure the bath temperature. No evidence of temperature variation was detected with either bath in the electrical measurements described below.

The circuit used to determine the resistance, R, of the tube filament, the current, i, through it, and the potential drop, V, across it, is represented in Fig. 2. The filament, F, and the calibrated box, D, served essentially as end coils to the 1 m. slide wire, AB, in a bridge circuit having boxes, S and Q, as ratio arms. A mercury rocker switch consisting of two rows of eight cups

linked in pairs (shown just above AB in Fig. 2) permitted interchange of F and D in the bridge. On interchange the balance point on the slide wire was shifted by an amount l cm. such that,

$$(R - R_d) = \rho l, \tag{1}$$

where R_d denotes the known resistance of D, and ρ represents the resistance per centimeter of the slide wire.* The potential drop, V, was measured with
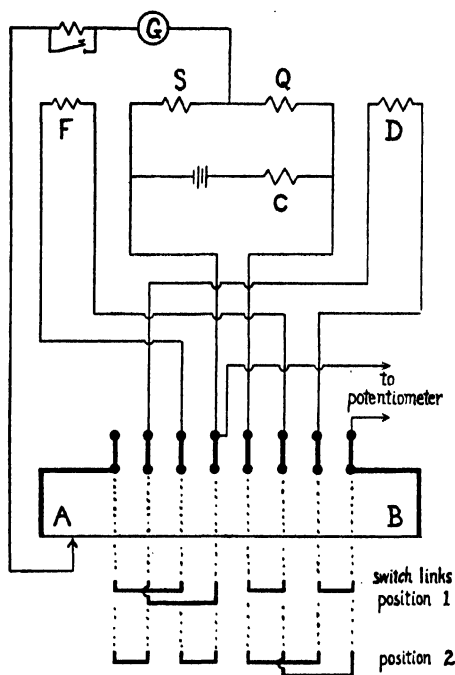
FIG. 2.

a Leeds and Northrup Student potentiometer with a certified standard cell when the switch was set to Position 2; that across D (V_d) was measured when the switch was set to Position 1. The current, i, was calculated from $i = V_d/R_d$; it was adjusted by means of the resistance box, C.

No variation in the value of ρ (0.005615 $\pm$ 0.000003 ohm per cm.) was detected for the range of currents used in these experiments. The slide wire was calibrated for uniformity along its length. The sensitivity of the galvanometer G (1.3 μV per mm.) was sufficient to permit a balance to the nearest 0.1 mm. on the slide wire with the minimum filament current. Potential drops were measured to 0.05% or better. Filament currents ranged from about 0.01 to about 0.05 amp. In general, the bridge was operated with 500 ohms in S and Q and about 25 ohms in D.

---

* *Strictly speaking, Equation (1) should contain the resistance difference between the leads to F and to D from the switch, but this did not exceed 0.00005 ohm.*

In making a determination, a steady current of about 0.01 amp. was passed through the filament with the tube inserted in the bath at the desired temperature. Thermal equilibrium was attained in two to three minutes as shown by the constancy of the filament resistance with time. At least four readings were made of the shift l in the balance point on interchanging F and D, and V and V_d were determined. The procedure was repeated with three additional filament currents, requiring in all from 20 to 25 min. The mean ρl values were plotted against the filament power dissipation, $P = V. V_d/R_d$, and the conductivity, k, was calculated from the slope and the $P = 0$ intercept of the curve in accordance with Equation (7). The magnitudes of the various experimental quantities are illustrated by the following figures for an intermediate filament current.

$$R_d = 24.217 \pm 0.001\ \Omega \qquad i = 0.02958 \pm 0.00002\ \text{amp.}$$
$$V_d = 0.7165 \pm 0.0003\ \text{v.} \qquad \rho l = 0.3705 \pm 0.0003\ \Omega$$
$$V = 0.7255 \pm 0.0003\ \text{v.} \qquad P = 0.02146 \pm 0.00002\ \text{w.}$$
$$l = 54.75 \pm 0.02\ \text{cm.}$$

Theoretical Considerations

If, for the conductivity tube described, the absence of convection and of temperature discontinuities at solid–liquid boundaries is assumed, and if it is further supposed that conduction of heat from the filament is entirely radial, it may be shown easily that for thermal equilibrium

$$P = kG(T - T_i) = J(T_i - T_0), \tag{2}$$

where P and k are expressed respectively in watts and cal. sec.$^{-1}$cm.$^{-1}$ per degree C., and $T, T_i,$ and T_0 denote the temperatures of the filament, the sample–Pyrex interface, and the bath, in °C. The tube constants G and J are described by

$$\left. \begin{aligned} G &= 26.30\ h/\ln(r_i/r) \\ J &= 0.0686\ h/\ln(r_0/r_i) \end{aligned} \right\} \tag{3}$$

where r and h denote respectively the radius and length of the filament spiral, in cm., and r_i and r_0 represent the internal and external radii of the Pyrex tube. In calculating the numerical factor for the latter equation, the conductivity of Pyrex was taken to be 0.00261 cal. sec.$^{-1}$cm.$^{-1}$ per degree C. at 25° C. (7, Vol. 5, p. 217); as will appear later, this value need not be known with high accuracy.

Since in practice the temperature of the filament, T, exceeds that of the bath, T_0, by less than 5° C., one may write to a high degree of approximation

$$(T - T_0) = (R - R_0)/\alpha_0 R_0, \tag{4}$$

where R and R_0 denote the filament resistance at T and T_0, and α_0 represents the temperature coefficient of resistance appropriate to the range T_0 to T. It follows from Equations (2) and (4) that

$$k = P/G\left(\frac{R - R_0}{\alpha_0 R_0} - \frac{P}{J}\right), \qquad (5)$$

or one may write

$$P = \frac{kG}{\alpha_0 R_0(1 + kG/J)} \cdot R - \frac{kG}{\alpha_0(1 + kG/J)} \qquad (6)$$

On this basis, a plot of P vs. R should yield a straight line having a $P = 0$ intercept of R_0 and a slope σ such that

$$k = \sigma\alpha_0 R_0/G(1 - \sigma\alpha_0 R_0/J) \qquad (7)$$

The terms P/J in Equation (5), kG/J in Equation (6), and $\sigma\alpha_0 R_0/J$ in Equation (7) are introduced because of the temperature drop across the Pyrex walls of the tube, and may be considered as small correction terms. J need not be known with high accuracy, but errors in G cause similar errors in k. Since r_i and r enter Equation (3) logarithmically, errors introduced in G by inaccuracies in aligning the filament with the tube axis are of minor importance except with very small diameter tubes. The uncertainty in h is of more importance. The filament spiral is opened out for a short distance near each weld, and it is difficult to judge with high accuracy the value to be used for the effective spiral length. For this reason mainly, the error in G as calculated from tube geometry may be as high as 4%. Once the validity of the basic assumptions has been established, however, more accurate values of G may be obtained by standardizing the tubes with suitable liquids of known conductivity.

The Validity of the Method

The results of some preliminary tests with water suggested the presence of convection in the conductivity tubes used. A series of experiments was therefore performed to seek for any possible dependence of single determinations on tube diameter, filament power input, and the viscosity of the test substance. A value for the 'apparent' conductivity was calculated from Equation (5) for each determined filament resistance and power input. Since G and J were calculated from Equation (3) for this part of the work, the apparent conductivities obtained with a given tube may be subject to a systematic error of about 4% introduced in specifying tube geometry. Some typical data are given in Table I.

It is evident from Table I that the apparent conductivity of liquids with the viscosity of ethyl alcohol or less increased progressively with increasing power input when large diameter tubes were used. Even with the smallest power input the values obtained were commonly significantly greater than the literature values. Furthermore, reduction of the tube diameter caused both of these characteristics to appear less strongly; with a diameter of 0.33 cm. the

dependence on power input was undetectable and the apparent conductivities agreed with accepted values.   The conductivities for viscous liquids such as glycerol were independent of power input and tube diameter, and agreed with the accepted values.   The behavior described by the data is typical of effects produced by convection, which apparently was present with low viscosity liquids in the larger tubes but not with the more viscous samples.   The reason for the difference between this finding and Hutchinson's statement (6) that the method does not suffer from convection is not clear.

TABLE I

THE 'APPARENT' CONDUCTIVITY AT 25° C. FOR VARIOUS SUBSTANCES LISTED IN ORDER OF INCREASING VISCOSITY

Substance	Tube diam., cm.	App. $k(\times 10^5$, cal. sec.$^{-1}$ cm.$^{-1}$ per degree C.) for stated power inputs ($\times 10^3$, w.; expressed approximately)			
		2	9	22	38
Acetone*	1.266	57	55	61	65
	0.667	51	49	49	54
Gasoline	1.016	38	40	44	46
	0.667	37	36	39	41
	0.330	29	28	28	28
Distilled water†	1.270	144	150	154	161
	0.330	138	132	136	139
Ethyl alcohol**	1.270	53	51	56	61
	0.667	47	47	49	52
	0.330	44	45	45	43
Glycerol*†	1.266	69	68	68	68
	0.667	70	69	70	71
	0.330	64	68	67	67
Napalm–gasoline gel (3.5%)	1.270	27	28	28	28
	0.667	28	29	29	29

* Laboratory grade; k = 0.00043 c.g.s. units (7, Vol. 5, p. 227).

† k = 0.00143 c.g.s. units (2).

** Laboratory grade, denatured; k = 0.00045 and 0.00042 c.g.s. units for water contents of 5 and 0% respectively (3).

*† U. S. P. grade, determined water content less than 2%; k = 0.00069 and 0.00068 c.g.s. units for water contents of 2 and 0% respectively (2).

Aside from the occurrence of convection under certain conditions, the basic assumptions stated in the section on theoretical considerations appear to be good approximations.   Heat losses by conduction through the filament leads were less than 0.4% of the power input as estimated on the basis of Gregory and Archer's analysis (5).   The filament resistance vs. power input curves are straight lines (Fig. 3, A) as required by Equation (6), except under conditions in which convection is serious (Fig. 3, B).   Finally, under appropriate conditions the method yields results in agreement with those obtained by

others using different methods. For example, the average values for the conductivity of glycerol at 25° C. calculated from the slopes and intercepts of P vs. ρl curves obtained with tubes of 1.270, 1.266, 1.248, 1.161, 1.016,
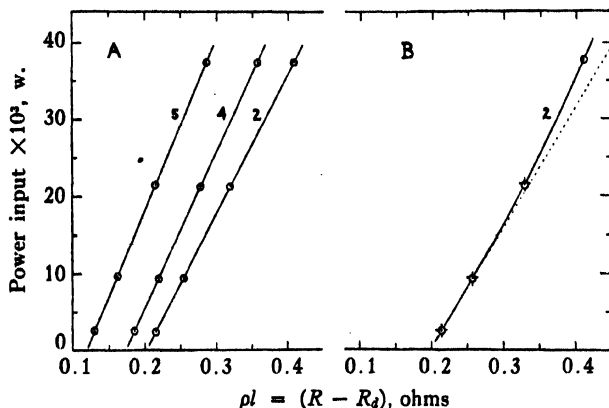
FIG. 3. *Experimental curves for (A) glycerol and (B) acetone, at 25° C. The number attached to each curve refers to the tube used; the internal diameters of tubes, 2, 4, and 5 were respectively 1.266, 1.016, and 0.667 cm. In curve B the symbols ⊙ and + represent measurements taken in the order of increasing and decreasing power input respectively; the broken line is straight.*

0.667, 0.330, and 0.330 cm. internal diameter were respectively 0.000680, 0.000688, 0.000696, 0.000705, 0.000708, 0.000717, 0.000681, and 0.000665 cal. sec.$^{-1}$cm.$^{-1}$ per degree C. The conductivity lies between 0.00068 and 0.00069 (footnote to Table I). Since a G value found from Equation (3) was used in the calculations the above values are subject to the systematic error mentioned previously. Standardization of the tubes consisted in adjusting the G values so that the data for each tube yielded a conductivity of 0.000680 cal. sec.$^{-1}$cm.$^{-1}$ per degree C. The standardized G values were used in the work with Napalm–gasoline gels.

Application of the theory of the section on theoretical considerations to experimental data permits calculation of various quantities not directly measured. The following figures for glycerol at 25° C. indicate the magnitude of the temperature difference across the sample and across the Pyrex tube walls. With a tube of 1.266 cm. diameter, $(T - T_i)$ and $(T_i - T_0)$ were respectively 0.14° and 0.0014° C. at a power input of 0.002430 w., and 2.12° and 0.022° C. at an input of 0.03770 w. The corresponding figures for a tube of 0.330 cm. diameter were 0.11° and 0.0045° C. at an input of 0.002544 w. and 1.52° and 0.070° C. at an input of 0.03985 w. The tube diameters as well as the power inputs are at opposite ends of the range investigated.

Results for Napalm–gasoline Gels

The gels were prepared by mixing Napalm with a commercial grade of gasoline and maintaining mechanical stirring for half an hour. A gel having 5% Napalm concentration contained 5 gm. of Napalm per 100 gm. of gel. Measurements were made on samples that had been freshly mixed and on

samples aged for several months, but since no difference in conductivity was detected no distinction has been made in presenting the results.   The measurements on gasoline alone were made with a tube of 0.330 cm. diameter; the conductivities agree fairly well with those obtained by extrapolating the *k* vs. Napalm concentration curves to zero concentration (Fig. 4).

Napalm concentration, % by weight
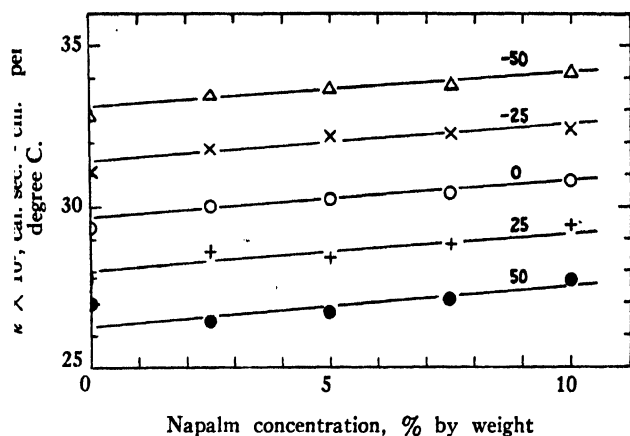
FIG. 4.   *The thermal conductivity of Napalm–gasoline gels.   The plotted points are experimental values, the lines were calculated from the empirical relation given in the text.   The number attached to each curve refers to the temperature in Centigrade degrees.*

Mean data based on 67 determinations are given in Table II; the average deviation of individual results from the mean was 1.1%.   As shown by Fig. 4, the data are represented to 1% by the relation

$$k \times 10^5 = 29.7 - 0.068T + 0.11C,$$

where T and C denote respectively the temperature, °C., and percentage Napalm concentration by weight.   Changes in concentration, despite their marked effect on some of the properties of the gels, produced relatively slight changes in the thermal conductivity.

TABLE II

THE THERMAL CONDUCTIVITY OF NAPALM–GASOLINE GELS

Temp., °C.	$k \times 10^5$ (cal. sec.$^{-1}$ cm.$^{-1}$ per degree C.) for stated Napalm concentration				
	0%	2.5%	5.0%	7.5%	10%
50.0	27.0	26.4	26.7	27.1	27.7
25.0	27.8	28.6	28.4	28.8	29.4
0.0	29.4	30.0	30.2	30.4	30.8
−25.0	31.1	31.8	32.2	32.3	32.4
−50.0	32.8	33.5	33.7	33.8	34.2

A Note on the Temperature Coefficient of Resistance of Unaged Tungsten Filaments

The use of I. C. T. data for the temperature coefficient of aged tungsten filaments (7, Vol. 6, p. 136) led to high values for the thermal conductivity of known liquids. Determined values for the coefficient of the unaged filaments used were about 20% smaller than the I. C. T. figure. Two methods of measurement were employed. (1) Determinations of the resistance change $\triangle R$ caused by a temperature change $\triangle T$ ranging from 2° to 8° C. were made with a thinly lacquered filament supported in the constant temperature bath. The lack of dependence of the resistance on filament current indicated that the filament was closely at the bath temperature. The temperature was measured to 0.01° C. with the bath thermometer, or at −25° and −50° C. with a calibrated copper–constantan thermopile (three couples). The coefficient appropriate to T_0 and R_0 was calculated from $\alpha_0 = \triangle R / \triangle T \, R_0$. The resistance measurements were made with the bridge previously described. (2). R_0 values obtained from the intercepts of the P vs. ρl curves of conductivity data at bath temperatures from −50° to 50° C. were plotted against the corresponding T_0 values. The coefficient at each working temperature was calculated from the slope of the curve and the R_0 value at that temperature.

A summary of the data is given in Table III. The 'Method 1' values are the means of from three to six determinations. The 'Method 2' values are based

TABLE III

THE TEMPERATURE COEFFICIENT OF RESISTANCE FOR UNAGED TUNGSTEN FILAMENTS

T_0 , °C.	Method	$\alpha_0 \times 10^4$, per degree C.	Mean $\alpha_0 \times 10^4$
50.00	2	35.2 ± 0.3	35.2
25.00	1	38.1 ± 0.2	38.3
	2	38.6 ± 0.3	
0.00	1	42.7 ± 0.2	42.8
	2	42.8 ± 0.3	
−25.00	1	48.0 ± 0.2	48.1
	2	48.2 ± 0.3	
−50.00	1	54.6 ± 0.2	54.7
	2	54.8 ± 0.3	

on all the conductivity data, which involved results for at least two different tubes at each working temperature. The data are described to better than 1% by the relation

$$\alpha_0 \times 10^5 = 427 - 1.89 T_0 + 0.0088 T_0^2 - 0.000021 T_0^3.$$

References

1. BATES, O. K.   J. Ind. Eng. Chem. 25 : 431.   1933.
2. BATES, O. K.   J. Ind. Eng. Chem. 28 : 494.   1936.
3. BATES, O. K., HAZZARD, G., and PALMER, G.   J. Ind. Eng. Chem. 10 : 314.   1938.
4. BATES, O. K., HAZZARD, G., and PALMER, G.   J. Ind. Eng. Chem. 33 : 375.   1941.
5. GREGORY, H. and ARCHER, C. T.   Proc. Roy. Soc. (London), A, 110 : 91.   1926.
6. HUTCHINSON, E.   Trans. Faraday Soc. 41 : 87.   1945.
7. INTERNATIONAL CRITICAL TABLES.   McGraw-Hill Book Co., Inc., New York.   1929.

CHOOSING AN EMULSION AND PROCESSING TECHNIQUE FOR DAYLIGHT AERIAL PHOTOGRAPHY[1]

By L. E. Howlett

Abstract

Experiments are reported that show the relations existing between gamma, useful exposure range for aerial photography, maximum resolving power, and emulsion speed as determined by the resolving power criterion. Aero Super XX and Panatomic X, processed in various ways, were used for the experiments. The results are used to deduce the proper choice of emulsion and processing technique for ordinary daylight aerial photography where the main requirement is the acquisition of information.

Purpose of the Experiment

In a previous communication (1) a resolving power criterion was proposed for selecting the photographic exposure that, for aerial photography, can be considered inversely proportional to the emulsion speed. Such a method gives appropriate emphasis to the importance of obtaining information. This is generally the principal user requirement in aerial photographic operations. It was shown that, although numerical determinations of speed by the proposed method have to be made by a subjective estimate of the limit of resolution, good and certainly quite adequate agreement can be attained at different times by a number of different observers of varying experience in such work.

The present discussion reports investigations to determine the relation between speed, as determined by the resolving power method, and certain other physical characteristics of two emulsions, when several different processing techniques are employed. Two emulsions, Aero Super XX and Panatomic X, and three developers were studied, D-19*b*, DK-20, and DK-60*b*. The processing time was varied to secure a wide range of gammas.

Experimental Procedure

Sensitometric printings were made from a resolving power step tablet. On each density step were three identical resolving power targets. A target consisted of a series of three line units. The series in respect of size had as a common ratio $\sqrt[4]{2}$. In a unit the lines were equal in width and to the space separating them. The line length was nine times the separation. The lines were lighter than the density step forming the background. The logarithm of the brightness ratio was 0.2. The exposure time was one-thirtieth of a second. The illumination was equivalent to mean noon sunlight modified by a Wratten No. 12 filter. The usual controls necessary for accurate sensitometry were employed.

After processing the printings of the resolving power step tablets, the maximum resolving power attained on each step was read with the aid of a binocular microscope. The magnification and illumination were adjusted so that reading conditions led to the highest evaluation of the resolving power. From the results a curve was plotted to relate resolving power with the logarithm of the exposure.

The shortest exposure, which gave 90% of the maximum resolving power attained on the negative material for each particular processing technique, was taken as inversely proportional to the speed of the material for that technique.

Discussion of Results

A very large number of resolving power – log exposure curves were obtained, but their complete presentation here would hardly be justified. Accordingly a typical one is shown in Fig. 1. The normal characteristic curve has been
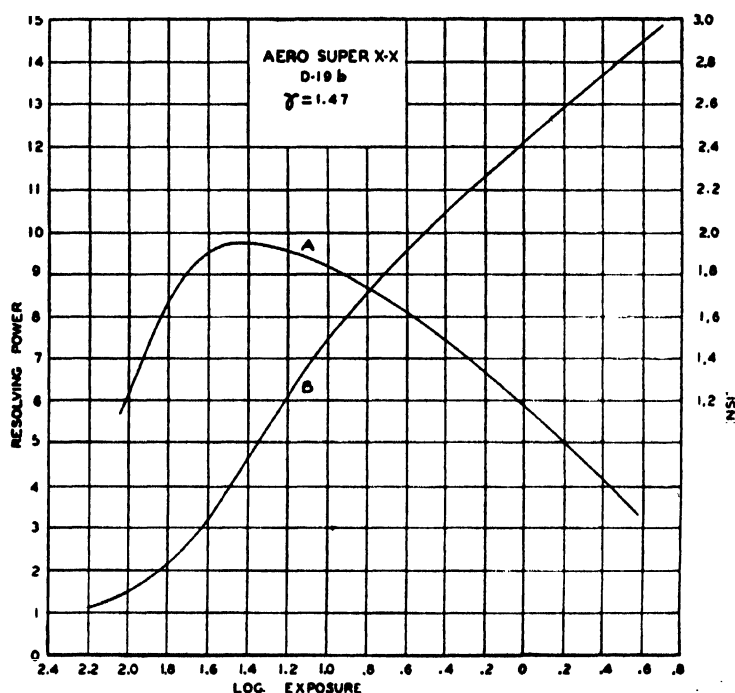
Fig. 1. *A typical resolving power – log exposure curve (A) with the density – log exposure curve (B).*

included. Ordinates refer to the step number of the smallest target resolved and to the density of the step. The exposure axis is the negative logarithm of the exposure in meter-candle seconds. It will be noted that in the sample given there is a relatively short range of exposures over which 90% maximum

resolving power can be obtained. This seems to be a general condition except for the finer grained emulsions at low gammas. The range is the important one for aerial photography and, to utilize it fully, accurate exposures must be made.

Repetition of the speed determinations for a specific emulsion and processing technique, at widely different times and by different observers, showed the same reproducibility of results that was reported previously (1). It is interesting to record that, early in the experiments reported here, concern was caused by obtaining from a series of tests an average log exposure for 90% resolving power on Aero Super XX at a gamma of 1.4 which differed by 0.12 from the results previously reported (1). On investigation the records revealed a difference in the emulsion number for the two experiments. Fortunately, some of the material bearing the original emulsion number was still available. Speed determinations were repeated, and the results demonstrated that no discrepancies existed in measurements of material bearing the same emulsion number, but that a speed difference on the resolving power basis really existed between the two emulsion batches.

Graphical presentation of the results is the easiest way to show the general conclusions that can be drawn from the large mass of experimental data.

Fig. 2 presents the negative logarithms of the exposures, which correspond to 90% maximum resolving power for particular processing techniques, plotted against gamma. Speed increases with gamma for both emulsions.
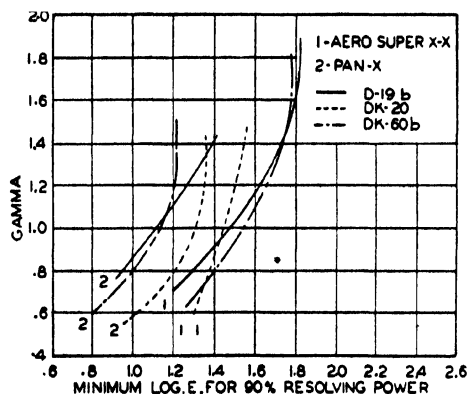
FIG. 2. *The relation between gamma and minimum log exposure for 90% maximum resolving power.*

Fig. 3 shows the maximum resolving powers attained by different processing techniques plotted against gamma. It will be noted that for each emulsion the resolving power is only moderately affected by processing. The extreme range of resolving power for Aero Super XX is just about two steps and for Panatomic X a little less. The highest values are obtained only by great

sacrifice of speed. There is in general a difference of about one step between the resolving powers of the two emulsions for the same developer and the same gamma.
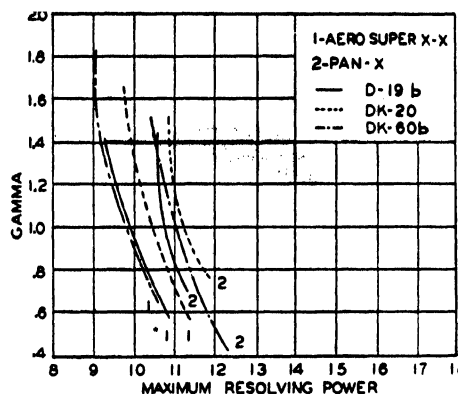
FIG. 3. *The relation between gamma and maximum resolving power.*

Fig. 4 gives the range of log exposure over which it is possible to obtain at least 90% of the maximum resolving power of each emulsion for each processing condition plotted against gamma. With both emulsions the range decreases
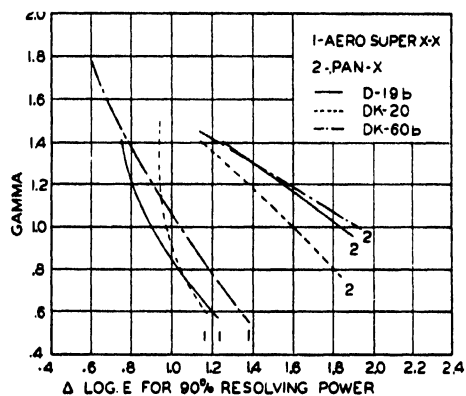
FIG. 4. *Relation between gamma and* Δ *log exposure over which 90% maximum resolving power can be obtained.*

continuously with increasing gamma for each developer. For a particular gamma the range is not greatly affected by a change of developer for Aero Super XX, but with Panatomic X some considerable differences are apparent. At low gammas the latter emulsion has very long ranges over which 90% maximum resolving power may be obtained. This characteristic no doubt accounts for its popularity in miniature photography. For the same purpose with this emulsion DK-20 will be the preferred developer, since it gives a slightly higher resolving power and a higher emulsion speed than the other two.

Choice of an Emulsion and Processing Technique for Aerial Photography

In choosing an emulsion and processing technique for aerial photography a suitable compromise must be made between speed, resolving power, and the range of exposure over which 90% of the maximum resolving power of the emulsion can be attained. The desirable condition would be to have the three factors at a maximum simultaneously, since this condition leads to the greatest recovery of information and tolerates greater errors in exposing. Unfortunately a compromise must be made. Provided resolving power is not unduly sacrificed, and providing the range of exposure over which 90% of maximum resolving power can be obtained is not reduced below the average brightness range of the subject from the air, speed is of great importance. The majority of aerial photographic lenses presently available perform better when stopped down to $f/11$ or $f/16$. High performance aircraft are extensively used in aerial photographic operations and short exposures are essential to avoid excess image movement unless some form of compensation is provided. Consequently, any slight increase in the absolute resolving power of the material that is gained by a significant sacrifice of emulsion speed can be quite illusory. Indeed, in certain circumstances it might actually lead to a smaller recovery of information. For high altitude photography (20,000 ft.) it can probably be accepted that the average log brightness range corresponds to about 0.75. Consequently, this can be taken as the minimum exposure range over which it is essential to obtain 90% of the maximum resolving power. At lower altitudes longer ranges are required.

For general aerial photographic operations the greater speed of Aero Super XX makes it preferable to Panatomic X. The maximum resolving power of Panatomic X is slightly greater, but it is doubtful whether advantage can be taken of the fact in practice on account of the much lower speed. D-19*b* and DK-60*b* lead to the highest speed with Aero Super XX, and this considerable increase of speed does not entail too costly a sacrifice of resolving power. Since D-19*b* leads to a slightly higher speed than DK-60*b*, the preference will be given to it since the other characteristics are, within experimental error, the same. No advantage is to be gained from the slightly greater speeds obtainable at gammas above 1.4, since the range over which 90% resolving power can be attained has been reduced below the acceptable limit of 0.75. It will be shown in a later communication that if the information is to be recovered by way of paper prints there are other considerations which suggest that gamma should not exceed about 1.4.

Of the emulsions and processing techniques tested, it is clear that Aero Super XX developed in D-19*b* to a gamma of about 1.4 is the most desirable combination for aerial photography. Other combinations equivalent to or better than this one are probably available. Further studies are being made to investigate this situation.

♪ Reference

1. HOWLETT, L. E.   Can. J. Research, A 24 : 1.   1946.

A SIMPLIFIED BROADSIDE DIPOLE ARRAY[1]

By J. H. Bell[2]

Abstract

A broadside dipole array, or 'billboard', with a greatly simplified feed and matching system, is described. Radiation patterns compare favorably with those of the conventional billboard.

Introduction

The two most difficult problems inherent in the design of a billboard array are:

(1) To obtain the proper phasing and feed of the dipoles for patterns with minimum side lobes and maximum gain;

(2) To match the antenna, particularly when there are many dipoles placed in parallel.

In the conventional type of billboard array each dipole is fed separately from a complex feeder network behind the reflecting screen. The purpose of this paper is to describe a billboard array in which this feeder system is almost completely eliminated, and the matching problem is simplified, without deterioration in the radiation patterns.

The Problem

It was required to construct an antenna to operate at 90 Mc. per sec. The antenna was to be mounted on a tower 200 ft. high, and was to rotate continuously at 4 r.p.m. The array was to have maximum gain and sharpness of radiation pattern commensurate with its physical size. Operational conditions as applied to the function of the antenna limited the vertical beam width to a minimum of 30°. Consideration of the mechanical conditions limited the size of the antenna to approximately 14 ft. high and 44 ft. in width.

The physical dimensions quoted above allowed the possibility of a billboard array of 21 half-wave ($\lambda/2$) elements, i.e., seven elements wide by three elements high, and horizontally polarized.

The Array

To gain simplicity in feed and matching, a vertical stack of three seven-element horizontally polarized collinear antennas was used (See Fig. 1). The phasing of the individual dipoles in the collinears was accomplished by means of quarter-wave stubs, which projected back through the reflecting screen.

The spacing between the collinears was one-half wave length. Each collinear was fed at its midpoint, and the main point of the feed was at the center of the middle collinear.
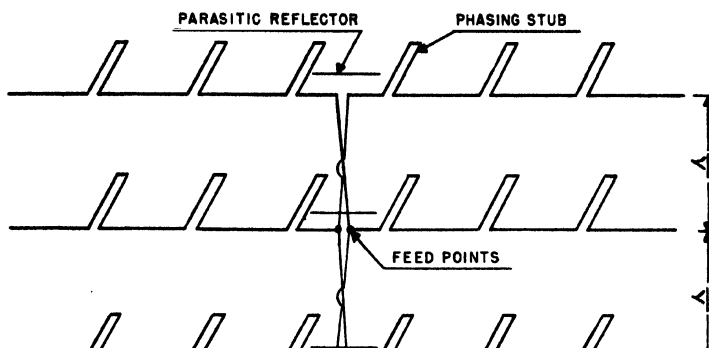
FIG. 1. *The schematic diagram of the collinear antennas. The screen is placed at a distance of λ/8 behind the radiators, and the phasing stubs project backwards through the screen.*

A parasitic reflector was placed at a distance of 25 cm. behind the center element of each collinear. The reflector caused the center element to be driven harder. This fact, accompanied by the natural taper in the power distribution along the array due to radiation, minimized the side lobes. The screen, made of horizontal lengths of No. 12 gauge copperweld wire, with a vertical spacing of 3 in., was constructed of such a size as to give an overlap of λ/8 all around the array.

The radiation pattern (field strength) is given in Fig. 2. The beam width at half field strength is 18°, the side lobes are less than 14% of maximum, and
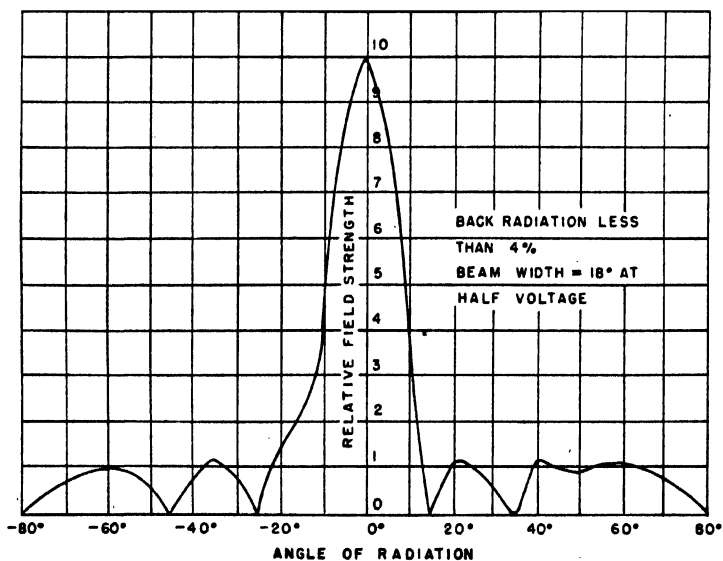
FIG. 2. *The horizontal radiation pattern of the array.*

the back radiation is less than 4%. As the array was to be used for common transmitting and receiving, the actual radar pattern is effectively the power pattern (see Fig. 3).
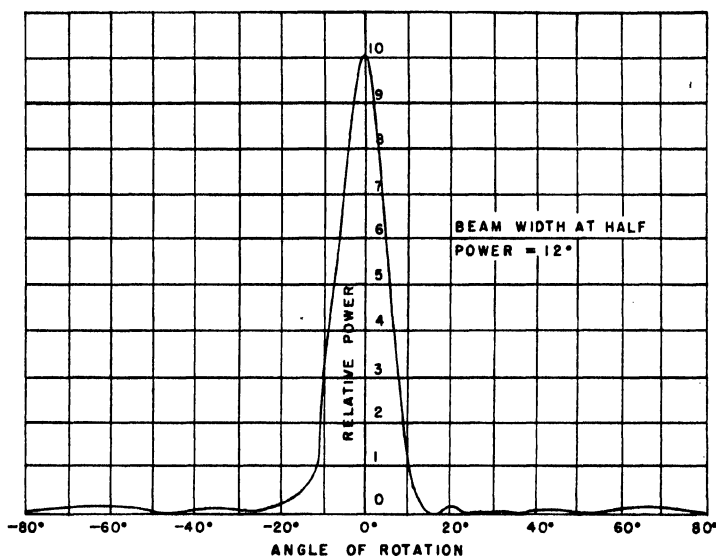
FIG. 3. *The effective radar pattern of the array.*

As the impedance of each collinear was in the neighborhood of 500 ohms, the impedance of the array turned out to be 165 ohms resistance, with very little reactance. This value made it very easy to match into with either open wire or coaxial line. The array was matched into a 400-ohm open wire line by means of a quarter-wave transformer.

The bandwidth of the array is nearly the same as for an equivalent array of conventional design, since the error in the phasing of the dipoles, when operating off frequency, is nearly the same in both cases.

The array itself was constructed of 5/16 in. brass tubing, mounted on a frame of 2 by 2 in. dressed oak. The brass work was mounted on Johnston type No. 65 insulators. The insulators were kept as far as possible from high voltage points. The array was subjected to powers as high as 300 kw. peak without any arc-over.

The feeding of the array during rotation was accomplished by means of inductive coupling rings, patterned after an English design. These consisted of two flat, tuned rings separated by a Faraday shield. There were no sliding contacts.

Conclusions

The main features of this array are:

(1) The simplicity of the feed system. There is only one point of feeding, eliminating the necessity of having feeders strung around behind the array.

(2) By means of the natural power taper and use of the central parasitic reflectors, the spurious radiation is kept to a minimum.   The pattern obtained is equal in all respects to that obtained using the conventional billboard.

(3) Using three arrays, of fairly high impedance, in parallel simplifies the matching problem.   There is only one point to be matched.   At that point the impedance is such as to make matching simple.   Furthermore, as elements are added to each collinear, the impedance increases.   Thus it is possible to build an array whose impedance actually increases as dipoles are added.

A POSITIVE ION SOURCE[1]

By A. J. BAYLY[2] AND A. G. WARD[2]

Abstract

Positive ions are formed in a low pressure electrodeless discharge which is excited by the radio-frequency field of a coil coupled to a 15 Mc. per sec. oscillator. The ions are extracted from the discharge through a pumping canal (2 mm. in diameter × 12 mm. in length) by a simple arrangement of electrodes. After further focusing and acceleration to 50 kv., the beam current at the target is 500 μa. and the focal spot is 6 mm. in diameter. Magnetic analysis has shown that the beam consists of 50% protons when using hydrogen in the discharge and 60% deuterons when using deuterium. Gas is supplied to the source at the rate of 15 cc. per hr.

Introduction

Protons or deuterons, accelerated to high energies, are used as tools for nuclear research, and for other purposes. The usefulness of the accelerators producing these high energy particles may be measured in terms of the maximum energy of the particles, the energy spread of the beam, the maximum current of atomic ions, and other criteria of a similar nature. Since the performance of an accelerator is closely related to that of its positive ion source, a list of the desirable properties of ion sources that are used in such accelerators can be compiled. The source should have a high efficiency as measured both by the ratio of the number of emergent atomic ions to the number of emergent gas molecules and by the ratio of atomic ion current to total beam current. The ion beam from the source must be suitably collimated. The source should give an adequate output of ions, various accelerators requiring ion currents from a few microamperes to many milliamperes. Other desirable properties are ruggedness, long life, and low power consumption.

Many positive ion sources have been described in the literature, and they can be classified in three main groups. The first group, 'Canal-ray Sources', use a high voltage, cold cathode discharge to produce ions, the useful beam emerging from the source through a small hole in the cathode. Papers by Bouwers, Heyn, and Kuntke (2) and Craggs (3) contain data on this kind of ion source, and many references to earlier work. In the second group, 'Capillary Arc Sources', a low voltage, high current discharge is passed through a constriction or capillary in order to produce a region of intense ionization. Positive ions are removed from this discharge either by diffusion through a small hole or by an electrostatic extracting field. Sources described by Lamar, Buechner, and Van de Graaff (6) and Zinn (9) are good examples of this group. The third group of sources are characterized by the use of a magnetic field to prevent the escape of electrons from the discharge, thus allowing the formation

of an intense plasma of electrons and positive ions. In sources of this type described by Finkelstein (4) and Ardenne (1) a reflection principle is also used. Electrons from the cathode are constrained by the magnetic field to oscillate between two electrodes at cathode potential until their energy is spent in excitation and ionization. In this way the effective path length of the electrons is increased and the discharge can be operated at a greatly reduced pressure.

The positive ion source described in this paper does not belong in any of the three groups discussed above. An electrodeless discharge is used to produce the positive ions, which are then extracted from the discharge through a pumping canal by a suitable arrangement of electrodes.

Preliminary Experiments

Experiments on the design of a positive ion source were undertaken as part of the work involved in the design and construction of a 50 kv. accelerator. A simple glass capillary source, shown in Fig. 1, was used in the first experiments*. The discharge was produced by a radio-frequency oscillator coupled to two external electrodes, and an electrostatic field was used to extract positive ions from the discharge through a canal of small diameter. Beam currents of 200 μa. were obtained, which contained 20% protons.
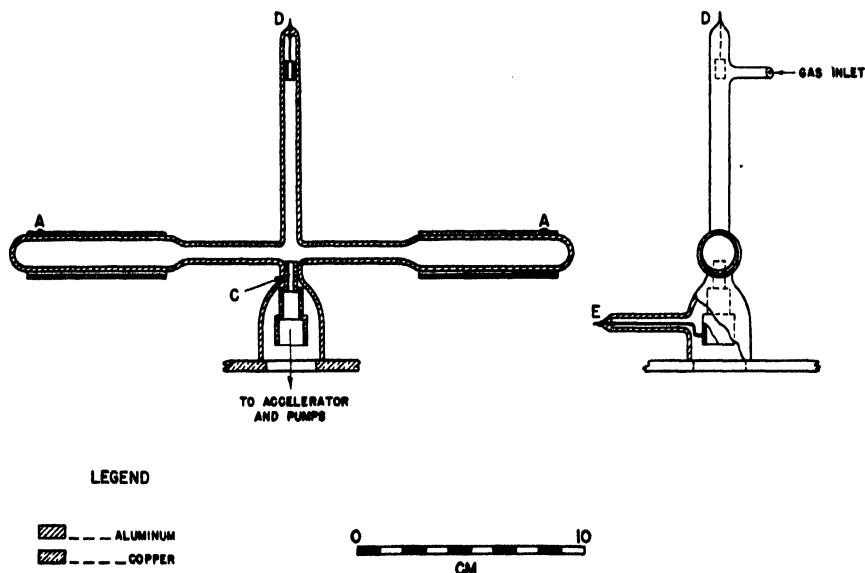
FIG. 1. *Capillary type ion source. Radio-frequency voltage was supplied to the external electrodes A, A, to excite a discharge. Positive ions were extracted from the discharge through the canal, C, by a steady voltage of approximately 2 kv. between electrodes D, E. Legend for aluminum should show crosshatching.*

* *Dr. D. Roaf, former member of the United Kingdom staff, Chalk River Laboratory, began the design of the accelerator and made preliminary investigations of this capillary source excited by radio-frequency.*

Radio-frequency excitation of the discharge has two apparent advantages. The surface enclosing the discharge region can be made of Pyrex glass, and the experience of other workers (5, 6) has shown that this should give a high percentage of atomic ions in the discharge. Since no electron-emitting cathode is required, the metal exposed to the discharge is only that associated with the extracting electrodes, and the emission failures and indeterminate life of cathodes are avoided.

The properties of this capillary type source were not thoroughly explored. Although the beam current was limited by local heating in the capillary, a better design for the electrodes would probably have improved the performance. Recurring breakages of the rather fragile source were troublesome, and the alternative design of ion source shown in Fig. 2 was investigated. This design was suggested by the source described by Thonemann (8), which was published at this stage of the experiments.
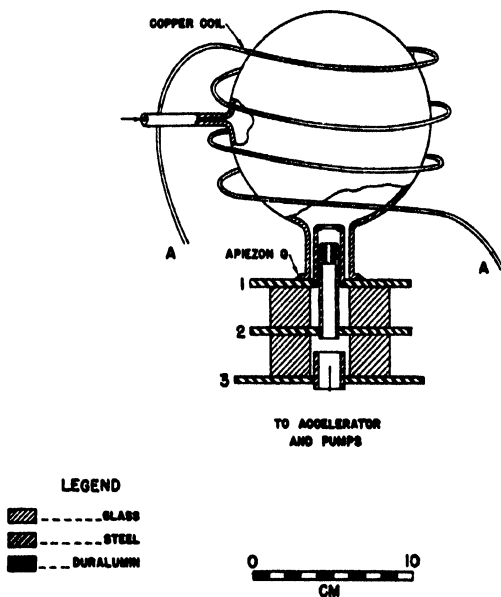
Fig. 2. *Radio-frequency type ion source. The copper coil was connected to the oscillator at the points A, A. Positive ions were extracted from the electrodeless discharge in the inverted Pyrex bottle by a suitable voltage between Electrodes 1 and 2. A further accelerating voltage between Electrodes 2 and 3 was used to focus the ion beam.*

In the initial measurements made on this source beam currents of 300 μa. were obtained, and the proton current was 14% of the total current when hydrogen was used in the discharge. With a deuterium discharge the deuteron current was 29% of the total beam current. By a variation of parameters such as the size and shape of the Pyrex flask and the geometry of the electrodes the performance was markedly improved.

Final Arrangement

The arrangement of the ion source used at the present time is shown in Fig. 3. The flask in which the discharge takes place is a 600 cc. Pyrex chemical reagent bottle. The rim of the bottle is ground flat to give uniform contact with the metal electrode. The vacuum seal at this point is made with
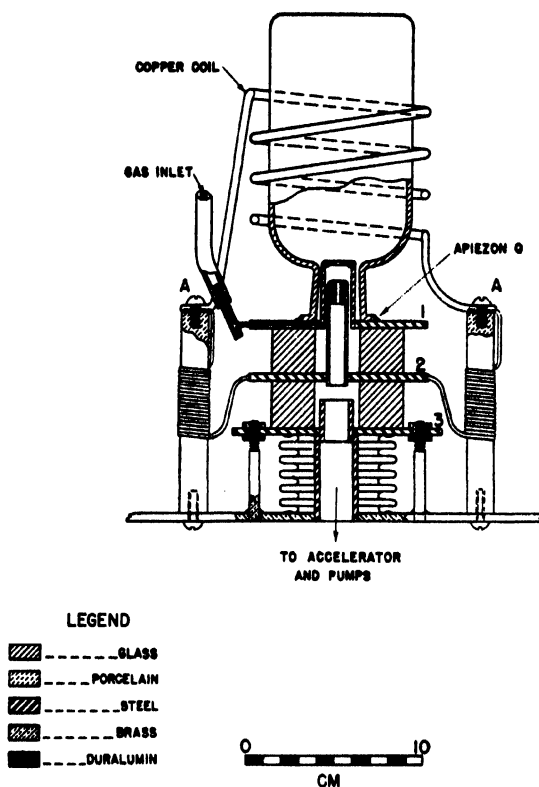
FIG. 3. *Improved model of the radio-frequency type ion source.*

Apiezon Q. A bottle of this shape, with the neck fitting closely on the electrode system and a rapid increase of diameter at the level of Electrode 1, gave optimum results. A strong discharge occurs near the electrode and a minimum of metal surface is exposed to the discharge.

The exciting coil is mounted concentrically with the axis of the bottle. It is made of four turns of $\frac{1}{4}$ in. diameter copper tubing, and the inside diameter of the coil is chosen to clear the walls of the bottle by approximately $\frac{1}{4}$ in. The coil is mounted on two porcelain pillars, and radio-frequency choke coils have been wound on these pillars. The ends of the choke coils remote from the exciting coil are connected to Electrode 2, Fig. 3. The radio-frequency power is supplied through two isolating condensers and a simple parallel wire transmission line; connections are made to the coil at the terminals *A,A*, Fig. 3. In this way the 15 Mc. per sec. oscillator is isolated from the 50

kv. applied to the source.   A push-pull type oscillator is used with an input power of 400 w., but it is not known how much radio-frequency power is used in exciting the electrodeless discharge.   The light emitted by the discharge is roughly equal to that from a 15 w. electric light, and a small fan with a 1/10 h.p. motor gives adequate cooling.

The dimensions of the electrode system are shown in Fig. 4.   The electrodes are made of mild steel with the exception of the two duralumin parts shown in the figure.   Duralumin was used for these parts to minimize sputtering from positive ion bombardment.   With this source no trouble has arisen
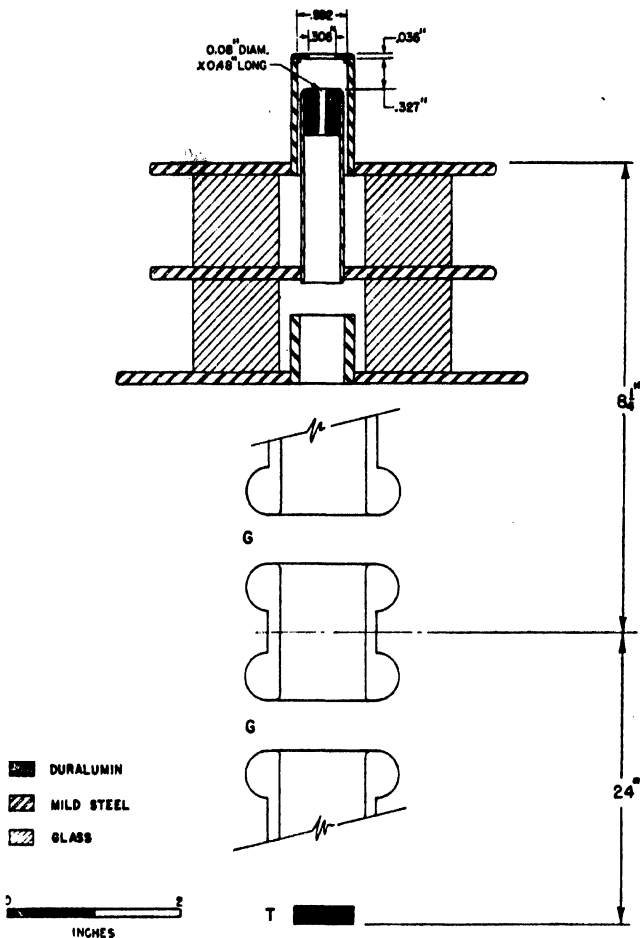
FIG. 4.   *Arrangement of the ion source electrode assembly, the main accelerating gaps, G, G, and the target, T.*

from this cause since the discharge appears to remove sputtered material from the Pyrex surface as quickly as it is deposited.   It is therefore possible that an electrode system made entirely of mild steel would be satisfactory.   In this source the limitation on applied voltage between the upper two electrodes

is set by sparking, and mild steel electrodes would raise this limiting voltage. The electrodes are spaced with glass disks, and Vinyl-seal resin has been used to make the vacuum seals. An assembly jig was used to assure reasonable alignment of the components.

Hydrogen or deuterium is supplied to the discharge from a 3 liter reservoir at reduced pressure. It passes through a suitable capillary leak, glass stopcock, and enters the discharge through the inlet tube in Electrode 1, Fig. 3. Variation of the pressure in the reservoir is used to alter the gas pressure in the discharge. When the operating conditions are normal, gas is used at the rate of 15 cc. per hr. The pressure in the discharge, calculated from the gas flow and dimensions of the pumping canal, is about 10^{-2} mm.

Positive ions are extracted from the discharge by a voltage applied between Electrodes 1 and 2, Fig. 3, Electrode 1 being positive with respect to Electrode 2. A further voltage applied between Electrodes 2 and 3 accelerates and focuses the ion beam emerging from the small diameter hole in Electrode 2. These voltages, designated as extracting and focusing voltages, are supplied by two variable 0 to 10 kv., 10 ma., power supplies. The power supplies are fed with mains voltage through a one-to-one transformer with insulation for 50 kv. between the primary and secondary windings.

Experimental Results

Data on the operation of the source under normal conditions are given in Table I. The color of the discharge provides a good indication of the behavior of the source. Normally the discharge, which fills the bottle, is deep red,

TABLE I

OPERATING DATA AND PERFORMANCE OF THE RF ION SOURCE (FIG. 3)

Gas consumption	15 cc. per hr.
Pressure in discharge	$\sim$10 $\times$ 10^{-3} mm. mercury
Pressure beyond canal	$\sim$5 $\times$ 10^{-6} mm. mercury
Power used in oscillator	450 w.
Oscillator frequency	15.5 Mc. per sec.
Extracting volts	1.2 kv.
Focusing volts	7.5 kv. for 50 kv. acceleration
Current normally obtainable	500 μa.
Maximum current obtained	750 μa.
Atomic ion content	51% from H_2 discharge
	57% from D_2 discharge
Ion current density at canal	$\sim$16 ma. per cm.^{2}
Ion current density at target	$\sim$0.65 ma. per cm.^{2}

and the lines of the Balmer series are very prominent when viewed through a spectroscope. If a small air leak is present, the discharge is pale pink or white. When the discharge is turned on after the apparatus has just been pumped down from atmospheric pressure, it requires one or two hours' operation before the discharge regains its red color. When the operating pressure is raised to about twice normal the discharge assumes a ring shape;

a reduction of pressure to about one-half normal causes the intensity to decrease rapidly, and at still lower pressures only a faint blue glow remains. This glow disappears completely when the gas supply is turned off, but fluorescence of the flask walls can still be observed. Decreasing the radio-frequency power produces similar changes in intensity and the discharge tends to flicker.

Positive ions are extracted from the discharge by a voltage between Electrodes 1 and 2 (Fig. 3). The arrangement of the electrodes is such that a beam of ions is focused through the small canal in the second electrode. For a given intensity of discharge there is an optimum extracting voltage corresponding to a maximum beam current passing through the canal, and this optimum voltage increases as the intensity of the discharge is increased. The relations between extracting voltage, beam current, and intensity of the discharge can be explained qualitatively in terms of the position of the plasma boundary. This boundary acts as a positive ion emitter, with a current density per unit area proportional to the intensity of the discharge. The boundary adjusts its position with variation of voltage and intensity of discharge so that the positive ion current corresponds to space charge limited conditions. When no extracting voltage is applied the plasma projects through the aperture in Electrode 1. As the voltage is increased the plasma retracts, and eventually is concave towards this electrode. As the plasma boundary moves with voltage, the focusing properties of the ion gun alter, and the operating voltage is chosen to give best focusing of the ion beam through the canal. Under normal operating conditions, this optimum occurs at 1200 v., and a current of about 1.5 ma. is taken from the power unit supplying this voltage.

When the positive ions pass through the canal they are accelerated by a further voltage between Electrodes 2 and 3 (Fig. 3). Adjustment of this focusing voltage is used to maintain the focus at the target for variations of the main accelerating potential between 10 and 50 kv. Although this electrostatic lens produces a converging effect on the beam, when it is used in combination with the two main accelerating gaps (G, Fig. 4) an increase of the voltage on this lens causes the beam at the target to diverge. This effect arises since the increased voltage of the positive ions entering the main accelerating gaps leads to an increase in the focal length. The first crossover of the beam after leaving the canal occurs at the target.

The relative positions of the ion source, main acceleration gaps, G, and the target, T, are also shown in Fig. 4. The high voltage is divided equally between the two gaps. For measurements of beam current the target, T, was replaced by a Faraday cylinder with appropriate bias voltages and limiting stops to avoid errors in measurement due to secondary electrons.

It has been found that the useful beam current increases from about 200 μa. at 15 kv. to 500 μa. at 50 kv. if the beam size at the target is maintained by appropriate variation of the focusing voltage. The increase in this voltage

as the over-all voltage is increased draws an increasing number of ions into the beam at the expense of ion current striking the interior walls of Electrode 2 (Fig. 3).

The percentage composition of the beam has been determined with a magnetic analyzer. This was placed at the position normally occupied by the target, and ion currents were measured in a Faraday cylinder after 180° deflection in a magnetic field. The resolution was such as to allow complete separation of the mass peaks as far as mass 6, and was determined primarily by the beam diameter at the entrance to the analyzer (of the order of 6 mm.) and the diameter of the aperture in front of the Faraday cylinder (of the order of 1 cm.). Flat-topped peaks were obtained as the magnetic field was varied, corresponding to one component of the analyzed beam sweeping across the aperture in front of the Faraday cylinder. The mean radius of curvature in the analyzer was 5 cm., and the analyses were normally made with an over-all voltage of 15 kv.

A series of measurements taken with the ion source operating normally are given in Table II. In addition to those peaks listed in Table II, very small peaks were observed which corresponded in energy to atomic ions produced by the breaking up of molecular ions after they had been accelerated to the

TABLE II (*a*)

TYPICAL ANALYSIS OF HYDROGEN BEAM

Mass	1	2	3	Others
Peak current, μa.	91	37	51	—

Mass 1 content = 51%.

TABLE II (*b*)

ANALYSES OF DEUTERIUM BEAM

(Currents in microamperes)

Mass	1	2	3	4	5	6	Mass 2 content, %
Run 1	4	64	2½	17	2	10	62
Run 2	4	50½	2½	17	4½	15	52
Run 3	4	57	3	19	4	14½	57
Run 4	4½	66	2½	18	3	19	58

Average Mass 2 content = 57%.

maximum voltage. The beam current used in taking these measurements was about 200 μa. The higher percentage of atomic ions when deuterium gas is used, as compared with that when using hydrogen gas, is a real effect.

It could arise from the difference in the impurities in the gases, since commercial samples were used. The 'hydrogen' was stated to be 99.5% H_2 with O_2 as the main impurity, while the 'deuterium' was 95% D_2 with H_2 as the main impurity.

The percentage of atomic ions in the beam increases gradually as the pressure is reduced, but the total beam current decreases more rapidly. The normal operating pressure has been chosen to give good percentages of atomic ions and a reasonable rate of gas consumption, but the performance of the source does not depend markedly on the pressure, and variations of 25% are easily tolerated.

Various workers have reported an improvement in proton percentage when gas mixtures are used in the discharge (5, 7). We have tried mixtures of hydrogen with helium, argon, water vapor, and oxygen. In all cases the color of the discharge changed from red, obtained with hydrogen, to blue, and the proton current was reduced.

The characteristics of various types of ion source are listed in Table III. Representative sources have been chosen for each of the three types listed in the Introduction. From an inspection of the data given in this table it can

TABLE III

COMPARISON OF ION SOURCES

Type of source	Canal ray		Capillary arc			Reflection type with magnetic field	Electrode-less discharge
			Metal probe	Metal capil-lary	Glass capil-lary		
Reference	Bouwers, Heyn, and Kuntke (2)	Craggs (3)	Zinn (9)	Lamar, Buechner, and Van de Graaff (6)		Ardenne (1)	Bayly and Ward
Pressure in discharge, μ	20	150	30	≥20	≥20	0.5	10
Power input, w.	2000	400	235	385	135	∼5	450
Canal dimensions, diameter X length, mm.	3 X 5	1.5 X 2.5	1 X 6	0.8 X 0	0.8 X 0	—	2 X 12
Maximum ion current, ma.	0.6	1.8	4.3	1.0	1.5	0.5	0.75
Percentage atomic ions	30?	45	20	20	60	20	60
Maximum energy spread, ev.	35,000?	20,000?	9000?	∼13	∼30	?(Low)	1200?
H_2 consumption, cc. per min. at 760 mm.	3.5	6.5	0.16	0.38	0.6	0.17	0.24
Ratio of protons to gas molecules, %	0.07	0.17	7.5	0.74	2.1	0.85	2.7

be seen that the radio-frequency type of ion source has a performance comparable to that of the best of the other sources. It should be noted that the values given for energy spread are maximum possible values. In the cases of

the Capillary Source with a metal probe (9) and the Radio-frequency Source the great majority of the ions in the beam have a relatively small energy spread, probably less than 100 ev.

Conclusion

The positive ion source described in this paper has operated satisfactorily for several months. The ruggedness, simplicity of operation, and good performance render it well suited for many of the uses for which positive ion sources are required. Improvements in the performance can probably be made by a variation of the electrode geometry and an investigation of the changes produced by varying the frequency of the oscillator used to excite the discharge.

Acknowledgments

References

1. ARDENNE, M.v. Physik. Z. 43 : 91. 1942.
2. BOUWERS, A., HEYN, F. A., and KUNTKE, A. Physica 4 : 153. 1937.
3. CRAGGS, J. D. Proc. Phys. Soc. London, 54 : 439. 1942.
4. FINKELSTEIN, A. T. Rev. Sci. Instruments, 11 : 94. 1940.
5. LAMAR, E. S., BUECHNER, W. W., and COMPTON, K. T. Phys. Rev. 51 : 936. 1937.
6. LAMAR, E. S., BUECHNER, W. W., and VAN DE GRAAFF, R. J. J. Applied Phys. 12 : 132. 1941.
7. LORRAIN, P. Can J. Research, A, 25 : 338. 1947.
8. THONEMANN, P. C. Nature, 158 : 61. 1946.
9. ZINN, W. H. Phys. Rev. 52 : 655. 1937.

GAMMA RAYS PRODUCED IN THE FISSION OF U²³⁵ [1]

BY B. B. KINSEY[2], R. C. HANNA[3], AND D. VAN PATTER[4]

Abstract

This paper describes measurements which have been made on the coincidence counting rate between the fissions produced in an ionization chamber and the discharges of a Geiger counter. By determining the absolute efficiency of the counter, the total energy emitted in the form of γ-radiation was estimated to be about 4.6 ± 1.0 Mev. Measurements have been made on the range of the electrons projected from an aluminum radiator placed between the ionization chamber and two thin-walled counters. From this experiment, the average energy of the radiation appears to be about 2.5 Mev. The result is confirmed by absorption measurements in lead. The absorption curve indicates a fairly homogeneous radiation and gives some evidence for the existence of a softer component with an energy of about 500 kev.

Introduction

It was thought that if γ-rays are emitted in the process of fission, a study of these radiations might yield useful information concerning the mechanics of the process. As a first attempt in this direction, the total energy emitted in the form of γ-radiation, and the hardness of this radiation, has been measured. The coincidence method has been used throughout in order to distinguish γ-rays produced in this way from γ-radiation resulting from the neutron source and from neutron capture in the sample of uranium and in surrounding objects.

The Coincidence Method

Fissions are produced by exposing a thin layer of uranium oxide to thermal neutrons. The layer is deposited on the collector electrode of an ionization chamber connected to a linear amplifier. A Geiger counter is placed nearby; the pulses created by the fissions and by the Geiger counter are fed into a mixing unit. The coincidences recorded are of two kinds, genuine coincidences produced by radiations emitted simultaneously with the fission process and chance coincidences. If q_f is the rate at which the pulses produced by the fissions operate the circuits of the mixing unit, and N is the number of fissions produced in the uranium per second, then $q_f = N\epsilon_f$, where ϵ_f is the efficiency of the ionization chamber and the circuits associated with it. If ϵ_γ is the efficiency of production of discharges in the Geiger counter by radiations emitted by the fission process, the genuine coincidence counting rate is $q_c = N\epsilon_f\epsilon_\gamma$. Von Droste and others (3, 7) have shown that the efficiency of a Geiger counter for γ-radiation is approximately proportional to the energy of the radiation, provided that the walls of the counter are thick enough and made of material of medium atomic weight. Therefore the probability that a

γ-ray of energy E_r, emitted in the fission process, produces a pulse in the mixer is kE_r, where k is a constant, determined by calibration, that depends on the nature of the counter and on the geometry of the experimental arrangement. The probability that a pulse is produced by the gamma-rays of all energies associated with a single fission is:

$$\Sigma n_r k E_r \ = \ k \Sigma n_r E_r \,,$$

where n_r is the average number of quanta per fission of energy E_r. Thus

$$\epsilon_\gamma \ = \ k \Sigma n_r E_r \ = \ k E_0 \,,$$

where E_0 is the total energy emitted in γ-rays per fission. The coincidence counting rate is therefore:

$$q_c \ = \ q_f k E_0 \,.$$

Hence

$$E_0 \ = \ \frac{1}{k} \frac{q_c}{q_f} \ .$$

The total energy of the radiation may thus be measured in terms of the ratio of the genuine coincidence rate to the fission rate when the absolute efficiency of the counter is known. The use of the coincidence method enables the γ-radiation associated with the fission process to be measured separately from that resulting from other processes.

The energy of the radiations has been studied by an adaptation of the method of Mitchell and Langer (6). Two counters, with thin walls of duralumin, were placed side by side and close together with their axes parallel and coplanar with that of the ionization chamber. A thick sheet of aluminum between the ionization chamber and the first counter serves as a radiator of secondary electrons. The triple coincidence rate between the ionization chamber and the two counters is measured and plotted as a function of the thickness of aluminum absorbers placed between the latter. The thickness of aluminum for which the genuine coincidence counting rate is reduced to one-half can be used as a measure of the energy of the radiation if this radiation is assumed to be homogeneous in energy.

To determine the degree of homogeneity of this radiation a study has been made of its absorption in lead. This has been done by placing lead sheets between the chamber and a thick-walled counter adjacent to it.

Apparatus

The first experiments were made with a neutron source consisting of a mixture of beryllium powder with several curies of polonium, equivalent in neutron production to about half a gram of a radium–beryllium mixture. We are indebted to the Health Division of this Laboratory for the loan of this source. In subsequent experiments a 1.2 gm. radium–beryllium source was used. With the polonium source, roughly equal numbers of neutrons and

γ-rays are emitted and it was considered that, with this source, the background of γ-radiation would be less intense than with a radium–beryllium source. However, it was found later that a higher neutron flux could be obtained with the radium source for the same background of γ-radiation if the counters were screened from the source by thicker plates of bismuth.

The neutron source and screening arrangements are shown in Fig. 1.
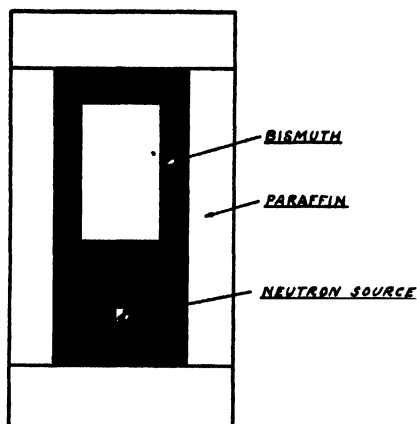
FIG. 1.   *Neutron source and screens.*

A large cylindrical cavity in paraffin wax—10 in. in diameter—was formed by a paraffin cylinder and cylindrical paraffin plates at top and bottom. The neutron source was placed in the center of massive cylinders of metallic bismuth. Four inches of bismuth were used to screen the source from the enclosure in which the ionization chamber and counters were installed. A bismuth cylinder with walls 2 in. thick screened the counters from the capture radiation produced by the neutrons in the paraffin and another bismuth disk, 2 in. thick, closed the top of the cavity. With the radium–beryllium source mentioned above, the flux of thermal neutrons in the enclosure was measured with the aid of a boron trifluoride counter and found to be of the order of 1000 thermal neutrons per sq. cm. per sec.

The ionization chamber used in these experiments was constructed with platinum electrodes, mounted in a lead glass tube. A total of 25 mgm. of a sample of uranium oxide, enriched in U²³⁵ by a factor of about 20 to 1, was deposited—as uniformly as possible—on a thin platinum sheet with an area of about 25 sq. cm. This sheet was rolled to form a cylinder, 8 cm. in length, to make one electrode of the ionization chamber. The other electrode consisted of a cylinder of platinum somewhat longer than the first, and concentric with it. After some preliminary heating *in vacuo*, the chamber was filled with pure argon at atmospheric pressure and sealed off. Under these conditions, the time taken to create the pulses produced by the fissions is determined by

the mobility of free electrons moving in the electric field between the electrodes. With 1000 v. between the electrodes, the collection time of the electrons is less than a microsecond. To preserve the sharp front of these pulses as they are formed at the collector of the ionization chamber, the latter was connected to a linear amplifier of the 'fast' type with an upper frequency limit of about 2 Mc.

Measurement of the Total Energy

For these measurements the ionization chamber was supported centrally in the enclosure shown in Fig. 1 and contained in an aluminum tube joined at its ends to a thin, perforated steel sheet. Four similar aluminum tubes, parallel to the first, were disposed at equidistant positions about it, and served as supports to locate the Geiger counters. Several copper-walled Geiger counters were made up for this purpose, each about 1 in. in diameter with an active portion about 8 cm. in length. They were filled with a mixture of argon (9 cm. pressure) and alcohol (1 cm. pressure). Owing to the very high counting rates which were unavoidable in these measurements, it was essential to refill the counters after two or three days of continuous use.

The distance between the axes of the tubes containing the ionization chamber and the Geiger counters was made as small as possible—4.4 cm. The location of the counters and the ionization chamber with respect to each other was a matter of considerable importance in securing reproducibility in the measurements. To minimize errors which might result from inaccuracy in location, two Geiger counters were therefore used successively and the results were averaged.

The measurements fall into two parts: (a) measurement of the ratio of the coincidence rate between the ionization chamber and a Geiger counter to the fission rate in the chamber, and (b) the absolute calibration of the counter in the same conditions.

(a) THE FISSION-γ COINCIDENCE RATE

In order to verify that the results obtained were independent of instrumental conditions, a number of measurements were made with different coincidence resolving times and with different potentials across the ionization chamber. The counting rates in the Geiger counters were considerable—about 200 per sec.—so that it was necessary to correct for chance coincidences. This correction was measured directly in each case, by determining the coincidence rate between the fissions and the pulses produced by another Geiger counter mounted outside the thermal neutron enclosure, screened from it and operated by a separate source of γ-rays at a similar counting rate. The coincidence-resolving time was calculated from the usual formula, $q_{ch} = 2q_f q_1 \tau$, where q_1 is the counting rate in this external counter and τ is the resolving time.

With the polonium source, the fission counting rate was nearly constant throughout the period of these experiments—about six weeks—at about 1.9 fissions per second. With the radium source, slight variations in the screening

arrangements were made from time to time, with the result that varying fission rates were used, up to 4.4 fissions per second.   Fig. 2 is a typical bias curve—one of many—obtained with a discriminator connected to the output of the
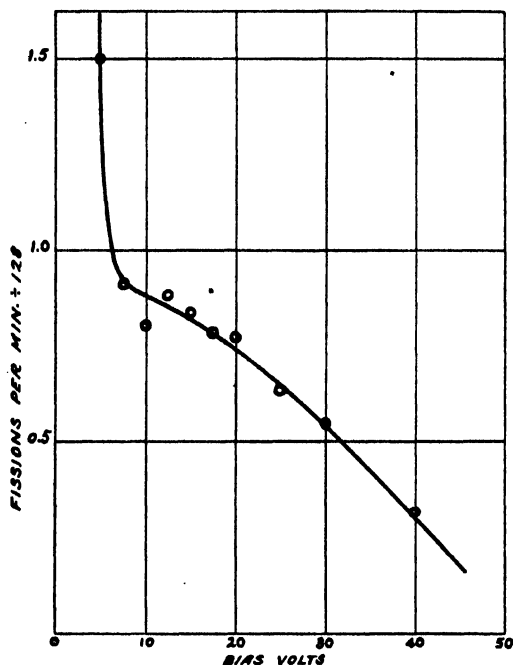
FIG. 2.   *Bias curve for fission pulses.*

amplifier.   In order to operate the multivibrator circuits of the mixer unit, the magnitude of the pulses must exceed a certain threshold.   The gain of the amplifier connected to the ionization chamber was adjusted so that the natural α-particles produced pulses lying below this threshold and only fissions would work the mixer.   The threshold was equivalent to pulses of about 10 v. peak, the gain was fixed so that the knee of the bias curve came just below this amount.   Above it, the bias curve is nearly flat.   Thus, the efficiency of counting fissions is nearly unity and independent of the gain.

The results are collected in Table I.   The Series A refer to one counter, the Series B to another.   The errors given are the statistical errors of the counts. It will be seen that there is no significant change in the coincidence rate with different potentials across the ionization chamber; nor is there any significant variation of the coincidence rate with the resolving time.   The error in ϵ_γ will depend on the statistical accuracy with which the fission counting rates have been measured and on the accuracy of location of the counters with respect to the ionization chamber.   The average value of ϵ_γ for all results is 3.0 $\pm$ 0.2 $\times$ 10⁻⁴.   It is probably accurate to 10%.

TABLE I

FISSION-γ COINCIDENCES

(All counting rates in units of 128)

Counter	Total coinc. rate/hr.	τ μsec.	Corrected chance rate/hr.	Genuine rate/hr.	q_f per min.	$\epsilon_\gamma \times 10^3$
Polonium–beryllium source						
A	0.32 ± .03	6.8	0.22 ± .02	0.10 ± .04	0.9	
A	0.30 ± .03	3.5	0.125± .01	0.18 ± .03	0.9	
HT 860v.	0.24 ± .03			0.15 ± .05	0.9	
A 640v.	0.29 ± .04	1.8	0.10 ± .02	0.19 ± .05	0.9	
	0.31 ± .04			0.20 ± .04	0.9	
420v.	0.25 ± .03		0.08 ± .03	0.17 ± .04	0.9	
A	0.20 ± .02	1.5	0.05 ± .01	0.15 ± .02	0.9	
A	0.23 ± .01	0.66	0.03 ± .005	0.20 ± .01	0.9	
A	0.21 ± .01	0.66	0.024± .002	0.19 ± .01	0.9	
B	0.34 ± .015	7.0	0.17	0.17 ± .01	0.9	
B	0.206± .01	0.7	0.033	0.17 ± .01	0.9	
			Weighted mean	0.18 ± .01		3.3 ± 0.3
Radium–beryllium source						
A	0.454± .015	2.6	0.22	0.234± .03	1.0	2.4
A	0.61 ± .02	2.6	0.356	0.254± .03	1.0	2.6
A	0.835± .02	2.9	0.45	0.38 ± .03	1.9	3.3
B	0.59 ± .02	1.85	0.27	0.32 ± .03	2.0	2.7
			Mean			2.8 ± 0.3

(b) CALIBRATION OF THE GEIGER COUNTERS

To a sufficient accuracy, the efficiency of counting of these Geiger counters is proportional to the energy of the radiation. Provided that the quantum energy emitted in fission is not too different from the energy of the, γ-radiation used to calibrate the counters, calibration at one energy is sufficient. For this purpose the 2.62 Mev. radiation emitted in the transition ThC″ ⟶ ThD was chosen and the absolute strength of the source determined by measuring coincidences between the various products involved in the branching disintegration, ThC ⟶ ThD. The results were checked by similar measurements with the long-period cobalt isotope.

About 65% of the atoms of ThC disintegrate with β-emission to form ThC′. This is a short-lived body with a period of the order of 10^{-7} sec. (4). The remainder (35%) emit α-particles of lower energy giving ThC″, a body which may be isolated from the thorium active deposit by the method of recoil. The calibration was made in two ways, firstly, with the aid of a source of ThB in transient equilibrium, and secondly, with a source of pure ThC″.

3×10^{-7} sec.

ThC′

β α

β

ThB ────→ThC   ThD

10.6 hr.

α β

ThC″

3.2 min.
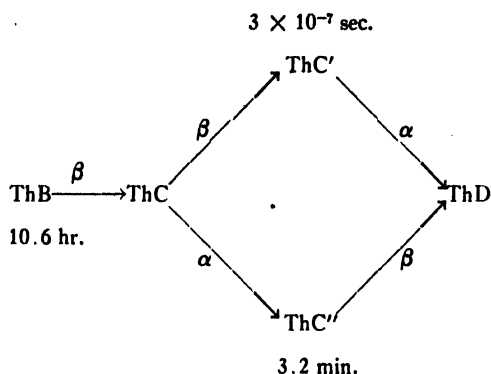
In the first calibrations with subsidiary apparatus, the coincidence counting rates between α- and β-particles has been measured, correcting for the fact that not all the β-particles detected follow the transition ThC ⟶ ThC′ ⟶ ThD. This measurement gives the rate of disintegration of ThC′ and, hence, that of ThC″. The active deposit was then placed in the counter assembly in the position normally occupied by the uranium layer and the counting rate for γ-rays determined. Following von Droste, 70.5% of this counting rate was assumed to be due to the 2.62 Mev. radiation.

In the second calibration, the source of ThC″ was placed in the location of the uranium layer and its absolute activity determined by measuring coincidences between a γ-counter, used in the fission measurements, and a thin-walled β-counter nearby. It was assumed that each disintegration of ThC″ leads to the emission of two γ-rays in cascade, one of 2.62 Mev. and the other of 0.58 Mev. It is by no means certain that all disintegrations of ThC″ follow this course, but it does seem established that very nearly one quantum of the 2.62 Mev. radiation follows every transition (1). The contribution of the lower energy radiations being in proportion to their energies and to their intensities, the error involved in the result will be negligible if the assumption is made that 0.58 Mev. is the mean energy of these radiations.

(1) The α–β Coincidences

A source of ThB was deposited on a thin foil of aluminum (about 5 mgm. per sq. cm.) by the method of recoil from a radiothorium preparation. A small fraction of this source was selected—about a millimeter or two in diameter—and secured to a thin aluminum base which was mounted on a wire frame placed centrally in the aluminum tube supporting the ionization

chamber. For coincidence measurements the wire frame was mounted
equidistant between the openings of two thin-walled counters each closed by
a mica window of about 4.5 mgm. per sq. cm. thickness. Of these counters,
the one was operated as a normal Geiger counter with an argon–alcohol
filling, the other, facing the active surface, was filled with pure argon and
used as a proportional counter. The stopping power of the materials between
the active deposit and the sensitive portion of this counter was sufficient to
stop all the 4.6 cm. α-particles due to the disintegration of ThC and to allow
only those to be detected which were due to the disintegration of ThC' (8.6
cm. range). The total stopping power between the active surface and the
β-counter was about 15 mgm. per sq. cm. The β-particles recorded are
divisible into a hard and a soft variety, the hard type resulting from the disinte-
gration of ThC'' and ThC; the soft type arise from the disintegration
ThB $\longrightarrow$ ThC and the internal conversion electrons due to the 0.24 Mev.
γ-ray originating in this transition. The number of these electrons is approxi-
mately 0.25 electron per disintegration of ThB. A considerable fraction of the
softer β-radiation will be absorbed in the small amount of material between
the active surface and the β-counter. Absorption curves were made with
aluminum absorbers to determine the fraction of the β-counting rate which was
due to the higher energy β-particles. Fig. 3 is a typical absorption curve.
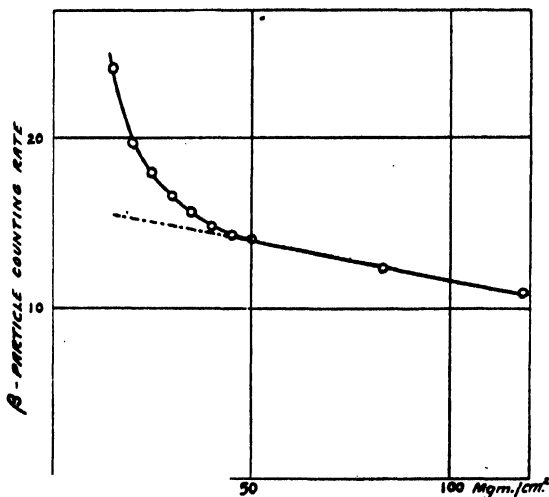
FIG. 3. *Absorption of β-particles.*

The first portion of the curve, where the absorption is most marked, is assumed
to represent the β-particles of ThB and the internal conversion electrons
referred to above; the flatter, linear portion which follows is due to the higher
energy electrons, and if this curve is extrapolated back to zero absorption an
estimate can be made of the fraction of the observed β-radiation which is due
to ThC and ThC''. From the curve, and to an accuracy of 10%, we find that
this quantity is 0.65.

If, then, N is the number of atoms of ThB disintegrating per second, N will also represent the rate of disintegration of ThC, because the time allowed for the preparation of the active deposit was always sufficient to obtain equilibrium between the two elements. If q_α, q_β, $q_{\alpha\beta}$ represent the counting rates of the α-particles, β-particles, and of coincidences, ϵ_α, ϵ_β the efficiencies* of the counters, and μ that fraction of the β-particles observed which are due to the disintegration of ThC and ThC″ ($\mu = 0.65$), then:—

$$q_\alpha = N\epsilon_\alpha \times 0.65$$

$$\mu q_\beta = N\epsilon_\beta$$

$$q_{\alpha\beta} = N\epsilon_\alpha\epsilon_\beta \times 0.65,$$

whence

$$N = \mu q_\alpha q_\beta / q_{\alpha\beta}$$

(the factor 0.65 representing the proportion of ThC atoms disintegrating to form ThC′). The number of disintegrations of ThC″ occurring per second is given by $N'' = 0.35N$. If Q_γ is the counting rate in the γ-counters when the source is placed in the central position normally occupied by the ionization chamber, the efficiency for the detection of the 2.62 Mev. radiation is obtained from the relation:

$$\epsilon_\gamma = 0.70\, Q_\gamma / N'',$$

using von Droste's result already referred to.

Some care is necessary in inserting numerical quantities into these equations. In the first place, the source is decaying continuously, so that counting rates have to be referred to a standard time, which in this case was taken to be the mean time of the coincidence run. The observed value of q_β is to be corrected for the γ-counting rate and the background rates due to other γ-sources in the vicinity and the result referred to this standard time. The coincidence rate is to be corrected for the chance rate. The chance rate was measured by determining the coincidence rate between the α-particles and the pulses produced by an external Geiger counter, operated at approximately the same counting rate. The result gives a measure of the coincidence-resolving time; it is then corrected to allow for differences between the counting rate of the external counter and the β-counting rate in the coincidence measurements and for any differences between the α-counting rates. The γ-counting rate of the thick-walled counters, Q_γ, was determined for each of two counters, in four distinct positions of the foil holding the active deposit, corresponding to the plane of the foil lying in the plane containing its center and the axis of a Geiger counter, or perpendicular to it. The mean of these eight measurements, corrected to the standard time, is taken as Q_γ. Table II gives the

---

* ϵ_β refers to the electrons produced in both branches of the transition ThC ⟶ ThD, and is assumed to be the same for both.

TABLE II

α–β COINCIDENCES

(Counting rates in units of 128 per min.)

Expt.	τ sec. $\times 10^6$	q_α	q_β	$q\beta$ Corr.	$q_{\alpha\beta}$	Chance rate		$q_{\alpha\beta}$ Corr.	$N''\times$ 10^{-4} sec.$^{-1}$	Q_γ	ϵ_γ $\times 10^3$
						Ext.	Corr.				
A	1.1	120	143	134	0.494	0.078	0.077	0.417	1.88	21.6	1.7
B	7.0	81	102	91	0.474	0.206	0.196	0.278	1.45	14.4	1.5
C	4.4	49	58	53	0.493	0.078	0.056	0.437	0.32	5.3	2.5

results of three measurements. The first two measurements (A and B) were made on the same source at times 5.5 hr. apart, and with different resolving times. It will be seen that the values for ϵ_γ agree closely. The third measurement (C) was made with a different source and with different efficiencies for collection of α- and β-particles. The result for ϵ_γ is appreciably higher. In all these measurements the same value of μ is assumed, viz., 0.65. The fifth column in the table gives the β-counting rate corrected for the γ-counting rate. The correction was made by interposing a thick plate of aluminum between the source and the β-counter. The correction is relatively high owing to the high γ-ray background in the laboratory. The seventh and eighth columns give, respectively, the chance rate—as measured directly with the external counter—and as corrected to allow for the different conditions in the coincidence arrangement. This latter result is subtracted from the results of the sixth column to give the figures in the ninth column, which are used to calculate N''. The mean of these three measurements gives:

$$\epsilon_{2.62} = 1.9 \times 10^{-3}.$$

(2)· *The β–γ Coincidences*

The source of ThC'' was deposited on a thin layer of aluminum about 1 sq. cm. in area, mounted on the wire frame used in the previous measurements. The experiments were performed with the frame situated in the middle of the aluminum tube used to support the ionization chamber. A hole in the wall of this tube allowed β-particles to emerge and operate a thin-walled β-counter. As observed above, this method allows the efficiency of the Geiger counters used in the fission-γ coincidences to be measured directly by using these counters to detect the γ-radiation. The source of ThC'' was prepared by recoil from a source of ThB in equilibrium with its products. The purity of the source was tested by plotting decay curves of the activity produced; no impurity was detected.

The procedure followed was to measure the total number of β and γ counts and coincidence counts in a period comprising several lifetimes of the radioactive deposit (usually 15 to 18 min.). A rough value of the efficiency of detecting the γ-rays is then given by the ratio of the total coincidence counts to the total β-counts. To correct for coincidences due to cosmic rays, and

for the background counting rate in the β-counter, the total number of counts is again measured in a period of time equal to that of the first period and immediately following it. Let $p_{\beta\gamma}$ and p_β represent the total number of coincidences and the total number of β-particles respectively, recorded in the first period, $p'_{\beta\gamma}$ and p'_β the corresponding quantities for the second period. If ϵ_γ is the total efficiency for the detection of the γ-rays in this transition, then ϵ_γ is given by the equation:—

$$\epsilon_\gamma(1 + \tau N) = (p_{\beta\gamma} - p'_{\beta\gamma})/(p_\beta - p'_\beta) \cdot (1 + \epsilon'_\gamma/\epsilon_\beta),$$

where τ is the resolving time of the mixer, ϵ_β and ϵ'_γ are the β and γ efficiencies of the β-counter, and N is the number of atoms of ThC'' disintegrating per unit time at the commencement of the first period. If the activity has decreased to xN at the end of this period, the equation is accurate to small quantities of the order of $(N\tau)^2$, $xN\epsilon_\beta\tau_0$ and $xN\tau$, where τ_0 is the dead time of the β-counter*. Three different resolving times were selected and four measurements were made in each case corresponding to the four positions of the source with respect to the Geiger counter. The results are given in Table III; the measured values of ϵ_γ are corrected to allow for the effect of the 0.58 Mev. radiation. In making this correction, it is assumed that the counting rates due to the two γ-rays are in direct proportion to their energies; to allow for this, the value of the efficiency calculated from the figures in the fourth column of Table III are multiplied by the factor 0.82 to give the efficiency for the 2.62 Mev. radiation. The ratio $\epsilon'_\gamma/\epsilon_\beta$ is approximately 7%.

The errors given in the fourth and fifth columns are the statistical errors in counting. The results show considerable deviations among themselves. To a certain extent this is due to the low statistical accuracy of the coincidence measurements, the total number of coincidences recorded in a run varying between 30 and 800, depending on the strength of the source and the geometrical arrangement. The differences between the mean values of ϵ_γ for different resolving times do not appear to be significant. It is possible that

---

* *This equation is calculated on the following basis:*

     It is assumed that the β-counting rate is big enough to warrant correction for the dead time and that the γ-counting rate is low enough to ignore it. The coincidence rate is to be corrected for the chance coincidences; the cosmic ray coincidence rates are eliminated from the result by taking the differences between the quantities $p_{\beta\gamma}$ and $p'_{\beta\gamma}$ assuming that this rate is not seriously affected by the dead time. The difference between p_β and p'_β eliminates the background counting rate of the β-counter. To this approximation, a simple calculation gives:

$$\frac{p_{\beta\gamma} - p'_{\beta\gamma}}{p_\beta - p'_\beta} = \epsilon_\gamma \cdot \frac{1 - N(1 + x)^2 (\epsilon_\beta\tau_0/2 - \tau)}{1 - N\epsilon_\beta\tau_0/2 \cdot (1 + x)^2} \cdot (1 - \epsilon'_\gamma/\epsilon_\beta),$$

which reduces to the equation given above, where terms of the order of $(N\tau)^2$, $xN\epsilon_\beta\tau_0$ and $xN\tau$ are neglected. The dead time of the Geiger counters was determined by measuring the deviation from linearity of the plot of the logarithmic decay of the ThC'' source. It was found to be about 150 μsec. In these measurements ϵ_β was usually of the order of 2%. Thus, N being of the order of 10^4, the quantity $N\epsilon_\beta\tau_0/2$ is of the order of a few per cent and has a negligible effect on the result. For a period of 15 min., $x = 0.025$ and terms containing x are negligible.

TABLE III

β–γ COINCIDENCES

τ, μsec.	$N \times 10^{-4}$sec.$^{-1}$	τN, %	$\dfrac{p_{\beta\gamma} - p'_{\beta\gamma}}{p_\beta - p'_\beta} \times 10^3$	$\epsilon_{2.62} \times 10^3$
0.5	4.2	3	1.73 ± .12	1.46 ± .09
	5.5	3	1.47 ± .14	1.24 ± .11
	2.5	1	1.75 ± .10	1.51 ± .08
	7.0	4	1.73 ± .10	1.45 ± .08
			Mean	1.42
2.9	2.1	6	2.03 ± .16	1.67 ± .12
	1.6	5	1.77 ± .17	1.46 ± .13
	0.7	2	1.36 ± .20	1.18 ± .16
	1.0	3	1.20 ± .20	1.03 ± .17
			Mean	1.34
5.3	2.7	14	2.63 ± .11	1.98 ± .10
	2.4	13	2.38 ± .13	1.82 ± .10
	4.0	21	1.93 ± .16	1.33 ± .10
	4.4	22	3.06 ± .12	2.06 ± .08
			Mean	1.80
			Mean	1.5 ± .15 × 10^{-3}

some genuine coincidences were lost at the lower resolving time; experiments which have been made to test this point indicate that the loss is not serious until the resolving time is reduced below 0.5 μsec. The mean value is

$$\epsilon_{2.62} = 1.5 \pm 0.15 \times 10^{-3}.$$

The measurements of the efficiency for the 2.62 Mev. radiation by the two methods do not agree very well but probably not worse than might be expected from the crudity of the methods. However, even this low accuracy is sufficient for rough measurements of this type. Taking the mean of the two methods, we obtain

$$\epsilon_{2.62} = 1.7 \pm 0.2 \times 10^{-3}.$$

To estimate the total energy emitted as γ-rays, this result must be compared with that for the efficiency of the fission γ-rays. The total energy radiated is thus found to be 4.6 Mev.

(3) *Calibration with Co^{60}*

To check on the figures obtained above, the counters have been calibrated by measuring the γ–γ coincidences produced in them when a sample of active cobalt is placed in the location of the fission chamber. Deutsch, Elliott, and Roberts (2) have shown that the β-particles emitted by the long period radioactive body (5.3 years) are associated with two γ-rays emitted in cascade, one with energy 1.10 Mev. and the other with 1.30 Mev. After

making the usual corrections for chance coincidences, the γ-ray efficiency, calculated from the ratio of the γ–γ coincidence rate to the γ-counting rate in either counter, will represent the efficiency for the mean energy of this radiation, viz., 1.20 Mev. If ϵ_γ represents this mean efficiency, q_c and q_γ the coincidence and γ-counting rates, then:

$$\epsilon_\gamma = q_c/q_\gamma \cdot (1 + q_\gamma \tau_0),$$

where τ_0 is the dead time.

The results are given in Table IV. A and B refer to two runs with the same source under slightly different conditions, C to a run with another weaker

TABLE IV

γ–γ COINCIDENCES WITH Co⁶⁰

(Counting rates in units of 128 per min.)

Run	Background rate	Mean γ-rates		Coincidence rates $\times 10^{-3}$			$\epsilon_\gamma \times 10^3$
		Counter 1	Counter 2	Total	Chance	Genuine	
A	4	196	193	0.260 ± .007	0.123 ± .005	0.137 ± .009	0.77 ± .06
B	4	204	206	0.281 ± .007	0.137 ± .005	0.144 ± .009	0.77 ± .06
C	4	104	100	0.107 ± .002	0.034 ± .001	0.073 ± .002	0.80 ± .02
D	4.5	85.9	83.4	0.061 ± .001	0.022 ± .001	0.039 ± .0015	0.79 ± .02

source, D to a third source, weaker still. The coincidence resolving time was $0.76 \pm 0.02 \ \mu$sec. The errors given in Table IV are the statistical errors of counting. From this table we find that the mean value of ϵ_γ is $0.78 \pm 0.02 \times 10^{-3}$. This gives 4.6 Mev. for the total energy of radiation in the fission process, in agreement with the previous result.

In the following pages it will be shown that the hardness of the fission radiation is about the same as that of the 2.62 Mev. radiation of ThD. Our result for the total energy makes it reasonable to assume that no very high energy radiation is emitted and that the counter efficiency is indeed linear in the energy range concerned. To test the linearity at low energies the efficiency for the radiations from radioactive gold has been measured in a similar manner. These radiations consist of two γ-rays of nearly equal intensity and energies, 280 and 440 kev. and a weaker γ-ray of 70 kev. (5). The efficiency was found to be 3.2×10^{-4}. This result is about one-fifth of the efficiency of the ThD radiation; the ratio of the sum of the energies of the gold radiation to 2.62 Mev. is rather more than this.

It seemed possible that a fraction of the measured efficiency of the fission radiations was due to recoiling nuclei in the Geiger counter produced by fast secondary neutrons associated with fission. A rough estimate of this effect gives a total contribution to the efficiency of about 1.10^{-5},—a negligible

amount. To test this possibility, the Geiger counter was operated in the proportional region, just below the threshold*. The gas amplification of the counter was certainly sufficient to allow all recoil nuclei to operate the mixer, because the total counting rate far exceeded any reasonable value for the counting rate of the recoils that might have been anticipated. Two runs were taken, each over a period of many hours, with $\tau = 1.8$ μsec. In both cases, the coincidence rates observed were only slightly in excess of the chance rates to be expected; 50% in one experiment and 20% in the other. The net result is a maximum possible contribution to the efficiency due to neutrons of about 6×10^{-5}. This is negligible in comparison with the observed efficiency.

In view of the fact that the uranium layer in the ionization chamber is extended over a length of about 8 cm., and the thorium active deposits used in the calibration experiments were effectively point sources, it seemed necessary to determine whether a correction should be applied to the measured efficiencies to allow for this difference. This was done by plotting a curve of the γ-counting rate in the Geiger counter as a function of the position of the thorium source along the axis of the tube which serves as a support for the ionization chamber. The correction to be applied was found to be less than 5% of the total efficiency, and consequently it has been ignored in the preceding calculations. The possibility was also examined that scattering from the walls of the bismuth enclosure would increase the measured efficiency for detection of the fission radiation, as contrasted with that for the thorium radiations, for which the calibration work was performed with the apparatus outside the enclosure. No detectable difference in the counting rate of a Geiger counter was observed when the apparatus with a thorium source in position was placed inside or outside the enclosure.

The Absorption of Secondary Electrons in Aluminum

To measure the quantum energy of the radiation, the apparatus indicated in Fig. 4 was set up. The ionization chamber, I, used in previous experiments, was mounted in a steel box together with two thin-walled duralumin counters,

FIG. 4. *Arrangement for measurements of absorption of secondary electrons in aluminum.*

G, with their axes lying in a plane. The chambers and the counters with their leads were screened electrically from each other. An aluminum plate, P, —$\frac{1}{4}$ in. thick—serves as the radiator of secondary electrons set free by the fission γ-radiations produced in the chamber. Thin plates of aluminum, Q,

---

* *The counter was connected to the mixer through a fast amplifier.*

were placed between the two counters and were used to study the absorption of the secondary electrons. In order to give the optimum counting rates the counter farthest from the ionization chamber was made bigger than the other (1.5 in. in diameter as compared with 1 in.). The experimental procedure consisted in measuring the triple coincidence rate between the fission chamber and the two counters as a function of the thickness of the aluminum plates.

For this experiment, the 1.2 gm. radium–beryllium source was used. The steel box was placed inside the container indicated in Fig. 1. The bias curve of the fissions produced in the chamber was similar to curves previously obtained; the counting rate for fissions was about 3.4 fissions per sec., the single counting rates in the Geiger counters, about 400 per sec. Since the efficiency for counting triple coincidences in these circumstances is much lower than in the simple arrangement used in previous experiments, the coincidence counting rates observed were exceedingly low. Most measurements involved about 100 hr. of continuous operation. To ensure the maximum stability of the electrical apparatus, all the electrical units were fed from constant voltage transformers. To make certain that power or tube failures over the counting periods would not affect the result, the reading of the meter recording triple coincidences was plotted against the time. Failures of the equipment could be detected by interruptions in the straight lines obtained in this way. The triple mixer used in these measurements was similar, in principle, to the double mixer previously used.

The correction for the chance coincidence rate amounted to about 20% of the genuine rate in most cases. The chance rate between random counts in the three counters was negligible; the high value for the correction arose from the fact that some electrons produced externally, or some electrons produced by radioactive atoms in the counter walls, could traverse both Geiger counters, causing coincidences between them. With no absorber between the counters, this coincidence rate was about 30 per sec. The correction was determined by measuring the triple coincidence rate between these two counters and another situated outside the bismuth enclosure and operated with a separate radioactive source. The equivalent resolving time was calculated from the formula:

$$q_{ch} = 2q_1 q_{\beta\beta} \tau,$$

where q_1 is the counting rate in the external counter and $q_{\beta\beta}$ is the coincidence rate between the thin-walled counters. To verify that the electrical conditions, in fact, did remain constant, the resolving times were measured for each absorber and often several times during the course of a run. This quantity varied very little from 0.90 μsec.

The results are given in Table V. The 'chance rate' was calculated from the formula above, when q_1 is made equal to the fission counting rate.

TABLE V

Absorption of secondary electrons in aluminum

(Coincidence rates in units of 128 per hr.)

Absorber thickness, mgm. Al per sq. cm.	0	50	110	145	190	335
Total coincidence rate	0.036	0.027	0.026	0.0122	0.0173	0.0103
Chance rate	0.007	0.006	0.005	0.004	0.0035	0.0024
Genuine rate	0.029	0.021	0.021	0.0081	0.014	0.0079

The results of these measurements are plotted in Fig. 5. The statistical errors in counting are indicated for each point. For purposes of comparison a similar curve has been taken for the absorption of the secondary electrons
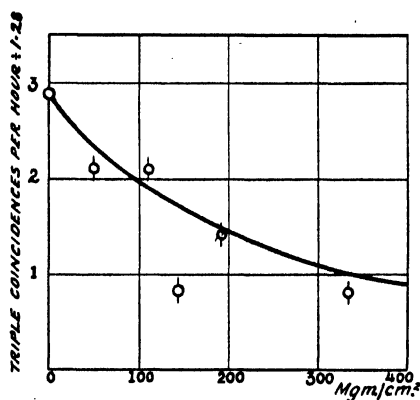
FIG. 5. *Absorption of secondary electrons in aluminum. Full line: absorption curve of electrons due to the 2.6 Mev. radiation of ThD.*

ejected by the radiation of ThB in equilibrium with its products. In this case, the thorium active deposit was surrounded by a lead cylinder 1 cm. in radius. The walls of the counters were each about 30 mgm. per sq. cm. in thickness. Under these conditions, the electrons observed are due almost entirely to the 2.62 Mev. radiation. The fission radiation would thus appear to have a similar hardness.

Absorption in Lead

To test the results of the previous section, the absorption of the fission radiation in lead was examined. The arrangement is shown diagrammatically in Fig. 6. A thick-walled Geiger counter was mounted with its axis about

9 cm. from the axis of the ionization chamber and screened from it electrically. Flat lead plates about 2 in. wide were introduced between the two. The coincidence rate between the fissions and the pulses in the Geiger counter were studied as a function of the thickness of the lead. The neutron source was the 1.2 gm. radium–beryllium source used in previous measurements.
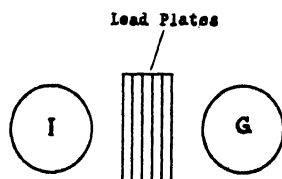
FIG. 6.   *Arrangement for absorption measurements in lead.*

Owing to the relatively low efficiency of detection of the fission radiation in this arrangement, the chance coincidence correction is high. The resolving time chosen for these measurements was 0.70 μsec.; separate measurements of this resolving time were made for each absorber to check possible deficiencies in the electrical apparatus. The measured values seldom differed from the mean by more than 2 or 3%. All the electrical equipment was operated from mains supplied through constant voltage transformers. The fission counting rate was about 3.7 fissions per sec. The counting rate in the Geiger counter was about 360 per sec. This counter was removed and refilled at intervals.

The results are given in Table VI. The chance coincidence rates were measured, as before, by determining the rate of coincidence between the fissions and the pulses produced by an external Geiger counter.

TABLE VI

ABSORPTION OF FISSION RADIATION IN LEAD

Absorber thickness, gm. per sq. cm.	Coincidence rates per hour in units of 130		
	Total	Chance	Genuine
0	0.198	0.062	0.136
3.5	0.161	0.063	0.098
5.7	0.184	0.062	0.122
7.3	0.142	0.062	0.080
11.4	0.144	0.073	0.071
17.0	0.125	0.069	0.056
24.3	0.102	0.060	0.042
27.9	0.103	0.060	0.043

The results in Table VI are plotted in Fig. 7, together with an absorption curve for the radiation of the thorium active deposit for comparison. The statistical errors of the points in the fission radiation curve are indicated by

the vertical lines. The contribution of the 2.62 Mev. radiation of ThD amounts only to 54% of the total at zero absorption; von Droste gives 70% for this figure. Presumably the difference is due to the greater likelihood of the softer radiations being scattered into the counter from those parts of the lead absorbers situated outside the direct beam of radiation. To test whether the bismuth enclosure had any effect on the absorption curve of the fission radiation, two curves were made with the thorium radiation, one with the supporting box outside the enclosure, and one with it inside. After correcting for the decay of the source, to an experimental error of 1 or 2%, no difference could be detected between the two curves at any point.
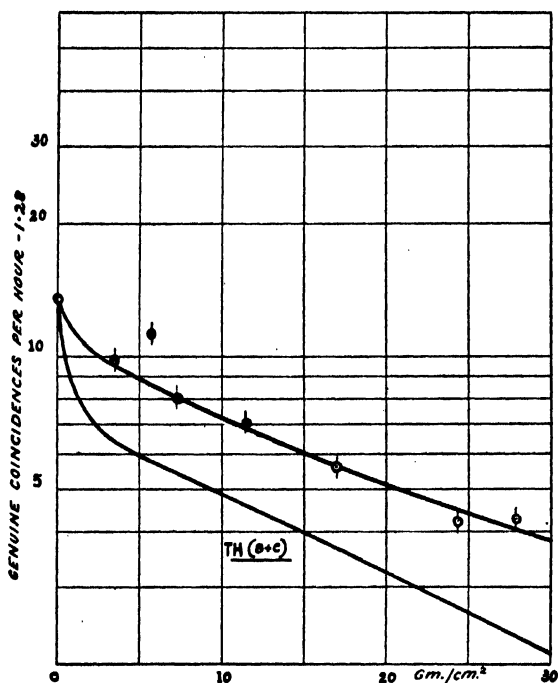
FIG. 7. Absorption of fission radiation in lead.

It will be seen that the average absorption of the fission radiation in lead is very similar to that of the hard component of the thorium radiation—about 0.043 sq. cm. per gm.—and that this absorption is very uniform. It would appear, from this, that the fission radiation is fairly homogenous. The previous measurements on the absorption in aluminum of the secondary electrons seem to eliminate the possibility that this radiation is, in reality, a much harder radiation with a similar lead absorption coefficient.

The absorption curve of Fig. 7 indicates the presence of a soft component in the fission radiation. An attempt was made to separate this soft component from the harder radiation by using a thin-walled counter as detector, with a

thin layer of gold (5 mgm. per sq. cm.) deposited on its inner surface. The gold layer would give a greater sensitivity for the lower energy radiation, the thin walls decreasing the sensitivity for detection of the harder component by reducing the number of secondary electrons ejected from the walls. These
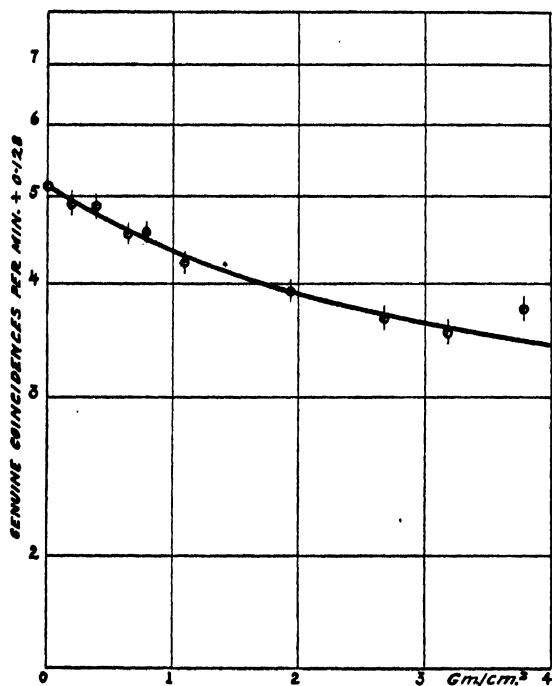
FIG. 8.   *Absorption of fission radiation in lead.*

TABLE VII

ABSORPTION OF FISSION RADIATION IN LEAD

Thickness of absorber, in gm./sq. cm.	Genuine coincidence rates $\times$ 10^3/128 per min.	
0	5.03 ± 0.4	5.14 ± 0.2
0.196	4.90 ± 0.2	
0.386	4.88 ± 0.2	
0.631	4.55 ± 0.2	
0.772	4.58 ± 0.2	
1.085	3.99 ± 0.2	4.45 ± 0.2
1.940	4.05 ± 0.2	3.81 ± 0.2
2.68	3.74 ± 0.2	3.65 ± 0.2
3.81	3.31 ± 0.2	3.77 ± 0.2
3.77	3.76 ± 0.2	3.82 ± 0.2

efforts were unsuccessful; for considerations of sensitivity, it was not possible to place the ion chamber and Geiger counter sufficiently far apart to reduce the relative number of Compton recoils produced at the walls of the ion chamber and passing into the counter. Following these attempts, an effort

was made to plot the absorption curve more carefully for small thicknesses of lead. The gold-lined counter was used (1.25 in. in diameter), placed with its axis 5.4 cm. from that of the ion chamber.   In these conditions, the chance rates were small in comparison with the genuine coincidence rates. The results are given in Table VII. The mean values of these measurements are plotted in Fig. 8. There would appear to be some soft radiation; the absorption coefficient is about 0.17 sq. cm. per gm., corresponding to an energy of some 500 kev. If this radiation really represents a homogeneous γ-ray, then inspection of the curves indicates that there is probably less than one quantum emitted per fission.

The full line connecting the experimental points in Fig. 7 is drawn to pass through the point for zero absorption and to follow the curve of Fig. 8 up to 4 gm. per sq. cm.   Thereafter, the best fit is made to the experimental values. It will be seen that the two curves agree quite well; one point at 5.7 gm. per sq. cm. lies rather far from the mean.

Conclusions

In addition to the possible existence of soft components, these measurements indicate that two radiations with an energy of 2.5 Mev. are emitted in each fission process.   Unfortunately, the sensitivity of the apparatus is not high enough to allow of the verification that two such γ-rays are emitted per fission, by observing γ–γ coincidences.   In view of the many different ways in which the fission process can occur, it is perhaps surprising that the radiation is so homogeneous.

Acknowledgments

References

1. ARNOULT, R.   Ann. phys. 12 : 241.   1939.
2. DEUTSCH, M., ELLIOTT, L. G., and ROBERTS, A.   Phys. Rev. 68 : 193.   1945.
3. DROSTE, G. F. VON.   Z. Physik, 100 : 529.   1936.
4. DUNWORTH, J. V.   Nature, 144 : 152.   1939.
5. FEATHER, N. and DAINTY, J.   Proc. Cambridge Phil. Soc. 40 : 57.   1944.
6. MITCHELL, A. C. G. and LANGER, L. M.   Phys. Rev. 52 : 137.   1937.
7. NORLING, F.   Phys. Rev. 58 : 277.   1940.

ANGULAR DISTRIBUTION OF NEUTRONS INSIDE A SCATTERING AND ABSORBING MEDIUM[1]

By P. R. Wallace[2]

Abstract

A method is developed for determining the moments of the angular distribution of monoenergetic neutrons diffusing inside a homogeneous medium. It is applicable to the 'asymptotic' region, i.e., the region in which surface effects may be neglected. In particular, a general derivation is given for the current-density relation, involving no assumptions about the relative cross sections for scattering and capture. The second moment is expressed in terms of derivatives of the density, and the analogous procedure for higher moments is indicated. Moments of the angular distribution relative to arbitrary directions in space are defined: general formulae and applications to special cases are given for the second moment. Comparison may be made with the results of elementary diffusion theory, in which the angular distribution is assumed to be essentially linear.

Introduction

A considerable amount of work has been done recently on the diffusion of neutrons in various types of media, in connection with the study of nuclear chain reactions. In so far as the diffusion of monoenergetic neutrons is concerned, the problem may be approached either through the 'elementary diffusion theory' (1, 4) of Fermi or through the more accurate 'transport theory' (2, 3). The latter involves the solution of an integro-differential equation and can be treated in general only with extreme difficulty. The greatest difficulties arise in connection with the regions close to irregularities of the medium (discrete sources, boundaries, etc.).

The present paper represents an effort to find out as much as possible about the *asymptotic* behavior of neutron distributions, that is to say, the behavior in regions sufficiently deep inside a homogeneous medium to justify the neglect of surface effects at boundaries and the effects of inhomogeneous sources. It is concerned with monoenergetic neutrons only.

· The method used is that of 'artificial sources'. The idea of this method is the following. Suppose one has a mass of scattering and absorbing material V_i of uniform properties inside which one wishes to determine the asymptotic neutron distribution. Outside V_i are materials with different and possibly inhomogeneous properties. Sources are assumed both in and outside V_i. An attempt might then be made to compensate for the difference in properties in these latter regions by introducing appropriate sources (or sinks) of neutrons, and then to treat the whole medium as homogeneous. Now the distribution of these sources will, of course, depend on ψ, the neutron density in the regions in question. If the density is known, due to a point source in an infinite medium whose properties are uniformly those of V_i, then the density every-

where may be written as an integral over the artificial sources outside V_i. In this we are led to an integral equation formulation of the problem. The kernel of the integral equation is the point source solution referred to.

While the method has a number of useful applications in the practical solution of neutron diffusion problems, we are concerned here primarily with the derivation from it of *general* results about asymptotic distributions.

General asymptotic relations have been derived from transport theory between density and current (zero and first-order moments of the angular distribution respectively) and the higher moments.

In particular, a general proof is given for the relation

Current $\propto$ — gradient (density)

and the general form of the proportionality factor is given:· this has been proved heretofore only for the limiting case of weak capture.

The Transport Equation and Moments of the Angular Distribution

Let us suppose that we have some general distribution of neutron sources in scattering and absorbing media of various properties. We shall designate the source distribution as

$$q(r_0 , \Omega_0); \tag{2.1}$$

this quantity is the number of neutrons being supplied in unit time per unit volume and per unit solid angle at r_0 radiating in the direction of the unit vector Ω_0. It is referred to as the density of sources.

The various media will be characterized by the constants

l = total mean free path,

α = ratio of total to capture mean free path.

We shall assume that we have a region of uniform properties (i.e., constant l, α and q), in the interior of which an *asymptotic* distribution is established. Let us designate this region V_i, and the rest of space V_e. We shall choose the unit of length equal to the value of l in V_i.

We describe the neutron distribution by the function $\psi(r, \Omega)$ such that $\psi(r, \Omega)dVd\Omega$ is the number of neutrons in the volume element dV whose directions are within the solid angle element $d\Omega$.

The transport equation (equation of continuity) appropriate to the problem is then

$$\Omega^i\psi_{,i} + \frac{\psi}{l(r)} = \frac{1 - \alpha(r)}{4\pi l(r)} \psi_0 + q(r, \Omega_0) , \tag{2.2}$$

where the summation convention of the tensor calculus is used and ',i' indicates differentiation with respect to co-ordinates x_i. Ω (with components $\Omega^i : i = 1,2,3$) is the unit directional vector and ψ_0 is the neutron density in the usual sense, i.e., the integral of ψ over all directions Ω. (For convenience, we have chosen the unit of time such that the velocity of our neutrons is unity.)

The terms in this equation have the following significance:

The first describes neutron efflux from a given volume and solid angle element. (It may be alternatively written div ($v\psi$).) The second describes the removal of neutrons by scattering or capture.

The first term on the right represents the density of neutrons scattered into $dVd\Omega$. $\dfrac{1 - \alpha}{l} = \dfrac{1}{l_s}$, where l_s is the scattering mean free path. We assume isotropic scattering throughout for simplicity, though the problem is not unduly complicated in the case of anisotropic scattering. Since the last term represents the source contribution, the equation is a statement of conservation: loss of neutrons from $dVd\Omega$ on the left, gain on the right.

(2.2) may be written

$$\Omega^i \psi_{,i} + \psi = \frac{1 - \alpha}{4\pi} \psi_0 + q + \sigma(V_e) \left[\left(1 - \frac{1}{l(r)} \right) \psi \right.$$
$$\left. + \frac{1}{4\pi} \left\{ \frac{1 - \alpha(r)}{l(r)} - (1 - \alpha) \right\} \psi_0 + q(r,\Omega_0) - q \right], \qquad (2.3)$$

where $\sigma(V_e)$ is a function whose value is unity in V_e and zero in V_i. The effect of the constant q outside the square bracket on the right hand side is simply to add a term q/α to ψ. For convenience we shall drop this term throughout.

It follows from (2.3) that the density in V_i is that from a certain distribution of (anisotropic) sources in V_e. We can designate these sources (the last term, in the square bracket, in (2.3)) by

$$\chi(r, \Omega_0), \qquad (2,4)$$

which is the density of sources, per unit volume and per unit solid angle.

The practical applications of the method to date have been concerned with certain special conditions. In the first place, so long as the first and third terms in the square bracket on the right hand side are concerned, they describe *anisotropic* sources, i.e., sources which do not radiate uniformly in angle. An integral equation with an *anisotropic* point source distribution as kernel results. This is very complicated. But in the special cases in which (a) q is isotropic everywhere and (b) the *total* mean free path l is a constant, the *anisotropic* sources disappear, and the problem is greatly simplified. In the case of plane problems, the condition (b) is not necessary, since a change of scale may be used to make the mean free path effectively constant.

The peculiar circumstances in which the method is most effective are those in which the inhomogeneities occur in small regions. Whereas the range of the integral in the integral equation is always infinite in the usual Wiener-Hopf formulation, it is then small in our formulation and the problem readily lends itself to approximate solution by iteration methods.

However, *none of the above restrictions are necessary for the derivation of the general results discussed in this paper.*

At an element of volume $dV(r)$ let the density per unit solid angle $d\Omega$, due to a point source at r_0 radiating in the direction Ω_0 in a homogeneous medium, be

$$Q(r - r_0, \Omega, \Omega_0) . \tag{2.5}$$

The density in V_i is, then,

$$\psi (r, \Omega) = \int_{\Omega_0} \int_{V_e} \chi(r_0, \Omega_0) Q(r - r_0, \Omega, \Omega_0) \, d\Omega_0 \, dV, \tag{2.6}$$

and from this the moments may be written down immediately (in terms of ψ in the region V_e). We are interested, however, in discovering relations between asymptotic forms of the lower moments which are independent of conditions in V_e.

The zero, first, and second moments are:

$$\psi^{(0)} (r) = \int_{\Omega_0} \int_{V_e} \chi(r_0, \Omega_0) Q^{(0)} (r - r_0, \Omega_0) \, d\Omega_0 \, dV, \tag{2.7}$$

$$\psi_i^{(1)} (r) = \int_{\Omega_0} \int_{V_e} \chi(r_0, \Omega_0) Q_i^{(1)} (r - r_0, \Omega_0) \, d\Omega_0 \, dV, \tag{2.8}$$

$$\psi_{ij}^{(2)} (r) = \int_{\Omega_0} \int_{V_e} \chi(r_0, \Omega_0) Q_{ij}^{(2)} (r - r_0, \Omega_0) \, d\Omega_0 \, dV, \tag{2.9}$$

where

$$\Phi_{i_1 i_2 \ldots i_n}^{(n)} = \int \Omega_{i_1} \Omega_{i_2} \ldots \Omega_{i_n} \Phi (\Omega) \, d\Omega ,$$

the integral being taken over the complete solid angle of directions Ω. Let us then consider the moments of Q.

Consider the transport equation (2.2) for a point source in a homogeneous medium. Let us define the three-dimensional Fourier transform:

$$\phi(k) = \int \chi(r) \, e^{i k \cdot r} \, dV(r) ,$$

for which the inverse transform is

$$\phi(r) = \frac{1}{(2\pi)^3} \int \phi(k) e^{-i k \cdot r} \, dV(k) .$$

If we take the three-dimensional Fourier transform from r- into k-space of (2.2), we get

$$\phi(k, \Omega, \Omega_0) = \frac{1}{1 - ik . \Omega} \left\{ \frac{1 - \alpha}{4\pi} \phi_{(0)} (k, \Omega_0) + \delta_2(\Omega, \Omega_0) \right\}, \tag{2.10}$$

where $\phi(k, \Omega, \Omega_0)$ is the Fourier transform of $Q(r, \Omega, \Omega_0)$, and $\phi_{(0)}$ is its zero moment with respect to Ω. $\delta_2(\Omega, \Omega_0)$ is the angular delta-function with the properties:

$$\delta_2(\Omega, \Omega_0) = 0 \text{ for } \Omega \neq \Omega_0,$$

and

$$\int \delta_2(\Omega,\ \Omega_0)d\Omega\ =\ 1.$$

It follows from (2.10) on integration over Ω, that

$$\phi_{(0)}\ (k,\ \Omega_0)\ =\ \frac{1}{1 - ik.\ \Omega_0}\ \frac{1}{\left(1 - (1 - \alpha)\ \dfrac{\tan^{-1}k}{k}\right)}, \tag{2.11}$$

and, on multiplying first by Ω^i, that

$$\phi^i_{(1)}\ (k,\ \Omega_0)\ =\ \frac{1 - \alpha}{1 - ik.\ \Omega_0}\ \frac{1 - \dfrac{\tan^{-1}k}{k}}{\left(1 - (1 - \alpha)\ \dfrac{\tan^{-1}k}{k}\right)}\ \frac{ik^i}{k^2} + \frac{\Omega^i_0}{1 - ik.\ \Omega_0}; \tag{2.12}$$

where $k = |k|$: these are immediate. We wish also to calculate $\phi^{ij}_{(2)}$. Now it may be shown on expressing the components of Ω in terms of polar co-ordinates with the vector k as axis, that

$$\int \frac{\Omega^i\ \Omega^j}{1 - ik.\ \Omega}\ d\Omega\ =\ 4\pi\ \left\{\frac{1}{2}\left[\frac{\tan^{-1}k}{k} - \frac{1}{k^2}\left(1 - \frac{\tan^{-1}k}{k}\right)\right]\delta_{ij}\right.$$
$$\left. +\ \left[\frac{3}{2}\frac{1}{k^2}\left(1 - \frac{\tan^{-1}k}{k}\right) - \frac{1}{2}\frac{\tan^{-1}k}{k}\right]\frac{k^i k^j}{k^2}\right\}, \tag{2.13}$$

so that

$$\phi^{ij}_{(2)}\ =\ (1 - \alpha)\ \frac{1}{1 - ik.\ \Omega_0}\ \frac{1}{1 - (1 - \alpha)\ \dfrac{\tan^{-1}k}{k}}$$

$$\frac{1}{2}\left[\frac{\tan^{-1}k}{k} - \frac{1}{k^2}\left(1 - \frac{\tan^{-1}k}{k}\right)\right]\delta^{ij} + \left[\frac{3}{2}\frac{1}{k^2}\left(1 - \frac{\tan^{-1}k}{k}\right)\right.$$
$$\left. -\ \frac{1}{2}\frac{\tan^{-1}k}{k}\right]\frac{k^i k^j}{k^2}\bigg\} + \frac{\Omega^i_0\ \Omega^j_0}{1 - ik.\ \Omega_0}. \tag{2.14}$$

By taking inverse transforms of (2.11), (2.12), and (2.14) we may deduce the zero, first, and second moments of Q. Letting $u = k/k$, we have

$$Q^{(0)}\ (r,\ \Omega_0)\ =\ \frac{1}{(2\pi)^3}\int \phi_{(0)}\ (k,\ \Omega_0)\ e^{-iku.r}\ k^2\ dk\ d\Omega_u, \tag{2.15}$$

and the higher moments may be written down similarly.

It should now be noted that, if we are interested only in *asymptotic* behavior in V_i, we may ignore the contributions from the *last* terms in (2.12) and (2.14), since these give only contributions from neutrons scattered in V_e but not yet having suffered a collision in V_i. Such contributions are part of the 'surface effects' which we are neglecting. In the other parts, Ω_0 occurs only through the factor

$$\frac{1}{1 - ik.\ \Omega_0}.$$

Let us now introduce

$$\int_{\Omega_0} \int_{V_s} \frac{1}{1 - i\mathbf{k} \cdot \Omega_0} \, \chi(\mathbf{r}_0, \, \Omega_0) \, e^{i\mathbf{k} \cdot \mathbf{r}_0} \, d\Omega_0 dV = f(\mathbf{k}) \,. \tag{2.16}$$

We may then, using (2.15) and the similar equations for $Q^{(1)}$ and $Q^{(2)}$ in (2.7) to (2.9), write the terms giving rise to asymptotic parts of the first moments of ψ as:

$$\tilde{\psi}^{(0)} (\mathbf{r}) = \frac{1}{2(2\pi)^3} \int f(\mathbf{k}) \, \frac{1}{1 - (1 - \alpha) \dfrac{\tan^{-1}k}{k}} \, e^{-i k u \cdot \mathbf{r}} \, k^2 \, dk \, d\Omega_u \,. \tag{2.17}$$

Similarly

$$\tilde{\psi}_i^{(1)} (\mathbf{r}) = \frac{i(1 - \alpha)}{2(2\pi)^3} \int f(\mathbf{k}) \, \frac{1 - \dfrac{\tan^{-1}k}{k}}{1 - (1 - \alpha) \dfrac{\tan^{-1}k}{k}} \, e^{-i k u \cdot \mathbf{r}} \, k u_i \, dk \, d\Omega_u \,, \tag{2.18}$$

and

$$\tilde{\psi}_{ij}^{(2)} (\mathbf{r}) = \frac{1 - \alpha}{2(2\pi)^3} \int f(\mathbf{k}) \, \frac{e^{-i k u \cdot \mathbf{r}}}{1 - (1 - \alpha) \dfrac{\tan^{-1}k}{k}} \left\{ \frac{1}{2} \left[\frac{\tan^{-1}k}{k} - \frac{1}{k^2} \left(1 - \frac{\tan^{-1}k}{k} \right) \right] \delta_{ij} \right.$$

$$\left. + \left[\frac{3}{2} \frac{1}{k^2} \left(1 - \frac{\tan^{-1}k}{k} \right) - \frac{1}{2} \frac{\tan^{-1}k}{k} \right] u_i u_j \right\} k^2 \, dk \, d\Omega_u \,. \tag{2.19}$$

Some Properties of Tensor Spherical Harmonics

It is convenient to introduce tensorial generalizations of ordinary spherical harmonics as follows: Let us define a radius vector $\mathbf{r}_v = r_v \mathbf{v}$ associated with a unit vector $\mathbf{v}$. Then we may write

$$T_{i_1 \ldots i_n}(v) = \frac{(-1)^n}{n!} \left[\left(\frac{1}{r_v} \right)_{,i_1 \ldots i_n} \right]_{r_v = 1}$$

the subscripts after the comma indicating differentiation with respect to the components of $\mathbf{r}_v$.

We call this the spherical harmonic tensor of order n formed from the vector $\mathbf{v}$.

The components of $T_{i_1 \ldots i_n}(v)$ are linear combinations of the 'surface harmonics' $P_n^m (\cos \theta) \, {\cos \atop \sin} \, m\phi$, θ and ϕ being the polar angles of $\mathbf{v}$. In particular, if we take the polar axis as the x_1-axis,

$$T_{(1)^n} = P_n(\cos \theta).$$

We may then state the following theorem, analogous to a familiar one in the theory of ordinary spherical harmonics:

$$e^{i\xi u \cdot v} = \Sigma \, i^n (2n + 1) j_n(\xi) C_n T_{i_1 \ldots i_n}(u) T_{i_1 \ldots i_n}(v) \,, \tag{3.1}$$

where

$$C_n = \frac{(n\,l)^2 2^n}{(2n)\,l}.$$ (3.2)

$j_n(\xi)$ is defined by

$$j_n(\xi) = \sqrt{\frac{\pi}{2\xi}}\; J_{n+\frac{1}{2}}(\xi),$$ (3.3)

where $J_{n+\frac{1}{2}}$ designates the Bessel function of order $(n + \frac{1}{2})$.

To prove the theorem it is necessary to show that, for any two unit vectors u and v,

$$C_n T_{i_1\ldots i_n}(u)\, T_{i_1\ldots i_n}(v) = P_n(u.v). *$$ (3.4)

Expanding $T_{i_1\ldots i_n}(u)$, by direct differentiation, we get

$$T_{i_1\ldots i_n}(u)\, T_{i_1\ldots i_n}(v) = \frac{1}{n!}\Big\{1.3.5\cdots(2n-1)\,u_{i_1}\cdots u_{i_n} - 1.3.5\ldots\ldots(2n-3)$$

$$\Sigma \delta_{i_1 i_2}\, u_{i_3}\cdots u_{i_n} + 1.3.5.\ldots(2n-5)$$

$$\Sigma \delta_{i_1 i_2}\,\delta_{i_3 i_4} u_{i_5}\ldots u_{i_n} + \ldots\Big\}\frac{(-1)^n}{n\,l}\left[\left(\frac{1}{r_v}\right)_{i_1\ldots i_n}\right]r_v = 1,$$

where the sums are taken over all possible combinations of subscripts in the Kronecker deltas. But now all except the first term goes out, all others involving Laplacians of $1/r_v$. Let us now choose the 1-axis in the direction of u. Then

$$T_{i_1\ldots i_n}(u)\, T_{i_1\ldots i_n}(v) = \frac{(2n)!}{2^n(n!)^3}(-1)^n\left[\frac{\partial^n}{\partial x_1^n}\left(\frac{1}{r_v}\right)\right]r_v = 1 = \frac{(2n)!}{2^n(n!)^2}P_n(u.v),$$

from which (3,4) follows.

Calculation of the Density $\psi^{(0)}$ in the Asymptotic Region

We shall expand $f(k)$ in spherical harmonics:

$$f(k) = \frac{1}{4\pi}\Sigma_n(2n+1)\,C_n f_{(n)}(k)\, T_{(n)}(u),$$ (4.1)

where the subscript '$_{(n)}$' indicates n indices $i_1\cdots i_n$. Then

$$f_{(n)}(k) = \int f(k)\, T_{(n)}(u)\, d\Omega_u. \dagger$$ (4.2)

Letting $r = r\,v$, $\quad e^{-iku.v} = \Sigma(-i)^m(2m+1)\,j_m(kr)C_m T_{(m)}(u)T_{(m)}(v).$ (4.3)

* The equation (3.1) reduces, with the help of (3.4), to the form given in Stratton, Electro-magnetic Theory, p. 409 (Equation 56) (McGraw-Hill, New York, 1941).

† See Appendix for proof.

Putting the expressions (4.2) and (4.3) into (2.17), and using the ortho-gonality of the T's of different order, and the fact that

$$T_{(m)}(v) \int T_{(m)}(u) T_{i_1 \cdots i_m}(u) d\Omega = \frac{(2m)!}{(m!)^2 2^m} \frac{4\pi}{2m+1} T_{i_1 \cdots i_m}(v) \dagger \qquad (4.4)$$

we get

$$\tilde{\psi}^{(0)}(r) = \frac{1}{2} \frac{1}{(2\pi)^3} \int_{-\infty}^{\infty} \frac{1}{1} \quad (1-\alpha) \frac{\tan^{-1}k}{k}$$

$$\Sigma_n(-1)^n(2n+1)C_n f_{(n)}(k)T_{(n)}(v)j_n(kr) \cdot k^2 dk = \frac{1}{2} \frac{1}{(2\pi)^3} \Sigma_n(-1)^n(2n+1)C_n T_{(n)}(v)$$

$$\int_{-\infty}^{\infty} \frac{f_{(n)}(k)j_n(kr)}{1 - (1-\alpha)\dfrac{\tan^{-1}k}{k}} \, k^2 dk . \quad (4.5)$$

Now from (2.16) it may be seen that $f(k)$ has no singularities for $|k| < 1$. Therefore the asymptotic contribution from the integral in (4.5) will arise from the poles at $k = \pm i\nu$, $(\nu < 1)$. Let us write

$$j_n(x) = \frac{1}{2}[h_n^{(1)}(x) + h_n^{(2)}(x)], * \qquad (4.6)$$

where

$$\left. \begin{array}{l} h_n^{(1)}(x) = \sqrt{\dfrac{\pi}{2x}} H_{n+\frac{1}{2}}^{(1)}(x) \\[4mm] h_n^{(2)}(x) = \sqrt{\dfrac{\pi}{2x}} H_{n+\frac{1}{2}}^{(2)}(x) \end{array} \right\} \quad \text{(Hankel functions)}$$

$$h_n^{(1)}(x) = e^{ix}\left[\text{polynomial in } \frac{1}{x}\right]$$

$$h_n^{(2)}(x) = e^{-ix}\left[\text{conjugate complex polynomial in } \frac{1}{x}\right] .$$

† *It will be sufficient to prove this result for the particular co-ordinate system in which the x_1-axis is in the direction of v. Then the only non-zero component of $T_{i_1 \cdots i_m}(v)$ is that for which $j_1 = \cdots = j_m = 1$, for which the right hand side becomes*

$$\frac{(2m)!}{(m!)^2 2^m} \frac{4\pi}{2m+1} P_m(1) ,$$

where, in fact, $P_m(1) = 1$.

But, by (3.4) and the expression (3.2) for C_n, the left hand side is

$$\frac{(2m)!}{(m!)^2 2^m} \int P_m(u \cdot v) T_{i_1 \cdots i_m}(u) d\Omega .$$

Since all the $T_{i_1 \cdots i_m}(u)$ except that for which $j_1 = \cdots = j_m = 1$ contain the azimuthal angle, integration over azimuth gives zero except in this case. In the case $j_1 = \cdots = j_m = 1$, however, the integral becomes

$$\int P_m^2 d\Omega = \frac{4\pi}{2m+1} .$$

The validity of (4.4) is therefore established.

* *For Bessel and Hankel functions and their interrelations, see for instance Stratton, Electromagnetic Theory (McGraw-Hill, New York, 1941), pp. 358, 359.*

The last integral in (4.5) may be broken up into

$$\frac{1}{2} \int_{-\infty}^{\infty} \frac{f_{(n)}(k) h_n^{(1)}(kr)}{1 - (1 - \alpha) \frac{\tan^{-1}k}{k}} k^2 dk + \frac{1}{2} \int_{-\infty}^{\infty} \frac{f_{(n)}(k) h_n^{(2)}(kr)}{1 - (1 - \alpha) \frac{\tan^{-1}k}{k}} k^2 dk .$$

We deform the first of these integrals about the upper half-plane, and the second about the lower.

Since the integrand has branch points at $-i$ and i the contours will be semicircular with cuts down the imaginary axis to these points. The contributions from the semicircles will vanish as the radius becomes infinite. The integrals along the edges of the cuts will vanish at least as e^{-r} as $r \longrightarrow \infty$, and will therefore be negligible for large r compared with the contributions from the poles at $-i\nu$, $i\nu$, $(\nu < 1)$. Taking only the asymptotic (pole) contributions, we get

$$\pi i \left[\frac{-i\nu(1 - \nu^2)(-\nu^2)}{\nu^2 - \alpha} \right] f_{(n)}(i\nu) h_n^{(1)}(i\nu r)$$

$$- \pi i \left[\frac{i\nu(1 - \nu^2)(-\nu^2)}{\nu^2 - \alpha} \right] f_{(n)}(-i\nu) h_n^{(2)}(-i\nu r)$$

where $i\nu$ is the zero of $\left[1 - (1 - \alpha) \frac{\tan^{-1}k}{k} \right]$ in the upper half-plane, i.e.,

$$\frac{\tanh^{-1}\nu}{\nu} = \frac{1}{1 - \alpha} = \frac{l_s}{l} , \tag{4.8}$$

where l_s is the scattering mean free path.

Therefore finally the asymptotic density is

$$\psi^{(0)\,(as)} = \frac{-1}{16\pi^2} \frac{\nu^3(1 - \nu^2)}{\nu^2 - \alpha} \Sigma_n (-1)^n (2n + 1) C_n T_{(n)}(v)$$

$$[f_{(n)}(i\nu) h_n^{(1)}(i\nu r) + f_{(n)}(-i\nu) h_n^{(2)}(-i\nu r)] . \tag{4.9}$$

In the particular case of a point source,

$$f = f_0/4\pi = \frac{\tan^{-1}k}{k} ; \tag{4.10}$$

only the first term in the series (4.9) remains, and we get

$$\psi^{(0)\,(as)} = \frac{1}{2\pi r} \frac{\nu^2(1 - \nu^2)}{(\nu^2 - \alpha)(1 - \alpha)} e^{-\nu r} .* \tag{4.11}$$

Calculation of the Current $\psi_i^{(1)}$ in the Asymptotic Region

Let us start with (2.18):

$$\widetilde{\psi}_i^{(1)} = \frac{i(1 - \alpha)}{2(2\pi)^3} \int f(k) \frac{1 - \frac{\tan^{-1}k}{k}}{1 - (1 - \alpha) \frac{\tan^{-1}k}{b}} e^{-iku\cdot r} k u_i dk d\Omega_u .$$

Cf. Bothe (2, 3).

We may write this

$$\tilde{\psi}_i^{(1)} = -\nabla_i \left\{ \frac{(1-\alpha)}{2(2\pi)^3} \int f(k) \frac{1 - \dfrac{\tan^{-1}k}{k}}{1 - (1-\alpha)\dfrac{\tan^{-1}k}{k}} e^{-iku \cdot r} dk d\Omega_u \right\}, \quad (5.1)$$

where ∇_i indicates the ith component of the gradient operator. The asymptotic part of the bracket may be calculated exactly as was $\psi^{(0)\,(as)}$ in the preceding section; it is in fact found to be

$$\frac{\alpha}{\nu^2} \psi^{(0)\,(as)},$$

so that

$$\boxed{\psi_i^{(1)\,(as)} = -\frac{\alpha}{\nu^2} \nabla_i \{\psi^{(0)\,(as)}\}.}$$

Thus we have the general form of the asymptotic current-density relation. As $\nu \longrightarrow 0, \dfrac{\alpha}{\nu^2} \longrightarrow \dfrac{1}{3}$, which is the value taken in the elementary diffusion theory. Expanding,

$$\frac{\alpha}{\nu^2} = \frac{1}{3}\left[1 + \frac{4}{5}\alpha + \frac{108}{175}\alpha^2 + \cdots\right]. \quad (5.3)$$

Calculation of $\psi_{ij}^{(2)}$ in the Asymptotic Region

The asymptotic part of $\psi_{ij}^{(2)}$ may be calculated from (2.19):

$$\psi_{ij}^{(2)} = \frac{1-\alpha}{2(2\pi)^3} \int f(k) \frac{e^{-iku \cdot r}}{1-(1-\alpha)\dfrac{\tan^{-1}k}{k}} \left\{ \frac{1}{2}\left[\frac{\tan^{-1}k}{k} - \frac{1}{k^2}\left(\frac{1-\tan^{-1}k}{k}\right)\right]\delta_{ij}\right.$$

$$\left. + \left[\frac{3}{2}\frac{1}{k^2}\left(1 - \frac{\tan^{-1}k}{k}\right) - \frac{1}{2}\frac{\tan^{-1}k}{k}\right] u_i u_j \right\} k^2 dk d\Omega_u .$$

We may write

$$\frac{1-\alpha}{2(2\pi)^3} \int f(k) \frac{e^{-iku \cdot r}}{1-(1-\alpha)\dfrac{\tan^{-1}k}{k}} \left[\frac{3}{2}\frac{1}{k^2}\left(1 - \frac{\tan^{-1}k}{k}\right) - \frac{1}{2}\frac{\tan^{-1}k}{k}\right] u_i u_j \cdot k^2 dk d\Omega_u$$

$$\left[\frac{1-\alpha}{2(2\pi)^3} \int f(k) \frac{e^{-iku \cdot r}}{1-(1-\alpha)\dfrac{\tan^{-1}k}{k}}\left[\frac{3}{2}\frac{1}{k^2}\left(1 - \frac{\tan^{-1}k}{k}\right) - \frac{1}{2}\frac{\tan^{-1}k}{k}\right] dk d\Omega_u \right\}.$$

$$(6.1)$$

The asymptotic part of the integral in the bracket may now be calculated by contour integration to be

$$\frac{1}{2}\frac{1}{\nu^2}\left(1 - 3\frac{\alpha}{\nu^2}\right)\psi^{(0)\,(as)}. \quad (6.2)$$

Similarly

$$\frac{1-\alpha}{2(2\pi)^3} \int f(k) \; \frac{e^{-i k u \cdot r}}{1 - (1 - \alpha)\frac{\tan^{-1}k}{k}} \; \frac{1}{2}\left[\frac{\tan^{-1}k}{k} - \frac{1}{k^2}\left(1 - \frac{\tan^{-1}k}{k}\right)\right] k^2 dk d\Omega_u$$

$$\approx \frac{1}{2}\left(1 - \frac{\alpha}{\nu^2}\right)\psi^{(0)\,(as)}.$$
(6.3)

asymptotically. It follows, then, that

$$\boxed{\;\psi_{ij}^{(2)\,(as)} = \frac{1}{2}\left(1 - \frac{\alpha}{\nu^2}\right)\psi^{(0)(as)}\,\delta_{ij} - \frac{1}{2\nu^2}\left(1 - \frac{3\alpha}{\nu^2}\right)\psi_{,ij}^{(0)(as)}\;}$$
(6.4)

Let us now define $\overline{\mu^2(n)}$ as the mean square cosine of the distribution with respect to the direction defined by the unit vector n, fixed in space. By definition

$$\overline{\mu^2(n)} = \psi_{ij}^{(2)\,(as)} n_i n_j / \psi^{(0)\,(as)}.$$
(6.5)

Substituting from (6.4) we find that

$$\overline{\mu^2(n)} = \frac{1}{2}\left(1 - \frac{\alpha}{\nu^2}\right) + \frac{1}{2\nu^2}\left(\frac{3\alpha}{\nu^2} - 1\right)\frac{1}{\psi^{(0)\,(as)}}\frac{\partial^2\psi^{(0)\,(as)}}{\partial n^2}$$
(6.6)

where $\dfrac{\partial}{\partial n}$ indicates differentiation in the direction n.

For very small capture cross section

$$\frac{3\alpha}{\nu^2} \approx 1 + \frac{4}{15}\nu^2$$

$$\frac{1}{2}\left(1 - \frac{\alpha}{\nu^2}\right) \approx \frac{1}{3} - \frac{2}{45}\nu^2$$

and therefore

$$\overline{\mu^2(n)} \approx \frac{1}{3} - \frac{2}{45}\nu^2 + \frac{2}{15}\frac{1}{\psi^{(0)\,(as)}}\frac{\partial^2\psi^{(0)\,(as)}}{\partial n^2}.$$
(6.7)

In the first approximation, this is independent of n, the angular distribution being isotropic. On the other hand, for large capture, $\alpha, \nu \longrightarrow 1$ and

$$\overline{\mu^2(n)} \approx \frac{1}{\psi^{(0)\,(as)}}\frac{\partial^2\psi^{(0)\,(as)}}{\partial n^2}.$$
(6.8)

If we wish to evaluate $\overline{\mu^2}$ relative to a direction which is not fixed in space (as, for example, the radial direction in spherical polar co-ordinates), we must put

$$n_i n_j \frac{\partial^2}{\partial x_i \partial x_j} = \frac{\partial^2}{\partial n^2} - n_j \frac{\partial n_i}{\partial x_j}\frac{\partial}{\partial x_i}.$$
(6.9)

In spherical polar co-ordinates, where $n_i = \dfrac{x_i}{r}$ this becomes $\dfrac{\partial^2}{\partial r^2}$. If $\psi^{(0)\,(as)}$ depends on r alone,

$$\nabla^2\psi^{(0)\,(as)} = \nu^2\psi^{(0)\,(as)} . \tag{6.10}$$

from which it follows that

$$\frac{1}{\nu^2\psi^{(0)\,(as)}} \frac{\partial^2\psi^{(0)\,(as)}}{\partial r^2} = 1 - \frac{2}{\nu^2 r} \frac{1}{\psi^{(0)\,(as)}} \frac{\partial\psi^{(0)\,(as)}}{\partial r} = 1 + \frac{2}{\alpha r}\bar{\mu} , \tag{6.11}$$

where $\bar{\mu}$ is the average cosine of the angular distribution relative to the radial direction. Therefore

$$\overline{\mu^2} = \frac{\alpha}{\nu^2} + \left(\frac{3\alpha}{\nu^2} - 1\right)\frac{1}{\alpha r}\bar{\mu} . \tag{6.12}$$

Let us consider two special cases here.

(a) If we have a point source,

$$\psi^{(0)\,(as)} = Q\frac{e^{-\nu r}}{r} ,$$

and since

$$\bar{\mu} = \frac{\displaystyle\int \left(\frac{\mathbf{r}}{r}\right) \cdot \mathbf{\Omega}\psi\,d\Omega}{\psi^{(0)}} = \frac{x_i}{r}\frac{\psi_i^{(1)}}{\psi^{(0)}} = -\frac{\alpha}{\nu^2}\frac{1}{\psi^{(0)}}\frac{\partial\psi^{(0)}}{\partial r} ,$$

we have

$$\frac{1}{\alpha r}\bar{\mu} = \frac{1}{\nu r} + \frac{1}{\nu^2 r^2} . \tag{6.13}$$

Therefore

$$\overline{\mu^2} = \frac{\alpha}{\nu^2} + \left(\frac{3\alpha}{\nu^2} - 1\right)\left(\frac{1}{\nu r} + \frac{1}{\nu^2 r^2}\right) \tag{6.14}$$

We note that $\overline{\mu^2}$ approaches a constant as $\nu r \longrightarrow \infty$, i.e., at distances large compared with a diffusion length. This may be seen to be an instance of a general result.

(b) If we are in an enclosed spherical region with sources outside,

$$\psi^{(0)\,(as)} = C\frac{\sinh \nu r}{r} .$$

Then, as in (a) above,

$$\frac{1}{\alpha r}\bar{\mu} = \frac{1}{\nu^2 r^2} - \frac{1}{\nu r}\coth \nu r, \tag{6.15}$$

which for small νr is

$$\approx -\frac{1}{3}\left(1 - \frac{1}{15}\nu^2 r^2\right) .$$

Therefore

$$\overline{\mu^2} \approx \frac{\alpha}{\nu^2} + \left(\frac{3\alpha}{\nu^2} - 1\right)\left[-\frac{1}{3}\left(1 - \frac{1}{15}\nu^2 r^2\right)\right] = \frac{1}{3} + \frac{1}{45}\left(\frac{3\alpha}{\nu^2} - 1\right)\nu^2 r^2 , \tag{6.16}$$

which indicates how the angular distribution departs from isotropy $\left(\overline{\mu^2} = \dfrac{1}{3}\right)$ as we go away from the center.

Evaluation of $\overline{\mu^2}$ in General

We may wish to express $\overline{\mu^2}$ relative to directions which are not fixed in space, and in non-Cartesian co-ordinate systems. For this purpose we must express in generalized co-ordinates $n^i n^j \nabla_{ij} \psi^{(0)\,(as)}$ and $\nabla^2 \psi^{(0)\,(as)}$. The tensorial forms of these quantities are $n^i n^j D_i D_j \psi^{(0)\,(as)}$ and $D^i D_i \psi^{(0)\,(as)}$, where D_i is the operation of covariant differentiation.

Now

$$n^i n^j D_i D_j \psi^{(0)\,(as)} = n^i n^j \left[\frac{\partial^2}{\partial x^i \partial x^j} - \left\{ {k \atop ij} \right\} \frac{\partial}{\partial x^k} \right] \psi^{(0)\,(as)}, \qquad (7.1)$$

$\left\{ {k \atop ij} \right\}$ being the Christoffel symbol of the second kind.[†]

Let us take a co-ordinate system in which $x^1 = s$ is distance measured normal to the surfaces of constant density (i.e., in the direction of the current). x^2, x^3 may be arbitrarily chosen co-ordinates in the surfaces of constant density. Let the indices α, β take the values 2, 3.[*] Now $\psi^{(0)\,(as)}$ depends only on s. From these facts, and the definition of the Christoffel symbol, it follows that

$$n^i n^j D_i D_j \psi^{(0)\,(as)} = \left[(n^1)^2 \frac{\partial^2}{\partial s^2} + \frac{1}{2} n^\alpha n^\beta \frac{\partial a_{\alpha\beta}}{\partial s} \frac{\partial}{\partial s} \right] \psi^{(0)\,(as)}. \qquad (7.2)$$

Consider next

$$\nabla^2 \psi^{(0)\,(as)} = a^{ij} D_i D_j \psi^{(0)\,(as)} = \nu^2 \psi^{(0)\,(as)}.[**] \qquad (7.3)$$

Calculating the Laplacian for the particular co-ordinate system in question, one finds

$$\nu^2 \psi^{(0)\,(as)} = \left[\frac{\partial^2}{\partial s^2} + \frac{1}{2} a^{\alpha\beta} \frac{\partial a_{\alpha\beta}}{\partial s} \right] \psi^{(0)\,(as)}. \qquad (7.4)$$

Substituting for the second derivative with respect to s in (7.2) above, we find

$$\overline{\mu^2}(n) = \frac{1}{2}\left(1 - \frac{\alpha}{\nu^2}\right) + \frac{1}{2\nu^2\,\psi^{(0)\,(as)}} \left(\frac{3\alpha}{\nu^2} - 1\right).$$
$$\left[(n^1)^2 \left\{ \nu^2\,\psi^{(0)\,(as)} - \frac{1}{2} a^{\alpha\beta} \frac{\partial a_{\alpha\beta}}{\partial s} \frac{\partial \psi^{(0)\,(as)}}{\partial s} \right\} + \frac{1}{2} n^\alpha n^\beta \frac{\partial a_{\alpha\beta}}{\partial s} \frac{\partial \psi^{(0)\,(as)}}{\partial s} \right]. \qquad (7.5)$$

But

$$-\frac{\alpha}{\nu^2} \frac{\partial \psi^{(0)\,(as)}}{\partial s} = \psi^{(1)} = \overline{\mu}\psi^{(0)},$$

and therefore

$$\overline{\mu^2}(n) = \frac{1}{2}\left(1 - \frac{\alpha}{\nu^2}\right) + \frac{1}{2}\left(\frac{3\alpha}{\nu^2} - 1\right)$$
$$\left[(n^1)^2 \left\{ 1 + \frac{1}{2\alpha} a^{\alpha\beta} \frac{\partial a_{\alpha\beta}}{\partial s} \overline{\mu}(n) \right\} - \frac{1}{2\alpha} n^\alpha n^\beta \frac{\partial a_{\alpha\beta}}{\partial s} \overline{\mu}(n) \right]. \qquad (7.6)$$

[†] See, for example, McConnell, Applications of the Absolute Differential Calculus. (Blackie, 1931) (pp. 140 ff.).

[*] The line-element is $d\sigma^2 = a_{ij} dx^i dx^j = ds^2 + a_{\alpha\beta} dx^\alpha dx^\beta$.

[**] McConnell, p. 151.

Let us suppose that we may choose the co-ordinates x^2 and x^3 in such a way that

$$a_{\alpha\beta} = s^2 \bar{a}_{\alpha\beta} , \tag{7.7}$$

where $\bar{a}_{\alpha\beta}$ do not depend on s . Then

$$\frac{1}{2\alpha} a^{\alpha\beta} \frac{\partial a_{\alpha\beta}}{\partial s} = \frac{1}{\alpha s} a^{\alpha\beta} a_{\alpha\beta} = \frac{1}{\alpha s} (a^{ij}a_{ij} - a^{11}a_{11}) = \frac{2}{\alpha s} , \tag{7.8}$$

and

$$\frac{1}{2\alpha} n^{\alpha}n^{\beta} \frac{\partial a_{\alpha\beta}}{\partial s} = \frac{1}{\alpha s} n^{\alpha}n^{\beta}a_{\alpha\beta} = \frac{1}{\alpha s} [1 - (n^1)^2] . \tag{7.9}$$

With the aid of these facts we may write

$$\overline{\mu^2}(n) = \frac{1}{2}\left(1 - \frac{\alpha}{\nu^2}\right) + \frac{1}{2}\left(\frac{3\alpha}{\nu^2} - 1\right)$$
$$\left[(n^1)^2\left\{1 + \frac{2}{\alpha s}\overline{\mu(n)}\right\} - \frac{1}{\alpha s}\{1 - (n^1)^2\}\,\overline{\mu(n)}\right]. \tag{7.10}$$

Now n^1 is the cosine of the angle which our direction n makes with the current. Designating $\bar{\mu}$ for the forward direction by $\bar{\mu}_0$,

$$\overline{\mu(n)} = n^1 \cdot \bar{\mu}_0 \tag{7.11}$$

and

$$\overline{\mu^2(n)} = \frac{1}{2}\left(1 - \frac{\alpha}{\nu^2}\right) + \frac{1}{2}\left(\frac{3\alpha}{\nu^2} - 1\right)$$
$$\left[(n^1)^2\left\{1 + \frac{2\bar{\mu}_0}{\alpha s} n^1\right\} - \frac{\bar{\mu}_0}{\alpha s} n^1 \{1 - (n^1)^2\}\right]. \tag{7.12}$$

Further we may write, by virtue of (5.2)

$$\bar{\mu}_0 = -\frac{\alpha}{\nu^2}\frac{\partial}{\partial s}\log \psi^{(0)} . \tag{7.13}$$

If we introduce

$$s_0 = \nu s , \tag{7.14}$$

$$\overline{\mu^2(n)} = \frac{1}{2}\left(1 - \frac{\alpha}{\nu^2}\right) + \frac{1}{2}\left(\frac{3\alpha}{\nu^2} - 1\right)\left[(n^1)^2\left\{1 - \frac{2n^1}{s_0}\frac{\partial}{\partial s_0}\log \psi^{(0)}\right\}\right.$$
$$\left. + \{1 - (n^1)^2\}\frac{n^1}{s_0}\frac{\partial}{\partial s_0}\log \psi^{(0)}\right]. \tag{7.15}$$

An interesting special case is the following: if we calculate $\overline{\mu^2}$ for a direction perpendicular to the current, we get, from (7.15) and (7.11)

$$\overline{\mu^2} = \frac{1}{2}\left(1 - \frac{\alpha}{\nu^2}\right),$$

which is completely independent of geometry, and of the particular position chosen.

We might also note the result, that at a sufficiently large distance in units of $1/\nu$, i.e., at a sufficiently large number of diffusion lengths, outside a closed surface containing all the sources, we get

$$\overline{\mu^2}(n) = \frac{1}{2}\left(1 - \frac{\alpha}{\nu^2}\right) + \frac{1}{2}\left(\frac{3\alpha}{\nu^2} - 1\right)(n^1)^2, \qquad (7.16)$$

which is again independent of geometry. This reduces to $\overline{\mu^2} = \frac{\alpha}{\nu^2}$ for $n^1 = 1$, i.e., n in the direction of the current.

Relation Between the Moments

Multiplying the transport equation (2.2) by Ω^j and integrating, we get, in the asymptotic region,

$$\psi^{(1)j} = -\psi^{(2)ij}{}_{,i}. \qquad (8.1)$$

Introducing

$$(\overline{\mu^2})^{ij} = \frac{\psi^{(2)ij}}{\psi^{(0)}}, \qquad (8.2)$$

so that

$$\overline{\mu^2}(n) = (\overline{\mu^2})^{ij} n_i n_j, \qquad (8.3)$$

we get

$$\psi^{(1)j} = -[(\overline{\mu^2})^{ij}\psi^{(0)}]_{,i}$$

$$= -(\overline{\mu^2})^{ij}\psi^{(0)}{}_{,i} - (\overline{\mu^2})^{ij}{}_{,i}\psi^{(0)}. \qquad (8.4)$$

If $(\overline{\mu^2})^{ij} = \frac{\alpha}{\nu^2}\delta^{ij}$ in the asymptotic region, this would reduce immediately to (5.2). However, it may be seen in fact that this is not so: $(\overline{\mu^2})^{ij}$ is not diagonalized, or even constant in space, in the asymptotic region.

To show this we use the asymptotic form of $(\overline{\mu^2})^{ij}$ derived from (6.4):

$$(\overline{\mu^2})^{ij} = \frac{1}{2}(1 - \alpha/\nu^2)\delta^{ij} + \frac{1}{2\nu^2}\left(\frac{3\alpha}{\nu^2} - 1\right)\frac{\psi^{(0)\ (as),\ ij}}{\psi^{(0)\ (as)}}. \qquad (8.5)$$

We see that $(\mu^2)^{ij}$ varies with position in the asymptotic region and does not reduce simply to a diagonal tensor. The second term on the right hand side of (8.4) is not negligible. It is only by combining the two terms (as may be immediately verified) that we get the relation (5.2).

Higher Moments

We note finally that the methods used in calculating moments up to the second can easily be extended to moments of higher order. In calculating the Fourier transforms of the higher moments, it is necessary to evaluate

$$\int \frac{\Omega^{i_1}\cdots\Omega^{i_m}}{1 - i\boldsymbol{k}\cdot\Omega}\,d\Omega$$

(see (2.10)), or alternatively,

$$\int \frac{T^{i_1\cdots i_m}(\Omega)}{1 - i\boldsymbol{k}\cdot\Omega}\,d\Omega. \qquad (9.1)$$

This is essentially the problem of determining the tensorial generalizations of the Legendre functions of the second kind, just as $T^{i_1 \cdots i_m}$ is the generalized Legendre function of the first kind (Legendre polynomial).

Designating the mth moment, $\int \Omega^{i_1} \cdots \Omega^{i_m} \psi d\Omega$, as $\psi^{(m) i_1 \cdots i_m}$, the mth moment relative to the direction of a unit vector n is

$$\overline{\mu^m}(n) = n_{i_1} \cdots n_{i_m} \psi^{(m) i_1 \cdots i_m}. \tag{9.2}$$

It is easily seen that asymptotically

$$\psi^{(m) i_1 \cdots i_m}$$

will be expressible in terms of derivatives of $\psi^{(0)}$ up to the mth. Conclusions about the nth moments relative to definite directions may be drawn as in the cases considered above.

APPENDIX

Expansion in Tensorial 'Spherical Harmonics'

The function $f(k) = f(ku)$ may be expanded in the form

$$f(ku) = \frac{1}{4\pi} \Sigma_n (2n + 1) \int f(ku') P_n(u \cdot u') d\Omega_u, \tag{A.1}$$

(see Byerly, Fourier's Series and Spherical Harmonics: (Ginn & Co., 1895) p. 211). But using the result (3.4), it follows that

$$f(k) = \frac{1}{4\pi} \Sigma_n (2n + 1) C_n \left[\int f(k') T_{(n)}(u') d\Omega_{u'} \right] T_{(n)}(u), \tag{A.2}$$

from which (4.1), (4.2) follow.

It should be noted that if we attempt to expand $f(k)$ in terms of the spherical harmonic tensors $T_{(n)}$, the coefficients $f_{(n)}$ will not necessarily be unique. For of the $\dfrac{(n + 1)(n + 2)}{2}$ components of $T_{(n)}$ (after taking account of symmetry in all pairs of indices), only $(2n + 1)$ are independent, because of the fact that the $\dfrac{n(n - 1)}{2}$ contractions with respect to two indices of $T_{(n)}$ vanish. There are an equal number of independent coefficients $f_{(n)}$. But if the symmetry and contraction conditions are applied also to the $f_{(n)}$'s, they also become uniquely determined, and have the values (4.2).

References

1. Bethe, H. A.   Rev. Modern Phys. 9 : 130-131.   1937.
2. Bothe, W.   Z. Physik, 118 : 401.   1941.
3. Bothe, W.   Z. Physik, 119 : 493.   1942.
4. Wallace, P. R. and Le Caine, J.   Elementary approximations in the theory of neutron diffusion.   National Research Council of Canada, Division of Atomic|Energy.   1946

THE INITIAL IONIZATION PRODUCED BY FISSION FRAGMENTS[1]

BY D. WEST

Abstract

The ionization produced by individual fission fragments over various lengths of track starting from the origin was measured in a pulse ionization chamber provided with a grid. The distribution of electron pulse sizes for the complete track showed the well known two peaks. As the length of track was diminished, the peaks corresponding to the high and low energy groups of fragments approached each other and merged together at a track length of about 6 mm. in nitrogen. In smaller distances measured from the beginning of the track the difference in ionization by the two groups of fragments was found to be small, and the two groups could not be resolved. From the progressive change in shape of the pulse spectrum it is tentatively concluded that the low energy group produces the greater initial ionization. The average energy spent in ionization by the fragments in the first 1.1, 2.3, and 5.3 mm. of their tracks was measured in nitrogen and found to be 7.6, 15.0, and 34.6 Mev. respectively. In the course of this work an effect due to the formation of negative ions by electron attachment was observed in the chamber filled with argon. Examination of this effect suggests that, at high collecting fields, formation of negative ions, perhaps in impurities such as oxygen and water vapor, is more pronounced in argon than in nitrogen.

Introduction

The general features of the loss of energy of fission fragments in passing through matter have been described by Bohr (2), who emphasized the essential differences in the mechanisms by which α-particles and fission fragments lose energy. In the first place, the effective charge of an α-particle is essentially equal to the nuclear charge during most of its range and decreases only towards the end of the range. On the contrary, the effective charge of a fission fragment is much less than the nuclear charge and decreases continuously from the beginning of the track. Consequently, the specific ionization of a fission fragment can be compared to that of an α-particle between the maximum in the Bragg curve and the end of its range. The energy region in which the specific ionization increases with decreasing velocity for particles as massive as fission fragments should occur at energies much higher than those actually attained in fission, while in the case of α-particles this region occurs at energies above one Mev. Thus, for α-particles the maximum value of the specific ionization occurs not far from the end of the range, while for fission fragments it actually occurs at the beginning of the tracks.

There is another mechanism by which charged particles lose energy in passing through matter: the 'indirect' ionization by nuclear collisions. This effect is of much greater importance for fission fragments than for α-particles. In fact, energy loss by nuclear collisions, which occurs with significant frequency only at the very end of the track of an α-particle, takes place all along the track of a fission fragment. However, even for a fission fragment, the amount of energy lost by this process is small in comparison to the energy lost by direct ionization, *except at the very end of the track.*

Calculations of the energy loss of fission fragments in passing through matter have been made by Lamb (11), Bohr (2), and Knipp and Teller (10). The detailed comparison of these calculations with experiment is, however, made difficult by the wide distribution in mass and energy of the fragments. The energy loss has been investigated in a cloud chamber by Bøggild, Brostrøm and Lauritsen (1). They used the recoil tracks that occur along the track of the fission fragment to deduce its velocity at various points. Their method is most accurate towards the end of the range where recoils are most frequent. Information about the initial part of the range was obtained by Lassen, who performed magnetic deflection experiments and deduced the initial effective charges of the light and heavy groups of fragments (12) and the effective charge and energy of the light group of fragments after they had traversed various thicknesses of mica (13). Lassen obtained results with which Bohr's theory does not agree in detail.

In view of this disagreement and the lack of more complete experimental data about the initial part of the range, a measurement of the initial ionization by fission fragments was undertaken.

Experimental Method

The principle of the method was as follows. A thin sample of fissile material, in this case uranium 233 (16), was placed at the center of a hemisphere. The sample holder and the hemisphere constituted two electrodes of a pulse ionization chamber. By varying the pressure of the gas in the chamber the ionization produced in various distances beginning at the origin of the track of a fission fragment could be investigated. The hemispherical arrangement ensures that the length of track in the gas is the same for all fragments. It was chosen in preference to a parallel-plate geometry and a well collimated beam of fission fragments to avoid loss of ionization in the channels of the collimator.

When the simple hemispherical chamber with two electrodes was filled with argon and tested, it was found to be unsatisfactory owing to the long collection time of positive ions in the electric fields that could be applied. Mr. D. H. Wilkinson suggested a form of grid chamber in which this difficulty is avoided. It was adopted for the experiment and is shown in Fig. 1. The hemispherical geometry is retained but the support for the source is made very small. The potential of the support is adjusted so that electrons produced by the ionizing fragments are not collected by it but move past to the collecting

electrode. A grid placed in front of the collecting electrode shields it from the effect of the motion of the positive ions. This grid consisted of a grating of parallel wires, 0.13 mm. in diameter, spaced at intervals of 1.4 mm., and it
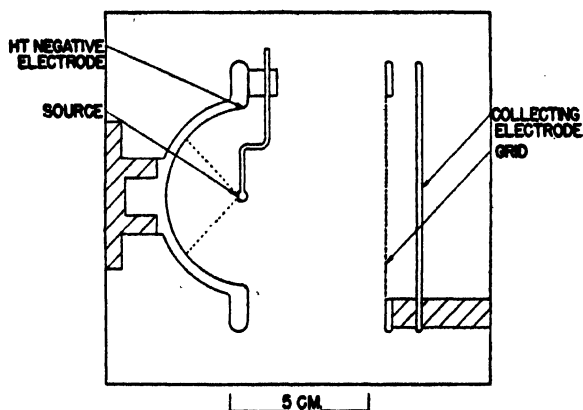
Fɪɢ. 1. *Sketch of pulse ionization chamber.*

was placed 1.1 cm. in front of the collecting electrode. According to the theory of grid chambers that has been given by Bunemann, Cranshaw, and Harvey (5), the residual effect of the positive ions produces a variation of less than 1% in the pulse size in this chamber.

The chamber was irradiated with neutrons in the low power, heavy water pile. The fission pulses were amplified by a linear amplifier, displayed on the screen of a cathode-ray oscilloscope, and photographed on 35 mm. film. The deflection on the screen varied linearly with the voltage applied to the input of the amplifier up to deflections corresponding to pulses of 200 v. A gain control that consisted of a bank of calibrated resistors constituting an anode load was used in the amplifier. It was placed in the first stage to ensure linearity at all gain settings. The bandwidth of the amplifier extended from 0.6 to 80 kc. per sec., at which frequencies the response fell to half of the maximum. This width was sufficient to ensure that the pulse height was independent of any variation of the collection time of the electrons that would be encountered in the experiment. The pulses on the oscilloscope screen were photographed on moving film. The horizontal sweep was not used. The direct spot of the stationary beam on the screen was covered with a narrow slit to eliminate fogging of the film along the base line. This arrangement gave a well defined base line on the photographic record from which precise measurements of the pulse heights could be made.

Preparation of the Fission Source

Since the initial ionization of the fission fragments is to be measured, the loss of energy in the layer of fissile material must be kept as small as possible. An idea of the amount of energy lost in the layer was obtained by calculating

the mean energy lost by an initially monokinetic group of fission fragments in a layer of thickness t. It was assumed that the relation between specific energy loss dE/dl and the residual range l is of the form

$$\frac{dE}{dl} = kl \, ,$$

where k is a constant. Over the initial part of the track this relation is a good approximation to the results of Bøggild, Brostrøm, and Lauritsen (1). The calculation was carried out for the case when the layer of fissile material was covered with a cylindrical collimator, since some collimation was found to be necessary. The behavior of the collimator was idealized by assuming that the number of particles emerging per unit solid angle is independent of the angle of emergence. Since in fact the number of particles per unit solid angle emerging from the collimator decreases almost linearly with the tangent of the angle of emergence, falling to zero at the maximum angle, the expression to be written for the mean energy loss will be an upper limit. The expression derived on the above assumptions is

$$\triangle E = \frac{E_0 t}{R} \left\{ \frac{1}{1 - \cos \alpha} \log \sec \alpha - \frac{t}{3R} \sec \alpha \right.$$

for $t \sec \alpha < R$,

where $\triangle E$ = mean energy spent in the layer by fragments that emerge from the collimator,

   E_0 = initial energy of the fragment,

   t = thickness of the layer,

   R = range of the fragment in the fissile material,

and α = maximum angle of emergence of fragments from the cylindrical collimator, measured from the normal to the layer.

The layer of fissile material was uranium oxide weighing about 0.04 mgm. per cm.^{2} The collimator consisted of holes, 0.75 mm. in diameter, drilled in a metal sheet 0.5 mm. thick. Considering the light group of fission fragments, which have an initial energy of about 90 Mev. and a range $R \sim 6$ mgm. per cm.^{2} in uranium oxide, the mean energy loss in the layer is about 1 Mev.

The error on the measured ionization in the gas of the chamber, caused by the loss of energy in the solid layer, depends upon the pressure of the gas. It is more important at low pressure and sets a lower limit to the pressure at which significant results can be obtained. However, the effect of the layer even at low pressures is not as important as it may appear at first sight.

Consider a solid layer of equivalent depth t of gas and a depth r of gas in the chamber. Fission fragments that originate in the bottom of the layer lose an amount of energy equal to that spent in the first t cm. of the range before they enter the gas. Thus in traversing the chamber they lose an amount of energy equal to that spent between t and $t + r$ (instead of between 0 and r). Hence the energy lost in the layer is replaced by an amount equal to the energy spent between r and $r + t$. The net effect is only a small reduction

in the energy spent in the gas, this reduction being a small fraction of the energy spent in the layer. The amount by which the energy spent in the gas is reduced can be estimated using the approximate energy-range relation given above. The maximum reduction in energy spent in the gas due to the thickness of the layer of fissile material chosen was estimated to be about 1% for a chamber depth equivalent to 1 mm. of air. The layer chosen (0.04 mgm. per cm.^{2}) was therefore sufficiently thin for the measurements.

The layer of fissile material was prepared by evaporating a solution of uranium nitrate in pyridine on a platinum foil. About 40 μgm. of U_3O_8 was converted to nitrate and dissolved in pyridine. This material was evaporated on 1 sq. cm. of foil in many stages. At the end of each stage of evaporation the deposit was ignited. The final deposit appeared to have a uniform yellow color. The gain in weight of the foil showed that no appreciable impurity had accumulated from the evaporation of the pyridine. A small portion of this layer was selected and used as the source.

Chamber Characteristics

In view of the unusual design of the chamber, a detailed study was made of the variation of pulse size with the voltages applied to the electrodes.

A sample of polonium was placed on the source electrode and the chamber filled with argon (99.8% pure) at a pressure just sufficient to prevent the α-particles from reaching the hemisphere. The potentials of the electrodes were adjusted to give the maximum pulse size, and the distribution of sizes was investigated. A well defined peak was obtained, but in addition about one-third of the pulses were of smaller sizes. These small pulses were shown not to be due to the thickness of the source. It was thought that electrons released near the rim of the hemisphere might be collected on the case of the chamber and hence not contribute to the pulse on the collecting electrode. This explanation was shown to be right, since the small pulses were, in fact, eliminated by placing a shallow collimator over the source. This collimator, described in the previous section, reduced the number of small pulses to less than 5% of the total. It limited the emission of ionizing particles to an angle that is indicated by dotted lines in Fig. 1.

The variation of pulse size with the potentials of the grid and source electrode was studied, the potential of the hemisphere being kept constant. (The electron-collecting electrode is connected to ground through a resistance.) Two of the characteristics obtained are shown in Fig. 2.

The grid characteristic (A in Fig. 2) has a well defined plateau when its potential is made sufficiently negative to prevent its collecting any electrons. At the upper end of the plateau there is a falling-off in mean pulse size, which is associated with a broadening of the spectrum of pulses. This is due to the increased ratio of leakage field (between hemisphere and case) to collecting field (between hemisphere and grid) as the potential of the grid is made more negative. The effect is similar to that produced by reducing the degree of

collimation of the source. In fact, the length of the plateau on the grid characteristic was found to depend on the degree of collimation used. As one would expect, the plateau was shorter when a wider collimator was used.
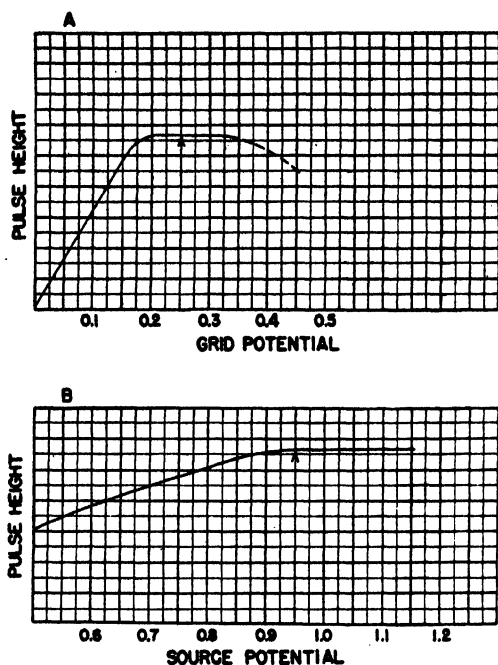
FIG. 2. A. *Graph of pulse height against the grid potential when the source potential was 0.95.*

B. *Graph of pulse height against the source potential when the grid potential was 0.25.*

Potentials are expressed in units of that of the hemisphere. The electron-collecting electrode is grounded through a resistance.

A characteristic (B) for the source electrode is also shown in Fig. 2. As the potential of the source is made more negative, fewer electrons are collected on it and the pulse height increases to a steady value. The potentials of source and grid that were chosen as optimum values are indicated by arrows in Fig. 2.

After the preliminary investigation of the characteristics of the chamber with polonium α-particles was completed, the saturation voltage needed to collect the ions produced by fission fragments was investigated at various pressures of argon. The voltages were applied to the electrodes by means of a potentiometer that varied the total voltage without changing the fractional voltages on the different electrodes. The pulse heights were measured directly on a graduated oscilloscope screen. The mean pulse size was determined at a series of applied voltages, and from the curve of mean pulse size versus applied voltage the saturation voltage was determined.

At a pressure (70 cm. of mercury) sufficient to stop the fragments in the gas of the chamber, saturation was obtained with −1400 v. applied to the

hemisphere. It is of interest to compare this voltage with that required to collect the ions from polonium α-particles at the same pressure of gas. In that case -300 v. on the hemisphere was required to produce saturation.

Investigation of the saturation characteristics for fission fragments at lower pressures of argon revealed a phenomenon that proved to be of importance and led to the use of nitrogen instead of argon.

In argon at a pressure of 10 cm. of mercury, the mean pulse size reached a maximum with -100 v. applied to the hemisphere. On increasing the voltage above 100 v. the mean pulse size decreased, and with -1000 v. the pulse size was only one-tenth of its maximum size. A similar behavior was observed at higher pressures. A check of the reproducibility of the phenomenon was made by refilling the chamber at 10 cm. pressure: the effect was observed again but the variation of the pulse size with voltage could not be reproduced exactly.

Observation of the pulse shape showed that the decrease of pulse height was associated with the appearance of a second pulse that occurred about one millisecond later. This delayed pulse rose much more slowly than the first and was consequently not amplified as much.

It was apparent from these observations that some electrons were becoming attached to gas molecules during their passage across the chamber. The negative ions so formed move much more slowly than the electrons, and, since a pulse is produced on the collecting electrode only after the ions have reached the grid of the chamber, the slow pulse from the negative ions is delayed with respect to that due to the electrons.

The lack of reproducibility of the phenomenon on refilling suggests that the negative ions are formed with impurities in the argon. The argon used was 99.8% pure; the effect, however, was also observed with argon 99.96% pure. The impurities were not identified, but for the purpose of the present argument they are assumed to be oxygen and water vapor. For both these molecules the probability of negative ion formation by electron attachment rises rapidly with electron energy above a certain region of energy (3, 4, 8). Direct measurements of electron attachment by oxygen or water vapor present in small amount in argon are not available. Nevertheless, it is believed that the range of electron energies attained in the present chamber extended into the region where the probability of electron attachment is rising rapidly. This would explain the dependence of the pulse size on the applied electric field. The collecting field in the region traversed by fission fragments is sufficient to collect electrons, but it would be inadequate to prevent recombination of positive and negative ions. Consequently, the fact that the negative ions produced a pulse rather than recombining with the positive ions is an indication that they were formed away from the positive ions, i.e., away from the region traversed by fission fragments (see Fig. 1).

One can thus visualize the effect as follows: the velocities of the electrons in the region beyond the sample, where positive ions are not produced, increase

with increasing field, so that the higher the field, the greater the amount of negative ion formation from impurities. These negative ions can now reach the collecting electrode notwithstanding their low mobility, because in the region considered there are no positive ions produced.

The effect described above introduces a serious difficulty for the measurement of the initial specific ionization of fission fragments when argon is used. The following considerations suggest that other gases may be more desirable in connection with this difficulty.

The motion of electrons in gases has recently been summarized by Healey and Reed (8). The motion under the action of an electric field is a diffusion process that is characterized by two velocities, the agitational velocity and the drift velocity. The drift velocity will determine the collection time of the electrons. It is the mean, in the direction of the field, of the generally much larger agitational velocities. It will be the agitational velocity that determines the formation of negative ions, however. Now the agitational velocity in argon is much higher than in most other gases for a given applied field. Consequently the degree of negative ion formation in impurities of oxygen and water vapor will be considerable even for very small quantities of impurity, as, for example, is indicated by the occurrence of negative ion formation in argon of 99.96% purity mentioned above.

In nitrogen the agitational velocity of electrons is much less than in argon for the same drift velocity. This is essentially due to the larger loss of energy that occurs in a collision of an electron with a nitrogen molecule. On this account one may expect nitrogen to be considerably less sensitive to impurity than argon and in particular that negative ion formation will be much less probable than in argon for a given drift velocity.

The nitrogen used was the commercial grade, which was purified by passing it over heated copper to remove oxygen. No indication of negative ion formation was obtained with this gas even with a field strength five times as great as that at which it became important in the case of argon. The voltage required to produce saturation of the pulses was, however, about twice as great as with argon under similar conditions. Consequently, it was decided to use nitrogen in order to avoid the extreme purity of gas that would have been required had argon been selected.*

Results

In order to verify that the operation of the apparatus as a whole (chamber and associated electronic equipment) was satisfactory, the distribution of the total energy of fission fragments from uranium 233 was measured at a pressure (72.5 cm. of mercury) sufficient to stop all the fragments in the chamber. Unfortunately it was not possible to use nitrogen for this measurement as the necessary saturation voltage could not be applied to the chamber owing

---

* *Margenau et al. (15) have shown that electron attachment in argon takes place to a measurable degree even after extreme precautions to remove impurities have been taken.*

to electrical breakdown. With argon the plateau on the characteristic of mean pulse size versus total voltage, however, extended from − 1600 to − 2000 v. (above which the decrease due to negative ion formation set in). Consequently, it was thought that even with argon this experiment on the total energy of fission fragments would give significant results for control purposes. The pulse heights were measured on the photographic record of the oscilloscope screen. The spectrum of pulses obtained for the total energy of fission fragments from uranium 233 is shown in Fig. 3, *A*. A calibration of the apparatus
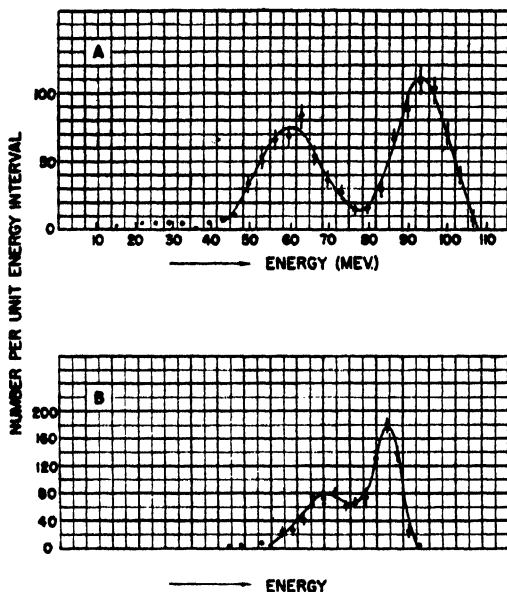
FIG. 3. *A. Energy distribution of 1038 fission fragments from uranium 233 in argon. The depth of the chamber exceeded the range.*

B. Energy distribution of 2040 fission fragments from uranium 233 in nitrogen, made with an electronic pulse analyzer. The depth of the chamber was equivalent to 8.8 mm. path in standard nitrogen. The analyzer was not calibrated in Mev., hence the abscissae are in arbitrary units proportional to the energy spent in ionization.

was obtained by photographing the pulses from polonium α-particles with a pressure of argon sufficient to absorb the whole track within the gas of the chamber. The calibration was performed at a different setting of the gain of the amplifier. Knowing the relative values of the gain in the two cases the energy of the fission pulses could be determined. The energy spectrum of the fission fragments is in close agreement with the energy spectra obtained by Jentschke (9) for the fission fragments from uranium 235 and uranium 238. It was concluded that the operation of the chamber was satisfactory.

The actual experiment on the initial ionization of fission fragments was carried out using nitrogen for the reasons already explained. A separate calibration was performed with polonium α-particles in nitrogen. In order to be able to apply this calibration to all subsequent measurements the gain

of the amplifier was measured in each case so that changes of gain could be allowed for. At each pressure the relation between the mean pulse height and high voltage was investigated, and a suitable collecting voltage chosen. The distributions obtained for the energy spent in ionization in the first 5.3, 2.3, and 1.1 mm. of the tracks in nitrogen reduced to normal temperature and pressure are reproduced in Figs. 4, *A*, 4, *B*, and 4, *C*, respectively. In these
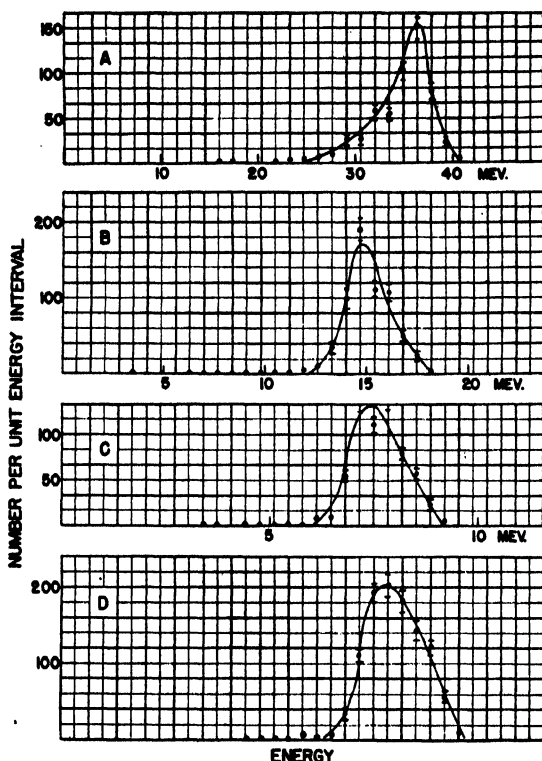
Fɪɢ. 4. *A. Energy distribution of 566 fission fragments from uranium 233 in nitrogen. The depth of the chamber was equivalent to 5.3 mm. path in standard nitrogen.*

B. 662 fragments. 2.3 mm. path in nitrogen.

*C. 680 fragments. 1.1 mm. path in nitrogen.**

D. 1274 fragments. 1.1 mm. path in nitrogen.

While the spectra in A, B, and C were obtained by the photographic method, that in D was obtained with an electronic pulse analyzer. As the analyzer was not calibrated in Mev. the abscissae are in arbitrary units.

spectra the energy lost by the two groups of fragments cannot be resolved. A definite separation into two groups can be made only at greater equivalent depths of the chamber. For instance, Fig. 3, *B*, shows the spectrum of pulse heights in the first 8.8 mm. of track. Here the two groups give energy losses that are sufficiently different for resolution.

* *Two experimental points have unfortunately been omitted. These lie just outside the upper border of the graph.*

The spectrum of pulses obtained with a depth of chamber equivalent to 1.1 mm. of nitrogen shows an interesting asymmetry (Fig. 4, *C*). A similar asymmetry is also evident for a depth equivalent to 2.3 mm. of nitrogen (Fig. 4, *B*). The spectrum rises more steeply on the low energy side in contrast to the behavior at depths of 5.3 mm. (Fig. 4, *A*) and 8.8 mm. (Fig. 3, *B*). This point was confirmed by repeating the measurement of the spectrum for a depth equivalent to 1.1 mm. using an electronic pulse analyzer (7), which was capable of giving better resolution than the photographic method. The spectrum of pulses is shown in Fig. 4, *D*, and its shape confirms the existence of the features observed using the photographic method. It is not possible to account for this behavior in terms of source thickness as energy losses in it would result in a more gradual rise on the low energy side of the peak. Consequently the observed spectra indicate the following.

1. The low energy group of fragments, represented by the left hand peak in the spectrum of total energies shown in Fig. 3, *A*, gives rise to a broader spectrum than does the high energy group. The ratio of the most probable energy of the low energy group to that of the high energy group is about 0.65, in agreement with earlier work (9).

2. In Fig. 3, *B* (equivalent depth of chamber = 8.8 mm. of nitrogen), the two peaks are closer together. If the left hand peak is again identified as the low energy group, the spectrum representing the low energy group is still broader than that representing the high energy group. The ratio of the energies spent by the two groups is now greater and equal to about 0.8.

3. In Fig. 4, *A* (equivalent depth of chamber = 5.3 mm. of nitrogen), the two peaks are no longer resolved, but the more gradual rise on the left hand side of the spectrum indicates that the ratio of the energies spent by the two groups is still less than unity.

4. In Figs. 4, *B*, and 4, *C*, (equivalent depths of chamber = respectively 2.3 mm. and 1.1 mm. of nitrogen), the two peaks are still unresolved, but the more gradual fall on the right hand side of the spectrum indicates that the ratio of the energies spent by the two groups of fragments has become greater than unity. In other words, the 'unresolved peaks' representing the two groups, which have gradually become closer together with decreasing pressure, have crossed over. In physical terms this means that the initial ionization of the low energy group is greater than that of the high energy group.

Finally, in Fig. 5 is plotted the mean energy spent in ionization by fission fragments in various distances from the beginning of the track obtained from these distributions. The mean energy spent in the first millimeter of the track in nitrogen at N.T.P. is 6.5 Mev.

Discussion

The conclusion that the initial ionization is greater for the low energy group of fission fragments than for the high energy group is in accord with the results

of measurements of the specific ionization of fission fragments made by Lassen (14), which were published after the completion of the present work.

There is a disagreement on this point among the various theoretical estimates of the initial ionization that have been made. The ratio of the energy spent in the first millimeter of track by the low energy group of fragments to that
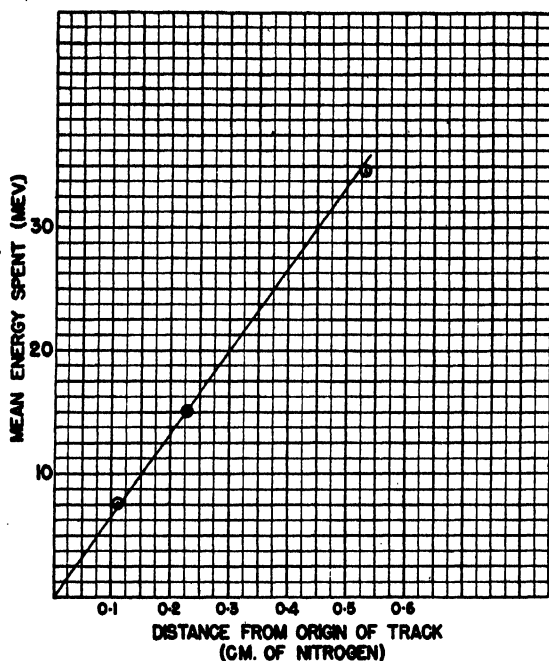
FIG. 5. *Graph of mean energy spent by the fission fragments (both groups) as a function of the distance from the source in nitrogen at N.T.P.*

spent by the high energy group is according to Bohr (2) less than unity. Lamb (11) and Knipp and Teller (10), on the other hand, obtain values for the ratio that are greater than unity. The results of the present work as well as those of Lassen mentioned above are thus in qualitative agreement with the predictions of Lamb and Knipp and Teller as far as the ratio of initial ionization by the two groups is concerned. It should be mentioned that evidence conflicting with the results of Lassen and the present work has recently been published by Demers (6) and Sherr and Peterson (17), who obtain a higher initial ionization by the high energy group of fragments.

Acknowledgments

References

1. BØGGILD, J. K., BROSTRØM,.K. J., and LAURITSEN, T.   Kgl. Danske Videnskab. Selskab. Math.-fys. Medd. 18 : No. 4.   1940.

2. BOHR, N.   Phys. Rev. 59 : 270.   1941.

3. BRADBURY, N. E.   Phys. Rev. 44 : 883.   1933.

4. BRADBURY, N. E. and TATEL, H. E.   J. Chem. Phys. 2 : 835.   1934.

5. BUNEMANN, O., CRANSHAW, T. E., and HARVEY, J. A.   Unpublished report, CRP-247. The use of grid chambers for α-ray analysis.   National Research Council of Canada. 1946.   (Report to be published.)

6. DEMERS, P.   Phys. Rev. 70 : 974.   1946.

7. FREUNDLICH, H. F., HINCKS, E. P., and OZEROFF, W. J.   Rev. Sci. Instruments, 18 : 90. 1947.

8. HEALEY, R. H. and REED, J. W.   The behaviour of slow electrons in gases.   Amalgamated Wireless (Australasia) Ltd., Sydney, Australia.   1941.

9. JENTSCHKE, W.   Z. Physik, 120 : 165.   1943.

10. KNIPP, J. and TELLER, E.   Phys. Rev. 59 : 659.   1941.

11. LAMB, W. E., Jr.   Phys. Rev. 58 : 696.   1940.

12. LASSEN, N. O.   Phys. Rev. 68 : 142.   1945.

13. LASSEN, N. O.   Phys. Rev. 69 : 137.   1946.

14. LASSEN, N. O.   Phys. Rev. 70 : 577.   1946.

15. MARGENAU, H., McMILLAN, F. L., Jr., DEARNLEY, I. H., PRARSALL, C. S., and MONT- GOMERY, C. G.   Phys. Rev. 70 : 349.   1946.

16. SEABORG, G. T., GOFMAN, J. W., and STOUGHTON, R. W.   Phys. Rev. 71 : 378.   1947.

17. SHERR, R. and PETERSON, R.   Rev. Sci. Instruments, 18 : 567.   1947.

SURFACE AREA MEASUREMENTS OF FINE POWDERS USING MODIFIED PERMEABILITY EQUATIONS[1]

By P. C. Carman and J. C. Arnell

Abstract

The several modified Kozeny equations for the measurement of the specific surface of fine powders by gas-permeability methods have been compared. The equations all give very similar surface area values for a set of experimental data. The physical significance of the empirical constants used is discussed and preference is indicated.

Introduction

Within the past two years, two very similar equations have been proposed as modifications of the Kozeny equation for the measurement of the surface area of very fine powders by gas-permeability methods. The use of the Kozeny equation for the determination of the specific surface of powders by the permeability method was first proposed by Carman (5) and was found to give values for the specific surface of a powder for particles having specific surfaces of less than about 5,000 sq. cm. per cc. that were in satisfactory agreement with other methods, such as sedimentation and microscope counting. It was found, however, that, as the particle size decreased and the specific surface increased, divergences were observed between the gas-permeability value of specific surface and that obtained by other methods. These divergences have been accounted for by modifying the Kozeny equation to account for the 'slip' that occurs when a gas flows through capillaries of the same order of magnitude as the mean free path of the flowing gas.

A comparison of two similar modifications of the Kozeny equation is presented in this paper.

Theoretical

The Poiseuille type of equation for capillaries of any shape takes the form (4),

$$u_e = \frac{m^2}{k_0 \eta} \cdot \frac{\Delta p}{L_e} , \qquad (1)$$

where u_e = actual velocity of the fluid through the bed in centimeters per second,

m = mean hydraulic radius in centimeters,

Δp = pressure drop across the bed in dynes per square centimeter,

k_0 = shape factor, whose value generally lies between 2 and 3 (4),

η = viscosity of the fluid in poises, and

L_e = actual length of path traversed by the fluid through the bed in centimeters.

For circular capillaries, $m = r/2$, where r = radius of the capillary, and $k_0 = 2$ and Equation (1) takes the form of the usual Poiseuille equation. Application of this equation to granular beds (4) by putting

$$u = u_e . \epsilon . \frac{L}{L_e} = \frac{Q}{A} ,$$

$$m = \frac{\epsilon}{S_v(1 - \epsilon)} , \quad \text{and}$$

$$k = k_0 . \left(\frac{L_e}{L}\right)^2 ,$$

leads to a form of the original Kozeny equation (7),

$$Q = \frac{A \triangle p}{k \eta L} \cdot \frac{\epsilon^3}{S_v^2(1 - \epsilon)^2} , \tag{2}$$

where u = approach (apparent) velocity of the fluid in centimeters per second,

ϵ = volume of pore space per unit volume (porosity),

L = length of bed in centimeters,

Q = rate of flow of the fluid in cubic centimeters per second,

A = cross-sectional area of the bed in square centimeters,

S_v = specific surface of the granules in square centimeters per cubic centimeter, and

k = Kozeny's constant, which is approximately equal to 5.

Rigden (9) applied the same considerations as used above to the classical Poiseuille equation corrected for 'slip', and arrived at an equation having the form:

$$Q = \frac{A \epsilon \triangle p}{k \eta L} \left[\left\{ \frac{\epsilon}{S_v(1 - \epsilon)} \right\}^2 + \frac{2 \epsilon x \lambda}{S_v(1 - \epsilon)} \right] , \tag{3}$$

where x = a constant, having the value of 0.874, and

λ = mean free path of the gas molecules.

Carman (6) has since pointed out that the slip correction factor used by Rigden was in the form used for circular capillaries, whereas, for granular beds, the correction should be larger than that used by Rigden. He recommends the use of a slightly modified equation used by Lea and Nurse (8, pp. 27-33), which may be written:

$$Q = \frac{A \epsilon \triangle p}{k \eta L} \left[\left\{ \frac{\epsilon}{S_v(1 - \epsilon)} \right\}^2 + \left(\frac{2}{f} - 1\right) \sqrt{\frac{\pi}{2} \frac{R_0 T}{M}} \frac{k_0 \eta \epsilon}{S_v(1 - \epsilon)p} \right]. \tag{4}$$

where f = fraction of molecules evaporated from the surface, or $(1 - f)$ = the fraction of molecules undergoing elastic collisions with the surface, and

$p = (p_1 + p_2)/2$ = mean pressure of the gas in dynes per square centimeter.

Arnell (1), by analogy with the Knudsen semiempirical equation for the flow of gas through capillary tubes at all pressures, arrived at the following equation:

$$Q = \frac{A \epsilon \Delta p}{k \eta L} \left[\left\{ \frac{\epsilon}{S_v(1 - \epsilon)} \right\}^2 + \frac{8}{3} \sqrt{\frac{2R_0 T}{\pi M}} \frac{k \eta \delta \alpha}{S_v(1 - \epsilon) p} \right] , \qquad (5)$$

where R_0 = gas constant in absolute units,

T = absolute temperature,

M = molecular weight of the gas,

δ = variable factor, having a value of approximately 0.9.

α = fraction effective void area and is given by the equation, $\log_{10}\alpha = 1.41\epsilon - 1.40$.

From a comparison of Equations (4) and (5), it is seen that the first terms or the right-hand sides are equal and identical to the simple Kozeny equation (Equation (2)). The second terms on the right-hand sides should also be equal, hence:

$$\left(\frac{2}{f} - 1 \right) \sqrt{\frac{\pi}{2} \frac{R_0 T}{M}} \frac{k_0 \eta \epsilon}{S_0(1 - \epsilon) p} = \frac{8}{3} \sqrt{\frac{2R_0 T}{\pi M}} \frac{k \eta \delta \alpha}{S_v(1 - \epsilon) p} ,$$

which reduces to:

$$\left(\frac{2}{f} - 1 \right) \sqrt{\frac{\pi}{2}} k_0 \epsilon = \frac{8}{3} \sqrt{\frac{2}{\pi}} k \delta \alpha .$$

If f is taken equal to 0.84 (6) and δ as 0.9 (1),

$$\left(\frac{2}{f} - 1 \right) \sqrt{\frac{\pi}{2}} \simeq \frac{8}{3} \sqrt{\frac{2}{\pi}} \delta ,$$

and actual equality is obtained, if $f = 0.79$, which is quite a reasonable value. Thus, if Equations (4) and (5) are identical,

$$\frac{\alpha}{\epsilon} \simeq \frac{k_0}{k} . \qquad (6)$$

Arnell (1) has defined α as a function of ϵ, which could be expressed by the equation $\log_{10}\alpha = 1.41\epsilon - 1.40$, and α/ϵ was therefore a variable, which increased with increasing porosity and approached 1 in the limit. Carman (4) defined k_0/k as equal to $(L/L_e)^2$, that is, he attributed this factor to the tortuous path that must be followed by a fluid in traversing a granular bed. Within the normal working range of porosities, k_0/k has been found to have a value that lies between 0.4 and 0.6, and k_0/k should be constant for any bed where the ratio of the actual length of path traversed, L_e, to the length of the bed, L, is a constant. It now is necessary to re-examine available data to determine whether α/ϵ (or its equivalent) increases with increasing porosity or remains approximately constant.

Calculations

It is possible to study this aspect of the permeability equation by recalculating the data quoted by Arnell (2) for the flow of air through beds of finely powdered quartz and inorganic pigment powders. Arnell originally evaluated

α, using his empirical relation between α and ϵ, and calculated the specific surface using only the second term on the right-hand side of Equation (5). The specific surface can also be calculated using the Kozeny part (first term) of either Equation (4) and (5) and then applying the result to give a value of α/ϵ. This has been done here and the results are given in Table I, together with the original specific surface values.

TABLE I

VALUES OF THE SPECIFIC SURFACE CALCULATED BY DIFFERENT METHODS FROM THE
EXPERIMENTAL DATA OBTAINED BY ARNELL (2) ON BEDS OF FINE POWDERS

Porosity, ϵ	Specific surface (original), S_v, sq.m./cc.	Specific surface (recalculated), S_v, sq.m./cc.	$\dfrac{\alpha}{\epsilon}$
Powdered quartz			
0.425	9	9.4	0.40
0.428	8	9.3	0.43
0.439	7	8.5	0.48
0.475	7	8.0	0.50
0.475	9	9.3	0.40
0.498	10	10.3	0.38
0.510	10	10.1	0.39
0.514	9	9.4	0.40
0.517	9	9.7	0.40
0.528	10	10.0	0.40
0.537	9	8.7	0.46
0.545	9	9.0	0.44
0.563	8	7.8	0.52
0.584	10	8.9	0.42
0.585	11	9.4	0.39
0.604	10	8.8	0.41
0.610	11	9.1	0.45
0.619	10	9.3	0.43
0.621	9	7.6	0.51
	9.1	9.1	0.43
Mapico Red No. 297			
0.636	32	46.3	0.61
0.677	34	39.9	0.63
0.692	40	43.2	0.54
0.718	40	37.3	0.56
0.721	41	40.2	0.55
0.752	44	33.5	0.55
0.766	40	39.8	0.61
	38.7	39.1	0.58
Mapico Yellow Lemon			
0.676	25	29.6	0.48
0.700	29	28.4	0.51
0.704	24	25.8	0.60

TABLE I—*Concluded*

VALUES OF THE SPECIFIC SURFACE CALCULATED BY DIFFERENT METHODS FROM THE
EXPERIMENTAL DATA OBTAINED BY ARNELL (2) ON BEDS OF FINE POWDERS—*Concluded*

Porosity, ϵ	Specific surface (original), S_v, sq.m./cc.	Specific surface (recalculated), S_v, sq.m./cc.	$\dfrac{\alpha}{\epsilon}$
Mapico Yellow Lemon—Concluded			
0.754	26	24.1	0.63
0.767	29	27.3	0.56
0.780	28	27.2	0.62
0.807	24	21.4	0.74
	26.4	26.3	0.59
Hydrated yellow iron oxide			
0.702	31	33.9	0.56
0.721	36	33.9	0.52
0.747	32	29.3	0.60
0.771	33	31.6	0.54
0.778	38	28.5	0.53
0.781	32	27.9	0.64
	33.5	30.9	0.57
Hydrated chromic oxide			
0.656	71	37	—
0.664	49	29	—
0.682	58	33	—
0.691	39	23	—
0.706	33	17	—
0.711	27	16	—
	46	26	
Pure red iron oxide			
0.479	10	12.4	0.48
0.491	13	15.1	0.39
0.543	12	12.6	0.42
0.552	12	12.2	0.44
0.568	10	10.5	0.51
0.583	12	11.0	0.48
	11.4	12.3	0.45
Pure chromic oxide			
0.464	13	14.9	0.34
0.487	13	11.7	0.35
0.493	11	13.8	0.39
0.521	11	7.7	0.43
0.526	11	7.7	0.40
	11.6	11.2	0.38

Discussion

Lea and Nurse (8, pp. 27-33), in discussing the modified equations, expressed no physical picture, but used a slip factor, Z, which on comparison with the equations previously discussed, gives the following equivalents:

$$\text{Equation (4)} \qquad Z = k_0 \left(\frac{2}{f} - 1 \right)$$

$$\text{Equation (5)} \qquad Z = \frac{16}{3\pi} \frac{\delta k \alpha}{\epsilon} = 7.65 \frac{\alpha}{\epsilon}, \qquad (7)$$

if $\delta = 0.9$ and $k = 5.0$.

Lea and Nurse have calculated the values of the slip factor, Z, for several powders.   It is of interest to consider these Z values and to convert them to values of α/ϵ by means of Equation (7).   These valuations are reproduced in Table II.

TABLE II

SLIP FACTORS AND VALUES OF α/ϵ FOR VARIOUS SUBSTANCES

(From Lea and Nurse (8, pp. 27-33))

Substance	Porosity	Slip factor, Z	α/ϵ
Cement 240	0.450	3.29	0.43
	0.475	3.25	0.43
	0.500	3.53	0.46
	0.525	3.27	0.43
Cement 299	0.475	3.32	0.43
Zinc dust	0.425	3.63	0.47
Lithopone	0.500	4.07	0.53
	0.540	3.53	0.46
	0.600	2.94	0.38
	0.650	3.77	0.49
Kaolin	0.500	2.73	0.36
	0.600	2.78	0.36
	0.625	3.21	0.42
	0.650	2.91	0.38

Rigden (9) found that his equation (Equation (2)) did not give a constant value for the specific surface of a powder over a range of mean pressures, but showed a fall-off in the value for the surface at low pressures.   This effect is due to the use of a constant, X, having too small a value.   By reading from his curves in Figs. 3 and 4 and using Table II of his paper, it is possible to recalculate Rigden's data using either the Lea and Nurse type equation or Equation (5) and thus obtain constant values for the specific surfaces.   The resulting values are given in Table III.

From the calculations in Tables I, II, and III, it appears that the values of α/ϵ lie, in general, within the range of 0.4 and 0.6 and show no real trend with increasing porosity.   This is the same range as was found for k_0/k

TABLE III

SLIP FACTORS AND VALUES OF α/ϵ FOR VARIOUS SUBSTANCES

(After Rigden (9))

Substance	Specific surface (original) S_v, sq.m./cc.	Slip factor, Z	$\dfrac{\alpha}{\epsilon}$	Specific surface (recalculated) S_v, sq.m./cc.
Portland cement	1.28	4.3	0.56	1.41
Rapid-hardening cement	1.55	3.4	0.44	1.58
Fine slate powder	2.80	3.9	0.51	3.05
Air-blown' slate	8.43	3.5	0.46	9.44

and it therefore seems reasonable to assume that Equation (6) is a true equality. The term k_0/k is expressed in terms of the increased length of the tortuous path, followed by a fluid in traversing a bed of granules, over the actual length of the bed, and, as it appeared in the derivation of the original Kozeny equation, it should appear in the modifying term. Also the ratio α/ϵ does not show a definite increase with increasing porosity, as it should by definition, and it therefore appears advisable to substitute k_0/k for α/ϵ in Equation (5) and to use it in the following form:

$$Q = \frac{A\,\epsilon\triangle p}{k\eta L}\left[\left\{\frac{\epsilon}{S_v(1-\epsilon)}\right\}^2 + \frac{8}{3}\sqrt{\frac{2R_0T}{M}}\,\frac{\delta k_0\eta\epsilon}{S_v(1-\epsilon)p}\right], \qquad (8)$$

where k_0 has a probable value of about 2.5.

It is now of interest to re-examine the permeability data on carbon blacks reported by Arnell (3) and compare the specific surface values of these blacks given by Equation (8) with those quoted in his paper. The carbon blacks are of particular interest in that the majority of the beds examined showed a constant mass flow over a fairly wide mean pressure range, so that only the second term on the right-hand side of Equation (8) enters into the calculation of specific surface.

In Table IV are presented the recalculated values of the specific surfaces of the carbon blacks using $k_0 = 2.5$ and $\delta = 0.96$ (3) in Equation (8), together with the original values obtained from the permeability data and electron microscope counting. Where the first term on the right-hand side of Equation (8) (Kozeny equation) could be applied, the data are included.

In general, the specific surfaces of the carbon blacks calculated by means of Equation (8) agree very closely with the original calculations. This fact lends support to the view that α/ϵ is probably equivalent to k_0/k and may be replaced by it. Further experimentation should be carried out to settle this point, but for the present either Equation (4) or Equation (8) may be used for the calculation of the specific surface of very fine powders where 'slip' occurs in the gas flow measurements.

TABLE IV

SURFACE AREAS OF CARBON BLACKS

(From Arnell (3))

Black	Porosity	Specific surface, sq.m./cc.			
		Permeability			Electron microscope
		Original	Equation (8)	Kozeny	
Kosmos 20	0.554 0.568 0.579	43 ⎫ 43 ⎬ 42 41 ⎭	50 ⎫ 48 ⎬ 48 45 ⎭	—	47
Kosmos 40	0.584 0.634 0.638	67 ⎫ 59 ⎬ 65 69 ⎭	74 ⎫ 60 ⎬ 68 70 ⎭	—	72
Shawinigan 100% Comp.	0.729 0.762 9.791	67 ⎫ 82 ⎬ 74 72 ⎭	57 ⎫ 66 ⎬ 59 55 ⎭	38 ⎫ 42 ⎬ 41 44 ⎭	78
Statex B	0.601 0.610 0.619 0.636 0.645	97 ⎫ 99 103 ⎬ 99 98 96 ⎭	104 ⎫ 105 107 ⎬ 103 97 102 ⎭	— — — — 73	72
Statex A	0.603 0.639 0.656	98 ⎫ 100 ⎬ 100 103 ⎭	104 ⎫ 101 ⎬ 102 101 ⎭	— — 89	86
Kosmobile 77	0.638 0.670 0.672 0.673 0.674 0.675 0.715 0.721	155 ⎫ 150 155 ⎬ 146 131 131 155 ⎭ 93 70	156 ⎫ 143 148 ⎬ 141 125 125 147 ⎭ 80 61	—	161
Dixiedensed HM	0.696 0.704 0.716	164 ⎫ 144 ⎬ 150 141 ⎭	150 ⎫ 129 ⎬ 134 124 ⎭	118 91 66	165
Kosmobile S	0.653 0.666 0.673 0.692 0.707 0.718	178 ⎫ 197 ⎬ 182 171 ⎭ 126 71 45	175 ⎫ 189 ⎬ 176 163 ⎭ 116 64 39	— — — — 43 —	162
Spheron 9	0.676 0.696 0.696	189 ⎫ 180 ⎬ 184 182 ⎭	179 ⎫ 164 ⎬ 170 166 ⎭	—	144
Voltex	0.707 0.717 0.765	344 ⎫ 328 ⎬ 326 306 ⎭	307 ⎫ 288 ⎬ 280 245 ⎭	—	220
Neo Spectra Mk. II	0.823 0.825 0.828	435 ⎫ 418 ⎬ 428 430 ⎭	309 ⎫ 296 ⎬ 303 303 ⎭	—	259

References

1. ARNELL, J. C.   Can. J. Research, A, 24 : 103.   1946.
2. ARNELL, J. C.   Can. J. Research, A, 25 : 191.   1947.
3. ARNELL, J. C. and HENNEBERRY, G. O.   Can. J. Research, A, 26 : 29.   1948.
4. CARMAN, P. C.   Trans. Inst. Chem. Engrs. London, 15 : 150.   1937.
5. CARMAN, P. C.   J. Soc. Chem. Ind. Trans. 57 : 225.   1938.
6. CARMAN, P. C. Nature, 160 : 301.   1947.
7. KOZENY, J.   Akad. Wiss. Wien. Math.-naturw. Klasse Sitzber 136 (Abt. IIa) : 271.   1927.
8. LEA, F. M. and NURSE, R. W.   Trans. Inst. Chem. Engrs. London, and Soc. Chem. Ind. Symposium on "Particle Size Analysis".   Advance copy, Feb. 4, 1947.
9. RIGDEN, P. J.   J. Soc. Chem. Ind. 66 : 130.   1947.

SOLAR ECLIPSE OBSERVATIONS OF THE IONOSPHERE[1]

By C. W. McLeish

Abstract

The results are presented of ionosphere measurements made in the region of totality during the eclipse of July 9, 1945. An analysis of the results shows effective recombination coefficients of 1.6×10^{-8} for E region, 1.4×10^{-8} for F_1 region, and 1.0×10^{-9} for F_2 region. Evidence of a variable coefficient for E region agrees with the suggestion of Massey and others of a high negative ion density at this level.

Introduction

Because the presence of the ionized regions of the atmosphere, commonly known as the ionosphere, is due mainly to absorbed ultraviolet energy from the sun, a solar eclipse affords an unusual opportunity to study the effect of a known change in radiation over a short period.

For the 1945 total eclipse in Canada, a site was chosen at Victoria Beach, Manitoba, on the shores of Lake Winnipeg. Fig. 1 is a general view showing the lorry, which housed the equipment, the antenna mast, darkroom hut, and supplies tent. This point (lat. 50°48'N, long. 96°32'W) was directly beneath the totality belt at the 200 km. level. Obscuration of the sun here was about 95% on the ground, 98% at 100 km., and 100% at 200 km. The eclipse occurred in the early morning, the sun's elevation being less than 7° on first contact and about 25° on fourth contact.

Observations

An automatic ionosphere recorder was constructed at the National Research Laboratories especially for the eclipse observations, and the equipment was set up on the site and in operation by July 5. Details of this equipment are to be found in the N.R.C. Radio Branch Report PRA No. 132 (3). Fig. 2 is a front view showing the transmitter–receiver rack on the left, the scanner and visual monitor center, and the camera recording unit on the right. The equipment produced virtual height versus frequency curves on 35 mm. film, covering the range 1 Mc. per sec. to 16 Mc. per sec. logarithmically in just over two minutes. Following an observational program laid down by the Canadian Radio Wave Propagation Committee for the ionosphere stations in Canada, records were obtained at 15 min. intervals throughout the month from July 5 to Aug. 5 except on the eclipse day when records were made at five minute intervals over an eight hour period (Fig. 3).

Conditions were quite disturbed for a few days preceding the eclipse when strong auroral displays were seen. Data for the eclipse day are compared with control data for three days before and three days after the event. Owing

to slight disturbances in the E region on July 6 and 12, data for these two days were eliminated in E region calculations.

The photographic records for the days July 6 to 12 inclusive have been carefully analyzed. Virtual heights of the ionized regions were read to an accuracy of 10 km. and critical penetration frequencies to ±0.05 Mc. per sec. The actual time of observation of any particular critical frequency was tabulated to the nearest half-minute.

Analysis of Results

The object of the following analysis is to investigate the general behavior of maximum electron density in each of the regions E, F_1, and F_2. The correlation between the observed values of maximum density during the ecl.pse and the values predicted by the simple recombination law, $\frac{dN}{dt} = q - \alpha N^2$, is studied for the three regions. Maximum electron density, N, is derived from the equation relating it to the critical penetrating frequency of the ordinary ray, $N = 1.24 \times 10^{-8} f^2$, where N is maximum electron density in the region in terms of electrons per cubic centimeter, q is ionizing rate at the level of maximum density N, in terms of electrons per cubic centimeter per second, α is recombination coefficient, and f is frequency in cycles per sec.

The following is the method of analysis used in interpreting the eclipse effects in the ionosphere. From the control data a normal day electron density curve for July 9 was drawn by interpolation for each of the three regions, F_1, E, and F_2 (Curve 1 in Figs. 4, 5, and 6). By assuming values of recombination coefficient, α, for each of the three regions the curve of ionizing rate, q, was drawn as Curve 2 in Figs. 4, 5, and 6. Making a further assumption that the ionizing rate at a given time during the eclipse was proportional to the visible area of the sun's disc, Curve 3 was constructed for each region. Finally by using values of q from Curve 3, the initial value of N and $\frac{dN}{dt}$ from Curve 1 at first contact, and the assumed value of α, curves were constructed graphically to satisfy the equation $\frac{dN}{dt} = q - \alpha N^2$. For each region several values of α were assumed and curves constructed although only those lying close to the observed points are shown.

Let us first consider the correlation shown for F_1 region results in Fig. 4. Because F_1 does not regularly appear until around 6 a.m. in July, Curve 1 is extrapolated beyond the mean of the observed values, back to the time of the beginning of the eclipse. Curves 4 and 5 are electron density curves calculated from assumed values of α of 0.7×10^{-8} and 1.4×10^{-8}. Observed points for F_1 maximum electron density are in fairly close agreement with the curve for $\alpha = 1.4 \times 10^{-8}$ except near the beginning of the eclipse. The deviation here is most probably due partly to error in extrapolation of the mean data and partly to the normal day to day spread in F_1 density. It can be seen that the minimum value of N for F_1 and the time after totality at which it occurs correspond quite closely to the curve for $\alpha = 1.4 \times 10^{-8}$.
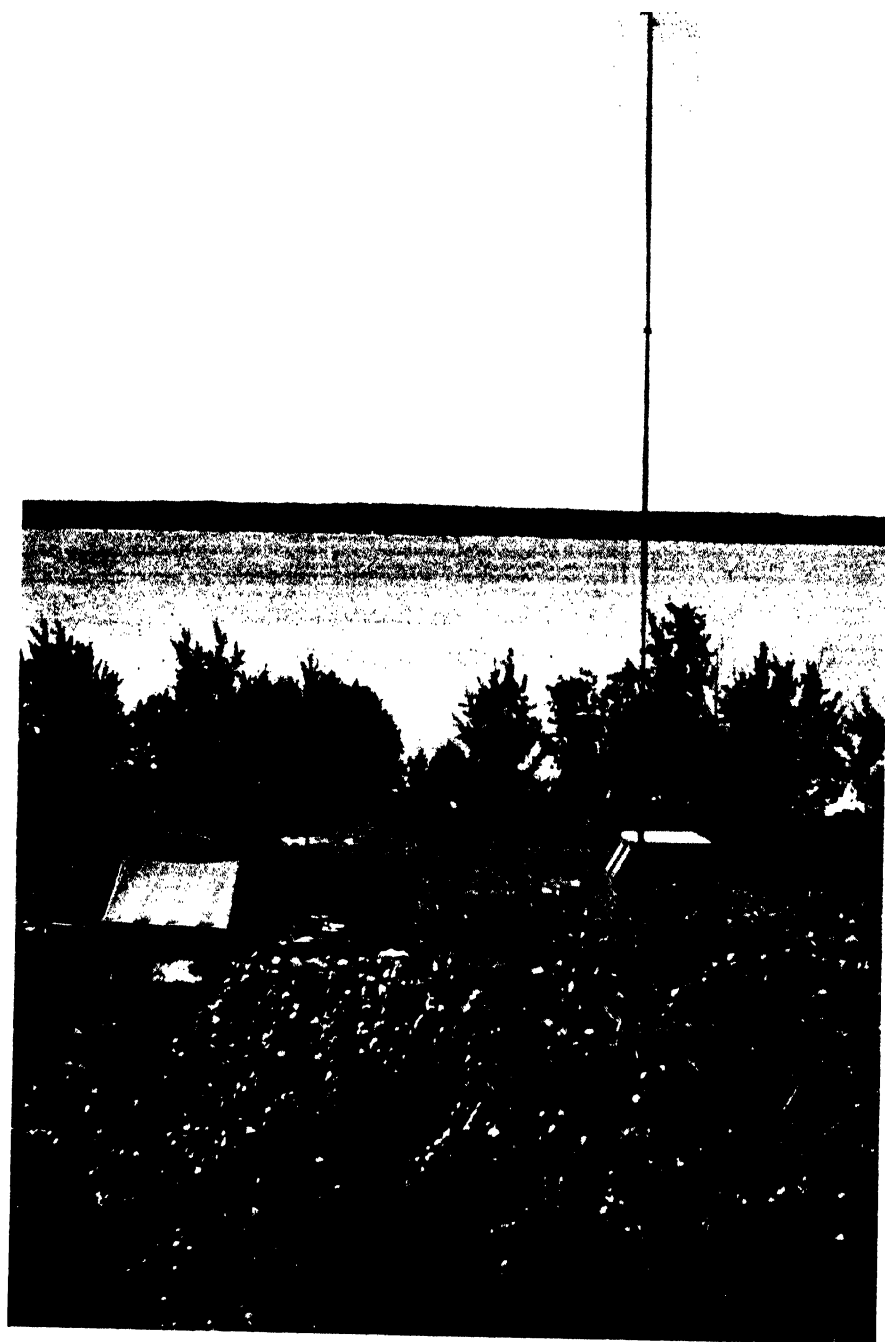
PLATE I

FIG. 1. *Site at Victoria Beach, Man.*

PLATE II

FIG. 2. *Automatic ionosphere recorder.*

PLATE III

07:05
JULY 9

07:25
JULY 9

07:50
JULY 9
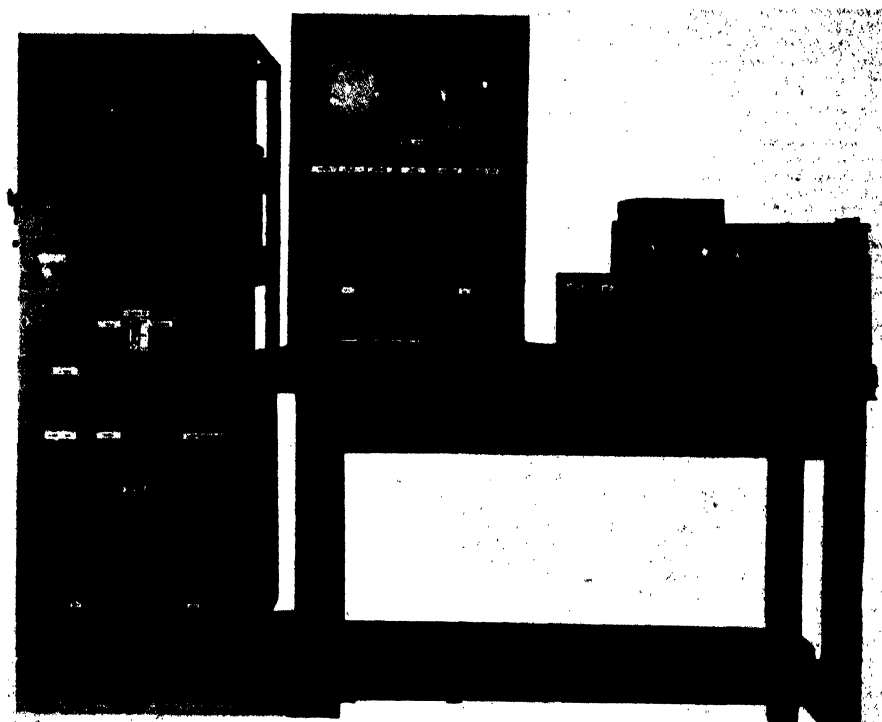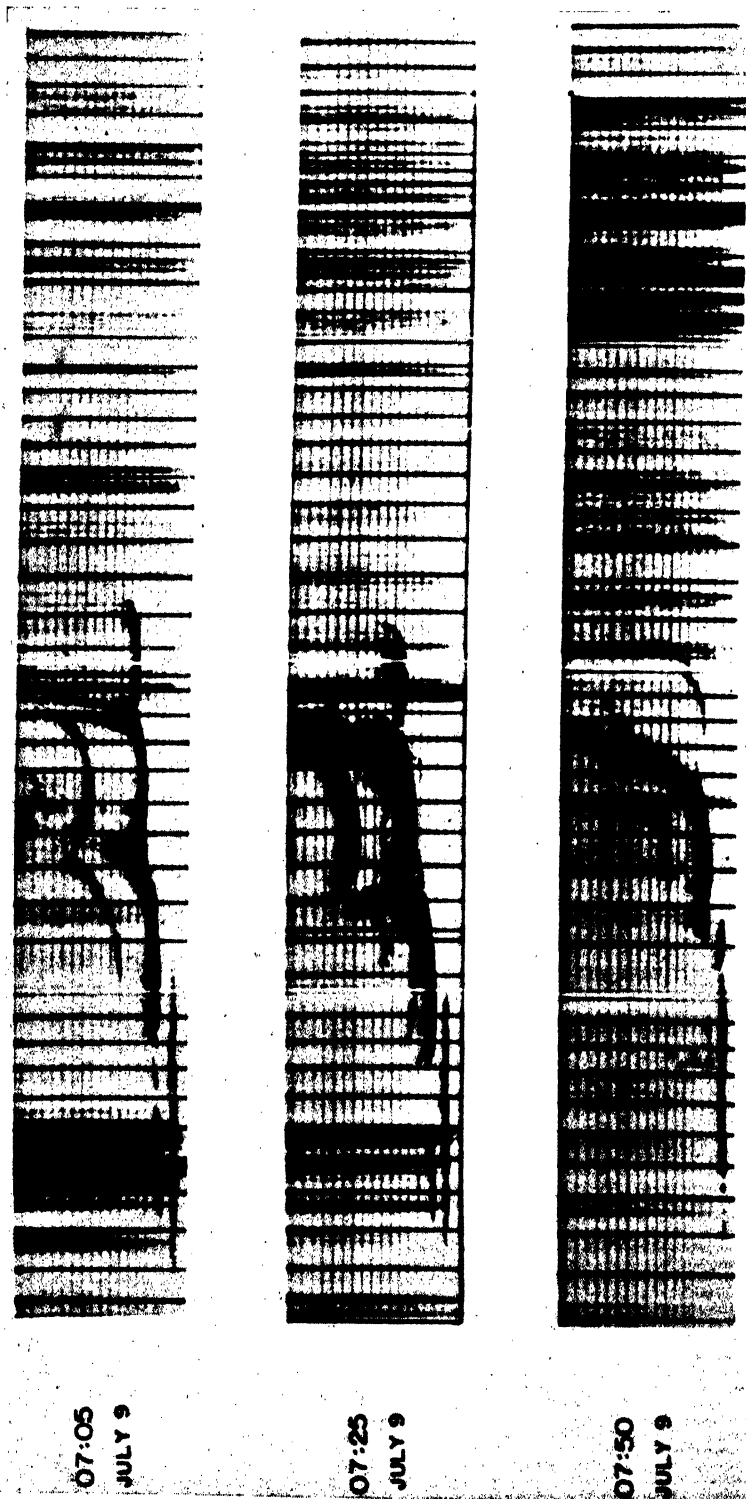
FIG. 3. *Eclipse day ionosphere records.*
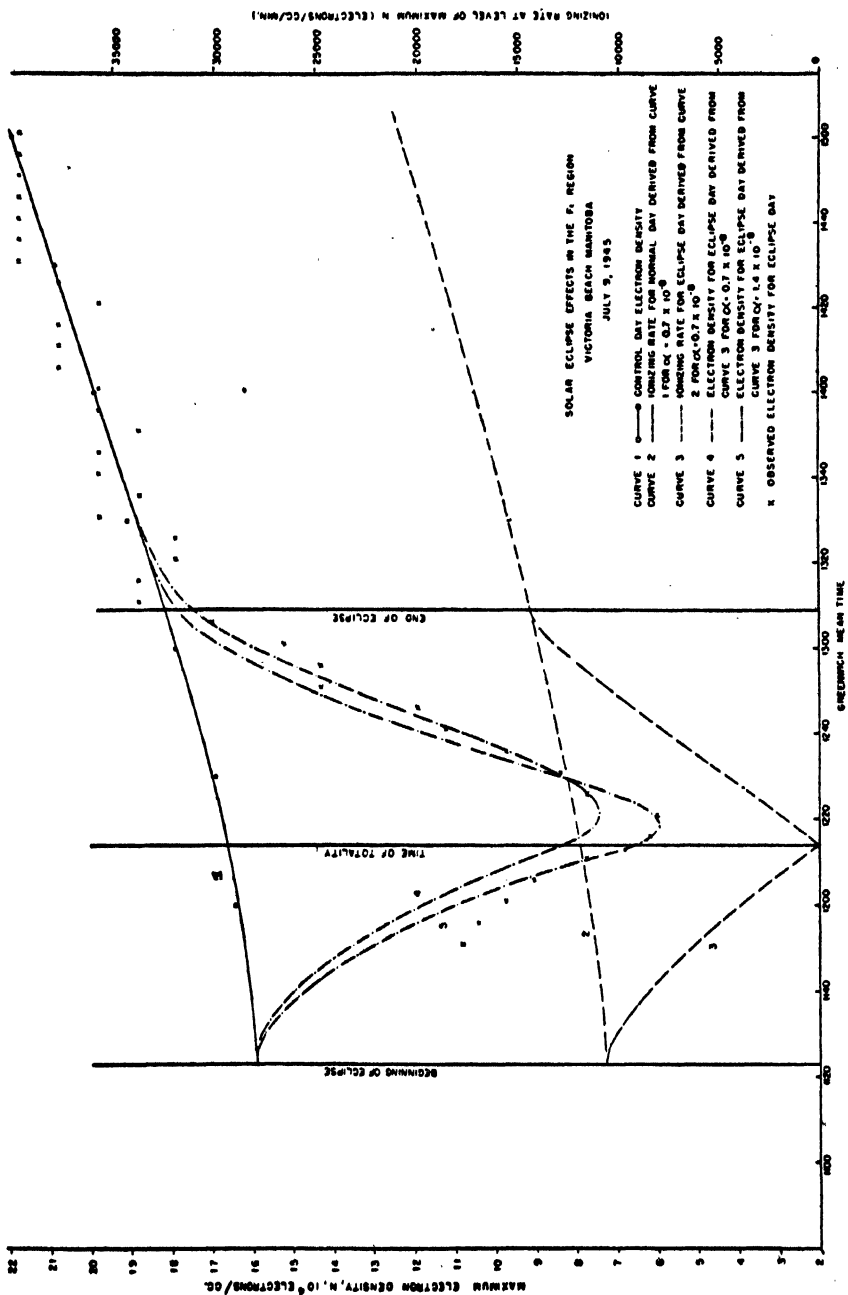
FIG. 4.

E region results do not show the same degree of correlation as observed for F_1. Fig. 5 shows derived curves for two assumed values of α of 1.6×10^{-8} and 1.9×10^{-8}. Curve 6 is a smooth curve showing the general trend of observed points. Although Curve 6 has the same minimum N falling at ·about the same delay time as the curve for $\alpha = 1.6 \times 10^{-8}$, interpretation of this is limited by the accuracy of the observations to a qualitative one, but the discrepancy may be either in the assumption that the sun's radiation is proportional to exposed area only, or in the assumption that the region obeys a simple recombination law. If one assumes that the sun's corona contributes a considerable proportion of the ionizing radiation so as to cause a more rapid fall and rise of q near first and fourth contacts, then one would expect a considerable ionizing rate at totality from the annular ring of the corona which is still exposed. To allow electron density to fall as low as that observed experimentally a large value of α must then be assumed. This, however, would not result in the same order of delay time for the minimum value of N as that observed (5 $\pm$ 1 min.). This alone would seem to rule out any large coronal effect, apart from the fact that none is definitely observed in results of the other regions.

On the interpretation that the region E obeys a different recombination law from the simple one assumed, measurements of the observed curve show a large change of effective recombination coefficient from near the time of first contact to totality. The measurements fit well with the conclusions of Massey, Bates, and others (1, 4) who show that there is probably a high concentration of negative oxygen ions at E region levels. This results in an effective recombination coefficient dependent on the ratio of ion density to electron density in a neutral medium (2). The equation of equilibrium given (1) is

$$\frac{dN}{dt} = q - \left(\alpha_e + \lambda\alpha_i + \frac{1}{N_+}\frac{d\lambda}{dt}\right)N^2 \qquad (1)$$

where N is electron density, electrons per cubic centimeter,

   N_+ is positive ion density, ions per cubic centimeter,

   λ is ratio of negative ion to electron density,

   α_e is recombination coefficient of electrons and positive ions, and

   α_i is the coefficient for electron transfer from negative to positive
       ions.

Probable values assigned to these coefficients are $\alpha_e = 5 \times 10^{-12}$ and $\alpha_i = 2 \times 10^{-11}$, which are derived from controlled laboratory experiments. Because λ is large we may simplify Equation (1) to obtain the approximation

$$\frac{dN}{dt} = q - \lambda\alpha_i N^2 \qquad (2)$$

in which it is assumed that $\frac{d\lambda}{dt}$ is small.
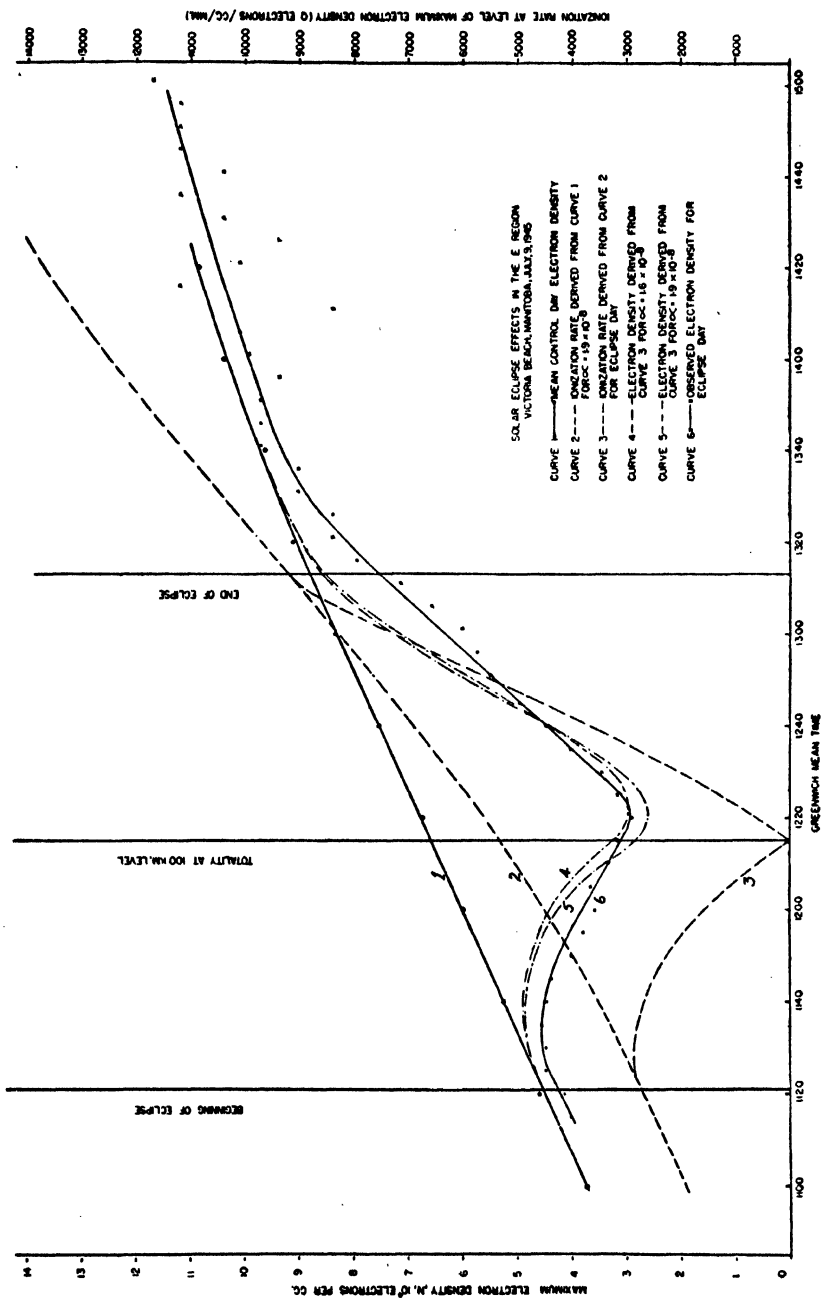
FIG. 5.

At the time 1127 1/2 G.M.T. the value of q reaches a maximum $\left(\frac{dq}{dt} = 0\right)$ so that at this point $\frac{d^2N}{dt^2} = -2N\lambda_1\alpha_i \frac{dN}{dt}$, where λ_1 is the negative ion electron ratio at this time. Measurements of Curve 6 in Fig. 5 give values at this time of $N = 4.50 \times 10^4$ electrons per cc., $\frac{dN}{dt} = 3.58$ electrons per cc. per sec., and $\frac{d^2N}{dt^2} = -0.0136$ electrons per cc. per sec.[2]

Thus,

$$\lambda_1\alpha_i = -\frac{\dfrac{d^2N}{dt^2}}{2N\dfrac{dN}{dt}} = 4.2 \times 10^{-8} \text{ (the effective coefficient),}$$

o

$$\lambda_1 = \frac{4.2 \times 10^{-8}}{2 \times 10^{-11}} = 2100.$$

The figure λ_1 may be correct only as to order of magnitude but serves as a useful comparison with the result obtained at totality (1215 G.M.T.), when, q being zero, $\frac{dN}{dt} = \lambda_2\alpha_iN^2$, where λ_2 is that occurring at 1215 G.M.T.

From the observed curve, $N = 3.1 \times 10^4$ electrons per cc. and $\frac{dN}{dt} = -7.69$ electrons per cc. per sec. Thus

$$\lambda_2\alpha_i = 0.8 \times 10^{-8}, \text{ (effective coefficient)}$$

or

$$\lambda_2 = \frac{0.8 \times 10^{-8}}{2 \times 10^{-11}} = 400.$$

The drop in λ from 2100 to 400 indicated here shows that the term $\frac{1}{N_+}\frac{d\lambda}{dt}$ is likely to be of account in this case.

F_2 region results are shown in Fig. 6. On the eclipse day and on the control days F_2 displayed much more irregularity of critical frequency than did either of the other two regions. The experimental results are, therefore, much less significant in this case. Curve 1, the mean control day density, shows a hump at about 1230 G.M.T. Checking the records for all the days in the eclipse month showed only a slight possibility of a systematic rise of critical frequency at this time. The apparent rise in fact may be due only to the difficulties of analysis, as it appears shortly after the separation of F_2 and F_1 regions. It was, therefore, assumed that the hump was a random variation effect, not smoothed out by control day data, which could not be accepted as a characteristic of the F_2 region. Curves 2, 3, and 4 were derived from Curve 1 (neglecting the hump) for an assumed effective recombination coefficient of 0.1×10^{-8}. It can be seen that the observed points, though badly scattered, show some correlation with the curve. Electron densities were lower both before and after the eclipse than those predicted from the control days, but are well within the expected day to day spread.
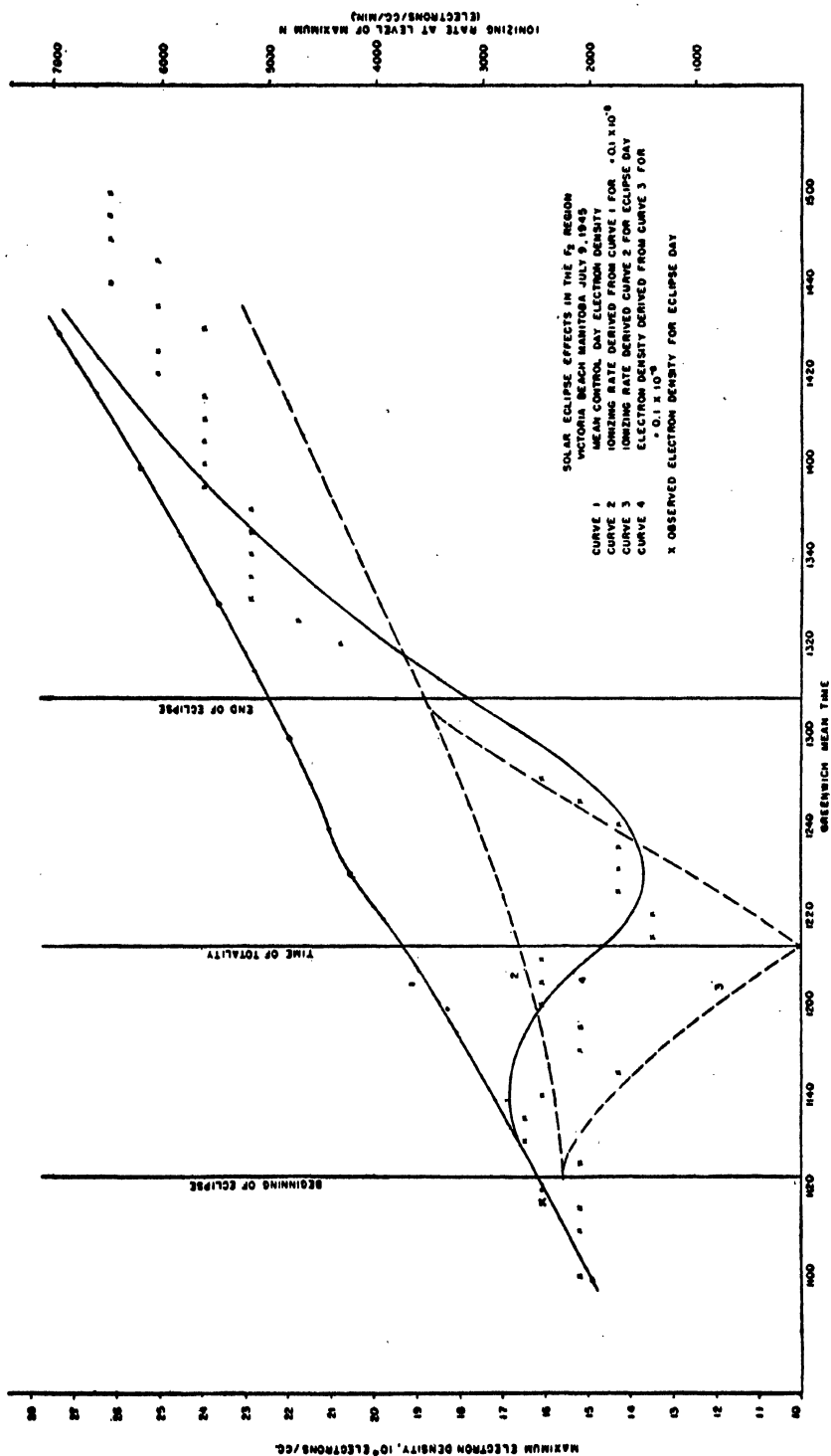
FIG. 6.

An interesting point to be noted is the absence of F_2 reflections for the time between 1251 G.M.T. and 1321 G.M.T. when F_1 maximum densities recovered rapidly enough to approach the F_2 densities in this interval. Absorption in F_1 was too great to allow observation of F_2 echoes during this time.

Conclusions

From the results derived from the eclipse observations at Victoria Beach some conclusions regarding the general behavior of the three main regions of the ionosphere may be drawn.

The F_1 region behaves as though it has a constant recombination coefficient of approximately 1.4×10^{-8}. It seems unlikely that negative gas ions are formed stably at the height 200 to 250 km.

The E region apparently has a varying effective recombination coefficient, the average value during the eclipse being about 1.6×10^{-8}. By making some approximations, the value of coefficient arrived at is about 4.2×10^{-8} soon after first contact, and 0.8×10^{-8} at totality. This shows a drop in ratio of negative oxygen ions to electrons from 2100 to 400 at totality.

The F_2 region shows a distinct eclipse effect but the quantitative analysis is limited by the experimental evidence. An effective recombination coefficient of the order of 1×10^{-9} seems to hold for this region.

It may be said that there is no experimental evidence of a coronal effect in the solar eclipse, and therefore the ionization due to the corona must be small compared with that due to the main body of the sun.

Acknowledgment

References

1. BATES, D. R., BUCKINGHAM, R. A., MASSEY, H. S. W., and UNWIN, J. J. Proc. Roy. Soc. London, A-170: 322. 1939.
2. FERRARO, V. C. A. Terr. Magn. Atm. Elec. 50 : 223. 1945.
3. FREEMAN, R. E. and MOTT, R. I. N.R.C. Radio Dept. PRA-132. 1945.
4. MASSEY, H. S. W. Proc. Roy. Soc. London, A-163 : 542. 1937.

A HIGH TEMPERATURE CONTROL CIRCUIT[1]

BRUCE C. LUTZ AND JOHN H. WOOD[2]

Abstract

This is an electronic circuit useful in the control of electric air-bath furnaces having a long time lag. The control is accomplished by means of a relay that shunts a portion of the resistance in series with the furnace winding. The thermometric device is a thermocouple connected in series with a mirror-type galvanometer and a variable voltage supplied by a potentiometer. The setting of the potentiometer selects the temperature at which the device will control. A light beam falling on the mirror is reflected to one of two photocells. One photocell closes the shunt by means of the described circuit and increases the current in the furnace. This condition is maintained until the beam moves across the second photocell, when the shunt is again opened. The device will control temperatures over 1000° C. within a precision of $\pm 2°$ C. over any desired length of time.

Introduction

The temperature control to be described here was designed for use over a wide temperature range with air-bath furnaces, electrically heated by covered resistance elements. A long time lag is an inherent property of this type of furnace. There are a number of temperature controls described in the literature (1, 3, 4) which will give a higher degree of precision but have limitations as to temperature range, power input to the furnace, or time lag.

The limitation in temperature range is usually imposed by the range of the platinum resistance thermometer. When a thermocouple is used as the thermometric device, the limit is determined by the refractory nature of the elements employed. Thus for a tungsten–molybdenum couple, temperatures in excess of 2000° C. may be controlled.

The furnace resistance wire is also a determining factor on the upper temperature limit. The furnace at present being thermostatically controlled has a nichrome element permitting operation up to 1000° C. However, a furnace is to be constructed employing tungsten windings, thus permitting temperatures in excess of 2000° C.

In the previous circuits, a thyratron was used in series with the furnace as a current regulator by controlling the relative phase of the grid voltage. The use of a thyratron has the advantage of a continuous control. However, such circuits are not applicable over a wide range of power consumption nor do they lend themselves readily to either frequent changes in the required temperature or to changes in the furnace windings. Also, the thyratron circuits depend upon the light intensity falling on a single photocell. It is felt that difficulties in maintaining a constant light source over long periods of time might arise and that, with a single photocell, there is a danger that the

light will move completely off the photocell if there is any appreciable time lag in the furnace. If the latter occurred all control would be lost.

The circuit to be described uses a relay to shunt a portion S (Fig. 1) of the series resistance and thus affords no practical limitation on the power delivered to the furnace. However, to gain in this respect continuous control
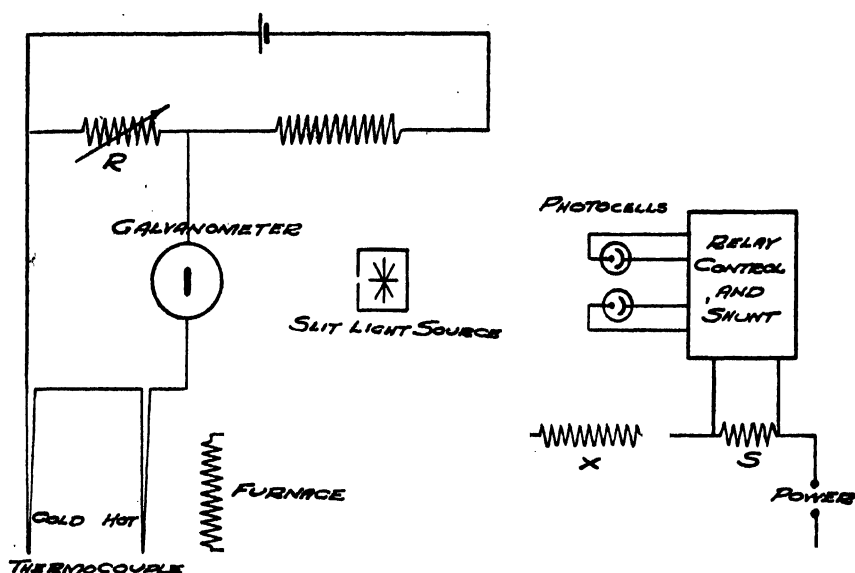
FIG. 1.

has been sacrificed; the effect of discontinuous control may be minimized by keeping the shunted portion of the series resistance as small as possible. The selection of a new controlled temperature has been simplified to two manual adjustments; the setting of the series resistance, X, for approximate temperature and the adjustment of the opposing e.m.f. for the thermocouple (Resistance R).

The chief advantage of this circuit is use of two photocells, one being employed to open and the other to close the shunt. If the light beam passes either cell, the proper action is accomplished as it does so and the light must eventually return to the opposite cell, no ill effects occurring as it repasses the first cell.

Description of the Circuit

The circuit of Fig. 2 consists of the following stages: the relay tube, 6F6, an Eccles–Jordan circuit (2) consisting of two 6C5's, and two pulse circuits functioning alternately. Each pulse circuit consists of an 884 used as a sawtooth generator, a 6F5 used as a bias amplifier, and a 927 phototube.

The relay, an Aminco 'supersensitive' mercury relay, is activated at 10 ma. and releases when the current is reduced to below 2 ma. The current is controlled by the bias on the 6F6 since this tube is in series with the relay. The

bias may be either of two values determined by the condition of the Eccles–Jordon circuit. This circuit (2) has two stable conditions, in either of which one tube is conducting while the other is cut off. When the right hand 6C5
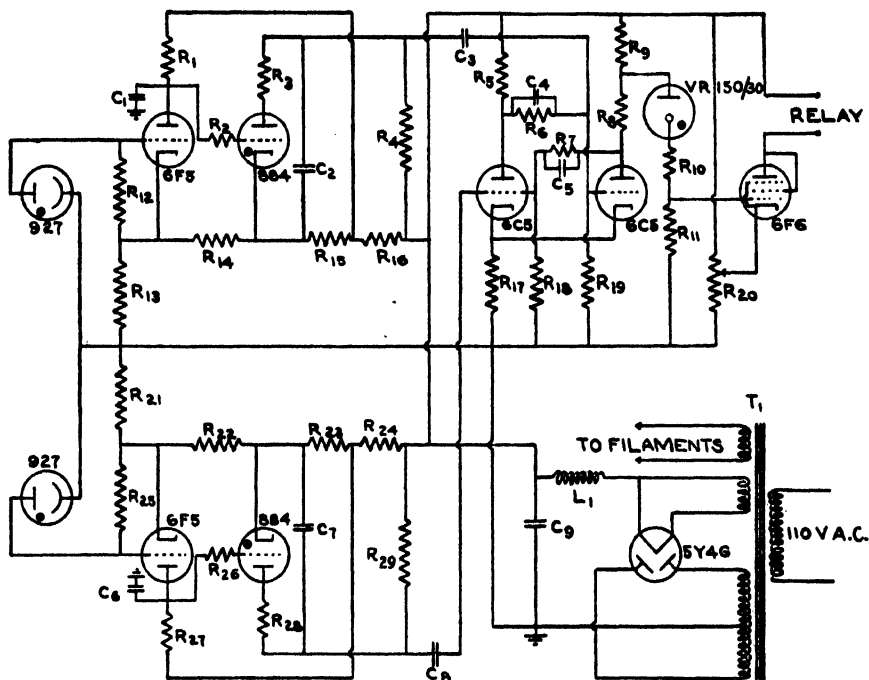
FIG. 2. $R_1 = R_{27} = 330\ K\Omega$. $R_2 = R_{26} = 10\ K\Omega$. $R_3 = R_{28} = 300\ \Omega$. $R_4 = R_{29} = 100\ K\Omega$. $R_5 = 50\ K\Omega$. $R_6 = R_7 = 400\ K\Omega$. $R_8 = 20\ K\Omega$. $R_9 = 25\ K\Omega$. $R_{10} = R_{11} = 100\ K\Omega$. $R_{12} = R_{25} = 5\ M\Omega$. $R_{13} = R_{21} = 15\ K\Omega$. $R_{14} = R_{22} = 25\ K\Omega$. $R_{15} = R_{23} = 5\ K\Omega$. $R_{16} = R_{24} = 25\ K\Omega$. $R_{17} = 20\ K\Omega$. $R_{18} = R_{19} = 100\ K\Omega$. $R_{20} = 10\ K\Omega$. $C_1 = C_6 = 0.005\ \mu fd$. $C_2 = C_7 = 0.03\ \mu fd$. $C_3 = C_8 = 0.01\ \mu fd$. $C_4 = C_5 = 0.35\ \mu fd$. $C_9 = 24\ \mu fd$. $L_1 = 30\ h$. $T_1 = Hammond\ type\ 275$.

is cut off, the bias on the 6F6 allows the tube to conduct the necessary 10 ma. to close the relay. When this 6C5 is conducting, the relay current is reduced below 2 ma. The VR150/30 in the voltage divider permits a maximum change in grid bias at the same time reducing the d–c. drop across the grid return resistor.

The Eccles–Jordon circuit is altered from one stable condition to the other by applying negative pulses to the grid of the tube to be cut off. These pulses are formed by passing a saw-tooth wave from a standard type 884 sweep circuit through a differentiating circuit. In Fig. 2 the upper 884 thyratron supplies negative pulses through the differentiating circuit, C_3 and R_{19}, to the grid of the right 6C5, cutting it off and closing the relay. In a similar manner the lower 884 functions to open the relay.

The saw-tooth wave is produced only when the bias on the thyratron is lifted to a point where the tube can 'fire'. This bias is controlled by a bridge circuit with a 6F5 forming a variable resistance element in one arm. When

the light falls on the corresponding photocell, the negative voltage drop across the grid return resistor of the 6F5 is increased, causing an increase in the resistance of this arm of the bridge, thus permitting the 884 to function. The 6F5 is a high-gain tube and care must be taken to prevent oscillation if the leads from the photocells are long. Since this is a d-c. amplifier, it is permissible to use a large by-pass condenser from plate to ground.

Operation of the Circuit

A high degree of precision is not claimed for this circuit. It was designed for a purpose requiring a precision of only $\pm 2°$ C. at high temperatures ($900°$ to $1500°$ C.), which it accomplished. If necessary this could be improved considerably by increasing the current sensitivity of the galvanometer and improving the optical system. The device has seen 1000 hr. of almost continuous operation and has given excellent performance throughout the period.

Acknowledgment

References

1. BENEDICT, M.   Rev. Sci. Instruments, 8 : 252.   1937.
2. ECCLES, W. H. and JORDON, F. W.   Radio Rev. 1 : 143.   1919.
3. WARING, C. E. and ROBISON, G.   Rev. Sci. Instruments, 14 : 143.   1943.
4. ZABEL, R. M. and HANCOX, R. R.   Rev. Sci. Instruments, 5 : 28.   1934.

THE PHOTOELECTRIC TEMPERATURES OF THE P CYGNI STARS[1]

By C. S. Beals and R. D. Hatcher[2]

Abstract

The photoelectric temperatures of 52 P Cygni stars of spectral type from A4 to O5 have been determined from emission lines by Zanstra's method. For approximately half the stars, accurate spectrophotometric measures of emission line intensities were available and for the remainder the intensities were estimated on the basis of published descriptions of spectra. The computed temperatures were found to range from 10,000° to 42,000° K. and after smoothing by graphical methods a temperature scale for the O, B, and A type stars showed the following values: A0, 16,000°; B0, 35,000°; O5, 40,000° K. Comparisons are made with temperatures derived by other methods and reasons are given for attributing greater weight to the values from B0 to O5 than to those in the lower range of the sequence.

Introduction

There are three principal methods now in use to determine the temperatures of stars, (A) the application of Planck's formula to the observed distribution of energy in the continuous spectrum (6), (B) the use of ionization formulae such as those of Saha in conjunction with observations of relative line intensities of atoms in different stages of ionization (10), (C) the determination of photoelectric temperatures on the basis of the intensity of emission lines relative to the continuous spectrum (14). A fourth method makes use of the Boltzmann formula for the distribution of atoms in excited states but it is of limited application among the early type stars (13). In the present paper data on the intensities of emission lines have been used to derive photoelectric temperatures for a number of stars of P Cygni type.

Theory of Method Used

Method (C), developed by H. Zanstra (14), was originally used to determine the temperatures of planetary nebulae. It has since been adapted to include stars that have around them envelopes such as may have their origin in the ejection of atoms from the surface of the star. This has been done for the Wolf Rayet stars, for a number of stars of P Cygni type, and for several novae by C. S. Beals (1, 3), for Nova Lacertae by A. McKellar (7), and for a number of Be stars by O. Mohler (9). It is particularly advantageous to have this method available in the case of the P Cygni stars since Method (A) is invalidated by the distortion of the continuous spectrum due to space absorption, and Method (B) is made difficult of application by the combination of emission and absorption in P Cygni type spectra.

The application of Zanstra's method involves the following assumptions,

(1) The star is assumed to be a black body radiator of temperature T, obeying Planck's radiation law.

(2) The envelope of the star is assumed to consist of atoms of one element only, and a majority of the atoms are assumed to be in the normal state.

(3) The ultraviolet starlight emitted by the star is completely absorbed beyond the ionizing frequency of the atoms present in the envelope, causing the ejection of photoelectrons.

(4) The photoelectrons recombine with the ionized atoms in the upper states of the atom and in a steady state the number of quanta of ultraviolet starlight absorbed is equal to the number of recombinations in any time interval.

The observational data required for the calculation are values of the quantity A_ν, where

$$A_\nu = \frac{L_p}{\nu \frac{\delta L_s}{\delta \nu}} , \tag{1}$$

where L_p represents the total energy in the emission line, of average frequency ν, and $\frac{\delta L_s}{\delta \nu}$ the total energy per frequency unit of the continuous spectrum for the same frequency. It has been shown by Beals (1, 3) that this quantity A_ν is equal to

$$A_\nu = \frac{1}{c} \int_{V_1}^{V_2} I \, dV , \tag{2}$$

where the V's are the velocity displacements from the center of the band to the edges, I is the intensity of the band relative to the continuous spectrum, and c is the velocity of light in kilometers per second. The quantity

$$\int_{V_1}^{V_2} I \, dV$$

is the equivalent width of the line expressed in units of velocity displacement.

On the basis of the above assumptions the theory as given by Zanstra leads to the equation

$$\int_{x_0}^{\infty} \frac{x^2}{e^x - 1} \, dx = \Sigma \frac{x^3}{e^x - 1} A_\nu , \tag{3}$$

where

$$x = \frac{h\nu}{kT} = \frac{1.432 \times 10^8}{\lambda T} ,$$

$$x_0 = \frac{h\nu_0}{kT} = \frac{1.432 \times 10^8}{\lambda_0 T} = \frac{11600 \, V_0}{T}$$

k is Boltzmann's constant, λ the wave length in angstroms, ν the frequency, V_0 the ionization potential in volts, ν_0 and λ_0 the ionizing frequency and wave length respectively, and the summation is carried out over all the visible emission lines for a particular atom. The equation is solved by trial in order

to determine the value of T. The temperature so determined is the 'photo-electric' temperature referred to in the title of this paper. A more detailed discussion of the theory and its application to individual observations has been given by Beals (3).

Observational Data and the Use of Estimates of Intensity

For a considerable number of the stars considered, spectrophotometric measures of equivalent width made at Victoria were available. These values of equivalent width were derived from plates calibrated with the aid of a rapidly rotating step sector (100 revolutions per second) placed in front of the slit of a calibrating spectrograph. The plates were analyzed with the aid of microphotometer tracings and the process of reducing the tracings to equivalent widths was greatly facilitated by a new intensitometer, which has been described elsewhere (2). The actual observations will be discussed in more detail in a forthcoming publication of the Dominion Astrophysical Observatory. To illustrate the general type of spectrum dealt with in this paper, portions of the spectra of two P Cygni stars have been reproduced in Plate I along with that of an ordinary absorption line star of early type for comparison.

In addition to those stars for which quantitative measurements of line intensity are available there are numerous others for which there are only general descriptions and in some cases published reproductions of spectra. Ordinarily it might be supposed that in such instances no significant calculation of temperatures could be made. However, as Zanstra has previously pointed out, this method of determining temperatures is very insensitive to observational error. This point may be illustrated by the following examples:—

(1) For the star H.D. 31293 taking the equivalent width of the line λ6563 of hydrogen to be 200 and using standard values for the ratios of H_α to H_β, H_γ and H_δ the temperature of the star was found to be 12,800° K. Then taking the value of the equivalent width to be 400, twice as much as before, and using the same ratios the value 13,500° K. was found.

(2) For higher values of the temperature the effect is more noticeable but again not very great. For the star H.D. 151804, using the measured value of the equivalent width of λ4686 He II and doubling the value, the temperatures of 40,800° and 42,800° K. were calculated, whereas, for the same star, measures on a different line from a different ion gave temperatures of 32,400° and 34,600° K. Since the method itself and the assumptions on which it is based involve uncertainties of the order of a few thousand degrees for individual stars, the errors due to the use of estimates are probably not very significant. Accordingly an estimate of line intensity has been made for every star for which a description is available and it is believed that a reasonable degree of confidence may be placed in the temperatures calculated from these estimated intensities.

In our calculations the temperature was calculated for both A_ν as measured or judged and for twice A_ν. This is the same as assuming first, that the

number of observed emission quanta is equal to the ultraviolet quanta absorbed, and second, that the observed are only half those absorbed. The first temperature may be regarded as a minimum temperature, and it will be denoted by T min. in our results.

It should be stated here that the temperatures obtained for the same star by using different atoms or ions show large differences, a result that naturally leads to doubts as to the accuracy of the method. These differences will be discussed in a later part of the paper.

Evaluation of the Integrals

For use in our calculations we require tables of the integral

$$I_1 = \int_{x_0}^{\infty} \frac{x^2}{e^x - 1} \, dx .$$

Zanstra (14) gives a table of this integral for values of x_0 between 0 and 11.0 as calculated by Debye's method. In our work the value of x_0 sometimes reaches values over 20 so that an extension is necessary. This can be seen from the formula,

$$x_0 = \frac{h\nu_0}{kT} \frac{11600 V_0}{T}$$

where V_0 is the ionization potential in volts and T the absolute temperature in degrees Kelvin. If we give V_0 a value of 25 v. or higher and T a value of 15,000° or less we reach values of x_0 near 20.

In calculating values for the integral beyond x_0 equal to 10 an approximation was made that will be shown to be justified. We require

$$\int_{x_0}^{\infty} \frac{x^2}{e^x - 1} \, dx \text{ when } x_0 > 10 .$$

If $x_0 > 10$, then $e^x > e^{x_0} \gg 1$, so that we may replace the above integral by

$$\int_{x_0}^{\infty} x^2 e^{-x} dx .$$

Integrating by parts:

$$\int_{x_0}^{\infty} x^2 e^{-x} dx = e^{-x_0}(x_0^2 + 2x_0 + 2) .$$

On testing this approximation we obtain the values of Table I.

TABLE I

x_0	$\int_{x_0}^{\infty} x^2 e^{-x} dx$	$\int_{x_0}^{\infty} \frac{x^2}{e^x - 1} dx$
10	0.00554	0.00554
5	0.2493	0.2500

PLATE I
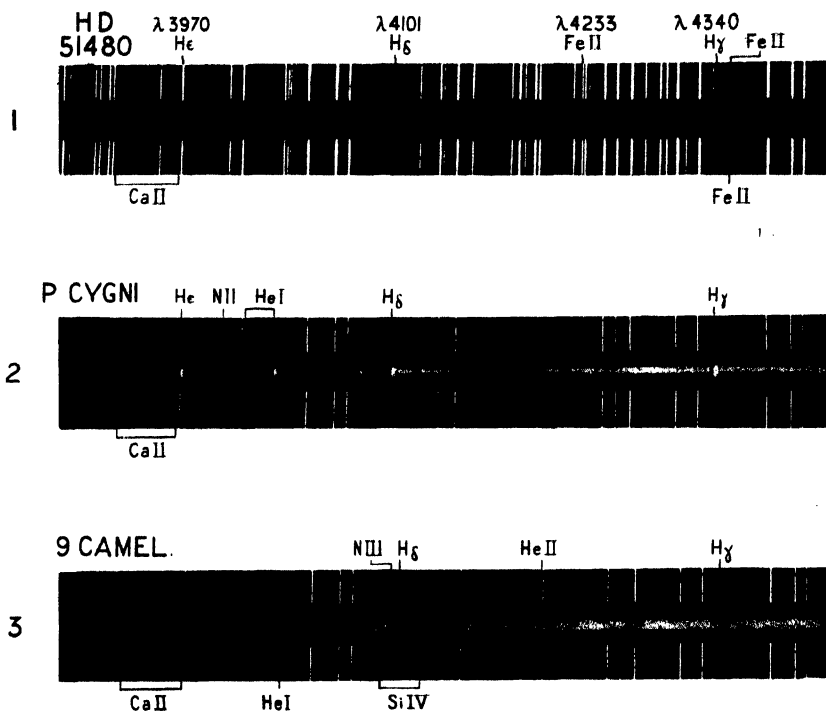
PLATE I

(1) and (2) Emission Line Stars of P Cygni Type.
(3) Ordinary absorption Line Star for comparison.

We thus see that even for values quite low in the table the approximation gives very good results.

Similarly we may calculate values of the second integral used by Zanstra. This is

$$\int_{x_0}^{\infty} \frac{x^3}{e^x - 1} dx ,$$

which becomes

$$\int_{x_0}^{\infty} x^3 e^{-x} dx ,$$

using a similar approximation.

Upon integration by parts as before this gives

$$e^{-x_0} (x_0^3 + 3x_0^2 + 6x_0 + 6) .$$

Trying $x_0 = 5$ we obtain 1.590 by this method, whereas the value by Debye's method is 1.594.

We shall however need numerical values for the first integral only and these as calculated according to the formula above are shown in Table II.

TABLE II

x_0	$\int_{x_0}^{\infty} x^2 e^{-x} dx$	x_0	$\int_{x_0}^{\infty} x^2 e^{-x} dx$
10.0	0.00554	16.0	0.0000326
11.0	0.00242	17.0	0.0000135
12 0	0.00104	18.0	0.00000551
13.0	0.000445	19.0	0.00000225
14.0	0.000188	20.0	0.000000911
15.0	0.0000786		

It may be noted that O. Mohler (9) gives a table calculated by an expansion method for values up to 15.5 in agreement with those given here.

Use of Graphs

To facilitate computation, graphs were drawn from which several of the values appearing in Equation (3) could be read off directly.

From (3)

$$x = \frac{h\nu}{kT} \frac{1.432 \times 10^8}{\lambda T} ,$$

where λ is the wave length in angstroms which for the range dealt with here varies from $\lambda 3700$ to $\lambda 6700$ approximately. Thus for any definite value of T a set of values of the quantity $\frac{x^3}{e^x - 1}$ may be calculated by giving values between $\lambda 3700$ and $\lambda 6700$. This was done initially for values of T of 10, 15,

20, 25, 30, 35, and 40 thousand degrees and this set of seven curves was used in the first few calculations, it being considered sufficient to interpolate between these to obtain the temperature to sufficient accuracy. Later, however, when it was noticed that most temperatures lay in the 10,000° to 20,000° K. group, extra curves were drawn for T equal to 12,500° and 17,500° K. and interpolations made between these values. Occasionally greater accuracy was used for special stars and interpolations between 1000 degree intervals were made. In such cases the values obtained were checked with those obtained by interpolating over wider intervals and it was noted that they agreed to a sufficient degree of accuracy. We cannot claim therefore that the values as given here are as precise as could be obtained by drawing many mc·e intervening curves but it is felt that the accuracy is amply sufficient for the purpose.

Treatment of Hydrogen Lines

As hydrogen played an important role in the spectra of these stars a method of shortening various calculations was devised, using an assumed value for the Balmer decrement.

It will be noted that the equivalent widths for the main Balmer lines in the star P Cygni are

$$H_\alpha : H_\beta : H_\gamma : H_\delta \quad = \quad 3660 : 783 : 325 : 205,$$

leading to the ratios $4.7 : 1.0 : 0.40 : 0.25$. Several of the other stars showed roughly these ratios and so where only H_α or H_γ had been measured it was assumed that the ratios held, and calculations were made accordingly. In come cases when the hydrogen lines showed values different from those given above, a separate calculation was made for the temperature. This ratio is not the Balmer decrement given by some authors, but its connection with it can be seen from References (1, 3). (The values given here are in each case relative to the continuous spectrum at the appropriate wave length.)

Classification

In most cases ordinary absorption line intensity ratios are not available for the P Cygni stars because of the blending of absorption and emission lines. The spectral classes included in the second column of Table III have therefore been determined from the general level of ionization in the stellar spectra. Dr. R. M. Petrie very kindly undertook to classify all stars for which data were available during a visit to this Observatory in January, 1947, and most of the designations in Table III are his. A more detailed discussion of the problems of the classification of the P Cygni stars will appear in a forthcoming publication of the Dominion Astrophysical Observatory. In the meantime it is believed that classifications are precise enough for the present purpose of determining a general relation between spectral class and temperature for the P Cygni stars.

Table of Results

The results of the calculations are given in the following table. Column (1) shows the star, (2) its classification, (3) the atom or ion encountered in its spectrum in emission, and its ionization potential, (4) the wave length of the line, (5) the equivalent width in kilometers per second (6) T min. and (7) T. In order to distinguish between the values of equivalent width that have been directly measured and those that have been estimated, the latter values are enclosed in parentheses.

It will be noted that many more lines occur for some stars than for others. This is either because the emission spectrum is more completely developed or because more complete data are available. In some instances where a spectrum shows marked variations the temperature has been calculated for more than one epoch, as in the case of the star H. D. 108.

TABLE III

TEMPERATURES OF THE P CYGNI STARS

Star	Class	Atom I.P.		λ	E.W., km./sec.	T min., °K.	T, °K.
H.D. 108 (1934–38)	O6–O7	H 13.54		6562.817	295	13,400	15,200
				4861.332	213		
				4340.468	92	.	
				4101.737	52		
(1944–45)				6562.817	82	10,500	11,100
				4861.332	18		
				4340.468	4		
				4101.737	3		
(1934–38)		CIII (47.67)		5696.0	32	36,300	38,300
				4647.40			
				4650.16	37		
				4651.35			
(1944–45)			.	5696.0	30	35,200	36,400
				4647.40			
				4650.16	8		
				4651.35			
(1934–38)		NIII 47.2		4640.64	64	37,200	39,700
				4634.16	33		
(1944–45)				4640.64	42	36,100	38,000
				4634.16	20		
(1934–38)		HeII 54.17		4685.682	47	40,500	42,300
1944–45)				4685.682	28	39,000	40,800
M.W.C.419	B9	H	13.54	4861.332	(200)	15,200	16,100
	.	FeII	16.16	4351.764	(75)	14,500	15,300
				4233.167	(75)		
H.D.7902	B5	H	13.54	6562.817	100	10,700	11,400

TABLE III—*Continued*

TEMPERATURES OF THE P CYGNI STARS—*Continued*

Star	Class	Atom I.P.		λ	E.W., km./sec.	T min., °K.	T, °K.
H.D.12953	A0	H	13.54	6562.817	65	10,300	10,800
C. o Ceti	B	H	13.54	4861.332	(345)	16,000	17,400
		HeI	24.48	6678.149	(114)	24,500	25,900
				5875.618	(270)		
				650			
				5015.675	(98)		
				4471.477	(70)		
		FeII	16.16	4351.764	(75)	14,500	15,300
				4233.167	(75)		
H.D.21389	B9	H	13.54	6562.817	(100)	10,700	11,400
H.D.31293	A0	H	13.54	6562.817	(200)	12,800	13,500
H.D.31648	A2	H	13.54	6562.817	(200)	12,800	13,500
H.D.32256	B	H	13.54	6562.817	(224)	12,600	13,200
				4861.332	(13)		
P Cygni Stars in Large Magellanic Cloud .	B	H	13.54	6562.817	(3660)	17,500	19,300
				4861.332	(783)		
				4340.468	(325)		
				4101.737	(205)		
				3970.074	(129)		
H.D.242257	B	H	13.54	4861.332	348	16,600	17,600
				4340.468	83		
				4101.737	77		
M.W.C.497	B	FeII	16.16	4351.764	(75)	14,500	15,300
				4233.167	(75)		
H.D.41511	AI	H	13.54	6562.817	360	13,400	14,600
H.D.45910 (1937)	B6	H	13.54	4861.332	158	14,700	15,800
(Av. 1939–44)				6562.817	1730	16,100	17,700
(25/3/39)				6562.817	815	14,900	16,000
(1943)				4861.332	81	13,500	14,700
(Av. 1923–24)		FeII	16.16	4351.764	88.3	15,000	15,800
				4233.167	88.3		
(1926)				4351.764	30.1	13,200	14,200
				4233.167	30.1		
(1943)				4351.764	46.6	13,800	15,100
				4233.167	46.6		
H.D.51480	B7	H	13.54	6562.817	2740	16,600	18,200
				4861.332	345		
				4340.468	103		
				4101.737	47		
				3970.074	21		

TABLE III—*Continued*

TEMPERATURES OF THE P CYGNI STARS—*Continued*

Star	Class	Atom	I.P.	λ	E.W., km./sec.	*T* min., °K.	*T*, °K.
H.D.51480	B7	FeII	16.16	4583.829	31	15,000	15,700
				4351.764	27		
				4233.167	68		
				4178.855	19		
				4173.450	22		
H.D.51585		H	13.54	6562.817	(100)	10,700	11,400
H.D.53179		H	13.54	6562.817	(100)	10,700	11,400
M.W.C.560		H	13.54	6562.817	(436)	13,200	14,400
				4861.332	(49)		
η Carinae		H	13.54	4861.332	(2349)	20,400	22,500
		FeII	16.16	4351.764	(225)	16,100	17,600
				4233.167	(225)		
H.D.94878		H	13.54	4861.332	(783)	17,500	19,300
H.D.94910		H	13.54	4861.332	(783)	17,500	19,300
		HeI	24.48	6678.149	(227)	25,900	27,800
				5875.618	(540)		
				650			
				5015.675	(197)		
				4471.477	(139)		
H.D.138403		H	13.54	4861.332	(783)	17,500	19,300
H.D.141969		H	13.54	4861.332	(392)	16,200	17,800
H.D.142983		H	13.54	6562.817	(360)	13,400	14,600
H.D.151804	O9	HeII	54.17	4685.682	(56)	40,800	42,800
		NIII	47.2	4640.64	(40)	38,000	40,400
				4634.16	(84)		
		CIII	47.67	5696.0	(16)	32,400	34,600
H.D.151895		H	13.54	4861.332	(392)	16,200	17,800
H.D.152236	B1	H	13.54	6562.817	(224)	12,600	13,200
				4861.332	(13)		
H.D.152408		HeII	54.17	4685.682	(28)	39,000	40,800
		NIII	47.2	4640.64	(42)	36,100	38,000
				4634.16	(20)		
H.D.160529	A4	H	13.54	6562.817	(100)	10,700	11,400
H.D.161044		H	13.54	4861.332	(783)	17,500	19,300
		OII	35.00	3727.33	(500)	33,300	35,800

TABLE III—*Continued*

TEMPERATURES OF THE P CYGNI STARS—*Continued*

Star	Class	Atom	I.P.	λ	E.W., km./sec.	T min., °K.	T, °K.
H.D.161114	A0	H	13.54	4861.332	(1600)	19,000	20,900
		FeII	16.16	4351.764	(150)	15,300	16,700
				4233.167	(150)		
M.W.C.272		H	13.54	4861.332	(45)	12,500	13,400
		HeI	24.48	6678.149	(170)	25,200	26,900
				5875.618	(400)		
				650			
				5015.675	(148)		
				4471.477	(105)		
		FeII	16.16	4351.764	(68)	14,400	15,200
				4233.167	(68)		
H.D.163296	A2	H	13.54	6562.817	(360)	13,400	14,600
H.D.168607	A0	H	13.54	4861.332	(392)	16,200	17,800
H.D.169226	B3	HeI	24.48	6678.149	(170)	25,200	26,900
				5875.618	(400)		
				650			
				5015.675	(148)		
				4471.477	(105)		
H.D.169454	B2	H	13.54	6562.817	436	13,200	14,400
				4861.332	49		
		HeI	24.48	5875.618	20	18,100	18,900
				650			
H.D.169515	B0	HeI	24.48	5875.618	(400)	25,200	26,900
				650			
		NIII	47.2	4640.64	(3)	30,000	32,000
				4634.16	(3)		
H.D.174638		HeI	24.48	5875.618	(400)	25,200	26,900
				650			
H.D.183143	B7	H	13.54	6562.817	(11)	10,100	10,300
H.D.187399	B8	H	13.54	6562.817	(224)	12,600	13,200
				4861.332	(13)		
H.D.188001	O7	H	13.54	6562.817	89.7	11,800	12,700
		HeI	24.48	5875.618	16.7	17,900	18,600
				650			
		NIII	47.2	4640.64	5.8	32,800	35,100
				4634.16	10.7		
		CIII	47.67	5696.0	44.0	35,300	36,500
H.D.190073	A1	H	13.54	6562.817	1304	15,400	16,600
				4861.332	190		
				4340.468	93		
				4101.737	45		
				3970.074	20		

TABLE III—*Continued*

TEMPERATURES OF THE P CYGNI STARS—*Continued*

Star	Class	Atom I.P.		λ	E.W., km./sec.	T min., °K.	T, °K.
H.D.190073	A1	FeII	16.16	5018.434	98	15,600	15,800
				4923.921	69		
				4583.829	24		
				4555.890	17		
				4534.166	6		
				4522.634	30		
				4515.337	16		
				4508.283	16		
				4351.764	23		
				4233.167	29		
		TiII	13.6	4571.971	22	12,700	13,300
				4549.622	29		
				4533.966	7		
				4501.270	23		
				4468.493	25		
				4443.802	23		
				4395.031	26		
				4300.052	15		
		ScII	12.8	4246.829	22	10.000	10,200
		CaII	11.82	3968.470	50	10,100	10,900
				3933.664	31		
H.D.190603	B2	H	13.54	6562.817	224	12,600	13,200
				4861.332	13		
		HeI	24.48	5875.618	14	17,600	18,200
				650			
P Cygni H.D.193237	B1	H	13.54	6562.817	3660	17,500	19,300
				4861.332	783		
				4340.468	325		
				4101.737	205		
				3970.074	129		
		HeI	24.48	6678.149	227	25,900	27,800
				5875.618	540		
				650			
				5047.736	15		
				5015.675	197		
				4921.929	62		
				4713.143	59		
				4471.477	139		
				4437.549	4		
				4387.928	25		
				4143.759	14		
				4120.812	22		
				4026.189	91		
				4009.270	5		
				3964.727	51		
				3871.819	3		
				3867.477	2		
		NII	29.49	6482.07	13.4	26,100	27,800
				5747.29	2.1		
				5710.76	8.5		

TABLE III—*Concluded*

TEMPERATURES OF THE P CYGNI STARS—*Concluded*

Star	Class	Atom	I.P.	λ	E.W., km./sec.	T min., °K.	T, °K.
P Cygni H.D.193137	B1	NII	29.49	5686.21	10.1		
				5679.56	28.0		
				5666.64	13.8		
				5007.316	19.8		
				5005.140	3.0		
				4643.086	24.5		
				4630.537	32.9		
				4621.392	15.0		
				4613.868	13.2		
				4607.153	14.4		
				4601.478	25.8		
				4447.033	6.6		
				3994.996	18.6		
				3955.851	6.7		
		CIII	47.67	5696.0	1.0	27,000	28,700
H.D.197345	A2	H	13.54	6562.817	11	10,100	10,300
H.D.198478	B2	H	13.54	6562.817	7.7	9,500	10,000
M.W.C.374	B5	FeII	16.16	4583.829	50.7	15,100	16,700
				4555.890	19.8		
				4549.467	29.3		
				4351.764	29.4		
				4233.167	27.7		
				4178.855	18.5		
				4173.450	20.9		
H.D.207757	O9	H	13.54	4861.332	(1566)	19,400	. 20,600
		HeI	24.48	6678.149	(340)	26,900	29,400
				5875.618	(810)		
				650			
				5015.675	(295)		
				4471.477	(219)		
H.D.218393	B8	H	13.54	6562.817	806	14,200	15,500
				4861.332	60.5		
				4340.468	7		
				4101.737	1		
		FeII	16.16	4233.167	17.9	12,500	14,700
H.D.221650 (Z Andromedae)		HeII	54.17	4685.682	123.4	43,200	45,600
		NIII	47.2	4640.64	42	36,100	38,000
				4634.16	20		
Companion of R Aquarii		HeII	54.17	4685.682	(80)	41,100	42,900
		NIII	47.2	4640.64	(46)	36,100	38,000
				4634.16	(20)		
H.D.223385	B9	H	13.54	6562.817	(100)	10,700	11,400

Discussion of Results

In discussing the validity of the results of this study it is important to bear in mind the fundamental limitation of the method, namely, that it claims only to set a minimum value for the temperature of a star. This limitation arises largely as a consequence of the two assumptions (a) that all the radiation to the violet of the ionizing frequency of an atom is absorbed in the process of photoelectric ionization and (b) that most electron captures are made in upper atomic levels.

Referring to assumption (a), even if it could be supposed that all, or a majority of the atoms in an envelope, were of one kind it might well happen in the case of incipient emission that the envelope would be of insufficient optical thickness for complete absorption and this would lead to too low an estimated temperature for the star. Also in a mixed atmosphere, owing to the existence of overlapping regions of absorption, assumption (a) could be realized only under very exceptional circumstances, and the failure of the assumption would again lead to too low a temperature.

There is thus no conflict between the different values of temperature derived for the same star by the use of lines of different atoms. Since each represents a minimum value, the highest calculated temperature (ordinarily derived from the atom of highest ionization potential) should correspond most closely to the true temperature of the star. Also, in the numerous instances where stars of the same spectral type exhibit different emission characteristics and therefore different photoelectric temperatures, the differences may be attributed mainly to the different optical thickness of their respective envelopes.

The assumption regarding electron capture in upper levels is also likely to result in too low rather than too high estimates of the stellar temperature. Here we have followed Zanstra in assuming that half the actual captures result in observable emission. In view of the work of Cillié (5) on the capture coefficients for hydrogen it would appear that most captures take place in the lower levels, the largest number being in the ground state. It is thus possible that considerably less than half the actual captures are made in atomic levels that result in emission lines in the spectral region actually observed and that all the calculated temperatures are somewhat too low.

Incomplete observation of the emission spectrum, which is inevitable in some instances, will have the same result and it would therefore appear that the results of this paper are likely to give rather conservative estimates of the temperatures attained by the O and B type stars.

On the Use of Ions other than Hydrogen

It should be noted that Zanstra's theory was developed for the case of the envelope of a star containing hydrogen only (3) because of the relative ease of the calculations for the hydrogen atom. We have not attempted further development of the theory for the more complex atoms and as a consequence the relation of the observed line intensities to the number of absorbed

ultraviolet quanta is more uncertain than for hydrogen. However, in the more important cases (HeII, NIII, CIII) we have made use of a single line or a single multiplet, and there would appear to be little likelihood that use of the observed intensities would result in an overestimate of the number of ultraviolet quanta. The original aim of the investigation to derive minimum temperatures is therefore preserved, although other considerations arise where the mechanism of fluorescence is involved.

Fluorescence Effects

Bowen's fluorescence mechanism (4) is another factor to be considered in analyzing these results. For completeness we shall give a short discussion along the lines used by McKellar (7) in treating the same phenomenon. Considering first the cycle for the hydrogen–helium case in which the line λ4686 of HeII is produced, the diagram of Fig. 1 shows quite clearly how this line may occur with anomalous intensity, to the exclusion of other lines in its series. Because of the large intensity of λ304 many of the helium ions will
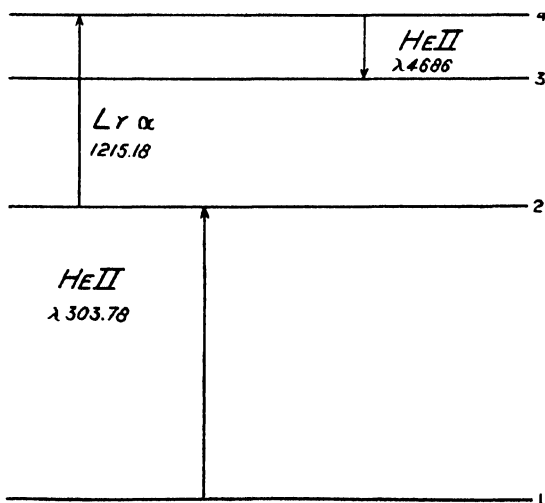
FIG. 1. *Fluorescence cycle for H and HeII.*

be in State 2 as represented on the diagram. Then because of a close coincidence with the very intense Ly$_\alpha$ line of hydrogen the ion may be moved up to State 4 by the absorption of a quantum of Ly$_\alpha$ and on falling back will produce the visible line λ4686, while other members of the series will be absent. The Ly$_\alpha$ line of hydrogen is λ1215.68 while that for helium is λ1215.18, so that it is seen that the coincidence is very close.

The HeII – OIII – NIII cycle is more complicated and consists of two close coincidences. Its mechanism may be seen from Fig. 2. The presence of the wave lengths λ4634–4640 of NIII unaccompanied by the strong lines λ4097–4103 is evidence for its occurrence.

In connection with the above mechanism of fluorescence McKellar makes the interesting comment that since each quantum of λ4640 due to Bowen's line absorption process follows from one of HeII 304 which resulted from the

NIII OIII HeII

^3PDF

LINES
λ3025 TO λ3760

^3SPD

^2D

^3P

LINES
λ4097 TO λ4642

^3P

^2S

λ303.799
λ303.693

λ303.780

λ374.434
λ374.442

λ374.436

λ452

^2P ^3P ^2S
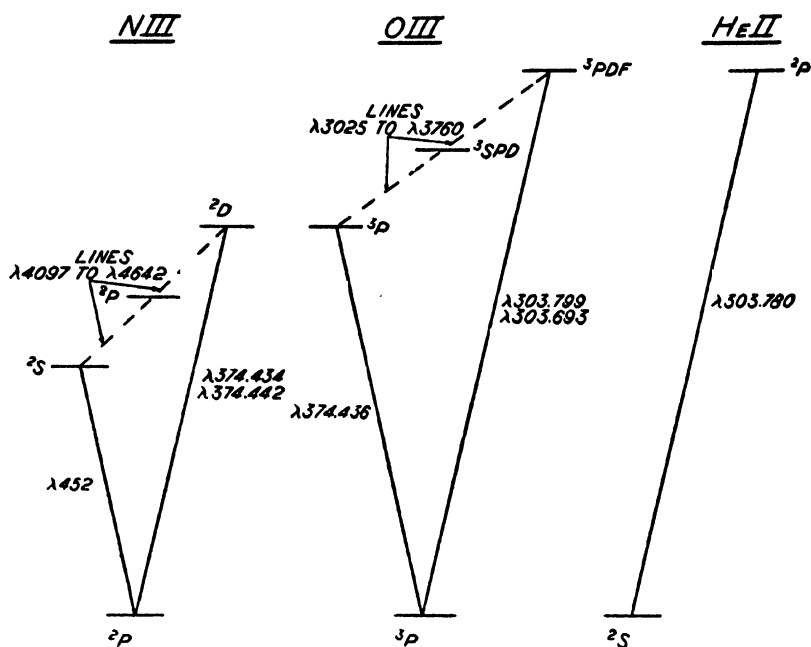
FIG. 2. *Fluorescence cycle for HeII, OIII, and NIII.*

photoelectric ionization of a HeII atom, then the λ4640 quantum should be considered as evidence of the presence of ultraviolet radiation beyond the ionizing frequency of HeII rather than of NIII. Similarly the λ4686 line should be considered as a line of hydrogen, and if so considered the calculated temperature of the star will in general be much lower. In the former case, taking λ4640 as a band of HeII and calculating the temperatures thus, the result obtained will not differ greatly from that found for NIII.

Because of the existence of the fluorescence mechanism it would appear that temperatures calculated on the basis of the lines of NIII and HeII would be somewhat unreliable although it is by no means certain that they would in all cases be too high. However since the action of the mechanism is to increase the intensity of the line it may be expected that such lines will lead to temperatures higher than those due solely to recombination. Fortunately in most instances where lines due to HeII and NIII appear there are also lines due to CIII which does not appear to be involved in the fluorescence mechanism. There is reasonable agreement between the temperatures calculated for CIII and for NIII and HeII although the latter are somewhat higher. In constructing Fig. 3 it was decided to make use of CIII only in

plotting the relation connecting temperature with spectral type, and it will be seen that the points for NIII and HeII are mostly above the curve.
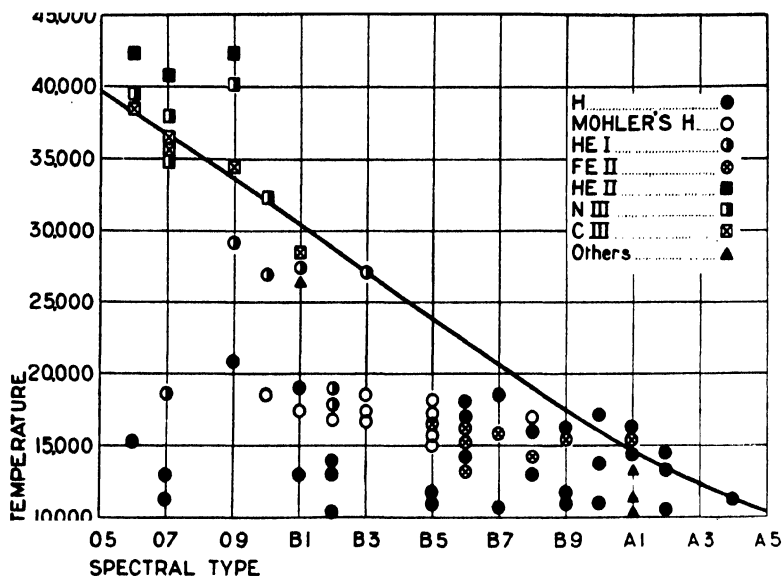
FIG. 3. *Relation between photoelectric temperature and spectra type for the P Cygni stars.*

The Stellar Temperature Scale for Early Type Stars

It will be noticed that the stars cover the range in the spectral sequence for spectral types O6 to A4. In Fig. 3 the photoelectric temperatures found have been plotted against spectral type. For the interpretation of the graph a few remarks are necessary. First, the points seen on the diagram are individual calculations for a star for a definite ion only and not an average for several ions in cases where several appeared. The curve is drawn through the highest points in each of the spectral classes, since the temperature determinations, as has been stated above, refer to minimum values, except in cases where the fluorescence effect may be acting. These latter are most noticeable at the O6 end of the sequence and as will be noticed they lie above the curve. Here the NIII and HeII determinations are generally greater than those for CIII for which no fluorescence effect or coincidences in line wave lengths have been found. The values of temperature from NIII and HeII have been disregarded in drawing the curve. Second, in addition to the values obtained by ourselves, there have also been introduced into the diagram the values of Mohler for the Be stars, principally B3 and B5 of which there were few in our group. These are indicated by open circles. Third, the sudden rise in temperature in the vicinity of B3 is due principally to the appearance in the spectra of measurable lines of ions of higher ionization potential than H, as for example HeI. If a sufficient variety of ions was available we would expect the area under the curve to be completely filled in.

It will also be noticed that temperatures derived from hydrogen do not show much variation with spectral type and the general appearance of the curve would indicate a series of steps for the different ions.

There are several discussions in scientific literature of the temperature scale of stars. One of the most recent is that of Kuiper (8), who also gives a diagram showing the log of the effective temperature against stellar sequence. R. M. Petrie (11) has also given a discussion of the temperatures of the O5–B0 stars. The values given for this part of the stellar sequence by the two writers are not in agreement, Kuiper giving 25,000° to 80,000°, whereas Petrie gives 28,000° to 36,000°. However, as Petrie has pointed out, Kuiper uses values obtained by Beals (3) for Wolf Rayet emission as being applicable to the associated O-type spectra, whereas it is now believed that a composite spectrum is really observed and that the emission line temperatures refer to the W star and not the O-type object.

It may be seen that for our curve the values obtained are, for B0, approximately 30,000°, although this is quite rough owing to lack of stars in this general region, and, for O5, an extrapolated temperature in the neighborhood of 40,000°. These figures are slightly higher than those in Petrie's corresponding classification. For the lower end of the scale our values are somewhat higher than those shown by Kuiper.

There are, as is well known, some doubts as to the validity of applying results from such unusual objects as the P Cygni stars to a determination of the general temperature scale of the stellar sequence. However the temperatures of the hotter stars are subject to so much uncertainty and the results of different investigators differ so widely among themselves that it is surely desirable to make full use of data from every possible source in attempting to arrive at a reliable conclusion. In the upper part of the scale involving the early O-type stars the presence of emission lines due to NIII, HeII, and CIII is a fairly normal feature and is shown by one of the typical stars of the group H.D. 188001. It would therefore seem quite permissible to make use of these lines to fix the temperature at this end of the scale.

Those early A-type stars that show P Cygni characteristics are on the other hand mostly quite unusual objects. A number of them have exceptional luminosities while in one or two instances it is suspected that the spectra are composite. As a consequence the present determination is probably entitled to less weight for the lower end of the range than for the O-type stars. From a number of converging lines of evidence the temperature scale has been fixed at 10,000° for class A0 and it will be noted from the diagram that our values are approximately 6000° higher. It should be pointed out however that Williams (12), on the basis of color temperatures, places the temperature of the A0 stars at 15,000° while the Greenwich observers (6) place them even higher so that it is by no means certain the present determination is in error.

For the O type stars it may be recalled that Petrie has derived temperatures of 28,000° to 36,000° while Payne (10) in an earlier work, gives 35,000° for the O stars as a class. The present determination (32,000° to 40,000°) is in

reasonably good agreement with these values and, since the discovery of the binary character of certain Wolf Rayet stars has explained the high values for the O's (65,000°) given by Kuiper, it now becomes possible to speak with some confidence of the order of magnitude of the temperatures in this part of the stellar sequence.

Acknowledgment

References

1. BEALS, C. S.   J. Roy. Astron. Soc. Can. 34 : 169.   1940.
2. BEALS, C. S.   J. Roy. Astron. Soc. Can. 38 : 65.   1944.
3. BEALS, C. S.   Pubs. Dominion Astrophys. Observ. Victoria, B.C. 6 : 93.   1934.
4. BOWEN, I. S.   Astrophys. J. 81 : 1.   1935.
5. CILLIÉ, G.   M.N. 92 : 820.   1932.
6. DYSON, Sir. F.   Observations of color temperatures of stars.   H.M. Stationary Office, London.   1932.
7. HARPER, W. E., PEARCE, J. A., BEALS, C. S., PETRIE, R. M., and McKELLAR, A.   Pubs. Dominion Astrophys. Observ. 6 : 317.   1937.
8. KUIPER, G. P.   Astrophys. J. 88 : 429.   1938.
9. MOHLER, O.   Pubs. Observ. Univ. Mich. 5 : 43.   1933.
10. PAYNE, C. H.   Stellar atmospheres.   Harvard Observ. Monograph No. 1.   1925.
11. PETRIE, R. M.   Pubs. Dominion Astrophys. Observ. Victoria, B.C. 7 : No. 21.   (In press).
12. WILLIAMS.   Pubs. Observ. Univ. Mich. 7 : 147.   1939.
13. WRIGHT, K. O.   Pubs. Dominion Astrophys. Observ. Victoria, B.C. 8 : No. 1.   (In press).
14. ZANSTRA, H.   Pubs. Dominion Astrophys. Observ. Victoria, B.C. 4 : 209.   1929.

A RADIO METHOD OF STUDYING THE YAW OF SHELLS[1]

By C. C. Gotlieb, P. E. Pashler, and M. Rubinoff[2]

Abstract

A new method of investigating the angular motion of a shell in flight is described. This is a radio method wherein the fuse of the shell is replaced by a high frequency transmitter and the radiated signal is recorded at a ground station. The theory of the method is given, the equipment described, and the procedure in the analysis of the records is discussed. Results of experiments are quoted and values of the force coefficients are deduced. In addition to those coefficients usually determined by jump card experiments, certain other coefficients, involving spin, are evaluated. The radio method of measuring yaw is compared with other methods.

I. Introduction

This paper contains an account of certain work in ballistics carried out by the authors at the Department of Physics, University of Toronto.

The subject of the work is a new method of investigating the angular motion of a shell in flight. This method was made possible by techniques originating in the radio proximity fuse development. Early in the fuse development it was found that the spin of the shell could be determined, and considerable attention was given to this both in the U.S. and Canada. Later, work was done at the University of Toronto in an effort to correlate certain features of spin recordings with secondary oscillations of the shell. The essential feature of the present method, however, was put forward by Mr. A. F. H. Thomson of the Directorate of Naval Ordnance (U.K.), who suggested a method for the measurement of the yaw angle of a shell.

In the radio method of investigating a shell's flight the fuse of the shell is replaced by a high frequency radio transmitter and the radiated signal is recorded at a suitably located ground station. The angular oscillations of the shell produce corresponding changes in signal level, and this paper describes how these fluctuations in signal strength may be used to determine the angular motion. The theory of the radio method is given, and, after certain simplifying assumptions are made, a formula suitable for application to experimental results is derived.

The angular motion of a shell in flight has been the subject of considerable study in the past. Most previous work has, of course, been devoted to problems of immediate practical concern in the design of projectiles. However, a fundamental study was made by Fowler, Gallop, Lock, and Richmond (2) who published their results just after the Great War. In their paper, a system of forces was assigned, the equations of motion were set up and solved approximately, and the theories were tested by experiment. In this paper the same force system and angular motion is assumed, and there follows a summary of those results that are employed in the radio method.

II. The Theoretical Background

1. THE FORCE SYSTEM

Let the instantaneous direction of the axis of the shell be represented in Fig. 1 by OA, and the instantaneous direction of motion of the center of mass O, by OP. By definition:

  (i) The plane AOP is the plane of yaw;

  (ii) The angle AOP is the angle of yaw, denoted by the letter δ;

  (iii) The angle of rotation of the plane of yaw about OP is the azimuth, denoted by the letter ϕ.
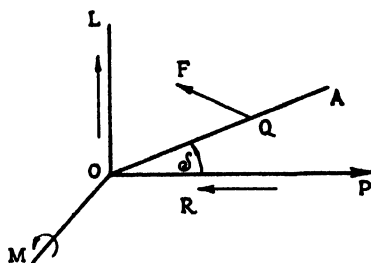
FIG. 1.

For the moment, we regard the shell as at rest and the air streaming past it with uniform velocity, v, equal and opposite to that of the shell. The aerodynamic forces can be represented through symmetry by a single force F, located in the plane of yaw, and acting through the center of pressure, Q, on the axis OA. The force F can be replaced, as shown in Fig. 1, by

  (i) The drag R, which acts through O in the direction of the air stream;

  (ii) The cross-wind force L, which acts through O in the plane of yaw, perpendicular to R, and is positive when it tends to move O in the direction from P to A;

  (iii) The moment M about O, perpendicular to the plane of yaw, and positive when it tends to increase δ.

The following forms are assumed for R, L, and M:

$$(1) \quad \begin{aligned} R &= \rho v^2 r^2 f_R(v/a,\ \delta) \\ L &= \rho v^2 r^2 f_L(v/a,\ \delta) \sin \delta \\ M &= \rho v^2 r^3 f_M(v/a,\ \delta) \sin \delta, \end{aligned}$$

where ρ is the density of the air, r the radius of the shell, and a the velocity of sound in the undisturbed medium.

These equations are of the most natural form to make the force coefficients f_R, f_L, and f_M, of no physical dimensions. Since L and M vanish with δ through symmetry, the factor $\sin \delta$ is included explicitly in order that f_L, f_M, may have non-zero limits as $\delta \to 0$. Further discussion of the dependence of the force coefficients on the constants of the medium (diameter of molecules, ratio of specific heats, etc.) is given in § 1.01 of the paper by Fowler et al.

In practice the direction of the axis of the shell changes relative to the direction of motion.   We assume that R, L, and M are unaltered by the angular velocity of the axis, but that the effect of the angular motion of the axis of the shell can be represented by the introduction of a damping couple, H, called the "yawing moment due to yawing" and acting in such a way as directly to diminish the resultant angular velocity, ω, of the axis of the shell, as shown in Fig. 2.
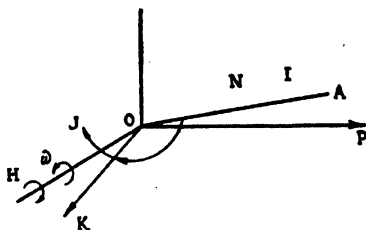
There is a possible effect due to the spin N of the shell about its axis.   It is assumed that the spin does not affect any of the preceding force components but gives rise to additional components.   There will be a couple I which tends to reduce N.   When the shell is yawed, there will be a sideways force K', analogous to that producing swerve on a tennis ball, which need not act through O but which must act normal to the plane of yaw, if it is not to alter R or L, as assumed.   The force K' can be represented by an equal force K through O and a couple J about O.   The complete effects of spin can be represented, therefore, by the addition of the couples I and J and the force K, acting as shown in Fig. 2.

These forces are represented by the equations:

$$(2) \quad \begin{aligned} H &= \rho v \omega r^4 f_H(v/a, \dots) \\ I &= \rho v N r^4 f_I \\ J &= \rho v N r^4 f_J \sin \delta \\ K &= \rho v N r^3 f_K \sin \delta \end{aligned}$$

As before, the force coefficients are of no physical dimensions.   Moreover, these force coefficients may depend appreciably on other arguments, such as $\omega r/v \cdot$ and δ.

In deriving the equations of motion, Fowler *et al.* were able to simplify the algebra by defining new coefficients by the equations:

$$(3) \quad \begin{aligned} M &= \mu \sin \delta \\ L &= \kappa m v \sin \delta \\ H &= hB\omega \\ I &= -AN\Gamma \\ J &= AN\gamma \sin \delta, \end{aligned}$$

where A and B are, respectively, the moments of inertia of the shell about longitudal and transverse axes through the center of gravity, and m is the mass of the shell.

The complete force system is seen to consist of seven components; of these, by far the most important are R, L, and M; then, somewhat less important, H. Only one relation between the forces is available, that between R, L, and M. For shells of given shape moving in a given manner, the forces R and L are independent of the position, O, of the center of gravity, while the moment M varies with the position of O. If M_1 and M_2 are the values of M corresponding to positions O_1 and O_2, then

(4) $M_1 = M_2 + O_1O_2(L \cos \delta + R \sin \delta)$,

where $O_1 O_2$ is positive when O_1 is nearer the base than O_2. For small yaw, this equation reduces to:

(5)   · $f_{M_1} = f_{M_2} + \dfrac{O_1O_2}{\cdot} (f_L + f_R)$.

This is the only method of finding f_L .

2. Description of the Angular Motion

We consider here only what Fowler *et al.* call "Motion of Type α". This type of motion occurs in the early part of all trajectories, and for the whole of a trajectory whose initial elevation is less than 45° and muzzle velocity greater than a few hundred feet per second. The characteristic feature of Type α motion is that the axis of the shell and the direction of motion of the C.G. deviate only by small angles from the tangent to the corresponding plane trajectory. To simplify the treatment to be employed here, the assumption is made that the directions of motion in the plane trajectory and in the actual trajectory are parallel for that region of the trajectory under investigation (up to six seconds from the instant of firing). This assumption can be justified to experimental accuracy in this case by reference to Sections 3.64 and 3.65 of Reference (2). The following system of axes is chosen; the $O1$ axis is the direction of motion of the center of gravity; the $O2$ axis is the upward normal; and the $O3$ axis is horizontal and to the right as viewed from the gun (Fig. 3).
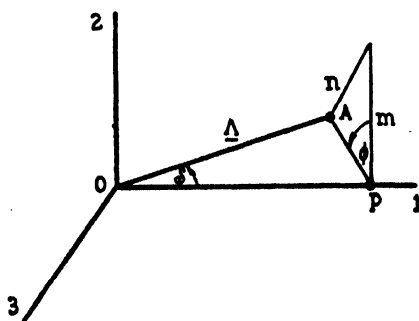
Fig. 3.

OA is the axis of the shell, which is represented by the unit vector Λ. Λ has components l, m, and n (the direction cosines of OA). The angle of yaw δ is, by definition, the angle between $O1$ and OA; and ϕ, the angle of orientation,

is specified as the angle between the plane $AO1$ and the plane $1O2$. l, m, and n are related to δ and ϕ by:

$$
\begin{aligned}
l &= \cos \delta \\
(6) \qquad m &= \sin \delta \cos \phi \\
n &= \sin \delta \sin \phi.
\end{aligned}
$$

The assumptions made by Fowler, Gallop, Lock, and Richmond in treating motion of Type α are the following:

  (i) The $O1$ axis makes a slowly varying angle θ with the horizontal, so $\dot{\theta}$ is small compared to the spin N,

 (ii) The yaw δ is small (less than, say, $7°$),

(iii) The total effect of the components h, κ, Γ, γ, is small, so that all terms other than those of the lowest order in δ can be neglected.

The stability factor for a spinning shell is defined as

$$
(7) \qquad s = \frac{A^2 N^2}{4 B \mu}.
$$

It is found that the condition for stability is that s be greater than unity. This is, of course, analogous to the condition for stability of a spinning top.

When this condition is satisfied, the following solution is found for the equations of motion in the terms of the direction cosines, l, m, and n: (these equations follow directly from those of § 4.0 in the Fowler paper)

$$
m = \tfrac{1}{2}(\alpha + \beta) \cos 2\pi \int_{t_1}^{t} (n_1 + n_2)dt - \tfrac{1}{2}(\alpha - \beta) \cos 2\pi \int_{t_2}^{t} (n_1 - n_2)dt,
$$

(8)

$$
n = \tfrac{1}{2}(\alpha + \beta) \sin 2\pi \int_{t_1}^{t} (n_1 + n_2)dt - \tfrac{1}{2}(\alpha - \beta) \sin 2\pi \int_{t_2}^{t} (n_1 - n_2)dt,
$$

where:

$$
\tfrac{1}{2}(\alpha + \beta) = \tfrac{1}{2}(\alpha_0 + \beta_0) \left(\frac{\Omega_0 \sigma_0}{\Omega \sigma} \right)^{\!\frac{1}{2}}
$$

$$
\exp. \left\{ - \tfrac{1}{2} \int^{t} \left[(h + \kappa) + \frac{1}{\sigma} (h - \kappa + 2\gamma - \Gamma) \right] dt \right\}
$$

(9)

$$
\tfrac{1}{2}(\alpha - \beta) = \tfrac{1}{2}(\alpha_0 - \beta_0) \left(\frac{\Omega_0 \sigma_0}{\Omega \sigma} \right)^{\!\frac{1}{2}}
$$

$$
\exp. \left\{ - \tfrac{1}{2} \int^{t} \left[(h + \kappa) - \frac{1}{\sigma} (h - \kappa + 2\gamma - \Gamma) \right] dt \right\}
$$

and α_0, β_0, t_1, and t_2 are arbitrary constants of integration, and

$$
\Omega = \frac{AN}{B}, \quad \sigma = \sqrt{1 - 1/s}, \quad n_1 = \Omega/4\pi, \quad n_2 = \Omega\sigma/4\pi,
$$

$$
(n_1 + n_2) = \Omega(1 + \sigma)/4\pi, \qquad (n_1 - n_2) = \Omega(1 - \sigma)/4\pi.
$$

The subscript zero is used to give a variable its value at the muzzle.

In Equation (8) it is seen that the vertical component m, and the horizontal component n, of the motion of the axis, are composed of two periodic terms. One, called the nutational term, consists of a damped oscillation of instantaneous frequency $(n_1 + n_2)$ and instantaneous amplitude $\frac{1}{2}(\alpha + \beta)$. The other, called the precessional term, is a damped oscillation of frequency $(n_1 - n_2)$ and amplitude $\frac{1}{2}(\alpha - \beta)$. The ratio of these two frequencies for the projectiles employed here was about 10 to 1. An exaggerated graph of m is shown in Fig. 4 with the contribution of each term shown separately.

$(n_1 + n_2)$ term. $(n_1 - n_2)$ term.   m.
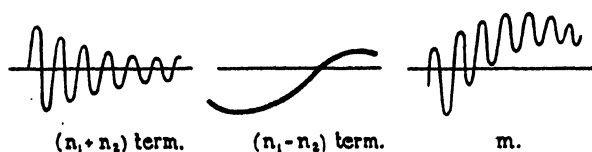
FIG. 4.

From a continuous record of the vertical component m it is possible to deduce all the force coefficients previously defined except f_R, f_I, and f_K. f_M can be derived from $(n_1 + n_2)$ and $(n_1 - n_2)$; f_L may be determined from the values of f_M found for various positions of the centers of gravity of the shells. f_H and f_J may be determined by evaluating the exponents of decay of $\frac{1}{2}(\alpha + \beta)$ and $\frac{1}{2}(\alpha - \beta)$. f_I can be determined directly from the radio trace, by a method to be described in Section IV. f_R must be determined by chronograph measurements of the retardation of the forward motion of the shells.

III. The Radio Method

1. QUALITATIVE DESCRIPTION OF THE METHOD

The Thomson radio method of yaw measurement depends on the fact that for a radio fused shell, the radiation in a direction making an angle θ with the axis of the shell is very closely proportional to $\sin \theta$. This is most nearly true in the region up to 10° from the axis to the rear.

The electric axis of the shell as a radiator comes close to, but seldom coincides with, the physical axis of symmetry. A small angle between the two will be assumed in deriving the fundamental equations, but will be taken as zero in the present section.

If a receiver be located on the instantaneous axis of the shell extended, no signal will be received. For a small angular displacement of the axis, the electric field intensity at the receiver will be proportional to the sine of the angle between the axis and the line joining the shell and the receiver (line of sight). If the receiving antenna be oriented to respond, say, to the vertical component of the electric field, the signal received will be proportional to the vertical component of the angular displacement (Fig. 5). Thus the received signal will be zero when the axis is deflected horizontally, to the right or left, and will reach a maximum value when the axis is deflected vertically either

up or down.   There is no method of distinguishing between these up and down deflections, and there is no means of determining the absolute value of the angular displacement from a receiver record.
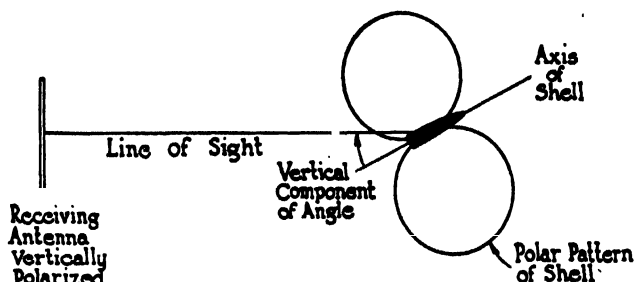
FIG. 5.

These difficulties are overcome for yaw measurement by locating the antenna so that there is always an angle between the axis and the line of sight in excess of the expected yaw angle, and by orienting the antenna to respond only to radiation polarized in the plane of this angle.   To do this, the antenna is located in the plane of the trajectory, a distance ahead of the gun, and oriented to respond only to vertically polarized radiation, as in Fig. 6.
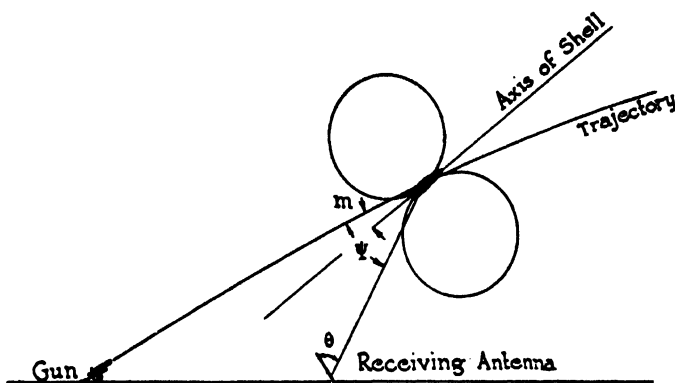
FIG. 6.

The signal will then be proportional to $\sin(\psi + m)$, where ψ is the angle between the line of sight and the tangent to the trajectory, and m is the vertical component of the angle between the axis of the shell and the tangent to the trajectory.   The mean signal level is approximately proportional to $\sin \psi$. Hence the ratio $\sin(\psi + m)/\sin \psi$ is equal to the ratio between the instantaneous and mean signal levels (Fig. 7).   From a knowledge of the trajectory and the geometry of the receiver and gun locations, it is possible to find the angle ψ as the shell moves through space.   Then knowing the value of ψ it is possible to determine m.   By proper choice of Q.E. and the distance gun to antenna, it is possible to arrange that ψ stays reasonably constant over a

desired region of the early part of the trajectory. For example, in certain of the experiments discussed later, ψ lay between $4\frac{1}{2}°$ and $3°$, from one to five seconds time of flight.
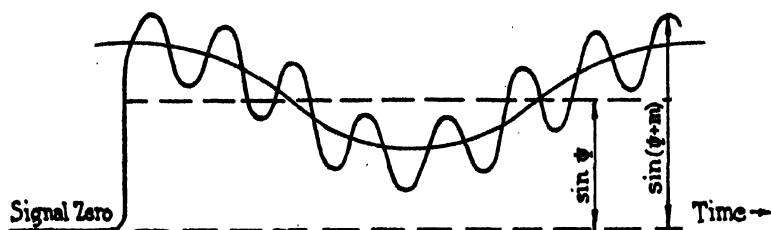
FIG. 7. *Receiver record.*

2. DERIVATION OF THE FUNDAMENTAL EQUATIONS OF THE RADIO METHOD

(a) Assumptions

The following are the assumptions in the derivation of the fundamental equations of the radio method:

(i) The polar pattern of the radiation from the shell is sinusoidal, i.e., the field strength E is proportional to the sine of the angle between the electric axis of the shell as a radiator, and the direction of propagation.

(ii) The electric axis Σ of the shell is inclined to the geometric axis, Λ, of the shell by an angle ϵ.

(iii) The radiation from the shell is plane polarized; i.e., E lies in the plane containing the electric axis Σ and the direction of propagation.

(iv) The receiving antenna responds only to the component of E lying in the plane containing the antenna, and the direction of propagation.

(b) Antenna Voltage Due to a Shell in Space

For the general case of a radiating shell, located and oriented arbitrarily in space, we define the following vectors:

(i) Λ, a unit vector coinciding with the geometric axis of the shell,

(ii) Σ, a unit vector coinciding with the electric axis of the shell,

(iii) R, a unit vector in the direction of propagation, i.e., a line joining the C.G. of the shell and the reference point of the receiving antenna,

(iv) E, the electric field vector at the receiving antenna, given by:

$$(10) \qquad E = \frac{K}{r}\{R \times (R \times \Sigma)\},$$

where K is a scalar proportionality factor depending on power, wave length, etc., and r is the distance from the shell to the receiving antenna.

(v) A, a unit vector in the direction of the antenna axis. The voltage induced by a field E in an infinitesimal dipole can be expressed as:

$$V = c\,E\,.\,A,$$

where c is a scalar quantity depending on wave length, units, etc. For a directional array, we may write:

$$V = E \cdot A \, F(\theta, \chi)$$

where θ is the polar angle measured from A;

χ is the azimuthal angle measured from an arbitrary plane through A;

and $F(\theta,\chi)$ is a scalar function, such that $F(\theta,\chi)/c$ represents the gain of the array relative to the dipole.

Then, substituting for E from Equation (10):

(11)
$$V = \frac{K}{r} F(\theta,\chi) \, A \cdot \{R \times (R \times \Sigma)\}$$

$$= \frac{K}{r} F(\theta,\chi) \, A \cdot \{R(\Sigma \cdot R) - \Sigma\}$$

To determine the components of these vectors we employ the system of axes, $O1$, $O2$ and $O3$, previously defined (Fig. 8). Let $O1$, $O2$, $O3$ represent unit vectors on their corresponding axes.

Fɪɢ. 8.
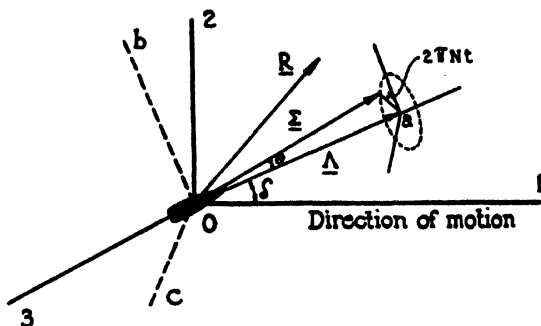
Λ makes an angle δ (the yaw angle) with $O1$, and the plane of $O1$ and Λ makes an angle ϕ (the angle of orientation) with the $1O2$ plane.

(12) $\therefore \Lambda = \cos \delta \, O1 + \sin \delta \cos \phi \, O2 + \sin \delta \sin \phi \, O3.$

At O we define another unit triad, Oa, Ob, Oc. In it $Oa = \Lambda$, Ob is in the plane of $O2$ and Λ, Oc is perpendicular to Oa and Ob. The electric axis Σ passes through the center of gravity, and makes an angle ϵ with Λ. Owing to the spin N, of the shell, Σ rotates with angular velocity $2\pi N$ about Λ.

Then in the $a\,b\,c$ triad, reckoning the angle $2\pi Nt$ from the aOb plane:

(13) $\Sigma = \cos \epsilon \, Oa + \sin \epsilon \cos 2\pi Nt \, Ob + \sin \epsilon \sin 2\pi Nt \, Oc.$

To transform the Σ vector into the $1\,2\,3$ triad we require the components of Oa, Ob, Oc, referred to the $1\,2\,3$ triad:

$$Oa = \cos \delta \, O1 + \sin \delta \cos \phi \, O2 + \sin \delta \sin \phi \, O3,$$

and Ob, Oc are determined as unit vectors perpendicular to Oa. For δ small, so that $\sin \delta \approx \delta$, $\cos \delta \approx 1$, these reduce to:

(14) $Oa = O1 + \delta \cos \phi\, O2 + \delta \sin \phi\, O3$
             $Ob = -\delta \cos \phi\, O1 + O2$
             $Oc = -\delta \sin \phi\, O1 + O3.$

Substituting the above values for Oa, Ob, and Oc, in Equation (13), with the additional approximation that ϵ is small, so that $\sin \epsilon \approx \epsilon$, $\cos \epsilon \approx 1$, $\epsilon\delta \approx 0$ we find:

(15) $\Sigma = O1 + (\delta \cos \phi + \epsilon \cos 2\pi Nt)O2 + (\delta \sin \phi + \epsilon \sin 2\pi Nt)O3.$

R lies in the $1O2$ plane, and the angle between R and $O1$ is ψ, and therefore:

(16) $R = \cos \psi O1 + \sin \psi O2.$

A lies in the $1O2$ plane, inclined to R by the angle θ, so that

(17) $A = \cos (\psi + \theta)O1 + \sin (\psi + \theta)O2.$

Substituting these values in Equation (11), we have:

$$V = \frac{K}{r} F(\theta, \chi) \sin \theta\, (\sin \psi - \cos \psi\, \delta \cos \phi - \epsilon \cos 2\pi Nt)$$

If we arrange in the experiments that ψ remains small, so that $\sin \psi \approx \psi$, $\cos \psi \approx 1$, and compressing $F(\theta,\chi) \sin \theta$ into $f(\theta)$, (since χ is nearly constant for an actual trajectory), this may be written:

(18) $V = \frac{K}{r} f(\theta)\, (\psi - \delta \cos \phi - \epsilon \cos 2\pi Nt).$

When the spin is not of immediate interest ϵ is put equal to zero to obtain:

(19) $V = \frac{K}{r} f(\theta)\, (\psi - m).$

3. The Equipment

The equipment required for measurement of yaw by the radio method is the following:

(i) A radio fuse that can be fitted to standard artillery shells and that radiates a signal approximately as assumed in III – 2,

(ii) A receiving antenna, responding to vertically polarized radiation,

(iii) A radio receiver, tuned to the frequency of the signal from the fuse, and whose output voltage is proportional to the input voltage from the antenna,

(iv) A cathode ray oscilloscope, permitting the output voltage to be photographed,

(v) A timing device, indicating on the film record (1) the time when the gun is fired and (2) the time at any subsequent point on the film.

The equipment developed for this work is described in this section. In Part (a) the fuse, or radio sonde, is discussed, in (b) the antenna, and in (c) the receiver, and its associated apparatus.

PLATE I
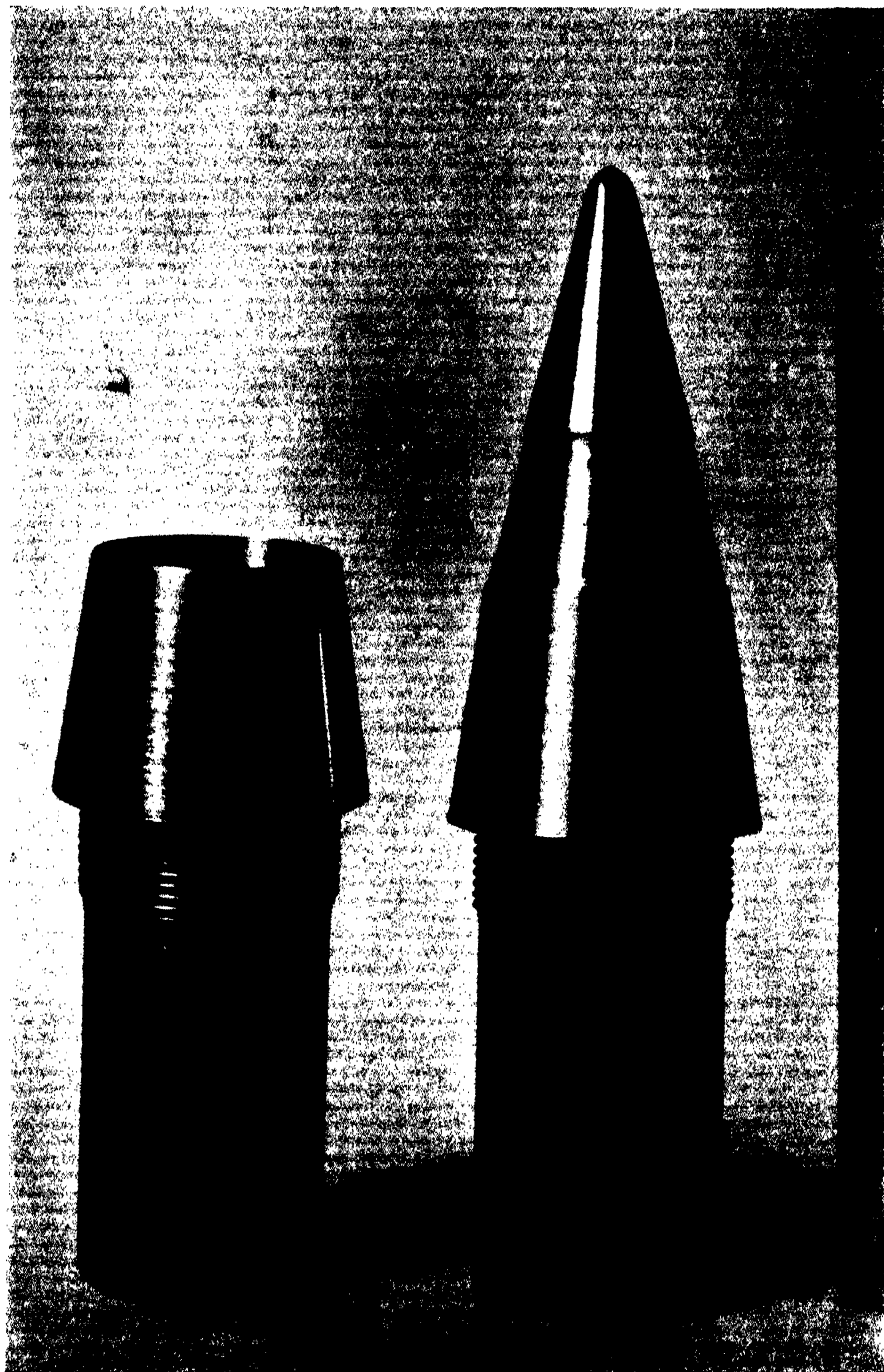
FIG. 9. *The yaw fuse.*

(a) *The Radio Sonde*

The requirements of the radio sonde are:

, (1) The polar radiation pattern at the rear of shell must be sinusoidal, and must be a figure of revolution whose axis nearly coincides with the axis of the shell.

(2) Power radiated must be sufficient to give signals well above the noise level of the receiver, even when the shell is at the largest distance from the receiver.

(3) The frequency must be capable of adjustment in the laboratory, so that, on firing, the sonde frequency will lie as nearly as possible at the mid-band of the receiver.

(4) The frequency drift of the unit over the useful time of flight must be small.

(5) The variation in output power over the useful time of flight must be small.

A photograph of the sonde is shown in Fig. 9. The oscillator circuit is conventional, but of course employs rugged (V.T. Fuse) components. The battery is a regular V.T. Fuse battery.

Requirement (1) was attained by using the lowest possible frequency. The portion of the polar pattern actually used is that not exceeding 20° from the axis of the shell at the rear. Stationary tests were made in a large open field to check this region. The shell was supported by a polystyrene rod about 6 ft. long. The axis of the shell was horizontal and the shell was rotated about a vertical axis. Relative field strengths were then measured a few hundred feet away. These tests indicated that the polar pattern was sinusoidal in the required region, as closely as measurable. In addition, within the accuracy of these tests, the electric axis and the geometric axis of the shell appeared to coincide. As discussed in Section IV – 5(a), this is not strictly accurate.

Requirement (3) was met by taking special care with the oscillator coil, and by using, for final tuning, a number of nose caps of different sizes. This gave sufficient adjustment to bring all the frequencies within the desired range.

Requirement (4) of small frequency drift was checked by following a number of units in flight with a narrow-band receiver. These tests did not reveal any frequency drift.

Requirement (5) of no power drift was checked in the laboratory. Over relatively long periods (several minutes) no change in power output could be detected.

(b) *The Receiving Antenna*

The requirements of the receiving antenna are:

(1) A directivity pattern that discriminates in azimuth against reflections from behind and from the sides.

(2) Independence of effects due to variations in ground conditions.

(3) In the region of maximum reception a response that is independent of elevation over a range of about 10° and of azimuth over a range of at least 4°.

(4) A radiation resistance to match the 50 ohm characteristic impedance of the coaxial cable to the receiver.

(5) Maximum possible gain over a half-wave dipole.

(6) Portability and ease of assembly in the field.

(7) Provision for tilting in the vertical plane to investigate any part of the trajectory.

It was decided to use a 90° corner array, but to provide it with a ground screen in order to ensure the second requirement above. This type of antenna was first investigated by Kraus (4), whose conclusions can be summarized as follows: (1) the physical dimensions of the array are not critical, (2) a power gain of 10 is possible using a 90° corner, and (3) for dimensions smaller than two wave lengths, the performance of corner arrays equals that of parabolic reflectors and horns.

The directivity patterns of the antenna in azimuth and in elevation are shown in Figs. 10 and 11.
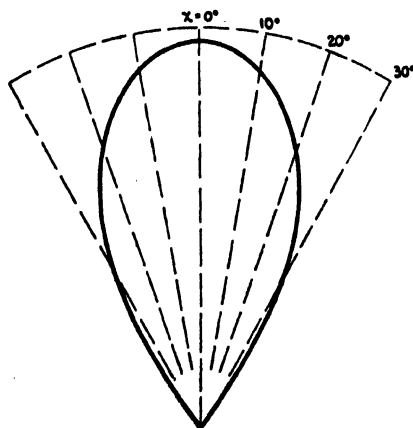
FIG. 10. *Directivity pattern of antenna in azimuth ($\theta = 90°$).*
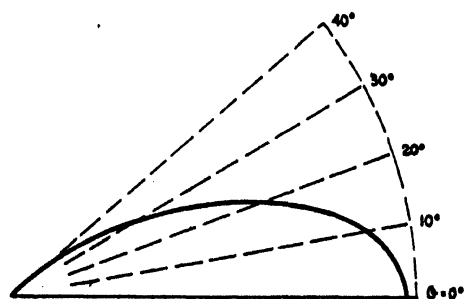
FIG. 11. *Directivity pattern of antenna in elevation ($\gamma = 0°$).*

(c) The Receiving System

The requirements of the receiver are:

(1) Ability to find the signal within 0.5 sec. of firing of the shell.

(2) A sensitivity adequate for good photography for the trajectory region under investigation.

(3) A means of recording the amplitude of the radio-frequency signal.

(4) Linearity of output with input.

(5) Insensitivity to line voltage fluctuations.

(6) A method of providing an accurate time scale from the instant the gun is fired.

Fig. 12 shows the block diagram of the receiving system.
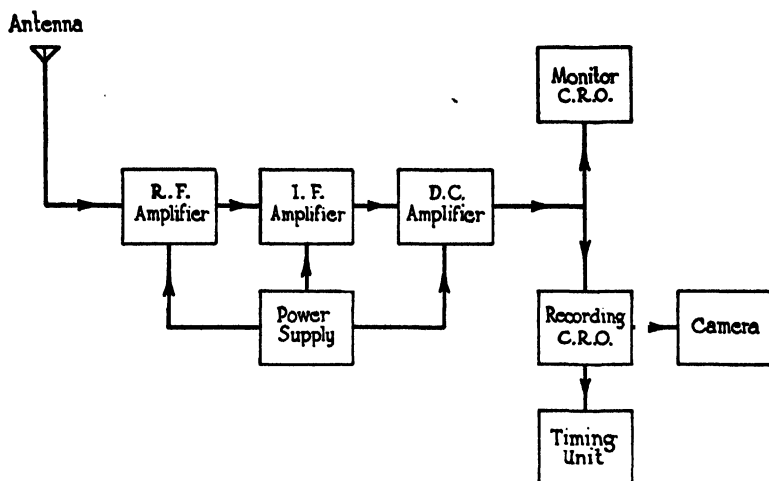
FIG. 12.   Block diagram of receiving system.

Since the yaw is largest very early in flight, it is essential that there be as little delay as possible in obtaining a usable signal. Moreover it is necessary to hold this signal once it is found, since tuning the receiver would affect its output and make yaw measurements impossible. Therefore it was decided that manual tuning during shell flight was undesirable, and that a fixed-frequency, broad-band receiver would meet the requirements best. Because the sondes may show a certain frequency spread there was included a tuning condenser on the local oscillator. Before each round is fired the receiver is tuned to the laboratory measured frequency for that sonde. Nevertheless a bandwith of a few megacycles is desirable, because a sharply tuned receiver would respond to frequency drift as a change in signal strength which could not be distinguished from changes due to variations of orientation and distance of the shell. Automatic frequency control was considered as a means of eliminating this difficulty, but it was found unnecessary.

Preliminary calculations and experience with the proximity fuse indicated that to ensure good signals over a 25 sec. time of flight it would be necessary to employ a high sensitivity receiver. This problem of high sensitivity and wide band was exactly that which had been overcome in the construction of radar receivers, and it was decided that it would be simplest to modify such a receiver. The frequency was adjusted to cover the desired range, and a switch was introduced, thus permitting the gain to be altered in six fixed steps. For linearity of response, a diode detector was employed.

Recording the carrier level of the radio-frequency signal requires direct coupling between the detector and final indicator, the cathode ray oscillograph. A direct-coupled amplifier consisting of a single 6AC7 was employed for this purpose.

Sometimes it is an advantage to listen to the spin modulation of the sonde. For this there is an A.F. amplifier and speaker.

The d-c. amplifier is followed by two 3 in. cathode ray oscilloscopes, one with a green tube for monitoring, the other blue for photographing. The no-signal voltage on the C.R.O. plates is that of the d-c. amplifier plate, i.e., 175 v. Therefore, the high voltage must be specially insulated to make centering and focusing possible. A horizontal sweep voltage may be applied to the monitor if desired. Because of the vertical motion of the film the recording tube is rotated 90° so that horizontal deflections on it correspond to vertical deflections on the monitor.

In order to relate the instantaneous position of the shell in space to the corresponding point on the trace it is necessary to put a time scale on the records. This was provided by a series of timing marks at intervals of 1/100 sec., about 1/6 in. apart on the film. These are obtained by photographing a narrow slit illuminated by a neon bulb, pulsed from an independent timing unit.

The master timekeeper is a 1000 c.p.s. tuning fork oscillator (General Radio Type 813-A). The output of the oscillator is fed into a peak clipper and thence to a step circuit. By careful adjustment of the cathode voltage of the step tube, the step circuit is made to trigger an asymmetrical multi-vibrator at the beginning of the seventh step. Another four milliseconds are allowed for the step circuit to discharge; thus the full cycle is completed in 1/100 sec. The multi-vibrator delivers a 300 v. pulse of 10 μsec. duration to the neon bulb. Examination of the wave form of the voltage across the neon bulb shows that the firing time repeats itself to better than 1 μsec.

A fiducial mark for the time scale is obtained by momentarily switching a resistor in parallel with the plate load of the d-c. amplifier. This introduces a sharp rise of short duration on to the trace. The switch is operated by the pressure from the blast of the gun. The moving part is a copper disk about 3 in. in diameter. The whole switch is mounted in a box and placed to the side and slightly behind the muzzle of the gun. The time delay in switch operation was measured by a separate chronograph trial and the necessary correction was made for each round.

The zero signal position of the C.R.O. spot is extremely sensitive to voltage fluctuations, especially to the I.F. screen voltage, the d-c. amplifier heater and the high voltage of the C.R.O.   The primary source of power for most of the trials was a 60 cycle, 1500 w., Homelite gasoline generator.   This has quite stable operation for its type, but surges of ± 5 v. occurred frequently. Therefore it was decided to use power supplies stabilized by negative feedback. A similar type of unit is used in the 700 v. supply of the C.R.O.'s and here also the stability is more than adequate.   The heater voltage of the d-c. amplifier is supplied by a 6 v. storage battery.   The heater voltages on the R.F. and I.F. amplifiers are not critical.   The over-all system is such that rapid generator fluctuations do not affect the spot position appreciably.   A slow change causes a steady drift but this is negligible over the 20 sec. time of flight of a single round.

The Recording Camera employed is the General Radio Oscillograph recorder, Type 651-AE, with lens 651-PI.   This is a continuous drive camera taking either 16 or 35 mm. film; 35 mm. film (Kodak Super XX) was used throughout on this work.   For photography the lens is opened to $f/1.5$. The maximum writing speed is about 56 in. per sec.

The complete equipment is held in a shockproof steel rack and can be mounted in a three ton Dodge truck in which complete equipment for trials is carried.

IV. The Experiments and Experimental Results

1. DESCRIPTION OF THE EXPERIMENTS

Experiments were performed using the radio method to measure yaw of the 25 pr. shell.   The firings were performed on Nov. 15, Nov. 23, and Dec. 3, 1945.   The Artillery Proof Establishment of the Inspection Board of the United Kingdom and Canada, at Hamilton, Ontario, supplied guns, propellant, and gun crews.   The firings were held at the Winona Rifle Range of the Department of National Defence.

The gun employed was the 25 pr., firing H.E. MK. I. D, streamline shell. All rounds were fired with normal full charge at a quadrant elevation of 20°, from a barrel in the first quarter of wear.   The gun was located about 300 yards from the shore, and pointed over Lake Ontario.   The antenna was located 227.4 ft. in front of, and 6.1 ft. below, the muzzle of the gun, in the vertical plane containing the trajectory.   A mound of earth, 20 ft. high by 30 ft. thick was located between the antenna and recording station, and the gun.

The velocities and retardations of all rounds fired were measured by officers. of the Canadian Armament Research and Development Establishment, Valcartier, Quebec, using the counter chronographs and photoelectric screens normally used in these measurements.   At the trial, measurements were made of temperature, relative humidity, and wind velocity at ground level. The mass, the transverse and longitudinal moments of inertia through the center of gravity (A and B), and the position of the center of gravity, were

determined for all rounds fired. In order to determine f_L by Equation (5) shells of three different mass distributions were fired. In one group sulphur filling was employed, in another, lead, and in the third, a steel plug was placed at the nose beneath the fuse. This produced a range of positions of the centers of gravity of about $\frac{3}{4}$ in.

2. Description of the Trace

A typical trace is reproduced in Fig. 13. The following are salient points:

(i) In the region one to three seconds, three frequency components are evident:

(a) A high frequency, of about 250 c.p.s., with fairly small amplitude. This is the spin N.

(b) A medium frequency, of about 20 c.p.s., with amplitude of the order of one-quarter film width. This is the $(n_1 + n_2)$ term of the vertical component, m, of the shell's angular motion (see Section II – 2).

(c) A low frequency, of about 2 c.p.s., with amplitude of the same order as (b) above. This is the $(n_1 - n_2)$ term.

(ii) The $(n_1 + n_2)$ component is gradually decreasing in amplitude, until three seconds, when it has almost wholly disappeared. There is, meanwhile, no marked change in the $(n_1 - n_2)$ component, or in the spin.

(iii) In the region one to two seconds, the level of the entire trace is shifting downwards. Later, it remains almost constant, when the decrease due to $f(\theta)/r$ nearly balances the increase due to increasing ψ.

Certain other points should be noted. Through the middle of the film there is a series of small rectangles. These are the timing light marks, 1/100th sec. apart. They are numbered every 1/10th sec. Before the point marked zero, the trace is at the lower edge of the film, in a steady straight line. At zero time, and following it for 0.15 sec. there are several jogs in the film. These are caused by the pressure switch, actuated by the gun blast. At about 0.2 sec. the first signal is received, but it is so great as to send the trace off scale. By about 0.8 sec. the signal has decreased and is on scale after that. The sudden jump in the height of the trace at 2.2 sec. is caused by a scale change. When the receiver operator saw the signal becoming too low on the monitor oscilloscope, he switched the receiver to a higher gain position, causing this discontinuity.

3. Procedure and Theory of Analysis

The voltage at the receiving antenna, due to the shell in space, is:

$$(18) \qquad V = \frac{K}{r} f(\theta) \left(\psi - \delta \cos \phi - \epsilon \cos 2\pi N t \right).$$

The trajectory of the shells, of course, must be known to permit analyses of the records. The trajectory data specifically required are: the distance along the line of sight from the antenna to the shell; r, the angle between the

PLATE II

0.8   0.4   0.3   0.2   0.1

1.0   0.9   0.8   0.7   0.6

1.7   1.6   1.5   1.4   1.3   1.2

2.3   2.2   2.1   2.0   1.9   1.8

2.9   2.8   2.7   2.6   2.5   2.4

3.5   3.4   3.3   3.2   3.1   3.0

4.1   4.0   3.9   3.8   3.7   3.6   3.5

4.7   4.6   4.5   4.4   4.3   4.2

5.1   5.1   5.4   5.0
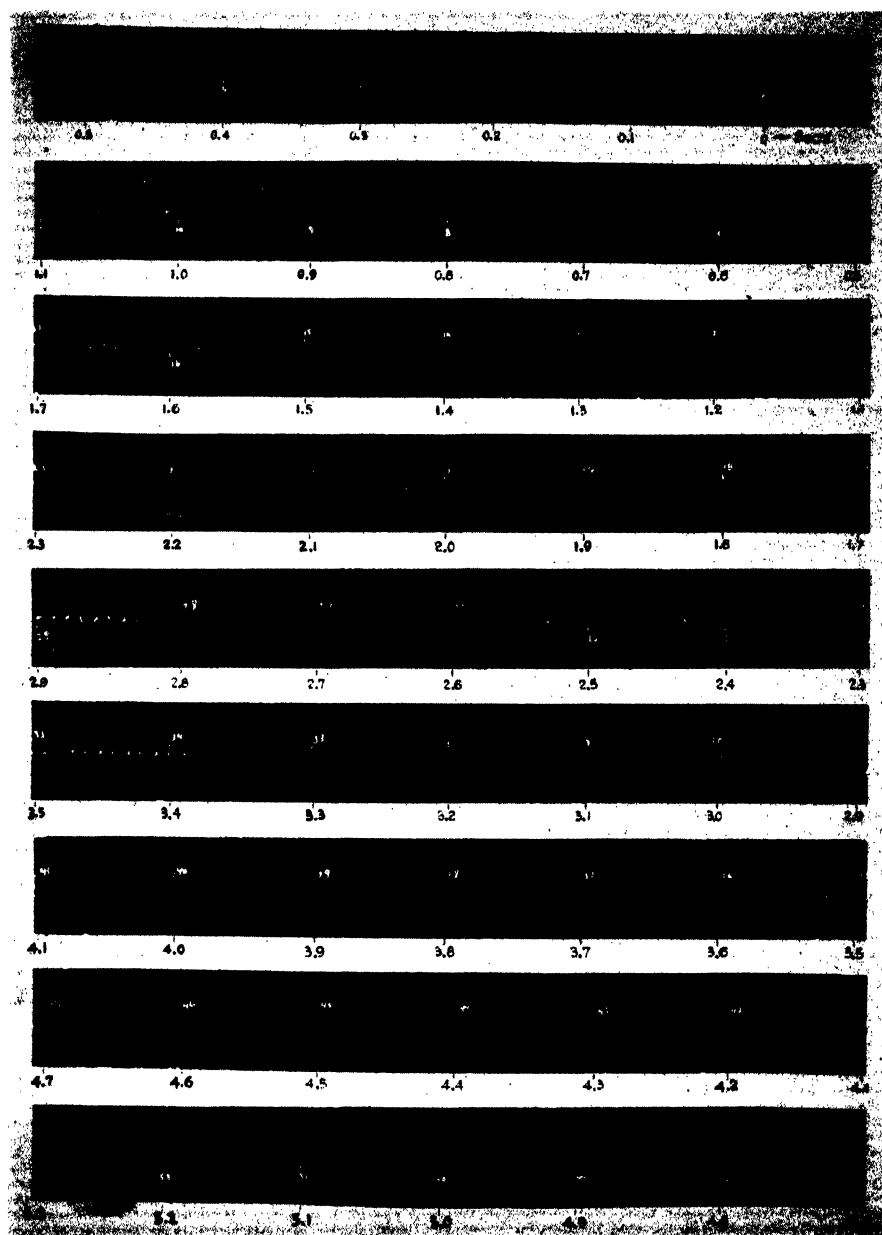
FIG. 13. *Photographic trace of Round 67. 0 to 5.3 sec.*

PLATE III
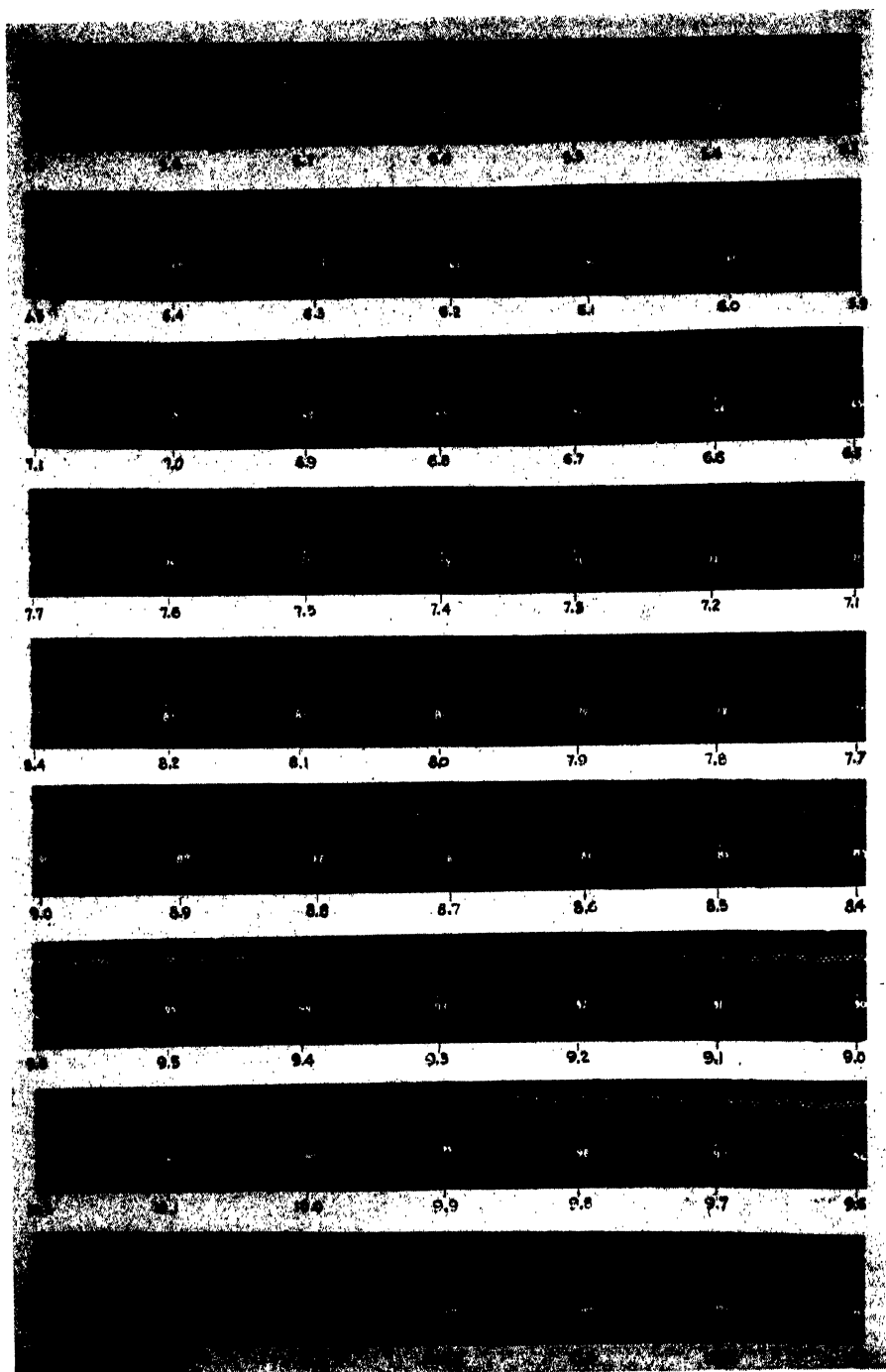
FIG. 13, *continued, 5.3 to 10.8 sec.*

line of sight and the tangent to the trajectory, ψ; and the angle between the line of sight and the reference axis of the antenna, θ (Fig. 6). These can be determined from the trajectory and from the position of the antenna relative to the gun. From these data, and from the calculated response pattern of the antenna, values of $\dfrac{f(\theta)}{f(\theta_1)}\dfrac{r_1}{r}$ and ψ were tabulated and plotted against time. r_1 and θ_1 are the values of r and θ at one second. It was necessary to calculate the trajectory of these shells, since the shape of the yaw fuse is different from the fuses regularly employed. A short-arcs method was used for this purpose, the ballistic coefficient being determined by a separate retardation trial.

(a) Preliminary Steps

To facilitate measurements, enlarged copies of the trace were made by projecting its image on to continuous graph paper, and tracing it in pencil. The complete motions of the oscilloscope spot and the timing dots were carefully reproduced. A magnification of about seven was employed, and, since the distance between sprocket holes on the film is 1 in., the working traces were 7 in. wide.

The first operation on the graph paper was to smooth out the spin modulation, either by estimating the mid-point directly or by drawing the envelopes of the peaks and taking the curve midway between.

(b) The Analysis

H, the height of the curve above the zero signal level, is a linear* function of the input voltage V; i.e.,

$$H = gV.$$

By Equation (19)

$$V = K\frac{f(\theta)}{r} (\psi - m), \text{ spin being smoothed out.}$$

Hence

(20) $$H = gK\frac{f(\theta)}{r} (\psi - m).$$

It is useful to define two new quantities, as follows:

(i) The variable E, where

(21) $$E = \frac{r}{r_1}\frac{f(\theta_1)}{f(\theta)} H = g\frac{f(\theta_1)}{r_1} K(\psi - m).$$

The factor $g\dfrac{f(\theta_1)}{r_1}$, which is constant, will be included in K hereafter, so that the dimensions of K become inches displacement on the graph, per degree angular displacement of the shell's axis. That is, we write

$$E = K(\psi - m).$$

---

* There is a slight 'foot' on the input vs. output of the receiver, but since this can be eliminated by addition of a small constant to H, or use of the input–output curve itself, the above discussion is not in error.

E was calculated from H for several hundred points on each trace, using Equation (21), and the curve of $\dfrac{r}{r_1}\dfrac{f(\theta_1)}{f(\theta)}$.

· (ii) The variable G, where

$$(22)\quad G = E - K'\psi = - Km + (K - K')\psi,$$

where K' is a constant, the first approximation to K.

The purpose of the remaining preparatory work was to replace the curve of H by a curve of G. The latter is proportional to m, to a good approximation, since the contribution of $(K - K')\psi$ is very much smaller than the contribution of Km. Thus G is a more suitable graph for analysis of the shell's motion.

It was not difficult, by inspecting the curve of H, to locate approximately the times of the maxima and minima of the low frequency modulation. It was assumed, for this approximation, that at the time t_m , midway between a maximum and a minimum, this low frequency gives no contribution to the trace amplitude. By inspection, or by drawing the envelope of the peaks of the medium frequency $(n_1 + n_2)$, it was possible to estimate the contribution of this frequency component at the time t_m . Thus a good estimate could be made of the trace amplitude for zero vertical component of yaw, i.e., $m = 0$. But then $E = K\psi$, and since ψ is known at all times, this permitted an estimate of K, known as K', to be made. In general K' lay within 5% of the K finally determined.

From the values of K' obtained at a series of points on the trace, from the tabulated values of ψ, and from the values of E, G was calculated by Equation (22). A graph of G versus time was then superimposed on the original tracing of H. Two curves, G_1 and G_2, the envelopes of the maxima and minima, respectively, of the $(n_1 + n_2)$ term, were drawn. A graph typifying the curves G and the envelopes G_1 and G_2 is shown in Fig. 14.
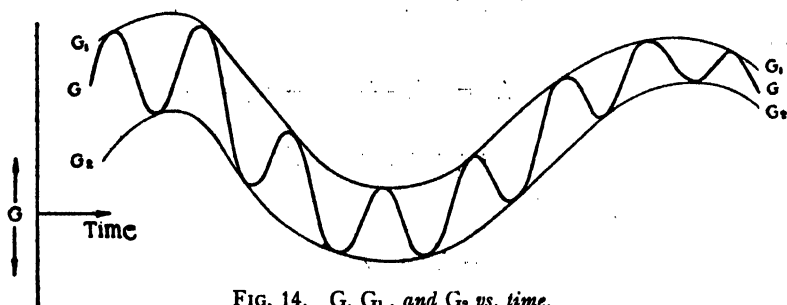
FIG. 14. G, G_1 , and G_2 vs. time.

The equations of these curves are:

$$(23)\quad G = - K\left[\tfrac{1}{2}(\alpha + \beta) \cos 2\pi \int_{t_1}^{t} (n_1 + n_2)\, dt - \right.$$

$$\left. (\alpha - \beta) \cos 2\pi \int_{t_0}^{t} (n_1 - n_2)\, dt \right] + (K - K')\psi.$$

$$(24) \quad G_1 = -K\left[-\tfrac{1}{2}(\alpha + \beta) - \tfrac{1}{2}(\alpha - \beta)\cos 2\pi \int_{t_2}^{t}(n_1 - n_2)dt\right]$$
$$+ (K - K')\psi.$$

$$(25) \quad G_2 = -K\left[\tfrac{1}{2}(\alpha + \beta) - \tfrac{1}{2}(\alpha - \beta)\cos 2\pi \int_{t_2}^{t}(n_1 - n_2)dt\right]$$
$$+ (K - K')\psi.$$

By adding Equations (24) and (25) we get:

$$(26) \quad S = G_1 + G_2 = K(\alpha + \beta)\cos 2\pi \int_{t_2}^{t}(n_1 - n_2)dt + 2(K - K')\psi.$$

(c) The Low Frequency

$(K - K')\psi$ is small compared to $K(\alpha - \beta)$, and changes slowly with time. Hence, at a maximum of S,

$$(27) \quad 2\pi \int_{t_2}^{t_{max}}(n_1 - n_2)\,dt = 2n\pi, \quad \text{and at the next minimum}$$

$$(28) \quad 2\pi \int_{t_2}^{t_{min}}(n_1 - n_2)dt = (2n + 1)\pi.$$

Combining Equations (27) and (28),

$$2\pi \int_{t_{max}}^{t_{min}}(n_1 - n_2)dt = \pi,$$

where t_{max} is the time of a maximum of S, and t_{min} is the time of the adjacent minimum. Assuming $(n_1 - n_2)$ is constant over this interval, we may write:

$$(29) \quad n_1 - n_2 = \frac{1}{2(t_{min} - t_{max})}.$$

This can, of course, be applied equally well from a minimum to a maximum of S.
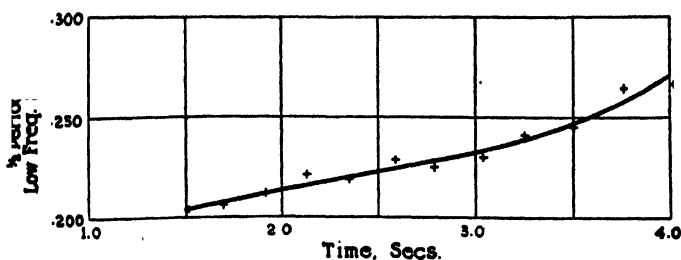
FIG. 15.   *Half-period of low frequency vs. time.   Round 89.*

The values of $(n_1 - n_2)$ for a typical round (No. 89) are plotted against time in Fig. 15, and a smooth curve drawn through them. The value of $(n_1 - n_2)$ employed to determine force coefficients were taken from such

curves for each round. These values, and their corresponding times, are shown in Table I, for each round.

TABLE I

Round No.	$(n_1 + n_2)$, c.p.s.	$(n_1 - n_2)$, c.p.s.	Time of evaluating $(n_1 - n_2)$, sec.
2	22.01	2.31	1.60
3	22.01	2.46	1.18
11	22.42	2.19	1.60
13	22.35	2.24	1.60
80	20.41	2.89	0.98
82	20.37	2.50	1.35
83	20.75	2.50	1.22
89	20.55	2.42	1.60
60	20.73	2.25	1.60
67	21.19	2.19	1.60

(d) The High Frequency

It was observed, for all rounds analyzed, that $(n_1 + n_2)$ was constant over the region in which it could be observed on the trace. Thus, it was readily determined by noting the times of its minima and maxima, and thereby calculating the mean period from the time taken for 10 or 12 complete cycles. The range generally used was that from one point in a low frequency cycle to the corresponding point on the next cycle.

In Table I, the values of $(n_1 + n_2)$ are shown for each round.

(e) Determination of K

From a knowledge of

$$2\pi \int_{t_1}^{t} (n_1 - n_2)dt$$

we can determine the times t_0 at which

$$\cos 2\pi \int_{t_a}^{t_0} (n_1 - n_2)dt = 0 .$$

Then from Equation (26) at such times:

$$S_0 = 2(K - K')\psi$$

(30) $$\text{or } K = K' + \frac{S_0}{2\psi} .$$

This determines K. If K differs from K' by more than 5%, the variation of ψ with time may have affected S sufficiently to impair the accuracy of the determination of $(n_1 - n_2)$, and hence the t_0. In this case, K as determined by Equation (30) must be regarded as a second approximation to the true K.

The process must then be repeated. In almost every case, repetition was found unnecessary. The values of K prior to the first scale change are shown in Table II, and with them, the corresponding K'.

TABLE II

Round No.	K, inches per degree	K', inches per degree
2	1.72	1.75
3	0.92	0.90
11	1.23	1.22
13	2.18	2.24
80	0.96	0.91
82	0.86	0.85
83	0.72	0.70
89	1.51	1.47
60	2.27	2.27
67	1.04	

(f) Determination of the Amplitudes

Adding and subtracting Equations (24) and (25) we have:

$$(31) \qquad \tfrac{1}{2}(\alpha - \beta) = \frac{G_1 + G_2 - 2(K - K')\psi}{2K \cos 2\pi \int_{t_2}^{t} (n_1 - n_2)dt}$$

$$(32) \qquad \tfrac{1}{2}(\alpha + \beta) = \frac{G_1 - G_2}{2K} \; .$$

Equations (31) and (32) were used to determine the yaw amplitudes.

A typical set of determinations of $\tfrac{1}{2}(\alpha + \beta)$, for Round 67, is plotted on semilogarithmic scales in Fig. 17. The corresponding least squares straight line is also plotted. Values of $\tfrac{1}{2}(\alpha - \beta) \cos 2\pi \int_{t_2}^{t} (n_1 - n_2)dt$ for the same round are plotted in Fig. 16.

4. THE DERIVED QUANTITIES

The quantities determined by direct measurement from the trace are the following:

Frequencies: Spin, $(n_1 + n_2)$, $(n_1 - n_2)$
Amplitudes: $\tfrac{1}{2}(\alpha + \beta)$, $\tfrac{1}{2}(\alpha - \beta)$.

In addition, the following quantities were determined, either by laboratory measurement, or by independent measurement at the trial:

The moments of inertia, A and B of the shell,
The position of the center of gravity,
The velocity and mean ballistic coefficient of the shell,
Meteorological data at the time of the trial.
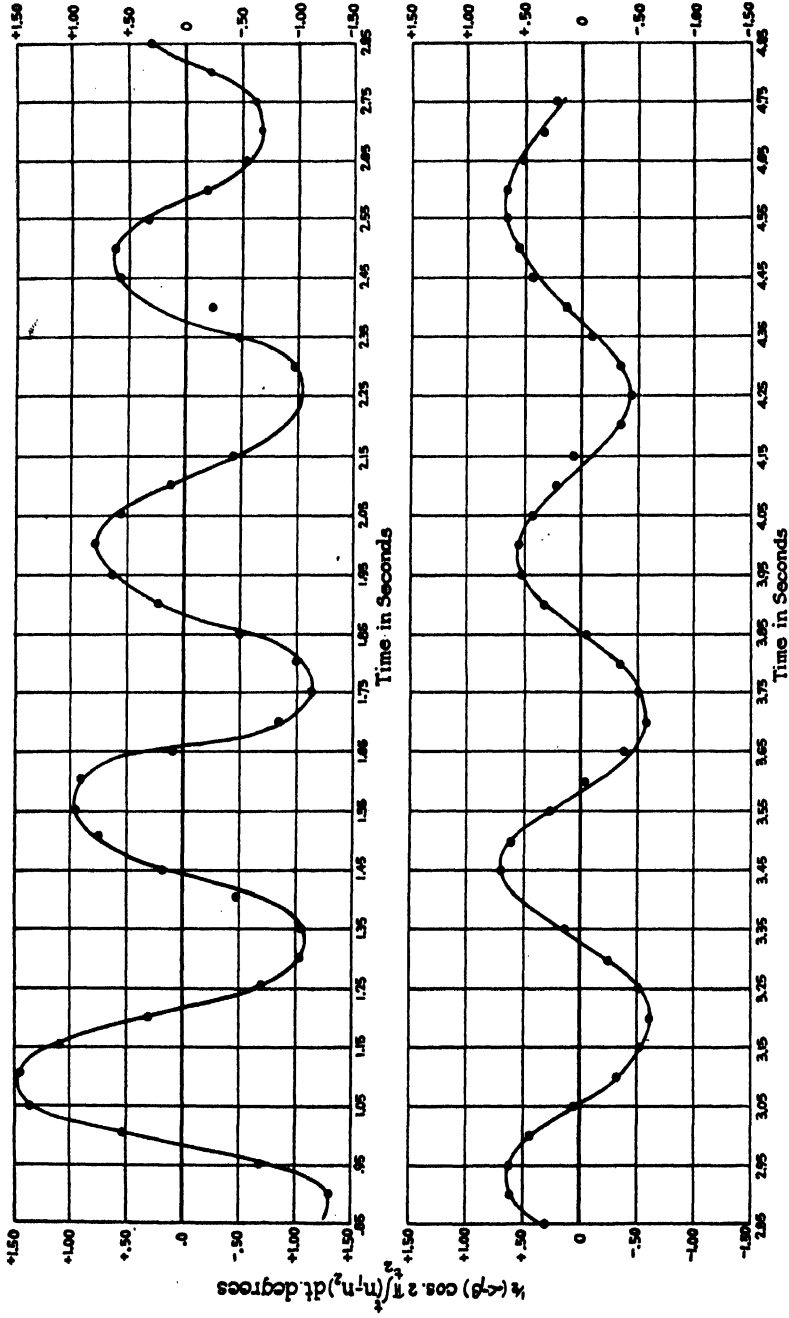
FIG. 16. $\frac{1}{2}(\alpha - \beta) \cos 2\pi \int_{t_2} (n_1 - n_2)dt.$ *Round 67.*
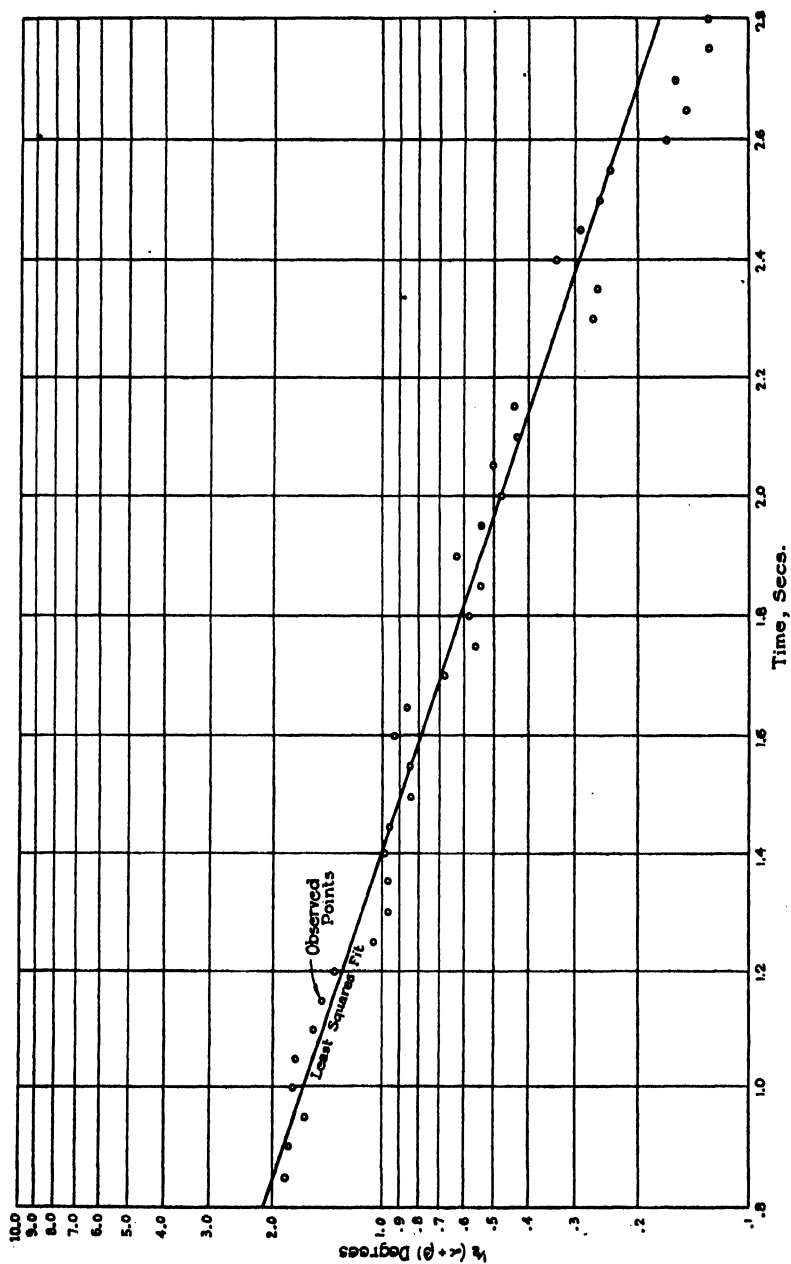
FIG. 17. $\frac{1}{2}(\alpha + \beta)$ vs. time. Round 67.

Certain of these measured values are shown in Table III.

TABLE III

| Round No. | Position of center of mass | | Mass, lb. | Axial moment of inertia, A lb-in.^{2} | Transverse moment of inertia, B lb-in.^{2} | Muzzle velocity, V $\dfrac{\text{ft.}}{\text{sec.}}$ |
	Type	Distance to base, in.				
2	Normal	6.64	24.97	40.42	418.9	1487
3		6.64	24.98	40.19	418.7	1486
11		6.62	24.95	39.93	413.0	1499
13		6.62	24.94	40.32	415.6	1491
80	Back	6.31	25.00	40.10	441.7	1495
82		6.33	24.97	40.21	445.2	1486
83		6.25	24.94	39.96	437.9	1498
89		6.27	24.98	39.94	439.1	1488
60	Forward	7.03	25.08	39.99	440.1	1490
67		7.03	25.11	39.94	433.6	1490

The velocities of the shells, as tabulated functions of time, were calculated by the standard methods of external ballistics. The force factors were then determined from the above data, as described in Sections IV – 4(a) and IV – 4(b), which follow.

(a) *The Overturning Moment Coefficient*

From Equation (9)

$$n_1 = \frac{\Omega}{4\pi}, \quad n_2 = \frac{\Omega\sigma}{4\pi}, \quad \sigma = \sqrt{1 - 1/s}.$$

Hence, adding $(n_1 + n_2)$ and $(n_1 - n_2)$ we obtain $\dfrac{\Omega}{2\pi}$.

Subtracting, we obtain $\dfrac{\Omega\sigma}{2\pi}$, and dividing n_2 by n_1 we obtain σ.

Then $\sigma^2 = 1 - 1/s$, whence $s = \dfrac{1}{1 - \sigma^2}$,

and since

$$s = \frac{A^2N^2}{4B\rho v^2 r^3 f_M}$$

(33) $$f_M(v/a) = \frac{A^2N^2}{4Bs\rho v^2 r^3} \cdot = \frac{\Omega^2 B}{4s\rho v^2 r^3} \cdot$$

$\Omega/2\pi$ may be obtained independently by the relation $\Omega = \dfrac{AN}{B}$, using the measured values of A, B, and the spin N. Using Ω determined in this way, and the measured values of $(n_1 + n_2)$, σ may be evaluated, since

$$(n_1 + n_2) = \frac{\Omega}{4\pi}(1 + \sigma).$$

This determination of σ is independent of $(n_1 - n_2)$, and permits another evaluation of s and f_M. The values of $\Omega/2\pi$ and f_M found by both methods are given in Table IV.

TABLE IV

Round No.	Time of determination of $(n_1 - n_2)$, sec.	$\Omega/2\pi$, c.p.s.		$f_M(v = 1350 f/s)$		Distance of C.G. from base, in.
		From $(n_1 + n_2)$ and $(n_1 - n_2)$	From N	From $(n_1 + n_2)$ and $(n_1 - n_2)$	From N and $(n_1 + n_2)$	
2	1.60	24.32	24.12	13.61	12.41	6.64
3	1.18	24.47	24.31	13.85	12.93	6.64
11	1.60	24.61	24.61	12.90	12.94	6.62
13	1.60	24.59	24.60	13.36	13.41	6.62
82	1.35	22.87	22.96	14.55	14.55	6.33
83	1.22	23.25	23.33	13.93	14.33	6.25
89	1.60	22.97	22.87	14.01	13.40	6.27
60	1.60	22.98	22.95	13.20	13.00	7.03
67	1.60	23.38	23.28	12.94	12.33	7.03

(b) *The Cross-wind Force Coefficient*

By comparing the values of f_M for shells of three different positions of the centers of gravity, the values of f_L may be deduced from Equation (5). Using the data of Table IV, f_M was plotted against position of center of gravity and a straight line fitted by least squares (Fig. 18). From the slope of this straight line it was found that $f_L = 2.0$, whence κ (as defined in equation (3)) = 0.18.
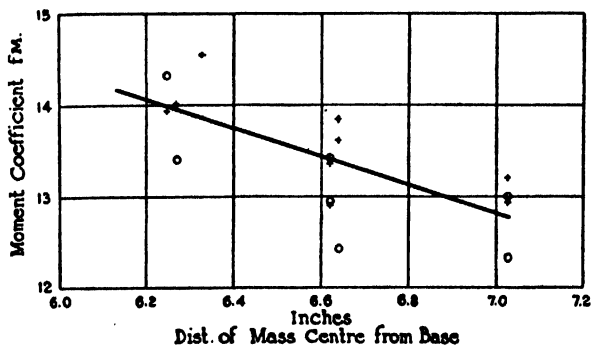
FIG. 18. f_M vs. *distance of mass center from base.*

(c) *The Damping Factors*

The quantities κ, h, γ, Γ, are called the 'damping factors', and are related to their corresponding force factors by Equation (3).

The determination of κ has been described above. Γ is determined from spin data as described in Section IV – 5.

TABLE V

Round No.	$\frac{1}{2}(\alpha_0 + \beta_0)$, degrees	Exponent, sec.$^{-1}$	$\frac{1}{2}(\alpha_0 - \beta_0)$, degrees	Exponent, sec.$^{-1}$	$h + \kappa$, sec.$^{-1}$	$\frac{1}{\sigma}(h - \kappa + 2\gamma - \Gamma)$, sec.$^{-1}$	σ	$h - \kappa + 2\gamma - \Gamma$, sec.$^{-1}$	κ, sec.$^{-1}$	h, sec.$^{-1}$	Γ, sec.$^{-1}$	γ, sec.$^{-1}$
2	4.23	1.32	0.81	0.09	1.41	1.23	0.82	1.01	0.18	1.23	0.01	−0.02
11	2.30	1.53	1.04	0.06	1.59	0.98	0.82	0.80	0.18	1.41	0.01	−0.21
13	2.96	1.02	2.24	0.25	1.27	0.97	0.82	0.63	0.18	1.09	0.01	−0.14
89	3.04	0.93	2.83	0.35	1.28	0.58	0.80	0.46	0.18	1.10	0.01	−0.23
60	2.20	0.87	1.36	0.34	1.20	0.53	0.80	0.42	0.18	1.02	0.01	−0.21
67	5.65	1.24	1.90	0.34	1.58	0.90	0.82	0.74	0.18	1.40	0.01	−0.24

The factors h and γ may be determined from the observed values of $\frac{1}{2}(\alpha + \beta)$ and $\frac{1}{2}(\alpha - \beta)$, using Equations (9). The best exponential curves of the form $y = Ae^{-bt}$ were fitted to the observed values by least squares. This involves neglecting the effect of variations of $\left(\dfrac{\Omega_0 \sigma_0}{\Omega \sigma}\right)^{\frac{1}{2}}$ and assuming that the exponents are linear functions of time. Consideration of the rate of change of $\Omega \sigma$ shows that $\left(\dfrac{\Omega_0 \sigma_0}{\Omega \sigma}\right)^{\frac{1}{2}}$ changes by only a fraction of a per cent per second. The assumption regarding the exponents can be justified by regarding the values obtained as averages. The semilogarithmic graph of $\frac{1}{2}(\alpha + \beta)$ against time in Fig. (17) shows that this procedure is reasonable.

By adding and subtracting the exponents of $\frac{1}{2}(\alpha + \beta)$ and $\frac{1}{2}(\alpha - \beta)$, $(h + \kappa)$ and $(h - \kappa + 2\gamma - \Gamma)$ can be determined. It is then possible to determine h and γ.

In Table V the values of $\frac{1}{2}(\alpha_0 + \beta_0)$, $\frac{1}{2}(\alpha_0 - \beta_0)$ and their corresponding exponents, are tabulated. The values of h, κ, Γ, and γ are also shown.

It will be noted that γ is negative. The significance of this is that the force K' acts behind the center of gravity, O, rather than in front.

5. Spin

(a) Modulation Amplitude

Equation (18) contains a term $\epsilon \cos 2\pi Nt$ which is a component varying at the spin frequency. For those times when $\delta \cos \phi = 0$ it follows that:

$$(34) \qquad \epsilon = \frac{h_s \psi}{\overline{H}},$$

where h_s is the height of the spin modulation on the trace and $\overline{H}$ = height of trace when averaged over a spin cycle. Measurements on the traces show that, to within experimental accuracy, ϵ remains constant throughout flight, so that the spin term in the signal is adequately explained by postulating the existence of an angle ϵ between the electric axis and the spin axis of the shell. For Round 67, ϵ was found to be $0.27°$, and for Round 89 it was $0.19°$.

(b) Measurement of Spin and Spin Decay

The small amplitude of spin modulation and the relatively low film speed make a statistical method of measurement necessary. Every tenth spin cycle on the trace was numbered, and ΔT_i, the observed time for 50 cycles, was obtained. N was thus calculated, and Fig. 19 shows a typical graph of spin against time. For each round a curve of the form $N = N_0 e^{-\Gamma t}$ was fitted by determining the least squares straight line:

$$(35) \qquad \log N = \log N_0 - \Gamma t.$$

The values of N_0 and Γ so found are listed in Table VI. For most rounds this equation was applied over a five or six second interval.

TABLE VI

Round	N_0, rev./sec.	Γ, sec.$^{-1}$	Round	N_0, rev./sec.	Γ, sec.$^{-1}$
2	253.7	0.0092	60	257.0	0.0109
3	256.2	0.0095	67	257.2	0.0109
11	259.0	0.0107	82	257.2	0.0123
12	254.8	0.0108	83	259.3	0.0115
13	257.8	0.0103	89	254.9	0.0087
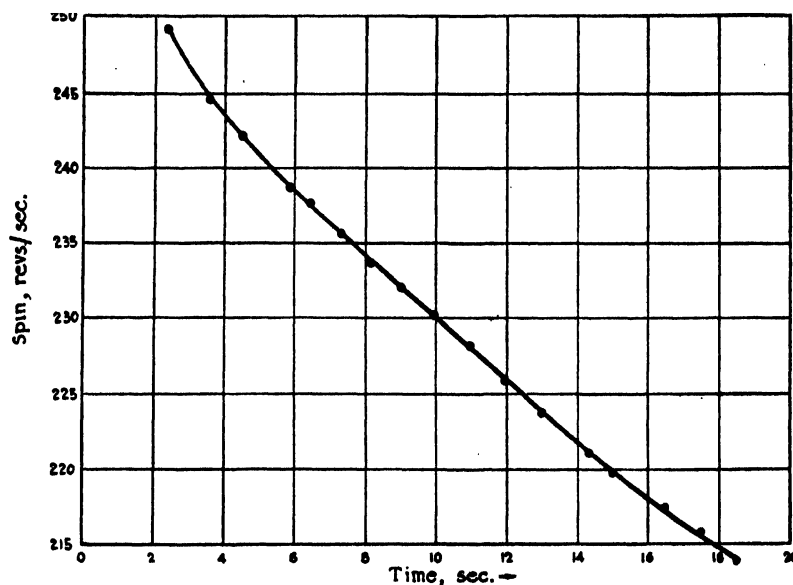
FIG. 19. *Spin. Round 12.*

Application of Equation (35) over shorter time intervals showed that there was a significant trend in Γ. This trend was investigated by determining Γ for two-second intervals, on five rounds. About 30 points were obtained, all but a few in the range 0 to 10 sec., and a smooth curve drawn through them. The mean distance of the points from the curve was about 3%. Using the relation connecting f_I, Γ, and the spin reducing couple, I,

$$\text{viz.:} \quad I = \rho v N r^4 f_I = -A N \Gamma \quad \text{(Equations (2) and (3))}$$

the curve of f_I versus time in Fig. 20 was obtained.

(c) Skin Friction

Spin decay results from friction due to the viscosity of the air and it is possible to estimate f_I from the theory of skin friction. The usual hydro-dynamic treatment is in terms of the boundary layer theory (3) according to which the shell is surrounded by a thin layer of air of which the inner surface is at rest relative to the shell, and the outer surface moves with the velocity

TABLE VII

CALCULATION OF f_I

Time, sec.	$M^* = V/a$	f_I from Γ	f_I from drag	Time, sec.	$M^* = V/a$	f_I from Γ	f_I from drag
0	1.368		0.0766	10	0.898	0.0715	0.0837
1	1.285	0.0808	0.0779	11	0.882	0.0719	0.0839
2	1.208	0.0772	0.0787	12	0.866	0.0733	0.0842
3	1.140	0.0735	0.0797	13	0.852	0.0754	0.0842
4	1.079	0.0720	0.0809	14	0.841	0.0772	0.0844
5	1.025	0.0706	0.0814	15	0.829	0.0801	0.0847
6	.987	0.0695	0.0819	16	0.820	0.0837	0.0850
7	.959	0.0692	0.0824	17	0.810	0.0872	0.0850
8	.935	0.0702	0.0832	18	0.802	0.0914	0.0850
9	.917	0.0709	0.0834				

* Mach number $= V/a$, where a $=$ velocity of sound in the undisturbed medium and V velocity of air stream.

$$(36) \qquad V^2 = v^2 + \left(\frac{Nr}{2\pi}\right)^2 .$$

of the air stream. Although the viscosity is small, the normal velocity gradient may be large, and the integrated effect of the shear stresses can give rise to an appreciable force. The drag is written in the form:

$$(37) \qquad D = \tfrac{1}{2}\rho V^2 C_f A ,$$

where C_f is a dimensionless coefficient,
and $A =$ area of surface $= 2\pi r L$ for a shell,
  ($L =$ effective length of shell $=$ length $+$ fuse correction).
  From this it follows that the spin reducing couple

$$I = \rho V\pi r^3 L N C_f ,$$

and comparing this with Equation (2):

$$(38) \qquad f_I = \frac{\pi L}{r}\frac{V}{v} C_f .$$

For turbulent flow Falkner has modified a theory of Karman's to show that (1):

$$(39) \qquad C_f = \frac{0.036}{(N_{RL})^{\frac{1}{7}}} ,$$

where $N_{RL} =$ the Reynold's number, $\dfrac{\rho VL}{\mu}$.

The values of f_I calculated from Equation (38) and those from the measured values of Γ are shown in Table VII and Fig. 20. It is seen that the magnitudes are in reasonable agreement but the shapes of the curves are different. It should be noted that the above theory for the drag does not take into account any possible changes in the nature of the equations of flow that occur in the

trans-sonic region. The minimum at 6.5 sec. corresponds to a Mach number of about one.
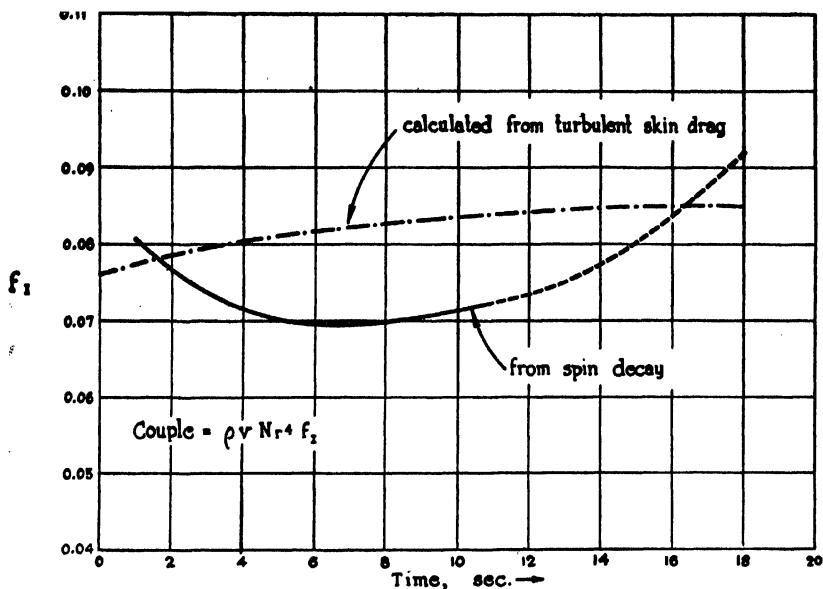
FIG. 20. *Coefficient of spin couple.*

It is of interest to see how much the drag due to skin resistance contributes to the total drag of a shell. The total force is due mainly to wave drag and is given by the empirical equation:

$$(40) \qquad D = \frac{m}{10^4 C} \frac{\rho}{\rho_0} v^2 P(u) ,$$

where

$$C = \text{ballistic coefficient},$$

and

$$P(u) \text{ is a tabulated function of } \left(\frac{v a_0}{a} \right)$$

$$(a_0 = \text{velocity of sound under standard conditions}).$$

From Equation (2) it follows that;

$$(41) \qquad \frac{\text{Skin drag}}{\text{Total drag}} = \frac{r^2 C 10^4 \rho_0}{m} \frac{f_I}{P(u)}$$

It is found that the skin drag contributes from 10 to 25% of the total drag, the fraction being least at $M = 1$.

V. Summary and Conclusions

1. Summary of Preceding Results

The system of forces acting on a shell in flight is described, after the analysis of Fowler, Gallop, Lock, and Richmond. The solutions of the equations of motion found by those authors are quoted, indicating the manner in which the

forces affect the angular motion.   A radio method of measuring this motion over a wide range of distances from the gun is described, the theory of the method is derived, and the equipment developed for the measurements is described.   An account of certain experiments using this method is given, and the photographic record is described.   The theory and examples of the analysis are given.   Results for some 10 rounds are quoted.   From these results, the force factors and damping coefficient have been deduced.   The overturning moment coefficient f_M has been determined at a velocity of 1350 ft. per sec.; and from values of f_M for shells of various mass distributions, the cross-wind force coefficient f_L, has been found.   Average values of the damping factors, h, and γ have been deduced by evaluating the exponents of the decay of the yaw angle.   By accurate measurements of spin, the spin decay exponent Γ has been determined, and the spin decay coefficient, f_I, has been evaluated at different times. f_I has also been calculated from hydrodynamic theory, and a comparison is made with the values determined by spin decay.

2. Comparison of the Radio and Other Methods

Prior to this development, two other methods of yaw measurements have been employed.   These are the jump card method and the photographic method.   The jump card method consists of firing a shell through a series of cardboards, spaced down a range.   By measurements of the shape and orientation of the resulting holes in the cards, it is possible to determine δ and ϕ.   The photographic method consists of firing a shell down a range, between pairs of cameras which photograph the shell in perpendicular planes, at a number of points down the range.   From these photographs, δ and ϕ may be determined.

It is possible at this point to compare the radio method with the jump card and photographic methods of yaw study.

The relative advantages of the radio method are:

   (*a*) It permits measurement over the whole trajectory;

   (*b*) It provides a continuous record;

   (*c*) No mechanical contact with the shell is required;

   (*d*) It permits measurement of the spin and spin decay;

   (*e*) The accuracy of all measurements is comparable with either card or photographic method, and for a number of quantities, e.g., nutation and precession frequencies, damping factors, it is better;

   (*f*) Measurements are not confined to a flat trajectory.

The relative disadvantages of the radio method are:

   (*a*) It requires special fuses and equipment;

   (*b*) The labor and time required for analysis is considerably greater;

   (*c*) Analysis requires independent determination of trajectory data.

Acknowledgments

The authors wish to acknowledge the considerable assistance of Professors E. F. Burton, C. Barnes, and V. G. Smith of this University, and Dr. D. C. Rose, of C.A.R.D.E. Valcartier. Proximity fuse components were made available by the co-operation of Dr. M. A. Tuve, O.S.R.D., Washington. Velocity measurements at the trials were made by Mr. P. T. Demos and Lt. J. Orr, R.C.A. The project was financed by the National Research Council of Canada.

References

1. FALKNER, V. M. Aircraft Eng. 15 : 65. 1943.
2. FOWLER, R. H., GALLOP, E. G., LOCK, C. N. H., and RICHMOND, H. W. Trans. Roy. Soc. London, A, 221 : 295. 1921.
3. HEMKE, P. E. Elementary applied aerodynamics. Prentice-Hall Inc., New York. 1946.
4. KRAUS, J. D. Proc. Inst. Radio Engrs. 28 : 513. 1940.
5. STRATTON, J. A. Electromagnetic theory. McGraw-Hill Book Company, Inc., New York and London. 1941.
6. TERMAN, F. E. Radio Engineers' handbook. McGraw-Hill Book Company, Inc. New York and London. 1943.

GRAVITY ANOMALIES IN NORTHWESTERN CANADA[1]

By M. J. S. Innes

Abstract

Free air, Bouguer, and isostatic anomalies are listed in a table of principal facts for 23 stations established by the Dominion Observatory in the area between latitudes 55 and 70 degrees, bounded on the east by Hudson Bay and on the west by Athabaska, Slave, and Mackenzie rivers. There is some evidence that the predominantly negative anomalies at stations in the Pre-Cambrian may be due to lack of isostatic adjustment following removal of glacial loads.

Introduction

The first gravity observations in northern Canada were made by the Dominion Observatory in 1921 when a series of pendulum stations were established along the water routes between Edmonton and the Mackenzie River delta (7). Observations were made at seven stations in the Arctic as far north as Cambridge Bay on Victoria Island on a combined gravity and magnetic airborne expedition in 1945. Three determinations were made at points along the Hudson Bay railroad in 1946. Altogether 23 stations have been established in the area between latitudes 55 and 70 degrees, bounded on the east by Hudson Bay and on the west by Athabaska, Slave, and Mackenzie rivers. The results of all observations are listed in Table I and are shown in Fig. 1.

To interpret the results of gravity observations the value of gravity is compared with theoretical values computed for the latitude and elevation of the station. Several methods of reduction may be employed. The observed value minus the computed value is the gravity anomaly. A positive anomaly represents an excess of gravity and a negative anomaly a deficiency. In this report three methods of reduction have been used, the free air, Bouguer, and the Hayford and Bowie isostatic reduction for a depth of compensation of 113.7 km. (7). The theoretical value of gravity at sea level for each station is computed from the International Gravity Formula* and is shown in the sixth column of Table I. The corrections that are applied to this value to obtain the computed value of gravity at the elevation of the station are shown in the next five columns of the table. The free air computed value is obtained by simply applying a negative correction for the elevation of the station above sea level to account for the diminution in gravity due to the

* Theoretical gravity (γ_0, in centimeters per second per second) at sea level for each station is obtained by substitution of the latitude φ of the station in the formula $\gamma_0 = 978.049$ $(1 + 0.0052884 \sin^2 \varphi - 0.0000059 \sin^2 2\varphi)$, adopted by the International Union of Geodesy and Geophysics. In this formula 978.049 is the most probable value of gravity at the equator, as deduced from numerous gravity observations at many places over the earth. The coefficients of $\sin^2 \varphi$ and $\sin^2 2\varphi$ are deduced from theoretical expressions for gravity on the adopted spheroid.

TABLE I

PRINCIPAL FACTS FOR GRAVITY STATIONS

No.	Name	Longitude ° '	Latitude ° '	Eleva-tion H, ft.	Theore-tical gravity, γ_0 gals	Eleva-tion	Topo-graphy A-O	Comp. A-O	$t+c$ 18-1	$t+c$ A-1	Computed gravity (free air), gals	Observed gravity, gals	Free air	Bouguer	Hayford-Bowie 113.7 km.
175	Churchill	94 09.3	58 46.0	17	981.826	- 2	+ 1	- 2	- 2	- 3	981.824	981.770	-54	-55	-51
174	Gillam	94 42.0	56 21.0	447	981.628	-42	+15	-11	- 3	+ 1	981.586	981.576	-10	-25	-11
173	Wabowden	98 37.9	54 54.5	759	981.507	-71	+26	-18	- 7	+ 1	981.436	981.416	-20	-46	-21
172	Brochet	101 39.5	57 53.0	1117	981.775	-105	+39	-28	- 7	- 5	981.670	981.651	-19	-58	-22
170	Cambridge Bay	105 04.1	69 07.4	6	982.562	0	0	- 5	0	- 5	982.562	982.515	-47	-47	-42
167	Stoney Rapids	105 49.5	59 15.5	727	981.865	-68	+25	-25	- 8	- 8	981.797	981.785	-12	-37	- 4
171	Ile à la Crosse	107 54.0	55 26.9	1385	981.553	-130	+48	-36	-13	- 1	981.423	981.409	-14	-62	-13
51	Chipewyan	111 08.8	58 42.7	750	981.822	-71	+24	-22	-14	-12	981.751	981.727	-24	-50	-12
62	Waterways	111 15.3	56 40.5	820	981.655	-77	+26	-36	-14	-24	981.578	981.555	-23	-51	+ 1
61	Lac la Biche	111 58.3	54 46.5	1801	981.495	-169	+60	-46	-18	- 4	981.326	981.322	- 4	-65	0
47	Resolution	113 40.5	61 10.1	500	982.014	-47	+17	-15	-11	- 9	981.967	981.946	-21	-38	-12
169	Coppermine	115 09.5	67 48.8	18	982.481	- 2	+ 1	- 8	- 3	-10	982.479	982.468	-11	-12	- 1
60	Kinuso	115 25.9	55 19.9	1922	981.543	-181	+65	-55	-20	-10	981.362	981.353	- 9	-75	+ 1
166	Fort Rae	116 05.7	62 49.3	515	982.138	-48	+18	-17	- 7	- 6	982.090	982.070	-20	-38	-14
43	Peace River	117 17.3	56 14.1	1063	981.619	-100	+34	-47	-25	-38	981.519	981.486	-33	-69	+ 5
44	Providence	117 39.3	61 21.2	512	982.028	-48	+17	-22	-13	-18	981.980	981.959	-21	-38	+ 3
168	Cameron Bay	117 54.4	66 03.7	128	982.367	-39	+14	-17	- 4	- 7	982.328	982.306	-22	-36	-15
59	Grand Prairie	118 47.5	55 10.3	2154	981.529	-203	+73	-59	-27	-13	981.326	981.321	- 5	-79	+ 8
45	Simpson	121 20.8	61 51.7	433	982.067	-41	+15	-20	-18	-23	982.026	982.008	-18	-33	+ 5
48	Liard River	123 47.5	59 58.5	525	981.922	-49	+16	-49	-26	-59	981.873	981.794	-79	-97	-20
46	Norman	125 34.4	65 54.0	285	982.287	-27	+ 9	-29	-16	-36	982.260	982.218	-42	-52	- 6
49	Good Hope	128 38.3	66 15.3	195	982.380	-18	+ 6	-20	-15	-29	982.362	982.344	-18	-25	+11
50	Arctic Red River	133 44.3	67 26.6	135	982.457	-13	+ 4	-18	-12	-26	982.444	982.438	- 6	-11	+20
	Mean anomaly with regard to sign												-24	-48	- 9
	Mean anomaly without regard to sign												24	48	13

PLATE I

FIG. 1. *Isostatic anomalies for a depth of compensation of 113.7 km. at gravity stations in northwestern Canada.*

increased distance from the center of the earth. For the Bouguer (modified) reduction a further positive correction is made for the attraction of the topography out to a distance of 103.5 miles (Hayford Zone O) from the station. For the Hayford and Bowie (6) reduction the theoretical value at sea level is first corrected for the elevation of the station and then for the topography of the whole earth and finally for the compensation corresponding to the topography. E. C. Bullard's (1) method for computing the effects corresponding to the lettered zones was used and maps of Canada based on Heiskanen's charts for Zones 10 to 1 were employed to obtain the corrections for these more distant zones.

Discussion of Results

If perfect isostatic equilibrium prevailed and if in the vicinity of the station there were no large masses differing in density from 2.67 (the value adopted as the mean density of the solid part of the earth) the isostatic anomalies would tend to be negligible. Isostatic anomalies for the 23 stations, grouped according to the geological formations (on which they are situated), are shown in Table II. There are seven Palaeozoic stations, five with negative anomalies

TABLE II

TABLE SHOWING ANOMALIES FOR THE VARIOUS STATIONS GROUPED ACCORDING
TO THEIR GEOLOGICAL FORMATIONS

Pre-Cambrian		Palaeozoic		Mesozoic	
Station number	Anomaly in cm./sec.^{2}	Station number	Anomaly in cm./sec.^{2}	Station number	Anomaly in cm./sec.^{2}
175	− .051	170	− .042	62	+ .001
174	− .011	171	− .013	61	.000
173	− .021	47	− .012	60	+ .001
172	− .022	44	− .003	43	+ .005
167	− .004	45	+ .005	59	+ .008
51	− .012	46	− .006	48	− .020
169	− .001	49	+ .011	50	+ .020
166	− .014	—	—	—	—
168	− .015	—	—	—	—
Mean anomaly with regard to sign	− .017	Mean anomaly with regard to sign	− .009	Mean anomaly with regard to sign	+ .002
Mean anomaly without regard to sign	.017	Mean anomaly without regard to sign	.013	Mean anomaly without regard to sign	.008

Note.—1 milligal = 1 × 10⁻³ cm. per sec.²

and two positive. The mean anomaly with regard to sign is −0.009 cm. per sec.² Five out of seven Mesozoic stations have positive anomalies. Only one Mesozoic station has a negative anomaly. The mean anomaly with

regard to sign for the Mesozoic stations is $+ 0.002$ cm. per sec.[2] All the nine Pre-Cambrian stations have negative anomalies and the mean anomaly is -0.017 cm. per sec.[2]

Similar results have previously been observed in Canada over all these formations, including the Pre-Cambrian. As Pre-Cambrian rocks are on the average most likely considerably heavier than normal, persistent negative anomalies over such an extensive Pre-Cambrian area point to a departure from isostatic equilibrium or overcompensation.

The center of the Pre-Cambrian area in question may have been near the center of the great Keewatin ice sheet during the Pleistocene period in North America. Coleman (2) describes the Keewatin as having at different times three main centers, the first to the west of Chesterfield Inlet, the second near Dubawnt Lake, and the third near the mouth of the Nelson River, the ice centers reaching an estimated depth of 12,000 ft. It has been well established by geological studies that, owing to the tremendous loads, glaciated areas were depressed far below present levels and that the land surface still stands lower than in preglacial times (4). Although the few statistics of rate of regional uplift that are available have been the subject of debate (3) it is generally agreed that equilibrium will be reached only after the termination of thousands of years.

Lack of isostatic equilibrium should then prevail in regions of postglacial upwarpings of the crust, gravity anomalies would be negative, and increasingly negative toward the area where the load was the greatest (5). The gravity measurements made over this large area exhibit to some extent this expected deficiency of gravity. Churchill and Cambridge Bay, both stations near the former center of the ice sheets, have negative anomalies of -0.051 cm. per sec.[2] and -0.042 cm. per sec.[2], respectively. On the other hand Arctic Red River and Good Hope near the Mackenzie River delta have positive anomalies, which is in agreement with geological evidence that this region was on the outer limits of the ice cap and was not disturbed by glaciation (2). There is also some evidence of algebraic decrease of the anomalies in passing from west to east. The area covered by the Prairie Provinces to the south and extending through the central United States is also for the most part one of positive anomaly.

Conclusion

The question whether the negative anomalies so predominant in this Pre-Cambrian area are due to lack of isostatic adjustment following removal of glacial loads cannot yet be definitely answered. Although the existing measurements of gravity suggest an affirmative answer, a greater density of gravity stations, especially in regions to the northeast, may present a different picture. It is hoped in the near future to make use of a gravimeter to extend the system of gravity measurements throughout this area in such a way as to answer some of the questions raised in this paper.

Acknowledgments

The writer wishes to acknowledge his indebtedness to Mr. A. H. Miller of the Dominion Observatory, Ottawa, for very helpful suggestions in the planning of the work and the preparation of the paper; and to the Royal Canadian Air Force who supplied air transportation in 1945.

References

1. BULLARD, E. C.   Trans. Roy. Soc. London, A, 235 : 445.   1936.
2. COLEMAN, A. P.   The last million years.   University of Toronto Press, Toronto.   1941.
3. COOKE, H. C.   Am. J. Sci. 240 : 144.   1942.
4. COOKE, H. C.   Trans. Roy. Soc. Can. 24 (IV) : 51.   1930.
5. DALY, R. A.   Strength and structure of the earth.   Prentice-Hall, Inc., New York.   1940.
6. HAYFORD, J. F. and BOWIE, W.   U.S.C.G.S.   Spec. Pub. No. 10.   1912.
7. MILLER, A. H.   Pubs. Dominion Observ. 8 : No. 6.   1923.

'

STUDIES IN HIGH FREQUENCY DISCHARGES[1]

By J. I. LODGE AND R. W. STEWART[2]

Abstract

A qualitative theory of the nature of high frequency discharges, with special reference to those developed by the use of external sleeve electrodes, is advanced on the assumption that the discharge is largely determined by its d-c. wall and space charges, and that the chief function of the high frequency field is to maintain the electron temperature. This theory leads to the conclusion that there must be a high negative wall charge under the electrodes, and a high radial field tending to drive positive ions to the walls. Thus each electrode has many of the characteristics of a cathode in a d-c. discharge. This conclusion is verified by the appearance of the high frequency discharge and by a careful examination of deposits resulting from the removal, by positive ion bombardment of the tube wall, of thin metallic films and of materials of which the discharge tube itself is composed.

Introduction

The marked effects of high frequency discharges in rarefied gases on the walls of discharge tubes have been observed by a number of workers. In 1933 Robertson and Clapp (8) discovered that a coating on the tube walls, formed previously by a pure electrodeless discharge (arrangement as in Fig. 1, *a*), was removed by a discharge maintained with external electrodes (as in Fig. 1, *b*), even though the deposit had resisted heat from a gas–oxygen flame. The removal occurred directly under the electrodes, and by moving the electrodes from place to place the entire tube was cleaned. Robertson and Clapp also found that when a clear tube, previously operated with external electrodes, was subsequently silvered by the Brashear process, a pattern in the silver was observable at the places where the electrodes had been.

About the same time, Banerji, Bhattacharya, and Ganguli (1, 2) discovered that various metallic and nonmetallic vapors were deposited by the action of a high frequency discharge with external electrodes, the deposit occurring in distinct regions which they associated with changes in the radial and transverse fields.

In 1938, Hay (4) made an extensive study of the removal and deposit of silver coatings by discharges obtained with external electrodes, using various gases, pressures, and frequencies. He found that the removal was of two types: "electrode effect", a strong removal directly under the electrodes, and

a "general removal", a much less marked effect opposite the various glows in the discharge. The silver was found to deposit in very sharply defined regions, with the deposits often showing marked fine structure.

Hay ascribed the electrode effect to positive ion bombardment, and gave evidence that the removal was associated with plasmas in the discharge. Since removal by positive ion bombardment suggests that the effect is not unrelated to the phenomenon of sputtering in a d-c. discharge, it was thought desirable to look for further evidence of this relation by extending Hay's work, using metals other than silver. Initially, the work done by one of us (R.W.S.) was undertaken with this object in view.
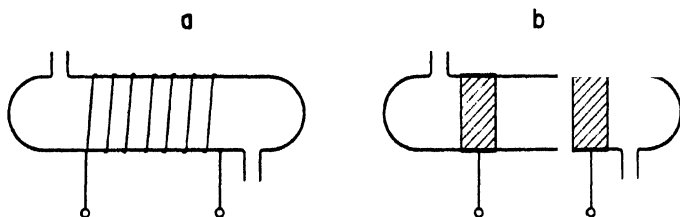
Fig. 1. *Two arrangements for exciting high frequency discharges:* (a) *electrodeless method;* (b) *external electrodes.*

When this work was under way, the other author (J. I. L.) was studying another aspect of the general problem of high frequency discharges. As both these investigations progressed, each of us observed a type of deposit that showed a marked interference pattern. As a careful examination of this deposit seemed likely to reveal interesting information concerning its nature and origin, as well as to shed further light on the complicated question of high frequency discharges, attention was shifted to a somewhat careful examination of this particular phenomenon.

At the same time, each of us, working independently, was able to make a preliminary comparison of conditions near an electrode in a high frequency discharge with those at the cathode in a d-c. discharge.

Experimental

The discharge was obtained in a tube around which, for the most part, two external electrodes were wrapped, as in Fig. 1, b. The high frequency power was developed by a series-fed Hartley oscillator, using an Eimac 250 TH tube supplied by a bridge type power supply, with variac control and with 866A mercury vapor rectifier tubes. The oscillator supplied up to 1000 w. at a frequency of about 6 Mc. per sec. A rotary switch and relay arrangement permitted the oscillator to be run intermittently.

Discharge tubes were mostly of Pyrex glass with an inside diameter of about 2.5 cm., although some tubes of larger diameter were used. Some experiments were conducted using quartz and polystyrene tubing.

In all cases, a Cenco Hyvac pump was employed to evacuate the discharge tube, and the pressure was controlled by means of a needle valve.

Thin glass strips, of dimensions about 15 cm. by 6 mm. by 0.5 mm., were coated by evaporation with semitransparent layers of silver, copper, aluminum, gold, and bismuth. The evaporation was carried out *in vacuo*, using the techniques described by Strong (11) and by Olsen, Smith, and Crittenden (7). A coated strip was placed in the bottom of the tube and an air discharge was then maintained in the tube. In all cases, removal similar to that found by Hay (4) was observed, although with some metals, notably aluminum, the removal was very slow. Fig. 2 is a contact print of a series of gold-coated strips left in the discharge for varying lengths of time. It will be noted that the removal occurs under the electrode and that outside the region of the electrode deposits have formed in sharply defined areas.

It was found that the relative rates of removal of various metals correspond roughly with sputtering rates as recorded in the literature, but since the pressures employed, from 0.05 to 1.5 mm. of mercury, were well above those normally used for sputtering, an exact comparison is hardly justified with the present data. It is hoped to continue this problem in the future.

DEPOSITS SHOWING INTERFERENCE PATTERNS

After runs of an hour or more, it was found that a transparent deposit showing thin film interference fringes formed on the part of the strip under an electrode. Fig. 3 is a photograph, taken in reflected sodium light, of such a strip. Close examination of the tube walls revealed that a similar deposit had formed on the inner walls of the tube, just beyond the boundaries of the electrodes. Fig. 4 is a photograph of a well developed deposit on the walls.

In addition to the film giving rise to the interference pattern, a narrow ringlike deposit of a different kind was observed on each side of the electrodes, about 2 mm. from them. This was composed of a grayish-white flaky substance. If an electrode was loose fitting at some point, this deposit and the interference film were formed on the tube walls underneath the loose region.

Temperature Control

In order to test whether or not the deposit showing interference fringes was due to evaporation arising from local heating, some observations were made with the electrodes and adjacent parts of the tube packed with dry ice. It was found that, although the interference pattern was not as well developed when dry ice was used as without it, the pattern persisted. Fig. 5 shows the patterns: (a) without dry ice, and (b) with dry ice. It would seem, therefore, that the fundamental cause of the formation of the deposits is not a thermal one, although further work on this point is desirable.

Effect of Pressure

The original deposits giving rise to the interference patterns were obtained at pressures of approximately 0.5 mm. In order to investigate the effect of

pressure, glass strips were exposed to the discharge at pressures of about 2 and 0.01 mm. At the higher pressure, the pattern obtained was much the same as that at 0.5 mm., except that it was confined to a smaller region, and the films on the tube walls were deposited a little closer to the electrodes. In the case of the lower pressure, the interference fringes showed an oval pattern for that part of the strip that was under the electrodes, and the deposits on the tube were formed at a greater distance from the electrodes. Fig. 6 is a photograph of the oval interference pattern observed on the strip.

Influence of Carrier Gas

In order to eliminate the possibility of vapors getting into the discharge f om the pump, a tube containing a *clear* glass strip was evacuated to a pressure of about 2 mm. of mercury, and sealed off. As the discharge ran, the pressure gradually dropped, owing to occlusion of the gas, until a discharge could no longer be maintained, but, owing to the initial high pressure, the strip was subjected to the discharge for a time great enough to give a pattern. Similar results were obtained with a sealed-off tube containing helium.

A trickle of hydrogen was allowed to pass into the discharge tube, the pressure being maintained at a constant value by means of a needle valve. In this case, a deposit formed on those portions of the strip under the electrodes, but an interference pattern could not be observed. A second run of much longer duration resulted in a similar deposit, which showed a little color at the edges when viewed with reflected white light. The deposit was quite thin and had a highly reflecting surface. In transmitted light it appeared brown.

Chemical Tests

An attempt was made to clean one of the Pyrex tubes so that it could be used again. It was first washed out with water. This removed the flaky deposit, which had formed at certain places under the electrodes, and most of the narrow ring-shaped deposit near the electrodes. Hot nitric acid, aqua regia, concentrated sodium hydroxide, and alcohol failed to remove the remainder of the ring-shaped deposit or the interference film.

The deposit obtained with hydrogen was unaffected by any of the above chemicals. Hydrochloric acid, sulphuric acid, and carbon disulphide were also tried, but without effect.

Quartz Tube

When quartz tubing was used the interference pattern was again formed, but there was no flaky deposit.

Index of Refraction

Since the deposits showing interference patterns failed to respond to any chemical reagents, the only properties that could be determined positively were optical ones. By means of an indicometer described elsewhere in this

PLATE I
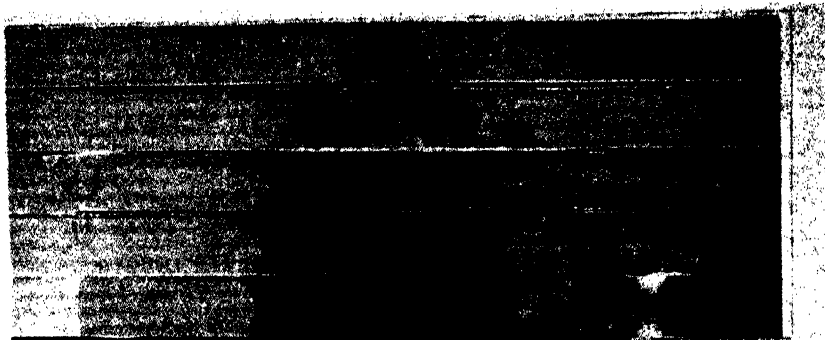
ELECTRODE

2

ELECTRODE
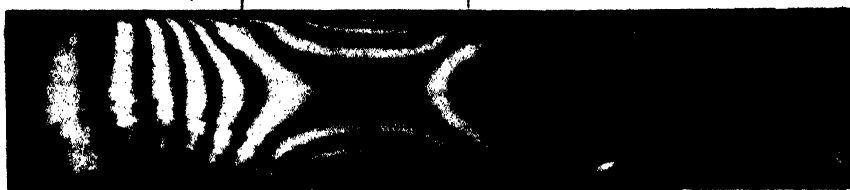
3

ELECTRODE

4

FIG. 2. *Contact print of a series of gold-coated strips of glass after being exposed to a high frequency discharge in air for various times. Note removal under electrode.*

FIG. 3. *Photograph, by reflected sodium light, of deposit showing interference pattern, on glass strip, in region under electrode.*

FIG. 4. *Photograph of deposit showing interference pattern, on tube walls, on either side of an electrode.*

PLATE II
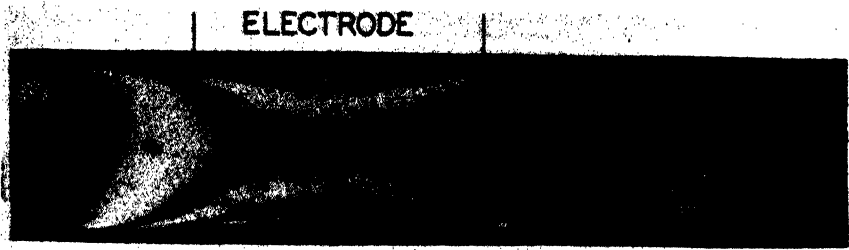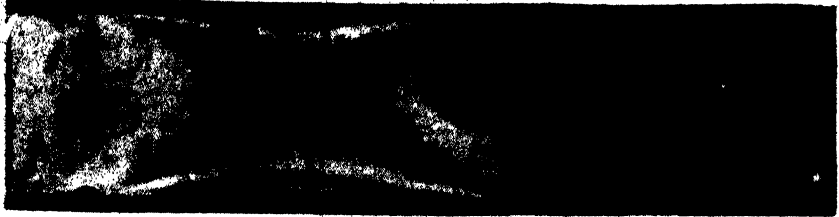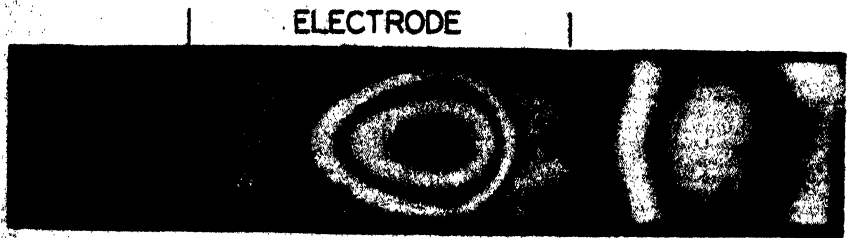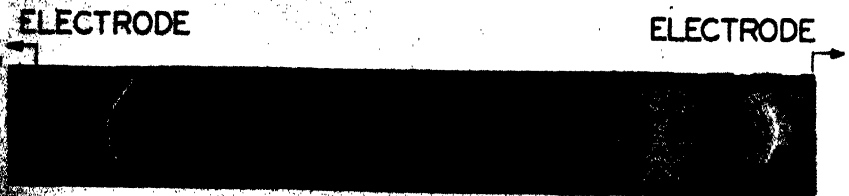
FIG. 5. *Interference pattern:* (a) *with electrodes at room or higher temperature;* (b) *with electrodes and adjacent parts of discharge tube packed in dry ice.*

FIG. 6. *Interference pattern under electrode, with discharge at very low pressure.*

FIG. 7. *Interference pattern on glass strip in polystyrene tube.*

issue (10) the index of the deposit was found to be about 1.497 ± 0.003, the same as that of silica in the form of cristobalite. The value of the index was identical whether the film was formed in Pyrex glass or quartz tubing.

Polystyrene Tube

In an effort to determine the extent to which the above phenomena depend on the silicate nature of the glass and quartz, some experiments were conducted using polystyrene tubing. It was found that a deposit could be quite easily obtained from polystyrene, forming just beyond the electrode region and also in the center of the tube between the electrodes. Little deposit formed on strips under the electrodes, but outside the electrode region the deposit was very marked (Fig. 7). When the tube had been washed out with alcohol, and also when it was allowed to become appreciably hot, a brownish deposit formed. If, however, no alcohol was used and the tube was kept cool, the deposit was quite colorless, although more translucent than transparent. The index of the deposit thus formed proved to be exceptionally low and to be a function of the thickness and of the time, increasing with both (10).

Spectrograms were taken of the light from the discharge in a polystyrene tube. The CO bands with heads at 4835 (0,1), 5198 (0,2), 5610 (0,3); the CO^+ bands at 2198.8 (0,0), 2299 (0,1), 2325 (1,2), 2419 (0,2), 2446 (1,3); the CO_2^+ bands at 2896, 2883, and the carbon line 2478 can be clearly seen in Fig. 8 (*a* and *b*). For purposes of comparison a spectrogram of light from a discharge in a Pyrex tube is shown in Fig. 8 *c*.

COMPARISON OF D-C. AND A-C. DISCHARGES

Since the removal near the electrode by high frequency discharges seemed to be of the same nature as cathodic sputtering, it was thought advisable to compare the conditions at the electrodes of a high frequency discharge with those at the cathode of a d-c. discharge. With this in view the following observations were made.

Direct Current Discharge with Internal Electrodes

Disk electrodes of diameter 2.25 cm. were placed 23.5 cm. apart inside a Pyrex glass tube whose internal diameter was about 2.5 cm. A d-c. discharge was operated with a potential difference of 750 v. between the electrodes, and a current of 5 ma. The widths of the cathode glow and cathode dark space were about 0.5 and 1.5 mm. respectively. To ensure cool operation, the rotary switch and the relay were used so that the discharge was on for 17.3 hr. out of a total of 117. At the end of this time, *there was a noticeable deposit on the walls at the cathode end of the tube, but none at the anode end.* Since the surface of the aluminum cathode had been roughened by the discharge, the deposit was assumed to be due to cathodic sputtering. On the walls very near the cathode, there was little, if any, deposit, but, as the distance from this

electrode increased, the deposit was more marked, its thickness reaching a maximum at a distance of about 1.5 to 2 mm., after which it gradually decreased. This maximum is nicely shown in Fig. 9, which also shows how rapidly the maximum thickness is attained on the electrode side.

High Frequency Discharge with Internal Disk Electrodes

With high frequency excitation, the electrodes used for the d-c. discharge were found to be unsuitable because their diameter was less than that of the tube and, if more than a certain amount of power was supplied, the discharge appeared on both sides of the disks. To prevent this, new electrodes were made that would just fit inside the tube.

At first only one electrode was used, one of the leads from the tank circuit being left unconnected. After a total run of 117 hr., some deposit showing an interference pattern in reflected light was visible near this electrode.

With two electrodes, similar patterns were obtained near each in only 13 hr. In this case, the oscillator could be adjusted to the load, and thus the power provided was much greater than when the single electrode was used. Fig. 10 is a photograph of the interference fringes near one of the electrodes.

External Disk Electrodes

Two glass windows were fastened to the ends of a short Pyrex glass tube 10 cm. long by means of polystyrene cement, and the two disk electrodes previously used for the d-c. discharges were placed *outside* the tube pressing against the windows. A high frequency discharge was induced in the tube, and after a total time of 89 hr. (net time is about one-seventh of this), interference fringes could be seen near each end of the tube.

Comparison of Appearance of D-C. and High Frequency Discharges

With internal electrodes and a pressure of the order of 1 mm., a typical direct current discharge in air was obtained. Starting at the cathode, the cathode glow, the Crookes dark space, the blue negative glow, the Faraday dark space, and the pink-red positive column followed in order. At the same pressure, the high frequency discharge had somewhat the same appearance, except that *each of the electrodes seemed to be an effective cathode*. Associated with each was a cathode glow, a Crookes dark space, a blue negative glow, a Faraday dark space, and a pink-red positive column, which was now in the central region. This was true with both internal and external disk electrodes. When external *sleeve* electrodes were used, the cathode glow and the Crookes dark space appeared at the wall parallel to, rather than normal to, the axis of the tube. Inside the Crookes dark space the region surrounded by the electrode was filled with the blue negative glow.

If only one electrode was used, either internally or externally, the discharge was essentially the same, except that the so-called 'positive column' tapered off at the end remote from the electrode, until it disappeared.

FIG. 8. *Spectra of high frequency discharge in air: (a) in Polystyrene tube, visible region;*
(b) in Polystyrene tube, ultraviolet region; (c) in Pyrex tube, visible region.

c

3914 N₂
3998 N₂
4059 N₂
I ST.
POSITIVE
N₂

b

2190 CO⁺
2299 CO⁺
2325 CO⁺
2419 CO⁺
2446
2478 C
2883 CO₂⁺
2896

a

3914 N₂
3942 N₂
3998 N₂
4059 N₂
4835 CO
4861 Hβ
5198 CO
5610 CO
6563 Hα

PLATE III

9

ELECTRODE

10
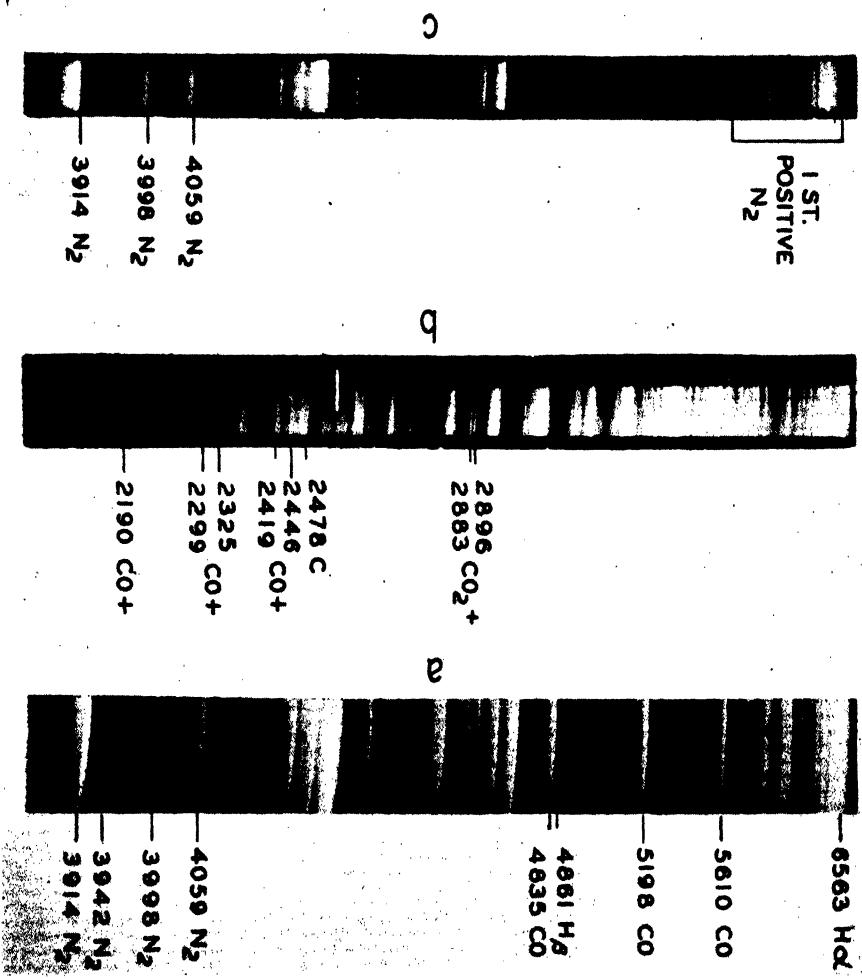
ELECTRODE

13

FIG. 9.   Deposit showing interference pattern near the cathode, on walls of a tube carrying a d-c. discharge.

FIG. 10.   Interference pattern near an internal disk electrode, on the walls of a tube carrying a high frequency discharge.

FIG. 13.   Photograph of the pattern on which measurements of thickness were made to obtain the dots plotted in Fig. 12.

Discussion

It is possible to explain many of the above facts by the following hypotheses concerning the mechanism of high frequency discharges.

That there is a similarity between the conditions at each electrode in a high frequency discharge and those at the cathode in a d-c. discharge is evident from the marked similarity in appearance. If this likeness is more than superficial, and if the electrode regions in the high frequency discharge are subject to strong positive ion bombardment, the removal of metals and non-metals in these regions can be considered to be due to a type of sputtering. It is thus worth while examining the conditions within a high frequency discharge tube.

To begin with, it should be noted that there is no justification for considering a high frequency discharge as a d-c. one in which the anode and cathode alternate every half-cycle. If this were true the positive column should be visible in the Faraday dark space, and this is emphatically not the case. On the other hand, as will appear later, it is useful to consider the high frequency discharge as essentially determined by the d-c. wall and space charges, the sole function of the high frequency field being to maintain the 'electron temperature'. Although the external sleeve electrode type of discharge will be considered, the fundamental conceptions are the same for any type of high frequency discharge, using either internal or external electrodes.

For stability, the total quantity of charge that crosses any cross section of the tube, or which reaches any wall in one cycle must be zero.

This means that Boltzmann's equation,

$$n = n_0 e^{\frac{qV}{kT}},$$

where n is the density of electrons at a point,

    q is the electronic charge,

    V the potential of the point,

    n_0 the density corresponding to $V = 0$,

    k Boltzmann's constant,

    T the absolute temperature,

holds not only radially, as in the case of d-c. discharges, but also axially, subject to the assumptions that high speed electrons, which cannot be said to be diffusing, are negligible in number, and that the net effect of the alternating field is zero over one cycle.

From this equation it can be seen that, in a potential gradient, the density gradient of electrons will be such that they will tend to diffuse against the field. This 'up-hill' diffusion is the key to the stability of the discharge in spite of the presence of d-c. fields.

Where the potential is lowest, not only will the electron density be lowest, but the field will be such as to tend to attract positive ions, so a high positive space charge will develop. In view of this high positive space charge, the only possible cause of the low potential is a high negative wall charge. This wall charge is again maintained by up-hill electron diffusion, this time to the walls. The number of electrons diffusing to the walls must exactly equal the number of positive ions reaching the wall by diffusion and repulsion from the positive space charge, plus the number of secondary electrons emitted.

The existence of a negative space charge is highly improbable. In order to have stability under such conditions, the positive ions, fewer in number than the electrons, would have to diffuse to the walls against the field due to this negative charge as fast as the electrons move under the influence of both field and diffusion. In view of the much greater mobility and coefficient of diffusion of the electrons (Kennard (5, p. 473) places them at many hundred times the values for the positive ions) this seems impossible.

The magnitude of the negative wall charge and positive space charge that can exist in a stable condition is determined by the ability of the electrons to diffuse against a field. This is dependent on the following relation, given by Kennard (5, p. 466), between the coefficient of diffusion and the mobility.

$$\frac{D}{U} = \frac{kT}{q} ,$$

where D is the coefficient of diffusion,

   U the mobility,

   T the absolute temperature,

   k Boltzmann's constant,

   q the ionic charge.

Thus, the greater the electron temperature, the greater the coefficient of diffusion relative to the mobility, and hence the greater the negative wall charge that can be maintained. The electron temperature will be maintained by the high frequency field, so the more intense that field, the higher the negative wall charge.

This wall charge is the dominant factor in determining the potential at any point, for where the positive space charge is largest, the potential is most negative. Thus, the potential surrounding a wall charge is worth examining in some detail.

Potential Distribution Due to a Wall Charge

Assume a uniform wall charge $q/cm.^2$ on the surface of a cylinder of radius a, the charged portion being $2b$ cm. long, and consider the potential produced at a distance x from the median plane of the charged portion, both on the axis and on the wall.

Potential on the axis is given by

$$V = q \int_{x-b}^{x+b} \int_{0}^{2\pi} \frac{a\,d\theta\,dx}{\sqrt{x^2 + a^2}}$$

$$= 2\pi aq \left\{ \sinh \frac{(x + b)}{a} - \sinh \frac{(x - b)}{a} \right\}.$$

Potential on the wall by

$$V = q \int_{x-b}^{x+b} \int_{0}^{\pi} \frac{2a\,d\phi\,dx}{\sqrt{x^2 + (2a\,\sin\phi)^2}}$$

The evaluation of the latter integral is given in Appendix A.

The results have been plotted in Fig. 11 for different values of b/a.
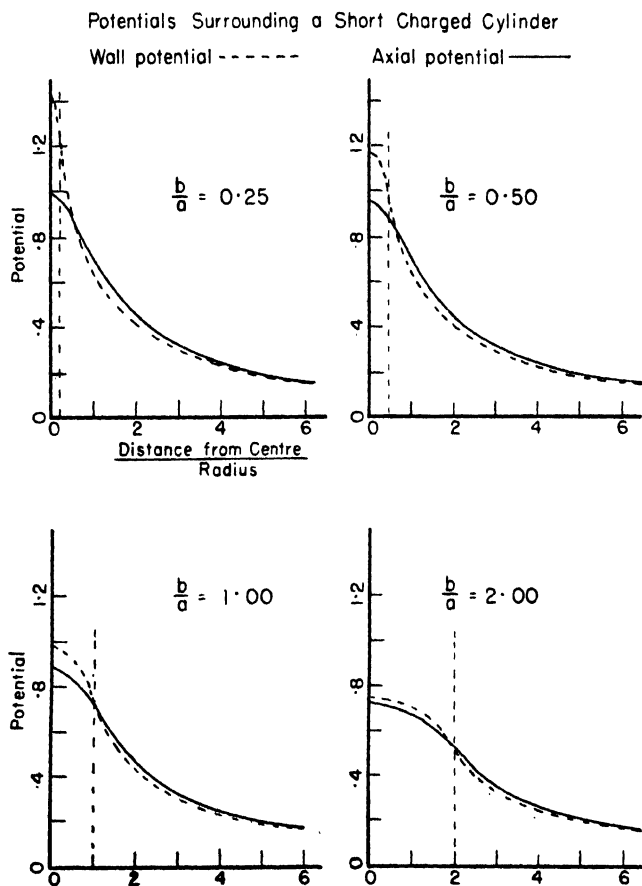
FIG. 11. *Graphs showing how potentials, on the tube wall and at axial points, due to a uniform cylindrical wall charge, vary with the distance from the center of the discharge.*

From the graphs in Fig. 11 it is seen that the radial field due to a wall charge is very small unless b/a is small. In general it is seen that there will be no radial field due to the wall charge unless the wall charge is not uniform. Indeed, if there is a high negative wall charge under the electrodes, the radial field between the *electrodes might actually be positive,** as can be seen from the graphs. Banerji and Ganguli (2) did observe such a change in sign of the radial field.

Role of High Frequency Field

The role of the high frequency field may now be examined. The potential distribution due to the charging of the electrodes will be somewhat similar to that of a uniform charge, to which Fig. 11 applies, the chief difference being that with our cylindrical electrodes, the charge tends to concentrate at the edges, the potential of the wall being constant under the electrodes, with a very steep gradient just outside. Since the general solution applicable to a short charged cylindrical conductor such as was actually used failed to respond to any method of attack at the writers' command, the approximation of a uniformly charged cylinder was used. Except right at the edges of the electrodes, the difference is slight.

The displacement of the ions because of this field will alter it somewhat, but that effect may reasonably be considered of second order magnitude compared with the field from the electrodes.

In view of the above, it can be seen from Fig. 11 that the only *radial* high frequency field of any consequence will be that directly under the electrodes. This, coupled with the fact that the greatest *axial* fields occur just outside the electrodes, means that the electrons under the electrodes may be expected to have very high temperatures, with the resulting high negative wall charge. If the alternating field is very intense, it may even make the radial field positive momentarily each cycle, despite the wall charge and positive space charge. Because of the high electronic mobilities this would greatly increase the flow of electrons to the walls.

Apart from the electrode region, the chief function of the high frequency appears to be to maintain the electron temperature. Townsend (12) found that the magnitude of the alternating field in the glows outside the electrode region was identical with that of the d-c. field in the positive column of a corresponding d-c. discharge.

Summary of Hypothesis

To summarize, a high frequency discharge is regarded as largely determined by the d-c. space and wall charges, notably the high negative wall charge under the electrodes. The function of the high frequency field is considered essentially to be to maintain the electron temperature.

---

* *Used herein to mean that potential increases as the radius increases.*

This hypothesis leads to the following conclusions.

1. There will be a negative radial field everywhere in the tube except possibly for a region a short distance outside the electrodes where the field due to the high wall charge under the electrodes changes sign.

2. This radial field will be very much more intense under the electrodes than elsewhere in the tube. This is in good agreement with the fact noted above, that the removal occurs only under the electrodes.

3. Because the radial field is largely caused by the positive space charge, it will increase as the wall is approached, being a maximum at the wall. (This can be seen from Boltzmann's equation. If there is a radial field, the potential near the wall will be less than on the axis, hence the number of electrons will be less, and since the field will tend to force the positive ions away from the center towards the walls, a positive ion sheath will develop near the walls, and most of the radial field will be in this region.) Confirmation of this conclusion will appear below.

4. No part of the above argument requires two electrodes, and it should hold equally well with only one. As has been pointed out above, a perfectly satisfactory discharge can be set up using only one external electrode.

The high positive ion bombardment resulting from the high radial field under the electrodes accounts for the removal of metals in this region. Sputtering of nonmetals has been shown to occur by Stark and Wendt (9), so the same phenomenon will explain the removal of the constituents of glass and polystyrene from the tube walls, such removal also occurring under the electrodes.

EXPLANATION OF DEPOSITS

As noted above, several different types of deposit were obtained, and deposition occurred in different regions.

The deposit showing an interference pattern, which, as already noted, for Pyrex and quartz tubes is probably cristobalite, always has smooth contours and, in general, is thickest near discontinuities. The nature of these deposits, examples of which are given in Figs. 3, 4, 5, and 6, indicates that the material is deposited by diffusion, as is evident from the following discussion. If we assume that the silica can be removed by the high bombardment at the walls under the electrodes, but not by the ions in the less intense fields over strips that are nearer the axis of the tube, the fact that the deposit is heaviest at the edges and corners is explained by the proximity of these regions to the source compared with the central portions. To work out a diffusion function for the inside of a tube containing a strip is extremely difficult, but it is possible to obtain a good approximation for diffusion to the walls outside the electrode region.

Assuming all the silica to originate under the electrodes and to diffuse to the walls, we have Laplace's equation

$$\triangle D = 0$$

within the tube, where D is the density of material at any point in the tube.

Using as boundary conditions $D = C$ under the electrodes and $D = 0$ elsewhere on the wall, we find that:

$$\frac{\partial D}{\partial r}\bigg|_{r=a} = \frac{2C}{\pi}\left[\sum_{n=1}^{n=\infty} - \left\{\left(1 - \frac{I_1(na)}{I_0(na)}\right)\sin(nb)\sin(nx)\right.\right.$$
$$\left.\left. + \cot\left(\frac{x+b}{2}\right) - \cot\left(\frac{x-b}{2}\right)\right]\right.$$

In this expression,

  a is the radius,

  $2b$ is the length of the electrode,

  x is the distance from the center of the electrode to the point under consideration,

  I_0 and I_1 are modified Bessel's functions of the first kind.

The derivation of the above expression is given in Appendix B.

The rate of flow to the wall at any point will be proportional to $\dfrac{\partial D}{\partial r}$

so the thickness of the deposit at that point at any time will also be proportional to this expression.

Fig. 12 shows the comparision of theoretical and experimental results. The curve is the theoretical one, given by the above equation. The points are experimental ones, taken from a photograph of the tube shown in Fig. 13, the fringes being considered as equal vertical interval contour lines. Points have been taken from the fringe patterns near both electrodes. The maximum thickness of the deposit for which the fringes could be separated was about 7 wave lengths (14 fringes), or about 2.5×10^{-4} cm. The thickness became greater than this as the electrode was approached, but the fringes were too close to be separated by the traveling microscope used.

The tube dimensions used in the theoretical calculation were those of the experimental set up. The agreement appears sufficiently satisfactory to support the contention that these deposits are laid down by diffusion to the walls.

Diffusion and Disk Electrodes

For comparison, the diffusion curves for disk electrodes have been calculated. Two theoretical curves have been plotted. For one, it was assumed that the diameter of the electrode at which the sputtering occurred was equal to the inner diameter of the tube, and that the density of the sputtered particles across the face of the electrode was uniform. Otherwise the boundary conditions were the same as in the case of the external electrodes already given.

The resulting equation is:

$$\frac{\partial D}{\partial r} = -C \sum_{n=1}^{n=\infty} \frac{2}{a} e^{-\frac{r_n}{a} x},$$

where r_n is the nth root of a Bessel function of the first kind of order zero, and the remaining symbols are the same as for the external electrode case.

Thickness of deposit
Dimensions - $a = 1 \cdot 0$
$\qquad b = \frac{\pi}{4}$
Curve - Theoretical
Points - Experimental

Thickness

Distance from electrode centre
(360° centre to centre)
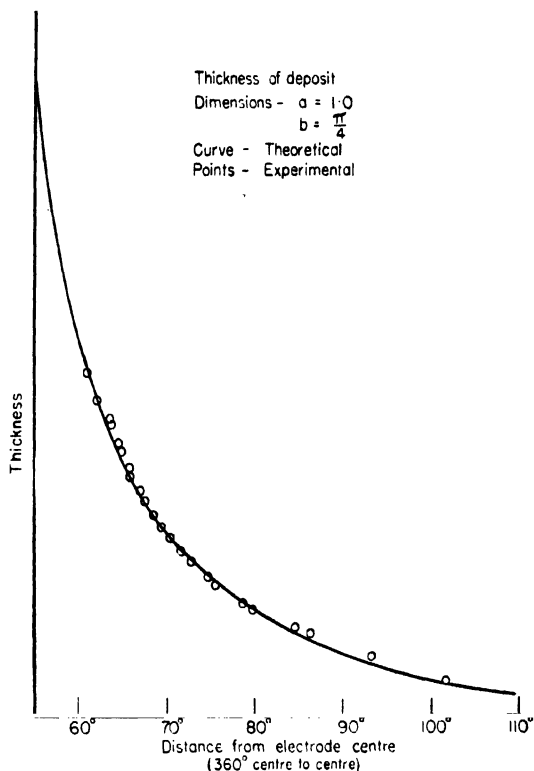
FIG. 12. *The curve shows how the thickness of a wall deposit, assumed to result from diffusion, should vary with the distance from the source. The dots are based on measurements of thickness obtained from an actual interference pattern.*

This curve is shown in Fig. 14, Graph 1.

For the second theoretical curve, only one boundary condition was changed. It had been observed that, after a high frequency discharge had passed between two polished aluminum disk electrodes for some time, the central part of each electrode had lost its polish but the outer parts had not. It was assumed for this second theoretical case, therefore, that the sputtering took place over an area having a diameter equal to two-thirds that of the tube. The boundary conditions thus are:

$$D(r,\infty) = 0; \; D(a,x) = 0; \; D(r,0) = C, \quad r < b$$
$$= 0, \quad b < r < a.$$

In this case $b = 2/3a$.
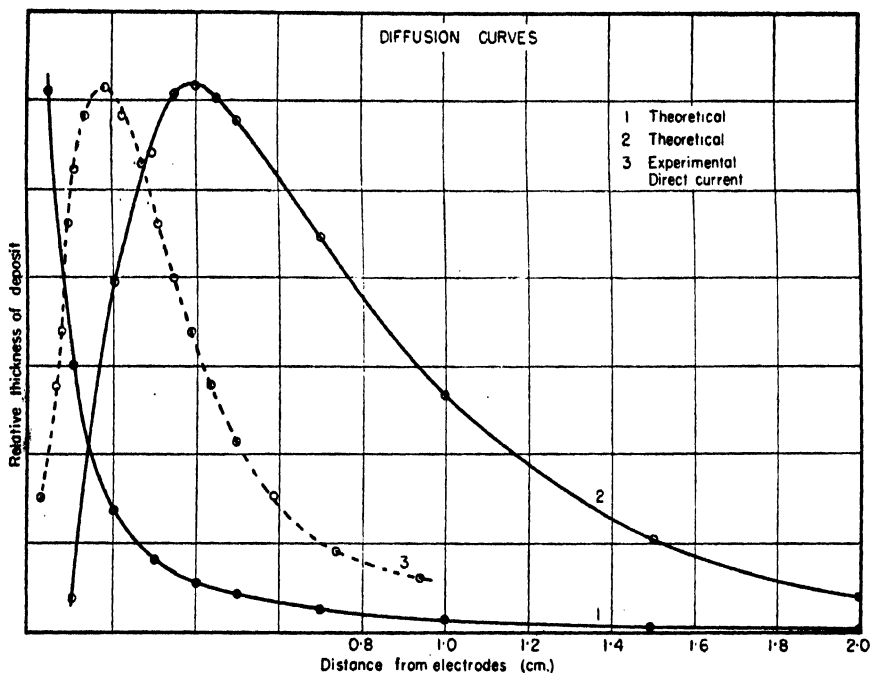
FIG. 14. *Graphs showing how the thickness of material deposited on tube walls by diffusion varies with the distance, when the source is a disk electrode. Graph 1 is based on the assumption that material is released from the whole face of the disk; Graph 2, on the assumption that the effective diameter of the disk is two-thirds the diameter of the tube. Graph 3 is based on actual measurements of thickness of the deposit showing fringes, reproduced in Fig. 9.*

With these boundary conditions, the solution to Laplace's equation is:

$$D = C \sum_{n=1}^{n=\infty} \frac{4}{3r_n} e^{-\frac{r_n}{a}z} \cdot J_0\left(r_n \frac{r}{a}\right) \cdot \frac{J_1\left(\frac{2r_n}{3}\right)}{\{-J_1(r_n)\}^2}$$

and

$$\frac{\partial D}{\partial r}\bigg|_{r=a} = -C \sum_{n=1}^{n=\infty} \frac{4}{3a} e^{-\frac{r_n}{a}z} \cdot \frac{J_1\left(\frac{2r_n}{3}\right)}{J_1(r_n)}$$

The values of $\dfrac{\partial D}{\partial r}\bigg|$ are plotted in Graph 2, Fig. 14.

Fig. 14, Graph 3, is an experimental curve taken from the photograph shown in Fig. 9. A comparison of the three curves of Fig. 14 also supports the contention that the mechanism of deposition is one of diffusion.   Evidence is also provided that the effective diameter of the electrode is somewhat less than its actual diameter.

Deposits at Low Pressure

The nature of the deposit on strips under the electrodes at low pressures, shown in Fig. 6, is probably due to the fact that at lower pressures the ionic free path is greater and hence the positive space charge is farther from the

walls. The edge of the strip is thus outside the space charge and under bombardment, as is the tube wall. The center of the strip is nearer the tube center, and hence under less bombardment. Apparently in this position the rate of deposition is greater than the rate of removal, and hence the deposit. At still lower pressures no deposit at all formed on the strip.

Flaky Deposits

The gray flaky deposits, which are formed in glass tubes but not in quartz ones, are probably constituents of glass other than silica, notably boron trioxide, sodium oxide, and aluminum oxide. The sharp localization of these deposits indicates that the material, rather than diffusing to the walls, is cast down by a field. If the particles generally take a positive charge in the discharge, there will be an excess deposit under or near the electrodes, where the particles will be re-removed, unless they are in some region where the radial field, and hence the positive ion bombardment, is reduced. Thus they will accumulate just outside the electrode region and under loose spots of the electrodes.

A similar explanation probably accounts for the localization of the metallic deposits. In this case the sputtering rate is much greater, and deposit will become greater than removal only at a considerably greater distance from the electrodes than for the flaky deposits.

Polystyrene

The location of the deposits in polystyrene indicates that the particles must pick up a negative charge in the discharge, for deposition occurs in the two places where the radial field is least negative, just outside the electrode region, and in the center of the tube between the electrodes.

The brown deposit observed on the walls of tubes that had either been cleaned with alcohol, or had been allowed to become hot, seems to be very similar to that obtained by Harkins and Gans (3), who found that a reddish brown solid formed very rapidly when a pure electrodeless discharge was run in benzene. They identified this as a complex hydrocarbon of formula $(CH)_n$. Carbon was also obtained, and in the presence of oxygen, carbon monoxide and water. In the work reported in this paper spectroscopic evidence has been found of the presence of carbon, carbon monoxide, and carbon dioxide in an air discharge in a polystyrene tube. Considering that benzene would be one of the chief products of the cracking of polystyrene, it is likely that the deposit found in this work is identical with that investigated by Harkins and Gans.

When no alcohol was used, and when the temperature was kept low, the brown deposit could be practically eliminated. The deposit then probably consists of polystyrene molecules, modified only slightly, if at all, by the discharge. It appears that the effect of the alcohol and of the heat is to make the polystyrene more susceptible to cracking in the discharge.

SPUTTERING

This investigation may cast some light on the general problem of sputtering, for, although the phenomenon has been known for many years, it has not yet been satisfactorily explained. Lewis (6), in her recent monograph, states that it is not known whether the particles emitted are atomic or molecular in size.

The observations on the silica deposits do not solve this problem, as the silicon could be removed as silica and, when the discharge was in air or in helium, could be deposited unchanged, or, with hydrogen the carrier gas, reduced to silicon either before or after deposition. On the other hand, the silicon could be removed in atomic form and oxidized in the discharge if all the oxygen was not removed by the hydrogen carrier gas. In either case we would expect silica to be deposited in air or helium and either silicon or silica in hydrogen. The mirrorlike deposit obtained with hydrogen as carrier gas could not be positively identified, but it was probably silicon.

With polystyrene, however, the evidence is very strong that the particles removed and deposited were fairly large molecules. As is pointed out in the accompanying paper (10), the evidence there presented suggests that the deposit is of polystyrene molecules, cast down into a rather loose mass. This indicates that in some cases at any rate, sputtered particles are at least of molecular size.

SUMMARY OF CONCLUSIONS

On the basis of the hypothesis that the high frequency discharge is essentially determined by the d-c. wall and space charges, differences in which are caused by differences in the electron temperature maintained by the high frequency field, it has been shown that there is a strong positive ion bombardment of the walls under the electrodes, and that the bombardment is of much lower intensity elsewhere in the discharge tube. This has been verified by a comparison of the nature of d-c. and high frequency discharges and by the fact that both metals and the materials of which the walls are made, whether of silicate or of an organic plastic nature, are removed in the electrode region by a process akin to sputtering. These materials are deposited in regions more or less remote from the electrodes, where the bombardment is reduced.

It is also shown that at least the particles of polystyrene removed by the positive ion bombardment are of molecular dimensions or larger.

Acknowledgments

to Prof. E. F. Burton of the University of Toronto for his kind donation
of the helium required for part of this investigation; and to many members of
staff of Queen's University for helpful co-operation.

In addition, grateful thanks are due the National Research Council of
Canada, whose generous award of a Studentship to one of us (R.W.S.) made
this work possible.

References

1. BANERJI, D. and BHATTACHARYA, D. Phil. Mag. [7] 17 : 313. 1934.
2. BANERJI, D. and GANGULI, R. Phil. Mag. [7] 15 : 676. 1933.
3. HARKINS, W. D. and GANS, D. M. J. Am. Chem. Soc. 52 : 5165. 1930.
4. HAY, R. H. Can. J. Research, A, 16 : 191. 1938.
5. KENNARD, E. H. Kinetic theory of gases. 1st ed. McGraw-Hill Book Company, Inc.,
     New York. 1938.
6. LEWIS, W. Thin films and surfaces. English Universities Press, London. 1946.
7. OLSEN, L. O., SMITH, C. S., and CRITTENDEN, E. C., Jr. J. Applied Phys. 16 : 425. 1945.
8. ROBERTSON, J. K. and CLAPP, C. W. Nature, 132 : 479. 1933.
9. STARK, J. and WENDT, G. Ann. Physik, 38 : 921. 1912.
10. STEWART, R. W. Can. J. Research, A, 26 : 230. 1948.
11. STRONG, J. Procedures in experimental physics. Prentice-Hall Inc., New York. 1938.
12. TOWNSEND, J. S. Phil. Mag. [7] 11 : 1112. 1931.

APPENDIX A

Potential on the Wall of a Tube, a Section of which is Uniformly Charged with a Charge Density q/cm.^{2}

Owing to the law of addition of potentials, this may be obtained from the
potential due to a uniform wall charge extending from $x = 0$ to $x = x$ (x being
the distance along the wall from the point under consideration) by subtraction.

Let tube radius $= a$, and ϕ the angle shown in Fig. 15.
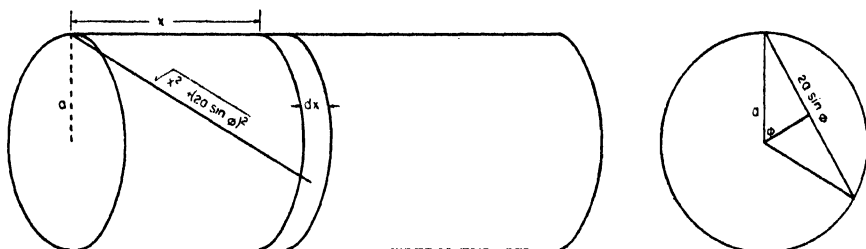
FIG. 15

$$V = q \int_0^x \int_0^\pi \frac{2a\, d\phi dx}{\sqrt{x^2 + (2a\sin\phi)^2}} = 2aq \int_0^x dx \int_0^\pi \frac{d\phi}{\sqrt{x^2 + 4a^2\sin^2\phi}}$$

$$= 2aq \int_0^x dx \int_0^\pi \frac{d\phi}{\sqrt{x^2 + 4a^2 - 4a^2\cos^2\phi}}.$$

Set $\theta = \phi - \pi/2$

$$V = 2aq \int_0^x \frac{dx}{\sqrt{x^2 + 4a^2}} \int_{-\frac{\pi}{2}}^{\frac{\pi}{2}} \frac{d\theta}{\sqrt{1 - \dfrac{4a^2}{x^2 + 4a^2} \sin^2\theta}}$$

$$= 4aq \int_0^x \frac{K\left(\dfrac{4a^2}{x^2 + 4a^2}\right)^{\frac{1}{2}}}{\sqrt{x^2 + 4a^2}} \, dx \quad \left(\text{since } \frac{4a^2}{x^2 + 4a^2} < 1 \text{ for } x > 0\right)$$

where $K(k)$ is the complete elliptic integral:

$$\int_0^{\frac{\pi}{2}} \frac{d\theta}{\sqrt{1 - k^2 \sin^2\theta}}$$

$$K(k) = \int_0^{\frac{\pi}{2}} \frac{d\theta}{\sqrt{1 - k^2 \sin^2\theta}} = \int_0^{\frac{\pi}{2}} \left(1 + \frac{k^2 \sin^2\theta}{2} + \frac{3k^4 \sin^4\theta}{2.4}\right.$$

$$\left. + \frac{1.3.5k^6 \sin^6\theta}{2.4.6} + \ldots\right) d\theta = \frac{\pi}{2} \left\{1 + \left(\frac{1}{2}\right)^2 k^2\right.$$

$$\left. + \left(\frac{1.3}{2.4}\right)^2 k^4 + \left(\frac{1.3.5}{2.4.6}\right)^2 k^6 + \ldots\right\},$$

which converges if $k^2 < 1$.

Therefore:

$$\frac{K\left(\dfrac{4a^2}{x^2 + 4a^2}\right)^{\frac{1}{2}}}{\sqrt{x^2 + 4a^2}} = \pi/2 \left(\frac{1}{\sqrt{x^2 + 4a^2}} + \left(\frac{1}{2}\right)^2 \frac{4a^2}{(x^2 + 4a^2)^{\frac{3}{2}}}\right.$$

$$\left. + \left(\frac{1.3}{2.4}\right)^2 \frac{4a^2}{(x^2 + 4a^2)^{\frac{5}{2}}} + \ldots\right).$$

Integrating term by term with respect to x;

$$V = 4aq \int_0^x \frac{K\left(\dfrac{4a^2}{x^2 + 4a^2}\right)^{\frac{1}{2}}}{\sqrt{x^2 + 4a^2}} \, dx = 2\pi aq \left[\ln \frac{(x + \sqrt{x^2 + 4a^2})}{2a}\right.$$

$$+ \left(\frac{1}{2}\right)^2 \frac{x}{\sqrt{x^2 + 4a^2}} + \left(\frac{1.3}{2.4}\right)^2 \left(\frac{x}{\sqrt{x^2 + 4a^2}} - \frac{x^3}{3(x^2 + 4a^2)^{\frac{3}{2}}}\right)$$

$$\left. + \left(\frac{1.3.5}{2.4.6}\right)^2 \left(\frac{x}{\sqrt{x^2 + 4a^2}} - \frac{2x^3}{3(x^2 + 4a^2)^{\frac{3}{2}}} + \frac{x^5}{5(x^2 + 4a^2)^{\frac{5}{2}}}\right) + \ldots\ldots\right]$$

(Integrals of the form $\displaystyle\int \frac{dx}{(x^2 + a^2)^{\frac{2n+1}{2}}}$ are obtained by the substitution

$$x = a \tan \theta)$$

Convergence

By Stirling's formula: $\displaystyle\frac{1.3.5 \ldots\ldots (2n-1)}{2.4.6 \ldots\ldots\ldots (2n)} = \frac{(2n)!}{(2^n n!)^2}$

$$\simeq \frac{\sqrt{4n\pi}\left(\dfrac{2n}{e}\right)^{2n}}{2n\pi\ 2^{2n}\left(\dfrac{n}{e}\right)^{2n}} \quad \frac{1}{\sqrt{n\pi}} \ .$$

Hence the term:

$$\frac{1.3.5\ldots\ldots(2n-1)}{2.4.6\ldots\ldots(2n)} \text{ approaches zero as } \frac{1}{\sqrt{n}} \text{ as } n \to \infty\ .$$

Thus in the series for V, if all the coefficients of $\dfrac{x}{\sqrt{x^2 + 4a^2}}$, $\dfrac{x}{(x^2 + 4a^2)^{\frac{3}{2}}}$

etc. are grouped, the resulting coefficients will be series of the form: $A \displaystyle\sum_n \frac{1}{n}$, which diverges.

However, if the series is left grouped as above, it is dominated by the limiting value as $x \to \infty$ since each term is positive and increases as x increases* which is:

$$\sum_n \left(\frac{1.3.5\ldots\ldots(2n+1)}{2.4.6\ldots\ldots(2n+2)}\right)^2 \left(1 - \frac{n}{3} + \frac{\dfrac{n(n-1)}{2!}}{5} - \ldots + \ldots + \frac{(-1)^n}{(2n+1)}\right).$$

But:

$$1 - \frac{n}{3} + \frac{\dfrac{n(n-1)}{2!}}{5} - \ldots + \ldots\ldots + \frac{(-1)^n}{(2n+1)} = \frac{2.4.6\ldots\ldots(2n)}{1.3.5\ldots\ldots(2n+1)} \quad **.$$

Thus each term in the dominating series is of the form:

$$\frac{1.3.5\ldots\ldots(2n+1)}{2.4.6\ldots\ldots(2n+2)} \cdot \frac{1}{(2n+2)} \simeq \sqrt{\frac{1}{(n+1)\pi}} \cdot \frac{1}{(2n+2)} = \frac{1}{(n+1)^{\frac{3}{2}} 2\sqrt{\pi}}.$$

Thus the series converges for all values of $x > 0$.

* *The derivative of this series is:*

$$\left(\frac{1}{2}\right)^2 \frac{4a^2}{(x^2 + 4a^2)^{\frac{3}{2}}} + \left(\frac{1.3}{2.4}\right)^2 \frac{(4a^2)^2}{(x^2 + 4a^2)^{\frac{5}{2}}} + \ldots\ldots$$

which is always positive.

** *Readily proved by expanding:*

$$\frac{2.4.6\ldots\ldots\ldots\ldots\ldots\ldots(2n)}{(1+x)(3+x)\ldots\ldots\ldots(2n+1+x)} \text{ in the form } \frac{a}{1+x} + \frac{b}{3+x} + \ldots + \frac{r}{2n+1+x}$$

and putting x = 0.

Alternatively, the matrix:

$$\begin{bmatrix} 1 & 0 & 0 & 0 & 0 & . & . \\ -1 & 2 & 0 & 0 & 0 & . & . \\ 0 & -2 & 3 & 0 & 0 & . & . \\ 0 & 0 & -3 & 4 & 0 & . & . \\ 0 & 0 & 0 & -4 & 5 & . & . \\ . & . & . & . & . & . & . \\ . & . & . & . & . & . & . \end{bmatrix}$$

may be used to speed convergence.

If $u_1 + u_2 + u_3 + \ldots + u_n + \ldots$ is a converging series in which $u_1 \ u_2 \ u_3 \ldots u_{n-1} > u_n > 0$, and $S_1, S_2, S_3 \ldots S_n \ldots$ is a sequence such that

$$S_n = u_1 + u_2 + \ldots + u_n,$$

and the S_n sequence is arranged as a column vector and premultiplied by the above matrix, the product will be a column vector, the terms of which form a sequence $R_1, R_2, R_3 \ldots \ldots R_n \ldots$, i.e.:

$$\begin{bmatrix} 1 & 0 & 0 & 0 & 0 & . & . \\ -1 & 2 & 0 & 0 & 0 & . & . \\ 0 & -2 & 3 & 0 & 0 & . & . \\ 0 & 0 & -3 & 4 & 0 & . & . \\ 0 & 0 & 0 & -4 & 5 & . & . \\ . & . & . & . & . & . & . \\ . & . & . & . & . & . & . \end{bmatrix} \begin{bmatrix} S_1 \\ S_2 \\ S_3 \\ S_4 \\ S_5 \\ . \\ . \end{bmatrix} = \begin{bmatrix} R_1 \\ R_2 \\ R_3 \\ R_4 \\ R_5 \\ . \\ . \end{bmatrix}$$

where

$$\begin{aligned} R_n &= nS_n - (n-1)S_{n-1} \\ &= S_n + (n-1)(S_n - S_{n-1}) \\ &= S_n + (n-1)u_n. \end{aligned}$$

But since $u_1 + u_2 + u_3 \ldots$ is a converging series of positive terms, $(n-1)u_n \to 0$ as $n \to \infty$.

Thus R_n approaches the same limit as does S_n as $n \to \infty$.

In some cases, as for example the above series for V, R_n converges more rapidly than S_n, and so the transformation is of considerable value in summing the series.

For small values of x, i.e. values of $x < 2a$, a different approximation for V is of value, as the convergence of the above series is extremely slow.

$$V = 4aq \int_0^{\frac{r}{2}} \frac{K\left(\frac{4a^2}{x^2 + 4a^2}\right)^{\frac{1}{2}}}{\sqrt{x^2 + 4a^2}} \, dx$$

$$\sqrt{\frac{4a^2}{x^2 + 4a^2}} \text{ , therefore: } k' = \sqrt{\frac{}{x^2 + 4a^2}}$$

From *Tables of Functions* (Jahnke and Emde) we have:

$$K(k) = L + \frac{L-1}{4} k'^2 + \frac{9}{64}\left(L - \frac{7}{6}\right)k'^4 + \cdots$$

where

$$L = \ln\frac{4}{k'} = \ln\frac{4\sqrt{x^2 + 4a^2}}{x}$$

Assume $x \ll 2a$, so neglect all terms in k'^n where $n > 3$. Approximate signs will not be used.

$$\frac{K}{\sqrt{x^2 + 4a^2}} = \frac{K}{2a}\left(1 - \frac{x^2}{8a^2}\right)$$

$$K = L\left(1 + \frac{k'^2}{4}\right) - \frac{1}{4}k'^2 .$$

Therefore:

$$\frac{K}{\sqrt{x^2 + 4a^2}} = \frac{1}{2a}\left[\ln\frac{4\sqrt{x^2+4a^2}}{x}\left\{1 + \frac{x^2}{4(x^2+4a^2)}\right\}\cdot\left\{1 - \frac{x^2}{8a^2}\right\} - \right.$$

$$\left. 4\ x^2 + 4a^2 \qquad - \frac{x^2}{8a^2}\right\}\right]$$

$$= \frac{1}{2a}\left\{\ln 8a\left(1 - \frac{x^2}{16a^2}\right) + \frac{x^2}{8a^2} - \ln x\left(1 - \frac{x^2}{16a^2}\right) - \frac{x^2}{16a^2}\right\} .$$

and thus:

$$V = 4aq\int_0^x \frac{K}{\sqrt{x^2 + 4a^2}}\,dx = 2q\left\{\left(\ln\frac{8a}{x}\right)\left(x - \frac{x^3}{48a^2}\right) + x + \frac{1}{72}\frac{x^3}{a^2}\right\} .$$

APPENDIX B

Diffusion of Material from under the Electrodes to the Walls

Assumptions:

1. That the situation between two electrodes when there are only two differs slightly from the situation with an infinite number of evenly spaced electrodes.

2. That the density of material just inside the walls under the electrodes is constant. This is at best a rough approximation, particularly towards the edges of the electrodes. However, at any appreciable distance from the electrodes the error should be slight.

3. The density of material just inside the walls outside the electrode regions is zero. This should be true if there is no appreciable sputtering except under the electrodes.

Choose as origin the center of an electrode region.

Choose unit length so that the distance center to center between electrodes = 2π, as shown in Fig. 16.
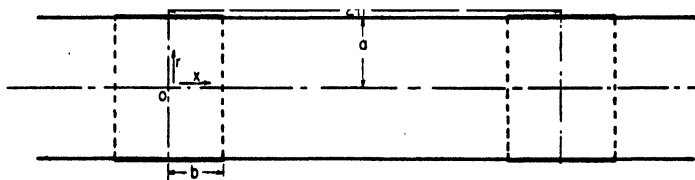
FIG. 16

In these units:

$$\text{Radius} = a$$

$$\text{Electrode length} = 2b$$

Laplace's equation in cylindrical co-ordinates:

$$\frac{\partial^2 D}{\partial x^2} + \frac{1}{r}\frac{\partial D}{\partial r} + \frac{\partial^2 D}{\partial r^2} = 0,$$

where D is the density of material at any point.

Then: for $-\pi < x < \pi$ the boundary conditions are:

$$D = C \quad |x| < b \qquad \text{(Assumption 2)}$$

$$D = 0 \quad |x| > b \qquad \text{(Assumption 3)}$$

D is periodic in x, with a period of 2π (Assumption 1).

To solve:

$$\frac{\partial^2 D}{\partial x^2} + \frac{1}{r}\frac{\partial D}{\partial r} + \frac{\partial^2 D}{\partial r^2} = 0$$

set

$$D = X(x) R(r).$$

Thus:

$$R\frac{d^2 X}{dx^2} + \frac{X}{r}\frac{dR}{dr} + X\frac{d^2 R}{dr^2} = 0$$

or:

$$\frac{1}{X}\frac{d^2 X}{dx^2} + \frac{1}{rR}\frac{dR}{dr} + \frac{1}{R}\frac{d^2 R}{dr^2} = 0.$$

Therefore:

$$\frac{d^2 R}{dr^2} + \frac{1}{r}\frac{dR}{dr} - n^2 R = 0 \quad (n \text{ arbitrary})$$

and:

$$\frac{d^2 X}{dx^2} + n^2 X = 0.$$

(1) $$\frac{d^2 X}{dx^2} + n^2 X = 0.$$

Therefore:

$$X = A_n \cos nx + B_n \sin nx \qquad n \neq 0$$

$$X = A_0 + B_0 x \qquad n = 0$$

Because of the choice of co-ordinates, and Assumption 1, X must be an even function.

Therefore:

$$B_0 = B_n = 0$$

and:

$$X = A_n \cos nx.$$

(2)
$$\frac{d^2 R}{dr^2} + \frac{1}{r} \frac{dR}{dr} - n^2 R = 0.$$

Solution for $n \neq 0$:

$$R = E_n I_0(nr) + F_n K_0(inr) \quad (E_n, \; F_n \text{ const.})$$

where:

I_0 is a modified Bessel's function of the first kind.

K_0 is a Bessel's function of the second kind.

Solution for $n = 0$:

$$R = F_0 \ln(r) + E_0.$$

However R does not become infinite as $r \to 0$, therefore:

$$F_n = F_0 = 0$$

and:

$$R = E_n I_0(nr) \qquad n \neq 0$$

$$R = E_0 \qquad n = 0$$

Therefore the desired solution to Laplace's equation is:

$$D = A_0 E_0 + \sum_{n=1}^{\infty} A_n E_n I_0(nr) \cos(nx).$$

At the wall:

$$D|_{r=a} = A_0 E_0 + \sum_{n=1}^{\infty} A_n E_n I_0(na) \cos(nx).$$

$$= C \quad |x| < b$$

$$= 0 \quad |x| > b$$

Thus for this series:

$$A_0 E_0 \qquad \frac{1}{2\pi} \int_{-b}^{b} C dx = \frac{bC}{\pi},$$

and:

$$A_n E_n I_o(na) = \frac{1}{\pi} \int_{-b}^{b} C \cos(nx)\, dx = \frac{2C}{\pi} \frac{\sin(nb)}{n}$$

or

$$A_n E_n = \frac{2C}{\pi} \frac{\sin(nb)}{n\, I_o(na)} .$$

Therefore:

$$D = \frac{bC}{\pi} + \frac{2C}{\pi} \sum_{n=1}^{n=\infty} \frac{\sin(nb)}{nI_o(na)}\, I_o(nr) \cos(nx).$$

The amount of material going to the walls and being deposited is proportional to: $\left.\dfrac{\partial D}{\partial r}\right|_{r=a}$.

Hence the amount deposited in any finite region between $x = x_1$ and $x = x$ is proportional to:

$$\int_{x_1}^{x} \frac{\partial D}{\partial r}\, dx = \frac{2C}{\pi} \sum_{n=1}^{n=\infty} \frac{\sin(nb)\,\sin(nx)}{nI_o(na)}\, I_1(na) + \text{const. (if } x_1 \text{ and } x > b).$$

(This device is employed to avoid having to deal with a series without the factor of convergence $1/n$.)

$$\lim_{n\to\infty} \frac{I_1(na)}{I_0(na)} = 1.$$

Now:

$$\frac{\sin(nb)\,\sin(nx)}{n} = \frac{\cos n(x - b)}{n} - \frac{\cos n(x + b)}{n}$$

and

$$\sum_{n=1}^{n=\infty} \frac{\cos(ny)}{n} = -\ln(2 \sin y/2)^*.$$

Differentiating, we get:

$$\frac{\partial D}{\partial r} \quad \frac{2C}{\pi}\left[\sum_{n=1}^{\infty} \left\{ 1 - \frac{I_1(na)}{I_o(na)} \sin(nb) \cos(nx) \right. \right.$$

$$\left. \left. + \cot \frac{(x - b)}{2} - \cot \frac{(x + b)}{2} \right] \right.$$

The convergence is supplied by the fact that:

$$\left. 1 - \frac{I_1(na)}{I_o(na)} \right\} \to 0 \text{ as } n \to \infty$$

as about $\dfrac{1}{2n}$, and the factor $\sin(nb) \cos(nx)$ alternates in groups of terms, the sum of the terms in each group being nearly equal. The number of terms in each group depends on x.

* Carslaw—Fourier's Series and Integrals, 3rd ed., p. 241. MacMillan and Co. 1930.

The Cesàro triangular matrix:

$$
\begin{array}{llll}
1 & & & \\
1/2 & 1/2 & & \\
1/3 & 1/3 & 1/3 & \\
1/4 & 1/4 & 1/4 & 1/4
\end{array}
$$

was used to obtain a more rapidly converging series.

A METHOD FOR THE DETERMINATION OF THE INDEX OF REFRACTION OF THIN TRANSPARENT FILMS[1]

BY R. W. STEWART[2]

Abstract

The index of refraction of thin films deposited on an optical flat is obtained by comparison of the fringe system set up in the film with that in the air gap between the film and another optical flat. The use of the method is illustrated by application to films produced in high frequency discharge tubes. Films produced in Pyrex glass and quartz tubes are shown to be silica in the form of cristobalite. Films produced in polystyrene tubes prove to have an index of refraction that is very low and is a function of the thickness.

Introduction

During the progress of an investigation of the effect of high frequency discharges on tube walls, reported elsewhere in this journal (2), a thin deposit of transparent material was obtained after a run of an hour or more. This deposit, which shows typical thin film interference fringes, formed both on the tube walls outside the electrode region and on thin strips of glass placed within the tube and under the electrode. It proved to be both mechanically hard and chemically inert. Films deposited on top of metallic coatings resisted concentrated nitric acid and strong bases, although prolonged immersion resulted in the dissolving of the underlying metal so that the material could then be rubbed off. The deposit itself, however, could be rubbed vigorously without damage.

Since the total quantity of material in these films was very small (2×10^{-5} cc. spread over 2 cm.^{2} would be a large deposit) and the maximum thickness observed was about 3×10^{-4} cm., analysis by ordinary methods would be very difficult, particularly in view of the chemical inertness of the films. It was thus thought advisable to get some indication of the nature of this deposit by determining its index of refraction by a method suggested by the recent work of Tolansky (6) on the optical determination of the irregularities of crystal surfaces. A p eliminary note regarding the method has been published (3).

In addition to the films obtained in Pyrex glass tubes, deposits were obtained in tubes made of polystyrene. For this plastic the index was found to vary with thickness. Most methods of determining the index of refraction of small samples of transparent materials are based on the fact that when two trans-

parent media are in contact the boundary surface will reflect light unless the indices are identical. The index found is thus essentially a surface one and is valid only for homogeneous materials. The method described in this paper has the peculiar characteristic of measuring the index of *whatever is changing in thickness*, and is thus particularly useful in cases where the index is a function of the thickness.

Apparatus and Procedure

An optically plane glass plate of dimensions about 15 by 20 by 5 mm. was covered by evaporation with a mirrorlike metallic coat whose coefficient of reflection was about 0.6. The plate was then placed in a discharge tube so that one end protruded about 3 mm. outside the region surrounded by one of two external electrodes. The tube was then operated for about 10 hr., so that a considerable deposit was laid down on top of the metal. Fig. 1, Plate I, photographed by reflected sodium light, shows the resulting pattern. Another similar semitransparent metallic coat was then formed by evaporation on top of the deposit, and also on top of a second optical flat of the same dimensions as the first. The two plates were placed with their coated faces together in a device designated herein as an *indicometer*, which could be accurately adjusted until the plates were less than 0.1 mm. apart, and sufficiently parallel to give observable interference fringes in the air gap. Adjustment was fine enough that the number and direction of the fringes could be controlled to give any desired set of conditions.

If the indicometer was then viewed in reflected or transmitted monochromatic light, two sets of superimposed multiple reflection fringes were visible, one in the deposit and the other in the air gap. In Fig. 2, Plate I, an enlarged photograph taken in transmitted sodium light, the points A and B are on the same fringe in each set. Thus they are points at which both the thickness of the air gap and of the film, and therefore the distances between the two glass surfaces, are equal. Since both the glass surfaces are optically plane, the distance between them is constant along the line AB, and is also constant along any line parallel to AB.

If the number of fringes due to reflection within the medium showing the original interference pattern is a in any line segment parallel to AB, and the number due to reflection in the air gap is b in the same line segment, the index of refraction of the medium is a/b, since along the line segment the change in thickness of the air gap is entirely due to the change in thickness of the film. This method is independent of any sudden phase changes at the boundary, as this change would cause only a fringe shift, not a change in the *number* of fringes between two points. Similarly it is independent of the thickness of the metal mirrors or of any other uniform layer, as long as this thickness is uniform.

The indicometer is shown in Fig. 3. The screws on the sides clamp the glass plates in place, while the plate, *A*, is held to the frame only by the three screws in the face. By adjusting these screws, which have a very fine pitch,
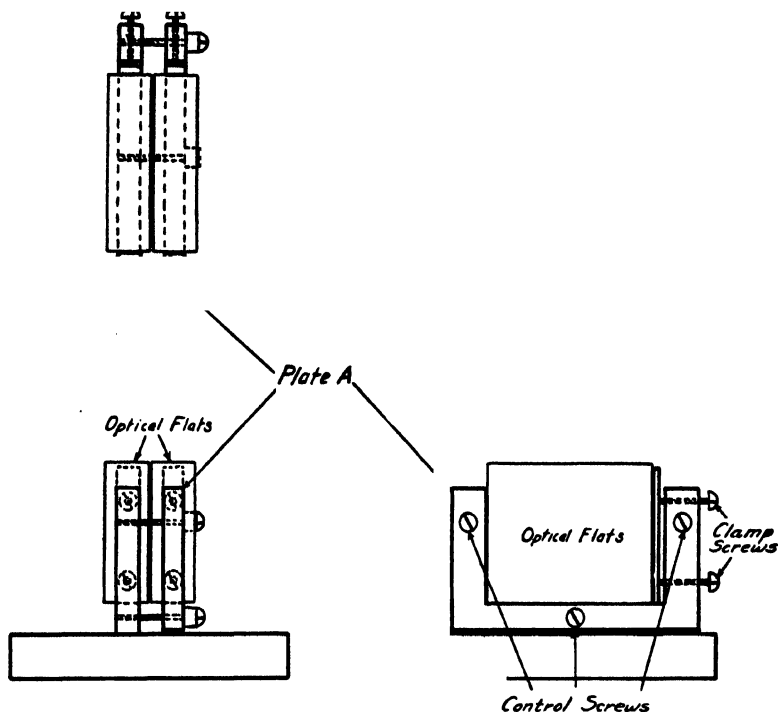
FIG. 3. *Diagrams showing the mechanical arrangement for mounting and adjusting the optical flats in the indicometer.*

any desired alignment can be attained. The number of fringes in the surface can be controlled within one, and the direction within a few degrees. In practice it was found advisable to have the two sets of fringes meet as nearly at right angles as possible.

Observations

Pyrex Glass and Quartz Tubes

Films were obtained in Pyrex glass tubes with the plate originally coated with half-mirror surfaces of silver, magnesium and aluminum. The gas was air at a pressure of about 1 mm. of mercury.

The indices observed, for sodium light, were:

On silver	1.489 ± 0.012
On magnesium	1.488 ± 0.008
On aluminum	$1.484 \pm 0.006.$

The estimates of precision were computed by Goodwin's method (1).

PLATE I
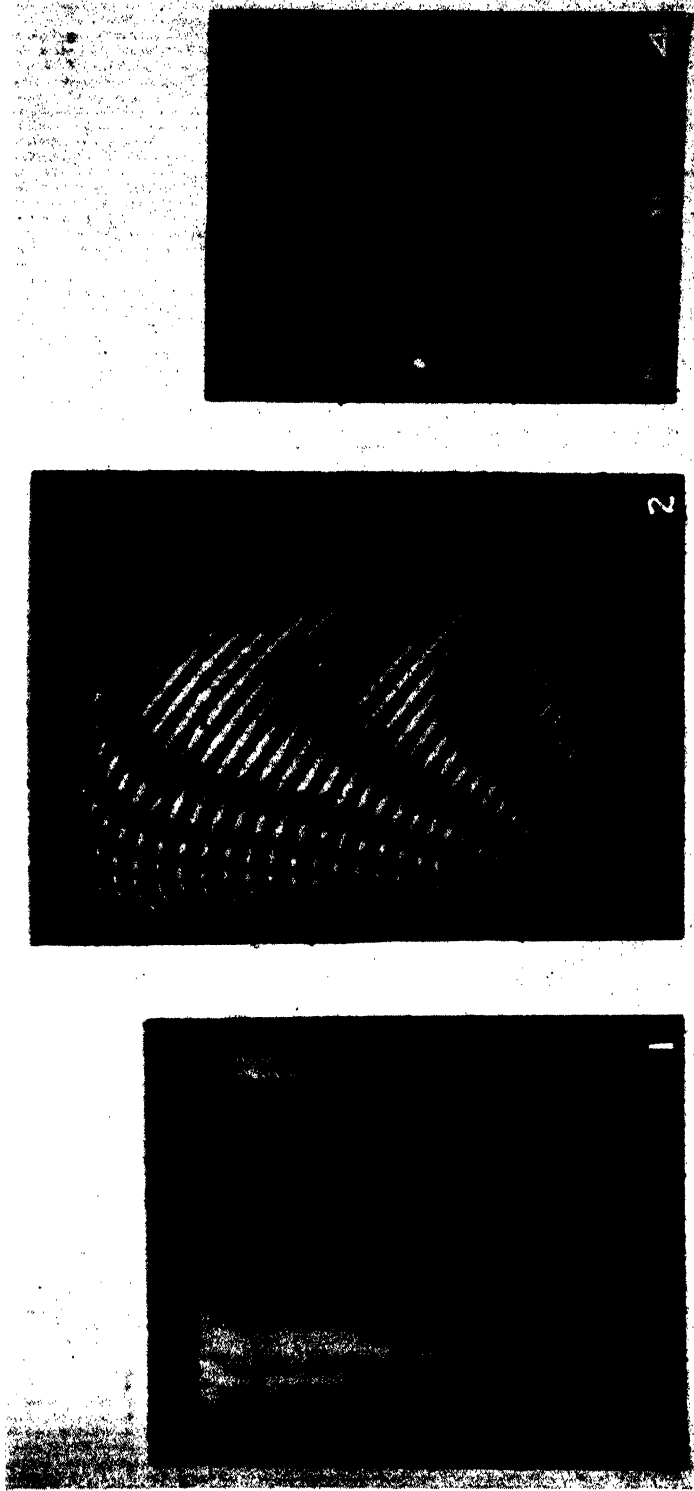
FIG. 1. *Interference pattern observed, by reflected sodium light, on an optical flat originally placed near an electrode inside a tube carrying a high frequency discharge.* FIG. 2. *Photograph by transmitted sodium light showing two sets of fringes: (a) due to the original deposit on an optical flat; (b) due to multiple reflections in the narrow air gap between this flat and a second silvered flat nearly parallel.* FIG. 4. *Photograph of an interference pattern obtained by an air discharge in a polystyrene tube.*

A typical set of values, taken for a film deposited on magnesium, is as follows:

a	b	Index $= a/b$	Deviation from mean
4.0	2.65	1.51	0.023
3.5	2.2	1.59	0.103
3.5	2.4	1.46	0.027
3.0	2.05	1.46	0.027
3.0	2.0	1.50	0.013
3.0	2.15	1.40	0.087
3.0	2.1	1.43	0.057
3.0.	2.0	1.50	0.013
2.0	1.35	1.48	0.007
3.0	1.95	1.54	0.053
		Mean: 1.487	Mean dev.: 0.041

Therefore, reliability of mean: $\dfrac{0.041}{\sqrt{10}} = 0.013$

Index of refraction: 1.487 ± 0.013.

A series of three such groups of 10 readings was taken in each case, each group from a different photograph with the fringes at a different angle. These three figures were then averaged to give the final recorded value.

The index was also measured for a film obtained by running a discharge in a quartz tube, the value being 1.487 ± 0.006.

Polystyrene Tubes

With the deposit obtained in the polystyrene tube, such as is shown in Fig. 4, the index appeared to be abnormally low and a function of the thickness. A deposit of this type was left to stand for some four months, and the index again measured. Although the number of fringes due to reflection in the deposit was nearly the same before and after this period, the deposit shrank appreciably in volume, so that the index, while still a function of the thickness, was considerably greater than before shrinkage. The graph in Fig. 5 shows the index plotted as a function of the thickness before shrinkage.

A deposit was also obtained in a tube made from the new plastic 'Textolite'.* In this case the index was also found to be very low (of the order of 1.37), but it has not yet been determined with sufficient accuracy to prove whether or not it is a function of thickness.

* *Trade name of a plastic manufactured by the General Electric Company, Plastics Division, Pittsfield, Mass.*
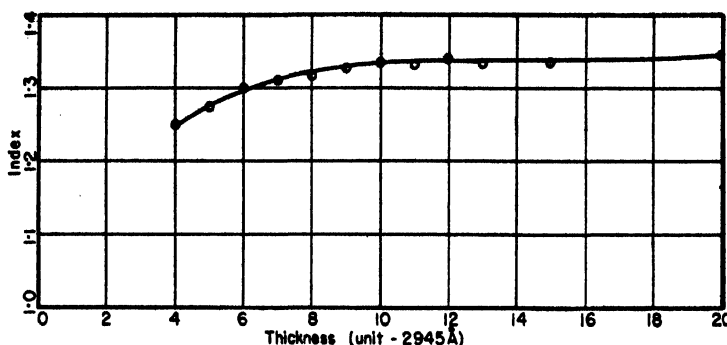
FIG. 5. *Graph showing the variation of the index of refraction with thickness for a deposit formed in a polystyrene tube.*

Conclusions

The indices of refraction of deposits obtained in Pyrex glass and quartz tubes are identical, within experimental error, averaging about 1.487 for sodium light. This fact, coupled with its transparency and chemical inertness, strongly indicates that the deposit is silica in some form.

The *Handbook of Chemistry and Physics* gives the following forms of silica with the corresponding indices of refraction.

Cristobalite	1.487, 1.484
Lechatelierite	1.46
Quartz	1.544, 1.553
Tridymite	1.469, 1.470, 1.471
Amorphous, opal	1.41 – 1.46

The only index that falls within the limits of experimental error is that of cristobalite, which is almost exactly equal to the average value found in these experiments. It is not to be expected that the slight degree of anisotropism would be observable. Cristobalite is the form taken by silica crystallized at high temperatures. Sosman (4, p. 110) states that silica depositing from the gaseous state must be either micro-amorphous or cristobalite. The evidence is therefore strong that these deposits are silica in the form of cristobalite.

No such definite conclusion can be drawn as to the nature of the deposit formed in the polystyrene tube. That a new transparent organic solid could be created in the discharge is not probable, and we are forced to consider the deposit as basically polystyrene. Since, on the whole, hydrocarbons become more and more volatile as their molecules become less and less complex, the fact that this deposit withstood the high vacuum of the evaporating apparatus indicates that its molecules must be quite large.

Massive polystyrene, however, has an index of refraction of about 1.60, whereas, even after standing for four months, the maximum index of the deposit did not exceed 1.45. The shape of the curve in Fig. 5 indicates a sort of packing down process. It is explained most easily by considering the top layer of the deposit to be more open in structure, with index about 1.25, the

deposit becoming more compact with additional deposition until the index reaches about 1.35. With the passage of time the molecules gradually rearrange themselves into a more compact mass, so that the index increases. (Note that the indicometer does not measure average index. As has been pointed out above, the index that is measured is that of the material which varies in thickness. If, as is logical, the surface layer in the polystyrene deposit is uniform, the index that was measured is that of the *bottom* of the deposit.)

To get a tentative explanation of the very low index found, lower than that of any organic compound of which the writer has knowledge, it is necessary to examine the nature of the polystyrene polymer itself. The polystyrene molecules are very long and thin, and ordinarily these molecules are aligned. According to Staudinger (5) this alignment exists even in the amorphous state. Now if the individual polystyrene molecules, instead of being crystallized out of a solution, were thrown down at random like a handful of sticks, there would be a large number of open spaces in the material, and the index would be expected to be low. This hypothesis also makes probable the packing down action, suggested above.

On the basis of this hypothesis, the amount of open space in the deposit would be:

$$\frac{1.60 - 1.25}{1.60 - 1.00} = 58\% \text{ at the top,}$$

$$\frac{1.60 - 1.35}{1.60 - 1.00} = 42\% \text{ at the bottom before shrinkage, and}$$

$$\frac{1.60 - 1.45}{1.60 - 1.00} = 25\% \text{ at the bottom after shrinkage.}$$

These figures neither help, nor detract from, the hypothesis.

Acknowledgments

References

1. GOODWIN, H. M. Elements of the precision of measurements. Geo. H. Ellis Co., Boston. 1905.
2. LODGE, J. I. and STEWART, R. W. Can. J. Research, A., 26 : 205. 1948.
3. ROBERTSON, J. K., STEWART, R. W., and LODGE, J. I. Nature, 158 : 703. 1946.
4. SOSMAN, R. B. The properties of silica. Chemical Catalogue Company, Inc., New York. 1927.
5. STAUDINGER, H. Ber. 62 : 2893. 1929.
6. TOLANSKY, S. Proc. Roy. Soc. London, A, 184 : 41. 1945.

A COMPARISON OF THE X-RAY DIFFRACTION AND NITROGEN ADSORPTION SURFACE AREAS OF CARBON BLACKS AND CHARCOALS[1]

By J. C. Arnell and W. M. Barss

Abstract

The surface areas, as determined from X-ray diffraction and low temperature nitrogen adsorption data, were compared for a number of carbon blacks and activated charcoals. Comparative data were also obtained on samples of charcoal at various stages of activation and after calcination. The X-ray diffraction data indicated that all the samples examined were composed of small graphitelike crystallites of the same order of magnitude, which had specific surfaces of about 2500 to 3000 sq. m. per cc. The nitrogen adsorption surface of a highly activated charcoal was found to be about equal to the X-ray surface. It is suggested that the crystallite surface represents the potential adsorption surface of a carbonaceous material and, providing that crystal growth does not occur during activation, the activation process makes these surfaces available to external adsorbate.

Introduction

The determination of the surface areas of activated charcoals and carbon blacks from nitrogen adsorption isotherms measured at the temperature of liquid air has been well tested (4; 5, pp. 1–36). A method of determining the ultimate particle (crystallite) size, and consequently the maximum surface area, of the same materials from X-ray powder photographs has been developed by Warren (8), based on the original formula of Scherrer (7). There have been, however, very few comparative measurements between the two methods.

During the recent war a few isolated results obtained in the United States indicated that the nitrogen adsorption surface of a highly activated charcoal was of the same order of magnitude as the surface calculated from X-ray diffraction data. More recently, Zettlemoyer and Walker (9) have found fairly good agreement between the two methods for active magnesia having a surface of 300 sq. m. per gm., but found that the nitrogen surface deviated below the X-ray surface in a regular manner as the surface decreased.

Considerable data are available for various types of carbonaceous materials ranging from carbon blacks (2) to coals and chars from various wood components (3, pp. 176–231; 6). These materials all appear to be made up of small graphitelike crystallites, characterized by a random layer lattice. In each crystallite the carbon atoms form two-dimensional plane hexagonal nets separated by essentially the same spacing as in graphite, but with random orientation about a normal to the layers. The carbon–carbon distances within

the nets and between layers are remarkably constant for the many different kinds of carbonaceous materials studied and the same is also generally true for the crystallite dimensions.

Comparative data are presented here for a number of carbon blacks and activated charcoals, both in their original states and after heat treatment.

Theoretical

As the individual crystallites of a substance become smaller than 1000 Å, the diffraction lines in its X-ray powder photograph progressively broaden. Scherrer proposed the following formula for calculating the average dimensions of simple cubic crystals (7):

$$L_c = \frac{0.94\lambda}{B \cos \theta},$$ (1)

where L_c = average crystallite dimensions, perpendicular to the particular set of diffracting planes in the lattice, in Ångström units,

λ = wave length of the X-radiation in Ångström units,

B = angular width of the line at half its maximum intensity in radians, and

θ = Bragg angle of the diffraction maximum in degrees.

B must be corrected for the instrument width, that is, the width of the half-maximum of the intensity curve for very large particles. This correction is usually applied in the following form:

$$B^2 = B'^2 - b'^2,$$ (2)

where B' = measured width of the half-maximum in radians, and

b' = correction for instrument width in radians.

Other formulae have been derived by other workers, but all are of the same form as Equation (1), except that the numerical constant has varied from 0.89 to 1.0.

In identifying the diffraction maxima from carbonaceous materials, it is customary to use the Miller indices for a hexagonal system, such as are used for graphite, even though only limited types of reflection are possible because of the random orientation of the parallel hexagonal nets in the nongraphitized materials. The unit cell parameter, a, is the separation of the adjacent carbon atoms in a net and the parameter, c, is twice the separation of the parallel nets. Thus, the (00.2) diffraction halo is a normal three-dimensional effect to which the ordinary Scherrer formula applies, although Warren (8) recommends 0.89 as the best value for the constant. On the other hand, the (10) halo arises from the diffraction of the X-ray beam by the two-dimensional arrays of atoms in the hexagonal nets and is displaced in the direction of

smaller Bragg angles from the position of the three-dimensional (10.0) diffrac-
tion line of graphite.   Warren has considered the case of such cross lattice lines
and has derived the following formula in which the constant of the Scherrer
equation becomes 1.84:

$$L_a = \frac{1.84\lambda}{B \cos \theta} \tag{3}$$

where L_a = average crystallite dimension across the plane of the hexagonal
          rings in Ångström units.

From the original Scherrer equation (with the constant equal to 0.89), the
average crystallite dimension normal to the carbon layers, L_c, can be deter-
mined.   From the θ value corresponding to the position of the (00.2) halo,
the distance between layers (i.e., $c/2$ = half the c axis of the unit cell) within
the crystallite can be calculated from the Bragg equation.

$$\lambda = 2d_{c/2} \sin \theta, \tag{4}$$

where $d_{c/2}$ = distance between layers within the crystallite.

The average crystallite dimension across the layers of carbon atoms, L_a,
can be obtained from Equation (3).   From the θ value corresponding to the
observed (10) halo may be subtracted a correction factor (8):

$$\triangle(\sin \theta) = 0.16\lambda/L_a, \tag{5}$$

which will give the θ value corresponding to the (10.0) line of graphite.
From this, in turn, the length of the a axis of the graphite unit cell can be
calculated.

If the graphitelike crystallites are assumed to be cylinders having a diameter
of L_a and a height of L_c, it is possible to calculate the specific surface of a
collection of such cylinders.   The specific surface is given by:

$$S_{v(\text{x-ray})} = \frac{2L_a + 4L_c}{L_aL_c} \times 10^4, \tag{6}$$

where $S_{v(\text{x-ray})}$ = specific surface of the assumed cylindrical crystallites in
            square meters per cubic centimeter.

The procedures for determining the areas by nitrogen adsorption have been
described many times recently (4; 5, pp. 1–36) and will not be repeated here.
Nitrogen isotherms were obtained on evacuated samples at liquid air tem-
peratures.   The areas of the carbon blacks were calculated from BET plots
(4, p. 153), while those of the charcoal samples were calculated from Langmuir
plots (4, p. 71) as the isotherms showed no indications of multilayer formation.
The surface area values were converted from area per unit weight to area per
unit volume, by multiplying by the density as determined by X-ray diffraction.

Results

The specific surfaces of a number of carbon blacks had been previously
measured by three different methods (1): low temperature nitrogen adsorption,
gas permeability measurements, and electron microscopy, and this study was

extended to include X-ray measurements. The new data are presented in Table I, along with the nitrogen surfaces.

TABLE I

SPECIFIC SURFACES OF CARBON BLACKS

Carbon black	Spacings		Dimensions		Specific surface	
	$c/2$, Å	a_0, Å	L_c, Å	L_a, Å	X-ray, sq.m./cc.	Nitrogen, sq.m./cc.
Thermax	3.54	2.43	16.2	42.5	2350	14
Kosmos 20	3.53	2.40	15.0	37	2410	46
Kosmos 40	3.57	2.41	15.0	32	2580	80
Statex B	3.55	2.41	14.8	32.0	2600	93
Shawinigan	3.47	2.43	22.2	54.8	1630	94
Statex A	3.57	2.43	14.8	35.8	2470	145
Kosmobile 77	3.54	2.45	13.7	30.5	2770	200
Spheron 9	3.56	2.40	14.5	32.5	2610	225
Dixiedensed HM	3.57	2.40	14.9	29.6	2700	250
Kosmobile S	3.54	2.43	14.3	33.4	2580	290
Voltex	3.66	2.43	12.4	37	2700	1150
Neo Spectra Mk. II	3.52	2.41	16.0	42	2200	1650

In order to investigate the effect of heating on the crystallite size, samples of the Neo Spectra Mk. II carbon black were studied after heating for various periods of time in an evacuated quartz tube. The results are listed in Table II.

TABLE II

SPECIFIC SURFACES OF NEO SPECTRA MK. II CARBON BLACK AFTER CALCINATION

Treatment	Spacings		Dimensions		Specific surface	
	$c/2$, Å	a_0, Å	L_c, Å	L_a, Å	X-ray, sq.m./cc.	Nitrogen, sq.m./cc.
None	3.52	2.41	16.0	42	2200	1650
3 hr. at 1200° C.	3.61	2.45	13.9	43.2	2370	1600
6 hr. at 1200° C.	3.65	2.44	14.3	49.1	2070	730
16 hr. at 1200° C.	3.68	2.41	—	-–	—	710

This study was extended to include a number of activated charcoals. A commercial coconut charcoal was examined after various periods of steam activation and then the final charcoal sample (after eight days' steaming) was heated for various periods of time in an evacuated quartz tube before study. The results are given in Table III, together with similar data on calcined samples of two zinc chloride activated wood charcoals.

TABLE III

SPECIFIC SURFACES OF ACTIVATED CHARCOALS AT VARIOUS STAGES OF ACTIVATION AND AFTER CALCINATION

Treatment	Spacings		Dimensions		Specific surface	
	$c/2$, Å	a_0, Å	L_c, Å	L_a, Å	X-ray, sq.m./cc.	Nitrogen, sq.m./cc.
Coconut shell charcoal (commercial samples)						
After 1 day's steaming	3.64	2.43	12.6	40.3	2580	1120
After 3 days' steaming	3.72	2.45	11.1	43.8	2720	1550
After 5 days' steaming	3.67	2.44	11.5	51.4	2520	1820
After 7 days' steaming	3.68	2.44	10.9	45.6	2700	2210
After 8 days' steaming	3.79	2.44	10.4	49.0	2740	2750
2 hr. at 1000° C.	3.70	2.44	10.5	47.3	2750	2830
2 hr. at 1200° C.	3.71	2.44	10.5	50.9	2690	2320
6 hr. at 1200° C.	3.78	2.44	10.2	47.2	2810	2250
ZnCl₂-activated maple flour charcoal (laboratory sample)						
None	3.74	2.45	10.7	26.8	3360	—
2 hr. at 1000° C.	3.70	2.43	10.8	27.2	3320	3150
2 hr. at 1200° C.	3.68	2.41	11.1	38.3	2870	3210
6 hr. at 1200° C.	3.78	2.45	9.9	48.9	2840	2950
ZnCl₂-activated wood charcoal (commercial sample)						
None	3.70	2.44	11.8	42.7	2630	2400
3 hr. at 1200° C.	3.63	2.39	11.8	42.8	2630	2600
6 hr. at 1200° C.	3.58	2.41	11.4	42.1	2700 ·	2500

Discussion

All of the samples listed above show the same general values for the spacings between the carbon atoms in adjacent planes ($c/2$) and in the hexagons (a_0) and are in agreement with previously reported values (2; 3, pp. 176–231).

The carbon blacks and the activated charcoals all have very similar crystallite dimensions and, in consequence, the specific surfaces calculated for the crystallites are all of the same order. As there is fairly good agreement between the specific surfaces of highly activated charcoals, determined by low temperature nitrogen adsorption and from X-ray diffraction (Table III), it seems probable that the potential adsorbing surface of an activated carbon is the external surface of the small graphitelike crystallites, which apparently form the basis of all carbonized materials.

The samples of coconut shell charcoal at various stages of activation (Table III) all show the same X-ray specific surface, while the nitrogen adsorption surface increases as the activation proceeds. It is therefore possible to visualize the activation process as one that opens up the charcoal structure by the

PLATE I
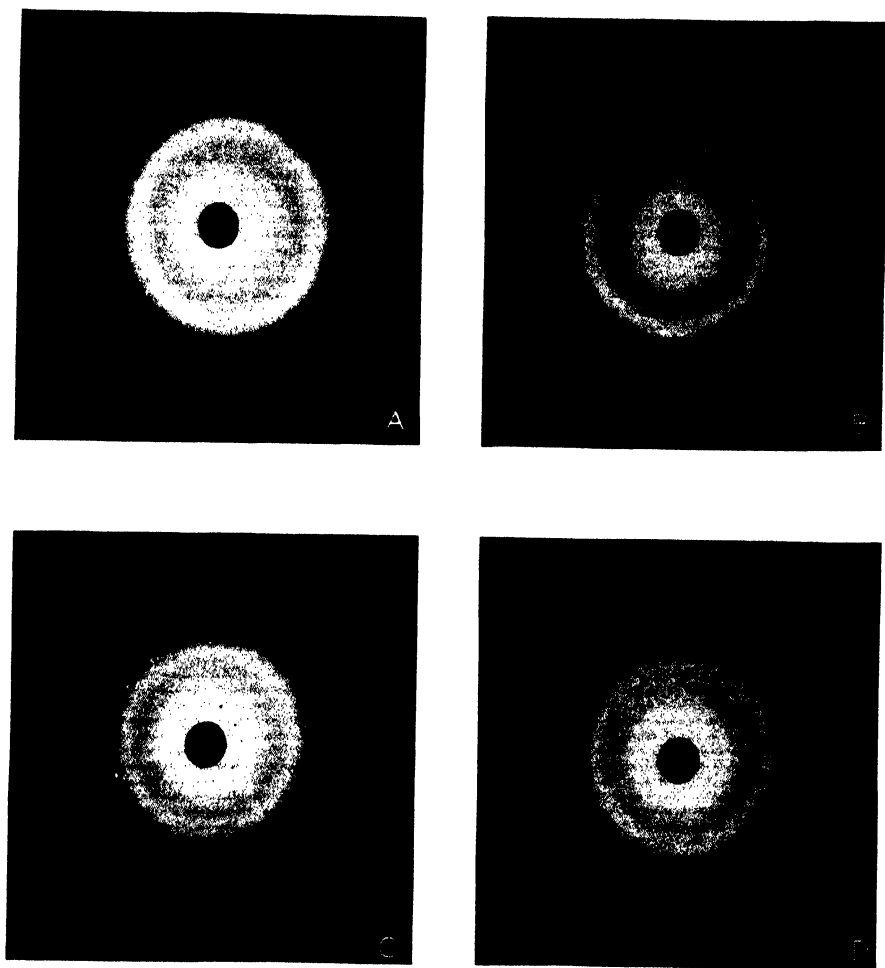
FIG. 1. *X-ray diffraction photographs of Neo Spectra Mk. II carbon black. A. Original sample. B. Heated for three hours at 1200° C. C. Heated for six hours at 1200° C. D. Heated for 16 hr. at 1200° C.*

removal of amorphous carbon from between the crystallites or by the separation of the crystallites due to thermal expansion during the heating process, followed by a subsequent contraction of the crystallites. Either process would allow the molecules of the adsorbate to reach the crystallite surfaces where adsorption takes place, without any necessity for change in the crystallite dimensions.

If this is the case, then it would appear that it should be possible to activate by heating with or without the use of a gas almost any material that consists essentially of carbon. Such activation, however, is not possible if the material tends to exhibit crystal growth under normal activating conditions. Biscoe and Warren (2) studied the effect of calcination on a sample of Spheron Grade 6 carbon black, and their results, which are reproduced in Table IV, show crystallite growth very clearly.

TABLE IV

EFFECT OF CALCINATION ON THE CRYSTALLITE DIMENSIONS OF SPHERON GRADE 6 CARBON BLACK

(After Biscoe and Warren (2))

Treatment	Spacings		Dimensions		Specific surface, sq.m./cc.
	$c/2$, Å	a_0, Å	L_c, Å	L_a, Å	
None	3.55	2.45	12.7	20.0	3570
2 hr. at 760° C.	3.52	2.42	14.4	22.6	3160
2 hr. at 1040° C.	3.47	2.46	14.9	28.0	2770
28 hr. at 1040° C.	3.55	2.43	14.9	29.8	2690
2 hr. at 1500° C.	3.48	2.44	24.9	44.2	1710
2 hr. at 2000° C.	3.46	2.44	32.3	55.8	1340
10 hr. at 2000° C.	3.47	2.43	35.5	60.5	1220
2 hr. at 2800° C.	3.45	2.46	40.0	65.2	1110

Neo Spectra Mk. II carbon black shows another example of crystal growth as a result of calcination. While the data in Table II show little change in the crystallite dimensions following the heating, which is more or less in line with the data in Table IV for the heating of Spheron Grade 6 carbon black at 1040° C., crystal growth does occur, however, as the nitrogen surfaces in Table II indicate, and is shown in the X-ray diffraction photographs of the four samples of Neo Spectra Mk. II carbon black, reproduced in Fig. 1. It can be seen in the photographs, that while little change occurs in the diffuse diffraction ring, discrete spots indicating macrocrystals are apparent in the photograph of the sample heated for six hours at 1200° C., and after 16 hr. heating at 1200° C., a sufficient number of macrocrystals have been formed to give the outlines of a new ring. The fact that this new ring is spotty, while the diffuse rings remain diffuse, suggests that crystal growth takes place at a relatively small number of 'centers' rather than throughout the aggregate.

On the other hand, the three activated charcoals show little change in either the crystallite dimensions or the nitrogen adsorption surface as a result of six hours' heating at 1200° C. The nitrogen adsorption surface of the coconut shell charcoal shows a slight decrease after calcination. This may or may not be significant.

Conclusions

From the broad X-ray diffraction bands obtained on a number of activated charcoal samples, the crystallite dimensions of the graphitelike ultimate particles of the structure could be estimated. The specific surfaces, calculated from the crystallite dimensions, showed good agreement with the low temperature nitrogen adsorption surface for highly activated charcoals.

It is suggested that these crystallites form the adsorption surface of an activated carbon, and the activation process, by the removal of some of the material, opens the structure sufficiently for the adsorbate to diffuse to the crystallite surfaces.

As all carbonized materials show crystallites of similar dimensions, all might be considered as capable of activation. However, many substances, such as carbon blacks, exhibit marked crystallite growth under normal activation conditions and, in consequence, the potential adsorption surface disappears while the structure is being opened to make it accessible.

Activated charcoals show little crystallite growth on calcination and it would appear that resistance to such growth is the first requirement of a carbonized material suitable for high temperature activation.

Acknowledgments

References

1. ARNELL, J. C. and HENNEBERRY, G. O. Can. J. Research, A, 26 : 29. 1948.
2. BISCOE, J. and WARREN, B. E. J. Applied Phys. 13 : 364. 1942.
3. BLAYDEN, H. E., GIBSON, J., and RILEY, H. L. The ultrafine structure of coals and cokes. The British Coal Utilization Research Association, London. 1944.
4. BRUNAUER, S. The adsorption of gases and vapors. Princeton Univ. Press, Princeton, N.J. 1943.
5. EMMETT, P. H. *In* Advances in colloid science. Vol. 1. *Edited by* E. O. Kraemer. Interscience Publishers, Inc., New York. 1942.
6. RILEY, H. L. Quarterly Revs. (Chem. Soc., London) 1 : 59. 1947.
7. SCHERRER, P. Nachr. Ges. Wiss. Göttingen, 96. 1918. *Abstracted in* Chem. Abstracts, 13 : 2624. 1919.
8. WARREN, B. E. Phys. Rev. 59 : 693. 1941.
9. ZETTLEMOYER, A. C. and WALKER, W. C. J. Phys. Coll. Chem. 51 : 763. 1947.

MEASUREMENT OF THE ENERGIES OF α-PARTICLES[1]

By T. E. Cranshaw[2] and J. A. Harvey[3]

Abstract

The energies of the α-particles from weak preparations of several new radio-active substances were measured in a grid ionization chamber filled with argon. The accurately·known energies of α-particles from several well known sources were used for calibration. The voltage pulses produced by electron collection from the tracks were amplified in a linear amplifier of high stability and con-verted into flat-topped pulses. An accurately known voltage was subtracted, and the small residual pulses were further amplified. The frequency distribution of pulse sizes was recorded on an electronic pulse analyzer.

The final values of the energies are as follows:

$_{92}U^{233}$, 4.823 ± 0.003; $_{89}Ac^{225}$, ·5.801 ± 0.010; $_{87}Fr^{221}$, 6.298 ± 0.010; $_{85}At^{217}$, 7.023 ± 0.010; $_{84}Po^{213}$, 8.336 ± 0.005; and $_{94}Pu^{239}$, 5.159 ± 0.005 Mev.

The ionization–energy curve in argon was found to be linear within experi-mental error for α-particles of energy 5 to 9 Mev. Extrapolation of this line determines an intercept of 85 kev. at zero ionization.

Introduction

This paper describes a rather powerful method of measuring the energies of α-particles from weak sources and its application to several new radio-active substances. Absolute measurements were derived with the aid of α-particles of accurately known energies. The principles involved are (1) that the total ionization produced in a gas by an α-particle is very nearly proportional to its initial energy, and (2) that the electron pulse from the ionization in an argon-filled grid chamber is nearly proportional to that ionization. The principal advantage over other methods of measuring the energies of α-particles is that a large surface area (several square centimeters) of source and a large solid angle for α-particle emission can be used. The method adopted here is therefore particularly suitable for long-lived elements, which have low specific activities.

The resolving powers of the various methods for measuring the energies of α-particles differ considerably. The highest resolution is obtained in the magnetic spectrograph, such as that used by Chang (3), where the width of the line at half-maximum was about 10 kev. On the other hand, only one α-particle in about 5000 reaches the detector, and the source is limited to a small area. Usually, some of this resolution is sacrificed for greater utilization of the source, and the width at half-maximum may then reach 30 kev. With the grid chamber used in the present work and a source of polonium 210, the width of the line at half-maximum was ultimately reduced to 50 kev. (1).

Ionization Chamber

The ionization chamber contained two plane parallel electrodes, 10 cm. square and 6 cm. apart, with a grid of parallel wires placed 1.4 cm. from the electron-collecting electrode. The wires in the grid were 0.10 mm. in diameter (No. 38 gauge) spaced 2 mm. apart. In another paper (1) it will be shown that this grid is adequate for shielding the electron-collecting electrode from the induced effect of the slowly moving, positive ion component of the ionization. A negative potential of 1200 v. was applied to the high tension electrode, which produced a field sufficient to collect all the electrons from the track of an α-particle. The potential of the grid was chosen so that it did not collect electrons (1). The chamber could be filled with argon (99.8% pure) to a pressure of 3 atm.

A small hinged platinum plate was attached to the negative electrode. The source of α-particles whose energy was to be measured was mounted on one side of the plate, and the two standard sources of α-particles chosen for comparison were mounted on the other side. By rotating the chamber the hinged plate could fall over and take up either of two positions close to the negative electrode. Thus the α-particles from the 'unknown' source and the standards could be analyzed alternately under identical conditions.

The source on each side of the hinged plate was covered with a simple collimator, which was a sheet of 1/32 in. aluminum drilled with 1/8 in. holes. Without the collimator the distribution of pulse sizes was not symmetrical about the maximum but had a tail on the low energy side. These small pulses may have been caused by α-particles that had lost an appreciable amount of energy in the source and those scattered backwards from the support with energy loss.

Electronic Equipment

The voltage pulses produced on the collector were amplified in a linear amplifier of high stability to a level of about 50 v. and converted into flat-topped pulses. An accurately known voltage was then subtracted, and the small residual pulses underwent further amplification. A distribution of frequency of occurrence against size was then obtained using a pulse analyzer ('kicksorter') (6).

(a) Linear Amplifier

In order to obtain a high signal-to-noise ratio the head amplifier was mounted directly on to the ionization chamber. This amplifier is shown in Fig. 1. It consists of a high-gain low noise triode that feeds through a cathode-follower, the cathode load of which is mounted inside the main amplifier and used as a stepped gain-control. The triode operates with feedback through the grid-anode capacity and this gives a stabilized gain of about 10 times.

The main amplifier, shown in Fig. 2, is made up of two similar stages; each a three-tube ring circuit with a gain of 200. The very large negative feedback round the ring ensures high gain-stability and accurately linear amplification.

The gain was found to be stable to 1 part in 1000 over several hours. The two stages are separated by an adjustable bandwidth control made up of a
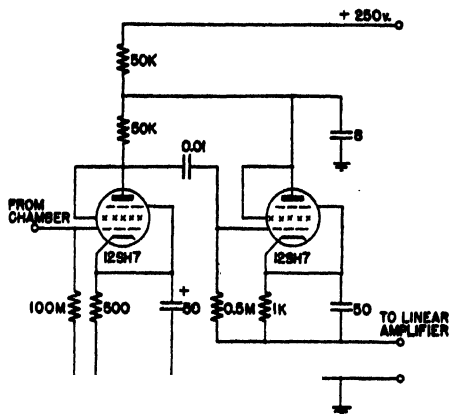
FIG. 1. Head amplifier.
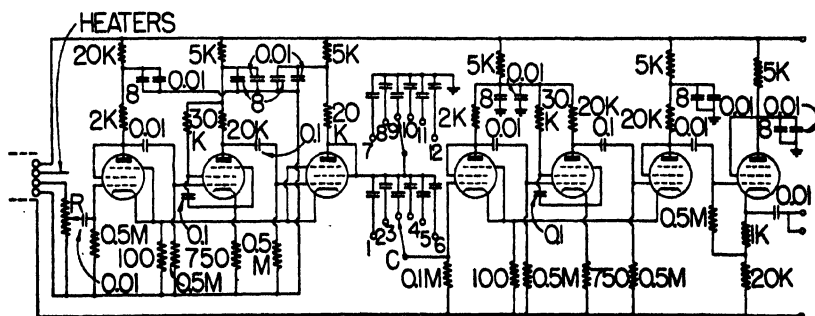
FIG. 2. Negative feedback amplifier. Tubes are 12SH7's. Resistance R consists of the following series: 1750, 1250, 750, 500, 250, 175, 125, 75, 50, 25, 50 ohms. Capacity C is made up as follows: No. 1, 0.001; No. 2, 0.0005; No. 3, 0.00025 μf; No. 4, 100; No. 5, 50; No. 6, 20 μμf.; No. 7, 0.001; No. 8, 0.0005; No. 9, 0.00025 μf.; No. 10, 50; No. 11, 20 μμf.; No. 12, off.

'differentiating' time constant, which determines the rate of fall of the output pulse, and a smoothing time constant, which restricts the high frequency response and fixes the rate of rise of the output pulse.

The collection time—that is, the time for the collector voltage to rise to its final value—is about 1μsec., but depends somewhat on the orientation of the α-particle track in the chamber. This variation, however, does not affect the output pulse amplitude if the differentiating time constant is made sufficiently long. (It cannot be increased indefinitely, however, as this would increase the grid-current noise.)

The smoothing time constant is adjusted to be somewhat longer than the collection time. This avoids significant dependence of output amplitude on collection time. The reduction in high frequency response is also valuable in reducing shot noise. All other coupling time constants in the amplifier are kept long to avoid overshooting.

The pulse at the output of the linear amplifier (a cathode-follower) has, then, an exponential rise and fall adjustable by the bandwidth control.   In this experiment the time constants used were respectively 5 and 25 μsec.

(b) Cutoff Amplifier

It has previously been remarked that the spread in amplitude of the pulses produced was only about 1%.   To obtain an accurate value for the mean pulse height it is clearly desirable to extend this spread over a considerable part of the working range of the pulse analyzer (50 to 150 v.).

A simple biased amplifier that amplifies the difference between the pulses at the output of the linear amplifier (say 49 to 51 v.) and a bias level of 48 v. would not, however, be satisfactory.   The residual pulses undergoing amplification would clearly be very short, necessitating a very wide-band amplifier. Furthermore, the length of a residual pulse would vary rapidly with the amplitude of its parent pulse.   With any reasonably attainable bandwidth (and the already relatively fast pulses at the amplifier output) there would be in consequence an appreciable non-linearity, the smaller, shorter residual pulses being amplified less than the larger, longer ones.

This difficulty is removed if the parent pulses are rectangular in shape—the residual pulses are then of equal length independent of their amplitude, and the effect of a finite amplifier bandwidth is the same on all.

This shaping is accomplished by the first part of the cutoff amplifier circuit shown in Fig. 3.   A cathode-coupled Kipp relay V_1, V_2 produces a square wave of amplitude 100 v. and adjustable duration (40 to 2000 μsec.) from any input pulse of amplitude greater than about 13 v.   This positive square wave is applied to the grid of the cathode-follower V_4 and cuts off·the diode D_4.   This allows the condenser C to charge through the diode D_3 to the peak amplitude of the input pulse, which is applied to D_3 through a cathode-follower V_3.

The condenser C retains this charge until the recovery of the Kipp relay swings V_4 cathode to earth potential and discharges C through D_4.   A very small fraction of the charge on C leaks away through R, but the fall in potential during the length of the square wave required is negligible.

The detailed behavior of the diode condenser-charging circuit is somewhat involved.   Owing to the imperfect cutoff characteristics of diodes the exact level to which the cathode rises depends on the input pulse shape and the size of the reservoir condenser used.   A small hump is produced owing to the diode self-capacity.   Provided that C is small enough to avoid saturation of D_3 or V_3, these are second-order effects and reduce to two terms—a constant and a term proportional to the input pulse; that is, a small 'zero-error' plus a small change in the gain.   (The latter is still independent of pulse amplitude.) The 'zero error' and gain were determined experimentally (see below) using pulses of exactly similar shape.

Tube V_5 is merely a buffer stage to isolate C and R.   The bias voltage is subtracted from the now square pulse on the grid of V_6.   The diode D_5 passes only that part of the pulse above earth potential, that is, the difference between
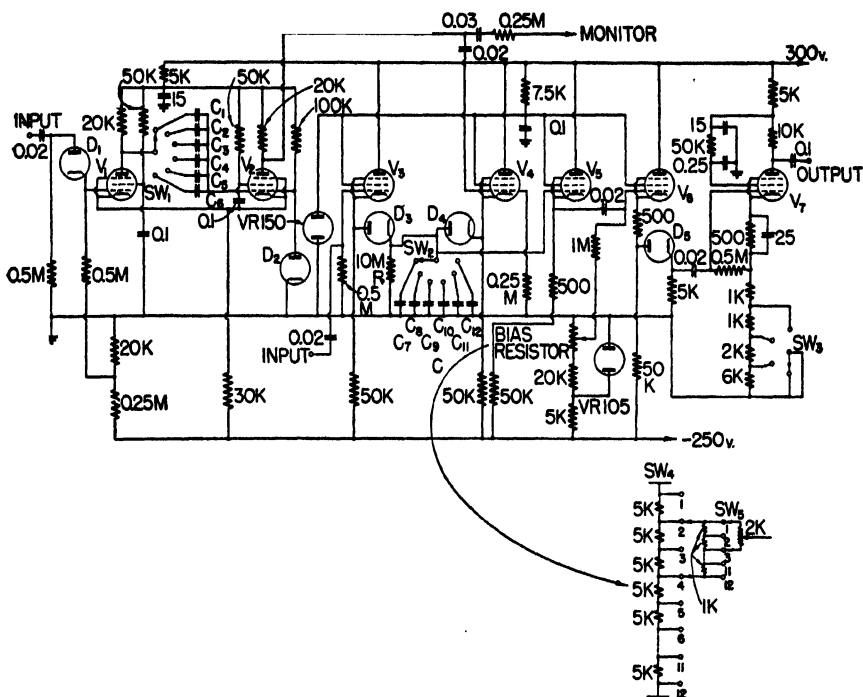
FIG. 3.   *Cutoff amplifier.   Tubes V_1 to V_7 are 6AC7's; D_1 to D_5 EA 50's.   Resistances are shown in ohms, capacities in microfarads.   Further components are as follows: C_1, 0.005; C_2, 0.002; C_3, 0.001 μf.; C_4, 500; C_5, 200; C_6, 100 μμf.; C_7, 0.01; C_8, 0.005; C_9, 0.002; C_{10}, 0.001 μf.; C_{11}, 500; C_{12}, 200 μμf.*

the input pulse amplitude and the bias voltage, plus a 'zero-error' due to the grid bases of the cathode-follower tubes.   The numerical value of this is reduced by the insertion of a 500-ohm resistor in the cathode circuit of V_6. The diode D_5 operates linearly at outputs greater than about $\frac{1}{3}$ v.

The bias voltage is obtained from a potentiometer chain consisting of 11 selected $5K$ wire-wound resistors, not differing by more than one ohm, connected in series.   To equalize these to an accuracy of better than 1/100% they are shunted by selected resistors of nominal value 2 Megohms.   Eleven selected $1K$ wire-wound resistors are connected in series, and by means of a switch can be connected across any two consecutive $5K$ resistors.   Similarly a $2K$ wire-wound potentiometer can be connected across any two consecutive $1K$ resistors.   With this bias arrangement it is possible to obtain bias voltages whose relative values are accurate to 1/100%.

V_7 is simply an output tube stabilized by negative feedback.   Its gain can be adjusted in four convenient steps.   It feeds directly into the pulse analyzer. A description of this instrument has been published (6).

Sources

The activity of the sources was of the order of a few hundred counts per minute. They were prepared by evaporating drops of the active substances in solution on to gold or platinum foils. The energies of the α-particles used for calibration were taken from Seaborg's Table (12) and are listed in Table I. The energies of the α-particles from four members of the $(4n + 1)$-series* were known to be about 5.8, 6.3, 7.0, and 8.3 Mev. from earlier work in this laboratory. For their precise measurement, sources of thorium active deposit and polonium 210 were used to give reference energies. The energy of the α-particles from uranium 233 (13) was measured by comparison with the α-particles from radium 226 and polonium 210. For plutonium 239 the s'.andards were radium 226 and radon 222. The ionization–energy curve was determined with the α-particles from three sources—radium 226 and its products, thorium active deposit, and polonium 210. In this case the thorium active deposit and polonium were mounted on one side of the hinged plate, and the radium source on the other side. This arrangement prevented overlap of the pulse distributions due to α-particles at 5.998 and 6.054 Mev., also at 5.298 and 5.486 Mev. (Table I).

TABLE I

ENERGIES OF α-PARTICLES USED FOR CALIBRATION

Element	Mass number	Energy of α-particle, Mev.
Radium	226	4.791
Polonium	210	5.298
Radon	222	5.486
Radium A	218	5.998
Thorium C	212	6.054
Radium C'	214	7.680
Thorium C'	212	8.776

Experimental Procedure

(a) *Method 1*

In the first method the gain and bias on the cutoff amplifier were chosen so that the pulses from the two standard sources, bracketing the 'unknown' source, were counted on the pulse analyzer in two groups of channels close to the ends of the bank of 20 channels. For instance, when the energy of the α-particles from uranium 233 (known to be about 4.8 Mev.) was to be measured, radium 226 and polonium 210 were used as standards. The middles of the pulse distributions for radium and polonium α-particles occurred at channels Nos. 5 and 17 respectively. By inverting the ionization chamber,

* *The chain of decay products of uranium 233, which form part of the new $(4n + 1)$ radioactive series, was discovered independently by English et al. (4, 5) of the Montreal Laboratory and Hagemann et al. (10) of the Argonne Laboratory. The present paper contains a detailed portion of this work at the Montreal Laboratory, which was summarized in a brief publication (5).*

alternate runs could be taken on the α-particles from uranium 233.   By linear interpolation the energy of these α-particles was derived.   The results of a typical run are plotted in Fig. 4.

FIG. 4.   *Typical distributions on pulse analyzer, taken in Method 1.   The dotted lines are the loci of the mid-points of the diameters.   Upper curve: α-particles from uranium 233, peak at channel 5.75.   Lower curves: α-particles from radium 226 and polonium 210, peaks at channels 5.0 and 17.6.   Energy of uranium 233 α-particle = 4.791 + (5.298 − 4.791) 0.75/12.6 = 4.821 Mev.*

The linearity of response of the equipment was checked by feeding into the head amplifier 20 different-sized groups of artificial pulses.   However, since each distribution of α-particle pulses covers only two or three channels, a small error in the threshold of one of the relevant channels would make a large error in judging the position of the middle of the distribution.   For accurate work this method was therefore abandoned.   It should be noted, however, that the method is useful when the α-particle spectrum is almost unknown, for a wide range of energy can be quickly scanned.   It is also convenient for identifying several peaks of α-particles through a study of their decay with time.

(b) *Method 2*

In the second method the gain of the amplifiers was held fixed as in Method 1, but the bias voltage of the cutoff amplifier was varied to bring each distribution of α-particle pulses to the central position on the pulse analyzer (see below).

The gain of the cutoff amplifier could be chosen five times that used in Method 1. Consequently, the distributions covered more channels of the analyzer, and errors due to imperfections in the settings of the channels were correspondingly reduced. Moreover, since there were about eight points on each distribution curve, drifts in individual channels were revealed by irregularities showing in the curve.

The relation between the bias of the cutoff amplifier and the energy of the α-particles chosen as standards was investigated. Small deviations of the peaks from the chosen channel of the analyzer were measured, and corrections were applied to the bias reading. In order to make these corrections the relation between bias voltage and position of the distribution for input pulses of constant size was required. This was determined by feeding in uniform pulses from a generator and locating the positions of the distribution on the pulse analyzer for different bias settings. The number of the channel was plotted against the bias to give a straight line of required slope. The linear relation between bias and energy of α-particles was then used to determine the energy of the α-particles from the substance under investigation.

In order to find the position of most probable size in the distribution of α-particle pulses, the method of diameters was used. The distribution curve was drawn, and the point at which the locus of the mid-points of diameters intersected this curve was taken as the most probable size. An example is shown in Fig. 5.

In the investigation of the ionization–energy curve it was necessary to determine the bias threshold, i.e., the value of the bias that corresponds to zero pulse size. Ten groups of artificial pulses, whose amplitudes were in the ratio $1 : 2 : 3 : \ldots 10$, were fed through a small condenser to the input grid of the head amplifier. The bias necessary to bring each group in turn to the level of the standard channel was measured. The straight line plot of the bias against pulse size was extrapolated to zero size to yield the zero of the bias system.

Experimental Results

The experimental runs were usually 5 or 10 minutes each, and about 1000 α-particles were counted in each distribution. In the measurements with uranium 233, twenty-five runs were taken on both standards and 'unknown'. For the other members of the $(4n + 1)$-series, six runs each, and for plutonium 239, ten runs were taken. The final energies of the α-particles with the probable errors of the means are given in Table II.

Since these measurements were made, the signal-to-noise ratio was increased by a factor of nearly three, and the width of the polonium 210 line at half-maximum reduced to 50 kev. (1). About 40 kev. of this spread is due to noise and about 35 kev. due to thickness of source and straggling of ionization. With a new chamber of lower capacity and optimum selection of tubes the spread due to noise could likely be further reduced by the factor 2. Moreover,

thinner and more uniform sources and perhaps a more suitable gas could be used. With these improvements the width of a line such as that of polonium 210 could possibly be reduced to 30 kev. at half-maximum.
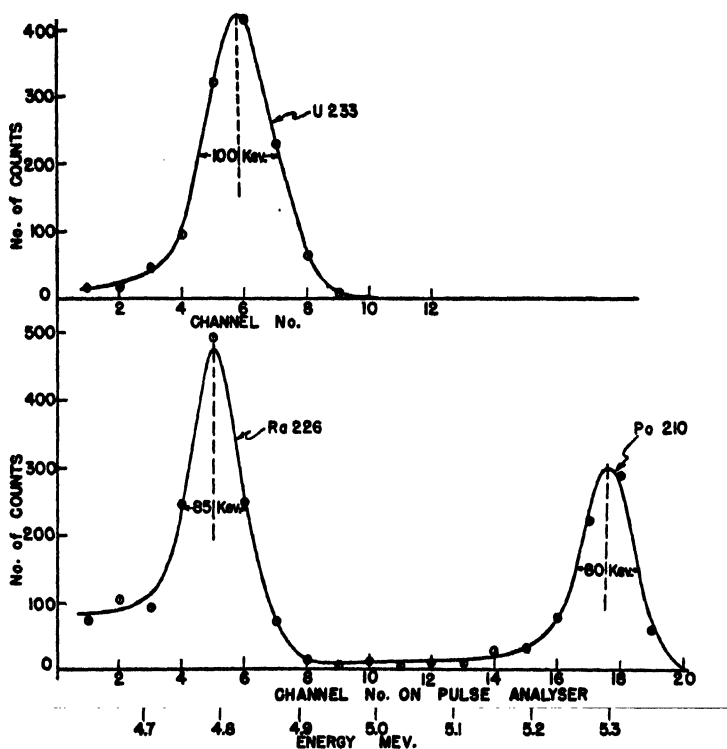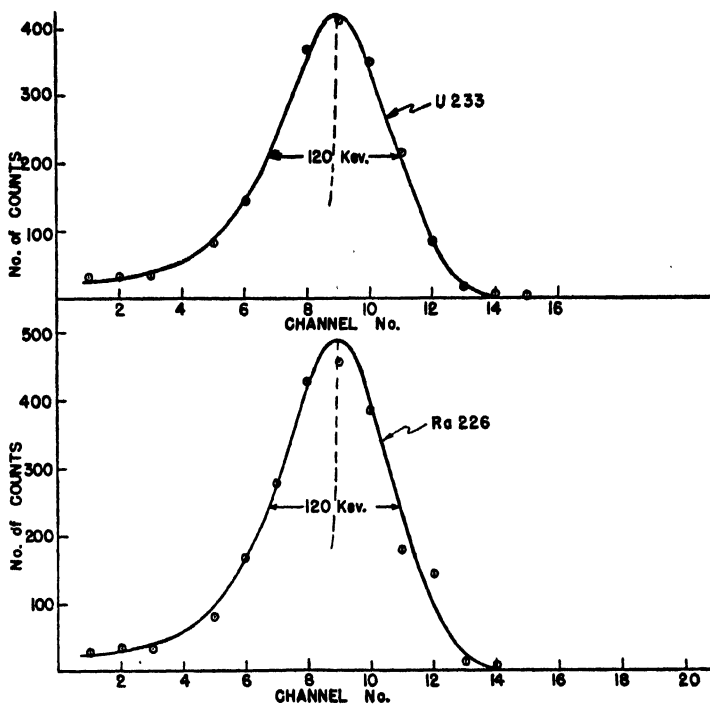

FIG. 5. *Typical distributions on pulse analyzer, taken in Method 2. The dotted lines are the loci of the mid-points of the diameters. Upper curve: α-particles from uranium 233, peak at channel 9.0, bias 8,075. Lower curve: α-particles from radium 226, peak at channel 9.0, bias 8,015. The peak of the distribution of α-particles from polonium 210 is at channel 9.0 when the bias is 8,960. A shift of 1 channel is caused by 54 bias units or 29 kev. in α-particle energy. Energy of uranium 233 α-particle = 4.791 + (5.298 − 4.791) 60/945 = 4.823 Mev. (10,000 bias units correspond to 50 K, the maximum available in the bias resistor, or to $\frac{50}{70} \times 105$ v. = 75 v.)*

TABLE II

DERIVED ENERGIES OF α-PARTICLES

Substance	Energy, Mev.	Substance	Energy, Mev.
$_{92}U^{233}$	4.823 ± 0.003	$_{85}At^{217}$	7.023 ± 0.010
$_{89}Ac^{225}$	5.801 ± 0.010	$_{84}Po^{213}$	8.336 ± 0.005
$_{87}Fr^{221}$	6.298 ± 0.010	$_{94}Pu^{239}$	5.159 ± 0.005

The energy of the α-particles of plutonium 239, measured in the present experiment, may be compared with that derived from their mean range in air, measured by Chamberlain, Gofman, Segrè, and Wahl (2). This is 3.675

cm. relative to a mean range of 3.842 cm. for the α-particles from polonium 210. Stout and Jones (15) have derived 5.144 Mev. for the energy of the plutonium α-particle from these ranges and the range–energy relation of Holloway and Livingston (11). This value is in reasonable agreement with 5.159 $\pm$ 0.005 Mev. found in the present experiment.

Ionization–Energy Curve

The ionization pulse sizes were measured for the α-particles from the seven radioactive substances given in Table I, which cover the energy range 5 to 9 Mev. The pulse size was found to vary linearly to 0.1% with the energy of the α-particles, using the method of least squares. Artificial pulses of 10 different amplitudes in the ratio 1 : 2 : 3 : . . . . . 10 were fed into the amplifier and their output size against input size was linear to 0.1%. From these two straight lines the ionization–energy line was drawn, which extrapolates to the energy axis with an intercept of 85 kev. in argon. This value was the mean of three separate experiments, each with two determinations of pulse size, and its probable error is 10 kev. The intercept on the energy axis is taken as an indication that the ionization–energy relation is curved for low values of the α-particle energy.

The average energy W in electron volts spent in producing an ion pair in a gas traversed by an α-particle has been the subject of numerous investigations. L. H. Gray (8) has summarized the work up to 1942. He has, in effect, interpolated for W for various initial energies of the α-particle in air on the basis of a modified Gerbes formula. Gerbes (7) measured the total ionization produced in air by initially monokinetic electrons over the range 300 to 60,000 ev. He observed a progressive increase in W with decreasing energy of the electrons that is well represented by the formula:

$$W = 31.62 + \frac{5.27}{\sqrt[4]{E}\sqrt{E_i}} \pm 0.08 \text{ ev. per ion pair,} \qquad (1)$$

where E is the initial energy of the electron in kev. and E_i is the ionization potential (1.7×10^{-2}) in kev. Gray calculated the total ionization produced by an α-particle of given initial energy on the assumptions that both the primary ionization and the secondary δ-ray ionization are represented by a formula of the Gerbes type. Best agreement with experiment was obtained by changing the second constant of Equation (1) from 5.27 to 2.6.

We find that Gray's adjusted data for the average energy loss W per ion pair produced in air by an α-particle of initial energy E in Mev. can be satisfactorily represented by the formula:

$$W = 32.75 + \frac{6.5}{\sqrt{E}}. \qquad (2)$$

This formula is particularly applicable in the region 2 to 8 Mev. It gives 35.1 and 35.6 ev. per ion pair for the α-particles of radium C' (7.680 Mev.) and polonium (5.298 Mev.) respectively. These are in good agreement with the measurements prior to 1943 reviewed by Gray, and with the measurements from Stetter's laboratory (14). From the latter work $W = 7.680 \times 10^6/220,300 = 34.9$ and $W = 5.298 \times 10^6/148,200 = 35.7$ ev. per ion pair for these α-particles.

A formula of the type shown by Equation (2),

$$W = A + \frac{B}{\sqrt{E}}, \tag{3}$$

can be tried for the ionization of an α-particle of initial energy E in argon. Suitable values of the constants A and B have to be determined. Let I_1 and I_2 represent respectively the total number of ion pairs produced in argon by α-particles of initial energies E_1 and E_2. The average energy losses per ion pair are given by

$$W_1 = \frac{E_1}{I_1} \quad \text{and} \quad W_2 = \frac{E_2}{I_2}. \tag{4}$$

Choosing $E_1 = 5$ Mev. and $E_2 = 8$ Mev. and noting the linear relation found in the present experiments,

$$\frac{I_2}{I_1} = \frac{8.00 - 0.085}{5.00 - 0.085} = 1.6104.$$

From these relations

$$\frac{W_1}{W_2} = 1.0065 \quad \text{and} \quad \frac{A}{B} = 14.1.$$

Stetter (14) quotes 186,200 and 148,200 for the numbers of ion pairs produced in argon and air respectively by a polonium α-particle. The former leads to $W = 28.5$ ev. per ion pair, while the ratio is 1.256. Using Equation (2) as a good representation of Gray's adjusted data for air and this ratio, it follows that $W = 28.3$ ev. per ion pair for a polonium α-particle traversing argon. Adopting the latter value of W at $E = 5.298$ Mev., the best values of the constants for argon that can be derived from the present experiments are

$$A = 27.5 \quad \text{and} \quad B = 1.9,$$

$$\text{or } W = 27.5 + \frac{1.9}{\sqrt{E}}. \tag{5}$$

The agreement of our results with the classical measurements of Gurney (9) appears reasonably close. There is some uncertainty about the exact energies of the α-particles in Gurney's experiments, and these were concerned with α-particles of lower energy than in our experiments. The ratio of the ioniza-

tion in argon to that in air, measured by Gurney, is about 3 to 4% higher than the ratio predicted by Equations (2), (4), and (5) over the range of energy he observed.

Acknowledgments

The authors wish to thank Mr. A. C. English for preparing the radioactive sources, and Dr. B. W. Sargent and Mr. G. C. Hanna for assistance in preparing this paper for publication.

References

1. BUNEMANN, O., CRANSHAW, T. E., and HARVEY, J. A.   Unpublished report, CRP-247. The use of grid chambers for α-ray analysis.   National Research Council of Canada. 1946.   (Report to be published.)
2. CHAMBERLAIN, O., GOFMAN, J. W., SEGRÈ, E., and WAHL, A. C.   Phys. Rev. 71 : 529. 1947.
3. CHANG, W. Y.   Phys. Rev. 69 : 60.   1946.
4. ENGLISH, A. C.   Unpublished report, MC-145.   The (4n + 1) radioactive series.   National Research Council of Canada.   1945.
5. ENGLISH, A. C., CRANSHAW, T. E., DEMERS, P., HARVEY, J. A., HINCKS, E. P., JELLEY, J. V., and MAY, A. N.   Phys. Rev. 72 : 253.   1947.
6. FREUNDLICH, H. F., HINCKS, E. P., and OZEROFF, W. J.   Rev. Sci. Instruments, 18 : 90. 1947.
7. GERBES, W.   Ann. Physik, 23 : 648.   1935.
8. GRAY, L. H.   Proc. Cambridge Phil. Soc. 40 : 72.   1944.
9. GURNEY, R. W.   Proc. Roy. Soc. London, A, 107 : 332.   1925.
10. HAGEMANN, F., KATZIN, L. I., STUDIER, M. H., GHIORSO, A., and SEABORG, G. T.   Phys. Rev. 72 : 252.   1947.
11. HOLLOWAY, M. G. and LIVINGSTON, M. S.   Phys. Rev. 54 : 18.   1938.
12. SEABORG, G. T.   Rev. Modern Phys. 16 : 1.   1944.
13. SEABORG, G. T., GOFMAN, J. W., and STOUGHTON, R. W.   Phys. Rev. 71 : 378.   1947.
14. STETTER, G.   Z. Physik, 120 : 639.   1943.
15. STOUT, J. W. and JONES, W. M.   Phys. Rev. 71 : 582.   1947.

MEASUREMENT OF THE HALF-PERIOD OF POLONIUM 213[1]

By J. V. Jelley[2]

Abstract

In the recently discovered $(4n + 1)$ radioactive series, bismuth 213 transforms to polonium 213 by β-emission. The latter rapidly transforms by α-emission to lead 209. The present paper describes a measurement of the half-period of polonium 213. A preparation of radium 225 was placed between two Geiger–Müller counters. One detected β-particles while the other detected α and β-particles. Coincidences were counted with a modified Rossi circuit. The pulse-width on the grid of one of the tubes of the coincidence unit was made variable, while the pulse-width on the other remained fixed. The pulse-width associated with the counter that responded only to β-particles was chosen to be variable. Coincidences were counted as a function of the pulse-width. Corrections were made for accidental coincidences and exact coincidences arising from other causes. The final value for the half-period T of polonium 213 is $T = 4.2 \pm 0.8$ μsec. A subsidiary experiment to determine the half-period of thorium C' gave the value $T = 0.34 \pm 0.06$ μsec. in reasonable agreement with measurements by other workers.

Introduction

In the recently discovered $(4n + 1)$ radioactive series (7, 8, 9) there occurs a short-lived α-active body that occupies a position in the series similar to those of radium C', thorium C' and actinium C' in the other three radioactive series. This body is polonium 213, which is produced by the β-decay of bismuth 213 and transforms by α-decay to lead 209. The relevant portion of the series proceeds as shown in Fig. 1 (7). It was clearly of interest to measure the half-period of polonium 213 and to see whether it shows a departure from the Geiger–Nuttall relation similar to those for the C' bodies. This paper describes such a measurement.
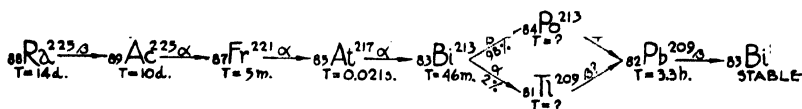
FIG. 1. *Part of the $(4n + 1)$ radioactive series.*

From the known energy of the α-particles (3, 8) and the Geiger–Nuttall relation, the half-period was estimated to lie in the region of microseconds or milliseconds. The coincidence method of measuring short periods could therefore be readily applied (5, 11). Two Geiger–Müller counters were used to detect the β-particles from bismuth 213 and the α-particles from polonium 213. The pulses from the counters were applied to a coincidence amplifier with a variable resolving time. The coincidence counting rate was measured as a

function of the resolving time. Corrections were applied for (1) the accidental coincidence rate, and (2) exact coincidences arising from other causes.

Geiger–Müller Counters

A Geiger–Müller counter was used for the detection of the α-particles since a grid-ionization chamber utilizing electron collection and an associated fast amplifier were not available. If an ionization chamber having slow pulses and an associated amplifier had been adopted, time delays between genuine coincidences from the two detectors, of the same order of magnitude as those under investigation, would have been introduced. A compensating delay-circuit introduced into one of the two channels of the coincidence unit would have added considerable complications. Recently, systems working with delayed coincidences have, however, been successfully used (4).

Two mica window Geiger–Müller counters were mounted horizontally to reduce the cosmic ray coincidence rate to a minimum. These are shown in Fig. 2. In order to obtain best counting geometry the spacing between the
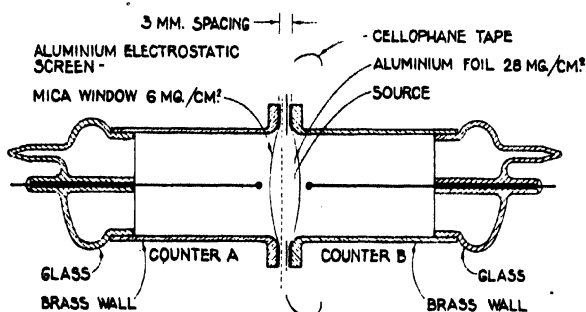
FIG. 2. *Geiger–Müller counters arranged to detect $\beta - \alpha$ coincidences. Counter A detects β-particles, while counter B detects α and β-particles.*

ends of the counters was reduced to a practical minimum—about 3 mm. The source was deposited over an area of about 12 mm.² on a thin aluminum foil weighing 28 mgm. per cm.² This was in turn mounted on a strip of cellophane tape, which was stretched across the window of one of the counters, the deposit being on the side of the foil opposite that to which the tape was attached. The counters and their cathode-followers were entirely surrounded by a lead housing. This expedient, although it increased the cosmic ray coincidence rate, was necessary to shield against γ-rays from neighboring sources in the laboratory.

The half-period of thorium C′ was measured as well as that of polonium 213. The measured value of the former, standing in reasonable agreement with previous measurements, was taken as evidence that the equipment was working satisfactorily for the determination of half-periods of the order of microseconds. In both experiments the thickness of the aluminum foil was sufficient to stop the α-particles of maximum range. In both cases, however,

the α-particles could penetrate the mica window of one counter, which weighed 6 mgm. per cm.^{2}. The energy of the α-particles of polonium 213 is 8.336 Mev. (3, 8), which corresponds to a mean range of 7.89 cm. in air at 15° C. and 760 mm. pressure or 11.4 mgm. per cm.^{2} in mica. The α-particles of thorium C' have an energy of 8.776 Mev., a mean range of 8.56 cm. in air and 12.3 mgm. per cm.^{2} in mica.

In the experimental arrangement counter A is actuated by β-particles and counter B by α and β-particles. Both counters also respond, though at lower efficiency, to γ-rays.

Electronic Equipment

A schematic arrangement of the electrical equipment is shown in Fig. 3. Steps were taken to reduce circuit delays to a minimum, to obviate the necessity of amplifiers as usually used by others in this field (1), and to produce pulses with steep and sharply defined 'front edges'. Two cathode-followers
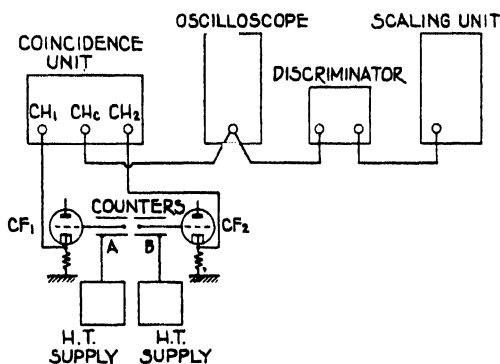
FIG. 3. *Schematic diagram of experimental arrangement.*

CF_1 and CF_2 were mounted close to the counters. RCA 6AK5 miniature pentodes were used for this purpose. The negative pulses, about 50 v. in amplitude, were taken from these by screened cables to the inputs CH_1 and CH_2 of the two channels of a Rossi coincidence unit. The circuit was arranged so that the pulse-width or time-gate on the grid of *one* of the tubes of the coincidence unit was made variable, while the pulse-width on the other remained fixed. In both experiments—with thorium C' and polonium 213—the α-particle is emitted *after* the β-particle. Thus, the time-gate τ_1 associated with counter A, the one responding only to β-particles, is chosen to have the variable width. This is shown in Fig. 4, for the case in which an α-particle pulse has arrived in channel CH_2 within the time interval τ_1 after the arrival of a β-particle in channel CH_1 and for which a coincidence is recorded. The time-gate was varied by altering the time constant in the grid circuit of one tube of the Rossi circuit (switch S in Fig. 5).

The output pulses appearing at CH_c in Fig. 3 were taken through a discriminator to a scaling unit. An oscilloscope was also included for monitoring

purposes. The individual counting rates at CH_1 or CH_2 could be similarly determined.
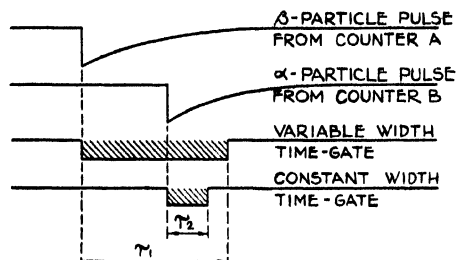
Fig. 4. *Illustrating a coincidence between a β-particle detected in counter A and an α-particle in counter B.*
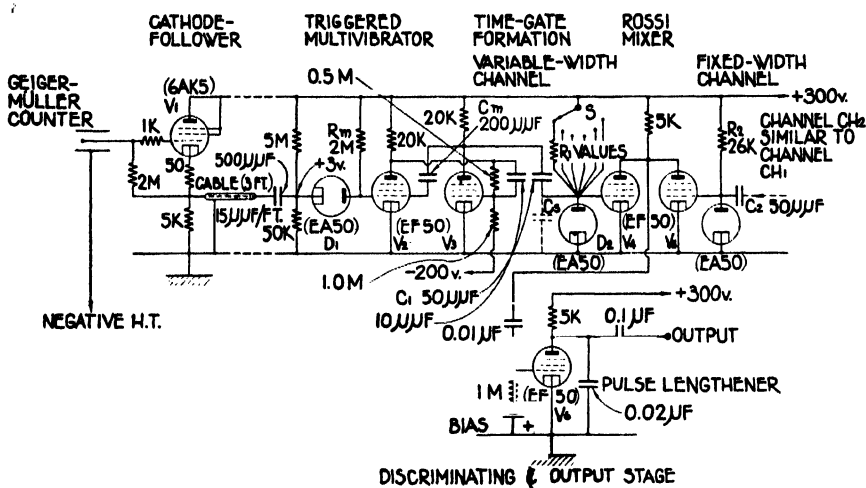
Fig. 5. *Detailed diagram of electronic circuit.*

The coincidence unit is shown in detail in Fig. 5 and the wave-forms in Fig. 6. Tube V_1 is the cathode-follower. Tubes V_2 and V_3 form a Kipp relay, which produces a negative square-wave of fixed amplitude and duration on the anode of V_3 when triggered by a negative pulse on the grid of V_2. The duration is set by the components R_m and C_m to be longer than the maximum value of the delay-time determined by R_1 and C_1, but not so long as to produce appreciable counting losses due to pulses overlapping. Diode D_1 serves two purposes, (1) as a fixed-bias discriminator and (2) as a 'buffer' stage to prevent interaction of V_1 and $V_2 - V_3$ when the multivibrator has been 'fired'. The wave-form on the anode of V_3 is utilized to form the time-gate τ_1 on the grid of one of the Rossi tubes, V_4. Tube V_6 performs the function of a discriminating and pulse-lengthening stage.

The circuit is symmetrical in both channels except that in the channel of variable time-gate, shown in Fig. 5, the resistance R_1 is selected by means of the switch S over a range from $26K$ to $10M$ ohms in 10 stages.

Two factors that represent developments of the earlier circuits employed in the coincidence technique (1, 11) are (1) the introduction of the cathode-followers close to the Geiger–Müller counters, and (2) a modification in the

<small>COUNTER OUTPUT VIEWED AT CATHODE OF D₁</small>
<small>APPROX. 50v.</small>
<small>ANODE OF V₃</small>
<small>APPROX. 200v.</small>
<small>ASYMPTOTIC TO v₀ (H.T.)</small>
<small>CURRENT IN D₂ & GRID OF V₄</small>
<small>GRID OF V₄</small>
<small>GRID BASE OF V₄</small>
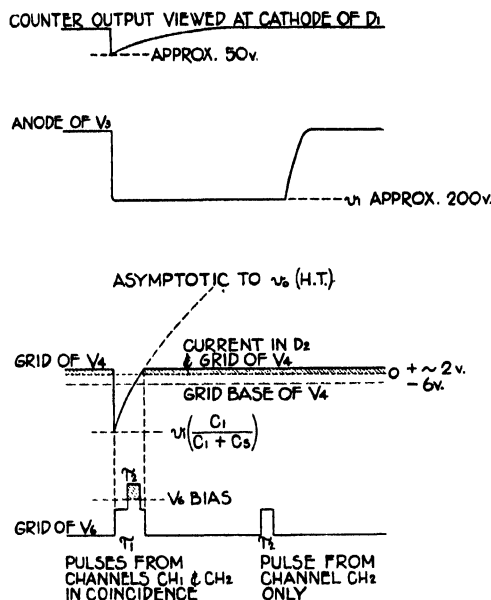
F<small>IG</small>. 6.   *Wave-forms to illustrate the operation of the coincidence circuit.*

method of pulse differentiation at the grids of the Rossi tubes.   The latter enables pulses of rather shorter duration (for given circuit components) and with steeper 'back edges' to be produced.   The normal grid-leak R_1 is taken to the positive H.T. line instead of to earth, and tube V_4 operates normally at zero or with slightly positive voltage on the grid.   Diode D_2 is introduced to ensure that the grid potential of V_4 is definite (approximately $+ 1$ v.) and to protect the grid of V_4 against excessive grid current.

If v_0 denotes the voltage of the positive H.T. line and v_1 the amplitude of the wave-form present on the anode of V_3, the amplitude of the wave-form on the grid of the Rossi tube V_4 is given by

$$v_1 \left(\frac{C_1}{C_1 + C_s} \right) , \qquad (1)$$

where C_1 is the capacity of the coupling condenser and C_s is the sum of the stray capacities of the grid-circuit of V_4 and the diode D_2.   It will then be seen that the width of the time-gate τ_1 as the wave-form crosses the grid-base of V_4 is related to the time-constant of the circuit $R_1 C_1$ by the equation:

$$v_0 = \left[v_0 + v_1 \left(\frac{C_1}{C_1 + C_s} \right) \right] e^{-\tau_1 / R_1 (C_1 + C_s)} . \qquad (2)$$

A similar equation holds for the time-gate τ_2 of the other channel. With the values of the voltages and components met with in practice, τ_1 is considerably less than $R_1 C_1$.

Determination of Resolving Times

The following symbols are defined:

N_1 = Counting rate for the channel counting β-particles;

N_2 = Counting rate for the channel counting $(\alpha + \beta)$-particles;

τ_1 = Duration of the time-gate on the variable-width or β-counting channel of the coincidence unit;

τ_2 = Duration of the fixed time-gate on the $(\alpha + \beta)$-counting channel,

$f = \tau_1 + \tau_2$;

$S1, S2, \ldots S10$ = Switch positions selecting R_1 (Fig. 5) and thus altering τ_1 ;

N_A = Counting rate of accidental coincidences.

(Counting rates are expressed as counts per minute, time intervals in microseconds.)

The determination of the resolving times for the various switch positions $S1, S2, \ldots S10$ was carried out by measuring the accidental coincidence rate N_A when the two counters were actuated by two independent sources of β-radiation. During this experiment the two counters were separated by approximately 6 ft. and enclosed in separate lead housings.

The equation

$$N_A = \frac{N_1 N_2 \tau}{60} \times 10^{-6} \qquad (3)$$

was used to determine τ from the measured values N_1, N_2 and N_A. The cosmic ray coincidence rate with this arrangement was negligible.

Table I gives the results of these measurements, and the calculated values of τ, including standard errors, for the various switch positions.

TABLE I

DETERMINATION OF RESOLVING TIMES

Switch S position	R_1, ohms	N_1	N_2	N_A	τ, μsec.
1	26K	4915	4922	0.41 ± 0.03	1.02 ± 0.08
2	42K	4925	5085	0.70 ± 0.04	1.68 ± 0.10
3	54K	5345	4895	0.77 ± 0.03	1.77 ± 0.07
4	67K	5475	4960	1.00 ± 0.06	2.21 ± 0.13
5	70K	5540	4975	1.39 ± 0.08	3.03 ± 0.18
6	103K	5585	5115	1.90 ± 0.13	3.99 ± 0.27
7	262K	5360	4670	4.83 ± 0.32	11.6 ± 0.8
8	520K	5425	4335	8.32 ± 0.48	21.2 ± 1.2
9	2M	5445	4125	28.0 ± 0.7	74.8 ± 1.9
10	10M	5430	3900	85.0 ± 2.0	241 ± 6

Test of Coincidence Unit with Exact Coincidences

In order to test whether there were any measurable differential delays between the two channels, either in the counters or circuits, coincidence measurements were made with the normal experimental arrangement (Fig. 2) and a source that emits a large percentage of 'exactly' coincident particles. Protactinium 233 was chosen for the purpose. The β-emission is followed by γ-rays that are highly internally converted (6). The delay between the primary β-particle and the conversion electron is probably of the order of 10^{-13} sec.

Let N'_C = measured coincidence rate.

If the coincidence apparatus is behaving properly, the quantity $N'_C - N_A$ should be independent of the resolving time of the apparatus.

The results of this experiment are given in Table II. The values of $N'_C - N_A$ in Column 6 are reasonably constant. This proves that differential delays between the two channels are negligible over the range of values of τ permitted by the circuit constants.

TABLE II

TEST OF COINCIDENCE UNIT WITH EXACT $\beta - \beta$ COINCIDENCES

(The cosmic ray coincidence rate was about one count per minute.)

Switch S position	N_1 (± 48)	N_2 (± 63)	N'_C	N_A (calc.)	$N'_C - N_A$
1	2340	3930	183 ± 3.5	0.2	183 ± 3.5
2	2270	3840	189 ± 3.6	0.3	189 ± 3.6
3	2240	3910	186 ± 3.5	0.3	186 ± 3.5
4	2240	4030	193 ± 3.6	0.3	193 ± 3.6
5	2270	3970	187 ± 3.5	0.5	187 ± 3.5
6	2240	3970	185 ± 2.0	0.6	184 ± 2.0
7	2270	3910	193 ± 3.5	1.7	191 ± 3.5
8	2305	3930	187 ± 3.5	3.2	184 ± 3.5
9	2305	3930	197 ± 4.0	11.3	186 ± 4.0
10	2145	3930	224 ± 4.0	34	190 ± 4.0
				Average	187

Method of Analyzing Coincidence Measurements to Determine Short Half-Periods

The measured coincidence rate is made up of the following contributions:

(1) 'Exact' coincidences arising from cosmic rays;

(2) 'Exact' coincidences arising from other background effects, for instance a β-particle passing through both counters in succession;

(3) 'Exact' coincidences caused by radiations from the radioactive source, such as $\beta - \gamma$ coincidences if the β-decay has associated γ-rays, or $\gamma - \gamma$ coincidences if γ-rays are emitted in cascade by the source;

(4) 'Accidental' coincidences, which arise from two unrelated events causing counts in the two counters of such a time correlation that they record as a coincidence;

(5) 'Delayed' coincidences of the $\beta - \alpha$ type, arising from the short half-period under investigation.

It should be noted that 'exact' coincidences of Types 1 and 2 form a constant background. On the other hand, 'exact' coincidences of Type 3 will vary with the source strength. In the case of a source containing two or more radioactive bodies, the counting rate of Type 3 coincidences will vary with time in a manner determined by the amount of each radioactive body present and the contribution to the coincidence rate arising from the disintegration of each body.

The 'accidental' coincidence rate, Type 4 coincidences, has been determined in the usual way from the product of the counting rates in the two counters and the resolving time. Since, in some instances, as many as 10% of the counts in one counter are time correlated with the counts in the other counter, the above procedure used to calculate the 'accidental' coincidence rate is only approximate (Equation (3)). However, the 'accidental' coincidence rate is in most cases negligible, and an accurate calculation would have little influence on the analysis of the results.

The following additional symbols are defined:

N'_C = Measured coincidence rate;

N_A = Counting rate of accidental coincidences (Type 4);

N_B = Counting rate of 'exact' coincidences that form a background independent of the source (Types 1 and 2);

$N_C = N'_C - N_A - N_B$;

N_D = Delayed coincidence rate of the $\beta - \alpha$ type, arising from the short half-period under investigation;

N_{DO} = Asymptotic value of N_D when τ_1 is very large compared with the half-period for α-decay;

N_E = 'exact' coincidence rate arising from activities in the source (Type 3);

$N_{co} = N_E + N_{DO}$.

(Counting rates are expressed in counts per minute. A bar over the symbol, e.g., $\bar{N}_D$, is used to denote a counting rate which has been corrected for source decay to a constant source strength.)

From the previous discussion it is seen that

$$N_C = N_D + N_E \tag{4}$$

$$\text{and } N_D = N_{DO}(1 - e^{-\lambda\tau_1}), \tag{5}$$

where λ is the transformation constant of the α-active body, and

$$N_A = \frac{N_1 N_2 \tau}{60} \times 10^{-6} . \tag{3}$$

In analyzing the data for the half-period of the short-lived radioactive body, the following procedure was used.

(a) Calculate N_A from the relevant values of N_1, N_2 and τ;

(b) Evaluate $N_C = N'_C - N_A - N_B$. (The value of N_B throughout these experiments was taken to be about 1.0 count per minute, which is, strictly speaking, only the cosmic ray portion.);

(c) Correct the values of N_C for readings taken during the decay of the source to a constant source strength, obtaining $\bar{N}_C$ for the various values of τ;

(d) From an inspection of the values of $\bar{N}_C$ for values of τ very large compared with the half-period for α-decay verify that $\bar{N}_C$ is constant within the experimental error of these readings and then choose the average value as $\bar{N}_{CO}$;

(e) Since

$$\bar{N}_C = \bar{N}_E + \bar{N}_{DO}(1 - e^{-\lambda \tau_1})$$

$$= \bar{N}_{CO} - \bar{N}_{DO}\, e^{-\lambda \tau_1}, \tag{6}$$

it follows that

$$\bar{N}_{CO} - \bar{N}_C = \bar{N}_{DO}\, e^{\lambda \tau_1} e^{-\lambda \tau} = \text{constant } e^{-\lambda \tau}. \tag{7}$$

Consequently, the desired transformation constant, λ, can be found from the slope of the line in the semilogarithmic plot of

$$\bar{N}_{CO} - \bar{N}_C \quad \text{against } \tau.$$

Measurement of the Half-Period of Thorium C′

As a preliminary experiment to the measurement of the half-period of polonium 213, it was thought desirable to test the apparatus on thorium C′, whose period had previously been measured by other experimenters (2, 5). Thorium active deposit on an aluminum foil was used as the source. Thorium B is collected in the emanation, and it transforms successively to thorium C, thorium C′, and thorium D. The results of the experiment are shown in Table III and Fig. 7.

The elapsed times t to the mid-points of the measured coincidence runs are given with reference to the first. These are used to correct N_C for decay of the source, yielding $\bar{N}_C$. The amounts of thorium B and thorium C present depend on the duration of collection of the active deposit and the elapsed time from the end of collection to the mid-point of the coincidence measurement. Unfortunately these times were not recorded. The best that can be done now is to fit the measured rates $N_C = N'_C - N_A - N_B$ at the various times t tabulated for switch positions 10 to 5 inclusive. The associated times τ are so long that the rates N_D due to $\beta - \alpha$ coincidences only have their asymptotic

TABLE III

MEASUREMENTS TO DETERMINE HALF-PERIOD OF THORIUM C′

Switch S position	t, hr.	N_1 (± 47)*	N_2 (± 75)*	N'_C	N_A (calc.)	N_C ($N_B = 1$)	$\bar{N}_C$	$\bar{N}_{CO} - \bar{N}_C$ ($\bar{N}_{CO} = 353 \pm 2$)
10	0	2240	5600	401 ± 7	50	350	350	(+3 ± 8)
9	0.15	2335	5600	364 ± 7	16	347	347	(+6 ± 8)
8	0.45	2270	5500	359 ± 4	4	354	355	(−2 ± 8)
7	0.70	2340	5440	357 ± 7	2	354	357	(−4 ± 8)
6	1.13	2270	5440	353 ± 5	1	351	359	(−6 ± 6)
5	1.61	2310	5310	339 ± 4	1	337	351	(+2 ± 5)
4	2.06	2270	5150	330 ± 5	1	328	349	(+4 ± 6)
3	2.45	2175	4980	307 ± 4	0	306	332	21 ± 5
2	3.03	2175	4980	281 ± 3	0	280	313	40 ± 4
1	3.56	2045	4860	203 ± 4	0	202	233	120 ± 5

* *Standard errors for N_1 and N_2; each reading represents a count for one minute only.*

FIG. 7. *Measurements to determine the half-period of thorium C′. The coincidence rates in counts per minute are plotted semilogarithmically against the resolving times τ in microseconds.*

values N_{DO} (independent of the half-period of thorium C' and of τ), and N_C has the asymptotic value $N_{CO}(= N_{DO} + N_E)$.

The value of N_{DO} depends only on the number of atoms of thorium C that disintegrate per minute. The 'exact' coincidence rate N_E depends jointly on the numbers of atoms of thorium B and thorium C that disintegrate per minute. From the Rutherford–Soddy theory of successive transformations one expects that $N_{CO}(= N_{DO} + N_E)$ would vary with the time t from the end of the collection time in the emanation according to

$$Ae^{-\lambda_1 t} - Be^{-\lambda_2 t},$$

where λ_1 and λ_2 are the well known transformation constants of thorium B and thorium C respectively and A and B are constants. It is found that the measured coincidence rates N_{CO} for switch positions 10 to 5 inclusive are well represented by

$$N_{CO} = 390.5\,e^{-\lambda_1 t} - 37.2\,e^{-\lambda_2 t}, \tag{8}$$

where t takes the values in Column 2 of Table III. It is then necessary to assume that the subsequent decay, for switch positions 4 to 1 inclusive, follows

$$N_C = 390.5\,e^{-\lambda_1 t} - 37.2\,e^{-\lambda_2 t}. \tag{9}$$

The values of N_C were accordingly corrected for decay to zero time (Column 8).

The value chosen for $\bar{N}_{CO}$ is 353 $\pm$ 2 counts per minute. As shown in the previous section (Equation (7)), the logarithms of $\bar{N}_{CO} - \bar{N}_C$ are plotted against τ (Table I), and the required half-period of thorium C' is derived from the slope of the straight line (Fig. 7). The final result for the half-period is

$$T = 0.34 \pm 0.06\ \mu\text{sec.}$$

The spacing of the values of τ at the consecutive switch positions is rather wide for the measurement of such a short half-period. However, the derived value is in reasonable agreement with other measurements: 0.3 $\pm$ 0.1 μsec. (Dunworth (5)), 0.26 $\pm$ 0.04 μsec. (Bradt and Scherrer (2)), and 0.30 $\pm$ 0.015 μsec. (Hill (10)).

Measurement of the Half-Period of Polonium 213

A sample of radium 225 was prepared as a source of polonium 213. From the portion of the $(4n + 1)$-series shown in Fig. 1 it is seen that the amount of polonium 213 follows the decay of the actinium 225 rather closely. The radium 225 was used in this experiment 21 days after its preparation. The reduction in the disintegration rate of actinium 225 over one day, the duration of each run, is estimated at 1.2% from the Rutherford–Soddy theory of successive transformations. It is therefore unnecessary to correct for the decay of the source. Two independent runs were made on two successive days. The measurements are shown in Table IV and Fig. 8. The final value of the half-period is

$$T = 4.2 \pm 0.8\ \mu\text{sec.}$$

Unfortunately, the values of τ chosen for the circuit are not spaced in the optimum manner for accuracy of the half-period. However, a stronger source would have been necessary to make better use of larger and better spaced values of τ, and this was not available.

The result of this experiment was included in the brief communication published last year (8). The half-period of polonium 213 given in the present paper supersedes that listed (4.4 μsec.) in reference (8).

When the Geiger–Nuttall plot is made for the $(4n + 1)$-series, it is seen that polonium 213 shows a deviation in the same sense as the C' -bodies in the other radioactive series.

TABLE IV

MEASUREMENTS TO DETERMINE HALF-PERIOD OF POLONIUM 213

Switch S position	N_1 (± 30)*	N_2 (± 53)*	N_C'	N_A (calc.)	N_C ($N_B = 1.1$)	$N_{CO} - N_C$
			First run			$N_{CO} = 75.5 \pm 1.5$
10	842	2702	84.8 $\pm$ 1.9	9.1	74.6	(+0.9 $\pm$ 2.4)
9	917	2834	80.6 $\pm$ 2.1	3.2	76.3	(−0.8 $\pm$ 2.6)
8	917	2887	77.5 $\pm$ 2.1	0.9	75.5	(0.0 $\pm$ 2.6)
5	908	2784	44.7 $\pm$ 1.5	0.1	43.5	32.0 $\pm$ 2.1
4	906	2923	41.2 $\pm$ 1.5	0.1	40.0	35.5 $\pm$ 2.1
3	926	2857	37.2 $\pm$ 1.4	0.1	36.0	39.5 $\pm$ 2.1
2	901	2826	(48.6 $\pm$ 1.7)†	0.1	(47.4)	(28.1)†
1	886	2844	32.4 $\pm$ 1.2	0	31.3	44.2 $\pm$ 1.9
			Second run			$N_{CO} = 79.7 \pm 1.5$
10	924	2944	92.5 $\pm$ 1.9	11.0	80.4	(−0.7 $\pm$ 2.4)
9	942	2784	83.4 $\pm$ 1.5	3.3	79.0	(+0.7 $\pm$ 1.9)
8	924	2999	79.2 $\pm$ 2.0	0.9	77.2	(+2.5 $\pm$ 2.5)
7	861	2960	72.2 $\pm$ 1.9	0.5	70.6	9.1 $\pm$ 2.4
6	893	2897	52.3 $\pm$ 1.6	0.2	51.0	28.7 $\pm$ 2.2
5	937	2890	42.6 $\pm$ 1.5	0.1	41.4	38.3 $\pm$ 2.1
4	829	2925	38.3 $\pm$ 1.1	0.1	37.1	42.6 $\pm$ 1.9
3	811	2967	35.2 $\pm$ 1.3	0.1	34.0	45.7 $\pm$ 2.0
2	887	2817	33.2 $\pm$ 1.3	0.1	32.0	47.7 $\pm$ 2.0
1	832	2816	28.6 $\pm$ 1.2	0	27.5	52.2 $\pm$ 1.9

* Standard errors for N_1 and N_2; each reading represents a count for one minute only.

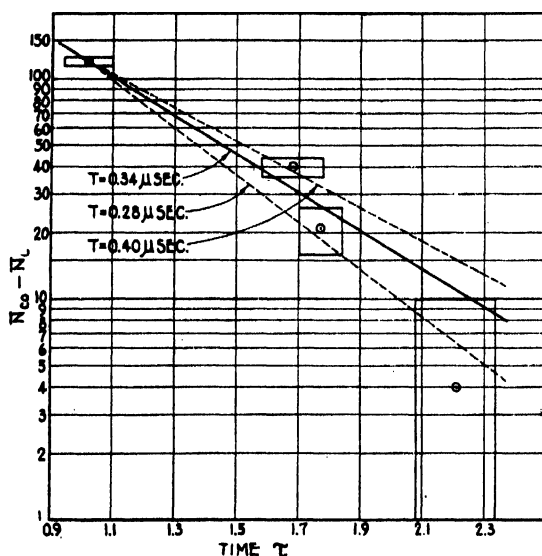*† Rejected; perhaps vitiated by electrical interference.*
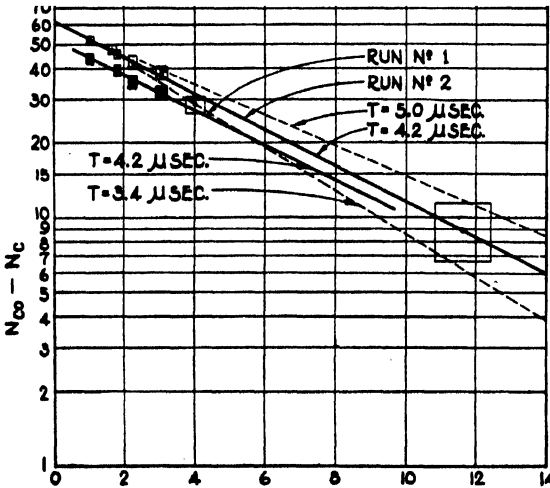
FIG. 8.   *Measurements to determine the half-period of polonium 213.   The coincidence rates in counts per minute are plotted semilogarithmically against the resolving time τ in microseconds.*

Acknowledgments

The author wishes to thank Dr. A. N. May and Mr. A. G. Ward for their interest and valuable advice during the experiment, and Mr. A. C. English and Dr. L. G. Elliott for preparing the radioactive sources. Dr. B. W. Sargent and Mr. A. G. Ward have generously assisted in preparing this paper for publication.

References

1. BRADT, H. and SCHERRER, P.   Helv. Phys. Acta, 16 : 251.   1943.
2. BRADT, H. and SCHERRER, P.   Helv. Phys. Acta, 16 : 259.   1943.
3. CRANSHAW, T. E. and HARVEY, J. A.   Can. J. Research, A, 26 : 243.   1948.
4. DE BENEDETTI, S. and McGOWAN, F. K.   Phys. Rev. 70 : 569.   1946.
5. DUNWORTH, J. V.   Nature, 144 : 152.   1939.
6. ELLIOTT, L. G.   Private communication.   1945.
7. ENGLISH, A. C.   Unpublished report, MC-145.   The (4n + 1) radioactive series.   National Research Council of Canada, 1945.
8. ENGLISH, A. C., CRANSHAW, T. E., DEMERS, P., HARVEY, J. A., HINCKS, E. P., JELLEY, J. V., and MAY, A. N.   Phys. Rev. 72 : 253.   1947.
9. HAGEMANN, F., KATZIN, L. I., STUDIER, M. H., GHIORSO, A., and SEABORG, G. T.   Phys. Rev. 72 : 252.   1947.
10. HILL, J. M.   Private communication.   1948.
11. ROTBLAT, J.   Proc. Roy. Soc. London, A, 177 : 260.   1941.

HEAT TRANSFER WITH SURFACE BOILING[1]

By J. W. Knowles

Abstract

These experiments were undertaken to investigate the transfer of heat from solid surfaces to flowing water. The bulk temperature of the cooling water was below the boiling point, and the surface temperature of the heat transfer tube went to about 100° C. above the boiling point. Water velocities ranged up to 10 ft. sec.$^{-1}$ and heat fluxes up to 720 w. cm.$^{-2}$. The non-dimensionless heat transfer constant a in the Dittus and Boelter formula $(Nu) = a(Re)^{0.8} (Pr)^{0.4}$, which under normal forced convection has a value of 2.30×10^{-2}, increased to four times the normal value under the surface boiling conditions. It is shown graphically that the constant a bears a simple relation to the heat flux and the length–diameter ratio for surface temperatures below a certain value. For constant heat flux and volume flow rate, the surface temperature rises with rising bulk liquid temperature until it reaches the certain value of the surface temperature referred to above. The surface temperature then remains constant with further rise in the bulk liquid temperature until conditions become too unstable for measurements.

Introduction

The main object of this investigation was to study the transfer of heat from a solid surface to flowing water when the temperature of the solid surface was above the boiling point. Information on surface boiling is of general interest owing to its possible bearing on the design of steam engines, and it is of particular importance in the design of atomic reactors where irregularity in the boiling rate might lead to operating difficulties. The data on heat transfer by surface boiling to a moving fluid is meager. In previous experiments (1), the metal surface has been heated by high pressure steam. This leads to difficulties in determining the surface temperature from the properties of the steam, because the variations in the heat transfer, caused by the condensation of the steam on the inside surface, are uncertain. Also, it is difficult to determine the surface temperature by the use of a thermocouple embedded below the metal surface if the metal wall is only slightly thicker than the thermocouple, because the presence of the thermocouple disturbs the heat flow through the wall.

In the following experiment, an electrically heated stainless steel heat transfer tube was used in order to avoid some of these difficulties and to obtain high heat fluxes from moderate power supplies. The outside surface temperature of this tube was calculated from the electrical energy dissipated in the tube and the temperature registered by a thermocouple inside the tube.

Experimental

A flow diagram of the heat exchange unit is given in Fig. 1. The heat transfer column, Fig. 2, was the only part of the heat exchange unit that was

altered during the experiment. Different diameters and lengths of glass and stainless steel tubes were used, as summarized in Table I.
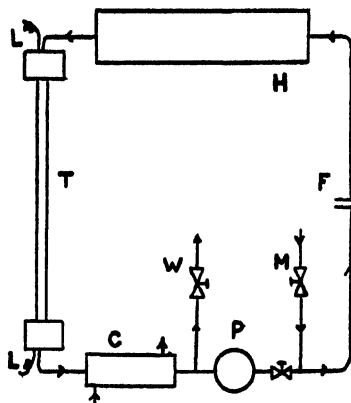
FIG. 1. *Flow diagram for heat exchange unit,*

L, power leads.
T, heat transfer tube.
C, water cooler.
W, water pressure regulator.

P, pump.
M, main inlet (hot).
F, calibrated flowmeter.
H, heater coil, 60 kw. max.
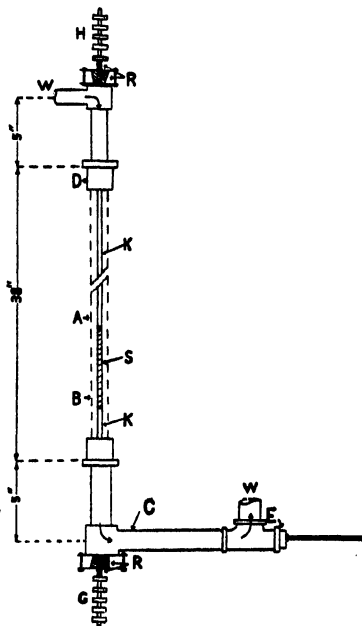
FIG. 2. *Heat transfer column,*

H and G, electric conductors.
W, water inlet and outlet.
K, 0.25 in. copper conductors.

A, glass tube.
S, stainless steel heated section.
E, thermometer and thermocouple.

R, spring to prevent heater rod from buckling when the rod expands through rubber ring.
B, C, and D, indicate positions discussed in the text.

Copper–constantan thermocouples were used for the following temperature measurements.   The internal temperature T_1 of the stainless steel tube was measured at 2 cm. above the lower solid copper conductor, Fig. 3.   The outside
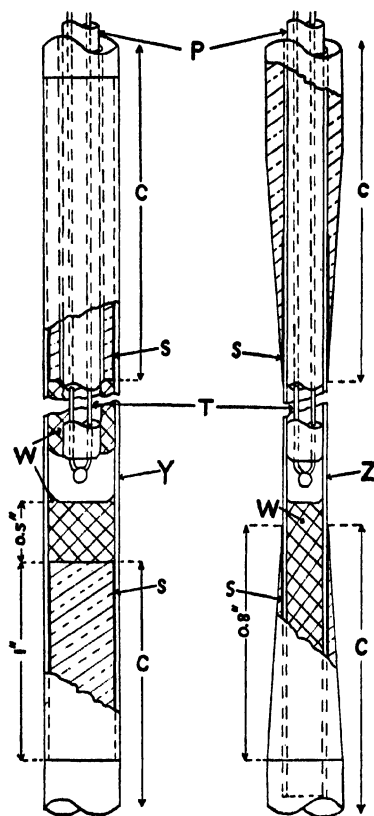
FIG. 3.   Heater elements.

C, copper tube and copper rod conductors,   W, glass wool.
T, thermocouples.   P, porcelain insulators.
Y, stainless steel tube (0.25 in. O.D.).   S, solder joints.
Z, stainless steel tube (0.12 in. O.D.).

surface temperature of the stainless steel tube at this position, also indicated by B, Fig. 2, was calculated from the known heat flux and tube temperature T_1. Drawing a thermocouple up the inside of the heat transfer tube, when it was heated, showed the temperature gradient to be approximately 0.2° C. in.$^{-1}$. Thus, any error in the internal temperature T_1 caused by conduction along the thermocouple leads was negligible.   To measure the inlet bulk temperature T_2 of the cooling water before it reached the heated section S, a thermocouple was soldered to a thin copper strip, which was in turn clamped to the outside of the glass tube at A, Fig. 2.   To measure the bulk outlet temperature at point E, Fig. 2, a thermocouple and a precision thermometer, accurate to 0.2° C., were immersed directly in the flowing water.   The thermometer

required five minutes longer than the thermocouples to reach equilibrium conditions, and thus was used only for standardization.

The thermocouples were standardized between 30° and 130° C. against the thermometer at E, Fig. 2. The temperature of the water circulating in the closed system was varied between 30° and 130° C. by means of the heater, H, Fig. 1. During standardization no power was supplied to the heat exchange unit. Temperature readings up to 230° C. were obtained by a linear extrapolation of the thermocouple standardization.

The whole heat transfer column from D to E, Fig. 2, was insulated with 1 cm. of glass wool and from 2 to 3 cm. of cotton wool packing. Any error due to insulation imperfections was assumed insignificant, as it was present in both the standardization and the actual experiment.

A pressure gauge accurate to 2% registered the pressure at position C, Fig. 2. The pressure at C was equal, within 1%, to the pressure at B, the lowest point on the heated tube where boiling occurred. It was for this point on the heated tube that all heat transfer coefficients were calculated. The pressure at point C was held at 26.0 lb. in.$^{-2}$ gauge, or 40.6 lb. in.$^{-2}$ absolute throughout all the experiments.

When an experimental run was made, the heat flux and the rate of water flow to the heat transfer tube were kept constant. The input bulk water temperature T_2 was increased by decreasing the water flow through the water cooler, C, Fig. 1. Equilibrium temperature conditions were considered to have been reached when the inlet bulk temperature T_2 varied by no more than 0.2° C. during the two minute interval required to take all the readings and to repeat the first temperature reading T_2. At a sufficiently high input water temperature, the cooling water failed to transfer the heat from the hot surface because of heat insulation caused by steam formation. This input temperature is called 'the breakdown point'. Near breakdown, the temperature measurements were accepted if the input temperature was rising no faster than 1° C. in two minutes.

Accuracy of Measurements

All temperatures were measured to an accuracy of ±0.5° C. Heat flux and flow rates were measured to better than ±1%. Thus, for the large temperature difference experienced, the heat transfer coefficient h was accurate to about ±2%, and was reproducible within this limit. A calculation of the temperature of the cooling water at E, Fig. 2, was made for all experiments from a knowledge of the heat input and the flow rate. This calculated temperature agreed with the measured temperature at E, Fig. 2, to within 1%.

All the stainless steel heat transfer tubes were highly polished before use and were repolished after one hour of continuous use. The Montreal tap water that was used produced no visible dirt film deposit on these tubes after four hours of continuous moderate boiling in the tube. Under heavy boiling in the tube, the polish disappeared beneath a dirt film in about 15 min., and a

distinct red coating was produced after 30 min. Continuous running of the boiling heat transfer for 24 hr., at a heat flux of 200 w. cm.$^{-2}$ and a flow rate of 99 gm. sec.$^{-1}$ cm.$^{-2}$, produced a dirt film 0.05 mm. thick, but did not produce any lowering of the heat transferred. At very high boiling rates and at heat fluxes greater than 200 w. cm.$^{-2}$, any dirt film that had formed was pulled almost completely off by the scouring action of the bubbles.

Description of Surface Boiling

The boiling on the heat transfer tube was very similar to that observed by C. H. Brooks and W. L. Badger (1). When the surface temperature of the stainless steel tube was a few degrees above the boiling point, long chains of bubbles formed at distinct nuclei on the heated surface. The main body of the bubble streams stayed close to the stainless steel tube, and a fine spray of bubbles extended out further into the cooling water. As the surface temperature was increased, the chains of bubbles projected further into the water flow, the fine spray extended to the outside walls, and the central heater tube became obscured by the moving steam bubbles. When the heat flux or the input temperature T_2 was increased sufficiently, the surface boiling became very unstable, and regularly spaced clouds of bubbles travelled down the heat transfer tube. On passing this unstable condition, called the 'breakdown" point, the bubble size would increase suddenly, and if the electric power were not shut off immediately the stainless steel tube would fuse. When using the smaller tube, $D = 0.47$ cm., Table I, a volume of steam would be produced that would force the water up and down the transfer tube away from the center of the disturbance, and would stop the water pump. The central stainless steel tube would be violently shaken, and the outer glass tube shattered if the stainless steel tube came into contact with it. With the larger tube, $D = 1.00$ cm. the cooling water always remained flowing, and no outer glass tubes were broken.

Correlation of Heat Transfer Data

In order to correlate the results, it was found necessary to distinguish two boiling regions. The basis for this distinction shows itself in the following procedure. If one keeps the heat flux in the heat transfer tube and the mass flow rate constant, and gradually raises the bulk water temperature, the surface temperature of the heat transfer tube also will increase at first. At a certain value of input bulk temperature, at which vigorous boiling is occurring in the heat transfer column, the surface temperature of the heat transfer tube will cease to rise with increasing bulk temperature, as shown in Figs. 9 and 10. This effect of constant surface temperature will extend over a range of from 5° to 20° C. of increasing bulk temperature, depending on the heat flux and the flow rate, before the breakdown bulk temperature is reached.

The region in which the surface temperature rises normally with increasing bulk temperature is termed the normal boiling region. The constant surface temperature region is termed the critical boiling region.

TABLE I

LENGTH OF HEATER SURFACE, L; HYDRAULIC DIAMETER, DIFFERENCE BETWEEN THE INNER AND OUTER DIAMETER OF THE WATER ANNULUS, D

No.	L, cm.	Area of heated surface, cm.	D, cm.	Area of annulus, cm.	Mass flow rate, gm.sec.$^{-1}$cm.$^{-2}$	L/D
1*	30.55	60.3	0.47	0.63	285	64.3
2	30.55	60.3	0.47	0.63	108	64.3
3	30.55	60.3	1.00	1.79	302	30.5
4	30.55	60.3	1.00	1.79	210	16.1
5	76.2	150.8	1.00	1.79	99.0	75.9
6	30.55	60.3	1.00	1.79	99.0	30.4
7	7.62	15.1	1.00	1.79	99.0	7.6
8	7.62	15.1	0.47	0.63	77.0	16.1
9**	29.5	29.4	1.32	2.09	279	22.3
10	29.5	29.4	1.32	2.09	86.1	22.3

* In Series 1 to 8 the heater tube was ¼ in. or 0.63 cm. diameter.
** In Series 9 and 10 the heater tube was ⅛ in. or 0.32 cm. diameter.

The correlation of all results was based on finding variations in a of the well known Dittus and Boelter relation (2),

$$Nu = a(Re)^{0.8}(Pr)^m,$$

$Re = \dfrac{(DG)}{\mu}$, which is the Reynolds dimensionless criterion;

$Pr = \dfrac{(c\mu)}{K}$, which is the corresponding Prandl criterion;

$Nu = \dfrac{(hD)}{K}$, which is the corresponding Nusselt criterion;

D = the hydraulic diameter of the space through which the water flows, and is equal to the difference between the inner and outer diameters of the water tube in centimeters;

G = the mass flow rate in grams per square centimeter;

μ = the viscosity of the cooling water, c.g.s.,

K = the thermal conductivity of the cooling water, c.g.s.;

c = the specific heat of the cooling water, c.g.s.;

h = the liquid to surface coefficient of heat transfer, calculated from

$$h = \frac{q}{t_s - t_B}$$

q = the heat flux in watts per square centimeter;

t_s = the surface temperature;

t_B = the bulk temperature.

This equation was found to fit the heat transfer points for normal boiling by choosing $m = 0.4$. Pr and Re were computed with the arithmetic averages of surface and bulk temperature at B, Fig. 2, rather than with the bulk tem-
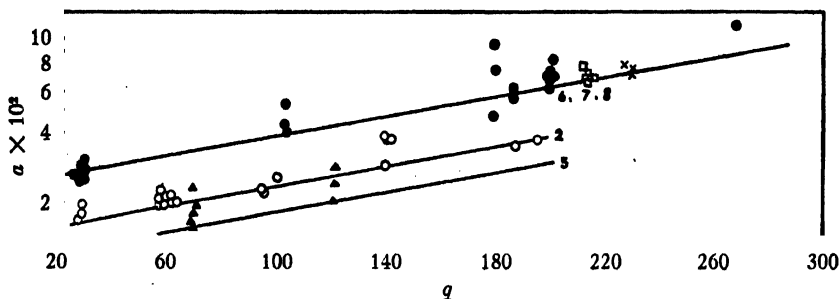
FIG. 4. *Log* a *versus heat flux* q *watts per square centimeter, for low mass flow rates. The numbers refer to Table I, 2—open circles; 5—triangles; 6—solid circles; 7—squares; 8—crosses.*
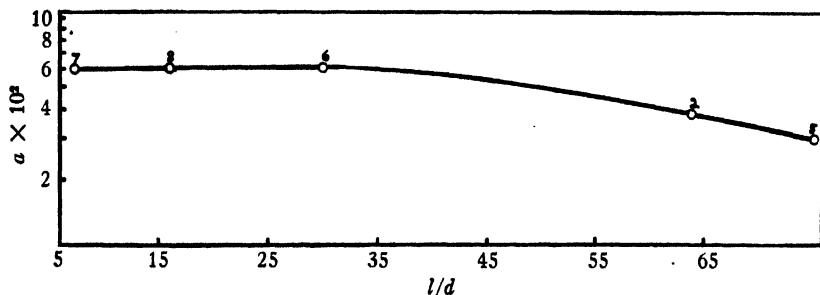
FIG. 5. *Log* a *versus length/diameter for a heat flux of 200 w. cm.$^{-2}$. Mass flow rates from 77 to 108 gm. sec^{-1} cm.$^{-2}$. The numbers refer to Table I.*
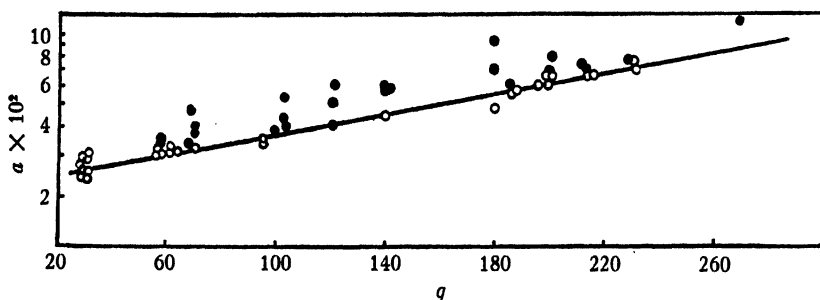
FIG. 6. *Log* a *versus heat flux* q *watts per square centimeter. Before the constant surface temperature is reached, open circles; after the constant surface temperature is reached, solid circles.*

perature alone, since better over-all correlation of data was obtained with the former.

Without surface boiling the average value of a is 0.023. With rapid surface boiling the measured values of a were much higher than this value. In Fig. 4 the points indicated by any one type of symbol represent the variation of a

with heat flux q for the length–diameter ratio and flow rate given in Table I. These values of a include results from the normal boiling and critical boiling regions.   Each straight line in Fig. 4 represents the variation of a with q for
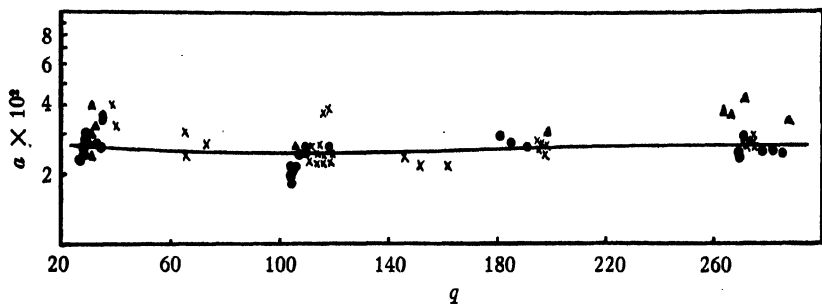
FIG. 7.   Log a versus heat flux q watts per square centimeter, for high mass flow rate. Table I, No. 4, triangles; No. 3, solid circles; No. 1, crosses.
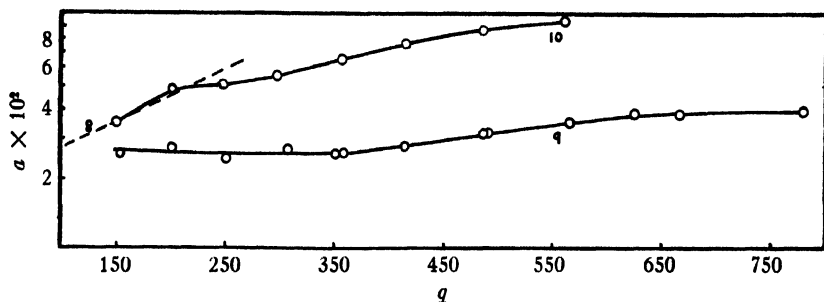
FIG. 8.   Log a versus heat flux q watts per square centimeter, for high heat fluxes.   The numbers refer to Table I.

values of a in the normal boiling region with a given geometry and flow rate. Values of a in the critical boiling region with a given geometry and flow rate are always greater than the values of a for normal boiling.

Reference to Table I shows that as the length–diameter ratio increases, the straight lines of Fig. 4 are shifted parallel to themselves towards lower values of a.   This lowering of a with increasing length/diameter is represented in Fig. 5 for $q = 200$ w. cm.$^{-2}$.   By multiplying all the values of a represented by a given symbol in Fig. 4, by a constant factor, the parallel lines in Fig. 4 may be brought into coincidence with line 7, Fig. 4.   This is shown in Fig. 6. The line drawn through the open circles in Fig. 6 represents the heat correlation for normal boiling.   The experimental points above the line, represented by solid circles, are the value of a in the critical boiling region.

For high mass flow rates, $(G = 279$ gm. sec.$^{-1}$ cm.$^{-2})$, the effect of surface boiling on heat transfer became noticeable only at heat fluxes above 260 w. cm.$^{-2}$, Fig. 7.   The constant surface temperature effect was observed also at these high flow rates, but there was no consistent evidence in the correlation

of points from which to conclude that the highest a values plotted in Fig. 7 were caused by this effect.

The effect of surface boiling on the heat transfer constant a at heat fluxes above 200 w. cm.$^{-2}$, is shown in Fig. 8. Curve 10, Fig. 8, is a plot of a for low mass flow rates, $(G = 86$ gm. sec.$^{-1}$ cm.$^{-2})$. Curve 10 was obtained with
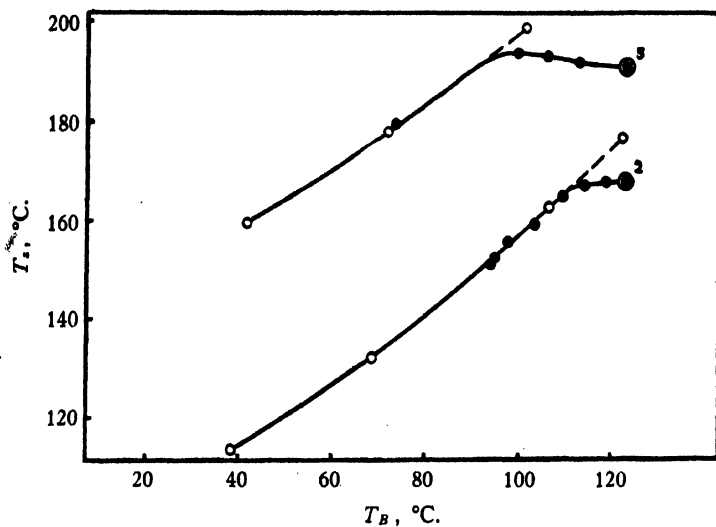
FIG. 9
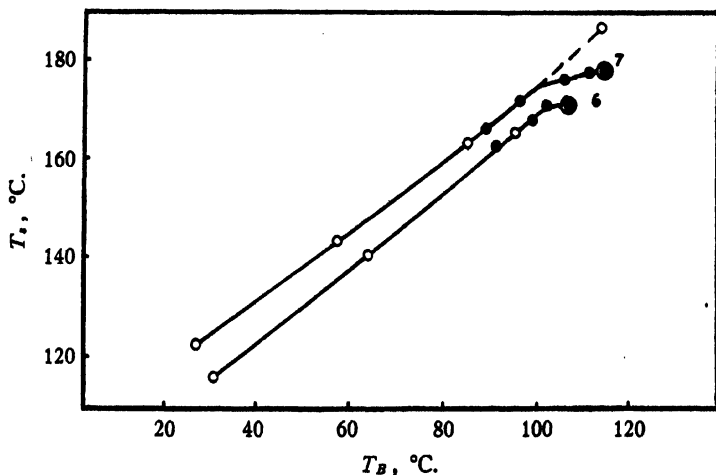
FIG. 10

FIGS. 9 AND 10. *Outside surface temperature of stainless steel tube* T_s °C. *versus bulk temperature of cooling water at B, Fig. 2,* T_B °C. *Values calculated from the Dittus and Boelter equation using values of a from Fig. 4, open circles; experimental values near breakdown, solid circles; experimental values at breakdown, double circles. Curve 5,* q = 69.3 w. cm.$^{-2}$; *Curve 2,* q = 59.1 w. cm.$^{-2}$; *Curve 7,* q = 214 w. cm.$^{-2}$; *Curve 6,* q = 201 w. cm.$^{-2}$. *The curve numbers refer to Table I.*

apparatus of the same length/diameter ratio as that of Curve 8, but of different heater diameter (see Table I). Curve 8, Fig. 4, replotted as a broken line in the same figure with Curve 10 shows that the agreement is satisfactory.

At low heat fluxes and high flow rates, Curve 9, Fig. 8, and the curve of Fig. 7 agree well, although the results of Fig. 7 were obtained with a heater tube of a different diameter than that of Curve 9, Fig. 8; Table I. Curve 9 shows clearly that for mass flow rates of 279 gm. sec.$^{-1}$ cm.$^{-2}$, which correspond to Reynolds numbers of the order of 1.5×10^5, the effect of surface boiling became noticeable only at heat fluxes above 300 w. cm.$^{-2}$.

Conclusion

All physical properties in the Dittus and Boelter equation depending on the cooling water temperature were taken at the arithmetic average of the surface and bulk water temperatures. Similar calculation, using the bulk temperature instead of the arithmetic average temperature, gave the same general agreement as that shown by the graphs, but the values of a were higher by from 10% to 20% and showed more scatttering when one attempted to correlate results in the manner shown in the graphs.

However when either the bulk or the average temperature is used the experimental data presented can be correlated in a consistent manner by assuming a length–diameter effect, Fig. 5. The lowering of the heat transfer coefficient a with increasing heated length probably occurred because bubbles produced by the heat transfer did not collapse immediately in the cooling water, and so caused an accumulation of steam when the heated section of the tubes was sufficiently long.

The constant surface temperature effect shown in Figs. 9 and 10 was present in all experimental arrangements, and if further experimental data had been obtained these regions could have been mapped out completely. Qualitatively, for the same heat transfer column dimensions and rate of flow, the surface temperature tended to remain constant over a wider range of bulk temperatures at the higher values of heat fluxes.

The experiments show that, for normal boiling, heat transfer conditions can be correlated with the usual Dittus and Boelter relation if one takes account of the variations of a with the heat flux and length–diameter ratio. If one uses an irreversible source process for the production of heat, such as the stainless steel heat transfer tube used here, or atomic energy, the critical boiling region has a broad constant temperature range which may serve as a safety indicator between normal boiling and the dangerous breakdown point. Thus, under such conditions, it should be safe to operate in the normal boiling region. With suitable geometry the surface temperature of the stainless steel may be from 80° to 100° C. above the boiling point. At high heat fluxes and low flow rates the transfer coefficient can increase by a factor of 4 and still have stable conditions.

Acknowledgments

The author wishes to express his gratitude to Dr. S. G. Bauer for his suggestion of the problem and his guidance, and to Dr. W. H. McAdams for his helpful criticism.

References

1. BROOKS, C. H. and BADGER, W. L.   Trans. Am. Inst. Chem. Engrs. 33 : (No. 3) 392. 1937.
2. BOARTS, R. M., BADGER, W. L., and MEISENBURG, S. J.   Trans. Am. Inst. Chem. Engrs. 33 : 363. 1937.

THE VIBRATIONAL CONSTANTS OF ACETYLENE[1]

By NORMA MORGENROTH NORDIN AND R. N. H. HASLAM

Abstract

On the basis of the work done by Darling and Dennison on the water vapor molecule, the vibrational constants of acetylene are calculated, taking into account the resonance interaction arising from the near equality of the fundamentals ν_1 and ν_2. Seventeen band centers are known experimentally. The band centers depend on the 10 constants χ_i, χ_{ik} and γ, which are functions of the potential constants. The expressions for the vibrational energies of the band centers are set up, those for interacting doublets or triplets being found by perturbation methods. The 10 constants are determined and the positions of eight bands calculated to check the results. The agreement is very satisfactory. The positions of 10 other bands not yet observed are predicted.

Introduction

The rotation vibration spectrum of the acetylene molecule has been studied by many investigators such as A. Levin and C. F. Meyer (6), G. Herzberg and J. W. T. Spinks (5), G. W. Funke and G. Herzberg (2), G. Glockler and C. E. Morrell (3), and R. Mecke and R. Ziegler (7). It has been definitely shown from the spectrum that the molecule is linear and symmetrical. There are five normal modes of vibration, shown in Fig. 1.

In the Raman spectrum there are two strong lines at 1973.8 and 3373.7 cm.$^{-1}$, which can be attributed to ν_2 and ν_1 respectively. A weak Raman doublet at 589 and 646 cm.$^{-1}$ has been interpreted as the two branches of the third Raman active vibration, ν_4.

In the infrared two strong absorption bands at 3287 and 729.1 cm.$^{-1}$ are found, and are due to ν_3 and ν_5 respectively. A third band at 1328.1 cm.$^{-1}$ has been interpreted as a combination of ν_4 and ν_5.

It may be noted that some of the earlier authors used different notations. The nomenclature used in this paper is that adopted by Herzberg (4), and not that used by Darling and Dennison (1).

The ordinary and photographic infrared regions have many other combination bands. The assignment of the overtone bands has been the subject of many discussions, one of the latest of these being that given by Wu (8). In all the work done so far there have been discrepancies when constants calculated from some of the bands have been used to calculate positions of other bands.

It was suggested by Herzberg (4) that these discrepancies might be due to a mutual perturbation of the levels v_1, v_3 and $v_1 - 2$, $v_3 + 2$ with other v's being equal. Since the values of the fundamentals v_1 and v_3 are very close together, this perturbation may be expected to be fairly strong.
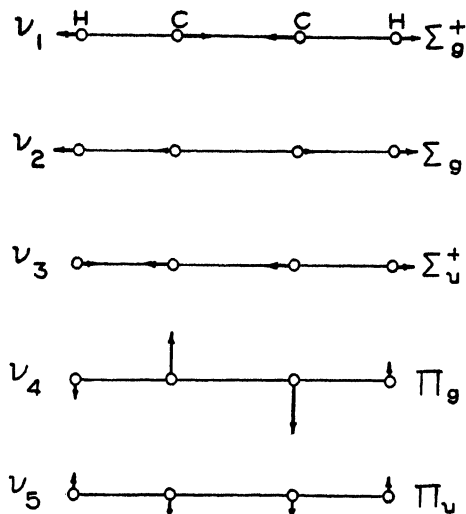
FIG. 1.

This is not a first order resonance effect since v_1 and v_3 possess different symmetry properties. In a linear symmetrical molecule the only normal vibrations that may occur are those belonging to the species Σ_g^+, Σ_u^+, π_g and π_u. In the case of acetylene, v_1 belongs to the species Σ_g^+, and v_3 to the species Σ_u^+. That is, one is unchanged for reflection at the center of the molecule, and the other changes sign. Therefore the first class is characterized by v_3 being an even integer, and the other by v_3 being odd. Levels that may interact are thus of the type $(v_1, v_2, v_3, v_4, v_5)$ and $(v_1 - 2, v_2, v_3 + 2, v_4, v_5)$. Overtone bands of this type are observed in the spectrum of acetylene, for example, (20100) and (00300) found at 9835.1 and 9639.8 cm.$^{-1}$, and (21100) and (01300) found at 11782.9 and 11600.1 cm.$^{-1}$.

A successful calculation of the energy values of the water vapor molecule, taking into account the resonance between v_1 and v_3, has been carried out by Darling and Dennison (1). Although the acetylene molecule is linear, and the water vapor molecule is nonlinear, the calculations for the two are very similar. The method of calculation is as follows.

The expression for the Hamiltonian function is that given by Darling and Dennison, namely,

$$H = \tfrac{1}{2} \sum_{\alpha\beta} \mu^{\frac{1}{4}} (P_\alpha - p_\alpha) \mu_{\alpha\beta} \mu^{-\frac{1}{2}} (P_\beta - p_\beta) \mu^{\frac{1}{4}} + \tfrac{1}{2} \sum_k \mu^{\frac{1}{4}} p_k \mu^{-\frac{1}{2}} p_k \mu^{\frac{1}{4}} + V.$$

The P_α's are the components of the total angular momentum, the p_α's are the components of the vibrational angular momentum, the $\mu_{\alpha\beta}$'s are the components of a determinant μ that contains the moments of inertia; and the p_k's are the momenta conjugate to the normal co-ordinates, q_k.

An expression for the vibrational energy is found, using perturbation theory. To obtain the expression for the energies of perturbing levels in doublets and triplets, the method used is to diagonalize the portion of the Hamiltonian matrix which contains the interacting states.

The Vibrational Energy

For all bands considered, v_4 and v_5 are equal to zero, that is v_1, v_2, and v_3 alone are present. To obtain the position of the band centers the components of the total angular momentum, P_α, are set equal to zero. The remaining Hamiltonian then becomes, as for water vapor:

$$H = \tfrac{1}{2}\Sigma_k \mu^{\frac{1}{4}} p_k \mu^{-\frac{1}{2}} p_k \mu^{\frac{1}{4}} + V.$$

The potential V is written as a power series in the normal co-ordinates, and must necessarily be even in q_3.

$$
\begin{aligned}
V = \ &\tfrac{1}{2}(\lambda_1 q_1^2 + \lambda_2 q_2^2 + \lambda_3 q_3^2) \\
&+ \tfrac{1}{3}(a_1 q_1^3 + a_2 q_2^3 + a_3 q_1^2 q_2 + a_4 q_1 q_2^2 + a_5 q_1 q_3^2 + a_6 q_2 q_3^2) \\
&+ \tfrac{1}{4}(b_1 q_1^4 + b_2 q_2^4 + b_3 q_3^4 + b_4 q_1^2 q_2^2 + b_5 q_1^2 q_3^2 + b_6 q_2^2 q_3^2).
\end{aligned}
$$

To obtain the expression for V in terms of the dimensionless variables x_i the following substitutions are made. Since

$$x_i = 2\pi\sqrt{\frac{\omega_i c}{h}}\, q_i$$

we write

$$q_i^2 = \frac{h}{4\pi^2 \omega_i c}\, x_i^2 \; ; \qquad \lambda_i = 4\pi^2 \omega_i^2 c; \qquad a_i = \frac{hc}{2}\left[\frac{1}{2\pi}\sqrt{\frac{h}{\omega_i c}}\right]^3 \alpha_i$$

and

$$b_i = \frac{hc}{2}\left[\frac{1}{16\pi^4} \cdot \frac{h^2}{\omega_i^2 c^2}\right]\beta_i .$$

The ω_i's are the normal frequencies.

Therefore

$$
\begin{aligned}
\frac{V}{hc} = \ &\tfrac{1}{2}(\omega_1 x_1^2 + \omega_2 x_2^2 + \omega_3 x_3^2) \\
&+ (\alpha_1 x_1^3 + \alpha_2 x_2^3 + \alpha_3 x_1^2 x_2 + \alpha_4 x_1 x_2^2 + \alpha_5 x_1 x_3^2 + \alpha_6 x_2 x_3^2) \\
&+ (\beta_1 x_1^4 + \beta_2 x_2^4 + \beta_3 x_3^4 + \beta_4 x_1^2 x_2^2 + \beta_5 x_1^2 x_3^2 + \beta_6 x_2^2 x_3^2).
\end{aligned}
$$

The quadratic terms constitute the zero order potential, the cubic terms constitute the first order potential, and the quartic terms constitute the second order potential.

The zero order Hamiltonian equation is written

$$H^\circ = \tfrac{1}{2} \sum_{i=1}^{3} p_i^2 + \tfrac{1}{2}hc(\omega_1 x_1^2 + \omega_2 x_2^2 + \omega_3 x_3^2).$$

We replace p_i by

$$\frac{h}{2\pi i} \frac{\partial}{\partial q_i},$$

which is equal to

$$\frac{h}{i} \sqrt{\frac{\omega_i c}{h}} \frac{\partial}{\partial x_i}$$

since

$$\frac{dx_i}{dq_i} = 2\pi \sqrt{\frac{\omega_i c}{h}};$$

p_i^2 is replaced by

$$- h\omega_i c \frac{\partial^2}{\partial x_i^2}$$

and is then allowed to operate on Ψ. Remembering that $H\Psi = W\Psi$ we see that the equation may be written

$$\omega_1 \frac{\partial^2\Psi}{\partial x_1^2} + \omega_2 \frac{\partial^2\Psi}{\partial x_2^2} + \omega_3 \frac{\partial^2\Psi}{\partial x_3^2} + \left(\frac{2W}{hc} - \omega_1 x_1^2 - \omega_2 x_2^2 - \omega_3 x_3^2\right)\Psi = 0$$

If $\Psi = \Psi_1(x_1). \ \Psi_2(x_2). \ \Psi_3(x_3)$ and $W = W_1 + W_2 + W_3$ we have three separable equations of the form

$$\frac{d^2\Psi_i}{dx_i^2} + \left(\frac{2W_i}{hc\,\omega_i} - x_i^2\right)\Psi_i = 0 \qquad i = 1, 2, 3$$

The solution of the equation is

$$\Psi_i = N_i e^{-\frac{x_i^2}{2}} H_{v_i}(x_i),$$

where

$$N_i = \left[\frac{1}{\pi^{\frac{1}{2}} 2^{v_i} v_i!}\right]^{\frac{1}{2}}$$

and

$$W_i = hc(v_i + \tfrac{1}{2})\omega_i.$$

The zero order wave function is given by

$$\Psi = N e^{-\frac{x_1^2}{2}} e^{-\frac{x_2^2}{2}} e^{-\frac{x_3^2}{2}} H_{v_1}(x_1) H_{v_2}(x_2) H_{v_3}(x_3),$$

with

$$N = \left[\frac{1}{\pi^{\frac{3}{2}} 2^{v_1 + v_2 + v_3} v_1! v_2! v_3!}\right]^{\frac{1}{2}}$$

The zero order energy W° is written

$$W^\circ = hc[(v_1 + \tfrac{1}{2})\omega_1 + (v_2 + \tfrac{1}{2})\omega_2 + (v_3 + \tfrac{1}{2})\omega_3].$$

$\dfrac{W^\circ}{hc}$ is usually replaced by G°. Therefore,

$$G^\circ = \tfrac{1}{2}(\omega_1 + \omega_2 + \omega_3) + v_1\omega_1 + v_2\omega_2 + v_3\omega_3.$$

The first order correction to the energy is given by

$$W' = \int \Psi^* H' \Psi d\tau = \int H' \Psi^2 d\tau,$$

where

$$H' = hc[\alpha_1 x_1^3 + \alpha_2 x_2^3 + \alpha_3 x_1^2 x_2 + \alpha_4 x_1 x_2^2 + \alpha_5 x_1 x_3^2 + \alpha_6 x_2 x_3^2].$$

Therefore

$$G' = N^2 \int (\alpha_1 x_1^3 + \ldots + \alpha_6 x_2 x_3^2)\ e^{-x_1^2} e^{-x_2^2} e^{-x_3^2}\ H_{v_1}^2 H_{v_2}^2 H_{v_3}^2 dx_1 dx_2 dx_3$$

Upon integrating, each term is found to be equal to zero, hence the first order correction to the energy is zero.

The second order correction to the energy is given by

$$W'' = \int H'' \Psi^2 d\tau + \sum_{a \neq b} \frac{\left\{ \int \Psi_a H' \Psi_b d\tau \right\}^2}{W_a^o - W_b^o},$$

Ψ_a is the wave function for the state (v_1, v_2, v_3).

Ψ_b is the wave function for the state (u_1, u_2, u_3).

$$H'' = hc[\beta_1 x_1^4 + \beta_2 x_2^4 + \beta_3 x_3^4 + \beta_4 x_1^2 x_2^2 + \beta_5 x_1^2 x_3^2 + \beta_6 x_2^2 x_3^2].$$

The first term when integrated gives

$$\frac{1}{hc} \int H'' \Psi^2 d\tau = \frac{3}{2}(\beta_1 v_1^2 + \beta_2 v_2^2 + \beta_3 v_3^2) + \frac{v_1}{2}(3\beta_1 + \beta_4 + \beta_5)$$

$$+ \frac{v_2}{2}(3\beta_2 + \beta_4 + \beta_6) + \frac{v_3}{2}(3\beta_3 + \beta_5 + \beta_6) + \beta_4 v_1 v_2$$

$$+ \beta_5 v_1 v_3 + \beta_6 v_2 v_3 + \frac{3}{4}(\beta_1 + \beta_2 + \beta_3) + \frac{1}{4}(\beta_4 + \beta_5 + \beta_6).$$

The second term is expanded into the expression

$$\sum_{a \neq b} \frac{hc \left\{ \int \Psi_a \alpha_1 x_1^3 \Psi_b d\tau + \int \Psi_a \alpha_2 x_2^3 \Psi_b d\tau + \ldots + \int \Psi_a \alpha_6 x_2 x_3^2 \Psi_b d\tau \right\}^2}{W_a^o - W_b^o}.$$

Each integral is considered separately and the values of (u_1, u_2, u_3) which give a nonzero result are found. Let I_1 represent $\int \Psi_a \alpha_1 x_1^3 \Psi_b d\tau$, and I_2 represents $\int \Psi_a \alpha_2 x_2^3 \Psi_b d\tau$. Each integral is found to have nonzero values for four sets of u-values. I_3, I_4, I_5, and I_6 representing the terms in α_3, α_4, α_5, and α_6 respectively, each are found to have nonzero values for six sets of u-values.

The Γ's for the same values of u_1, u_2, u_3 must be collected and substituted into $\sum\limits_{a \neq b} \dfrac{\left\{\int \Psi_a H' \Psi_b d\tau\right\}^2}{W_a^0 - W_b^0}$ which gives rise to 24 terms. After squaring and collecting, the terms with equal powers of the v's are collected. The result added to the term $\int H'' \Psi^2 d\tau$ gives the second order correction to the energy.

The complete expression for the energy may be written

$$G = G_o + X_1 v_1 + X_2 v_2 + X_3 v_3 + X_{11} v_1^2 + X_{22} v_2^2$$
$$+ X_{33} v_3^2 + X_{12} v_1 v_2 + X_{13} v_1 v_3 + X_{23} v_2 v_3$$

G_o is the summation of all constant terms: X_i, X_{ii}, and X_{ik} have the same form as for water vapor (1, p. 132).

The Resonance Interaction in Doublets

The consideration of the resonance interaction between the states (v_1, v_2, v_3) and $(v_1 - 2, v_2, v_3 + 2)$ does not affect the calculation of the constants. The determinant containing the interacting states for a doublet is

$$\begin{vmatrix} H_{kk} - G, & H_{kJ} \\ H_{Jk}, & H_{JJ} - G \end{vmatrix} = 0.$$

k refers to the state (v_1, v_2, v_3) and J to the state $(v_1 - 2, v_2, v_3 + 2)$.

$$H_{kk} = \int \Psi_k^* \overline{H} \Psi_k d\tau \qquad \text{and} \qquad H_{kJ} = H_{Jk} = \int \Psi_k^* \overline{H} \Psi_J d\tau.$$

$\overline{H}$ is the total Hamiltonian, and to a second order approximation is given by

$$\overline{H} = H^\circ + \lambda H' + \lambda^2 H''.$$

To the same order of approximation Ψ_k is given by

$$\Psi_k = \Psi_k^\circ + \lambda \Psi_k' = \Psi_k^\circ + \lambda \sum\limits_{m \neq k} \frac{\int \Psi_m^{\circ *} H' \Psi_k^\circ d\tau}{W_k^\circ - W_m} \cdot \Psi_m^\circ \cdot$$

Similarly

$$\Psi_J = \Psi_J^\circ + \lambda \sum\limits_{P \neq J} \frac{\int \Psi_P^{\circ *} H' \Psi_J^\circ d\tau}{W_J^\circ - W_P^\circ} \cdot \Psi_P^\circ \cdot$$

The expression for H_{kJ} is given by

$$\int [\Psi_k^{\circ *} + \lambda \sum\limits_{m \neq k} A_m \Psi_m^{\circ *}] [H^\circ + \lambda H' + \lambda^2 H''] [\Psi_J^\circ + \lambda \sum\limits_{P \neq J} A_P \Psi_P^\circ] d\tau.$$

In the expansion, terms are taken to only a second order approximation.

$$H_{kJ} = \int \Psi_k^{\circ *} H'' \Psi_J^\circ d\tau + \sum\limits_{m \neq k} A_m \int \Psi_m^{\circ *} H' \Psi_J^\circ d\tau + \sum\limits_{P \neq J} A_P \int \Psi_k^{\circ *} H' \Psi_P^\circ d\tau.$$

The first term, given by ·

$$N_k N_J \int (\beta_1 x_1^4 + \ldots \dot{} + \beta_6 x_2^2 x_3^2) e^{-x_1^2} e^{-x_2^2} e^{-x_3^2} H_{v_1} H_{v_1-2} H_{v_2} H_{v_3} H_{v_3+2} dx_1 dx_2 dx_3 ,$$

upon integration reduces to

$$\tfrac{1}{4}\beta_5 [v_1(v_1 - 1) \, (v_3 + 1) \, (v_3 + 2)]^{\frac{1}{2}} .$$

The second term consists of two factors, each depending on H'.

$$\sum_{m \neq k} A_m \int \Psi_m^{0*} H' \Psi_j^0 d\tau = \sum_{m \neq k} \frac{\int \Psi_m^{0*} H' \Psi_k^0 d\tau}{W_k^0 - W_m^0} \cdot \int \Psi_m^{0*} H' \Psi_j^0 d\tau .$$

The terms in each factor having the same v-values give rise to nonzero products. The resonance between ν_1 and ν_3 is due to the near equality of the fundamental frequencies ω_1 and ω_3. These frequencies may be assumed to be equal in a second order approximation. When ω_3 is replaced by ω_1, the expression for

$$\sum_{m \neq k} A_m \int \Psi_m^{0*} H' \Psi_j^0 d\tau$$

becomes

$$\left[v_1(v_1 - 1) \, (v_3 + 1) \, (v_3 + 2) \right]^{\frac{1}{2}}$$

$$\left[-\frac{1}{2} \frac{\alpha_5^2}{\omega_1} + \frac{1}{4} \frac{\alpha_1 \alpha_5}{\omega_1} + \frac{1}{8} \frac{\alpha_3 \alpha_6}{(2\omega_1 - \omega_2)} - \frac{1}{8} \frac{\alpha_3 \alpha_6}{(2\omega_1 + \omega_2)} \right] .$$

The third term,

$$\sum_{P \neq J} A_P \int \Psi_k^{0*} H' \Psi_P^0 d\tau,$$

gives the same result. Thus

$$H_{kJ} = \left[v_1(v_1 - 1) \, (v_3 + 1) \, (v_3 + 2) \right]^{\frac{1}{2}}$$

$$\left[\frac{1}{4} \beta_5 - \frac{\alpha_5^2}{\omega_1} + \frac{1}{2} \frac{\alpha_1 \alpha_5}{\omega_1} + \frac{1}{4} \frac{\alpha_3 \alpha_6}{(2\omega_1 - \omega_2)} - \frac{1}{4} \frac{\alpha_3 \alpha_6}{(2\omega_1 + \omega_2)} \right]$$

$$= \tfrac{1}{2} \gamma \left[v_1(v_1 - 1) \, (v_3 + 1) \, (v_3 + 2) \right]^{\frac{1}{2}} ,$$

where the interaction constant γ is given by

$$\gamma = \frac{1}{2} \beta_5 - \frac{2\alpha_5^2}{\omega_1} + \frac{\alpha_1 \alpha_5}{\omega_1} + \frac{\alpha_3 \alpha_6}{2(2\omega_1 - \omega_2)} - \frac{\alpha_3 \alpha_6}{2(2\omega_1 + \omega_2)} .$$

This is the expression given by Darling and Denn$\hat{i}$son (1, p. 133) except for a factor of 2 in the α-terms (which however does not affect the following calculations).

Then to obtain the energy of the components of a doublet, the following determinantal equation must be solved

$$
\begin{vmatrix} H_{kk} - G, & \dfrac{b}{hc} \\[2mm] \dfrac{b}{hc}, & H_{JJ} - G \end{vmatrix} = 0,
$$

where

$$
b = hcH_{kJ} = \tfrac{1}{2}hc\gamma[v_1(v_1 - 1)\,(v_3 + 1)\,(v_3 + 2)]^{\frac{1}{2}}
$$

This may be written

$$
G^2 - G(H_{kk} + H_{JJ}) - \left(\frac{b}{hc}\right)^2 + H_{kk}H_{JJ} = 0.
$$

The solution is

$$
G \qquad (H_{kk} + H_{JJ}) \pm \sqrt{\left(H_{kk} - H_{JJ}\right)^2 + \left(\frac{2b}{hc}\right)^2}
$$

The roots are thus the average of the unperturbed levels, plus or minus—one-half the square root of (the square of the difference of the unperturbed levels, plus the square of the separation due to the interaction).

The Resonance Interaction in Triplets

To obtain the roots of a triplet (v_1, v_2, v_3), $(v_1 - 2, v_2, v_3 + 2)$, $(v_1 - 4, v_2, v_3 + 4)$ the determinant containing the interacting states must be solved.

$$
\begin{vmatrix} H_{kk} - G, & H_{kJ}, & H_{kR} \\[2mm] H_{Jk}, & H_{JJ} - G, & H_{JR} \\[2mm] H_{Rk}, & H_{RJ}, & H_{RR} - G \end{vmatrix} = 0
$$

k refers to the state (v_1, v_2, v_3), J to the state $(v_1 - 2, v_2, v_3 + 2)$, and R to the state $(v_1 - 4, v_2, v_3 + 4)$. The expression for $H_{kJ} = H_{Jk}$ has already been found. A similar calculation gives an expression for $H_{JR} = H_{RJ}$.

$$
H_{JR} = \int \Psi_J^{\circ*}H''\Psi_R^{\circ}d\tau + \sum_{m \neq J} A_m \int \Psi_m^{\circ*}H'\Psi_R^{\circ}d\tau + \sum_{P \neq R} A_P \int \Psi_J^{\circ*}H'\Psi_P^{\circ}d\tau .
$$

Ψ_J° and Ψ_R° have the usual form, and A_m and A_P are given by

$$
A_m = \frac{\int \Psi_m^{\circ*}H'\Psi_J^{\circ}d\tau}{W_J^{\circ} - W_m^{\circ}} \; ; \qquad A_P = \frac{\int \Psi_P^{\circ*}H'\Psi_R^{\circ}d\tau}{W_R^{\circ} - W_P^{\circ}}
$$

The calculation is exactly similar to that for doublets, with v_1 replaced by $v_1 - 2$ and v_3 replaced by $v_3 + 2$.

Thus

$$H_{JR} = H_{RJ} = \tfrac{1}{2}\gamma[(v_1 - 2)(v_1 - 3)(v_3 + 3)(v_3 + 4)]^{\frac{1}{2}}.$$

The expression for H_{kR} is given by

$$H_{kR} = \int \Psi_k^{o*} H'' \Psi_R^o d\tau + \sum_{m \neq k} A_m \int \Psi_m^{o*} H' \Psi_R^o d\tau + \sum_{P \neq R} A_P \int \Psi_k^{o*} H' \Psi_P^o d\tau .$$

All terms when integrated are equal to zero. Hence $H_{kR} = H_{Rk} = 0$. The determinantal equations may be written

$$
\begin{array}{ccc}
H_{kk} - G, & \dfrac{b}{hc}, & 0 \\[2mm]
\dfrac{b}{hc}, & H_{JJ} - G, & \dfrac{a}{hc} \qquad 0 \\[2mm]
0, & \dfrac{a}{hc}, & H_{RR} - G
\end{array}
$$

and

$$b = \tfrac{1}{2}hc\gamma[v_1(v_1 - 1)(v_3 + 1)(v_3 + 2)]^{\frac{1}{2}}$$

$$a = \tfrac{1}{2}hc\gamma[(v_1 - 2)(v_1 - 3)(v_3 + 3)(v_3 + 4)]^{\frac{1}{2}}.$$

Thus

$$G^3 - [H_{kk} + H_{JJ} + H_{RR}]G^2$$

$$+ \left[H_{kk}H_{JJ} + H_{JJ}H_{RR} + H_{RR}H_{kk} - \left(\frac{a}{hc}\right)^2 - \left(\frac{b}{hc}\right)^2 \right]G$$

$$- H_{kk}H_{JJ}H_{RR} + \left(\frac{b}{hc}\right)^2 H_{RR} + \left(\frac{a}{hc}\right)^2 H_{kk} = 0.$$

Knowing the constants and the v-values for any triplet, a cubic equation may be set up and the roots found by approximation.

The Numerical Results

Seventeen bands of acetylene whose positions are known are shown in Table I. Nine of the bands were used to calculate the force constants, X_i and X_{ik}, taking no account of the resonance interaction. These are marked

TABLE I

v_1	v_2	v_3	Position, cm.$^{-1}$	v_1	v_2	v_3	Position, cm.$^{-1}$
0	1	0	1973.8*	0	1	3	11600.1*
0	0	1	3287.0*	2	1	1	11782.9*
1	0	0	3373.7*	1	0	3	12675.7
1	1	1	8512.1*	0	2	3	13532.4
0	3	1	9151.7*	1	1	3	14617.0
0	1	1	5250	0	0	5	15600.2
1	0	1	6500	0	1	5	17518.8
0	0	3	9639.8*	1	0	5	18430.2
2	0	1	9835.1*				

with an asterisk. The two with the v-values of (011) and (101) were not used in the calculations as these were measured with very small dispersion and thus their positions are not well known.

The values of the constants were thus found to be,

$X_1 = 3366.2$ cm.$^{-1}$ $X_{11} =$ 7.5 cm.$^{-1}$ $X_{12} =$ -10.75 cm.$^{-1}$

$X_2 = 1981.0$ " $X_{22} =$ -7.2 " $X_{13} = -107.15$ "

$X_3 = 3323.87$ " $X_{33} =$ -36.87 " $X_{23} =$ -4.5 "

It is evident that if the resonance interaction is considered an additional band will be needed to evaluate the X_i's and X_{ik}'s and γ, the interaction constant. The equations used are given below. For doublets, the general expression

$$G = \tfrac{1}{2}(H_{kk} + H_{JJ}) \pm \tfrac{1}{2}\sqrt{\left(H_{kk} - H_{JJ}\right)^2 + \left(\frac{2b}{hc}\right)^2}$$

was used to derive the equations.

v_1 v_2 v_3

0 1 0 $X_2 + X_{22} = 1973.8$ (1)

0 0 1 $X_3 + X_{33} = 3287.0$ (2)

1 0 0 $X_1 + X_{11} = 3373.7$ (3)

1 1 1 $X_1 + X_{11} + X_2 + X_{22} + X_3 + X_{33} + X_{12} + X_{13} + X_{23}$
$= 8512.1$ (4)

0 3 1 $3X_2 + 9X_{22} + X_3 + X_{33} + 3X_{23} = 9151.7$ (5)

2 0 1 $X_1 + 2X_{11} + 2X_3 + 5X_{33} + X_{13}$
$+ \tfrac{1}{2}\sqrt{(2X_1 + 4X_{11} - 2X_3 - 8X_{33} + 2X_{13})^2 + 12\gamma^2}$
$= 9835.1$ (6)

0 0 3 $X_1 + 2X_{11} + 2X_3 + 5X_{33} + X_{13}$
$- \tfrac{1}{2}\sqrt{(2X_1 + 4X_{11} - 2X_3 - 8X_{33} + 2X_{13})^2 + 12\gamma^2}$
$= 9639.8$ (7)

2 1 1 $X_1 + 2X_{11} + X_2 + X_{22} + 2X_3 + 5X_{33} + X_{12} + X_{13} + 2X_{23}$
$+ \tfrac{1}{2}\sqrt{(2X_1 + 4X_{11} - 2X_3 - 8X_{33} + 2X_{12} + 2X_{13} - 2X_{23})^2 + 12\gamma^2}$
$= 11782.9$ (8)

0 1 3 $X_1 + 2X_{11} + X_2 + X_{22} + 2X_3 + 5X_{33} + X_{12} + X_{13} + 2X_{23}$
$- \tfrac{1}{2}\sqrt{(2X_1 + 4X_{11} - 2X_3 - 8X_{33} + 2X_{12} + 2X_{13} - 2X_{23})^2 + 12\gamma^2}$
$= 11600.1$ (9)

1 0 3 $2X_1 + 5X_{11} + 2X_3 + 5X_{33} + 3X_{13}$
$- \tfrac{1}{2}\sqrt{(2X_1 + 8X_{11} - 2X_3 - 8X_{33})^2 + 36\gamma^2} = 12675.7$ (10)

Some difficulty was encountered in the solution of these 10 equations. The first nine can be reduced to the following two equations,

$$(-12X_{33} - 247.1)^2 + 12\gamma^2 = (195.3)^2.$$
$$[-12X_{33} - 247.1 - 2(-19.75 - 3X_{23})]^2 + 12\gamma^2 = (182.8)^2$$

These can most easily be solved by assigning an arbitrary value to one of the three unknowns. The value of X_{23} was varied, and the constants were determined each time and substituted into Equation (10) to find the best check with the observed position of this band. When $X_{23} = +3$ the calculated position of the band is 12675.6 cm.$^{-1}$, the observed position is 12675.7 cm.$^{-1}$, so this value of X_{23} was used. The constants are now

$$X_1 = 3405.1 \text{ cm.}^{-1} \qquad X_{11} = -31.4 \text{ cm.}^{-1} \qquad X_{12} = -25.75 \text{ cm.}^{-1}$$
$$X_2 = 1984.75 \text{ ``} \qquad X_{22} = -10.95 \text{ ``} \qquad X_{13} = -99.65 \text{ ``}$$
$$X_3 = 3313.4 \text{ ``} \qquad X_{33} = -26.4 \text{ ``} \qquad X_{23} = +3.0 \text{ ``}$$
$$12\gamma^2 = 33267 \qquad\qquad |\gamma| = 52.65$$

When the positions of the bands (011), (101), (023), and (113) are calculated, the values are found to agree favorably with the observed positions.

In the spectrum of acetylene there are also found three bands each of which is one root of a triplet. They are the bands (005), (015), and (105) found at 15600.2, 17518.8, and 18430.2 cm.$^{-1}$ respectively.

The determinant for each triplet was set up and solved. The results are given below.

The triplet (401), (203), and (005) has the determinant

$$\begin{vmatrix} H_{kk} - G, & 3\sqrt{2}.\gamma & 0 \\ 3\sqrt{2}.\gamma & H_{JJ} - G, & \sqrt{10}.\gamma \\ 0, & \sqrt{10}.\gamma & H_{RR} - G \end{vmatrix} = 0$$

$$H_{kk} = 4X_1 + 16X_{11} + X_3 + X_{33} + 4X_{13} = 16006.4$$
$$H_{JJ} = 2X_1 + 4X_{11} + 3X_3 + 9X_{33} + 6X_{13} = 15789.3$$
$$H_{RR} = 5X_3 + 25X_{33} = 15907.0$$

The roots were found to be 15633.8, 15841.51, and 16223.42 cm.$^{-1}$

For the triplet (411), (213), (015) the determinant has the same form, but the H's are now

$$H_{kk} = 4X_1 + 16X_{11} + X_2 + X_{22} + X_3 + X_{33} + 4X_{13} + 4X_{12} + X_{23} = 17880.2$$
$$H_{JJ} = 2X_1 + 4X_{11} + X_2 + X_{22} + 3X_3 + 9X_{33} + 2X_{12} + 6X_{13} + 3X_{23} = 17720.6$$
$$H_{RR} = X_2 + X_{22} + 5X_3 + 25X_{33} + 5X_{23} = 17895.8.$$

The roots are 17516.78, 17867.2, and 18097.23 cm.$^{-1}$

The determinant for the third triplet, (501), (303), (105), is

$$\begin{vmatrix} H_{kk} - G, & \sqrt{30}.\gamma & 0 \\ \sqrt{30}.\gamma & H_{JJ} - G, & \sqrt{30}.\gamma \\ 0, & \sqrt{30}.\gamma & H_{RR} - G \end{vmatrix} = 0$$

$$H_{kk} = 5X_1 + 25X_{11} + X_3 + X_{33} + 5X_{13} = 19029.25$$

$$H_{JJ} = 3X_1 + 9X_{11} + X_3 + 9X_{33} + 9X_{13} = 18738.45$$

$$H_{RR} = X_1 + X_{11} + 5X_3 + 25X_{33} + 5X_{13} = 18782.45.$$

The roots are 18370.73, 18926.05, and 19235.19 cm.$^{-1}$

There is no way of distinguishing between the v-values for the observed band of each triplet, since the perturbation makes each level a mixture of all three unperturbed levels.   One unperturbed level may be said to predominate in each root.

Using the values of the constants found in this paper, the positions of 10 bands not yet observed were predicted.   These values are shown in Table II,

TABLE II

A SUMMARY OF THE RESULTS

v_1	v_2	v_3	Observed position, cm.$^{-1}$	Calculated values	
				No resonance interaction	With resonance interaction
0	1	0	1973.8		
0	0	1	3287.0		
1	0	0	3373.7		
1	1	1	8512.1		
0	3	1	9151.7		
0	1	1	5250	5256.3	5263.8
1	0	1	6500	6553.65	6561.05
0	0	3	9639.8		
2	0	1	9835.1		
0	1	3	11600.1		
2	1	1	11782.9		
1	0	3	12675.7	12692.03	12675.6
3	0	1	—		13022.5
0	2	3	13532.4	13545.98	13530.7
2	2	1	—		13716.6
1	1	3	14617.0	14641.58	14613.65
3	1	1	—		14941.05
1	1	2	—		11611.7
3	1	0	—		11867.2
1	0	3	—		9152.15
1	3	1	—		12348.5
1	1	0	—		5321.75
0	3	3	—		15429.2
2	3	1	—		15638.6
4	0	1	⎫	16443.2	⎫
2	0	3	⎬ 15600.2	15759.28	⎬ 15633.8
0	0	5	⎭	15697.6	⎭
4	1	1	⎫	18369.5	⎫
2	1	3	⎬ 17518.8	17698.08	⎬ 17516.78
0	1	5	⎭	17648.9	⎭
5	0	1	⎫	19769.75	⎫
3	0	3	⎬ 18430.2	18841.53	⎬ 18370.73
1	0	5	⎭	18535.55	⎭

which gives a summary of all the results.   The observed positions of all bands, including the three belonging to triplets, are shown in the second column.   In the third column the values are calculated using the constants

found when no resonance interaction is considered. For each of the three triplets, three values are recorded corresponding to the three sets of v-values. In the fourth column the values are calculated using the constants found when the resonance interaction is considered. For the triplets only the one root closest to the observed value is recorded, since no one root can be identified wholly with any one set of v-values.

By comparing the calculated values with the observed values it is quite evident that the agreement for the fourth column is much more marked than for the third column. Thus the results justify the assumption that the previous discrepancies in the work on acetylene were due to the mutual perturbation of the levels $(v_1, v_2, v_3, v_4, v_5)$ and $(v_1 - 2, v_2, v_3 + 2, v_4, v_5)$. That the perturbation consideration may be carried on to triplets is a further justification of the assumption.

Acknowledgment

References

1. DARLING, B. T. and DENNISON, D. M. Phys. Rev. 57 : 128. 1940.
2. FUNKE, G. W. and HERZBERG, G. Phys. Rev. 49 : 100. 1936.
3. GLOCKLER, G. and MORRELL, C. E. J. Chem. Phys. 4 : 15. 1936.
4. HERZBERG, G. Infrared and Raman spectra of polyatomic molecules. Vol. 2 of Molecular spectra and molecular structure. D. Van Nostrand Company, Inc., New York. 1945.
5. HERZBERG, G. and SPINKS, J. W. T. Z. Physik, 91 : 386. 1934.
6. LEVIN, A. and MEYER, C. F. J. Optical Soc. Am. 16 : 137. 1928.
7. MECKE, R. and ZIEGLER, R. Z. Physik, 101 : 405. 1936.
8. WU, T. Vibrational spectra and structure of polyatomic molecules. National University of Peking, Peiping, China. G. E. Stechert & Company, New York, London. 1939.

SENSITIVITY AND EXPOSURE GRAPHS FOR RADIUM RADIOGRAPHY[1]

By H. E. JOHNS AND C. GARRETT[2]

Abstract

The radiography of steel by the use of the gamma rays from radium is discussed. The thickness of lead front screen which yields the maximum intensifying effect is determined and the action of the front screen discussed. Sensitivity curves are obtained using a slotted wedge steel penetrameter for a number of the commonly used types of X-ray film. It is shown that the thickness of the lead front screen which produces the maximum density on the film is not necessarily the most useful thickness for gamma radiography. The most useful thickness is determined from penetrameter sensitivity curves. The importance of these sensitivity curves for routine gamma ray testing is indicated.

Introduction

Several methods have been used in the past for the selection of the proper exposure factor required to give a suitable radiograph of a casting. The method developed in the National Research Council by Laurence, Ball, and Archibald (1) has been found very satisfactory for X-rays. The basis of the method is a wedge penetrameter (see Fig. 3) in which slots have been cut whose depth at any point is a constant percentage of the thickness of the wedge. Slots of depth 1, 2, 3, 5, and 10% are usually sufficient for the adequate testing of a film. This wedge penetrameter is then X-rayed for a series of exposures and the films developed in a standard way (2). Examinations of such films will reveal that the 2% slot is observable for a certain range of thicknesses of the wedge and for a certain range of exposure factors. This will be discussed in detail later.

This method, which has been developed primarily for use in X-ray work, has been extended by the authors to the field of gamma radiography. For gamma radiography Nodwell and Morrison (2) have measured the densities obtainable with a selection of films for different exposure factors. Although their results are of considerable use and interest, the authors feel that differential sensitivity (i.e., a knowledge that a flaw of a given percentage thickness will be made visible) is of much greater importance. It is customary in taking radiographs to use a lead front screen and a thicker lead back screen. These lead screens produce a certain amount of intensification (i.e., increase in density for a given exposure factor) and also reduce the blurring effect of scattered radiation. It is found that a certain thickness of lead front screen produces the maximum density for a given thickness of casting. It does not follow that this "optimum" thickness will give also the greatest differential sensitivity. This latter question can be answered by the use of the wedge penetrameter. The intensification of the front screen will be discussed first and then the sensitivity curves.

The Optimum Thickness of Lead Front Screens

In what follows in this section the "optimum" thickness of front screen will be defined as the thickness which produces the maximum density on the film. Later we will see that this is not the sole criterion for the choice of a front screen.

To find this "optimum" thickness a series of steel blocks from 0.5 to 3.0 in. thick were radiographed using a step wedge front screen made up of sheets of lead having thicknesses of 0.001, 0.002, 0.003, 0.006, 0.012, 0.018, 0.024, and 0.030 in. in immediate contact with the film and separated from the steel by the standard Kodak cardboard film holder. A series of radiographs with different exposure factors was taken using "No Screen" film backed by 0.030 in. of lead. The radium was held in a brass cup of wall thickness 0.125 in. The films were developed in Kodalk for five minutes at 20° C. and standard agitation was carried out (2). Densities were measured on a Marshall densitometer and are plotted against exposure factor (mgm. × min. per in.²) as in Fig. 1. (Film of density 1.0 will transmit 0.1 of the incident light; film of density 2.0 will transmit 0.01 of the incident light.)
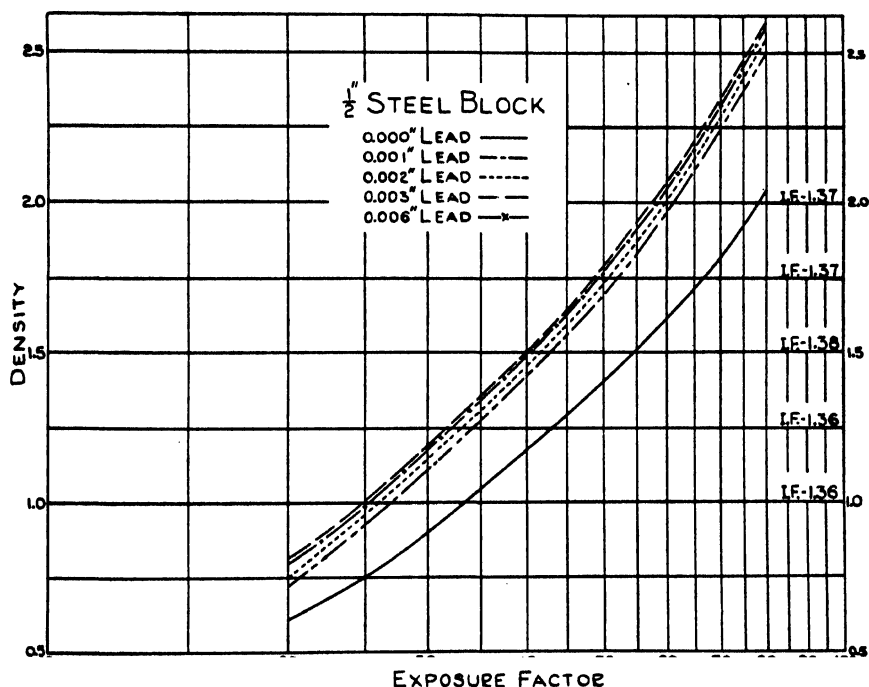
FIG. 1. *Density versus exposure factor for "No Screen" film, developed in "Kodalk" at 20° C. for five minutes with standard agitation. Radium filter, 0.125 in. brass. Back screen, 0.030 in. of lead in contact with the film. Front lead screen as indicated.*

The intensification factor due to the front screen is defined as the ratio of two exposure factors, the first made with no lead front screen and the second made with a lead front screen, in such a way as to produce an equal density on

the film. For example from Fig. 1 we see that density 1.0 requires an exposure factor of 34.0 when no lead front screen is used and 25.0 when a 0.003 in. lead front screen is used. The intensification factor is therefore 1.36. For densities 1.25, 1.50, 1.75, and 2.00 the intensification factors are 1.36, 1.38, 1.37, and 1.37 respectively, giving an average of 1.37. In a similar way the intensification factors for other thicknesses of the lead front screens and other thicknesses of steel block were obtained. These are shown graphically in Fig. 2. It will be seen that as the thickness of the steel block is increased the
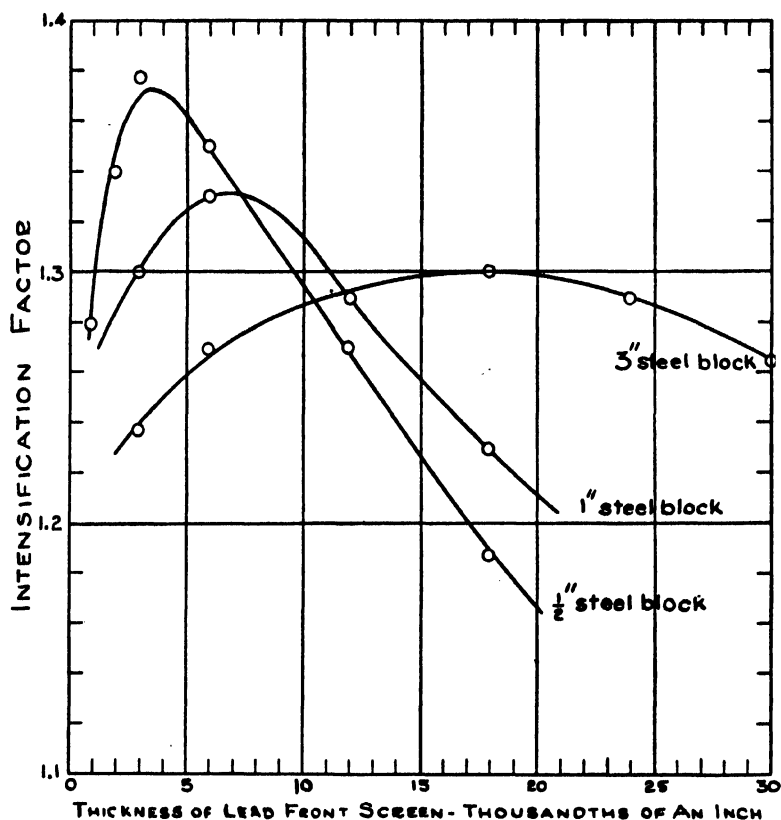
· FIG. 2. *Intensification factor versus thickness of lead front screen for steel, 1/2, 1, and 3 in. thick.*

"optimum" thickness of lead front screen also increases. At the same time the actual value of the maximum intensification obtainable decreases slightly. If the optimum thickness of lead front screen is plotted against the thickness of steel block a linear relation will result. For example the optimum thicknesses of lead front screens are 0.003, 0.006, 0.012, 0.018 in. for steel of thicknesses 0.5, 1.0, 2.0, and 3.0 in. respectively.

To give further information concerning the actual action of the lead intensifying screen the following experiments were carried out using a 0.50 in. steel block and "No Screen" film. Results similar to those shown in Fig. 1

were obtained for a number of different arrangements of steel, lead, Kodak cardboard film holder, and film as indicated below. From these it was found that density 1.50 was obtained for the exposure factors given below.

(a) The steel was separated from the film by the cardboard film holder. Exposure factor, *54.8*.

(b) The steel was placed in *direct* contact with the film. Exposure factor, *49.8*

(c) The steel was placed immediately against the lead front screen (0.003 in. lead) which was in contact with the film. Exposure factor, *40.2*.

(d) The steel was placed on the film holder and the lead front screen (0.003 in. lead) was in direct contact with the film inside the film holder. Exposure factor, *40.0*.

The exposure factors for (c) and (d) are essentially the same, as one would expect owing to the negligible absorption of the gamma rays in the cardboard film holder. (b) gives an intensification of 1.10 over (a). This means that a steel front screen would give an intensification of approximately 1.10. (c) and (d) give an intensification of 1.36 over (a).

The reason for this general behavior of lead front screens can be seen from the following considerations. At the lower face of the steel block there is equilibrium between the electrons (photoelectrons and Compton electrons) and the electromagnetic radiation (gamma rays, Compton scattered radiation, and fluorescent radiation) all characteristic of steel. The cardboard film holder will absorb for practical purposes all the electrons from the steel and in their place will appear the corresponding electrons from cardboard. If a sheet of lead is inserted between the film and cardboard whose thickness is equal to the maximum range R of the electrons, then all the electrons from the cardboard will be stopped and in their place will appear the electrons originating in the lead. Since gamma rays from Radium C eject essentially the same number of Compton electrons from equal masses of cardboard and lead, the intensification must be due mainly to photoelectrons. The photoelectric absorption by lead is greater than by cardboard, so more photoelectrons will be produced in the lead foil than were stopped, giving a net intensifying action. When the steel block is placed in *direct* contact with the film there is an increase in density over that when the cardboard casette is used but a decrease in density as compared with the use of the cardboard casette and the lead front screen. This result is of course due to the photoelectric absorption being greater in lead than in steel. If a lead casting were being radiographed no increase in density would result by the use of a lead front screen if the casting could be placed in direct contact with the film.

If the lead front screen is thicker than R the electrons produced at the front of the screen will be stopped before they reach the film anyway, and only those produced within the range R of the back of the intensifying screen can

affect the film. The front part of the foil has merely served to reduce the intensity of the gamma rays, so a reduction in the intensifying action results. This general picture serves to explain also why a thicker front screen is needed for thicker pieces of steel. As the steel thickness is increased, the softer components from the radium are filtered out and the average range of the photo-electrons produced increases. The maxima in Fig. 2 are however broad because of the inhomogeneity of the gamma rays from radium, and because the electrons are not all ejected in the forward direction, nor from the same depth.

Penetrameter Sensitivities of Different Types of X-Ray Films

In the last section the thickness of lead front screen which produced the maximum density was considered as "optimum", but one is primarily interested in the penetrameter sensitivity or differential sensitivity (i.e., a knowledge that a flaw of a given percentage thickness will be made visible). This was obtained by the method described by Laurence, Ball, and Archibald (1) for several types of X-ray films and the variation of this sensitivity with the thickness of the lead front screen measured. All films were developed in Kodalk at 20° C. for five minutes and given standard agitation (2). The radiation from the radium was filtered by 0.125 in. of brass in all cases. The films were viewed using the methods outlined in (1).

A steel wedge suitable for gamma radiography, 10 in. long, 4 in. wide, and of maximum thickness 4 in. was made and is illustrated in Fig. 3. When radiographs of such a wedge are taken using a distance from source to film of 24 in.

THE SLOTTED WEDGE PENETRAMETER
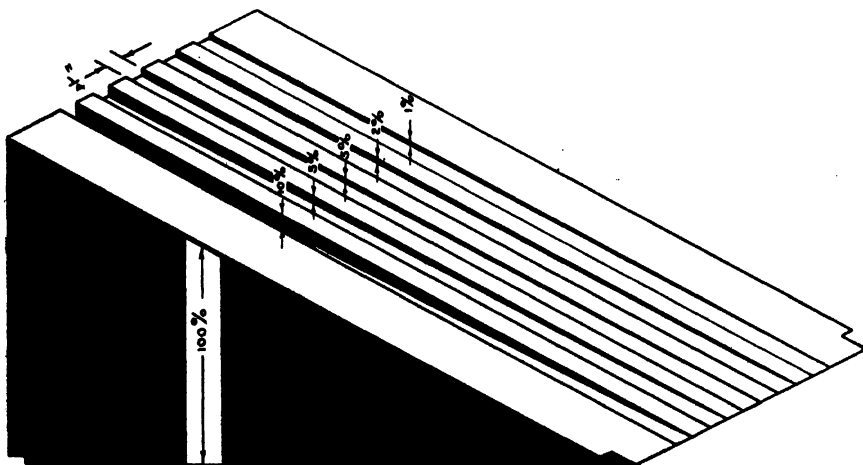
FIG. 3. *Slotted steel wedge penetrameter.*

certain errors related to the shortness of this distance arise. This is illustrated in Fig. 4. The wedge is made so that $EF/FG = PQ/QR$ but on the film the slot PQ' will appear on the wedge of thickness $Q'R'$ and $\dfrac{PQ'}{Q'R'} \neq \dfrac{PQ}{QR}$.
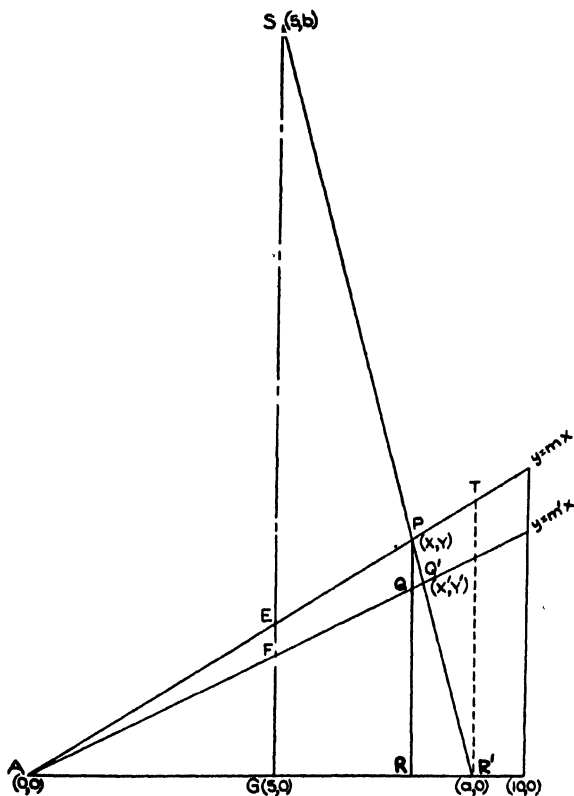
FIG. 4. *Diagram of steel penetrameter showing how distortion arises when short source to film distances are used.*

Hence for points along the film from A to R the effective percentage depth of the slot changes. Another error arises from the fact that the points along the film from A to R do not all receive the same exposure factor, since they are different distances from S. Corrections for these errors can be made easily.

In Fig. 5, the penetrameter sensitivity for "No Screen" film with 0.015 in. lead front screen and 0.030 in. lead back screen are shown both for the original measurements (solid lines) and when all corrections are made (dotted curves). The difference between these sets of curves is smaller than the probable error of the measurements so that for the other films no corrections of this kind were carried out. From Fig. 5 we see that under the ideal conditions obtainable with the penetrameter, the 1% slot was not visible but that the 2% slot was visible in steel of thickness greater than 0.6 in. For 1.0 in. the exposure

factor must lie between 100 and 300 in order to detect a 2% flaw. For 2.0 in. of steel the exposure factor should be somewhere in the range of 200 to 650. If a casting consisted of two thicknesses of 3.0 and 1.0 in. two exposures of
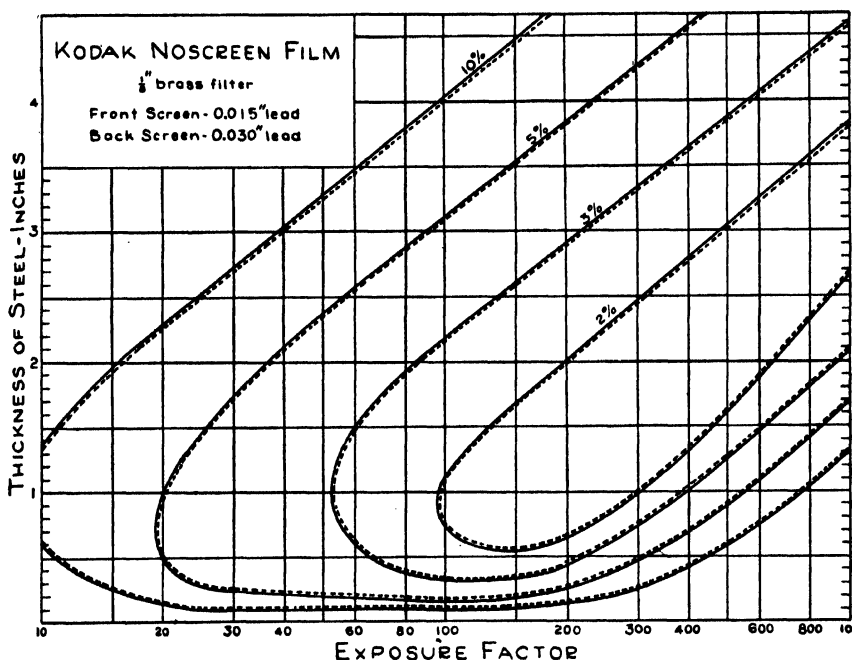
FIG. 5. *Penetrameter sensitivity curves for Kodak "No Screen" film. Solid lines were uncorrected for distortion, while dotted lines show the results after all corrections are carried out. Front screen, 0.015 in. lead; back screen, 0.030 in. lead. Standard development. The percentages marked on the graph give the percentage thickness of the slot in the wedge penetrameter which can just be detected.*

the casting would be required if one used "No Screen" film and a 0.015 in. lead front screen. From Fig. 5 we see that exposure factors of 200 and 600 would be satisfactory*.

The effectiveness of the lead front screen in determining the penetrameter sensitivity is illustrated in Figs. 6, 7, and 8 where results similar to Fig. 5 are shown but with lead front screens of thickness 0.000, 0.030, and 0.060 in. It will be seen that the area enclosed within the 2% sensitivity curve is greatest for 0.030 in. of lead front screen, and smallest for no lead front screen. For most purposes then, a 0.030 in. lead front screen is the most useful for "No Screen" film. For no lead front screen (Fig. 6) the area enclosed by the 2% curve is quite small showing that such a sensitivity can be only just obtained. When a thick lead front screen is used, scattered radiation from the casting

---

* *The width of the 2% area of course determines the allowable latitude in the exposure factor for a given thickness of casting. The height of the 2% area determines the range of casting thickness which may be examined with one exposure.*
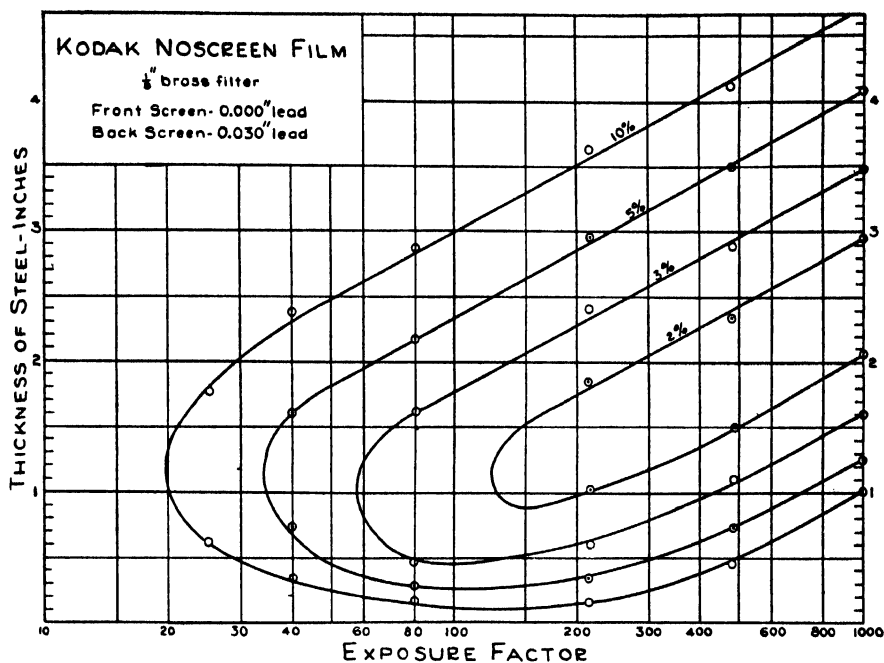
FIG. 6. *Penetrameter sensitivity curves for Kodak "No Screen" film. Front screen, 0.000 in. lead; back screen, 0.030 in. lead. Standard development.*
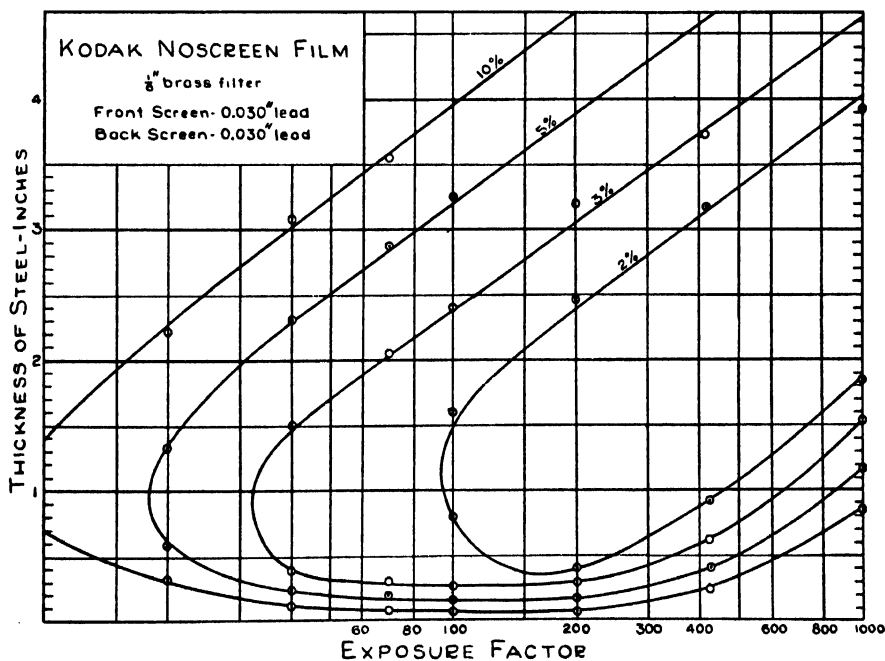
FIG. 7. *Penetrameter sensitivity curves for Kodak "No Screen" film. Front screen, 0.030 in. lead; back screen, 0.030 in. lead. Standard development.*

is more severely cut down so that the sensitivity which can be obtained is increased. However, when the thickness of the lead front screen is increased beyond a certain value, the penetrameter sensitivity obtainable decreases. This is illustrated in Fig. 8. Beyond a certain value the lead front screen serves only to absorb the primary beam without introducing much extra
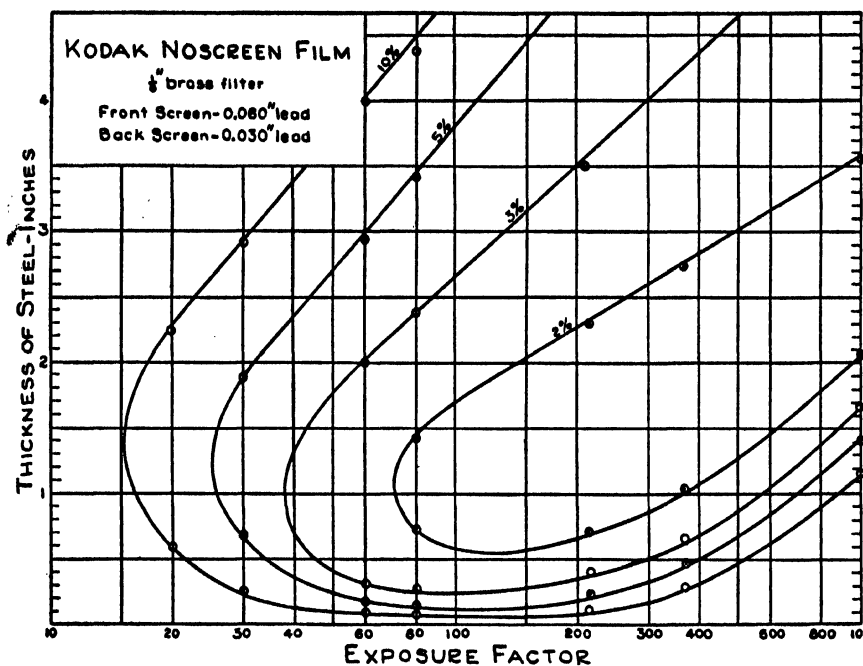
FIG. 8. *Penetrameter sensitivity curves for Kodak "No Screen" film. Front screen, 0.060 in. lead; back screen, 0.030 in. lead. Standard development.*

discrimination against the scattered radiation. Fig. 7 illustrates the fact that a 2% sensitivity can be obtained in a 0.5 in. steel block at exposure factor from 130 to 250 when 0.030 in. lead front screen is used. From Fig. 2 we saw that maximum intensification was achieved in a 0.5 in. steel block using 0.003 in. lead front screen. The great difference between the thickness of lead front screen to produce maximum differential sensitivity and that which gives maximum intensification (i.e., shortest exposure for a given density) is quite apparent.

Similar penetrameter sensitivity curves are shown in Figs. 9 to 14 for Kodak A film, Kodak Blue Brand, Dupont 506, and Ansco Superay A, for a variety of front screen filters. The information presented in Figs. 5 to 14 is summarized in Table I, in which is shown the thickness range of steel which can be radiographed, using radium, to give a 2% sensitivity and the exposure factor required for this sensitivity for five varieties of film and for different thicknesses of lead front screen.
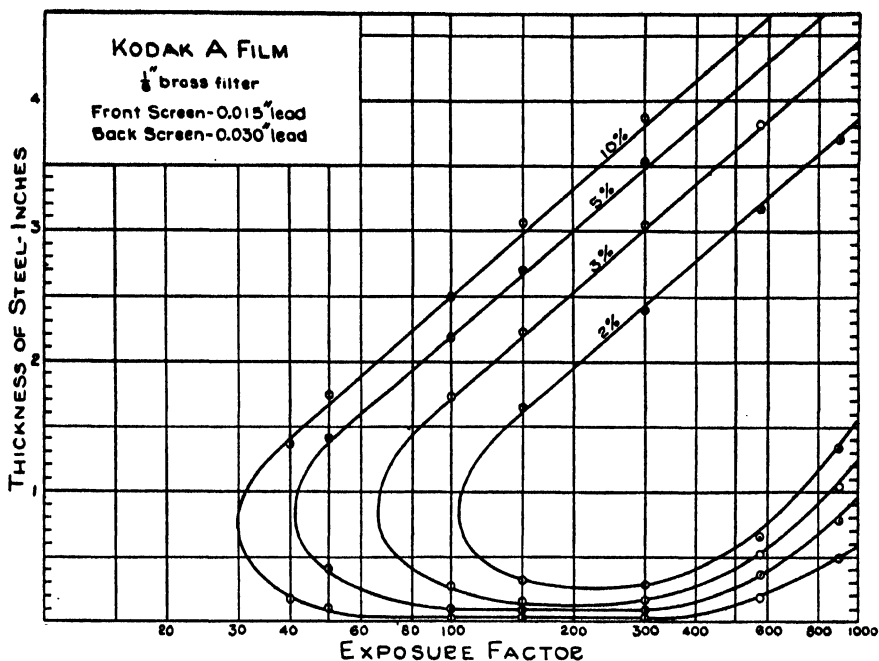
FIG. 9. *Penetrameter sensitivity curves for Kodak A film. Front screen, 0.015 in. lead; back screen, 0.030 in. lead. Standard development.*
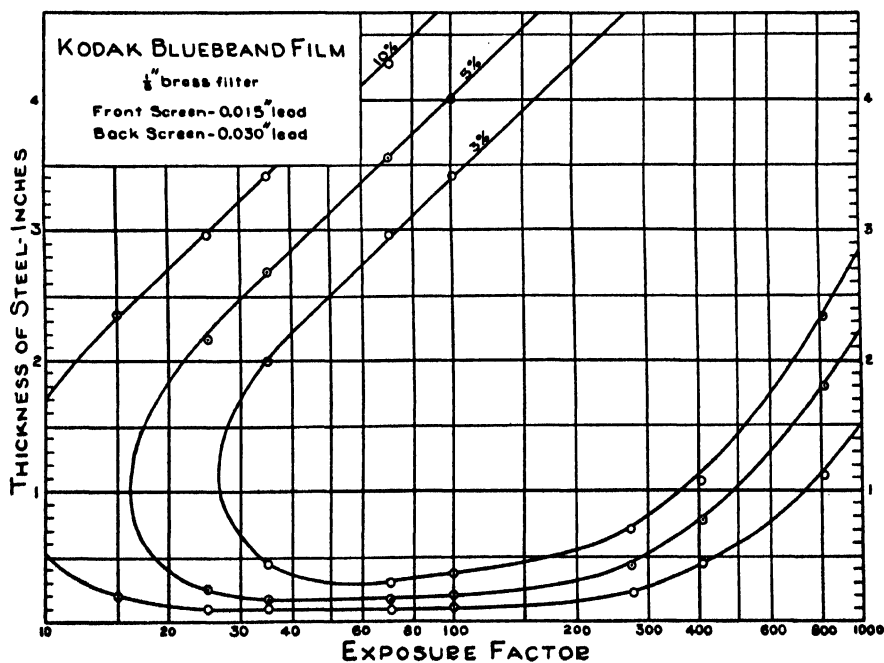
FIG. 10. *Penetrameter sensitivity curves for Kodak Blue Brand film. Front screen, 0.015 in. lead; back screen, 0.030 in. lead. Standard development.*
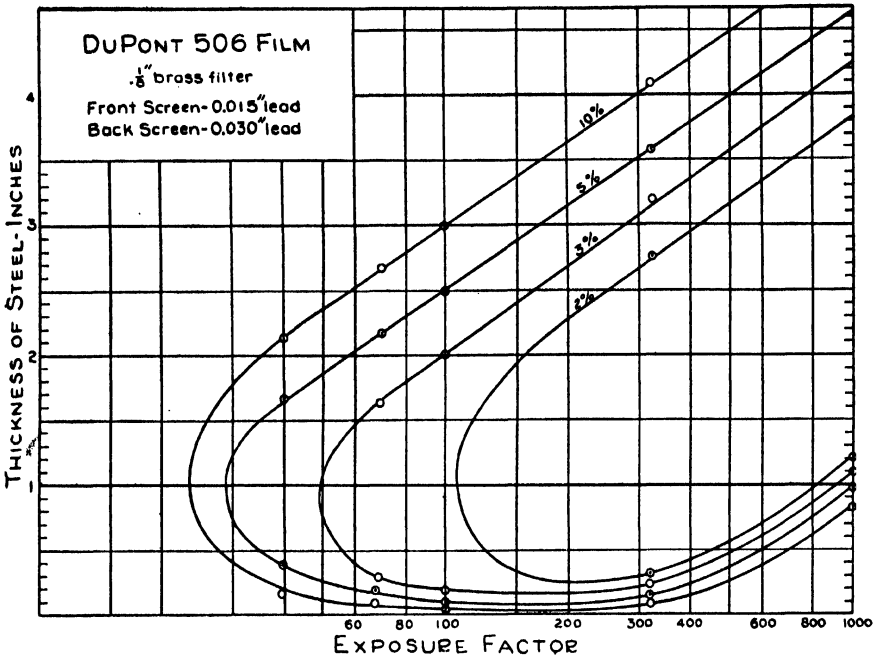
FIG. 11.   *Penetrameter sensitivity curves for Dupont 506 film.   Front screen, 0.015 in. lead; back screen, 0.030 in. lead.   Standard development.*
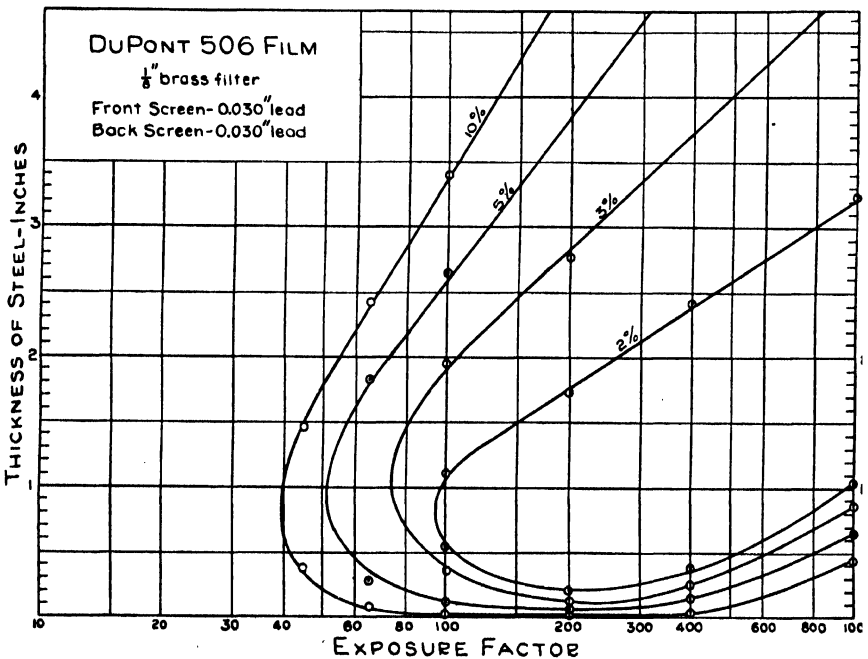
FIG. 12.   *Penetrameter sensitivity curves for Dupont 506 film.   Front screen, 0.030 in. lead; back screen, 0.030 in. lead.   Standard development.*
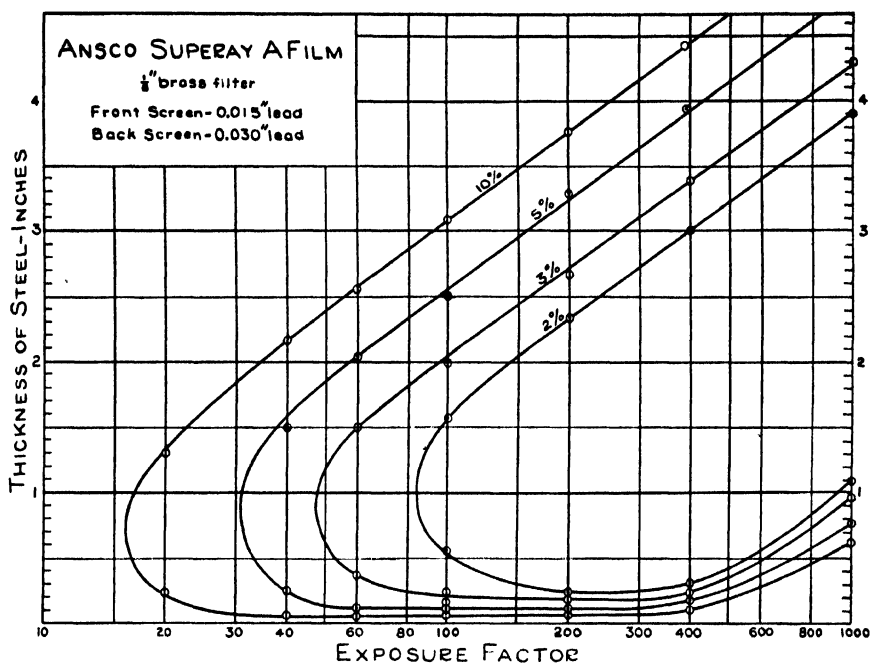
FIG. 13. *Penetrameter sensitivity curves for Ansco Superay A film. Front screen, 0.015 in. lead; back screen, 0.030 in. lead. Standard development.*
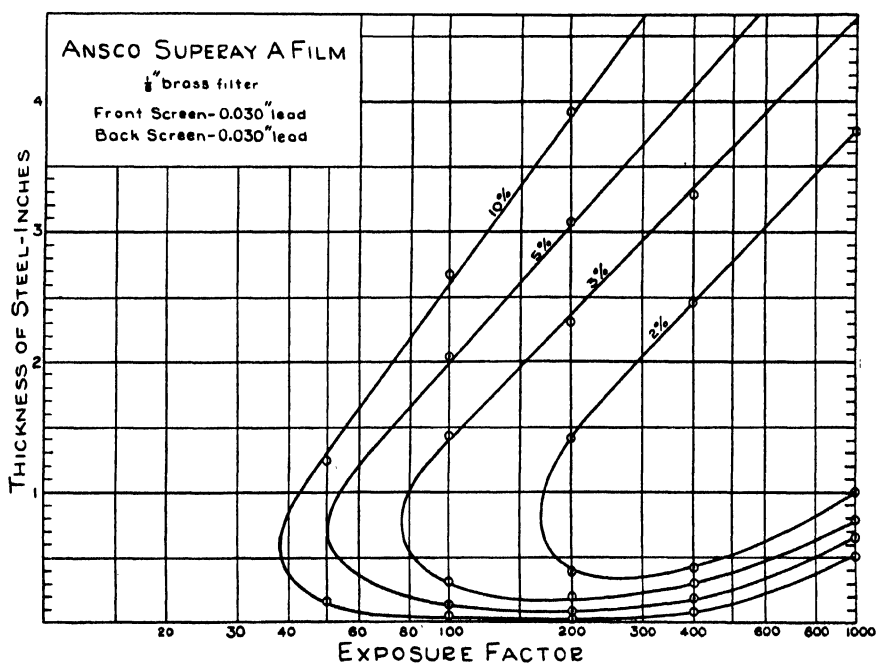
FIG. 14. *Penetrameter sensitivity curves for Ansco Superay A film. Front screen, 0.030 in. lead; back screen, 0.030 in. lead. Standard development.*

TABLE I

SUMMARY OF RANGES OF THICKNESS OF STEEL IN WHICH A 2% FLAW MAY BE DETECTED FOR DIFFERENT EXPOSURE FACTORS, TYPES OF FILM, AND THICKNESSES OF LEAD FRONT SCREENS

Film	Lead front screen, in.	Exposure factor, mgm. × min./in.³					
		80	100	150	200	400	1000
		Range of thickness of steel in which 2% flaw may be detected, in.					
Kodak "No Screen" Film	0.000			0.9 to 1.5	1.0 to 1.75	1.3 to 2.3	2.1 to 2.9
	0.015		0.75 to 1.1	0.6 to 1.6	0.7 to 2.0	1.3 to 2.75	2.7 to 3.8
	0.30		0.8 to 1.5	0.4 to 2.1	0.4 to 2.4	0.9 to 3.1	1.9 to 4.0
	0.043	1.1 to 1.6	0.8 to 1.9	0.6 to 2.2	0.6 to 2.4	0.9 to 2.7	1.8 to 3.5
	0.060	0.75 to 1.4	0.6 to 1.7	0.6 to 2.0	0.65 to 2.3	1.1 to 2.8	2.1 to 3.6
Kodak A	0.015			0.3 to 1.6	0.25 to 1.9	0.4 to 2.75	1.6 to 3.8
Kodak Blue Brand		2% not observable					
Dupont 506	0.000					0.7 to 1.7	1.3 to 2.8
	0.015			0.3 to 1.9	0.25 to 2.25	0.4 to 2.9	1.2 to 3.8
	0.030		0.6 to 1.1	0.3 to 1.5	0.25 to 1.75	0.4 to 2.3	1.1 to 3.2
Ansco Superay A	0.000					0.7 to 1.9	1.2 to 2.7
	0.015		0.5 to 1.6	0.3 to 2.1	0.25 to 2.3	0.3 to 3.0	1.1 to 3.9
	0.030				0.4 to 1.4	0.4 to 2.4	1.0 to 3.8

Discussion

Table I and Figs. 5 to 8 indicate that when "No Screen" film is used a lead front screen 0.030 in. thick will in general enable one to "examine" with a 2% technique the maximum thickness range of casting. The exposure factor required is 100 or greater. In general, thicker or thinner front screens will reduce slightly the range of thickness in which a 2% sensitivity may be obtained. However for a limited range of thicknesses a thicker lead front screen (0.043 in. or 0.060 in.) can yield a 2% sensitivity at exposure factor 80.

Table I and Figs. 9, 11, and 13 indicate that for most purposes Dupont 506 and Ansco Superay A should be used with 0.015 in. lead front screens. For a given exposure factor the range of thicknesses which may be radiographed to give a 2% sensitivity is slightly greater for Ansco Superay A than for Dupont 506, Kodak A, or "No Screen" film although the differences are very slight. Sections of steel thinner than 0.50 in. can hardly be radiographed to give a 2% sensitivity using "No Screen" film. Steel in thicknesses down to 0.30 in. can be radiographed with a 2% technique about equally well at exposure factor 150 for either Kodak A, Dupont 506, or Ansco Superay A film. These results are in general agreement with those of Nodwell and Morrison (2).

It is impossible to include in this paper results such as these for all films but it is felt that in a place where many castings are being radiographed, penetrameter sensitivity curves of this type should be constructed by the use of a

wedge penetrameter and that exposures of castings should be planned on the basis of such information rather than from graphs relating density to exposure factor. It should be realized that in many cases the sensitivity indicated in Figs. 6 to 14 cannot be achieved owing to scattered radiation from a complicated casting, but such curves do enable one to plan the exposure technique for any casting quickly and with greater accuracy than is possible by other methods.

Acknowledgments

The authors wish to express their appreciation to the National Research Council of Canada for their financial support in this project and especially to Mr. A. Morrison of the Radiology Division of the National Research Council for his part in initiating this work and for his many helpful suggestions. Acknowledgments are due Prof. E. L. Harrington, Head of the Department of Physics of the University of Saskatchewan, for his continued support of the project and to Mr. A. H. Cox of the Instrument Shop, for his technical assistance.

References

1. LAURENCE, G. C., BALL, L. W., and ARCHIBALD, W. J. National Research Council of Canada Bulletin. 1942.
2. NODWELL, E. M. and MORRISON, A. National Research Council of Canada Bulletin No. 1134. July, 1943. *Also in* A.S.T.M. Bulletin, p. 25. March, 1944.

ABSORPTION MEASUREMENTS OF SOUND IN SEA WATER[1]

By G. J. Thiessen, J. R. Leslie[2], and F. W. Simpson

Abstract

Sound absorption measurements, made with a diverging beam in sea water, are given. They cover frequencies from 0.35 to 2.3 Mc. per second and are somewhat lower than those given by Richardson for fresh water. Conclusive comparison between these results and fresh water results cannot be made. Advantages of using long distances are discussed.

Introduction

Owing to the use of sound in underwater signalling and submarine detection, the war was responsible for a considerable revival of interest in the absorption of sound in water, particularly in the ultrasonic region. A number of investigators had already published results in the literature which seemed to indicate a large absorption band in the frequency region of 1 Mc. per sec. and lower. But variations by factors as large as 10 were fairly common, depending on the details of the particular experimental methods used. Thus at a frequency of 1 Mc. per sec., Sörensen (17) gets an amplitude absorption coefficient α of 0.0057 cm.$^{-1}$, Hartmann and Focke (8) get 0.014 cm.$^{-1}$, whereas Richardson's (16) value is 0.00045 cm.$^{-1}$ For comparison purposes, as many data as could be obtained to date are plotted in Fig. 2, where the amplitude absorption coefficient α and the attenuation in decibels per meter are plotted against the frequency. All results except the present are for fresh water.

Since the measurements were not all made at the same temperature they are reduced, wherever possible, to 20° C. and to this end the classical variation with temperature was used. From Stokes' well known formula the amplitude absorption coefficient α is given by

$$\alpha = \frac{8\,\pi^2 f^2\,\eta}{3\rho v^3}$$

where f is frequency, η is viscosity, ρ the density, and v the velocity of sound in the medium. Hence the temperature variation will depend on η, v, and ρ. Using the values for η and ρ from the International Critical Tables and the values for v from references (13) and (19), the results for $\frac{\alpha}{f^2}$ are plotted in Fig. 1.

For comparison purposes some experimental values from the literature are also shown in arbitrary units. The check is as close as the spread among experimenters' values, and thus justifies the use of the curve for reduction of values to the same temperature.
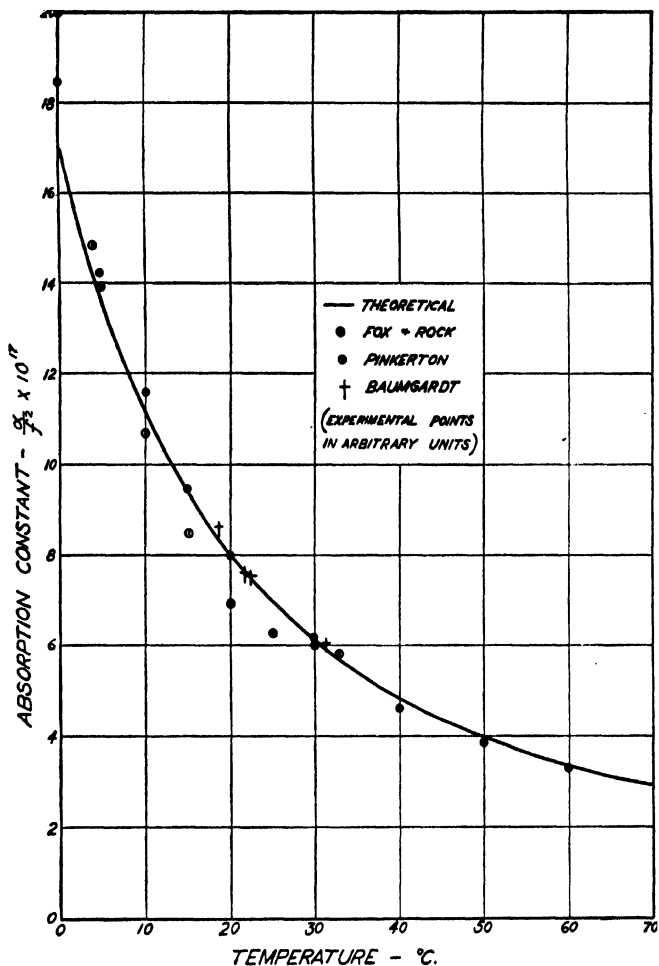
FIG. 1. *The variation of $\frac{\alpha}{f^2}$ as a function of temperature. The experimental values are in arbitrary units.*

The reproducibility for different investigators is probably not as poor as Fig. 2 would indicate. For instance, the values of Sörensen's have been definitely proved to be too high owing to radial resonances in the tube (5). Claeys, Errera, and Sack have, in fact, been able to get values even higher than those of Sörensen's by simply decreasing the diameter of the tube containing the water.

The second factor that has given rise to much of the discrepancy among the early results is absorption due to cavitation (15, p. 45). Boyle, Taylor, and Froman (4) have found that cavitation may begin at 0.03 w. per cm.^{2} and experiments on absorption as a function of intensity by Fox and Rock (18) bear this out, showing an increased absorption as the intensity is increased beyond about 0.04 w. per cm.^{2} The high frequency supply used by Hartmann and Focke was capable of an output of 100 w., and, since an efficiency of 10%
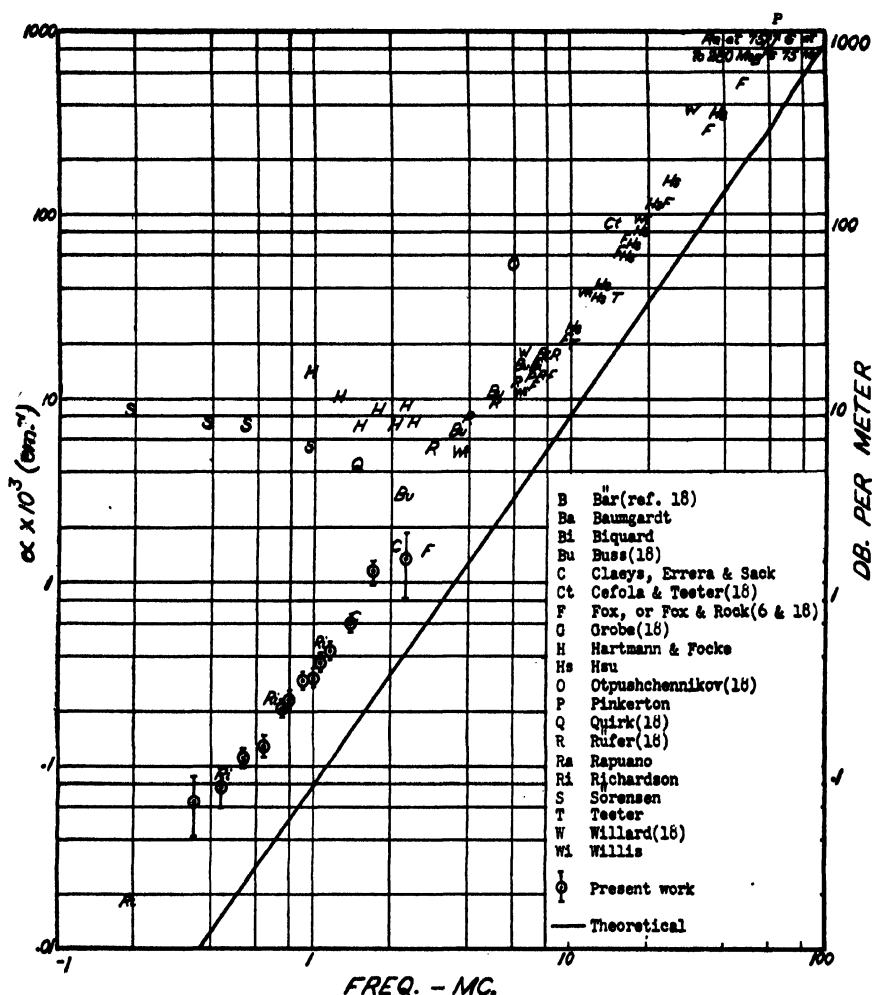
FIG. 2.   *The absorption coefficient* α *(cm.⁻¹) as a function of frequency.   The points W-W and P-P should really be joined by a straight line.   They were determined by calculation of* α *for the extreme frequencies from the average* $\frac{\alpha}{f^2}$ *as given by the corresponding authors.*

is easily obtained with quartz at resonance, this would give a possible intensity of 2.5 w. per cm.² for their crystal.   This is well in the cavitation region. Richardson, who believes that most radiation pressure methods require too high intensities for reliability, obtained the qualitative result that, whenever intensity was increased to the point of turbulence, the absorption coefficient was increased severalfold.

The remaining points, while suggesting more nearly a straight line, still spread out over a wide range, particularly at the lower frequencies.   The following factors have been suggested as possible causes of the scatter as well as of the discrepancy with theory:

(1) Energy is lost from the beam owing to scattering caused by local inhomogeneities of the water (e.g., crystallization). This was suggested by Lucas (11), and Biquard (2) also claims to have found evidence to substantiate this. Richardson and Pinkerton (12), however, have detected no scattered energies, though the latter has some secondary evidence of this in the change of the ratio of α(observed) to α(calculated) at temperatures below 15° C. Since the area over which the scattered radiation is spread is rather large, it is expected that this will be difficult to detect. It is probably worthy of notice that a radiation pressure detector was used by Biquard and since this is nearly nondirectional, it is possible that it may respond to radiation coming directly from the quartz crystal. The complicated directionality pattern of quartz is mentioned below.

(2) The assumption of plane waves is usually made, yet Richardson and Willard (18) have shown that there is an appreciable amount of divergence. Born (3) calls attention to the fact that both divergence and convergence are possible at distances generally used in absorption measurements. Specific corrections for this have been made only by Pinkerton, Willard, and Hsu (14), although some of the irregularities are no doubt smoothed out by the customary use of large detectors (see Fox and Rock, reference (18)).

(3) Another cause of divergence that is less easily corrected for, at short distances, is that due to variations in phase and amplitude across the crystal face. In calculating directionality patterns, it is usually assumed that the amplitude and phase across the face of the transmitting piston are constant. How far from valid this assumption may be is shown by pictures such as given by Hiedemann (reference (9), pages 9 and 11) or by Grobe (reference (7), page 335). Only by going to larger distances is it possible to tell accurately what the intensity changes, due to geometry, will be.

Apparatus and Method

The present work was done in Vancouver harbor where, through the courtesy of the Pacific (Coyle) Navigation Co. Ltd., the use of their dock was obtained. This afforded a stretch of water free from obstacles, for a distance of 30 m., where the depth varied from 4 to 6 m., depending on the tides. The temperature was also dependent on the tides, varying by approximately 1° on either side of 10° C. This variation was not corrected for, since this is beyond the accuracy claimed for the present experiments.

In the transmitter, X-cut rochelle salt was used. Four crystals 1 by ⅜ by ¼ in. had their ⅜ in. dimension ground down to 3/16 in., and were then connected in series-parallel, so that the ¼ by 1 in. faces were the transmitting faces. The crystals were mounted in a circular piece of bakelite, "vulcaloc" being used to stick them into place. The crystal surfaces usually protruded somewhat above the bakelite surface and, when the "vulcaloc" was dry, they were ground down flush with the bakelite. A thin rubber sheet from a

surgeon's rubber glove was then cemented over the whole face, thus effectively waterproofing it without interfering with the cooling effect of the water. The crystal mount was then mounted on one end of a cylindrical brass housing.

The cylindrical, brass, waterproof housing, $3\frac{1}{2}$ in. in diameter, contained two 6L6's connected in parallel, to supply the power to the rochelle salt crystals. They in turn were driven by a 6AG7 tube also contained in the same housing. Resistance plate loads were used throughout but no effort was made to secure a flat frequency response. The power and signal were supplied through cables from above water, a Clough Brengle signal generator being used as a source of the desired frequency.

The receiver was made of a small piece of crystal with dimensions $\frac{1}{4}$ by $\frac{1}{4}$ by 1/16 in., the larger face being the receiving face. This was set in polystyrene and covered with a polystyrene film, and then mounted on the end of a pre-amplifier housing, similar to the transmitter but smaller. The receiver was made small so that it would not have too sharp a directionality pattern and would thus facilitate the search for the center of the sound beam by reducing amplitude variations due to slight changes in orientation.

The preamplifier consisted of two 6AC7's, the first one being used as an amplifier while the second, connected as a cathode-follower, fed a concentric line to the amplifier above. The main amplifier was a superheterodyne all-band receiver with the audio stage removed. The a.v.c. voltage was con-trolled manually by means of a potentiometer, thus permitting the gain to be changed at will.

The procedure consisted of mounting the transmitter at a depth of about 2 to 3 m., depending on the tides, and sending the beam parallel to the floating dock toward the receiver. The receiver was mounted on the end of a long pole. It was not assumed that the center of the beam was along the line perpendicular to the crystal face, but the procedure involved rather a search for a maximum reading of the detector, as the two co-ordinates perpendicular to the approximate beam direction were varied. The distance between transmitter and detector was varied between 3 to 30 m., and since the sound pressure is given by

$$P_x = \frac{P_o e^{-\alpha x}}{x},$$

pressure measurements at two distances will enable the calculation of the amplitude absorption coefficient α. P_x is the sound pressure at distance x from the receiver. Up to 10 or 11 readings were taken for the same frequency and the error calculated statistically from the fluctuations of these readings about the mean.

Discussion of Results

The comparison of the present salt water results with those for fresh water cannot be made without some justification, and this lies mainly in the con-tradictory results in the literature. Claeys, Errera, and Sack found a decided

increase of the absorption coefficient with increasing salinity, so that for sea water (which is 3.0% salt, or about 0.5 mole per liter) $\frac{2\alpha}{f^2}$ should be very nearly doubled. Buss (18) on the other hand finds that 6.6% sodium chloride added to water has no appreciable effect on $\frac{2\alpha}{f^2}$ but that higher concentrations will cause a drop in this value. His actual values for $\frac{2\alpha}{f^2}$ seem very high but should still serve to show the effect of salinity. Rüfer (18) checks the values of Buss in an approximate way, also getting a decrease in absorption with increased salinity. However, the effect is so small that a 3.0% solution should not differ by more than 6% from fresh water at any of the frequencies that he used.

Thus, if the results of Buss and Rüfer may be accepted then, to within the accuracy claimed, the present results may be compared directly with fresh water results. If the results of Claeys, Errera, and Sack are given more weight, then the present results can only be considered to give an upper limit and would be approximately twice too high.

The values obtained for α are given in Table I, together with the corresponding statistical errors (calculated from the deviation from the mean). The figures in the fourth column are those for α corrected to 20° C. according to Fig. 1, and are the ones plotted in Fig. 2. The mean value for $\frac{2\alpha}{f^2}$ at 20° C. is about 71, and, if the values for the lowest and highest frequency are neglected owing to the large error, then the average $\frac{2\alpha}{f^2}$ comes to 70.

TABLE I

ABSORPTION COEFFICIENTS FOR VARIOUS FREQUENCIES

f, mc.	Db./m.	$\alpha \times 10^4$, cm.$^{-1}$	$\alpha \times 10^4$ (at 20°C.)	$\frac{2\alpha}{f^2} \times 10^{17}$ (at 20° C.)
0.355	0.080	0.92 ± 0.35	0.66	103
0.450	0.092	1.06 ± 0.18	0.76	74
0.550	0.138	1.59 ± 0.12	1.13	74
0.65	0.161	1.84 ± 0.09	1.31	62
0.75	0.233	2.90 ± 0.09	2.07	67
0.80	0.282	3.24 ± 0.14	2.32	71
0.90	0.350	4.03 ± 0.14	2.88	71
1.00	0.360	4.15 ± 0.28	2.97	60
1.08	0.440	5.10 ± 0.60	3.60	62
1.20	0.520	6.00 ± 0.37	4.30	71
1.45	0.720	8.30 ± 0.37	6.00	83
1.70	1.38	15.9 ± 1.5	11.3	78
2.30	1.61	18.4 ± 5.8	13.1	48

As is seen from the graph, the values check quite closely with the results of Richardson and those of Claeys, Errera, and Sack, who made measurements in this frequency region. Before definite conclusions can be drawn from this, it

will be necessary to repeat these experiments in fresh water, or at least to determine more conclusively the effect of salt on the absorption coefficient of water.

One of the reasons for fluctuations, particularly at low frequencies, was the reflection from the surface and bottom. This in fact set the lower limit to the frequencies that could be used and still result in reasonably consistent readings. The amount of surface reflection was usually judged by the fluctuations in the meter reading caused by waves and ripples when both transmitter and receiver were fixed. Bottom reflections were not, of course, as easily detected. These reflections can be expected to cause considerable trouble below 500 kc. for the water depths used, particularly since it becomes more necessary to get accurate readings owing to the decreasing absorption coefficient.

The high frequency limit was set by the fact that the directionality pattern became very complicated and the main beam might make any angle within 20° or so with the transmitter axis. Large side lobes would appear and show no axial symmetry. This made the hunt for the center of the beam difficult and resulted in the large error shown by the reading at the highest frequency. Furthermore, since the distances at these high frequencies have to be made necessarily shorter to obtain any signal, the correction for the difference in location of the actual source and the effective source (the latter is actually behind the former, see reference (20)) becomes quite important. Since this fact was not taken into account, the values at the highest frequency may be expected to be too low.

It is planned to continue experiments using relatively large distances, in both fresh and salt water.

References

1. BAUMGARDT, E. Compt. rend. 202 : 203. 1936.
2. BIQUARD, P. Compt. rend. 202 : 117. 1936.
3. BORN, H. Z. Physik, 120 : 383. 1943.
4. BOYLE, R. W., TAYLOR, G. B., and FROMAN, D. K. Trans. Roy. Soc. Can. 23 : 187. 1929.
5. CLAEYS, J., ERRERA, J., and SACK, H. Trans. Faraday Soc. 33 : 136. 1937.
6. FOX, F. E., and ROCK, G. D. Phys. Rev. 70 : 68. 1946.
7. GROBE, H. Physik. Z. 39 : 333. 1938.
8. HARTMANN, G. K. and FOCKE A. B. Phys. Rev. 57 : 221. 1940.
9. HIEDEMANN, E. Grundlagen und Ergebnisse der Ultraschallforschung. Walter De Gruyter & Co., Berlin W35. Printed by Metzger and Wittig in Leipzig. Archiv.—Nr. 525739. 1939.
10. HSU, E. T. J. Acoustical Soc. Am. 17 : 127. 1945.
11. LUCAS, R. Compt. rend. 201 : 1172. 1935.
12. PINKERTON, J. M. M. Nature, 160 : 129. 1947.
13. RANDALL, C. R. J. Research Natl. Bur. Standards, 8 : 79. 1932.
14. RAPUANO, R. A. Phys. Rev. 72 : 78. 1947.
15. RICHARDS, W. T. Rev. Modern Phys. 11 : 36. 1939.
16. RICHARDSON, E. G. Proc. Phys. Soc. London, 52 : 480. 1940.
17. SÖRENSEN, C. Ann. Physik, 26 : 121. 1936.
18. TEETER, C. E., JR. J. Acoustical Soc. Am. 18 : 488. 1946. (Other references given here.)
19. WILLARD, G. W. J. Acoustical Soc. Am. 19 : 235. 1947.
20. WILLIAMS, A. O., JR. J. Acoustical Soc. Am. 19 : 156. 1947.
21. WILLIS, F. H. J. Acoustical Soc. Am. 19 : 242. 1947.

THE γ-RAYS OF THORIUM CC''[1]

By S. C. Fultz[2] and G. N. Harding[3]

Abstract

At least two energy level schemes have been proposed for the ThC' nucleus, which is excited in the β-disintegration ThCC'. That of Ellis (1933) includes three γ-rays of energies 0.726, 1.62, and 1.80 Mev., the 1.62 Mev. ray being doubtful. The level scheme of Latyschev and Kulchitsky (1940) has eight γ-rays including one of energy 2.2 Mev., for which no corresponding long-range α-particle group has been observed. The two level schemes lead to widely differing values for the total γ-ray energy of ThCC'. In the present investigation a value for the total γ-ray energy of ThCC' has been obtained by measuring coincidences between the γ-rays of ThCC' and the subsequently emitted α-particles of ThC'. It is shown that this value (0.14 Mev.) favors the level scheme of Ellis, including only the γ-rays of energy 0.726 and 1.80 Mev., and taking the former as electric quadrupole. It was found that under certain conditions the external bremsstrahlung excited by the β-rays of ThCC' in the source-holder contributed appreciably to the coincidence rate. Precautions were taken to minimize this effect.

Introduction

In the β-disintegration ThC → ThC', the product nucleus may, in a certain fraction of the disintegrations, be left in an excited state. The de-excitation process occurs, according to Gamow (15), in one of two ways. Either the excitation energy is carried off by the α-particles subsequently emitted by ThC', thus giving rise to a long range group of α-particles; or the nucleus falls to a lower energy level by emission of a γ-ray. A close relationship between energies of γ-rays and energy differences of such groups of α-particles, therefore, would be expected.

Accurate measurements of the energies of ThC' α-particles were first made by Rosenblum and Valadares (25), who observed four groups corresponding to disintegration energies of 10.72, 9.78, 9.63, and 8.94 Mev. From the energy levels giving rise to these groups we might expect γ-rays of energies 1.78, 1.09, 0.94, 0.84, 0.69, and 0.15 Mev. originating from ThCC'. Further measurements were made by Rutherford, Wynn-Williams, Lewis and Bowden (27), and later by Lewis and Bowden (23), using improved techniques. The latter authors were able to detect only α-particle groups corresponding to disintegration energies of 10.744, 9.673, and 8·947 Mev., suggesting γ-rays of energies 1.797, 1.071, and 0.726 Mev.

Some measurements have also been made on the γ-rays of ThCC'. Ellis (12, 13), using a semicircular focusing magnetic spectrograph, examined the internal conversion electrons of thorium active deposit (ThB + C + C' + C''). Among the γ-rays which he identified were three which he attributed to ThCC'. These are of quantum energies 1.802, 1.623, and 0.726 Mev., of

which the first and last are in agreement with the measurements of Lewis and Bowden. The energy level scheme proposed by Ellis on the basis of these measurements is shown in Fig. 1, (a).
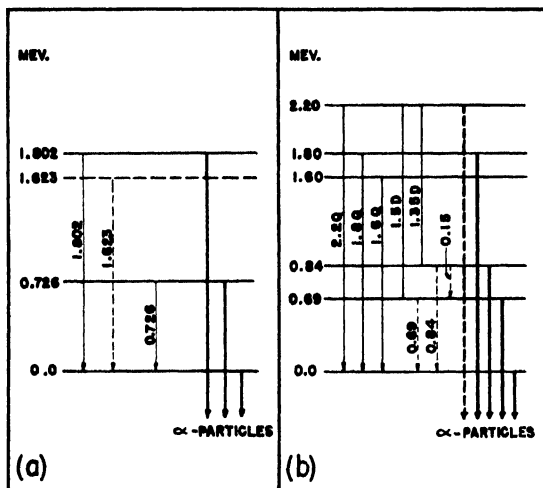
FIG. 1. *Energy levels of ThC' nucleus proposed by (a) Ellis and (b) Latyschev and Kulchitsky. Heavy lines denote α-particles, fine lines γ-rays.*

Alichanov and Dzelepov (1) examined the positron spectrum of thorium active deposit, using a semicircular focusing magnetic spectrometer, with two Geiger-Müller counters in coincidence. They identified hard γ-rays of energies 2.20, 1.80, 1.60, 1.50, and 1.35 Mev., which they attributed to the transition ThCC'. Measurements by Latyschev and Kulchitsky (22) on the recoil electron spectrum due to the γ-rays from thorium active deposit confirmed the measurements of Alichanov and Dzelepov on the energies of these hard γ-rays. The two sets of results from the Russian workers establish the multipolarities and intensities of these radiations. The error in the intensity measurements was estimated to be from 5 to 10%.

Of particular importance is the fact that these workers observed a 2.2 Mev. γ-ray which they attributed to ThCC'. If such an excitation level is present, one would expect to find a long range group of α-particles, corresponding to a disintegration energy of 11.15 Mev. Since the probability of emission of a long range α-particle increases more rapidly with excitation energy than the probability of the alternative process of γ-ray emission, this group of α-particles should be easily detectable, whereas Rutherford, Wynn-Williams, and Lewis (26) found, in a special search for α-particles of energy greater than 10.7 Mev., none having an intensity greater than 1/10,000 of the 10.7 Mev. group. A level scheme for ThC' proposed by Latyschev and Kulchitsky is shown in Fig. 1, (b).

In order to obtain further data on this problem, the authors undertook the measurement of the total γ-ray energy emitted per disintegration of ThCC'.

The total γ-ray energy expected, according to the two level schemes, will be the sum of contributions from all the γ-rays which are given in each of Tables I and II. The intensities of the hard radiations are those given by the

TABLE I

HARD* γ-RAYS OF ThCC′ AS SUGGESTED BY LATYSCHEV AND KULCHITSKY (22)

γ-ray energy, Q, Mev.	Intensity, p	Multipolarity	Energy per disintegration, p. Q, Mev.
2.20	0.027	Dipole	0.060
1.80	0.033	Quadrupole	0.060
1.60	0.054	Quadrupole	0.086
1.50	0.020	Dipole	0.030
1.35	0.019	Dipole	0.026

* In addition, there would be contributions from low energy γ-rays. As there has been no certain identification of low energy γ-rays arising from ThCC′, only the contribution of the 0.726 Mev. γ-ray (see Table II) will be added in evaluating the total γ-ray energy.

TABLE II

γ-RAYS OF ThCC′ AS SUGGESTED BY C. D. ELLIS (12, 13)

γ-ray energy, Q, Mev.	Intensity, p	Multipolarity	Energy per disintegration, p. Q, Mev.
1.80	0.033	Quadrupole	0.060
1.62	0.054	Quadrupole	0.088
0.726	⎰0.110	Quadrupole	0.080
	⎱0.339	Dipole	0.246

Russian workers. For the 0.726 Mev. radiation, the intensity is calculated from the measurements of Flammersfeld (14) using the theoretical internal conversion coefficients of Hulme (19) and Taylor and Mott (33). Intensity values are given in quanta per disintegration of ThC′.

A recent measurement by Johansson (20), who found the intensity of the 0.726 Mev. γ-ray to be 0.2 quanta per disintegration ThCC′, does not enable us to decide between the electric dipole and quadrupole values but is sufficient to rule out the possibility of this ray being magnetic dipole, in which case the intensity would be much lower.

The various possible values for the total γ-ray energy per disintegration according to the above level schemes are summarized in Table III. Since the multipolarity of the 0.726 Mev. γ-ray is uncertain, the values in Table III

have been calculated for two possibilities, electric dipole and electric quad-rupole. In the last row of Table III the total γ-ray energy has been evaluated on the basis of Ellis's level scheme, but omitting the contribution from the 1.62 Mev. γ-ray, the origin of which has not been established (13).

TABLE III

POSSIBLE VALUES FOR TOTAL γ-RAY ENERGY OF THCC′

Level scheme according to:	Total γ-ray energy in Mev. if 0.726 Mev. ray is:	
	Dipole	Quadrupole
Latyschev and Kulchitsky	0.508	0.342
Ellis	0.394	0.228
Ellis (excluding 1.62 Mev. radiation)	0.306	0.140

Experimental Method

The total γ-ray energy was determined by observing coincidences between the γ-rays of ThCC′ and the α-particles of ThC′D which are subsequently emitted with a half-period of about 0.3 μsec. (6). In order to ensure that no coincidences were lost in the interval between emission of γ-ray and α-particle, it was necessary to make the resolving time of the coincidence mixer greater than this interval. The resolving time was therefore varied between 0.6 and 4 μsec., and only those results used which lay on the flat portion of the curve of efficiency vs. resolving time (see Fig. 4). The source used was thorium active deposit, and the α-particles of ThCC″ were removed by absorption.

Under these conditions, the α-particle counting rate is given by (10)

$$q_\alpha = 0.65 \, N \, \epsilon_\alpha \, , \tag{1}$$

where N is the number of disintegrations of ThC in unit time, 0.65 is the fraction of this number disintegrating to produce ThC′, and ϵ_α is the efficiency of the α-counter. The counting rate for the γ-counter is given by

$$q_\gamma = 0.65 \, N \sum_i \epsilon_{\gamma i} \cdot p_i + 0.65 \, N \sum_j \epsilon_{Bj} \cdot p_j + S \, , \tag{2}$$

where p_i and $\epsilon_{\gamma i}$ are respectively the intensity and the efficiency of the γ-counter for a γ-ray i; p_j and ϵ_{Bj} are the corresponding quantities for a bremsstrahlung quantum j; and S is the counting rate due to γ-rays other than those of ThCC′. The bremsstrahlung will be discussed subsequently.

The total coincidence rate, which includes coincidences between ThC′D α-particles and ThCC′ γ-rays, plus those between ThC′D α-particles and bremsstrahlung arising from ThCC′ β-rays, is given by

$$q_c = 0.65 \, N \, \epsilon_\alpha \, (\sum_i \epsilon_{\gamma i} \cdot p_i + \sum_j \epsilon_{Bj} \cdot p_j) + 2\tau q_\alpha q_\gamma \, , \tag{3}$$

where τ is the resolving time of the coincidence mixer, and the last term on the right hand side is due to random coincidences. Dividing Equation (3) by Equation (1) yields the relation

$$\frac{q_c - 2\tau q_\alpha q_\gamma}{q_\alpha} = \sum_i \epsilon_{\gamma i} \cdot p_i + \sum_j \epsilon_{Bj} \cdot p_j . \quad (4)$$

The right hand side of Equation (4) gives the total efficiency of the γ-counter for all γ-rays and bremsstrahlung in coincidence with the α-particles of ThC'D.

For a given geometry, the efficiency of a thick-walled brass γ-counter is proportional (within about 6%) to the quantum energy of the incident radiation, particularly in the region of interest for this work, i.e., 0.5 to 2.6 Mev. (9, 10, 37). Considering a γ-ray of unit intensity, we have

$$Q_i = K \epsilon_{\gamma i} , \quad (5a)$$

where Q_i is the quantum energy of an incident γ-ray i, and K is a constant. When the radiation consists of several components of different intensities p, this becomes

$$\sum_i p_i Q_i = K \sum_i p_i \cdot \epsilon_{\gamma i} . \quad (5b)$$

Putting $p_i Q_i = E_i$, where E_i is the total γ-energy of a ThCC' γ-ray per disintegration ThCC', and using Equation (4), we get the simple expression

$$E_1 + E_2 + E_3 + \ldots = K \cdot \frac{q_c - 2\tau q_\alpha q_\gamma}{q_\alpha} - B , \quad (6)$$

where B represents the correction due to bremsstrahlung.

$$\text{or} \quad E_1 + E_2 + E_3 + \ldots = K \cdot \bar{\epsilon}_\gamma - B , \quad (7)$$

where $\bar{\epsilon}_\gamma$ denotes the total efficiency of the γ-counter for the ThCC' γ-rays. K can be determined by calibration with sources of known γ-energy, and the remaining quantities on the right hand side of Equation (6) are measurable. Thus the total energy of these rays $E_1 + E_2 + E_3 + \ldots$, can be determined.

APPARATUS

The α-particles were counted with a proportional counter constructed of brass tubing and filled with argon, having a central mica window 2.72 mgm. per sq. cm. thick. To absorb the α-particles of ThCC'', a screen of aluminum of thickness 7.01 mgm. per sq. cm. was placed between the source and the window, giving a total of 9.73 mgm. per sq. cm. The pulses were amplified by a high-gain broad-band amplifier before passing to the coincidence mixer. γ-rays were detected by a Geiger-Müller counter of conventional design constructed of brass tubing of wall thickness 1/16 in. and filled with a mixture of argon and ethyl alcohol. A two stage amplifier was used to amplify the pulses before passing to the coincidence mixer, which contained the usual Rossi circuit. Scales of 128 were used to record the total

number of α-counts, γ-counts, and coincidence counts over periods ranging from 4 to 15 hr., from which counting rates were calculated, corrections being made for decay of the source.

Sources of thorium active deposit were prepared by deposition on one side only of small pieces of platinum (0.10 gm. per sq. cm.) and aluminum (0.17 gm. per sq. cm.) foil, in a vessel containing an emanating preparation of radio-thorium. The foils were mounted at a fixed distance of 2 cm. from the γ-counter, with the active surface close to the window of the α-counter. In Fig. 2 is shown the geometrical arrangement of the counters.
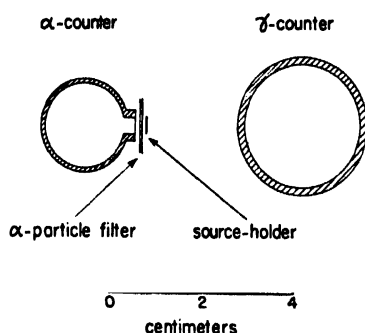
FIG. 2. *Arrangement of the counters.*

CALIBRATION OF THE γ-COUNTER WITH A Co[60] SOURCE

The γ-counter was calibrated by measuring its efficiency for γ-rays from a Co[60] source, keeping the geometrical conditions the same as before. Coincidences were observed between the β-rays and γ-rays of Co[60], the β-rays being detected in a thin-walled Geiger counter. The efficiency of the γ-counter was then determined by dividing the coincidence counting rate (corrected for random coincidences and cosmic ray background) by the β-ray counting rate. Co[60] is known to emit one β-ray and two γ-rays of average energy 1.20 Mev. per disintegration (8).

It was considered that a spurious increase in the coincidence rate might arise if a γ-quantum were to be scattered in the wall or window of the β-counter so that the recoil electron entered the β-counter while the scattered γ-quantum actuated the γ-counter. A simple calculation showed that if such an effect were present, the ratio of the β-γ to γ-γ coincidence rates for the Co[60] source would be less than 2. This ratio was measured in a separate experiment, and no change was observed when absorbers were placed to prevent scattered γ-quanta from the β-counter actuating the γ-counter. It was therefore concluded that no appreciable error in calibration could have been caused by such a process.

The possibility of obtaining coincidence counts between γ-rays and the X-rays caused by absorption of the β-rays was also considered. Calculations showed that this would have negligible effect on the measurements.

The mean value obtained from 10 measurements of the efficiency of the γ-counter for the γ-rays of Co^{60} was $(1.54 \pm 0.02) \times 10^{-3}$. Since there are two γ-rays per disintegration, of mean energy 1.20 Mev., this gives for K (Equation 7) the value $K = (1.56 \pm 0.02) \times 10^3$.

CALIBRATION OF THE γ-COUNTER WITH A THORIUM ACTIVE DEPOSIT SOURCE

An independent calibration of the γ-counter was obtained by measuring the counting rate, with the same geometry as before, due to γ-rays from a thorium active deposit source of known strength. The leakage rate in an ion chamber due to the γ-rays from this source was compared with that due to a radium standard; the source strength was calculated from these data, using the value found by Shenstone and Schlundt (28) for the relative strengths of ThC and Ra sources of equal γ-ray activity. The γ-rays of ThB were removed by filtration through lead.

Since the Ra standard was about 100 times stronger than the thorium active deposit, an ion chamber was used with the thorium active deposit which was about 10 times more sensitive than that used with the radium. The sensitivities of the chambers were compared later. Both chambers were constructed of aluminum; one was filled with argon and the other with hydrogen, both to a pressure of 20 atm. The leakage rates were measured with quartz fiber electrometers.

The results of three sets of measurements are given in Table IV.

TABLE IV

CALIBRATION OF γ-COUNTER WITH THORIUM ACTIVE DEPOSIT SOURCE

Trial No.	Source strength, disint. of ThB per sec.	γ-counting rate, counts per min.	γ-counter efficiency $\times 10^4$
1	3.02×10^5	1.714×10^4	9.37 ± 1.1
2	4.82×10^5	2.764×10^4	9.56 ± 0.9
3	3.81×10^5	1.843×10^4	8.1 ± 1.2
Mean			9.0 ± 0.6

The total γ-ray energy of thorium active deposit has been measured by L. H. Gray (17) who found the value 1.44 Mev. per disintegration of ThC. Using this figure, together with the efficiency quoted above, gives a value for the calibration constant $K = (1.60 \pm 0.11) \times 10^3$. This value agrees within the experimental error with that of $(1.56 \pm 0.02) \times 10^3$ obtained using a Co^{60} source.

The weighted mean of the two values is

$$K = (1.57 \pm 0.02) \times 10^3 .$$

Corrections for Bremsstrahlung

At the outset of this investigation, the very low result ultimately obtained for the total γ-ray energy of ThCC' was not foreseen, and hence it was not expected that corrections for bremsstrahlung arising from absorption of ThCC' β-rays in the source-holder would be important. The source-holders were therefore chosen without consideration of the maximum range of the electrons. In view of the low result, however, it later appeared necessary to estimate the magnitude of this effect, and subsequently to adjust the experimental conditions in order to reduce it to a minimum. Both inner and outer bremsstrahlung have to be considered.

The phenomenon of inner bremsstrahlung has been investigated theoretically by Knipp and Uhlenbeck (21) and experimentally by other workers (29, 31, 36). The results of Knipp and Uhlenbeck were used to calculate the inner bremsstrahlung of ThCC'. The effect on the results will be small. The value obtained in the calculation will indicate only the correct order of magnitude, since the calculation makes use of the Born approximation, which holds good only if $\frac{2\pi Z e^2}{hc} \ll 1$, whereas for ThC, $\frac{2\pi Z e^2}{hc} = 0.606$. In Fig. 3, the
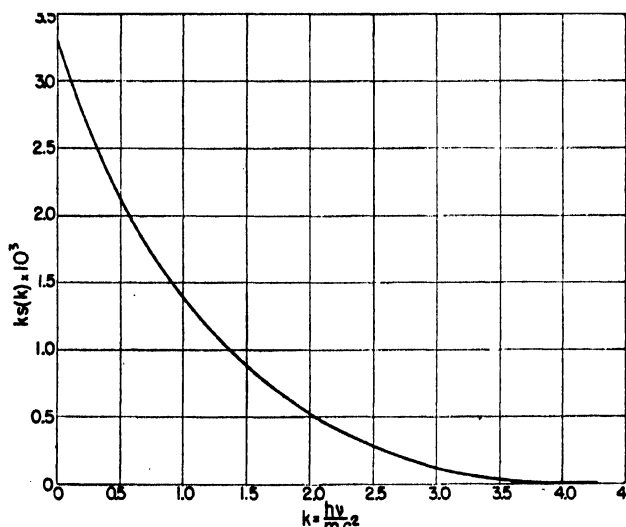
FIG. 3. *Inner bremsstrahlung in the transition ThCC'.*

total energy of radiation having quantum energy between k and $k+dk$, where $k = \frac{h\nu}{m_0 c^2}$, is plotted as a function of k. $S(k)$ is the total probability that a light quantum will be emitted in the energy range between k and $k+dk$, and is obtained by summing over all possible energies for the electron.

$$S(k) = \int_{1+k}^{W_0} dW_e \, p\,(W_e)\,\phi\,(W_e,k) ,\qquad (8)$$

where p (W_s) is the probability of obtaining a disintegration electron of energy W_s, ϕ $(W_s k)$ denotes the probability per unit energy range of electrons for production of radiation of quantum energy k, and W_0 is the maximum energy of the β-spectrum (including the rest mass m_0 of an electron). The β-ray distribution used in these calculations was that of Richardson and Leigh-Smith (24), which is discussed below. On numerically integrating the curve of Fig. 3, the value obtained for the total energy of the inner bremsstrahlung was found to be 1.76 kev. per disintegration of ThCC'. This is clearly negligible.

The outer bremsstrahlung arises from absorption of the energy of the β-rays by external atoms and is a mode of energy dissipation alternative to ionization by collision. Measurements have been made on the outer bremsstrahlung from different absorbers and for various sources of β-rays (2, 16, 29, 30, 32, 36), and the process has also been treated theoretically by Bethe and Heitler (3, 18). The total bremsstrahlung arising from the stopping of all the electrons in a thick plate can be calculated using the formulae of Bethe and Heitler and the β-ray energy spectrum.

In the case of an absorber of thickness less than the maximum range, it is necessary to subtract the bremsstrahlung which would be produced in the same material by those electrons which have passed through the absorber. To make such a calculation, it is necessary to determine the energy spectrum of these electrons. This was done in the following manner. The most probable energy of the electrons was obtained with the aid of Bloch's (4, 5) theory; their energy distribution was determined by an extrapolation of the data of White and Millington (35), and their number was found by a combination of these data with the results of Chadwick (7) and the absorption measurements of Varder (34).

The distribution of ThCC' β-rays was taken as the sum of Fermi curves corresponding to partial spectra with maxima of 2.248, 1.522, 0.625, and 0.446 Mev.; the total was taken from the results of Richardson and Leigh-Smith. The Fermi curve was used in preference to other distributions, because the latest measurements on β-spectra using refined techniques have been in close agreement with Fermi distributions, especially in the higher energy portions, which are of greatest interest in bremsstrahlung calculations. The largest contribution to the bremsstrahlung is made by the partial spectrum with maximum energy 2.248 Mev., which must comprise at least 80% of the ThCC' β-rays. Omitting the partial spectrum with a maximum energy of 0.625 Mev. (corresponding to the 1.62 Mev. level) and decreasing the intensity of the partial spectrum of maximum energy 1.522 Mev. (corresponding to the 0.726 Mev. level), from 0.14 to 0.08, in conformity with the conclusions of this work, will not therefore affect the bremsstrahlung calculations to any appreciable extent.

Initial measurements were made using source-holders of platinum foil (0.10 gm. per sq. cm.) and aluminum foil (0.17 gm. per sq. cm.). These thicknesses are not sufficient to absorb all the β-rays, some of which reached the

γ-counter wall. While it is possible to calculate the effect on the γ-counter of the bremsstrahlung arising from the source-holder, the effect due to bremsstrahlung excited in the counter wall cannot be estimated. In later measurements, therefore, all the β-rays emergent from the aluminum source-holder were absorbed in a plate of Lucite (polymethylmethacrylate). The experimental results obtained under these three sets of conditions are shown in Fig. 4, and the results of the calculation of the effect on the γ-counter of the external bremsstrahlung excited in the source-holder are given in Table V.

TABLE V

CALCULATED VALUES FOR OUTER BREMSSTRAHLUNG EXCITED IN THE
SOURCE-HOLDER (PER DISINTEGRATION ThCC′)

Foil substance	Thickness, gm./sq. cm.	Outer bremsstrahlung, kev.
Platinum	0.10	23.5
Aluminum	0.17	5.6

It has been well established that the intensity of outer bremsstrahlung is proportional to the atomic number of the target substance (29, 31, 36, 2). Hence all calculations were first worked out for aluminum, and the required result was obtained merely by multiplying this by the ratio of the atomic number of the absorber to that of aluminum.

The bremsstrahlung excited in the Lucite is estimated at 0.6 kev., which together with the inner bremsstrahlung of 1.76 kev., gives a total correction when both aluminum and Lucite absorbers are present, of 8 kev.

Several factors limit the accuracy of these figures. The results of Varder, which were used to obtain the distribution curve for the transmitted β-rays, hold accurately only for the geometry which he used, since the energy distribution of the transmitted β-rays changes with angle (11). In the work of White and Millington, foils were used having thicknesses up to a maximum of 17 mgm. per sq. cm. Extrapolating their results to the thicknesses used in this work probably introduced another source of error. However, it is felt that the error in these calculations should not be greater than 15 to 20%.

Results

The experimental data obtained are shown in Fig. 4. Efficiency values of the γ-counter for ThCC′ γ-rays are plotted against the resolving time of the coincidence mixer. The upper and center curves are based on data obtained using platinum and aluminum foil source-holders, respectively. The lower curve was obtained when the β-rays transmitted through the aluminum foil were absorbed in Lucite before reaching the γ-counter. It has been corrected for absorption of the 0.726 Mev. γ-ray in the Lucite. In taking the average

value for the efficiency, as given in Column 2 of Table VI, only those points on the flat portion of the curve, i.e., for which the resolving time was greater than 1 μsec., were used.
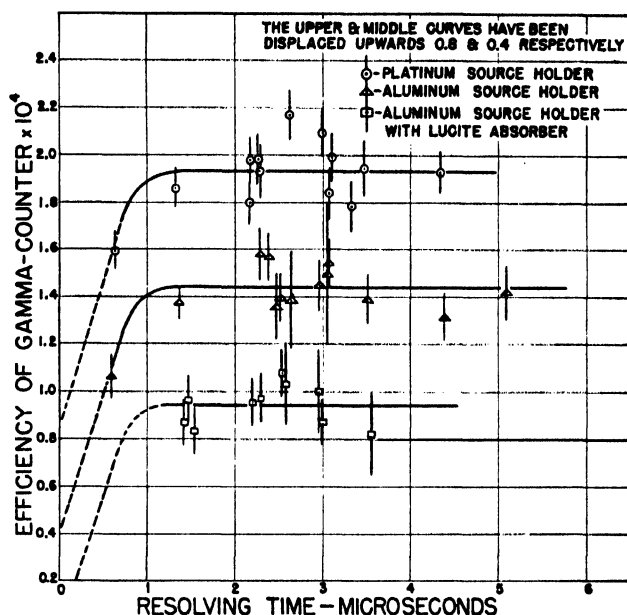
FIG. 4. *Experimental data on the efficiency of the γ-counter for γ-rays of ThCC'.*

In Table VI are given the mean values of the γ-counter efficiencies in the three cases, with the values of total γ-ray plus bremsstrahlung energy calculated from these efficiencies. Only in the third case, using an aluminum

TABLE VI

EXPERIMENTAL RESULTS ON THE TOTAL γ-RAY ENERGY OF THCC'

Calibration constant for the γ-counter: $K = (1.57 \pm 0.02) \times 10^3$

Source-holder	Efficiency of γ-counter $\bar{\epsilon}_\gamma \times 10^4$	Total γ-ray + bremsstrahlung energy, $K . \bar{\epsilon}_\gamma$, Mev.	Bremsstrahlung correction,** B, Mev.	Total γ-ray energy $K . \bar{\epsilon}_\gamma - B$, Mev.
Pt	1.14 ± 0.02	0.178 ± 0.007	0.026	0.152 ± 0.007
Al	1.04 ± 0.03	0.160 ± 0.006	0.008	0.152 ± 0.007
Al*	0.94 ± 0.03	0.147 ± 0.006	0.008	0.139 ± 0.006

* *With Lucite absorber of 1.4 gm. per sq. cm.*
** *Calculated values of bremsstrahlung considered good to 20%. An unknown amount of bremsstrahlung, which originates in the wall of the counter, must be added to the first two cases.*

source-holder and Lucite screen, is the correction for bremsstrahlung known completely, hence only in this case is the value calculated for the total γ-ray energy of ThCC' accepted.

Although the experiment was not of sufficient precision to determine the amount of bremsstrahlung accurately, at least the order of magnitude was found to be in agreement with calculated values. For example, the decrease in bremsstrahlung on changing the source-holder from platinum to aluminum, as obtained from Column 3, Table VI, is 18 ± 13 kev., which agrees in order of magnitude with that of 18 ± 6 kev. found from Column 4. This comparison neglects the difference in bremsstrahlung due to the transmitted β-rays for the two cases. According to the data of Column 5, the net bremsstrahlung due to these β-rays impinging on the wall of the γ-counter is 13 ± 13 kev., so that such a difference is small and is probably masked by the uncertainty in measurement.

The most probable error in the determination of the γ-counter efficiency for the case where the Lucite absorber was used, is 2.6%, and that for the constant of calibration is 1.3%. These give an experimental precision of about 4% in the total γ-ray energy (Column 3). Added to this will be an error of about 6% which is introduced through the assumption that a direct proportionality exists between the γ-counter efficiency and the quantum energy of the incident radiation. Hence the final result is considered to be accurate to within 10%.

Thus, the total energy of the γ-rays of ThCC' = 0.14 ± 0.014 Mev. per disintegration of ThCC'.

Discussion of Results

Applying Gamow's hypothesis to the measurements of Lewis and Bowden, it is found that the ThC' nucleus has two levels of excitation. These occur at 1.797 and 0.726 Mev., and may give rise to γ-rays having energies of 1.797, 1.071, and 0.726 Mev.

The measured value for the total γ-ray energy emitted per disintegration of ThC' is 0.14 Mev., and is in good agreement with the calculated value of 0.14 Mev. (see Table III), computed on the assumption that only the 1.80 and 0.726 Mev. γ-rays originate in the ThC' nucleus and that both are electric quadrupole. Addition of the 2.20 Mev. radiation would give a total energy of 0.200 Mev., which is in considerable disagreement with the measurements.

The present measurements indicate, therefore, that the energy level scheme for the ThC' nucleus suggested by the Russian workers is too complex and that there is no evidence in support of the presence of a 2.20 Mev. level of excitation.

Measurements were well advanced before it was realized that some of the recorded coincidences were between the bremsstrahlung and α-particles. Therefore, as stated above, only the data obtained with an aluminum source-holder and Lucite absorber have been utilized. The first two sets of data, however, give an indication of the amount of bremsstrahlung present, and this is seen to be of the same order as the calculated amount arising from the source-holder only (Table V). A more satisfactory arrangement would have been to make the source-holder from material of low atomic number, and

thick enough to absorb all the electrons from ThC. The observations on bremsstrahlung show the importance of considering this phenomenon when the coincidence method is used to investigate γ-rays of low intensity.

Acknowledgments

References

1. ALICHANOV, A. I. and DZELEPOV, V. P. Compt. rend. acad. sci. U.R.S.S. 20 : 113. 1938.
2. ARCIMOVITCH, L. A. and CHRAMOV, V. A. Bull. acad. sci. U.R.S.S. Série Phys. 5-6 : 757. 1938.
3. BETHE, H. and HEITLER, W. Proc. Roy. Soc. London, A, 146 : 83. 1934.
4. BLOCH, F. Ann. Physik, 16 : 285. 1933.
5. BLOCH, F. Z. Physik, 81 : 363. 1933.
6. BRADT, H. and SCHERRER, P. Helv. Phys. Acta, 16 : 259. 1943.
7. CHADWICK, J. Deut. Phys. Ges. Verh. 16 : 383. 1914.
8. DEUTSCH, M. and ELLIOTT, L. G. Phys. Rev. 62 : 558. 1942.
9. DROSTE, G. F. v. Z. Physik, 100 : 529. 1936.
10. DUNWORTH, J. V. Rev. Sci. Instruments, 11 : 167. 1940.
11. EDDY, C. E. Proc. Cambridge Phil. Soc. 25 : 50. 1929.
12. ELLIS, C. D. Proc. Roy. Soc. London, A, 138 : 318. 1932.
13. ELLIS, C. D. Proc. Roy. Soc. London, A, 143 : 350. 1933.
14. FLAMMERSFELD, A. Z. Physik, 114 : 227. 1939.
15. GAMOW, G. Nature, 126 : 397. 1930.
16. GRAY, J. A. Proc. Roy. Soc. London, A, 85 : 131. 1911.
17. GRAY, L. H. Proc. Roy. Soc. London, A, 159 : 263. 1937.
18. HEITLER, W. The quantum theory of radiation. Oxford University Press, London. 1944.
19. HULME, H. R. Proc. Roy. Soc. London, A, 138 : 643. 1932.
20. JOHANSSON, A. Arkiv. Mat. Astron. Fysik, A, 34, No. 9 : 1. 1947.
21. KNIPP, J. K. and UHLENBECK, G. E. Physica, 3 : 425. 1936.
22. LATYSCHEV, G. D. and KULCHITSKY, L. A. J. Phys. U.S.S.R. 4 : 515. 1941.
23. LEWIS, W. B. and BOWDEN, B. V. Proc. Roy. Soc. London, A, 145 : 235. 1934.
24. RICHARDSON, H. O. W. and LEIGH-SMITH, A. Proc. Roy. Soc. London, A, 162 : 391. 1937.
25. ROSENBLUM, S. and VALADARES, M. Compt. rend. 194 : 967. 1932.
26. RUTHERFORD, LORD, WYNN-WILLIAMS, C. E., and LEWIS, W. B. Proc. Roy. Soc. London, A, 133 : 351. 1931.
27. RUTHERFORD, LORD, WYNN-WILLIAMS, C. E., LEWIS, W. B., and BOWDEN, B. V. Proc. Roy. Soc. London, A, 139 : 617. 1933.
28. SHENSTONE, A. G. and SCHLUNDT, H. Phil. Mag. 43 : 1038. 1922.
29. SIZOO, G. J., EIJKMAN, C. and GROEN, P. Physica, 6 : 1057. 1939.
30. STAHEL, E. and COUMOU, D. J. Physica, 2 : 707. 1935.
31. STAHEL, E. and GUILLISSEN, J. J. phys. radium, 1 : 12. 1940.
32. STAHEL, E. and KIPFER, P. Helv. Phys. Acta, 9 : 492. 1936.
33. TAYLOR, H. M. and MOTT, N. F. Proc. Roy. Soc. London, A, 138 : 665. 1932.
34. VARDER, R. W. Phil. Mag. 29 : 725. 1915.
35. WHITE, P. and MILLINGTON, G. Proc. Roy. Soc. London, A, 120 : 701. 1928.
36. WU, C.-S. Phys. Rev. 59 : 481. 1941.
37. YUKAWA, H. and SAKATA, S. Sci. Papers Inst. Phys. Chem. Research, Tokyo, 31 : 187. 1937.

NOTICE

The Author and Subject Indexes for each of the sections, A, B, C, D, E, and F, of the *Canadian Journal of Research* for the year 1948 will be issued early in 1949.

THEORETICAL STUDY OF RAM-JET PROPULSION[1]

BY BOLESLAW SZCZENIOWSKI

Abstract

In ram-jet propulsion, artificial compression before combustion does not exist. Therefore, the only factors which may influence the increase in momentum, i.e., the thrust, are:

(1) The degree of initial dynamic compression by a diffuser;

(2) The shape of the combustion chamber;

(3) The variations of the rate of heat release along the tube;

(4) Air excess coefficient;

(5) Kind of fuel;

(6) Velocity of flight;

(7) Aerodynamic and heat losses.

This paper deals almost exclusively with the first four factors, i.e., with the theoretical case of an ideal gas and a perfect flow, with no heat or aerodynamic losses involved. The possible appearance of shock waves is disregarded. Neither are boundary layer phenomena discussed in this paper. The external fairing and the relation between the internal and external shape, as well as the influence of this relation on the actually obtainable thrust and efficiency, are also considered to be beyond the scope of the paper. General conclusions are drawn as to the optimum shape of the ideal engine from the standpoint of efficiency. It is found that air should be submitted initially to as high a dynamic compression as possible, i.e., using all kinetic energy available, after which a combustion chamber of constant cross section is used—and finally a nozzle. Another conclusion is that it is impossible to obtain a positive thrust with a combustion chamber of constant cross section, if no dynamic compression, by a diffuser, is initially applied. Special attention is drawn in the paper to the representation and interpretation of the ideal ram-jet cycle on the entropy diagram, this giving a clear picture of the relations between the energy released and the efficiency and thrust obtainable. The fact that in the flow through a tube of constant cross section with heat release (e.g., by combustion), the pressure may decrease even if ideal gas and perfect flow (with no losses involved) are concerned, is emphasized throughout the paper, as it seems that generally this fact is rather overlooked.

1. Denotations

Absolute pressure	P, lb. per sq. ft.
Absolute temperature	T, °Rankine
Specific volume	v, cu. ft. per lb.
Specific weight	$\gamma = 1/v$, lb. per cu. ft.
Velocity	c, ft. per sec.

Duct cross section area $\qquad$ A, sq. ft.

Air weight output $\qquad$ G_a, lb. per sec.

Fuel weight output $\qquad$ G_f, lb. per sec.

Mixture weight output $\qquad$ $G_m = (G_a + G_f)$, lb. per sec.

Work done per unit of time (power) $\qquad$ W, ft-lb. per sec.

Theoretical heat exchanged by 1 lb. of working
   medium (heat brought to the medium is
   assumed to be positive) $\qquad$ Q, B.t.u. per lb.

Specific heat at $P = $ Const. $\qquad$ c_p, B.t.u. per lb., °F.

Entropy $\qquad$ Φ, B.t.u. per lb., °F.

Gas constant of air $\qquad$ R_a, ft. per °Rankine

Gas constant of burning mixture $\qquad$ R_m, ft. per °Rankine

Isentropic exponent $\qquad$ $\kappa = c_p/c_v$

Thrust $\qquad$ (Th), lb.

Specific thrust $\qquad$ $\zeta = (Th)/G_a$

Unit thrust $\qquad$ $\epsilon = (Th)/A$, lb. per sq. ft.

Distance between cross-sections A and A_0 $\qquad$ x, ft.

Diffuser efficiency $\qquad$ η_d

Nozzle efficiency $\qquad$ η_u

External (propulsive) efficiency $\qquad$ η_{ex}

Internal (thermal) efficiency $\qquad$ η_{th}

Over-all efficiency $\qquad$ $\eta_0 = \eta_{ex}\eta_{th}$

Pressure efficiency $\qquad$ η_p

Efficiency expressing heat loss by conduction $\qquad$ η_h

Efficiency of pumping fuel $\qquad$ η_p

Air excess coefficient:

$$\lambda = \frac{\text{Actual mass of air involved for 1 lb. of fuel}}{\text{Mass of air necessary to burn completely 1 lb. of fuel}}$$

Weight of air theoretically necessary to burn
   completely 1 lb. of fuel $\qquad$ α, lb. per lb.

Lower heat value of 1 lb. of chemically correct
   air–fuel mixture $\qquad$ H_{m_0}, B.t.u. per lb.

Mechanical heat equivalent $\qquad$ $J = 778$ ft-lb. per B.t.u.

Terrestrial acceleration $\qquad$ $g = 32.174$ ft. per sec.^{2}

Standard conditions at sea level:

   $P_{st} = 14.72$ lb. per sq. in. $= 29.92$ in. of mercury $= 2120$ lb. per sq. ft.

   $T_{st} = 459.4 + 59 = 518.4$ °Rankine

Subscripts:

  0 — for surroundings

  1 — at the exit of a perfect theoretical cycle

  2 — after dynamic compression by a diffuser

  3 — after combustion

  4 — at the nozzle exit

Dimensionless coefficients:

  for pressure $\qquad\qquad\qquad\qquad\qquad \pi = P/P_0$

  for temperature $\qquad\qquad\qquad\qquad \tau = T/T_0$

  for specific volume $\qquad\qquad\qquad \nu = v/v_0$

  for velocity $\qquad\qquad\qquad\qquad\quad \sigma = c/c_0$

  for cross section $\qquad\qquad\qquad\quad \psi = A/A_0$

  for theoretical heat $\qquad\qquad\qquad \varphi = \dfrac{(\kappa - 1)JQ}{\kappa R T_0}$

  for lower heat value of burning mixture $\qquad \beta = \dfrac{(\kappa - 1)}{\kappa R T_0} \Pi_{m_0}$

  for entropy $\qquad\qquad \rho = \Phi/c_p = \dfrac{(\kappa - 1)J\Phi}{\kappa R}$

  Mach number $\qquad\qquad\qquad\qquad M = \dfrac{c}{}$

Abbreviations:

$$\frac{\alpha\lambda + 1}{\alpha\lambda} = \delta$$

$$1 + \frac{(\kappa - 1)}{2} M^2 = \mu$$

2. Flow of Gas Through a Duct of Variable Cross Section with Heat Release

The theoretical study of jet propulsion of any kind will not be entirely exact until a study has been made of the problem of flow through a duct of variable cross section with heat exchange (or, what has theoretically the same meaning, with heat release). Solving this problem and deriving hereafter special instances which may be useful in our case will provide the tools necessary to a further development of the jet propulsion theory. Such attempts have already been made and published (1, 7, 10); the paper by Dr. Samaras seems to be the most complete and adequate study to date.

Assume the general case of flow of an ideal gas, with no hydraulic or heat losses involved, through a tube of a cross section arbitrarily variable with the tube length (Fig. 1), in which heat is released (i.e., "introduced") at a rate likewise arbitrarily variable along the channel.

The initial values at the channel inlet are assumed to be A_0, P_0, T_0, c_0. At a certain distance x these values become A, P, T, c and they are functions of x, the movement being assumed to be steady, i.e., independent directly of time.
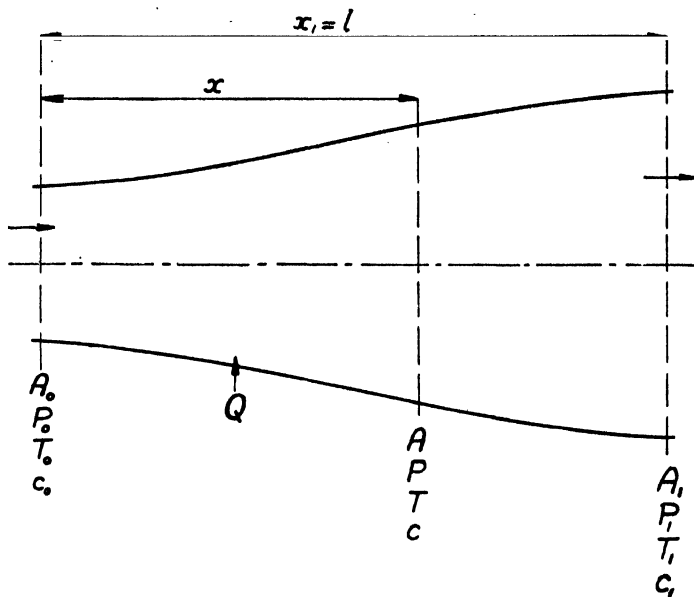
FIG. 1.

The form of duct is arbitrarily given as function of x:

$$\frac{A}{A_0} = \psi(x). \tag{1}$$

On the other hand, the amount of heat brought to the section $(0 - x)$ of the duct during the unit of time is also arbitrarily given in function of x:

$$GQ = F(x) \text{ B.t.u. per sec.} \tag{2}$$

The equation of state being:

$$P_0 v_0 = RT_0, \tag{3}$$

the output becomes:

$$G = \frac{A_0 c_0}{v_0} = \frac{A_0 c_0 P_0}{RT_0}. \tag{4}$$

In order to make clearer the significance of the function $F(x)$ assume that a certain amount of heat GQ_1 has been released along the distance $(0 - x)$ of the duct. If the rate of heat release were constant, i.e., the same on any element dx of the duct length, the form of function $F(x)$ would be

$$GQ = GQ_1 \frac{x}{x_1}.$$

As is known, three laws of conservation govern the flow of gas with heat exchange:

(1) Principle of conservation of mass, the mathematical expression of which for a steady flow is

$$\frac{AcP}{T} = \text{Const.} = \frac{A_0 c_0 P_0}{T_0} = RG; \tag{5}$$

(2) Principle of conservation of momentum, which may be represented by the equation of motion:

$$gRT\frac{dP}{P} + cdc = 0; \tag{6}$$

(3) Principle of conservation of energy, the mathematical expression of which is the first equation of thermodynamics:

$$dQ = c_p dT - \frac{1}{J} v \, dP,$$

which, if bound with the equation of motion, gives the so-called equation of aerothermodynamics which may be expressed in the integral form:

$$Q = \frac{\kappa R}{(\kappa - 1)J}(T - T_0) + \frac{1}{2gJ}(c^2 - c_0^2), \tag{7}$$

where $\dfrac{\kappa R}{(\kappa - 1)J}$ is the specific heat c_p.

Eliminating Q and G from (2), (4), and (7), and introducing dimensionless coefficients, Equation (7) becomes:

$$\tau = \mu_0 + \varphi(x) - (\mu_0 - 1)\sigma^2. \tag{8}$$

Next, eliminating A and T from (1), (5), and (8), Equation (5) becomes:

$$\pi = \frac{\tau}{\sigma\psi(x)} = \frac{\mu_0 + \varphi(x) - (\mu_0 - 1)\sigma^2}{\sigma\psi(x)}. \tag{9}$$

At the same time Equation (6) becomes:

$$\tau\frac{d\pi}{\pi} + \kappa M_0^2 \sigma d\sigma = 0. \tag{10}$$

Equations (8), (9), and (10) determine pressure π, temperature τ, and velocity σ, provided that φ and ψ are given. For instance, τ and π may be eliminated, thus giving:

$$\left[\frac{(\kappa - 1)}{2}M_0^2\sigma^2 - (\varphi + \mu_0) + \frac{\varphi'\psi}{\psi'}\right]\frac{\psi'}{\psi}dx +$$

$$\left[\frac{(\kappa + 1)}{2}M_0^2\sigma^2 - (\varphi + \mu_0)\right]\frac{d\sigma}{\sigma} = 0, \tag{11}$$

which defines the velocity in function of x, i.e., of Q, according to (2). The only difficulty is to find the integral form of Equation (11). As is seen, values of P, c, T depend both on the shape of the duct (ψ) and on variation of heat release (φ). Therefore these last two quantities as a whole—not only their initial and final values—*influence the obtainable thrust and efficiency of the ram jet engine.* This means that in a duct in which initial and final cross

sections, the total amount of heat released, and the initial values P_0, T_0, c_0 are given, the final values P, T, c may vary, according to the form of duct (ψ) and to the kind of variations of heat release (φ). As is seen, the phenomenon is different from that in an ordinary nozzle or diffuser, in which the heat release is considered to be nil, thus permitting the final values P, T, c to be in theoretical principle independent of the shape of the duct, provided the initial and final cross sections are given.

3. Special Case of Duct with Constant Cross Section

In this case $\psi = 1$; $\psi' = 0$, thus:

$$\tau = \mu_0 - (\mu_0 - 1)\sigma^2 + \varphi; \tag{12}$$

$$\tau = \pi\sigma; \tag{13}$$

$$d\pi + \kappa M_0^2 d\sigma = 0; \tag{14}$$

and after integration:

$$\pi + \kappa M_0^2 \sigma = (\kappa M_0^2 + 1). \tag{15}$$

These equations, when solved, give, in accordance with the results already published by the author (10):

$$\pi = \frac{(\kappa M_0^2 + 1)}{(\kappa + 1)} + \frac{\kappa}{(\kappa + 1)} \sqrt{(1 - M_0^2)^2 - 2(\kappa + 1)M_0^2\varphi} \; ; \tag{16}$$

$$\sigma = \frac{(\kappa M_0^2 + 1)}{(\kappa + 1)M_0^2} - \frac{1}{(\kappa + 1)M_0^2} \sqrt{(1 - M_0^2)^2 - 2(\kappa + 1)M_0^2\varphi} \; ; \tag{17}$$

$$\tau = \pi\sigma = \frac{[4\kappa\mu_0^2 - (\kappa + 1)^2]}{(\kappa + 1)^2(\kappa - 1)M_0^2} + \frac{2\kappa}{(\kappa + 1)} \varphi +$$
$$\frac{(\kappa - 1)(\kappa M_0^2 + 1)}{(\kappa + 1)^2 M_0^2} \sqrt{(1 - M_0^2)^2 - 2(\kappa + 1)M_0^2\varphi.} \tag{18}$$

Therefore:

$$\sigma = \frac{(\kappa M_0^2 + 1) - \pi}{\kappa M_0^2} \; ; \tag{19}$$

$$\tau = \frac{\pi}{\kappa M_0^2} [(\kappa M_0^2 + 1) - \pi] = \sigma[(\kappa M_0^2 + 1) - \kappa M_0^2\sigma]; \tag{20}$$

$$\pi + \kappa M_0^2 \nu = (\kappa M_0^2 + 1), \tag{21}$$

where $\nu = \dfrac{v}{v_0}$ represents the specific volume; and

$$\varphi = \frac{1}{\kappa}\left[\frac{(\kappa - 1)}{2\kappa M_0^2} - 1\right] + \frac{1}{\kappa}\left(1 + \frac{1}{\kappa M_0^2}\right)\pi - \frac{(\kappa + 1)}{2\kappa^2 M_0^2}$$
$$= (\kappa M_0^2 + 1)\sigma - \frac{(\kappa + 1)M_0^2}{2} \sigma^2 - \mu_0. \tag{22}$$

Discussion and graphical representation of these mathematical results have already been given in the author's publication cited above (10). The only detail that remains to be discussed, therefore, is the representation in the entropy diagram.

In order to define the entropy, express φ in function of temperature, eliminating σ from (20) and (22):

$$\varphi = \frac{(\kappa + 1)}{2\kappa} \tau - \frac{[(\kappa - 1)\kappa^2 M_0^4 + 2(\kappa + 1)\kappa M_0^2 - (\kappa - 1)]}{4\kappa^2 M_0^2} +$$

$$\frac{(\kappa - 1)}{2\kappa} (\kappa M_0^2 + 1) \sqrt{\frac{(\kappa M_0^2 + 1)^2}{4\kappa^2 M_0^4} - \frac{\tau}{\kappa M_0^2}}. \qquad (23)$$

The entropy

$$d\Phi = \frac{dQ}{T},$$

is in dimensionless form expressed by

$$\frac{\Phi}{c_p} = \frac{(\kappa - 1)J}{\kappa R} \Phi = \rho. \qquad (24)$$

Thus

$$d\rho = \frac{d\varphi}{\tau} = \frac{(\kappa + 1)}{2\kappa} \frac{d\tau}{\tau} - \frac{\frac{(\kappa - 1)}{2\kappa} d\tau}{\tau \sqrt{1 - \frac{4\kappa M_0^2}{(\kappa M_0^2 + 1)} \tau}}, \qquad (25)$$

and after integration

$$(\rho - \rho_0) = \ln \tau - \frac{(\kappa - 1)}{\kappa} \ln \left[\frac{(\kappa M_0^2 + 1)}{2} - \sqrt{\frac{(\kappa M_0^2 + 1)^2}{4} - \kappa M_0^2 \tau} \right]. \qquad (26)$$

The line representing this evolution in entropy diagram (τ, ρ) is limited both by a maximum of temperature

$$\tau_{max} = \frac{(\kappa M_0^2 + 1)^2}{4\kappa M_0^2}$$

for

$$(\rho - \rho_0)_e = \frac{(\kappa + 1)}{\kappa} \ln \left(\frac{\kappa M_0^2 + 1}{2} \right) - \ln(\kappa M_0^2),$$

and by a maximum of entropy

$$(\rho - \rho_0)_{max} = \frac{(\kappa + 1)}{\kappa} \ln \left(\frac{\kappa M_0^2 + 1}{\kappa + 1} \right) - \ln (M_0^2)$$

for

$$\tau_e = \frac{(\kappa M_0^2 + 1)^2}{(\kappa + 1)^2 M_0^2}.$$

In the latter case, according to (20), the velocity becomes:

$$\sigma_e = \frac{(\kappa M_0^2 + 1)}{(\kappa + 1)M_0^2} = \frac{\sqrt{\tau_e}}{M_0},$$

wherefrom $c_e = \sqrt{g\kappa RT_e}$; this is, therefore, the velocity of sound.

The tangent to the line of evolution at the initial point $\tau = 1$ is

$$\left(\frac{d\rho}{d\tau} \right)_{\tau=1} = \frac{(1 - M_0^2)}{(1 - \kappa M_0^2)};$$

$$\left(\frac{d\tau}{d\rho} \right)_{\tau=1} = \frac{(1 - \kappa M_0^2)}{(1 - M_0^2)},$$

while for the classic isobar:

$$\rho - \rho_0 = \ln \tau;$$

$$\frac{d\tau}{d\rho} = \tau;$$

$$\left(\frac{d\tau}{d\rho}\right)_{\tau=1} : 1.$$

The evolutions which occur in a tube of constant cross section for different values of M_0 are shown in entropy diagram in Fig. 2.
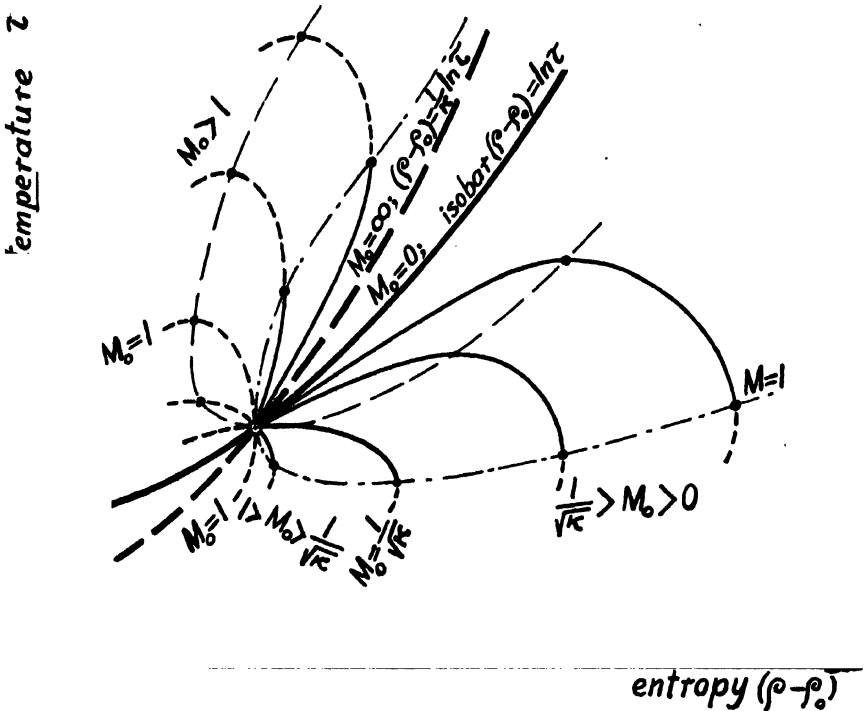
FIG. 2. *Thermodynamic evolutions in flow through a tube of constant cross section.*

The phenomenon of pressure variation with heat released in the perfect flow of a perfect gas through a tube of constant cross section is overlooked by the majority of students of dynamic propulsion, while this phenomenon is the more important the higher the velocity of flow in the combustion chamber. The results of computation given in this Section are, therefore, applied in the following Sections, instead of the generally admitted assumption $P = $ Const. for perfect gas and flow in a combustion chamber.

4. The Problem of Ram-jet Propulsion as Interpreted in Entropy Diagram

The ram-jet propulsion system may be, in general, represented by a duct as given in Fig. 1. The air enters section 0 at a velocity c_0, numerically equal to flight speed, but of opposite direction. The heat is released by combustion along the length $x_1 = l$ or along a part of it. The burnt gases leave at section 1 at a velocity c_1 which, if a certain increase in mass output due to fuel introduction is disregarded, must be higher than c_0, in order to obtain an increase in momentum, thus giving the necessary thrust.

Another essential condition, from the viewpoint of the performance of the engine as considered alone, is
$$P_1 = P_0,$$

i.e., the initial and final static pressures are the same and are equal to the atmospheric pressure. If the pressure P_1 is different from P_0, this will cause an additional loss of energy, apart from the additional static portion of thrust.

The mathematical form of the laws governing the phenomenon studied, as given by Equations (5), (6), and (7), may be rewritten as follows, taking into account the dimensionless coefficients:

$$\frac{\sigma\pi}{\tau}\psi = 1; \tag{27}$$

$$\tau\frac{d\pi}{\pi} + \kappa M_0^2\sigma d\sigma = 0; \tag{10}$$

$$\varphi = \tau + \frac{(\kappa - 1)}{2}M_0^2\sigma^2 - \mu_0. \tag{28}$$

Supposing for the moment that the pressure remains constant during the process, this latter will be represented in entropy diagram by the path $0 - 1$ of the isobar $P = P_0$ (Fig. 3). But, according to (10), the velocity will also remain constant. Thus, the thrust becomes nil here, if the mass output increase by adding fuel is disregarded. Such being the case, and remembering that, in general, $P_1 = P_0$, this isobaric path may be considered as the main skeleton line, which will serve as a comparative basis, while Equation (28) will serve as the main basis for discussion of energy exchanges. This latter equation may be rewritten as follows:

$$\varphi_1 = (\tau_1 - 1) + \frac{(\kappa - 1)}{2}M_0^2(\sigma_1^2 - 1), \tag{29}$$

where τ_1, σ_1, and φ_1 are the final values. As is seen, for isobaric evolution the total amount of energy introduced in form of combustion heat φ_1 is spent in increasing the "total heat", which is proportional to the temperature $(Q_1 = c_p T_1 - c_p T_0)$. In other words, the heat released served only to increase the internal energy of the gas, $c_v(T_1 - T_0)$, apart from a certain amount of external work done $(v_1 - v_0)P_0$ in "repulsing surroundings", due to the increase of specific volume $(v_1 - v_0)$.

The first term on the right side of Equation (29) thus represents the increase in "total heat", and the second the increase in kinetic energy, the only energy which is useful in our case.
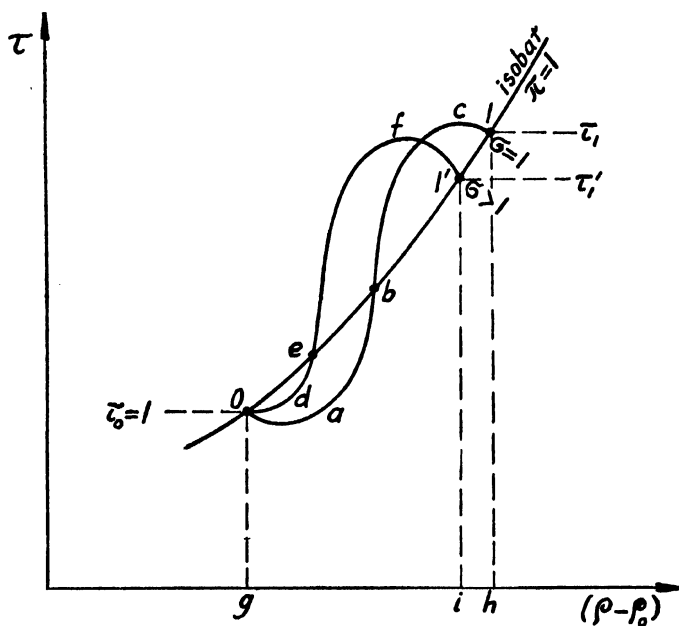
FIG. 3.

It is, of course, possible to apply any kind of evolution arbitrarily given, by forming appropriately the duct form, i.e., $\psi(x)$, provided the variation of the rate of heat release $\varphi(x)$ is given. Let, for instance, the evolution be arbitrarily given as $\pi = f_e(\tau)$. (Polytropic evolution, where $\pi = \tau^{\frac{m}{m-1}}$ with $m = $ Const. might serve here as an example.) Thus, Equations (27), (28), and (10) will give:

$$\kappa M_0^2 (\sigma^2 - 1) + 2 \int_1^\tau \frac{f_e'(\tau)}{f_e(\tau)} \tau d\tau = 0;$$

$$\frac{2}{\kappa M_0^2} \int_1^\tau \frac{f_e'(\tau)}{f_e(\tau)} \tau d\tau \; ; \tag{30}$$

$$\tau - 1 - \frac{(\kappa - 1)}{\nu} \int_1^\tau \frac{f_e'(\tau)}{f_e(\tau)} \tau d\tau = \varphi(x); \tag{31}$$

$$\psi(x) = \frac{\tau}{f_e(\tau) \left| 1 - \frac{\iota}{\kappa M_0^2} \int_1^\tau \frac{f_e'(\tau)}{f_e(\tau)} \tau d\tau \right|} . \tag{32}$$

Function $\varphi(x)$ being given, Equation (31) expresses τ in function of x; thus $\psi(x)$ will be found in function of x from (32).

Let the evolution be represented by the line $0abc1$. It is shaped arbitrarily, with the only condition that areas $0ab0$ and $11'bc1$ are equal. As the area comprised between the line of evolution, the two abscissae $0g$ and $1h$, and the path gh on abscissa axis, represents the total amount of heat φ_1 introduced, the evolution will really finish at point 1, the same as for an isobaric evolution.

If both the kind of fuel and the air excess coefficient are given, the total amount of heat released φ_1 remains the same for any evolution, and the same is true for the area below the line of evolution. On the other hand, in order to get positive thrust, the actual final point must be placed to the left of 1, say at $1'$, as there $\tau_1' < \tau_1$, thus $\sigma_1' > \sigma_0 = 1$. This means that the actual evolution, say $0def1'$, must be such as to have area $ef1'be$ larger than $0de0$, the difference being equal to $1hi1'$.

One important conclusion may be immediately drawn here: *if the combustion chamber, i.e., the part of the duct in which combustion occurs, has to be shaped for practical reasons as a tube of a constant cross section, it is impossible, in subsonic flight, to obtain positive thrust without prior dynamic compression by a diffuser.* This is to say that the ram-jet engine for a subsonic flight, as shown in Fig. 4, is impossible.
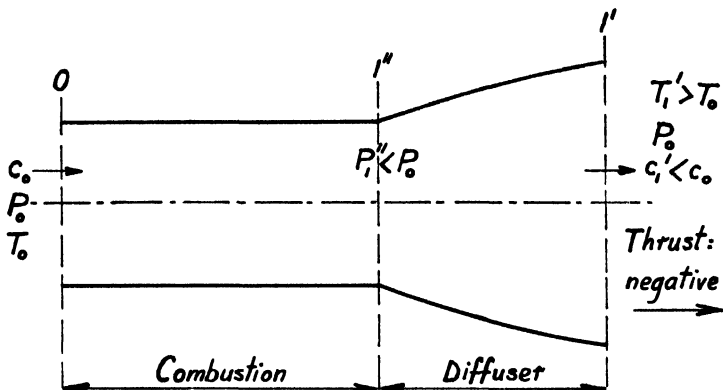
FIG. 4.

The corresponding graphical representation in entropy diagram is given in Fig. 5 for $M_0 < 1$ (subsonic region). Here the two shaded areas must be equal; thus, after isentropic compression $1'' - 1'$ of burnt gases, point $1'$ will be placed to the right of 1; consequently $\sigma < 1$ and thrust becomes negative.

Applying as combustion chamber a cone (in general curvilinear) of sufficient divergency, a line of evolution passing above the isobar $0 - 1$ is obtainable, with the final point $1'$ lying to the left of 1. Such a solution is, however, inefficient, as will be seen later.
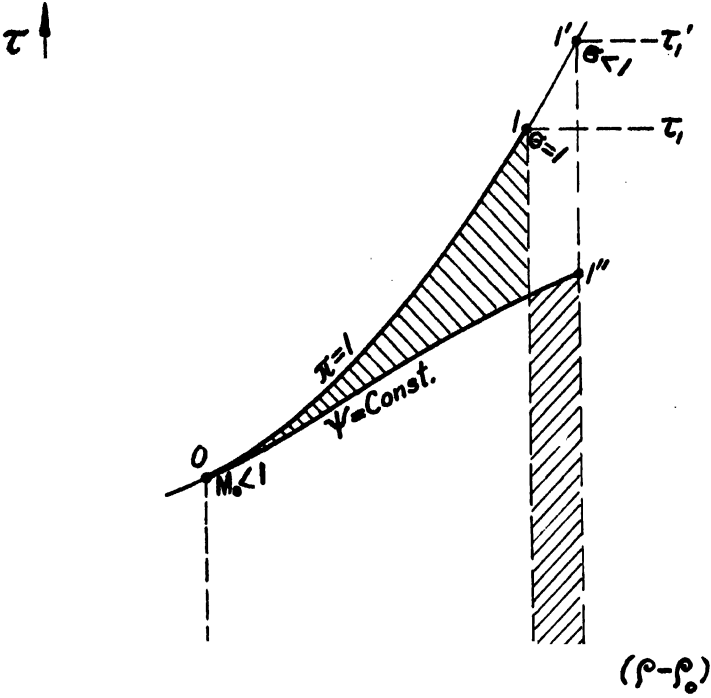
FIG. 5.

If the combustion chamber is to be of constant cross section type, prior
dynamic compression by a diffuser is unavoidable (see Figs. 6 and 7).
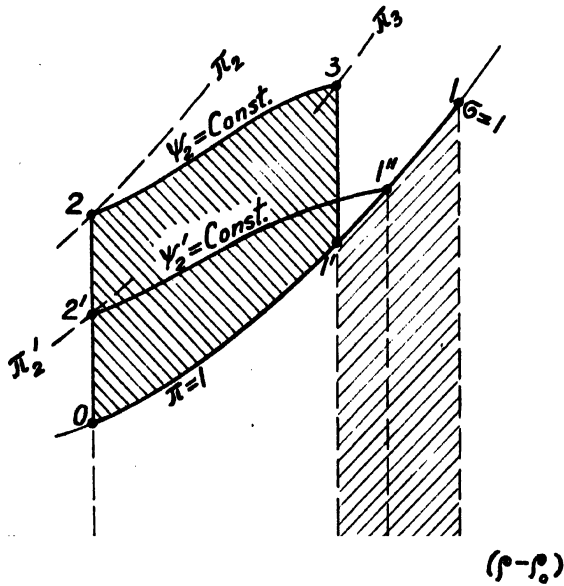
FIG. 6.
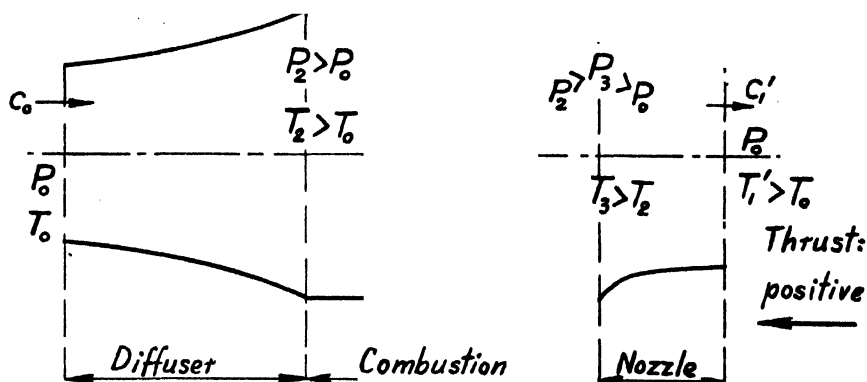
Fig. 7.

The prior compression ends here at a certain pressure $\pi_2 > 1$ at which the velocity σ_2 is still positive. The combustion being finished at 3, applying the nozzle to expand burnt gases from π_3 to $\pi_1' = 1$ is in general necessary. In a certain particular case when $\pi_2 = \pi_2'$ the nozzle is not necessary, the combustion being finished at $1''$, on isobar $\pi = 1$. If the prior dynamic compression is extended only to the pressure $\pi_2 < \pi_2'$, obtaining final pressure $\pi_1' = 1$ is no longer possible.

In the supersonic region, a combustion chamber with constant cross section and without the initial diffuser may give a positive thrust (see Figs. 8 and 9).
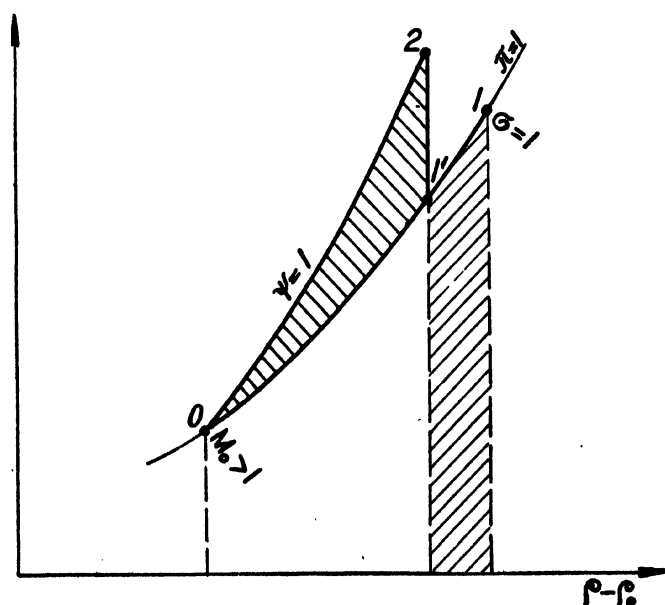
Fig. 8.
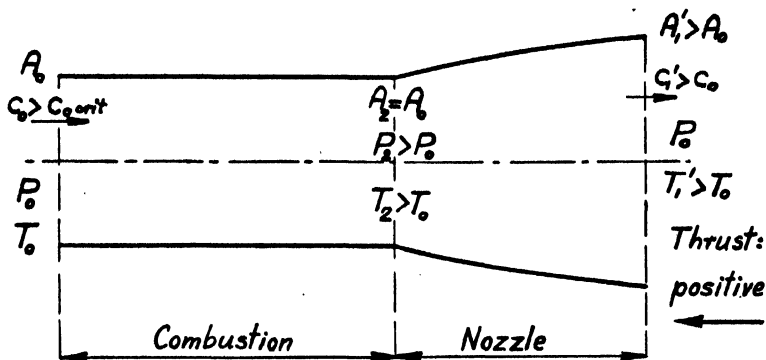
FIG. 9.

The nozzle to enable the expansion $2 - 1'$ is here divergent, as is needed in a supersonic region. Such a solution is, however, inefficient, as will be seen later.

In order to obtain the best working conditions of ram-jet engine, point $1'$ must be placed as far to the left of 1 as possible, according to (28). This will give both the maximum increase in velocity, i.e., maximum thrust and maximum efficiency, also minimum temperature, the total amount of heat φ_1 released by combustion remaining constant.

This is a geometrical problem, at least in part: to apply such a line of evolution which, together with the two abscissae and the path of abscissa axis, encloses a given area in such a manner as to have the difference $(\rho_1' - \rho_0)$ as small as possible, this being incidentally in accordance with the thermodynamic principle of minimum increase of entropy for maximum efficiency.

The first thing to be done is, therefore, an isentropic compression $0 - 2$ by a diffuser (Fig. 10), extended as far as possible. Of course, this is possible only up to $M_2 = 0$ and then the cross section becomes infinite. Although such a "perfect ram-jet engine" is not actually feasible, consider such an ideal case as the limit to which the actual solution has to approach as close as the actual conditions will permit. The corresponding form of the channel is symbolically represented in Fig. 11 for subsonic region and in Fig. 12 for supersonic.

In this case $M_2 = 0$ and, if on the line $2 - 3$ $\psi_2 = $ Const. $= \infty$, also $\sigma = \dfrac{w}{w_0} = $ Const. $= 0$, i.e., $\sigma_3 = \dfrac{w_3}{w_0} = 0$, and $\pi = $ Const. $= \pi_2 = \pi_3$, according to (16) and (17) where $M_0 = 0$ is put (which corresponds to $\sigma_2 = 0$). At the same time, it is found from (18), as a limit:

$$\frac{T_3}{T_2} = \frac{(\kappa - 1)JQ_4}{\kappa RT_2} + 1 = \frac{\varphi_4}{T_2} + 1.$$
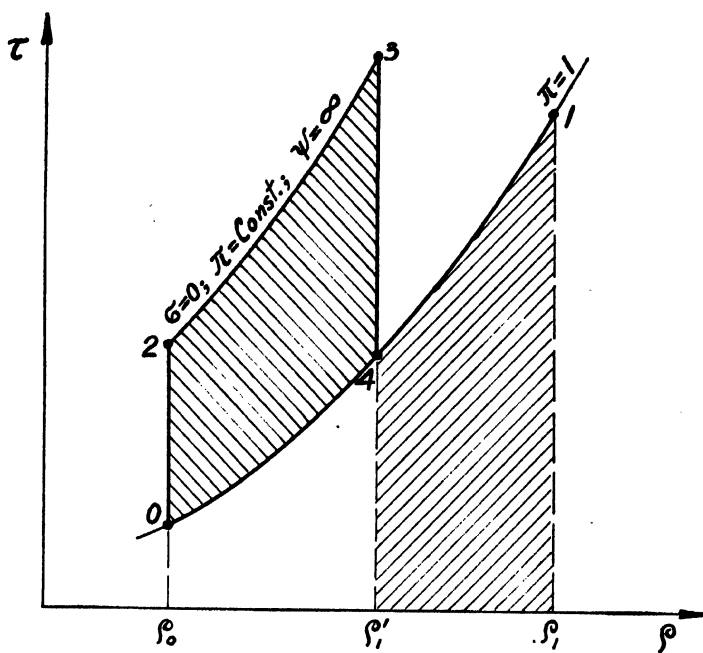
FIG. 10.
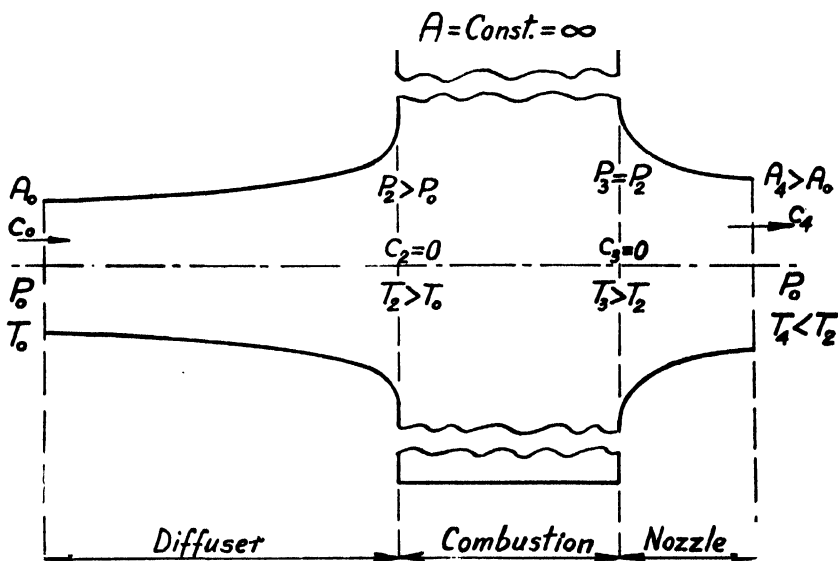
FIG. 11.

The evolution $0 - 2$ being simply isentropic, Equation (28) gives:

$$\tau = \mu_0 - \frac{(\kappa - 1)}{2} M_0^2 \sigma^2 = 1 + \frac{(\kappa - 1)}{2} M_0^2 (1 - \sigma^2);$$

$$\tau_2 = \mu_0 = 1 + \frac{(\kappa - 1)}{2} M_0^2, \tag{33}$$

$$A=Const.=\infty$$
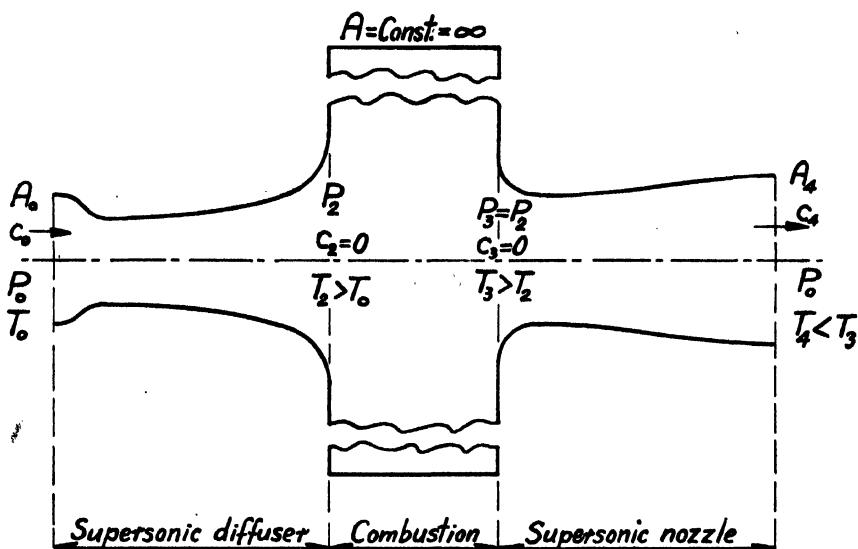
FIG. 12.

and Equation (10) gives:

$$\frac{d\pi}{\pi} + \frac{\kappa M_0^2 \sigma d\sigma}{\left[\mu_0 - \frac{(\kappa - 1)}{2} M_0^2 \sigma^2 \right]} = 0 \; ;$$

$$\frac{\pi^{\frac{\kappa-1}{\kappa}}}{\left[\mu_0 - \frac{(\kappa - 1)}{2} M_0^2 \sigma^2 \right]} = 1;$$

$$\sigma_2 = 0;$$

$$\pi_2 = \mu_0^{\frac{\kappa}{\kappa-1}} = \left[1 + \frac{(\kappa - 1)}{2} M_0^2 \right]^{\frac{\kappa}{\kappa-1}} = \pi_3 \; ; \qquad (34)$$

therefore

$$\tau_3 = \varphi_4 + \tau_2 = \left[1 + \frac{(\kappa - 1)}{2} M_0^2 + \varphi_4 \right]; \qquad (35)$$

$$\sigma_3 = 0.$$

Next comes the simple isentropic expansion $3 - 4$, similar to evolution $0 - 2$;

$$\frac{\tau_4}{\tau_3} = 1 + \frac{(\kappa - 1)c_3^2}{2g\kappa R T_3} \left(1 - \frac{c_4^2}{c_3^2} \right)$$

$$= 1 - \frac{(\kappa - 1)M_0^2 \sigma_3^2}{2\tau_3} \left(\frac{\sigma_4^2}{\sigma_3^2} - 1 \right) \; ;$$

$$\frac{(\kappa - 1)}{2} M_0^2(\sigma_4^2 - \sigma_3^2)$$

$$\tau_3 - \frac{(\kappa - 1)}{2} M_0^2 \sigma_4^2 = \tau_3 - (\mu_0 - 1)\sigma_4^2 \; ;$$

$$\pi_4 = 1;$$

$$\frac{\pi_4}{\pi_3} = \frac{1}{\pi_3} = \left(\frac{\tau_4}{\tau_3} \right)^{\frac{\kappa}{\kappa-1}} \; ;$$

therefore:

$$\tau_4 = \frac{\tau_3}{\pi_3^{\frac{\kappa-1}{\kappa}}} = 1 + \frac{\varphi_4}{1 + \frac{(\kappa-1)}{2} M_0^2}\ ; \tag{36}$$

$$\varphi_4 = \sqrt{\frac{\tau_3 - \tau_4}{\tau_2 - 1}} = \sqrt{\tau_4} = \sqrt{1 + \frac{\varphi_4}{\tau_2}} = \sqrt{1 + \frac{\varphi_4}{1 + \frac{(\kappa-1)}{2} M_0^2}}\ . \tag{37}$$

The final cross section will be

$$\psi_4 = \frac{\tau_4}{\sigma_4 \pi_4} = \sqrt{\tau_4} = \sqrt{1 + \frac{\varphi_4}{1 + \frac{(\kappa-1)}{2} M_0^2}}\ . \tag{38}$$

5. Thrust and Efficiencies of the "Perfect Ram-jet Engine"

The explanations of the thrust in a jet engine, as given in the technical literature, are sometimes misleading.   In order to avoid misunderstandings, the theoretical interpretation of the thrust is given below.

According to the law of conservation of momentum the sum of impulse and quantity of movement remains constant.   Consider a mass element dG of the thickness dx of the gas entering the duct at 0 (Fig. 1).   The force acting on this element in the direction of channel axis is $P_0 A_0$ and its momentum is $\frac{dG}{g} c_0$.   At the exit the corresponding values are $P_1 A_1$ and $\frac{dG}{g} c_1$.   Thus:

$$f_w + P_0 A_0 + \frac{c_0}{g} \int dG = P_1 A_1 + \frac{c_1}{g} \int dG,$$

where f_w is the force imparted to the gas by the duct walls.   The reaction of gas on the duct walls is, therefore, $(- f_w)$.   This is the internal reaction. On the other hand, supposing the duct to be at rest in an atmosphere of P_0 pressure, the external force acting on the duct walls will be $(A_1 - A_0)P_0$. Thus, assuming $P_1 = P_0$, the net thrust becomes:

$$Th = f_w - (A_1 - A_0)P_0 = \frac{(c_1 - c_0)}{g} \int dG = \frac{G}{g}(c_1 - c_0),$$

i.e., only the increase in momentum gives the thrust, provided the pressure is the same on both sides.

Taking as an example the duct of constant cross section, the thrust becomes, according to (16) and (17):

$$Th = (P_1 - P_0)A_0 + \frac{G}{g}(c_1 - c_0) - P_0(A_1 - A_0)$$

$$= P_0 A_0(\pi_1 - 1) + \frac{Gc_0}{g}(\sigma_1 - 1) = \frac{GRT_0}{c_0}(\pi_1 - 1) + \frac{Gc_0}{g}(\sigma_1 - 1)$$

$$\frac{Gc_0}{g}\left[\frac{1}{\kappa M_0^2}(\pi_1 - 1) + (\sigma_1 - 1)\right] = 0.$$

Let all idealizing assumptions so far made be conserved for a moment, and let the increase of mass by addition of fuel be disregarded. Thus the thrust will be:

$$Th = \frac{G}{g}(c_4 - c_0) \text{ lb.,}$$

and the "specific thrust" as calculated per 1 lb. of air output:

$$\zeta = \frac{Th}{G} = \frac{c_0}{g}(\sigma_4 - 1) = \frac{c_0}{g}\left[\sqrt{1 + \frac{\varphi_4}{1 + \frac{(\kappa - 1)}{2} M_0^2}} - 1\right] \quad (39)$$

The external efficiency:

$$\eta_{ex} = \frac{c_0(Th)}{\frac{G}{2g}(c_4{}^2 - c_0{}^2)} = \frac{2(\sigma_4 - 1)}{(\sigma_4^2 - 1)}$$

$$(\sigma_4 + 1) = \frac{2}{1 + \sqrt{1 + \frac{\varphi_4}{1 + \frac{(\kappa - 1)}{2} M_0^2}}} = . \quad (40)$$

The thermal efficiency (the only useful energy being the increase in kinetic energy):

$$\eta_{th} = \frac{G/2g(c_4^2 - c_0^2)}{JGQ_4}$$

$$= \frac{(\kappa - 1)M_0^2(\sigma_4^2 - 1)}{2\varphi_4} = \frac{\frac{(\kappa - 1)}{2} M_0^2}{\left[1 + \frac{(\kappa - 1)}{2} M_0^2\right]} . \quad (41)$$

The over-all efficiency:

$$\eta_0 = \eta_{ex}\eta_{th} = \frac{(\kappa - 1)M_0^2}{1 + \sqrt{1 + \frac{\varphi_4}{1 + \frac{(\kappa - 1)}{2} M_0^2}}} . \quad (42)$$

Thus, the conclusions for a "perfect ram-jet engine" are as follows:

(1) The specific thrust decreases with increasing altitude, while it increases with the total rate of heat release per 1 lb. of air output (i.e., with the total specific rate of heat release); it attains maximum value at a certain flight speed, being nil for $c_0 = 0$ and for $c_0 = \infty$.

(2) The external efficiency decreases with the total specific rate of heat release, while it increases with Mach number, i.e., with both the speed of flight and the altitude.

(3) The thermal efficiency is independent of the total specific rate of heat release, while it increases with the square of the initial Mach number, i.e., the square of flight speed has the same influence as the linearly increasing altitude.

(4) The over-all efficiency decreases with total specific rate of heat release and increases with Mach number.

(5) The maximum values of external and total efficiencies are obtained when the total specific rate of heat release is negligible:

$$(\eta_{ex})_{max} = 1.0;$$

$$(\eta_0)_{max} = \frac{\dfrac{(\kappa - 1)}{2} M_0^2}{1 + \dfrac{(\kappa - 1)}{2} M_0^2} = \eta_{th}.$$

In order to obtain in this case positive thrust, the air output must be infinitely large.

Rewriting Equations (40) and (42) for a certain given constant thrust *Th*, the following is obtained:

$$\sqrt{\frac{\varphi_4}{\mu_0} + 1} = 1 + \frac{g(Th)}{c_0 G};$$

$$\eta_{ex} = \frac{1}{1 + \dfrac{g(Th)}{2c_0 G}}; \tag{40'}$$

$$\eta_0 = \frac{\frac{1}{2}(\kappa - 1)M_0^2}{1 + \dfrac{g(Th)}{2c_0 G}}, \tag{42'}$$

while Equation (41) remains the same. As is seen, an increase in either flight speed or air output, as calculated per unit of thrust, is useful to improve efficiency.

It should be remembered here that the above conclusions are rather abstract, as they are based on assumptions of ideal gas and ideal flow, and of perfectly reversible thermodynamic process, excluding any friction and throttling losses, and also inlet shock wave phenomenon, the importance of which is actually considerable.

6. Perfect Ram-jet Engine with Mass of Fuel Involved

The next step to be accomplished in approaching actual conditions is to take into account the mass of fuel, other idealizing assumptions remaining valid.

In order to define more precisely the total rate of heat release, take first the chemically correct air–fuel mixture. The heat H_{m_0} released by burning 1 lb. of such a mixture, if regarded as a lower heat value, is incidentally constant and equals about 1130 B.t.u. per lb. for usual fluid fuels. The total specific rate of heat release φ_4 will, therefore, depend on the air excess coefficient λ.

The weight of air theoretically necessary to burn completely 1 lb. of fuel being denoted by α (for instance $\alpha \backsim 15.1$ for gasoline), thus, per 1 lb. of burning mixture:

$$Q_4 = Q_{2,3} = \frac{(\alpha + 1)}{(\alpha\lambda + 1)} H_{m_0}, \quad \text{B.t.u. per lb.;}$$

$$\varphi_4 = \varphi_{2,3} = \frac{(\kappa - 1)J}{\kappa RT_0} Q_{2,3}$$

$$= \frac{(\kappa - 1)J(\alpha + 1)H_{m_0}}{\kappa RT_0(\alpha\lambda + 1)} = \frac{(\alpha + 1)\beta}{(\alpha\lambda + 1)}, \tag{43}$$

where

$$\beta = \frac{(\kappa - 1)JH_{m_0}}{\kappa RT_0}. \tag{44}$$

The weight output of the active medium being G in compression $1 - 2$, it will be in combustion $2 - 3$ and in expansion $3 - 4$:

$$G_{2,3,4} = \frac{(\alpha\lambda + 1)}{\alpha\lambda} G = \delta G. \tag{45}$$

Equations (33) to (37) might be directly applied here to find temperatures, pressures, and velocities. This would be, however, an approximation only, which may raise the asymptotic limit of the external efficiency beyond 100%. To have all formulae theoretically exact, two quantities of energy, no matter how small they may actually be, must be taken into account.

The first is due to the fact that the fuel is introduced at the temperature T_0 ; it must, therefore, be reheated from T_0 to T_2. From the theoretical standpoint the same specific heat as for air will be applied here; therefore the actual amount of heat serving to raise the temperature of 1 lb. of the fuel–air mixture from T_2 to T_3 will be not Q_4 but

$$Q_4' = Q_4 - \frac{\kappa R}{(\kappa - 1)J} (T_2 - T_0) \frac{G}{\alpha\lambda} \times \frac{\alpha\lambda}{(\alpha\lambda + 1)G}$$

$$= \frac{(\alpha + 1)H_{m_0}}{(\alpha\lambda + 1)} - \frac{\kappa RT_0}{(\kappa - 1)J} \times \frac{(\tau_2 - 1)}{(\alpha\lambda + 1)} ;$$

$$\varphi_4' = \varphi_4 - \frac{(\tau_2 - 1)}{(\alpha\lambda + 1)} = \frac{(\alpha + 1)\beta - (\tau_2 - 1)}{(\alpha\lambda + 1)}. \tag{46}$$

The second quantity of energy lost is due to the fact that the fuel has to be delivered at the pressure P_2. This prior compression from P_0 to P_2 may be ideologically identical with the increase of kinetic energy of fuel from 0 to $\frac{c_0^2}{2g}$, as this was the kinetic energy of air at the intake, while for the fuel it was nil. The only means of doing this work is to utilize a small part of the kinetic energy of the gases leaving the engine, as there is no other way to drive auxiliaries—if the theoretical viewpoint is to be maintained. Thus the actual thrust will be diminished. Instead of the net work done by the thrust per unit of time

$$W = c_0(Th) = \frac{Gc_0}{g} (\delta c_4 - c_0),$$

it will be

$$W' = \frac{Gc_0}{g} (\delta c_4 - c_0) - \frac{Gc_0^2}{2g\alpha\lambda} \tag{47}$$

if any loss of energy which might occur here is disregarded. The actual net thrust will, therefore, be:

$$(Th)' = \frac{W'}{c_0} = \frac{G}{g} (\delta c_4 - c_0) - \frac{Gc_0}{2g\alpha\lambda} . \tag{48}$$

Applying now Equation (37) and those following, formulae as given below are obtained:

$$\tau_2 = 1 + \frac{(\kappa - 1)}{2} M_0^2 ;$$

$$\pi_2 = \left[1 + \frac{(\kappa - 1)}{2} M_0^2 \right]^{\frac{\kappa}{\kappa - 1}} = \pi_3 ;$$

$$\sigma_2 = \sigma_3 = 0;$$

$$\tau_3 = \tau_2 + \varphi_4' = \frac{(\alpha + 1)\beta + 1 + \alpha\lambda \frac{(\kappa - 1)}{2} M_0^2}{(\alpha\lambda + 1)} ;$$

$$\tau_4 = \frac{\tau_3}{\tau_2} = \frac{\varphi_4'}{\tau_2} + 1$$

$$= \frac{\left[(\alpha + 1)\beta + 1 + \alpha\lambda + \alpha\lambda \frac{(\kappa - 1)}{2} M_0^2 \right]}{(\alpha\lambda + 1) \left[1 + \frac{(\kappa - 1)}{2} M_0^2 \right]} ;$$

$$\pi_4 = 1;$$

$$\sigma_4 = \sqrt{\frac{\tau_3 - \tau_4}{\frac{(\kappa - 1)}{2} M_0^2}} = \sqrt{\frac{\tau_3}{\tau_2}} = \sqrt{\frac{\varphi_4'}{\tau_2} + 1}$$

$$= \sqrt{\tau_4} = \sqrt{\frac{(\alpha + 1)\beta + 1 + \alpha\lambda + \alpha\lambda \frac{(\kappa - 1)}{2} M_0^2}{(\alpha\lambda + 1) \left[1 + \frac{(\kappa - 1)}{2} M_0^2 \right]}} .$$

Thus, the final cross section:

$$\psi_4 = \delta \sqrt{\frac{\varphi_4'}{\tau_2} + 1} = \frac{\sqrt{\alpha\lambda + 1}}{\alpha\lambda} \sqrt{\frac{(\alpha + 1)\beta + 1 + \alpha\lambda + \alpha\lambda \frac{(\kappa - 1)}{2} M_0^2}{1 + \frac{(\kappa - 1)}{2} M_0^2}} . \tag{49}$$

Furthermore:

$$(Th)' = \frac{Gc_0}{g} \times$$

$$\frac{\left[\sqrt{\alpha\lambda+1}\sqrt{(\alpha+1)\beta+1+\alpha\lambda+\alpha\lambda\frac{(\kappa-1)}{2}M_0^2} - (\alpha\lambda+\tfrac{1}{2})\sqrt{1+\frac{(\kappa-1)}{2}M_0^2}\right]}{\alpha\lambda\sqrt{1+\frac{(\kappa-1)}{2}M_0^2}} .$$

$$\zeta' = \frac{(Th)'}{\upsilon}$$

$$= \frac{c_0}{g\alpha\lambda}\left[\frac{\sqrt{\alpha\lambda+1}\sqrt{(\alpha+1)\beta+1+\alpha\lambda+\alpha\lambda\frac{(\kappa-1)}{2}M_0^2}}{\sqrt{1+\frac{(\kappa-1)}{2}M_0^2}} - (\alpha\lambda+\tfrac{1}{2})\right] ;$$

$$\left. \right\} (50)$$

$$W' = c_0(Th)';$$

$$\eta_{ex} = \frac{W'}{\frac{G}{2g}(\delta c_4^2 - c_0^2)}$$

$$= \frac{2\left[\sqrt{\alpha\lambda+1}\sqrt{(\alpha+1)\beta+1+\alpha\lambda+\alpha\lambda\frac{(\kappa-1)}{2}M_0^2} - (\alpha\lambda+\tfrac{1}{2})\sqrt{1+\frac{(\kappa-1)}{2}M_0^2}\right]\sqrt{1+\frac{(\kappa-1)}{2}M_0^2}}{[(\alpha\lambda+1)\beta+1]} ; \qquad (51)$$

$$\eta_{th} = \frac{(\delta c_4^2 - c_0^2)}{JGQ_4\delta} = \frac{(\kappa-1)M_0^2[(\alpha+1)\beta+1]}{2(\alpha+1)\beta\left[1+\frac{(\kappa-1)}{2}M_0^2\right]} ; \qquad (52)$$

$$\eta_0 = \frac{(\kappa-1)M_0^2}{(\alpha+1)\beta}\left[\sqrt{\alpha\lambda+1}\frac{\sqrt{(\alpha+1)\beta+1+\alpha\lambda+\alpha\lambda\frac{(\kappa-1)}{2}M_0^2}}{\sqrt{1+\frac{(\kappa-1)}{2}M_i^2}} - (\alpha\lambda+\tfrac{1}{2})\right] \qquad (53)$$

The "unit thrust", as calculated by the unit of the cross section area, will be:

$$\epsilon_0 - \frac{(Th)'}{A_0} = \frac{c_0 P_0}{GRT_0}(\overline{in})$$

$$\frac{\kappa M_0^2 P_0}{\alpha\lambda}\left[\frac{\sqrt{\alpha\lambda+1}\sqrt{(\alpha+1)\beta+1+\alpha\lambda+\alpha\lambda\frac{(\kappa-1)}{2}M_0^2}}{\sqrt{1+\frac{(\kappa-1)}{2}M_0^2}} - (\alpha\lambda+\tfrac{1}{2})\right] . (54)$$

$$\epsilon_4 = \frac{(Th)'}{A_4} = \frac{\epsilon_0}{\psi_4}$$

$$= \kappa M_0^2 P_0 \frac{\left[\sqrt{\alpha\lambda+1}\sqrt{(\alpha+1)\beta+1+\alpha\lambda+\alpha\lambda\frac{(\kappa-1)}{2}M_0^2}-(\alpha\lambda+\tfrac{1}{2})\sqrt{1+\frac{(\kappa-1)}{2}M_0^2}\right]}{\sqrt{\alpha\lambda+1}\sqrt{(\alpha+1)\beta+1+\alpha\lambda+\alpha\lambda\frac{(\kappa-1)}{2}M_0^2}}.$$

$$(55)$$

Mathematical analysis of Equation (51) shows that η_{ex} attains the maximum value of 100% for $\lambda = \infty$, and continuously increases with λ. At the same time the specific thrust ζ' continuously decreases with increasing λ and becomes nil for $\lambda = \infty$, provided that $\mu_0 \leqslant 4[(\alpha + 1)\beta + 1]$, i.e.,

$$M_0 \leqslant \sqrt{\frac{2}{(\kappa - 1)} \{4[(\alpha + 1)\beta + 1] - 1\}}.$$

Considering now the initial Mach number as an independent variable, the external efficiency η_{ex} first increases with increasing M_0, attaining maximum value of 100% for

$$(M_0)_{e_1} = \sqrt{\frac{2}{(\kappa - 1)} (\alpha + 1)\beta},$$

and then decreases, becoming nil for

$$(M_0)_{e_2} = \sqrt{\frac{2}{(\kappa - 1)} \{4[\alpha + 1)\beta + 1](\alpha\lambda + 1) - 1\}}.$$

Of course, η_{ex} cannot be negative; therefore, the limit for the velocity of flight, expressed by the initial Mach number, is

$$M_0 \leqslant \sqrt{\frac{2}{(\kappa - 1)}\{4[(\alpha + 1)\beta + 1](\alpha\lambda + 1) - 1\}}, \qquad (56)$$

as far as the dynamical phenomenon is concerned, this value of M_0 corresponding to the conditions in which the loss in kinetic energy of gas mass leaving the engine becomes equal to the total increase in kinetic energy created by the engine. For $\lambda = \infty$, i.e., in a case in which the mass of fuel may be disregarded, the limit (56) gives, of course, $M_0 = \infty$, which means $c_0 = \infty$ if $T_0 > 0$.

Likewise, the specific thrust first increases with increasing M_0, attaining a certain maximum value which does not coincide with the maximum of η_{ex}, and then decreases, becoming nil together with η_{ex}, i.e., for the value of M_0 as defined by (56).

The maximum value of thermal efficiency, equalling 100%, is obtained for $(M_0)_{s_1} = \sqrt{\dfrac{2}{(\kappa - 1)}} (\alpha + 1)\beta$, according to (52), i.e., if thermodynamic means for creating energy are applied. In the limiting case φ_4' becomes nil, i.e., all the heat released by combustion is utilized only for the reheating of fuel from T_0 to the ram temperature T_2. It follows that $T_4 = T_0$ and $c_4 = c_0$, i.e., both exit heat loss and exit loss in kinetic energy are nonexistent, which is in accordance with 100% value of all efficiencies (η_{ex} ; η_{th} ; η_0). Of course, heat φ_4' cannot be negative; value $(M_0)_{s_1}$ is, therefore, a physical limit for the velocity of flight, as regarded from the theoretical viewpoint:

$$M_0 \leqslant \sqrt{\frac{2}{(\kappa - 1)} (\alpha + 1)\beta} . \tag{56'}$$

This limiting value is independent (at least apparently so) of the air excess coefficient, i.e., of the ratio G_f/G_a . It, therefore, seems to be valid in any general case, even for $G_a = \infty$, provided the thermodynamic means to create energy are applied. As the limit (56') is more restricted than (56), it must be considered as the actual one.

7. Semiperfect Ram-jet Engine with Finite Combustion Chamber Cross Section

In the actual jet engine the bulk diameter will, of course, be limited by practical conditions. In order to let the perfect ram-jet engine approach actual conditions, suppose that the maximum cross section, no matter where it may be placed in the engine, is given, all other idealizing conditions being maintained. The best results in such a semiperfect jet engine will, of course, be obtained when this maximum cross section occurs at point 2, i.e., just after dynamic compression, the combustion chamber cross section remaining constant, i.e., $A_3 = A_2$. The corresponding form of the engine working in subsonic region is represented in Fig. 13 and the graphical representation in entropy diagram in Fig. 14.
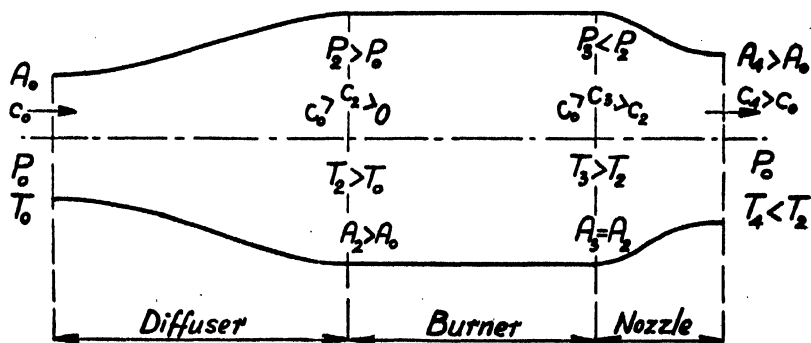
FIG. 13.
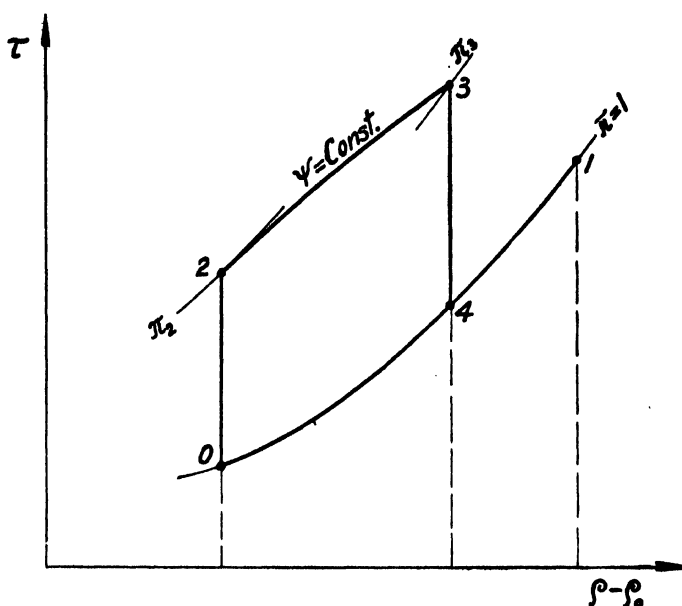
FIG. 14.

Another possible limitation is to consider the minimum admissible value for the velocity σ_2 after dynamic compression. Supposing that this value is given as $(\sigma_2)_{min}$, the following formulae are obtained:

$$\tau_2 = \left[1 + \frac{(\kappa - 1)}{2} M_0^2 (1 - \sigma_{2m}^2) \right] ; \tag{57}$$

$$\pi_2 = \tau_2^{\frac{\kappa}{\kappa-1}} = \left[1 + \frac{(\kappa - 1)}{2} M_0^2 (1 - \sigma_{2m}^2) \right]^{\frac{\kappa}{\kappa-1}} ; \tag{58}$$

$$\psi_2 = \frac{\tau_2}{\sigma_{2m}\pi_2} = \frac{1}{\sigma_{2m} \left[1 + \frac{(\kappa - 1)}{2} M_0^2 (1 - \sigma_{2m}^2) \right]^{\frac{1}{\kappa-1}}} ; \tag{59}$$

$$\varphi_{2,3} = \frac{(\alpha + 1)\beta}{(\alpha\lambda + 1)} ; \tag{60}$$

$$Q_{2,3} = \frac{\kappa R T_0}{(\kappa - 1)J} \varphi_{2,3} ;$$

$$\varphi'_{2,3} = \varphi_{2,3} - \frac{(\tau_2 - 1)}{(\alpha\lambda + 1)} = \frac{(\alpha + 1)\beta - \frac{(\kappa - 1)}{2} M_0^2 (1 - \sigma_{2m}^2)}{(\alpha\lambda + 1)} ; \tag{61}$$

$$\pi_3 = \frac{\pi_2^{\frac{1}{\kappa-1}}}{(\kappa + 1)} \left[(\kappa M_0^2 \sigma_{2m}^2 + \tau_2) + \kappa \sqrt{(\tau_2 - M_0^2 \sigma_{2m}^2)^2 - 2(\kappa+1)M_0^2 \sigma_{2m}^2 \varphi'_{2,3}} \right] ; \tag{62}$$

$$\sigma_3 = \frac{1}{(\kappa+1)M_0^2\sigma_{2m}}\left[(\kappa M_0^2\sigma_{2m}^2 + \tau_2) - \sqrt{(\tau_2 + M_0^2\sigma_{2m}^2)^2 - 2(\kappa+1)M_0^2\sigma_{2m}^2\varphi_{2,3}'}\right]$$

$$= \frac{\sigma_{2m}[(\kappa-1)M_0^2\sigma_{2m}^2 + 2(\tau_2 + \varphi_{2,3}')]}{(\kappa M_0^2\sigma_{2m}^2 + \tau_2) + \sqrt{(\tau_2 - M_0^2\sigma_{2m}^2)^2 - 2(\kappa+1)M_0^2\sigma_{2m}^2\varphi_{2,3}'}} \; ; \tag{63}$$

$$\tau_3 = \tau_2\frac{\sigma_3}{\sigma_{2m}} \times \frac{\pi_3}{\pi_2} = \frac{\sigma_3\pi_3}{\sigma_{2m}\tau_2^{\frac{1}{\kappa-1}}} \; ; \tag{64}$$

$$\tau_4 = \frac{\tau_3}{\pi_3^{\frac{\kappa-1}{\kappa}}} \; ; \tag{65}$$

$$\sigma_4 = \sqrt{\frac{(\tau_3 - \tau_4)}{\frac{(\kappa-1)}{2}M_0^2} + \sigma_3^2} \; ; \tag{66}$$

$$\psi_4 = \frac{\delta\tau_4}{\pi_4\sigma_4} = \frac{\delta\tau_4}{\sigma_4} \; ; \tag{67}$$

$$(Th)' = G\zeta' = \frac{Gc_0}{g}\left(\delta\sigma_4 - 1 - \frac{1}{2\alpha\lambda}\right) \; ; \tag{68}$$

$$\eta_{ex} = \frac{c_0(Th)'}{\frac{Gc_0^2}{2g}(\delta\sigma_4^2 - 1)} = \frac{2\left(\delta\sigma_4 - 1 - \frac{1}{2\alpha\lambda}\right)}{(\delta\sigma_4^2 - 1)} \; ; \tag{69}$$

$$\eta_{th} = \frac{Gc_0^2/2g\,(\delta\sigma_4^2 - 1)}{JGQ_{2,3}\delta} = \frac{(\kappa-1)M_0^2(\delta\sigma_4^2 - 1)}{2\delta\varphi_{2,3}} \; ; \tag{70}$$

$$\eta_0 = \eta_{ex}\eta_{th} \; ; \tag{71}$$

$$\epsilon_0 = \frac{(Th)'}{A_0} = \kappa M_0^2 P_0\left(\delta\sigma_4 - 1 - \frac{1}{2\alpha\lambda}\right) \; ; \tag{72}$$

$$\epsilon_2 = \frac{\epsilon_0}{\psi_2} \; ; \tag{73}$$

$$\epsilon_4 = \frac{\epsilon_0}{\psi_4} \cdot \tag{74}$$

Suppose, as an example:

Velocity of flight $c_0 = 600$ m.p.h. $= 880$ ft. per sec.;

Sea level, standard atmosphere;

$\kappa = 1.4$; $R = 53.3$ ft. per °Rankine;

Fuel: gasoline, $\alpha = 15.0$; $H_{m_0} = 1130$ B.t.u. per lb.;

Air excess coefficient: $\lambda = 4.0$;

Velocity at the combustion chamber inlet: $c_2 = 100$ ft. per sec.

This gives:

$$M_0 = 0.789; \qquad M_0{}^2 = 0.6225;$$
$$\sigma_{2m} = 0.1137; \qquad \sigma_{2m}{}^2 = 0.01292;$$
$$\tau_2 = 1.1221; \qquad \pi_2 = 1.497;$$
$$\psi_2 = 6.595; \qquad \sqrt{\psi_2} = 2.568;$$
$$\beta = 9.09; \qquad \varphi_{2,3} = 2.384; \qquad \varphi'_{2,3} = 2.383;$$
$$\delta = 1.017;$$
$$\pi_3 = 1.463; \qquad \sigma_3 = 0.362; \qquad \tau_3 = 3.490;$$
$$\pi_4 = 1.000; \qquad \tau_4 = 3.130; \qquad \sigma_4 = 1.739;$$
$$\psi_4 = 1.830; \qquad \sqrt{\psi_4} = 1.354;$$
$$\zeta' = 20.80 \text{ lb. per lb. per sec.};$$
$$\eta_{ex} = 0.734 = 73.4\%;$$
$$\eta_{th} = 0.1064 = 10.64\%;$$
$$\eta_0 = 0.0781 = 7.81\%;$$
$$\epsilon_0 = 1415 \text{ lb. per sq. ft.} = 9.67 \text{ lb. per sq. in.};$$
$$\epsilon_2 = 214.7 \text{ lb. per sq. ft.} = 1.475 \text{ lb. per sq. in.};$$
$$\epsilon_4 = 774 \text{ lb. per sq. ft.} = 5.330 \text{ lb. per sq. in.}$$

8. The Actual Ram-jet Engine

The aerothermodynamic process in an actual ram-jet engine will be as illustrated graphically in entropy diagram in Fig. 15.
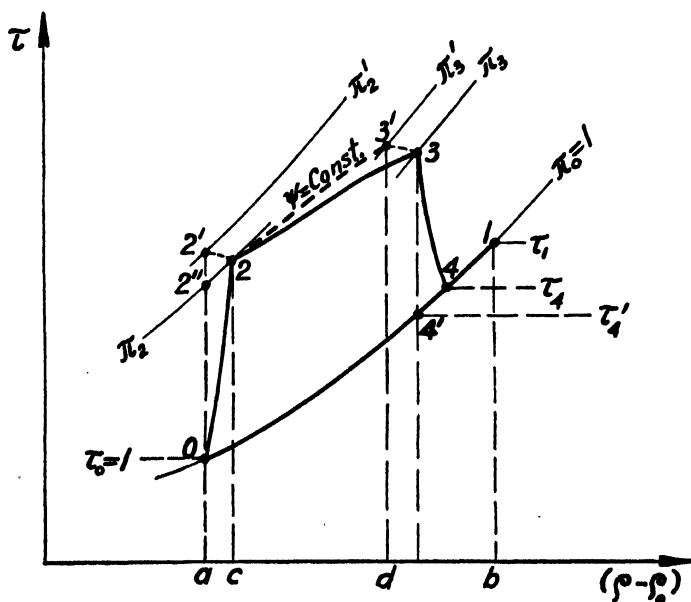
FIG. 15. *Entropy diagram of an actual ram-jet engine.*

Let the efficiency of the diffuser be η_d (probably of the order of 0.92); thus:

$$\frac{T_2'' - T_0}{T_2 - T_0} = \eta_d \; ;$$

$$\frac{P_2''}{P_0} = \frac{P_2}{P_0} \qquad \pi_2 \; \left(\frac{T_2}{T_0}\right)^{\frac{\kappa}{\kappa-1}} .$$

As equation of aerothermodynamics, in form (7) or (28), always holds true, even if throttling loss is involved, assuming that the process $0 - 2$ is adiabatic in the general sense of the term (i.e., that no heat exchange is involved), this process may be considered as an isentropic compression $0 - 2'$ accompanied by the throttling $2' - 2$. Thus

$$\tau_2 = \left[1 + \frac{(\kappa - 1)}{2} M_0^2 (1 - \sigma_{2m}^2)\right], \tag{75}$$

where σ_{2m} is assumed to be given. Therefore:

$$T_2'' = T_0 + \eta_d (T_2 - T_0);$$

$$\pi_2 = [(1 - \eta_d) + \eta_d \tau_2]^{\frac{\kappa}{\kappa-1}}$$

$$= \left[1 + \eta_d \frac{(\kappa - 1)}{2} M_0^2 (1 - \sigma_{2m}^2)\right]^{\frac{\kappa}{\kappa-1}} ; \tag{76}$$

$$\tag{77}$$

Pressure π_2' might be obtained if the evolution were isentropic, with no throttling loss involved and with the same cross section ψ_2.

The loss by incomplete combustion may be considered as nil, remembering the considerable air excess applied here, provided that the combustion chamber is properly designed. The loss of heat by conductivity is relatively small—of the order of 2%; this is due to the considerable magnitude of the heat release, as relating to the small surface corresponding to unit of flowing mass. Let the corresponding efficiency be η_h (probably about 0.98); thus:

$$\varphi_{2,3} = \eta_h \frac{(\alpha + 1)\beta}{(\alpha\lambda + 1)} ; \tag{78}$$

$$\varphi_{2,3}' = \varphi_{2,3} - \frac{(\tau_2 - 1)c_{p_f}}{(\alpha\lambda + 1)c_{p_a}} , \tag{79}$$

where c_{p_f}/c_{p_a} is the ratio of specific heats of fuel and air respectively; this ratio is so chosen as to take into account also the latent heat of vaporization of fuel. The actual value of this ratio is, therefore, about 10.

The gas constant and the isentropic exponent of the mixture during combustion are, of course, variable. The gas constant deviates only very slightly from that of air (this being due to a considerable air excess), and its mean

value may be evaluated as $R' = 53.0$. The mean value of the specific heat c_p' deviates much more from that of cold air, this being due mainly to the increase in temperature. It may be evaluated as $c_p' \backsim 0.28$ B.t.u. per lb., °F., in the case studied.

Therefore the isentropic exponent will be:

$$\kappa' = \frac{1}{1 - R'/c_p'J} = 1.322.$$

At the same time the formal value of Mach number M_0 will change to M_0':

$$M_0' = \sqrt{\frac{\kappa R}{\kappa' R'}}\, M_0 = 1.032\, M_0.$$

In actual practice the loss by heat conductivity is often overestimated, values of η_h being estimated as low as 0.88 and even 0.85. This is due to the fact that, in applying computation based on the assumption of an ideal gas, values of R and κ are usually kept constant during the whole process. As is seen, the actual value κ' during combustion deviates considerably from κ for cold gas. Thus, remaining in the field of theoretical computation, final results are found to be less optimistic, the influence of the changing value of κ with temperature being much stronger than the heat loss by conductivity.

If, for the moment, the "hydraulic" loss in the combustion chamber of constant cross section is disregarded, the final state after combustion will be π_3', σ_3', τ_3':

$$\pi_3' = \frac{\pi_2}{(\kappa'+1)\tau_2}\left[(\kappa' M_0'^2 \sigma_{2m}^2 + \tau_2) + \kappa'\sqrt{(\tau_2 - M_0'^2 \sigma_{2m}^2)^2 - 2(\kappa'+1)M_0'^2 \sigma_{2m}^2 \varphi_{2,3}'}\right] ; \tag{80}$$

$$\sigma_3' = \frac{1}{(\kappa'+1)M_0'^2 \sigma_{2m}}\left[(\kappa' M_0'^2 \sigma_{2m}^2 + \tau_2) - \sqrt{(\tau_2 - M_0'^2 \sigma_{2m}^2)^2 - 2(\kappa'+1)M_0'^2 \sigma_{2m}^2 \varphi_{2,3}'}\right]$$

$$\frac{\sigma_{2m}[(\kappa'-1)M_0'^2 \sigma_{2m}^2 + 2(\varphi_{2,3}' + \tau_2)]}{[(\kappa' M_0'^2 \sigma_{2m}^2 + \tau_2) + \sqrt{(\tau_2 - M_0'^2 \sigma_{2m}^2)^2 - 2(\kappa'+1)M_0'^2 \sigma_{2m}^2 \varphi_{2,3}'}]} ; \tag{81}$$

$$\tau_3' = \frac{\sigma_3' \pi_3'}{\sigma_{2m} \pi_2}\, \tau_2. \tag{82}$$

The actual pressure π_3 will, of course, be less and it might be evaluated according to the well known routine method, involving Reynolds number and hydraulic radius. The loss $(\pi_3' - \pi_3)$ is, in the case studied, of the order of 2%. For the sake of simplicity it may be defined by the "pressure efficiency" η_p as follows:

$$\pi_3 = \eta_p \pi_3', \tag{83}$$

where η_p is of the order of 0.98. More precisely:

$$\eta_p = 1 - 2.5\, M_0^2 \sigma_{2m}^2,$$

where the coefficient 2.5 was so chosen as to approach the actual conditions.

In actual practice the "hydraulic" loss of pressure during combustion is often overestimated, even if account is taken of the fact that some actual designs of burner are complicated and offer considerable resistance to flow through combustion chamber. This is due to the fact that the influence of heat exchange on pressure, as studied theoretically in Sections 3 and 4, is generally overlooked in actual computations, while this influence may be actually considerable, at least in case of high velocity.

As, in passing from 3' to 3, both the equation of continuity and the equation of aerothermodynamics hold true, the throttling phenomenon being adiabatic in the general sense of the term; thus:

$$\frac{\sigma_3 \pi_3}{\tau_3} = \frac{\sigma_3' \pi_3'}{\tau_3'} \; ;$$

$$\tau_3 = \tau_3' + \frac{(\kappa' - 1)}{2} M_0'^2 (\sigma_3'^2 - \sigma_3^2),$$

wherefrom:

$$\sigma_3 = \frac{\sigma_3'}{\eta_p} \left[1 + \frac{(\kappa' - 1)M_0'^2}{2\tau_3'} (\sigma_3'^2 - \sigma_3^2) \right] \; ;$$

$$\sigma_3 = \frac{\sigma_3'[2\tau_3' + (\kappa' - 1)M_0'^2 \sigma_3'^2]}{\sqrt{[(\kappa' - 1)M_0'^2 \sigma_3'^2 + \tau_3']^2 - (1 - \eta_p^2)\tau_3'^2} + \eta_p \tau_3'} \; ; \qquad (84)$$

$$\tau_3 = \frac{\eta_p \tau_3'}{\sigma_3'} \sigma_3 . \qquad (85)$$

Now let the efficiency of the nozzle be η_n (probably of the order of 0.96); thus:

$$\frac{T_3 - T_4}{T_3 - T_4'} = \eta_n \; ;$$

$$\pi_4 = 1;$$

$$\left(\frac{T_3}{T_4'} \right)^{\frac{\kappa'}{\kappa' - 1}} = \pi_3 \; ;$$

$$\tau_4 = \tau_3 \left[(1 - \eta_n) + \frac{\eta_n}{(\pi_3)^{\frac{\kappa' - 1}{\kappa'}}} \right] \; ; \qquad (86)$$

$$\sigma_4 = \sqrt{\sigma_3^2 + \frac{2}{(\kappa' - 1)M_0'^2} (\tau_3 - \tau_4)} \; ; \qquad (87)$$

$$\frac{\delta\tau_4}{\sigma_4} \qquad (88)$$

The efficiency of the pumping of fuel η_f is of the order of 0.10 only, as a part of final thrust is supposed to be utilized here; thus:

$$\zeta' = \frac{c_0}{g} \left(\delta\sigma_4 - 1 - \frac{1}{2\alpha\lambda\eta_f} \right) \; ; \qquad (89)$$

$$\eta_{ex} = \frac{2\left(\delta\sigma_4 - 1 - \frac{1}{2\alpha\lambda\eta_f}\right)}{(\delta\sigma_4^2 - 1)} \; ; \tag{90}$$

$$\eta_{th} = \frac{(\kappa - 1)M_0^2\eta_h(\delta\sigma_4^2 - 1)}{2\delta\varphi_{2,3}} \; ; \tag{91}$$

$$\eta_0 = \eta_{ex}\eta_{th} \; ; \tag{92}$$

$$\epsilon_0 = \kappa M_0^2 P_0 \left(\delta\sigma_4 - 1 - \frac{1}{2\alpha\lambda\eta_f}\right) \; ; \tag{93}$$

$$\epsilon_2 = \frac{\epsilon_0}{\psi_2} \; ; \tag{94}$$

$$\epsilon_4 = \frac{\epsilon_0}{\psi_4} \; . \tag{95}$$

Let, for example:

$c_0 = 880$ ft. per sec.; $c_2 = 100$ ft. per sec.;

sea level, standard atmosphere;

$\kappa = 1.40$; $R = 53.3$ ft. per °Rankine; $\lambda = 4.0$;

$\kappa' = 1.322$; $R' = 53.0$;

$\alpha = 15.0$; $H_{m_0} = 1130$ B.t.u. per lb.   ($\beta = 9.09$; $\delta = 1.017$);

$\eta_d = 0.92$; $\eta_n = 0.96$;

$\eta_h = 0.98$; $\dfrac{c_{p_f}}{c_{p_a}} = 10.0$;

$\eta_p = 0.98$; $\eta_f = 0.10$.

This gives:

$M_0 = 0.789$; $M_0^2 = 0.6225$;

$\sigma_{2m} = 0.1137$; $\sigma_{2m}^2 = 0.01292$;

$M_0' = 0.8135$; $M_0'^2 = 0.6625$;

$\tau_2 = 1.1221$; $\pi_2 = 1.448$;

$\psi_2 = 6.820$; $\sqrt{\psi_2} = 2.614$;

$\varphi_{2,3} = 2.536$; $\varphi_{2,3}' = 2.316$;

$\pi_3' = 1.414$; $\sigma_3' = 0.355$; $\tau_3' = 3.422$;

$\pi_3 = 1.386$; $\sigma_3 = 0.3573$; $\tau_3 = 3.374$;

$\pi_4 = 1.000$; $\tau_4 = 3.122$; $\sigma_4 = 1.578$;

$\psi_4 = 2.014$; $\sqrt{\psi_4} = 1.420$;

$\zeta' = 14.22$ lb. per lb. per sec.;

$\eta_{ex} = 0.6800 = 68.00\%$;

$\eta_{th} = 0.0724 = 7.24\%$;

$\eta_0 = 0.0492 = 4.92\%$;

$\epsilon_0 = 960$ lb. per sq. ft. $= 6.670$ lb. per sq. in.;

$\epsilon_2 = 140.8$ lb. per sq. ft. $= 0.978$ lb. per sq. in.;

$\epsilon_4 = 477.0$ lb. per sq. ft. $= 3.312$ lb. per sq. in.

It should be pointed out here that the property of a semiperfect ram-jet engine to have the higher efficiency, the closer the velocity σ_{2m} of flow in the combustion chamber is to zero, no longer exists in the actual engine. Of course, all the heat released in an actual engine is represented by the area $c23'd$, according to Fig. 15, as the two throttling phenomena $2' - 2$ and $3' - 3$ are adiabatic, and the expansion $3 - 4$, bound with a certain throttling, is also adiabatic. The heat released is also represented by the area $a01b$, the two areas being equal. As, however, in an actual engine point 2 is shifted to the right of 0 and point 4 is shifted to the right of $3'$, therefore, the higher the pressure π_2 (i.e., the lower the velocity σ_{2m}), the closer the point 4 is shifted to 1. It is therefore possible that the total efficiency does not increase continuously with π_2 but it passes through a maximum for a certain value of $\sigma_{2m} > 0$, at least at very high supersonic velocities of flight.

9. Conclusions

The main emphasis in this paper is placed on the theoretical background of the problem of ram-jet propulsion, while numerical calculation in regard to an actual engine, as given in Section 8, is only approximate.

The conclusion showing the necessity of applying both the diffuser for dynamic compression and the combustion chamber of constant cross section, as well as the nozzle at the rear, is rather disappointing, as this will result in considerable length of the whole unit. Fortunately, some recent solutions permitting a considerable shortening of the combustion chamber are just making their appearance. The same holds true for a diffuser. These questions are, however, beyond the scope of this paper.

The method of discussion on the basis of entropy diagram, as applied in this paper, seems to be successful; therefore, it will perhaps be desirable to apply it also in the case of a conventional turbo-jet engine.

References

1. CHAMBRÉ, P. and LIN, C.-C.   J. Aeronaut. Sci. 13 : 537.   1946.
2. EXERGIAN, R.   J. Franklin Inst. 237 : 401.   1944.
3. KEIRN, D. J. and SHOULTS, D. R.   J. Aeronaut. Sci. 13 : 411.   1946.   (See also references in that paper.)
4. MALINA, F. J.   J. Franklin Inst. 230 : 433.   1940.
5. MOSS, S. A. and FOOTE, W. R.   J. Aeronaut. Sci. 13 : 111.   1946.
6. REISSNER, H.   J. Aeronaut. Sci. 14 : 197.   1947.
7. SAMARAS, D. G.   Can. J. Research, F, 24 : 272.   1946.
8. SAMARAS, D. G.   Eng. J. 29 : 398.   1946.
9. SEIFERT, H. S., MILLS, M. M., and SUMMERFIELD, M.   Am. J. Phys. 15 : 1.   1947.
10. SZCZENIOWSKI, B.   Can. J. Research, A, 23 : 1.   1945.

REMARKS ON THE EXCITATION OF HYDROGEN AND HELIUM IN THE UPPER ATMOSPHERE[1]

By William Petrie

Abstract

A number of hydrogen and helium lines have been identified as features of the auroral spectrum. The relative intensities of these lines suggest that the excitation process is electron collision. Furthermore, the intensities of the helium lines indicate an "excitation temperature" of 4600°K., and the intensities of the hydrogen lines an "excitation temperature" of 7600°K.

Introduction

There is little doubt that on certain occasions hydrogen lines appear in the auroral spectrum. Vegard (15) has obtained spectra which show relatively strong lines at wave lengths coinciding with the first two members of the Balmer series. The rare appearance of these lines raises an interesting question regarding the source of the hydrogen and the excitation of the spectrum. It is not likely that hydrogen in the earth's atmosphere is the source of the observed Balmer spectrum, since we would then expect these lines to be a permanent feature of the auroral spectrum. This spectrum shows that excitation conditions in the upper atmosphere are sufficiently high to produce the Balmer lines, but little is known regarding the hydrogen content of the auroral region. The percentage by volume of hydrogen in dry tropospheric air is 5×10^{-5}. Owing to the differential densities of the various constituents of air, the percentage of hydrogen should increase with altitude. There is experimental evidence (11) to show that the percentage of helium is increasing at a height of 20 km.; and the same should be true to an even greater degree for hydrogen. On the other hand, the lighter gases are undoubtedly escaping from the upper atmosphere, which fact probably explains the usual absence of hydrogen lines from the auroral spectrum. Vegard (15) suggests that on occasions showers of hydrogen from the sun enter the earth's atmosphere; at such times the auroral spectrum shows the Balmer lines. This suggestion is very reasonable; it is known that solar "eruptive" prominences eject matter into space, and these prominences are largely hydrogen.

We will discuss the intensity distribution in the Balmer spectrum for different methods of excitation, and attempt to decide which method applies to the hydrogen lines in the auroral spectrum.

Excitation of the Balmer Spectrum

It might be thought that the hydrogen lines in the auroral spectrum are produced by the recombination of electrons and protons. Actually, we have no information on the proton content of the upper atmosphere, although

cosmic ray studies indicate that protons are present in this region.   If protons are supplied by the ionization of hydrogen or enter the atmosphere from an external source, we would expect the recombination process to operate continually and result in the hydrogen lines being a permanent feature of the auroral spectrum.   Quite apart from these considerations we will explain that the recombination process produces a spectrum in which the intensities of the lines H_α, H_β, H_γ decrease relatively slowly unless the temperature of the free electrons is very high.

To compute the relative intensities of the Balmer lines in a pure capture spectrum, we need to know the fractions of electrons captured on the various levels of the atom.   The number of captures per cubic centimeter per second per velocity range dv may be represented by the following expression,

$$N_v = N_i \, N_e \, v f(v) \, \sigma_n \, dv \qquad (1)$$

N_i = the number of protons per cubic centimeter,

N_e = the number of electrons per cubic centimeter,

$f(v)$ = the fraction of the electrons which have velocities between v and $(v + dv)$,

σ_n = the target area for capture on level n.

Kramers (8) has derived an expression for σ_n from the correspondence principle, i.e. $\sigma_n = \dfrac{K}{v^2 n^3 \nu}$.   The factor ν is obtained from the relation $h\nu = W_n + \dfrac{1}{2} mv^2$, W_n being the energy of level n measured from the ionization level.   Then $\sigma_n = \dfrac{2 \, h \, K}{v^2 \, n^3 \, (2 \, W_n + m \, v^2)}$.   If the velocity distribution of the free electrons is Maxwellian, then

$$f(v)dv = 4\pi \left(\frac{m}{2\pi k T_e}\right)^{\frac{3}{2}} v^2 e^{-\frac{1}{2}mv^2/kT_e} dv.$$

Then $N_v = N_i \, N_e \, 4\pi \left(\dfrac{m}{2\pi k T_e}\right)^{\frac{3}{2}} v^3 e^{-\frac{1}{2}mv^2/kT_e} \dfrac{2hK}{v^2 n^3 (2W_n + mv^2)} dv$.

The number of captures per cubic centimeter per second over all velocities

$$N = N_i \, N_e \, 4\pi \left(\frac{m}{2\pi k T_e}\right)^{\frac{3}{2}} \frac{2hK}{n^3} \int_0^\alpha \frac{v e^{-\frac{1}{2}mv^2/kT_e}}{(2W_n + mv^2)} \, dv .$$

We may write

$$N = \frac{C_1}{T_e^{\frac{3}{2}} n^3 2 W_n} \int_0^\infty \frac{v e^{-\frac{1}{2}mv^2/kT_e}}{(1 + C_2 v^2)} \, dv , \qquad (2)$$

where

$$C_1 = N_i \, N_e \, 4\pi \left(\frac{m}{2\pi k}\right)^{\frac{3}{2}} 2hK \quad \text{and} \quad C_2 = \frac{m}{2W_n} .$$

The integral is standard and results in a series the general term of which is

$$\frac{x!}{2\left(\dfrac{m}{2kT_e}\right)^{x+1}} \qquad 1, 2, 3, ------- \infty.$$

The intensities of the first three members of the Balmer series in a capture spectrum may be computed from the following expressions (14),

$$I(H_\alpha) = A_{32} h\nu_{32} [N_3 + N_4 X_{43} + N_5 X_{53} + N_6 X_{63} + -----]$$
$$I(H_\beta) = A_{42} h\nu_{42} [N_4 + N_5 X_{54} + N_6 X_{64} + N_7 X_{74} + -----] \qquad (3)$$
$$I(H_\gamma) = A_{52} h\nu_{52} [N_5 + N_6 X_{65} + N_7 X_{75} + N_8 X_{85} + -----],$$

where A_{n2} is the Einstein transition coefficient from levels n to 2, N_n the number of captures per second on level n, and X_{ni} the fraction of atoms in level n which reach level i by spontaneous emission. The X_{ni} values may be obtained from the following equation,

$$X_{n3} = \frac{1}{\displaystyle\sum_{i=1}^{n-1} A_{ni}} [A_{n3} + A_{n4} X_{43} + A_{n5} X_{53} + -----]. \qquad (4)$$

ΣA_{ni} is the total number of ways of leaving level n per second by spontaneous emission. We have used the A_{ni} and ΣA_{ni} values as computed by Menzel and Pekeris (10) to calculate X_{ni} values from (4). Substituting the X_{ni} and N values in Equations (3), we calculate the relative intensities of the first three members of the Balmer series. The results are approximately $3.5 : 1 : 0.3$. This result is for an electron temperature of 5000°K. The relative intensities are not sensitive to the temperature of the free electrons; at very high temperatures the intensities still decrease slowly. More accurate expressions for σ_n have been derived by Gaunt (5) and Cillié (4). Menzel and Baker (9) have presented a more accurate method of calculating Balmer intensities, and have pointed out the inaccuracies of the above approach. They give for the relative intensities of the first three members of the Balmer series in a capture spectrum the values $2 : 1 : 0.6$. Laboratory experiments on the recombination spectrum of hydrogen substantiate the theoretical result that the intensities decrease slowly. See for example the experiments of Herzberg (7). On the other hand, Vegard (15) gives the relative intensities of $H_\alpha : H_\beta$ in the auroral spectrum as $6 : 1$. Hence we can say with some certainty that the hydrogen lines in the auroral spectrum are not the result of electron and proton recombination.

A second possible but unlikely excitation process is the absorption of ultraviolet radiation from the sun. It is readily understood that the atmosphere is not exposed to short wave length solar radiation during the night, hence any excitation from this source must come about by absorption of energy during the day and the subsequent release of this energy at night. For example, oxygen and perhaps other molecules may absorb ultraviolet radiation and dissociate into atoms. During the night, recombination will take place, and the energy released in this process may excite certain constituents of the

atmosphere. However, there is no apparent dissociation and recombination process which will supply the energy necessary to excite hydrogen atoms and produce the observed intensity distribution in the spectrum. Furthermore, the observed intensity changes in auroral structure are difficult to explain by a radiation excitation process.

Collisional excitation is a process which will certainly operate to a certain extent in the upper atmosphere. It is well known that colliding electrons are effective in producing the hydrogen spectrum, and the many experiments with hydrogen discharge tubes indicate that the intensities of the Balmer lines decrease rapidly towards higher members of the series. For example, Bongers (3) has measured the intensities of the Balmer lines in a long discharge tube, and gives the relative intensities of the first three members of the series as 79 : 10 : 2. Since hydrogen cross-sectional areas for electron collision are not known, we are unable to compute the numbers of atoms excited to the various energy levels, and hence determine the intensities of the Balmer lines. However, the experimental evidence indicates that when hydrogen atoms are excited by electron impact the relative intensities of the Balmer lines are comparable to the relative intensities observed in the auroral spectrum. In a recent paper, Bernard (1) has attributed some fifteen lines in the auroral spectrum to the neutral helium atom. He shows that the intensity distribution in these lines is comparable to the intensity distribution in the spectrum of the radiation from a helium discharge tube. This evidence suggests that electron collisions are the source of the excitation of hydrogen and helium in the upper atmosphere. However, if hydrogen and helium atoms from the sun are incident on the earth's upper atmosphere, collisions between these particles and atmospheric atoms and molecules may produce both the hydrogen and helium lines as well as other features of the auroral spectrum.

Excitation Temperatures in the Auroral Region

The emission per cubic centimeter per second in a spectral line is given by $E_{nn'} = N_n A_{nn'} h \nu_{nn'}$, N_n being the number of atoms in the upper level involved in the production of the line. For a condition of thermal equilibrium, N_n may be represented by the Boltzmann law,

$$N_n = N_0 \frac{\tilde{\omega}_n}{\tilde{\omega}_0} e^{-X_n/kT} .$$

N_0 is the number of atoms in the ground level, $\tilde{\omega}_n$ and $\tilde{\omega}_0$ the statistical weights of levels n and the ground level, and X_n the excitation potential of level n. Hence,

$$E_{nn'} = N_0 \frac{\tilde{\omega}_n}{\tilde{\omega}_0} e^{-X_n/kT} A_{nn'} h\nu_{nn'} . \tag{5}$$

It is very unlikely that the auroral region as a whole approximates thermal equilibrium. However, free electrons may experience elastic collisions with other electrons, ions, or neutral atoms and molecules, inelastic collisions which result in the excitation of ions, atoms, or molecules, collisions of the second kind with ions, atoms, or molecules in excited metastable levels, free-

free transitions in the neighborhood of nuclei with the resulting emission of radiation, or capture by an ion with the emission of radiation. Bohm and Aller (2) have considered the motions of the free electrons in the atmosphere of a planetary nebula, and conclude that the process of elastic scattering is by far the most probable. Their arguments are quite general and probably apply to conditions in the upper atmosphere, in which case the free electrons will reach a velocity distribution which is close to a Maxwellian distribution. If this is so, atoms excited by collisions with these electrons will be distributed among the various energy levels according to the Boltzmann law. It is worth while then to apply Equation (5) to the intensities of the hydrogen and helium lines in the auroral spectrum. The relative intensities of the first two members of the Balmer series will be given by,

$$\frac{H_\alpha}{H_\beta} = \frac{\tilde{\omega}_3}{\tilde{\omega}_4} \frac{e^{-X_3/kT}}{e^{-X_4/kT}} \frac{A_{32}}{A_{42}} \frac{\nu_{32}}{\nu_{42}} .$$

Putting the equation in logarithmic form and expressing the χ-values in volts,

$$\log \frac{H_\alpha}{H_\beta} = \log \frac{\tilde{\omega}_3}{\tilde{\omega}_4} + \log \frac{A_{32}}{A_{42}} + \log \frac{\nu_{32}}{\nu_{42}} + \frac{5040\,(\chi_4 - \chi_3)}{T} . \qquad (6)$$

For the hydrogen levels the $\tilde{\omega}$ values are $2n^2$. Hence $\tilde{\omega}_3 = 18$, $\tilde{\omega}_4 = 32$. Also $A_{32} = 4.39 \times 10^7$, $A_{42} = 8.37 \times 10^6$, $\nu_{32} = 4.57 \times 10^{14}$, $\nu_{42} = 6.17 \times 10^{14}$, and $(\chi_4 - \chi_3) = 0.66$ volts. Substituting these values in (6) we find T is approximately 7600° K. The above results do not indicate whether or not the hydrogen energy levels are populated according to the Boltzmann law. On the other hand, this problem may be investigated by considering the intensities of the helium lines in the auroral spectrum. Table I gives the intensities of these lines as determined by Bernard, and other relevant data.

TABLE I

λ	$E_{nn'}$	Transition	$A_{nn'}$	$\tilde{\omega}_n$	χ_n	$\log D$
5876	6	$^3P - {}^3D$	64.7×10^6	15	23.0	23.70
4471	10	$^3P - {}^3D$	25.9×10^6	15	23.6	23.43
4026	4	$^3P - {}^3D$	12.8×10^6	15	23.9	23.16
5016	12	$^1S - {}^1P$	14.0×10^6	3	23.0	22.40
3965	6	$^1S - {}^1P$	8.13×10^6	3	23.6	22.27
4922	5	$^1P - {}^1D$	19.7×10^6	5	23.6	22.79
4388	4	$^1P - {}^1D$	8.67×10^6	5	23.9	22.49
4009	1	$^1P - {}^1D$	2.82×10^6	5	24.2	22.05

Writing Equation (5) in logarithmic form and letting $\dfrac{N_0}{\tilde{\omega}_0} h = C_1$, we have,

$$\log E_{nn'} = \log C_1 + \log \tilde{\omega}_n - \frac{5040\,\chi_n}{T} + \log A_{nn'} + \log \nu_{nn'}$$

Let $\tilde{\omega}_n A_{nn'} \nu_{nn'} = D$. Then,

$$\log \frac{E_{nn'}}{D} = \log C_1 - \frac{5040\,\chi_n}{T} . \qquad (7)$$

A plot of log $\frac{E_{nn'}}{D}$ against χ_n will produce a straight line if the energy levels are populated according to the Boltzmann law.   Fig. 1 shows this plot for the
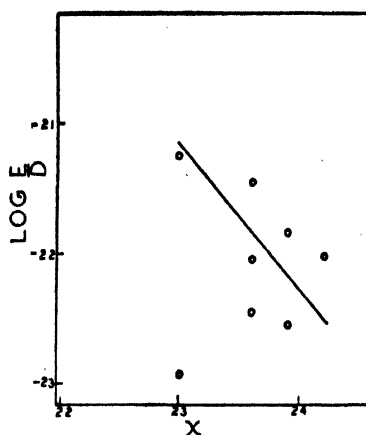
FIG. 1.   *The distribution of helium atoms in a number of energy levels.*

HeI lines.   It is apparent that deviations from the Boltzmann law are appreciable, and the slope of the line $\frac{5040}{T}$ simply gives an indication of the "excitation temperature" for the various energy levels.   The temperature obtained from this slope is 4600° K.   This method has been used by Goldberg (6) and Petrie (12) to compute the temperature of the solar chromosphere.

The results indicate that hydrogen and helium atoms are excited by particles which have velocities characteristic of a high temperature.   Similar results have been obtained by Petrie (13) from a study of the intensities of a number of OII lines in the auroral spectrum.   On the other hand, Vegard has found that the energy responsible for the excitation of nitrogen molecules is characteristic of a temperature of 300° K.   These results show that the upper atmosphere deviates considerably from a condition of thermal equilibrium. This condition is not surprising, since it is likely that different excitation mechanisms are operating in the upper atmosphere.   Certain features of the auroral spectrum are likely to result from collisions between atmospheric electrons and atoms or molecules.   "Excitation temperatures" computed from the intensities of these spectral features give information on the velocities of the particles involved.   On the other hand, if collisions between atmospheric particles and hydrogen or helium atoms from the sun are responsible for the appearance of hydrogen and helium lines in the auroral spectrum, then temperatures derived from these spectral features give information on the velocities of the incoming particles.   Detailed studies of the intensities of all auroral spectral features are necessary, if we are to understand fully the problem of auroral excitation.

References

1. BERNARD, M. R.   Compt. rend. 225 (7) : 352.   1947.
2. BOHM, D. and ALLER, L. H.   Astrophys. J. 105 : 131.   1947.
3. BONGERS, I. A.   Dissertation, Utrecht.   1927.
4. CILLIÉ, G. G.   Monthly Notices Roy. Astron. Soc. 96 : 771.   1936.
5. GAUNT, J. A.   Trans. Roy. Soc. London, A, 229 : 163.   1930.
6. GOLDBERG, L.   Astrophys. J. 89 : 673.   1939.
7. HERZBERG, G.   Ann. Physik, 84 : 553.   1927.
8. KRAMERS, H. A.   Phil. Mag. 46 : 836.   1923.
9. MENZEL, D. H. and BAKER, J. G.   Astrophys. J. 86 : 70.   1937.
10. MENZEL, D. H. and PEKERIS, C. L.   Monthly Notices Roy. Astron. Soc. 96 : 77.   1935.
11. PANETH, F. A.   Quart. J. Roy. Meteor. Soc. 63 : 433.   1937.
12. PETRIE, W.   J. Roy. Astron. Soc. Can. 38 : 137.   1944.
13. PETRIE, W.   Can. J. Research, A, 25 : 293.   1947.
14. PLASKETT, H. H.   Pubs. Dominion Astrophys. Observ. Victoria, B.C. 4 : 187.   1928.
15. VEGARD, L.   Geofys. Publikasjoner.   Norske Videnskaps.-Akad. Oslo. 12 (14) : 1.   1940.

GAMMA RAYS FROM THE DISINTEGRATION OF BORON BY SLOW NEUTRONS[1]

By B. Rose[2]

Abstract

The slow neutron disintegration of B^{10} yields two groups of α-particles, corresponding to the production of Li^7 in either the ground state or an excited state. The γ-radiation accompanying the de-excitation of the excited nucleus was studied. Boron in the form of boron trifluoride in a proportional counter was irradiated with slow neutrons from a Ra–α–Be source. Coincidences were counted between α-particle pulses in the proportional counter and γ-ray pulses in an adjacent Geiger–Müller counter. The ratio of the α–γ coincidence rate to the α-rate gave the product of the efficiency of the Geiger-Müller counter and the number of quanta emitted per boron disintegration. The absorption coefficient of the γ-radiation in lead was measured, and, by comparison with the absorption coefficients for the γ-radiation from Cu^{64} and Au^{198}, the energy was found to be 0.48 ± 0.015 Mev. The quantum efficiency of the Geiger-Müller counter for radiation of this energy was determined by calibration with standard sources of Co^{60} and thorium active deposit. Hence the number of quanta per boron disintegration was found to be 0.90 ± 0.08, in satisfactory agreement with the value to be expected from the relative abundance of the α-particle groups from this reaction.

Introduction

The slow neutron disintegration of B^{10} yields two groups of α-particles corresponding to the formation of the product nucleus Li^7 either in the ground state, or in a state of about 0.45 Mev. excitation. Measurements by Wilson (23) in a proportional counter, by Bøggild (3) and by Gilbert (8) in a cloud chamber, show that only 7% of the disintegrations go directly to the ground state. There should therefore be a γ-ray of energy about 0.45 Mev. accompanying 93% of the disintegrations, corresponding to the de-excitation of the Li^{7*} nucleus. Soft γ-rays from this reaction have been observed by Kikuchi, Aoki and Husimi (13). Wilson (23) observed $\alpha - \gamma$ coincidences and estimated the γ-ray energy by a very rough absorption measurement to be in the neighborhood of 0.5 Mev.

The object of the present investigation was to test the simple disintegration scheme suggested by the above results, and shown in Fig. 1, by measurement of the intensity and energy of the γ-ray.

Outline of Method

Boron, in the form of gaseous boron trifluoride contained in a proportional counter, was irradiated with slow neutrons from a 1.2 gm. Ra–α–Be source. The γ-radiation accompanying the neutron-induced disintegration of the

boron was detected in an adjacent aluminum-walled Geiger–Müller counter, of which the net efficiency for the energy of the radiation in question was determined by subsidiary experiments.

Let N disintegrations per minute be produced in the proportional counter,

ϵ_α be the efficiency of the proportional counter,

ϵ_{Li} be the efficiency of the Geiger–Müller counter for the Li^{7*} γ-ray,

λ be the number of quanta produced per disintegration,

and,

N_α and $N_{\alpha\gamma}$ be respectively the α- and genuine coincidence counting rates. Then $N_\alpha = N\epsilon_\alpha$; $N_{\alpha\gamma} = N\epsilon_\alpha\lambda\epsilon_{Li}$, so that $N_{\alpha\gamma}/N_\alpha = \lambda\epsilon_{Li}$.
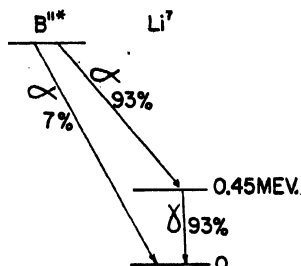
FIG. 1. *Disintegration scheme for the reaction* $B^{10}(n,\alpha)Li^7$.

The net efficiency of the Geiger–Müller counter was determined for the γ-radiation from Co^{60} by the use of a standard Co^{60} solution, and for the mixed γ-radiation from thorium active deposit by means of a source calibrated in terms of its α-particle activity.

The γ-ray energy was determined by measuring its absorption coefficient in lead, and comparing it with those of the γ-radiations from Cu^{64}, which is almost pure annihilation radiation (6), and from Au^{198}, which is predominantly of energy 0.408 Mev. (5, 16). Using the curves published by Bradt *et al.* (4), showing the variation of absolute efficiency of a Geiger–Müller counter with quantum energy, the net efficiency ϵ_{Li} may be determined for the energy of the γ-ray from the boron disintegration, and hence λ, the number of quanta per disintegration.

Measurement of $\lambda\epsilon_{Li}$

The proportional counter used was made of aluminum, of inside diameter $\frac{3}{4}$ in., active volume $2\frac{1}{2}$ in. long, and of $\frac{1}{8}$ in. wall thickness. It was filled with boron trifluoride to a pressure of 12 cm. of mercury. The Geiger–Müller counter was made of aluminum, with glass ends waxed in, the dimensions of the cathode being length 2 in., inside diameter 1 in. and wall thickness 0.9 mm. The arrangement of source and counters is shown in Fig. 2. The neutron source F was set in a bismuth block D, which was surrounded by eight inches of paraffin, E. The counters, A and B, were mounted in a light aluminum frame with their axes parallel and 36 mm. apart, and installed in a

bismuth block C, vertically above F and D. The function of the block D was to shield the Geiger–Müller counter A from the γ-radiation direct from the source F, and of the block C to shield it from γ-rays of neutron capture in the
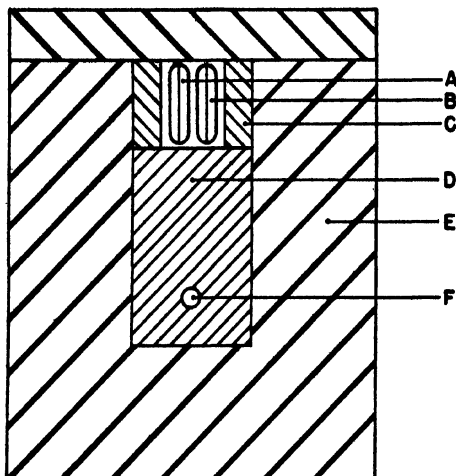
Fig. 2. *Experimental arrangement.* A, B, *counters*; C, D, *bismuth*; E, *paraffin*; F, *neutron source.*

paraffin. Bismuth was used in preference to lead as it is almost as efficient as lead for γ-ray shielding, and has a smaller slow neutron capture cross-section. The block D provided 11 in. of shielding, the block C 2.4 in. and together they reduced the γ-counting rate to approximately the same rate as that due to the activation of the aluminum cathode by the slow neutron flux (of the order of 1500 and 1000 counts per minute respectively). The latter rate was measured by removing the counter from the neutron flux and following the decay of the counting rate. The rate in the proportional counter was 2500 counts per minute.

The pulses from both counters, after amplification and discrimination, were fed into a Rossi coincidence circuit, and the ratio of the α-particle rate to the genuine coincidence rate was determined for coincidence resolving times of 0.25, 0.70 and 1.51 μsec. to ensure that no coincidences were lost. As the random coincidence rate at the longest resolving time was almost half the true coincidence rate, and the total coincidence rate was only about 0.7 count per minute, long counting periods were necessary. It was therefore decided to keep continuous check on the coincidence resolving time in order to be confident of the accuracy of the random coincidence rate. In alternate half hours, regularly spaced pulses from a pulse generator were fed into the Rossi circuit at 20,000 pulses per minute. The generator pulses and the coincidences between the generator pulses and those from the Geiger–Müller counter were counted, and from these figures and the measured γ-ray counting rate, the resolving time of the circuit was determined for each run. The ratio $N_{\alpha\gamma}/N_{\alpha}$

obtained was corrected for counting losses in the Geiger–Müller circuit, due to a 300 μsec. dead time in the discriminator. This long dead time was used throughout the experiment in order to minimize effects due to multiple pulsing in the Geiger–Müller counter. The dead time of the counter alone was 180 μsec. The circuit dead time was measured both by a counting loss determination and by direct measurement on an oscilloscope of known writing speed.

.It should be pointed out that there could arise coincidences due to a γ-ray and a neutron, emitted simultaneously from the source, being registered by the two counters. However, the cross section for the B^{10} $(n,\alpha)Li^7$ disintegration is very small except for slow neutrons. The slowing down process takes several microseconds in the great majority of cases. Hence the number of coincidences from this effect is negligibly small, owing to the coincidence resolving times used.

The values obtained are shown in Table I, the errors shown, as elsewhere throughout this paper being the standard errors. There is no significant difference in the values of $N_{\alpha\gamma}/N_\alpha$ obtained for the three resolving times. Therefore the mean of those values in Column 3 was taken, giving $(1.43 \pm 0.04)10^{-4}$.

In order to use Bradt and collaborators' curves, as mentioned earlier, it was necessary to correct this quantity for

(a) Back scattering into the Geiger–Müller counter from the block,

(b) Absorption in the wall of the proportional counter,

and

(c) Absorption in the wall of the Geiger–Müller counter.

These corrections were determined from subsidiary experiments using annihilation radiation from Cu^{64}, which was shown later to have an energy very similar to that of the γ-ray from Li^{7*}.

TABLE I

$N_{\alpha\gamma}/N_\alpha$ AS A FUNCTION OF COINCIDENCE RESOLVING TIME

Resolving time, μsec.	$N_{\alpha\gamma}/N_\alpha$, × 10^4	Mean value
0.23 (± 5%)	1.42 ± 0.11	1.38 ± 0.07
0.27 (± 6%)	1.34 ± 0.10	
0.68	1.25 ± 0.12	
0.71 } (± 3%)	1.53 ± 0.12	1.40 ± 0.07
0.71	1.43 ± 0.12	
1.54	1.64 ± 0.15	
1.52	1.36 ± 0.14	
1.46 } (± 2½%)	1.65 ± 0.16	1.52 ± 0.07
1.50	1.50 ± 0.15	
1.54	1.44 ± 0.15	

.The Cu⁶⁴ was prepared by irradiating electrolytic copper in the pile. After irradiation it was dissolved in nitric acid, the excess acid being neutralized with ammonia, and allowed to stand for two hours before use to remove the five minute activity due to Cu⁶⁶. The solution was then diluted to a volume equal to that of the active volume of the proportional counter. A dummy counter, made from a piece of aluminum tube of the same dimensions as the proportional counter, and coated inside with glyptal, was then substituted for the proportional counter and filled with active copper solution. The γ-ray counting rate was measured with the counter and dummy in the block C, closely surrounded by bismuth as in the coincidence experiment, and also measured with the counter and dummy remote from scattering material. After correction for source decay and the different background rates inside and outside the block, the counting rate was found to have increased by $1\frac{1}{2}\%$, owing to back-scattering.

To determine the absorption in the wall of the proportional counter, a half-cylinder of aluminum $\frac{1}{8}$ in. thick and closely fitting the wall of the dummy, was interposed between the Geiger–Müller counter and the dummy containing active copper solution. The reduction in the counting rate observed, after correction for background and source decay, showed an absorption of 5.8% in the wall of the proportional counter.

The absorption in the wall of the Geiger–Müller counter, which in this energy range is due entirely to the Compton process, is small since the wall is thin. The Compton absorption process will result in electrons of maximum energy 0.33 Mev. from a quantum of energy 0.5 Mev. Therefore a recoil electron produced in the counter wall at a distance from the interior of the counter greater than 0.1 gm. per sq. cm., the range of a 0.33 Mev. electron in aluminum (18), cannot produce a discharge in the counter. The total absorption in the counter wall cannot then be less than that due to the Compton absorption cross section alone in the portion of the wall that is more than 0.1 gm. per sq. cm. distant from the interior of the counter. The absorption cross section per electron for a 0.5 Mev. γ-ray is 10^{-25} cm.², and the thickness of that portion of the wall concerned 0.14 gm. per sq. cm. From these figures, we see that the absorption in the counter wall must exceed $\frac{1}{2}\%$.

An upper limit for the absorption in the counter wall may be made by assuming that it occurs at the same rate as in the wall of the proportional counter. The absorption in the wall of the proportional counter is due to the degradation of the radiation and to the production of recoil electrons. Since we have conditions of 'bad geometry', scattering into and out of the counter may be expected to compensate each other, so that the production of degraded radiation should be at the same rate in the two walls. However, the production of recoil electrons will be less effective in the wall of the Geiger–Müller counter than in the wall of the proportional counter, as argued in the previous paragraph. In this way we obtain $1\frac{1}{2}\%$ as an upper limit for the absorption in the wall of the Geiger–Müller counter.

We shall therefore take 1%, the mean of these two limits, as the best estimate of the absorption in the wall of the Geiger–Müller counter.

Hence the total correction to be made to the value of $N_{\alpha\gamma}/N_\alpha$ is an increase of 5%, giving

$$\lambda\epsilon_{\text{Li}} = (1.50 \pm 0.05)10^{-4}.$$

Calibration of the Geiger–Müller Counter

The thickness of the wall of the Geiger–Müller counter was considerably less than the maximum range of the recoil electrons from Co^{60} γ-radiation (1.16 and 1.32 Mev. γ-rays in cascade (11)) and from the hard component (2.62 Mev.) of the thorium radiation.   The wall thickness was therefore increased, by loading it with a close fitting split brass cylinder, to a mass 1.4 gm. per sq. cm., which is greater than the range of the recoil electron of maximum energy from the hardest component.   The same loading was used for both calibration measurements.

The Co^{60} was obtained in the form of a solution of which the specific activity had been determined by β–γ coincidence methods by Dr. W. B. Mann in this laboratory, by the National Bureau of Standards in Washington, and by the Oak Ridge standardization laboratory, with concordant results.   A known volume of this solution was diluted to a volume equal to that of the active volume of the proportional counter, introduced into the dummy counter, and the γ-ray counting rate determined.   After correction for source decay, background, and counting losses, the counts per γ-ray emitted from the dummy counter was found to be $(6.16 \pm 0.12)10^{-4}$.

Subsidiary experiments showed that the γ-ray sensitivity was almost independent of the total volume over a 3 cc. range of solution introduced into the dummy counter (and hence of the precise assumptions about the active volume of the proportional counter).   The sensitivity also varied very slowly with movements of the dummy counter along its axis, a movement of 1 cm. in this direction producing less than 1% difference in counting rate.

To determine the net efficiency of the counter for the γ-rays of Co^{60} and the geometry concerned, the counts per γ-ray must be corrected for self-absorption in the cobalt solution, absorption in the wall of the dummy counter, and absorption in the wall of the Geiger–Müller counter.

In order to measure the self-absorption, a linear source was prepared by filling a thin-walled glass tube of 2 mm. inside diameter with Co^{60} solution, the length of the source being equal to the length of the active volume of the counter.   The counting rates were determined for a position of the linear source in the dummy counter, and then immediately redetermined with the dummy counter filled with water.   In this way the change of counting rate due to the presence of the water was determined for each element of volume of the dummy counter.   The total self-absorption due to the water, determined by numerical integration, was 3 ± 1%.

The absorption in the wall of the dummy counter was determined as before, giving 4.5 ± 1%.

The absorption in the wall of the Geiger–Müller counter was determined by inserting an additional half-cylinder of brass of mass 1.06 gm. per sq. cm. between the dummy and the Geiger–Müller counter, closely fitting the latter. This reduced the counting rate by $5.5 \pm 1\%$. We may therefore over-estimate the absorption in the wall of the Geiger–Müller counter by assuming that it is the same per millimeter thickness as in the additional absorber, giving an absorption of 7%. We may underestimate it by assuming that it is due only to that thickness of the wall which exceeds the range of the fastest recoil electron. The latter would have an energy of 1.1 Mev. and therefore a range of 0.45 gm. per sq. cm. (18). The underestimate of the absorption is 5%. The mean of these two values was taken as the best value for the absorption in the counter wall, namely $6 \pm 1\%$.

The total value of the corrections to be applied is therefore about 14%. Hence the net efficiency of the Geiger–Müller counter for a γ-ray of energy 1.24 Mev. is $(7.02 \pm 0.21)10^{-4}$.

The difference between the efficiency of an aluminum and a brass counter was neglected here, since the brass loading increased the efficiency by a few per cent only in this case. It had to be considered, however, in the calibration with the thorium radiation, where a substantial portion of the efficiency was due to the brass.

In this method of determining the net efficiency of the Geiger–Müller counter for a volume source occupying the same position relative to it as did the proportional counter in the coincidence experiment, it has been assumed implicitly that the neutron-induced disintegration rate has its center of gravity at the geometric center of the proportional counter. This was investigated by measuring the counting rate in the proportional counter as a function of its position. The magnitude of the variation was such that the effective center of gravity of the disintegrations was displaced only a few millimeters from the geometric center. Displacements of the dummy counter by this amount were shown earlier to have a negligibly small effect on the counting rate in the Geiger–Müller counter, so that the assumption made is justified.

In order to calibrate the counter with a point source of thorium radiation, it was necessary to determine the effective center of gravity of the proportional counter relative to the Geiger–Müller counter. This was determined by the use of a point source of Co^{60} of which the strength relative to a standard Co^{60} solution was measured by γ-ray comparison. The counting rate was then measured as a function of the distance of the point source from the axis of the Geiger–Müller counter, and from the known strength of the source, that point on the equatorial plane determined at which the net efficiency of the Geiger–Müller counter was equal to that found by the calibration with the volume source. This was found to be at a distance of 37.8 ± 0.5 mm. from the axis of the Geiger–Müller counter, with the net efficiency changing by 6% per mm. at this point.

ROSE: γ-RAYS FROM THE DISINTEGRATION OF BORON BY SLOW NEUTRONS 373

This location for the center of gravity was in reasonable agreement with a determination made from a point by point exploration of the counting rate as a function of the position of the point source for various distances from the Geiger–Müller counter.

The thorium source was deposited on a thin aluminum foil, and after being allowed to decay for two hours to establish transient equilibrium, the α-particle activity was measured by counting α-particles from both sides of the foil simultaneously. The foil was then stuck with Scotch tape to a small Lucite holder and mounted in the frame at a distance of 36.7 mm. from the axis of the Geiger–Müller counter. The γ-ray counting rate was measured, and corrected for background, counting losses, and source decay to determine the γ-ray counting rate per α-particle emitted. This measurement was repeated with another source, the mean of the two values being $(6.97 \pm 0.14)10^{-4}$. This figure was then corrected for the slight displacement of the thorium source from the experimentally determined center of gravity of the proportional counter. The displacement was 1.1 ± 0.5 mm., so that the corresponding correction was a reduction by $6.5 \pm 3\%$.

It was also necessary to correct for the absorption in the wall of the Geiger–Müller counter. The weighted mean energy per γ-ray from a thorium active deposit source is 1.03 Mev., computed from the results of Johansson (12) and Latyschev and Kulchitsky (14). It was therefore assumed that the absorption in the counter wall would be the same as for the 1.24 Mev. γ-rays from Co^{60}, namely $6 \pm 1\%$, since the Compton cross section does not differ by more than 10% for these two energies. The net correction to be made was then $-0.5 \pm 3\%$.

Hence the mean efficiency of the counter for the thorium radiation was $(6.93 \pm 0.35)10^{-4}$ per α-particle. The experimentally determined ratio of the efficiencies for thorium and Co radiations was therefore

$$\epsilon_{Th}/\epsilon_{Co} = \frac{6.93 \pm 0.35}{7.02 \pm 0.21} = 0.99 \pm 0.06.$$

The ratio of the efficiencies was also computed from Bradt's curves for the variation of counter efficiency with quantum energy. The efficiency per α-particle was calculated by weighting the intensities of the various components by their relative efficiencies, for the softer components taking the efficiency for an aluminum cathode, for the radiations at 1.60 Mev. and 1.80 Mev. taking the mean of the efficiencies for aluminum and brass, and for the 2.2 Mev. and 2.62 Mev. radiations, taking the efficiency for a brass cathode. The efficiency for Co^{60} radiation was determined similarly, using the curve for an aluminum cathode. This gave the ratio of efficiencies

$$\epsilon_{Th}/\epsilon_{Co} = 1.07 \pm 0.05 \text{ (computed)}.$$

This agrees with the experimental value within the combined errors.

Absorption Coefficient in Lead of the Li^{7*} γ-Radiation

The energy of the Li^{7*} γ-ray was determined by comparing its absorption coefficient with those of the 0.511 Mev. annihilation radiation and the 0.408 Mev. γ-radiation of gold. The absorption coefficient was determined by measuring the α–γ coincidence rate as a function of the thickness of lead between the counters. Another proportional counter was used with twice the active volume of the one previously in use and filled with 30 cm. of boron trifluoride and 1.5 cm. of argon. A larger Geiger–Müller counter was also used, with a lead cathode. The counting rates were then approximately 10,000 counts per minute in each counter. The counters were installed in a different mounting which increased their separation to permit the insertion between them of 1½ cm. of lead, in the form of sheets of mean thickness 0.177 cm.

As the coincidence resolving time measured in the earlier part of the experiment had remained constant within statistical error, the continuous checking method was abandoned, but the resolving time, nominally ¼ μsec. was checked daily. Owing to the increased counting rates, it was possible to take several runs during a day with a small number of absorbers, the runs with a large number, when the genuine coincidence rate was equal to or less than the random rate, being carried out overnight. This had the advantage of avoiding any systematic drift of sensitivity of the counters producing a change in the measured absorption curve. The genuine coincidence rate varied from 4 to 0.25 counts per minute, and the counting periods from 40 min. to 16 hr. The rates obtained were corrected for counting losses in the Geiger–Müller circuit. The results obtained are shown in Table II. The errors shown are the standard errors of the number of counts. The average value of all determinations of the coincidence resolving time was used to determine the random coincidences.

TABLE II

$N_{\alpha\gamma}/N_\alpha$ AS A FUNCTION OF THICKNESS OF LEAD BETWEEN THE COUNTERS

Number of absorbers	Genuine coincidences	Random coincidences	$N_{\alpha\gamma}/N_\alpha$, $\times$ 10^4	Number of runs
0	1843	332	4.12 ± 0.11	5
1	508	119	2.88 ± 0.15	3
2	1211	379	2.14 ± 0.08	4
3	530	266	1.31 ± 0.08	2
4	856	578	0.96 ± 0.05	1
5	666	601	0.71 ± 0.05	1
6	1039	1231	0.53 ± 0.04	2
8	241	644	0.23 ± 0.04	1

A least squares fit to an exponential curve gave the absorption coefficient 1.98 ±0.11 cm.$^{-1}$, the error in this case being estimated by inspection.

Absorption Coefficient for 0.511 Mev. and 0.408 Mev. Radiation

Another dummy counter was substituted for the proportional counter and the pair of counters was installed in a lead block, so that the geometry was the same as in the absorption experiment. The dummy counter was then filled with a solution containing Cu^{64} prepared as before, and the absorption coefficient determined in the usual manner, using the same absorbers as in the coincidence absorption experiment, giving an absorption coefficient $\mu = 1.70$ cm.$^{-1}$

The absorption coefficient for the γ-radiation from Au^{198} was determined in the same way, giving $\mu = 2.55$ cm.$^{-1}$ Au^{198} was prepared by irradiating gold in the pile. The active gold was dissolved in aqua regia, the excess acid neutralized with ammonia, and the precipitated hydroxide redissolved in bromine water.

The γ-radiation from Cu^{64} consists of almost pure annihilation radiation, the admixture being a radiation of energy 1.35 Mev., with an intensity of one γ-ray per 40 ± 5 positrons (6). A computation based on the theoretical values of the good geometry absorption coefficients was made for this mixed radiation over the range of absorption used in these measurements, and showed that the mean absorption coefficient would be decreased by 0.03 cm.$^{-1}$ from the value for pure annihilation radiation. Since the measured absorption coefficients agreed closely with the theoretical values, this correction was applied directly, to give 1.73 cm.$^{-1}$ for the absorption coefficient for annihilation radiation.

The γ-radiation from Au^{198} consists principally of a line of energy 0.408 Mev. (5, 16), with possibly a weak admixture of softer components at 0.208 and 0.157 (16) of intensity less than 18% of that of the harder γ-ray. Computation based on the theoretical absorption coefficients showed that the effect of these components, even if present to the maximum intensity suggested, would be negligible after the first or second absorber, so that the measured absorption coefficient of 2.55 cm.$^{-1}$ needed no correction.

The absorption curves obtained are shown in Fig. 3. The statistical errors in the points on the Au^{198} and Cu^{64} curves are very small. The errors remaining, due to counter fluctuations, are difficult to estimate and are not shown. The curves for Au^{198} and Cu^{64} are each the mean of two separate determinations, which had no significant differences between them.

Energy of Li⁷* γ-Ray

From the measured absorption coefficients, and the assumption of a linear variation of absorption coefficient with energy, the energy of the Li^{7*} γ-ray was found to be 0.48 ± 0.015 Mev.†

† *Since this paper was written DuMond, Lind, and Watson (Phys. Rev. 73, 1392 (1948)) have published the very precise value 0.4112 ± 0.0001 Mev. for the energy of the γ-ray from Au^{198}. Although this value supersedes 0.408 Mev. assumed in the present paper, the derived energy of the Li^{7*} γ-ray given to two significant figures needs no alteration.*
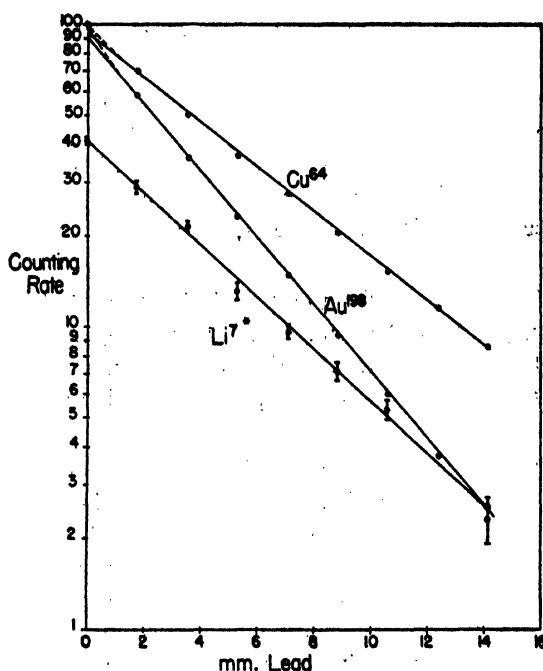
FIG. 3.   *Absorption curves of radiations from Li⁷*, Au¹⁹⁸, and Cu⁶⁴ with the same geometry.*

Number of Quanta per Boron Disintegration

From the curves given by Bradt and collaborators (4), we obtain the following efficiency ratios, in the manner described earlier.

$$\epsilon_{Li}/\epsilon_{Co} = 0.243; \qquad \epsilon_{Li}/\epsilon_{Th} = 0.226.$$

These ratios will be subject to a 5% standard error due to the 3% error in the γ-ray energy and an estimated 5% from the errors in Bradt's curves. We thus obtain for the efficiency of the counter for the γ-rays from Li⁷* the values 1.71×10^{-4} and 1.57×10^{-4} as determined from the calibrations with Co⁶⁰ and with thorium active deposit respectively. Weighting these results respectively by three and one, corresponding to the errors in the determination of ϵ_{Co} and ϵ_{Th}, we obtain for the weighted mean

$$\epsilon_{Li} = (1.67 \pm 0.13)10^{-4}.$$

From the previously determined value of $\lambda \epsilon_{Li}$ we obtain the value $\lambda = 0.90 \pm 0.08$.

Discussion

A summary of the work carried out before 1940 relating to the excited state of Li⁷ is contained in Graves' paper (10), and a later summary of work up to 1947 is given by Siegbahn (20, 21). Later work is included in Table III. There remain two distinct groups of values, centered around 0.485 Mev. and 0.455 Mev. respectively. There is no clear evidence for two different energy

levels being concerned, for in each case when two different reactions have been studied in the same instrument, the determinations have been in satisfactory agreement with each other. Siegbahn (20, 21) obtained 0.453 Mev. and 0.462 Mev. by measurement in a β-spectrometer of the γ-rays from the decay of Be^7, and from the inelastic scattering of α-particles by lithium. Lauritsen and collaborators' results (15) are shown in Table III. The present work is in better agreement with the high than the low value.

The value of λ determined here is in satisfactory agreement with the value to be expected from the disintegration scheme shown in Fig. 1. The energy available to the α-particles in this reaction is greater than the barrier height for the lithium nucleus, and therefore more disintegrations would be expected to pass to the ground state than to the excited state of Li^7, as is in fact observed in another reaction involving the same intermediate nucleus and end products, namely Be^9 (d,α)Li^7 (10) and in the similar reaction Li$^6(d,p)$Li^7 which yields two proton groups (19).

TABLE III

Author	Reaction	Measurement	Method	Energy of Li^{7*}, Mev.
Wilson (23)	B$^{10}(n,\alpha)$	Total disinteg- ration energy	Proportional counter	0.42 ± 0.05
Bøggild (3)	B$^{10}(n,\alpha)$	Total disinteg- ration range	Cloud chamber	0.42
Lauritsen et al. (15)	Li$^7(p,p')$Li^{7*}	γ-Energy	β-Spectrometer	0.48 ± 0.010
Lauritsen et al. (15)	Be$^9(d,\alpha)$Li^{7*}	γ-Energy	β-Spectrometer	0.48 ± 0.010
Strait et al. (22)	Be$^9(d,\alpha)$	α-Groups	Annular magnet	0.481†
Elliott and Bell (7)	B$^{10}(n,\alpha)$Li^{7*}	γ-Energy	β-Spectrometer	0.479 ± 0.005††
Present work	B$^{10}(n,\alpha)$Li^{7*}	γ-Energy	Absorption coefficient	0.48 ± 0.015

† *The value given by Strait et al. in the reference was changed to the value quoted here in the presentation of the paper before the American Physical Society.*
†† *This measurement was made after the present work had been completed.*

It is normally assumed that both the ground and first excited state of Li^7 have odd parity, and angular momentum 3/2 and $\frac{1}{2}$ respectively (9, 17). B^{10} has unit angular momentum (1) and is assumed to have even parity since it has an even number of particles (2). For this condition, the possible combinations of orbital angular momenta and spins are shown in the first part of Table IV. It will be clear that neither of these possible modes of disintegration can favor the production of the excited state of Li^7.

If, however, B^{10} has odd parity, the bias in favor of the excited state is readily explained. Remembering that the neutron and α-particle have even parity and that the reaction is produced by slow neutrons, it is necessary that the parity of the relative motion of the α-particle and of the residual nucleus be even. The possible combinations of angular momenta are given in the lower half of Table IV. It is clear that the only possible disintegration

that will favor the excited state is the last one, viz., that with zero relative angular momentum. The disintegration leading to the ground state will then have two units of orbital angular momentum, and in this case the penetrability is appreciably decreased.

TABLE IV

Parity of B^{10}	Angular momentum of B^{11*}	Relative angular momentum of α and Li	
		Ground state	Excited state
Even	3/2	1, 3	1
Even	$\frac{1}{2}$	1	1
Odd	3/2	0, 2	2
Odd	$\frac{1}{2}$	2	0

Acknowledgments

References

1. BETHE, H. A. Elementary nuclear theory. John Wiley & Sons, Inc., New York. 1947.
2. BETHE, H. A. Revs. Modern Phys. 9 : 69. 1937.
3. BØGGILD, T. K. Kgl. Danske Videnskab. Selskab., Math.-fys. Medd. 23, No. 4. 1945.
4. BRADT, H., GUGELOT, P. C., HUBER, O., MEDICUS, H., PREISWERK, P., and SCHERRER, P. Helv. Phys. Acta, 19 : 77. 1946.
5. CORK, J. M. Phys. Rev. 72 : 581. 1947.
6. DEUTSCH, M. Phys. Rev. 72 : 729. 1947.
7. ELLIOTT, L. G. and BELL, R. E. To be published.
8. GILBERT, C. W. See note at end of reference 23.
9. GOLDHABER, M. Proc. Cambridge Phil. Soc. 30 : 561. 1934.
10. GRAVES, E. R. Phys. Rev. 57 : 855. 1940.
11. JENSEN, E. N., LASLETT, L. J., and PRATT, W. W. Phys. Rev. 73 : 529. 1948.
12. JOHANSSON, A. Arkiv. Mat. Astron. Fysik, A, 34, No. 9. 1947.
13. KIKUCHI, S., AOKI, H., and HUSIMI, K. Nature, 137 : 745. 1936.
14. LATYSCHEV, G. D. and KULCHITSKY, L. A. J. Phys. U.S.S.R. 4 : 515. 1941.
15. LAURITSEN, T., FOWLER, W. A., LAURITSEN, C. C., and RASMUSSEN, V. K. Phys. Rev. 73 : 636. 1948.
16. LEVY, P. W. and GREULING, E. Phys. Rev. 73 : 83. 1948.
17. LIVINGSTON, M. S. and BETHE, H. A. Revs. Modern Phys. 9 : 245. 1937.
18. RASETTI, F. Elements of nuclear physics. Blackie & Son, Ltd., London & Glasgow. 1947.
19. RUMBAUGH, L. H., ROBERTS, R. B., and HAFSTAD, L. R. Phys. Rev. 54 : 657. 1938.
20. SIEGBAHN, K. Arkiv. Mat. Astron. Fysik, B, 34, No. 6. 1946.
21. SIEGBAHN, K. and SLÄTIS, H. Arkiv. Mat. Astron. Fysik, A, 34, No. 15. 1947.
22. STRAIT, E. N., STERGIOPOULOS, C. G., SPERDUTO, A., and BUECHNER, W. W. Bull. Am. Phys. Soc. 23, No. 3 : J6. 1948.
23. WILSON, R. S. Proc. Roy. Soc. London, A, 177 : 382. 1940-41.

SEARCH FOR A 3.20 MEV. γ-RAY IN THE DISINTEGRATION OF THORIUM C″ [1]

By R. E. Bell and L. G. Elliott

Abstract

In about 70% of the disintegrations, thorium C″ transforms to the ground state of thorium D by the emission of a β-ray and two successive γ-rays of energy 0.58 and 2.62 Mev. A search has been made for a γ-ray of energy 3.20 Mev. which would be emitted if a single radiative transition occurred. Using a source of radiothorium in equilibrium with its decay products, the secondary electrons ejected by the γ-rays from thin radiators of lead and uranium were analyzed in a magnetic lens spectrometer. No photoelectrons ejected by a 3.20 Mev. γ-ray were observed. If the γ-ray occurs its intensity is less than 0.2% of the intensity of the γ-ray at 2.62 Mev. This result is discussed in the light of the proposed disintegration schemes of thorium C″.

Introduction

Disintegration schemes have been proposed for the transition thorium C″ to thorium D by Ellis (8), Oppenheimer (13), and Arnoult (3). The last two of these are the most recent, and they agree well in their main features. The scheme suggested by Oppenheimer is shown in Fig. 1. According to this
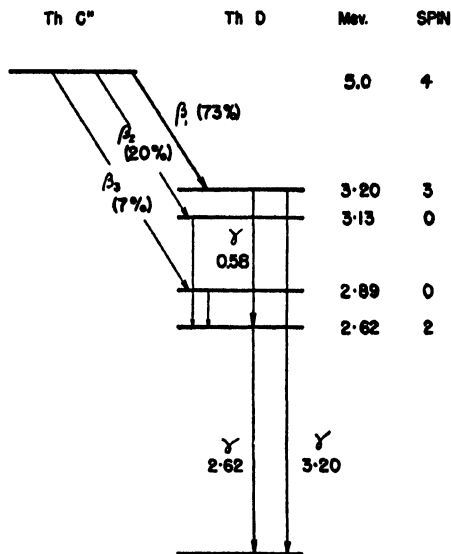
FIG. 1. *The disintegration scheme of thorium C″ according to Oppenheimer (13).*

scheme, 73% of the β-disintegrations of thorium C″ take place to an excited state of thorium D having an excitation energy of 3.20 Mev. De-excitation

of this state is supposed to occur mainly by the emission of two successive γ-rays of energies 0.58 and 2.62 Mev. respectively. The direct 3.20 Mev. transition to the ground state occurs, according to this scheme, in some fraction of the cases. Ellis (9) has commented on the importance of knowing the intensity of the 3.20 Mev. γ-ray in assigning nuclear spins in this disintegration scheme. The present paper reports a search for a 3.20 Mev. γ-ray, and gives an upper limit for its intensity which is well below the values previously reported.

Previous Work

The first suggestion of the existence of a 3.20 Mev. γ-ray from thorium C″ was made by Chadwick, Blackett, and Occhialini (4), who studied the positron-electron pairs produced in lead in a cloud chamber. They noticed a few pairs whose total energy seemed too great to be accounted for by the 2.62 Mev. γ-ray. Alichanow, Alichanian, and Kosodaev (1) studied the secondary electron spectrum produced in lead in a 180°-focusing β-ray spectrometer, and found photoelectrons which they ascribed to a γ-ray of energy 3.20 Mev. The intensity is described only as "small". A method similar to that of Chadwick *et al.* has been used by Zuber (16) and Simons and Zuber (14), who estimate the intensity of the 3.20 Mev. γ-ray as $12 \pm 6\%$ of that of the 2.62 Mev. γ-ray. Ellis (9) and Stetter and Jentschke (15) have attempted to detect the 3.20 Mev. γ-ray by observing the photodisintegration of the deuteron with a pulse ionization chamber and linear amplifier. The intensities quoted are 2 to 3% and 0.8% respectively. In all the work mentioned here the statistical accuracy has been very low, with the result that the quoted intensities vary by a factor of 15.

A 3.20 Mev. transition taking place by internal pair production has been observed by Alichanow and Dzelepow (2), who studied the resulting positrons in a 180°-focusing β-ray spectrometer. This result, however, does not imply that 3.20 Mev. γ-ray quanta are being emitted, and in fact Latyschev and Kulchitsky (12) failed to detect Compton recoil electrons from any 3.20 Mev. γ-rays from a source of radiothorium in equilibrium with its products.

It is worth noting that the two quoted investigations which employed β-ray spectrometers (1, 12) did not verify the relatively large intensities found by the other methods. Neither investigation, however, was directly concerned with the question of the existence of the 3.20 Mev. γ-ray, and no quantitative estimate of intensity was given in either case.

Experimental Method

In the present study a search was made for γ-rays in the energy region of 3.20 Mev. from sources of radiothorium in equilibrium with its products. The secondary electrons ejected from thin radiators of lead and uranium were studied using a thin magnetic lens β-ray spectrometer (6). The radioactive source is placed at one end of an evacuated cylinder about one meter in length

(Fig. 2), and a thin-window Geiger counter at the other end records the β-particles which have passed through the baffle system under the action of the focusing coil. The geometry of the instrument is kept fixed and the coil
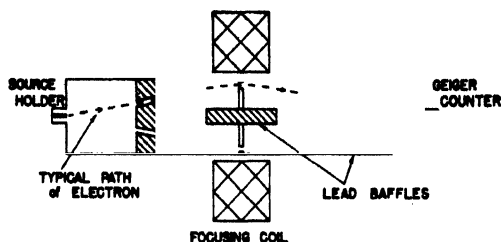
FIG. 2. *Schematic diagram of the magnetic lens β-ray spectrometer.*

current is varied to focus electrons of different momenta on the counter. Since no iron is used in the system, the current in the coil is exactly proportional to the momentum of the focused electrons.

The source, shown in Fig. 3, is covered with sufficient material of low atomic number (aluminum) to stop all the primary β-rays, and only the secondary electrons produced by γ-rays are observed. When no radiator of high atomic
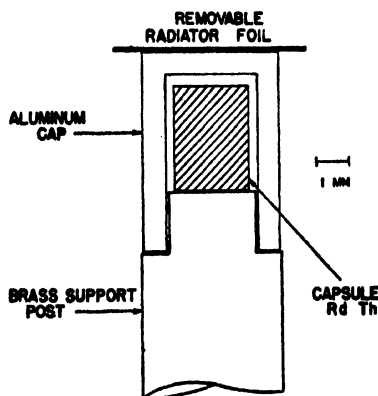
FIG. 3. *Diagram of the radiothorium source arrangement in the spectrometer.*

number is present on the source, the secondary electron spectrum consists almost entirely of Compton recoil electrons, for γ-ray energies of the order of magnitude considered here. When a thin radiator of high atomic number is placed over the source, there appears in addition to the Compton electron background a series of lines due to photoelectric conversion of the γ-rays. A typical pair of curves with and without the high atomic number radiator is shown in Fig. 4. Taking account of the fact that a particular γ-ray may be converted in the K, L, etc., shells of the atoms of the radiator, the difference

between the two curves is practically a line spectrum of the γ-rays from the source. It will be seen from Fig. 4 that this method is very sensitive to weak γ-rays of high energy because of the low counting background existing in that region.
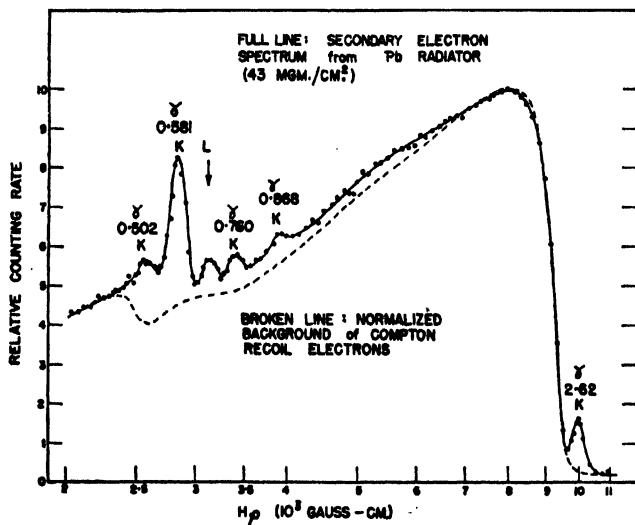
Fig. 4. *A typical pair of curves with and without the Pb radiator* (43 mgm. per cm.²), *showing the momentum distribution of the secondary electrons ejected by the γ-rays from the source of radiothorium in equilibrium with its decay products.*

In order to obtain the highest ratio of photoelectric line to Compton electron background, measurements were made on the 2.62 Mev. γ-ray using a series of radiators of different thicknesses. In the course of these measurements the first two runs were made with lead radiators ($Z = 82$) and the last two with uranium radiators ($Z = 92$). Since the photoelectric cross section varies approximately as the 4.5 power of Z (5), the change from lead to uranium gives roughly a 60% increase in the number of photoelectrons for a given radiator thickness. The results of these runs are shown in Fig. 5, the thickness of radiator being given above each curve. (The change from 43 mgm. per cm.² lead to 86 mgm. per cm.² lead was accompanied by improvements in the spectrometer alignment, accounting for the large improvement in line height in the case of the 86 mgm. per cm.² radiator.)

The uranium radiator of 82 mgm. per cm.² thickness was chosen as that giving the best visibility to the photoelectron line, having regard to the height of the line and its separation from the Compton background. The 150 mgm. per cm.² radiator gives a somewhat higher line, but the effect of electron scattering in the radiator prevents the line from reaching the height otherwise to be expected, and the scattered electrons, slightly degraded in energy, cause the line to be less well separated from the Compton background.
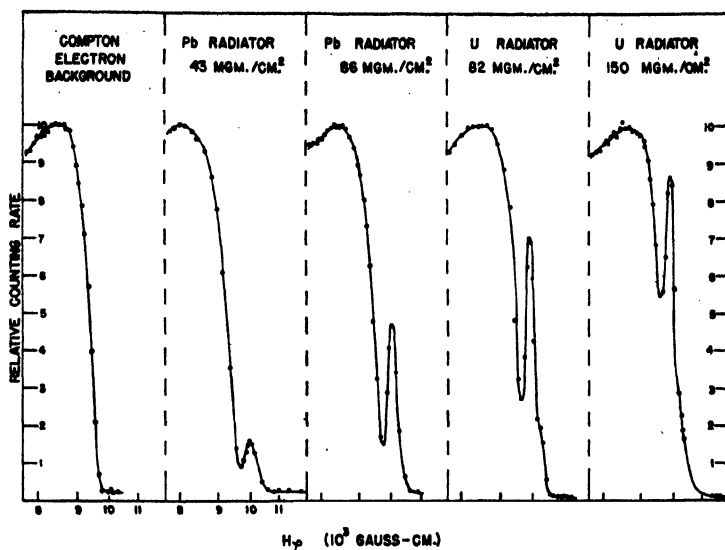
FIG. 5. Curves showing the variation in the height of the photoelectron line ejected by the 2.62 Mev. γ-ray of thorium C" from lead and uranium radiators of different thicknesses. The change from 43 mgm. per cm.² lead to 86 mgm. per cm.² lead was accompanied by improvements in the spectrometer alignment, accounting for the large improvement in line height in the case of the 86 mgm. per cm.² radiator.

Experimental Results

The result of a typical run in search of γ-radiation in the region of 3.20 Mev. is shown in Fig. 6, using the 82 mgm. per cm.² uranium radiator.   This curve
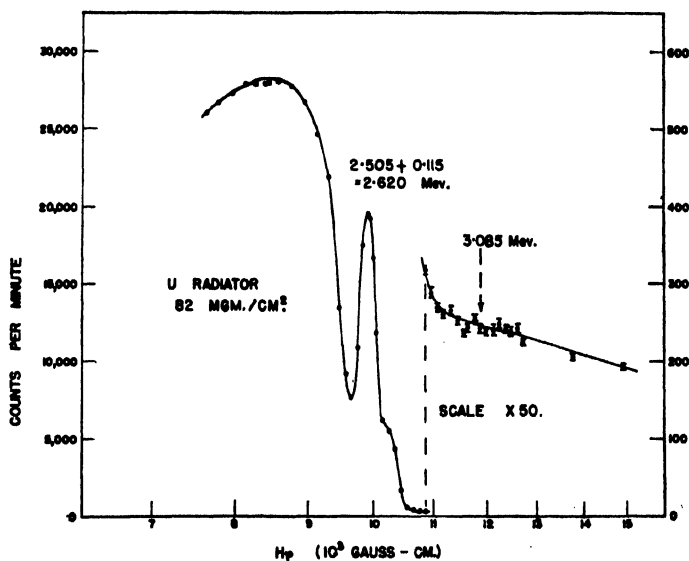
FIG. 6. The result of a typical run in search of γ-radiation in the region of 3.20 Mev. A line at 3.20 Mev. having an intensity of 0.2% of that of the 2.62 Mev. line would give a peak of 32 counts per minute at the point marked 3.085 Mev.

represents one of three runs of comparable accuracy over this energy region. The height of the 2.62 Mev. photoelectric conversion line, for reference, is 19,500 counts per minute. The ordinates of the curve in the high-energy region to the right of the 2.62 Mev. line have been expanded by a factor of 50. Taking account of the variation of the photoelectric cross section with energy, a 3.20 Mev. line having an intensity of 0.2% of that of the 2.62 Mev. line would give a peak of 32 counts per minute at the point marked 3.085 Mev. in Fig. 6. This line height corresponds to about three times the standard deviation of the points shown. No such line is detectable in any of the three runs taken, which demonstrates that the intensity of the 3.20 Mev. line must be less than 0.2% of that of the 2.62 Mev. line, and may be very much less than this amount or even zero.

Discussion of Results

The fact that a 3.20 Mev. excited state exists in thorium D is well attested by the results of Alichanow and Dzelepow (2), as well as by the fact that the 0.58 and 2.62 Mev. γ-rays have been shown to be emitted in cascade (7). The present study shows that direct γ-ray transitions from the 3.20 Mev. excited state to the ground state of thorium D are either very improbable or completely forbidden.

A theoretical estimate of the relative intensities of the γ-rays may be obtained from a formula quoted by Helmholtz (11), which gives the transition probabilities as follows: for electric 2^l-pole radiation of energy E, which occurs when the vector spin difference between the two states involved is l and the parity change is $(-1)^l$, the transition probability w is proportional to

$$\left(\frac{E}{23.7}\right)^{2l+1} \frac{1}{[1.3.5. . .(2l-1)]^2} ,$$

while for magnetic 2^l-pole radiation, which occurs when the vector spin difference is l and the parity change is $(-1)^{l+1}$, the transition probability w' is proportional to

$$\left(\frac{E}{23.7}\right)^{2l+3} \frac{1}{[1.3.5. . .(2l+1)]^2} .$$

Since both the 0.58 Mev. and 2.62 Mev. γ-rays are believed to be electric quadrupole radiations (10, 13), the three states involved have the same parity. Hence, according to Oppenheimer's disintegration scheme the 3.20 Mev. γ-ray is magnetic 2^3-pole radiation competing with the 0.58 Mev. electric 2^2-pole radiation. On this basis

$$= 0.0014.$$

On the data available the spin of the 3.20 Mev. level could be 4 instead of 3, in which case the 3.20 Mev. γ-ray is electric 2^4-pole radiation giving the same ratio $w_{3.20}/w_{0.58}$ as above. Taking into account the known intensity of the 0.58 Mev. γ-ray relative to the 2.62 Mev. γ-ray, the theoretical intensity ratio of the 3.20 Mev. γ-ray to the 2.62 Mev. γ-ray is 0.001.

From the present experimental results, the ratio of the intensity of the 3.20 Mev. γ-ray to that of the 2.62 Mev. γ-ray is known to be less than 0.002. This value is consistent with the theoretical estimate, but in view of the uncertainty in formulas of this type, the above agreement cannot be taken as a very positive support of the Oppenheimer disintegration scheme.

Acknowledgments

References

1. ALICHANOW, A. I., ALICHANIAN, A. I., and KOSODAEV, M. S. J. phys. radium, 7 : 163. 1936.
2. ALICHANOW, A. I. and DZELEPOW, B. Compt. rend. acad. sci. U.R.S.S. 20 : 113. 1938.
3. ARNOULT, R. Ann. phys. [11] 12 : 241. 1939.
4. CHADWICK, J., BLACKETT, P. M. S., and OCCHIALINI, G. Proc. Roy. Soc. London, A, 144 : 235. 1934.
5. DAVIDSON, Z. S. and LATYSCHEV, G. D. J. Phys. U.S.S.R. 6 : 15. 1942.
6. DEUTSCH, M., ELLIOTT, L. G., and EVANS, R. D. Rev. Sci. Instruments, 15 : 178. 1944.
7. DUNWORTH, J. V. Rev. Sci. Instruments, 11 : 167. 1940.
8. ELLIS, C. D. Report of the International Conference on Physics, London. 1934.
9. ELLIS, C. D. Proc. Phys. Soc. London, 50 : 213. 1938.
10. FLAMMERSFELD, A. Z. Physik, 114 : 227. 1939.
11. HELMHOLTZ, A. C. Phys. Rev. 60 : 415. 1941.
12. LATYSCHEV, G. D. and KULCHITSKY, L. A. J. Phys. U.S.S.R. 4 : 515. 1941.
13. OPPENHEIMER, F. Proc. Cambridge Phil. Soc. 32 : 328. 1936.
14. SIMONS, L. and ZUBER, K. Proc. Roy. Soc. London, A, 159 : 383. 1937.
15. STETTER, G. and JENTSCHKE, W. Physik. Z. 40 : 104. 1939.
16. ZUBER, K. Helv. Phys. Acta, 11-3 : 207. 1938.

ATTEMPT TO DETECT AN (n,2n) REACTION IN DEUTERIUM[1]

By L. G. Elliott[2], E. P. Hincks[2], and A. N. May[3]

Abstract

A detailed account is given of experiments carried out to detect an (n,2n) reaction in deuterium. A Po-α-Be neutron source was surrounded by a hollow aluminum sphere 30 cm. in diameter, which could be filled with heavy water. The sphere was surrounded by an effectively infinite medium of paraffin oil. The neutron density distribution outside the sphere was measured with a small boron trifluoride chamber (6 mm. diameter $\times$ 20 mm. long). The total integrated densities of neutrons were determined both with the sphere empty and filled with heavy water. After correcting for absorption of thermal neutrons by the heavy water, the aluminum sphere, and the source, and of fast neutrons by the oxygen of the heavy water, it is shown that the fraction of neutrons giving an (n,2n) effect is $0.1 \pm 2.7\%$. This indicates that the effect is less than both that predicted by Höcker's theory ($\sim 10\%$) and that reported from an earlier experiment by Halban and coworkers (18%). However it is in good agreement with measurements made by Fenning and Knowles ($1.4 \pm 5\%$).

Introduction

In 1941 Halban, Kowarski, Fenning, and Freundlich (10) at Cambridge University found an increase of $18 \pm 5\%$ in the number of neutrons from a Ra-α-Be source when it was surrounded by heavy water, after allowing for the photoneutrons produced by γ-rays from the source. This was interpreted as an (n,2n) process on deuterium caused by fast neutrons. Subsequently, it was frequently stated that this effect made an important contribution to the multiplication factor of chain-reacting piles using heavy water as the moderator. Critical analysis of the Cambridge experiment (9) has revealed that sources of error in the method, which were not fully taken into account, might give rise to the large positive result that was obtained.

Fenning and Knowles (8) repeated the Cambridge experiment in 1943 at the Montreal Laboratory. They also used a Ra-α-Be source, but avoided some of the sources of error in the earlier work. Their result $0 \pm 3\%$ for the neutron production by an (n,2n) reaction on deuterium, becomes $1.4 \pm 5\%$ when a correction is added for the fast neutron reaction on oxygen as described below.

In view of the uncertainty in the magnitude of the effect, it was decided to carry out a new determination with as great an accuracy as possible, and with thorough attention to all possible sources of error. This experiment was performed by the authors between November 1943 and August 1944 in the Montreal Laboratory of the National Research Council. The method used was similar in principle to that of Halban and coworkers, and of Fenning and Knowles, although differing in details.

The general method will be described briefly. A source of fast neutrons is placed at the center of a sphere, which may be alternately empty or filled with heavy water. Outside the sphere is an effectively infinite uniform medium in which all emergent neutrons are slowed down to thermal velocities, and subsequently captured. If Q is the total number of neutrons emerging in all directions from the sphere per unit time,

$$\frac{1}{\tau} \int_V \rho(x,y,z) dV,$$

where τ is the mean life of thermal neutrons in the external medium, $\rho(x,y,z)$ is the thermal neutron density at a point (x, y, z) in the medium, and the integral is taken over all space outside the sphere. If the neutron distribution is spherically symmetrical throughout the whole system, we can write $4\pi\rho(r)\ r^2\ dr$ for $\rho(x,y,z)\ dV$, where r is the distance from the center of the sphere. Moreover, if we use a neutron detector whose output I is accurately proportional to ρ everywhere, we can replace $\rho\ (r)$ by $aI(r)$, where a is a constant representing the efficiency of the detector. We may then write

$$= \frac{4\pi a}{\tau} \int_{r_1}^{\infty} I(r)r^2 dr,$$

where r_1 is the radius of the sphere, and $4\ \pi a/\tau$ is constant for a given experiment. The detector output I is therefore measured at various distances from the source, from the surface of the sphere outwards. When these values are multiplied by the corresponding values of r^2, and the product plotted as a function of the distance r, the area under the resulting curve may be used as a measure of the total number of neutrons emerging from the sphere in unit time. When the sphere is empty, this number is just the number of neutrons emitted by the source per unit time. Any $(n,2n)$ effect should appear as an increase in the total number of neutrons when the sphere is filled with heavy water. Corrections must be made for absorption of thermal neutrons by the heavy water when the sphere is full, absorption by the material of the sphere, and absorption by the source itself; these will be discussed in detail below.

The principal differences between this and the earlier measurements are the following:

(1) The use of a smaller sphere (30 cm. diameter instead of 60 cm.). This decreases the fraction of thermal neutrons captured by the heavy water and so makes the result less dependent on the measurement of the absorption cross section of the water. It also requires a smaller volume of heavy water. On the other hand the $(n,2n)$ effect will be almost as large in a 30 cm. as in a 60 cm. sphere, since the neutrons are ineffective after their energy has fallen below the 3.3 Mev. threshold for the reaction.

(2) The use of a Po-α-Be source instead of Ra-α-Be. This eliminates the production of neutrons in the heavy water by the $D^2(\gamma,n)H^1$ reaction, which complicated the previous measurements. Moreover, the proportion of high energy neutrons may be greater owing to the absence of the "Auger group" (2).

(3) The use of small boron trifluoride chambers for neutron density measurements. These have great reproducibility and low backgrounds when compared with "induced activity" detectors. Since the boron cross section is inversely proportional to the neutron velocity (13), the number of B^{10} disintegrations is accurately proportional to the mean thermal neutron density in the chamber. The degree to which the neutron absorption and finite size of the chambers might affect their representation of the true (undisturbed) neutron density in the medium was investigated by comparing them with thin dysprosium detectors.

Description of Apparatus

(1) Tank

The measurements were carried out in a rectangular iron tank, 90 cm. long, 60 cm. wide, and 60 cm. high. This was filled with paraffin oil (Imperial "Marcolix" medicinal paraffin: density 0.840 gm. per cm.³ at 22° C., and hydrogen content, 14.1% by weight.) The tank stood on a 30 cm.-thick layer of paraffin wax and was surrounded on the sides (but not on top) by 50 cm. of paraffin wax in the form of plates.

Fig. 1 is a vertical section of the tank showing the sphere and boron chamber mounted in position. These were supported from a steel frame that normally rested on the top edge of the tank, but which could be lifted out bodily and put on a separate stand for adjustments and measurements of distances.

(2) Sphere

The sphere was made of 0.5 mm. thick aluminum spun in two hemispheres and welded together. The outside diameter was 30.3 cm. A neck, 15 cm. long and 8.5 cm. in diameter, on the top of the sphere held a tight-fitting hollow aluminum plug, which was filled with paraffin oil during the measurements. Attached to the plug was a dural rod, which supported the source at the center of the sphere, and through the plug passed tubes by means of which the sphere could be filled with heavy water from a reservoir, or emptied, without disturbing the source. Clamping rings held the plug in the neck, and a neoprene gasket made a water-tight seal. Measurements with a cathetometer showed that the sphere was spherical to within 1 mm. in diameter, and that the source was central to within 1 mm.

The sphere was carried by a collar on the neck, and the collar in turn was clamped to two rods which were carried on the main frame. When the sphere was emptied, lead weights were placed on the collar to compensate for its buoyancy in oil, thus preventing distortion of the frame by a change in weight.

(3) Chamber

The chambers were 6 mm. in diameter, about 2 cm. long, filled with 1.5 atm. of boron trifluoride, and were a standard single-ended type made by N. Veall (16) in the Montreal Laboratory. Two chambers were used alternately for the experiment, and the sensitivity of each remained constant throughout.

The chamber was supported by a thin metal tube as shown in detail in Fig. 1. This, together with the preamplifier, was mounted on a carriage which slid on two rods of the main frame, so that the chamber could be moved longitudinally in the tank along a line normal to the surface of the sphere.
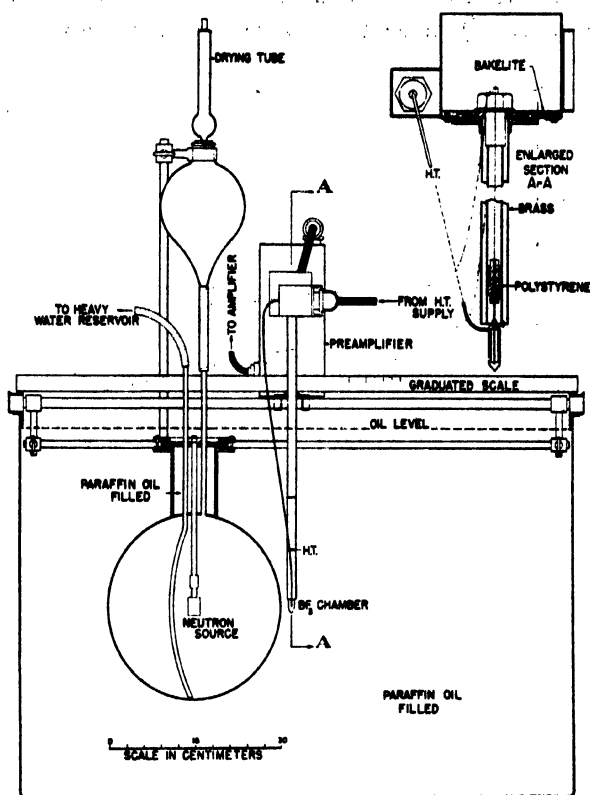
FIG. 1. Vertical section of apparatus showing sphere and boron trifluoride chamber mounted in oil-filled tank.

The use of an insulating medium such as paraffin oil in the tank had the advantage that the H.T. and collector leads could be brought out of the chamber without insulation, thus reducing the disturbance of the neutron distribution in the oil.

(4) Counting Apparatus

The electronic equipment used to count the pulses from the chamber comprised standard instruments used for similar work in the Montreal

Laboratory.   A linear amplifier, with a gain of about 10^5, was followed by a discriminator with variable bias, and a scale-of-128.   An oscilloscope was used for visual monitoring.

Considerable care was taken to reduce the background of spurious counts due to electrical pick-up in the laboratory.   Double screening of the lead from the chamber to the preamplifier input was used, and the earthing-connections in the preamplifier and first stages of the main amplifier were chosen to secure minimum sensitivity to pick-up.

The counting rate did not change appreciably with normal drifts in the characteristics of the electronic circuits.   The bias curves (counting rate vs. discriminator threshold) for the two chambers used are shown in Fig. 2.   The
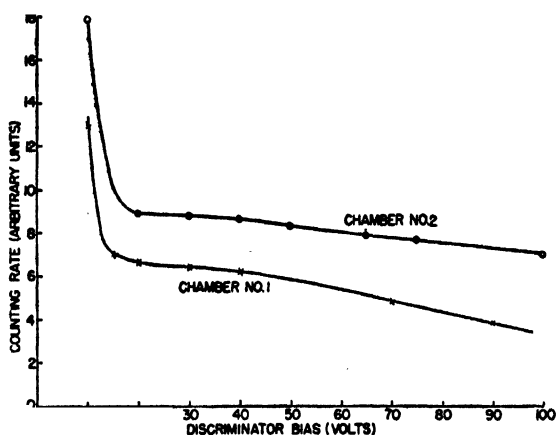
FIG. 2.   The bias curves for the two boron trifluoride chambers.

operating points were chosen on the sections of minimum slope, where it may be seen that a 1% change in amplifier gain would cause less than 0.1% change in counting rate.   The counting rate was also insensitive to small changes in H.T. voltage.   The H.T. supply was stabilized, and all the equipment was operated from a constant-voltage transformer.

(5) *Measurement of Distances*

It was important to measure the distance r from the center of the sphere accurately since a change of 1 mm. in r led in some cases to a 2% change in the intensity.   In some early runs the distances were measured by a scale placed along the top of the frame.   The scale was calibrated frequently by measurements with a cathetometer when the frame was outside the tank. In view of the possibility of small relative displacements of sphere and chamber when moving the frame, in later runs direct cathetometer observations were made through the surface of the oil.   The accuracy of this method was checked by measurements of a standard scale immersed in the oil.

(6) Dysprosium Detectors

Thin thermal neutron detectors were made by depositing dysprosium oxide (Dy_2O_3) on a 5 cm.^{2} area of aluminum foil. Two thicknesses of oxide were used, 1 mgm. per cm.^{2} and 2 mgm. per cm.^{2} The foils were supported in thin aluminum holders on thin brass rods. Distances between detectors and the sphere were determined by means of brass spacers. The detector activities were measured with standard cylindrical aluminum-wall counters (17) and scales-of-32.

(7) Source

The source consisted of 5 gm. of beryllium powder mixed with 0.5 curie of polonium and sealed in a brass holder. By comparison with a standard source it was found to be equivalent in neutron production to 0.07 curie of radon mixed with beryllium. Measurements made by H. Seligman at the Montreal Laboratory showed that the source did not decay appreciably during the whole period of measurement, so we can assume that the polonium is in equilibrium with radium D.

Experimental Results

Following the method outlined above, the neutron efflux from the sphere was derived by measuring the variation of neutron density with distance from the sphere. Each run therefore consisted of a sequence of counting rate determinations made at many points lying along a line normal to the sphere at various distances from it. About 10,000 counts were obtained at each point. Runs were taken with the sphere alternately empty and full of heavy water, and several complete sets of runs—each set comprising several emptyings and fillings—were made at intervals throughout the experiment. In comparable runs, the counting rates observed at a given distance repeated within the limits of statistical error (about 1%).

For analysis, the sets of runs were divided into two groups: those taken with one boron trifluoride chamber (No. 1) and those taken with the other chamber (No. 2). The results of these two groups were worked out separately in order to indicate the reproducibility that may be obtained by this method. Since the total number of measurements obtained in either group was large, measurements referring to approximately the same distance from the sphere have been lumped together in the following manner. Although the experimental procedure was to position the chamber at points which were an integral number of centimeters from the center of the sphere, as indicated by a meter scale attached to the frame, in general the accurate cathetometer reading showed a deviation from the integral position. The counting rate was corrected for this deviation by using the mean slope of the density curve at the point in question. All measurements thus corrected refer to integral distances, and measurements referring to the same distance were averaged. The final mean values of counting rates (I) at different distances from the center of the sphere for the two groups of runs are shown in Table I.

TABLE I

MEASURED INTENSITIES (COUNTS PER MINUTE) FOR EMPTY AND FULL SPHERES

Distance from center of sphere, r, cm.	Chamber No. 1		Chamber No. 2	
	Intensity, sphere empty, c.p.m.	Intensity, sphere full, c.p.m.	Intensity, sphere empty, c.p.m.	Intensity, sphere full, c.p.m.
15.2	660	2170	712	2260
16	655	1821	704	1930
17	640	1453	680	1545
18	604	1142	644	1215
19	560	877	596	926
20	510	665	544	705
21	460	500	490	527
22	410	373	436	395
23	—	—	385	297
24	314	218	337	226
25	—	—	293	174
26	233	126.5	252	135
27	—	—	216	106
28	172	78.8	184	84.5
29	—	—	156	68.2
30	127	51.9	132.5	55.3
31	—	—	112.5	45.0
32	92	34.9	95.8	36.7
34	67.2	24.1	69.8	25.2
36	48.5	17.2	50.7	17.8
38	35.0	12.5	37.0	12.7
40	25.3	9.0	27.0	9.05
42	18.3	6.4	19.75	6.52
44	13.2	4.6	14.3	4.70
46	9.70	3.3	10.5	3.39
48	7.10	2.4	7.62	2.45
50	5.23	1.7	5.61	1.78
52	3.85	—	4.16	1.32
54	—	—	3.08	—
56	—	—	2.29	0.7

The background count, taken with no source, was 0.03 counts per min. for both chambers. The constancy of this value, which was measured a number of times throughout the experiment, showed that spurious counts due to electrical pick-up, etc., were extremely unlikely. The contribution of the background is seen to be significant only for the points farthest from the sphere, and its effect on the area under the Ir^2 curve is negligible.

Some additional measurements were made with the sphere rotated about 180° through a vertical axis. In both the "full" and "empty" cases these agreed with the main results within 1%, showing that the source was well centered. Tests were also made with dysprosium detectors placed against the surface of the sphere at various latitudes, but again variation in intensity was found to be less than 1%.

The intensities given in Columns 2 and 3 (chamber No. 1) of Table I are plotted on a logarithmic scale against the distance r in Fig. 3. In the "empty" case the intensity is nearly constant near the sphere, corresponding to the

boundary condition $\partial\rho/\partial r = 0$ at the surface, and showing that there is little or no net generation or loss of thermal neutrons inside the sphere. At larger distances from the source ($r > 25$ cm.) the slope of the curve becomes
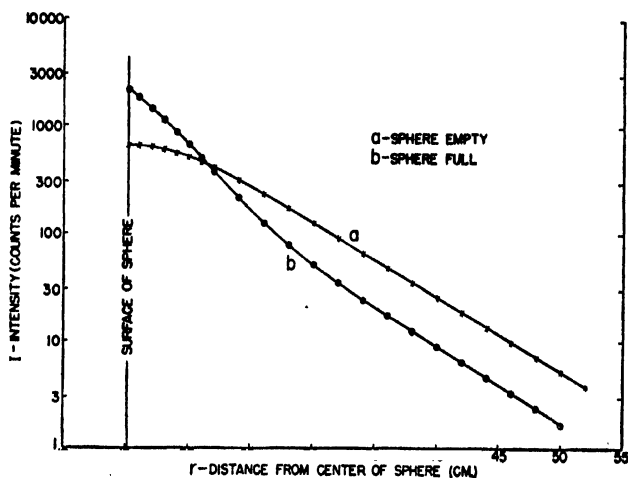
FIG. 3. *Logarithmic plot of the neutron intensity in the paraffin oil versus distance from center of the sphere: (a) sphere empty; (b) sphere filled with heavy water. (Chamber No. 1).*

nearly constant. This corresponds to an exponential decrease in density with a relaxation length of about 6.1 cm., which is characteristic of the energy of the fast neutrons from the source. The slope, however, decreases slightly with increasing distance, indicating a slight "hardening" of the neutrons.

The curve obtained with the full sphere shows quite different features. The slope near the sphere surface is large corresponding to a large outward flux of thermal neutrons generated in the sphere. For the same reason the intensity at the surface is larger than in the "empty" case. At $r = 21.4$ cm. the two curves cross. The "full" curve then straightens out at $r \sim 32$ cm. to become nearly parallel to the "empty" curve, but with about one-third the intensity. (The slope of the "full" curve actually appears to be slightly greater, the relaxation length for the exponential portion being 5.9 cm.) The comparison between the two curves in this region may be interpreted as showing that about one-third of the fast neutrons responsible for the exponential tail pass through the heavy water without much energy loss.*

The values of Ir^2 were calculated from the values in Table I, and plotted as a function of r. These curves for empty and full sphere in the case of chamber No. 1 are shown in Fig. 4. The area ($\int Ir^2dr$) under the "empty" curve between the surface of the sphere (r_1) and the outermost point measured (r_2) gives the total number of neutrons emitted by the source and absorbed by the paraffin oil inside a spherical volume of radius r_2. A correction for those

* *This agrees quantitatively with results obtained in preliminary experiments with a 20 cm. diameter sphere. In this case the same behavior was observed but the intensity of the "full" curve was one-half that of the "empty" one in the exponential region.*

neutrons captured outside this volume was made by assuming the exponential tail on each curve to continue to infinity. The corrected area for empty sphere may then be compared with that for the full sphere, which will be greater or less depending on whether there is a net generation or absorption of neutrons in the heavy water.
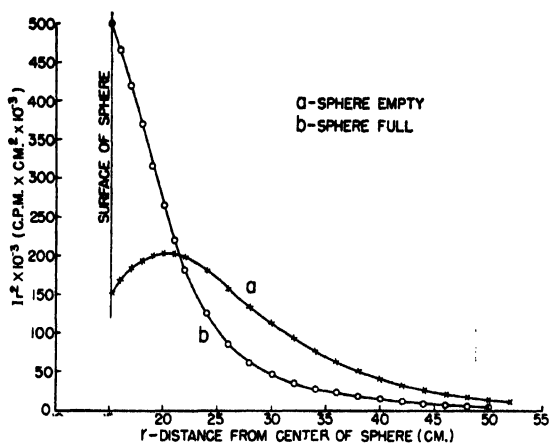
FIG. 4.   Plot of Ir^2 versus distance from center of the sphere: (a) sphere empty; (b) sphere filled with heavy water.   (Chamber No. 1).

Table II gives the results for the "empty" and "full" cases for each of chambers Nos. 1 and 2.   Column 3 gives the value of r_2 at the outer limit of measurement; Column 4, the area measured between $r_1 = 15.15$ cm. and r_2 ;

TABLE II

AREAS UNDER Ir^2 CURVES FOR EMPTY AND FULL SPHERE

Chamber	Sphere	Outer limit of measurement r_2(cm.) ($r_1 = 15.15$cm.)	Measured area r_1 to r_2 × 10^{-3}	Estimated area r_2 to ∞ × 10^{-3}	Total area r_1 to ∞ × 10^{-3}	Difference between "full" and "empty" areas × 10^{-3}	Difference as percentage of "empty" area
1	Empty	52	3509	91	3600	−185	−5.1
	Full	50	3380	35	3415		
2	Empty	56	3750	64	3814	−198	−5.2
	Full	56	3597	19	3616		

Column 5, the correction for $r > r_2$, or the estimated area under the curve from r_2 to infinity; Column 6, the total (corrected) area; Column 7, the difference—"full" area minus "empty" area—for each chamber; and Column 8, the same difference as a percentage of the total "empty" area.

The results for both chambers indicate that about 5% less neutrons are "observed" when the sphere is full than when it is empty. This immediately precludes the presence of a large positive $(n,2n)$ effect such as found by Halban *et al.* (10)*. However the absence of an $(n,2n)$ effect cannot be presumed until allowance has been made for all other effects that may alter the neutron balance when the sphere is filled with heavy water. These effects are individually small, and will be considered in later sections as corrections to the differences of Table II.

Errors

The sources of error in the measurements of neutron density distribution may be divided into four groups:

(1) Counting errors—

    (a) Statistical fluctuations,

    (b) Non-linearity of counting circuit,

    (c) Variations in sensitivity of boron trifluoride chamber and counting circuit.

(2) Failure of the boron trifluoride chamber to respond proportionally to the neutron density at all points of measurement.

(3) Imperfect extrapolation of the neutron distribution necessitated by the finite size of the paraffin oil medium.

(4) Errors in distance measurements.

The steps taken to minimize and estimate these errors will be discussed in turn.

(1) *Counting Errors.*—(a) Each point in each series of runs was obtained by observing more than 10,000 counts. Measurements were made at 1 cm. intervals over the greater part of the neutron distribution in the paraffin oil. Hence errors introduced in the area by statistical counting fluctuations are very small ($\ll 1\%$). (b) The counting circuit was tested at the highest counting rates used and found not to deviate from linearity by as much as 0.5%. (c) The constancy of the sensitivity of the chamber and counting circuit was frequently verified by observing the counting rate at a standard point close to the sphere.

(2) *Non-linearity of the Boron Trifluoride Chamber.*—To test whether the chamber was responding proportionally to the neutron density at all points in the paraffin oil, measurements were made with thin dysprosium detectors (described above) placed close to the sphere in both the "empty" and "full" cases. A further experiment was made with a stronger neutron source (600

---

* *The preliminary experiments with the 20 cm. diameter sphere similarly indicated the absence of any large effect.*

mc. Ra-α-Be), and the curves obtained with the chamber and thin dysprosium detectors at large distances from the sphere were compared. The shape of the neutron distribution obtained with 1 mgm. per cm.^{2} detectors was the same as that obtained with 2 mgm. per cm.^{2} detectors; this fact indicates that these detectors were sufficiently thin so as not to disturb appreciably the neutron distribution. The probable error in the detector measurements was 2%, and in all comparisons the agreement with the boron trifluoride chamber measurements was within this limit.

(3) *Extrapolation of the Neutron Distribution.*—There was no observable difference, even at the most distant point, between measurements taken with the oil tank alone and those taken with the tank surrounded on all sides by a 50 cm. thickness of paraffin wax. The residual area, obtained by extrapolating the measured curves to an infinite distance from the source, is the same to the required accuracy whether we assume either I or Ir^2 to decrease exponentially as r increases to infinity. It is seen in Table II, where the estimated residual area is given in Column 5, that it is less than 3% of the total area for each curve, so that any error introduced in the total area must be very small.

(4) *Distance Measurements.*—The distance measurements as described in the section on apparatus were reproducible to about 0.02 cm. The maximum error introduced by this uncertainty is 0.5% of the total neutrons in the differences between the full and empty sphere cases.

Corrections for Absorption of Thermal Neutrons

(1) *Absorption in the Heavy Water*

The fraction of neutrons absorbed by the heavy water depends upon the neutron density inside the sphere and the neutron lifetime in the water.

The distribution of neutron density within the sphere could be estimated with sufficient accuracy for this purpose from the density and the density gradient in the paraffin oil near the surface of the sphere. As a check one point was measured inside the sphere by fixing a thin dysprosium detector to the source rod. The estimated curve, together with the experimental point which lies on it, are shown in Fig. 5.

The neutron lifetime in the water is estimated in terms of that in the oil from the thermal neutron capture cross sections of the various nuclei involved, together with their relative abundances. In particular, we require a knowledge of the amount of hydrogen (H^1) contamination in the heavy water, since this is the nucleus chiefly responsible for the capture of thermal neutrons. It will be convenient and legitimate in the calculation of this correction to assume that the heavy water consists only of the molecules H_2O and D_2O, although in reality the hydrogen is found in the molecule HDO when in very small concentrations. P. Demers found both by freezing point and density

measurements that our heavy water contained 2.4% more ordinary water than did the main laboratory stock. Since the latter was known to have 0.6% ordinary water content, the actual contamination in our heavy water
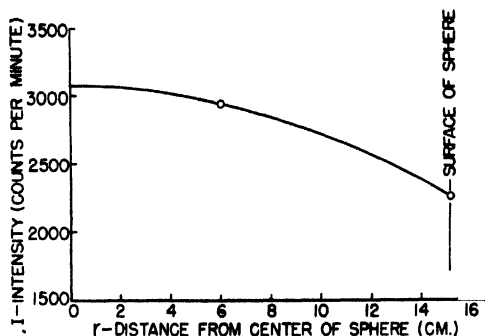
FIG. 5. *Neutron intensity inside the sphere when filled with heavy water. The solid line is estimated from the measurements outside the sphere; the circles are experimental points taken with dysprosium detectors. Both are normalized to the boron trifluoride chamber (No. 1) measurements at the surface of the sphere.*

was 3.0%. The ratio of the mean life for thermal neutrons in our heavy water (τ_s) to that in the paraffin oil (τ_{oil}) may be written

$$\frac{\tau_s}{\tau_{oil}} = \frac{d_{oil}}{d_s} \left(\frac{f_H \sigma_H + f_C \sigma_C/12}{f_{H_2O}\sigma_H/9 + f_{D_2O}\sigma_{D_2O}/20} \right)$$

where the symbols have the following meanings:

d_{oil} = Density of the oil (0.840 gm. per cm.[3]);

d_s = Density of the heavy water (1.10 gm. per cm.[3]);

f_H ≑ Fraction by weight of hydrogen in the oil (0.141);

f_C = Fraction by weight of carbon in the oil (0.86);

f_{H_2O} = Fraction by weight of H_2O in our heavy water (0.030);

f_{D_2O} = Fraction by weight of D_2O in our heavy water (0.97);

σ_H = Cross section for thermal neutron absorption per H atom;

σ_C = Cross section for thermal neutron absorption per C atom;

σ_{D_2O} = Cross section for thermal neutron absorption per D_2O molecule.

We take the values $\sigma_H = 0.30 \times 10^{-24}$ cm.[2]; $\sigma_C = 0.0045 \times 10^{-24}$ cm.[2]*. Sargent et al. (15) have measured the diffusion length for thermal neutrons in heavy water and give a value $(0.92 \pm 0.22) \times 10^{-27}$ cm.[2] for σ_{D_2O}. Substituting the above values we find for our heavy water

$$\frac{\tau_s}{\tau_{oil}} = 31.$$

* See for example, nuclear chart compiled by E. H. Segrè. Revised Sept. 1946. Addison-Wesley Press Inc., Cambridge, Mass.

To find the fraction f of neutrons absorbed by the heavy water we determine the ratio of the area A_s under the Ir^2 curve inside the full sphere (derived from the intensity curve of Fig. 5) to the total area A_{oil} under the corresponding curve outside (see Table II). Thus:

$$\frac{A_s}{A_{oil}} \quad \frac{\displaystyle\int_0^{r_1} Ir^2 dr}{\displaystyle\int_{r_1} Ir^2 dr}$$

$$= \frac{2690}{3415}$$

$$= 0.788.$$

Now

$$f = \left(\frac{A_s}{A_{oil}}\right)\left(\frac{\tau_{oil}}{\tau_s}\right)$$

$$= 0.788/31$$

$$= 0.025.$$

Thus the number of neutrons absorbed in the heavy water is 2.5% of the number absorbed outside the sphere. The probable error is estimated to be about 0.3%.

(2) *Absorption in the Aluminum Sphere*

The absorption in the aluminum can be estimated in a manner similar to that in the heavy water, where the net contribution is due to the differences in intensities at the sphere surface in the "empty" and "full" cases. The lifetime in pure aluminum can be derived from the absorption cross section for aluminum, but it is possible that the metal and the weld might contain impurities which would decrease the lifetime considerably. Analysis of samples of aluminum and welding rod showed traces of copper and silicon. The welding flux used contained lithium and boron, but tests of sample welds showed that simple washing removed all the flux.

To take into account the possibility of a large neutron absorption by impurities a test was made of the aluminum by a measurement with the 30 cm. sphere filled with pieces of aluminum sheet (totalling about 2.5 times the sphere weight) of the same kind as that used for the sphere. The area under the Ir^2 curve (Fig. 6, Curve a) was 0.6 ± 1.0% less than that in the case with the empty sphere, the shapes of the two curves being similar. Moreover, the thermal neutron density in the aluminum during this measurement was equal to the density in the empty sphere, which was 1/2.3 times the difference between the densities at the sphere surface in the "full" (of heavy water) and "empty" cases. Hence, this indicates a correction for absorption in the

aluminum sphere of $(0.6 \pm 1.0) \times 2.3/2.5 = 0.55 \pm 0.9\%$ of total neutrons. The value of the correction calculated from the lifetime, assuming pure aluminum, is 0.54%.
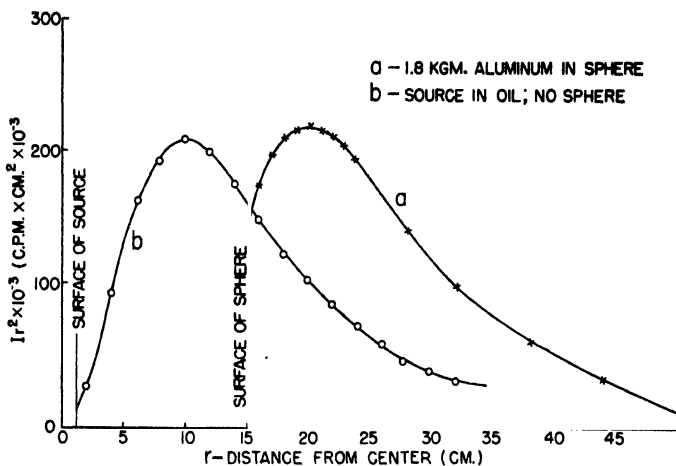
FIG. 6. *Plots of* Ir^2 *versus* r: (a) *source in sphere filled with pieces of aluminum sheet;* (b) *source placed directly in the paraffin oil.*

(3) Absorption in the Source

A test was made for the absorption of thermal neutrons in the source itself by placing the latter directly in the paraffin oil and integrating the density distribution. The Ir^2 curve under which the area is measured is shown in Fig. 6, Curve b. The increase in thermal neutron intensity at the source in this case over that with the empty 30 cm. sphere is about four times the difference in intensities between full and empty sphere. The difference in areas between the two cases is less than 1%. The correction for thermal neutron absorption in the source when comparing full and empty spheres is therefore less than 0.25% of total neutrons. The value calculated by assuming that all absorption is due to the brass container which holds the source is 0.11%.

(4) Absorption in Air

The absorption by the nitrogen of the air present when the sphere is emptied of heavy water is calculated to be 0.08% of total neutrons.

Correction for Absorption of Fast Neutrons

The absence of an increase in the number of neutrons on surrounding the source with heavy water may be interpreted to mean either that the effect of the $(n,2n)$ reaction with Po-α-Be neutrons is too small to be observed, or that it is masked by an equally large absorption of fast neutrons. For example, the following reactions between fast neutrons and O^{16} are known to occur:

$$O^{16} + n \longrightarrow C^{13} + He^4 - 2.3 \text{ Mev. (12, 7)}$$

$$O^{16} + n \longrightarrow N^{16} + H^1 - \sim 5 \text{ Mev. (5)}$$
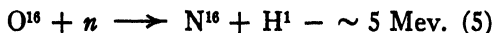
Pulses due to these reactions may be observed when chambers filled with oxygen are used with fast neutrons, and are a source of error if they are interpreted as recoils. If the cross section for these reactions is of the order of 10^{-25} cm² per atom, it would lead to an absorption in the heavy water of a few per cent of the fast neutrons from the source.

The following experiment was performed to determine whether the effect from any O^{16} reaction is appreciable. The neutron distribution outside a 15 cm. diameter sphere immersed first (a) in ordinary water, and then (b) in paraffin oil, was measured using (1) a Ra-γ-Be neutron source, and (2) a Po-α-Be source, at the center of the empty sphere. The Ir^2 curves for the four cases, $(a1)$, $(a2)$, $(b1)$ and $(b2)$ are shown in Fig. 7. The results from integration under these curves are given in Table III.
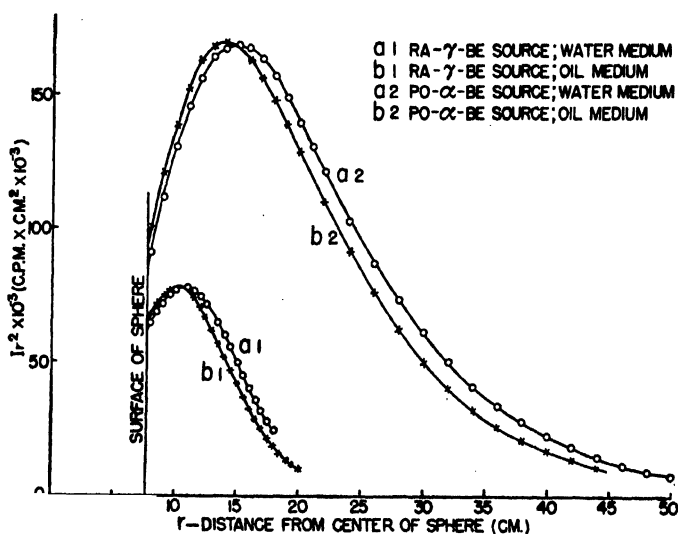
FIG. 7. *Plots of Ir^2 versus distance from center of sphere for a water medium (a) and an oil medium (b). Curves $(a1)$ and $(b1)$ are taken with a Ra-γ-Be source, while curves $(a2)$ and $(b2)$ are for a Po-α-Be source.*

TABLE III

COMPARISON OF AREAS UNDER Ir^2 CURVES TO DETERMINE THE EFFECT OF FAST NEUTRON REACTIONS ON OXYGEN

Source	$\int Ir^2 dr$ Water (a)	$\int Ir^2 dr$ Oil (b)	Difference in areas (water − oil)	Difference expressed as percentage of area for oil
Ra-γ-Be (1)	709	645	64	9.9 ± 1.5%
Po-α-Be (2)	3386	3180	206	6.5 ± 1.5%
Difference (1)–(2)				3.4 ± 2.1%

These results are interpreted in the following manner. The ratio of the area under the Ir^2 curve of case $(a1)$ to that of case $(b1)$ gives the ratio of the lifetimes for slow neutrons in ordinary water and paraffin oil. The difference

in areas expressed as a percentage of the area in case (b1) (Column (5)) is the fractional increase in lifetime of the Ra-γ-Be neutrons when the oil is replaced by water. We see that this increase is smaller for the Po-α-Be neutrons by an amount equal to 3.4% of the total neutrons. This effect, if real, can only be due to a greater absorption of the fast Po-α-Be neutrons by ordinary water than by paraffin oil. Our conclusion is consistent with the fact that the neutrons from the Ra-γ-Be source have energies below the threshold for the $O^{16}(n,\alpha)C^{13}$ reaction, while the Po-α-Be neutrons have energies above this threshold. In our heavy water experiment two-thirds of the fast neutrons were slowed down in the heavy water and one-third were slowed down in the paraffin oil which contains no oxygen. We estimate therefore that $2.2 \pm 1.6\%$ of the fast neutrons were lost by (n, α) or (n,p) reactions with the oxygen in the heavy water.

Conclusion and Discussion

The results of the measurements, together with the corrections, are summarized in Table IV. The decrease of 5.2% in the number of neutrons when the source is surrounded by heavy water is reduced to 2.1% when corrections

TABLE IV

SUMMARY OF RESULTS

Neutron absorption components	Difference as per cent of total neutrons: "full" case minus "empty" case	Estimated error, per cent of total neutrons
Neutrons absorbed in "infinite" paraffin medium	−5.2	±2.0
Neutrons absorbed in heavy water	+2.5	±0.3
Neutrons absorbed in aluminum sphere	+0.5	±0.9
Neutrons absorbed in source	+0.2	±0.1
Neutrons absorbed in air	−0.1	±0.0
Neutrons absorbed in entire system	−2.1	±2.2
Estimated fast neutrons absorbed in oxygen of heavy water	+2.2	±1.6
Net effect attributable to $(n,2n)$ reaction with deuterium	+0.1	±2.7

are made for absorption in heavy water, aluminum sphere, and source. Finally, when allowance is made for the fast neutron reaction with oxygen, we obtain an increase of $0.1 \pm 2.7\%$ which can be attributed to the $D^2(n,2n)H^1$ reaction.

Fenning and Knowles (8) in a repetition of the Cambridge experiment with a 60 cm. sphere and a Ra-α-Be source, found an effect due to the introduction of the heavy water equal to $-1.4 \pm 3\%$. However, this result does not take into account the absorption of fast neutrons by oxygen, and we have

estimated that when this correction is made the Fenning–Knowles experiment gives a value $+1.4 \pm 5\%$ for the $(n,2n)$ effect. Since both their experiment and the present one are consistent with the conclusion that the $(n,2n)$ effect is less than 3%, it seems that the value 18% found by Halban and coworkers must be due to experimental errors.

Höcker (11) has considered theoretically the $(n,2n)$ reaction with deuterium. He predicts a cross section that increases with the square of the excess neutron energy over the threshold, reaching a value 2×10^{-24} cm.^{2} at 10 Mev. We may combine this with the present information about the energy spectrum of Po-α-Be neutrons to calculate the effect to be expected on the basis of this theory. Thus the results of Richards, Speck, and Perlman (14)* and of Demers (6) give 10% and 30% respectively for the fraction of the neutrons from the source that would produce an $(n,2n)$ reaction in their first collision with deuterium. (Subsequent collisions are relatively unimportant because of the lower energy of the neutrons.) Since the present experiment shows that the effect with a Po-α-Be source is less than 3%, Höcker's values appear too large by a factor of at least three.

There is independent evidence that Höcker's cross sections are too large. Ageno et al. (1) found no appreciable difference between the total neutron cross section of deuterium as measured by beam experiments and the scattering cross section from the knocked-on deuterium nuclei at 13.5 Mev. At this energy Höcker's figures would lead to nearly every collision resulting in an $(n, 2n)$ reaction.

On the other hand, Bagge (3), in a cloud chamber investigation of recoil tracks in deuterium gas produced by fast neutrons from a Ra-α-Be source, found a group of tracks of about 10 cm. range in air which he ascribed to the protons from the $(n,2n)$ reaction. He estimated a mean cross section of 3×10^{-25} cm.^{2} per atom for neutrons of energy over 3.3 Mev. However, his interpretation of this group of tracks is doubtful, and even if it is correct the quantitative analysis of the results is complicated by the geometric conditions in the chamber—a point which is not adequately discussed in his paper.

The very similar reaction with fast protons, $D^2(p,n)2H^1$, has been studied by Barkas and White (4), who give a cross section that is much smaller than that to be expected from Höcker's theory.

Acknowledgments

* *We are indebted to Dr. Richards for communicating his results to us.*

We are indebted to Dr. B. W. Sargent for his valuable criticism of the manuscript of this paper.

References

1. AGENO, M., AMALDI, E., BOCCIARELLI, D., and TRABACCHI, G. C. Naturwissenschaften, 31 : 231. 1943.
2. AUGER, P. Compt. rend. 195 : 234. 1932.
3. BAGGE, E. Physik. Z. 43 : 226. 1942.
4. BARKAS, W. H. and WHITE, M. G. Phys. Rev. 56 : 288. 1939.
5. CHANG, W. Y., GOLDHABER, M., and SAGANE, R. Nature, 139 : 962. 1937.
6. DEMERS, P. Unpublished report, MP-74. Photographic emulsion study of Po-Be neutrons. National Research Council of Canada. 1945.
7. FEATHER, N. Nature, 130 : 237. 1932.
8. FENNING, F. W. and KNOWLES, J. W. Unpublished report, MP-41. Capture cross-section of heavy water for thermal neutrons; n-2n effect in deuterium. National Research Council of Canada. 1944.
9. FENNING, F. W. and KOWARSKI, L. Private communication.
10. HALBAN, H., KOWARSKI, L., FENNING, F. W., and FREUNDLICH, H. F. Unpublished report, Br-3. Evidence for the disintegration of deuterium by fast neutrons. British Atomic Energy Project. 1941.
11. HÖCKER, K. H. Physik. Z. 43 : 236. 1942.
12. MEITNER, L. and PHILIPP, K. Naturwissenschaften, 20 : 929. 1932.
13. RAINWATER, J. and HAVENS, W. W., JR. Phys. Rev. 70 : 136. 1946.
14. RICHARDS, H. T., SPECK, L., and PERLMAN, I. H. Phys. Rev. 70 : 118. 1946.
15. SARGENT, B. W., BOOKER, D. V., CAVANAGH, P. E., HEREWARD, H. G., and NIEMI, N. J. Can. J. Research, A, 25 : 134. 1947.
16. VEALL, N. J. Sci. Instruments, 24 : 331. 1947.
17. VEALL, N. and WILSON, M. Unpublished report, MP-60. Geiger-Müller counters used in Montreal laboratory. National Research Council of Canada. 1944.

THE EMISSION OF L RADIATION FOLLOWING INTERNAL CONVERSION OF γ-RADIATION IN HEAVY ELEMENTS[1]

BY B. B. KINSEY[2]

Abstract

The fluorescence yields of the L levels have been computed separately on the basis of radiation widths obtained from the work of Massey and Burhop, the widths of Auger transitions of the Coster–Kronig type measured by Cooper, and existing information on the widths of the L levels. In the case of fluorescence excitation, the total fluorescence yield calculated in this way is in general agreement with measurements of Lay. In the case of excitation by internal conversion of γ-radiation in the L levels, it is shown that the total fluorescence yield for elements in the vicinity of tantalum is appreciably less than the yield measured by Lay for fluorescence excitation, but that for the heavier elements near uranium, the yields should be comparable.

Introduction

The object of the present paper was to determine the fluorescence yield resulting from the internal conversion of γ-radiation in the L levels of the heavy elements and to determine the distribution of the energy in the spectrum. The L radiations emitted in the disintegration of RaD have been the subject of a careful study by Stahel (37). This author concluded that his results were consistent with the assumption that the γ-radiations produced by RaD are converted with nearly 100% efficiency; he based his results on the measurements of Lay (25) on the fluorescence yields obtained in fluorescence excitation. It is not clear that the use of Lay's results are relevant in this case because the relative excitations of the three levels by the fluorescence method are very different from that obtained with internal conversion. While the fluorescence excitations of the L_1, L_2, and L_3 levels are very roughly in the ratios of 1 : 2 : 3, the process of internal conversion in the L levels produces excitations in the ratios of 100 : 10 : 1. More recently, Frilley and Tsien (17) have examined the spectrum of the L radiation of RaD and have concluded that anomalies exist in the distribution of the energy among the various lines of the spectrum; in a later paper, Frilley et al. (16) point out that the distribution might be explained by the existence of Auger transitions of the type which have been discussed by Coster and Kronig (12).

This paper will show that there is no reason to suppose that an anomaly exists in the intensity distribution of the radiation emitted in the disintegration of RaD, although the quantitative information now available on the relative probabilities of the various Auger transitions which can occur does not make it possible to calculate the intensity distribution with any accuracy. In the following paper the author has described a measurement of the quantity of

L radiation emitted by ThC and RaD and has shown that the radiations emitted by the latter element are less than predicted by the assumption of 100% conversion of the γ-radiation.

The Relative Intensities in the L Spectrum

The emission lines of the L series cover a considerable range of energy, but the most intense lines, which comprise the α and β groups, are concentrated into two relatively narrow bands. The γ group of lines are of weaker intensity and of higher energy. The transitions to which the more important lines correspond are shown in diagrammatic form in Fig. 1.
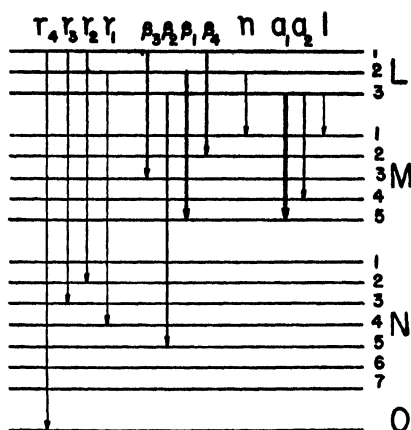
FIG. 1.   *Energy level diagram for lines of the L spectrum.*

In general, the relative intensities of the various lines of the L spectrum depend on three factors: the relative excitation of the three L levels, the fluorescence yield of each level (which is itself a measure of the proportions of radiative and nonradiative transitions), and the probability of Auger transitions shifting the vacancy produced in one level to another L level. A numerical evaluation of each of these three effects will determine the relative intensities of the radiations associated with the three levels as initial states. A determination of the relative intensities of all the lines in the spectrum would require further information on the relative probabilities of the radiations associated with one level.

In principle, then, the basis of the calculations for the radiations emitted following internal conversion could be checked by using the formulae for the relative intensities of the L radiations emitted in cathode-ray or fluorescence excitation and comparing the results with those of experiment. However, the relative intensities of the L radiations due to fluorescence radiations do not seem to have been measured, and the intensities observed in cathode ray excitation do not admit of easy interpretation owing to the existence of secondary effects.

Formulation of the Problem

A formula will now be obtained for the radiation probabilities of the three L levels, the three effects discussed in a previous paragraph being taken into account.

In the absence of nonradiative transitions in which the vacancy in one L level can be shifted to another L level, the intensities of the lines characteristic of one L level as an initial state depend only on the extent of the primary excitation. Let u_1, u_2, and u_3 be the probabilities that the levels L_1, L_2, and L_3 are ionized, such that $\Sigma u = 1$; and let f_1, f_2, and f_3 be the fluorescence yields. The total probability of emission of a quantum characteristic of the level L_s is then proportional to $u_s f_s$. If Γ_s is the total width of the level, the total radiation width is $\Gamma_s f_s$, and if x is the fractional probability of emission of radiation of a particular line from that level, its contribution to the radiation width will be $\Gamma_s f_s x$. The difference $\Gamma_s(1 - f_s)$ measures the probability of occurrence of nonradiating transitions from the level L_s. If, however, Auger processes are possible which shift the vacancy from one L level to another and produce a doubly ionized atom by ejection of an electron from a level of lower energy, the probability of excitation of a level L_s may depend on the primary excitation of the L level of higher energy. Let A_{rs} be the probability that a vacancy produced in the level L_r is transferred to the level L_s by a nonradiative transition, the other vacancy in the doubly ionized atom being in an M level or one of lower energy. The number of quanta radiated by the three L levels will then be given by the quantities q_1, q_2, and q_3, where:

$$q_1 = u_1 f_1$$
$$q_2 = f_2(u_2 + A_{12}u_1) \tag{1}$$
$$q_3 = f_3(u_3 + A_{23}(u_2 + A_{12}u_1) + A_{13}u_1).$$

In deducing these equations it has been assumed that the fluorescence yield of the state L_s, produced by a transition from the state L_r, is the same as in the case when the level L_s is excited by the primary process. The justification for this assumption is as follows. The probability per unit time of decay of the doubly ionized state is, to a first approximation, $\Gamma_s + \Gamma_p$, where Γ_s is the width of the L_s state and Γ_p is the width of the low energy state produced by the Auger transition. Let f_s be the fluorescence yield of the L_s level, and let f_s' be the effective fluorescence yield of this level in the doubly ionized state. When the L_s vacancy is filled first, the yield of radiation by transitions from L_s is $f_s'\Gamma_s/(\Gamma_s + \Gamma_p)$. When the low energy vacancy is filled first, the yield will be very nearly $f_s\Gamma_p/(\Gamma_s + \Gamma_p)$ since the new vacancy produced by this process will be of lower energy still and will have little effect on transitions from L_s. The total yield by transitions from L_s is therefore

$$(f_s\Gamma_p + f_s'\Gamma_s)/(\Gamma_s + \Gamma_p).$$

It will be shown that the most frequent double ionizations are vacancies in L_3 and either M_4 or M_5 (created by Auger transitions from L_1). The total width of the L_3 level is approximately equal to the total width of M_4 or M_5 in the case of heavy elements; hence approximately $\Gamma_s = \Gamma_p$. Moreover, f_s' must nearly equal f_s because the difference can result only from the vacancy in the M levels. The above expression, the total radiation yield by transitions from L_s, reduces to approximately f_s, as assumed in deriving Equations (1).

The Coster–Kronig Transitions

Transitions of the type which have just been described contribute to the coefficient A_{13}; it will now be shown that the greater part of that coefficient is derived from these transitions only, and that, to a first approximation, the other coefficients may be neglected.

The existence of an Auger transition, in which a vacancy in the L_1 level is filled to produce a vacancy in the L_3 level and another in the M levels, was invoked by Druyvesteyn (14) and others to explain the presence of the satellites of the line $L\alpha_1$ ($L_3 \rightarrow M_5$). These satellites, as is well known, are observed with appreciable intensity only for atoms with atomic numbers less than 50 and greater than 73. The explanation of this phenomenon was given by Coster and Kronig (12); they showed that the difference in the energies of the levels L_1 and L_3 should exceed that of the level M_5 corresponding to the element next above it in the periodic table. That the excitation of the satellites of the $L\alpha_1$ depends on the energy of the cathode rays exceeding the excitation potential of L_1 was demonstrated by Coster, Kuipers, and Huizinga (13) for Nb ($Z = 41$).

The probability of Auger transitions of this type, when permitted by the Coster–Kronig rule, depends, among other things, on the extent to which the wave function of the ejected electron overlaps the wave functions of the states of the atom involved in the transition. Only those electrons are ejected to an appreciable extent which can carry off an appreciable angular momentum. Further, those transitions will be most probable for which the energy of the ejected electron is least. For this reason transitions of the Coster–Kronig type are more probable than any others when they are permitted energetically. The increase in the probability of these transitions when the energy of the ejected electron is decreased has been demonstrated in experiments which have been made to determine the variation of intensity of the satellite line relative to the parent line as a function of atomic number (Z); as Z is increased, the satellite intensity increases to a maximum, followed by an abrupt decrease for atomic numbers within one or two units less than the maximum permissible by the energy condition of Coster and Kronig. This variation of the intensity of the $L\alpha$ satellites has been observed by Hirsh and Richtmeyer (21), and by Randall and Parratt (32); a similar intensity variation occurs in the satellites of $L\beta_2$ ($L_3 \rightarrow N_5$) which have been studied by Miss Pearsall (27). In the region of high atomic numbers, the intensities of the satellites of $L\alpha_1$ increase

abruptly at $Z = 74$, as shown in unpublished data of Shrader, quoted by Cooper (9). The onset of the transitions of the type $L_1 \to L_3 M_{4,5}$ must be accompanied by an increase in the width of the L_1 state and a decrease in its fluorescence yield. Consequently, at this point the intensities of the radiations with L_1 as the initial state must decrease relatively to those characteristic of L_2 and L_3. This phenomenon has been studied by Cooper in elements of highest atomic numbers and by Coster and de Langen (11) in elements in the region of silver.

Coster and Kronig (12) have also showed that an Auger transition is possible from the L_1 level to the L_2 level with the ejection of an electron from the M_4 or M_5 level for atomic numbers less than that of Nb ($Z = 41$). This has been demonstrated in experiments on the intensity of the satellites of the line $L\beta_1$, characteristic of the L_2 level. Hirsh (20) has shown that an intensity anomaly exists in the vicinity of atomic number 40, and his observations have been confirmed by de Langen (24), by measurements of the intensities of the satellites of $L\beta_1$ for Zr($Z = 40$), Nb(41), and Mo(42). De Langen (24) has also shown that the relative intensities of the L_1 lines, $L\beta_3$ and $L\beta_4$, increase relatively to that of $L\beta_1$, from Zr to Mo, owing to the decreasing probability of this Auger transition. For atomic numbers in the region of 70 and above, transitions of this type are not possible.

Transitions in which the vacancy is shifted from the L_2 to the L_3 level are possible, energetically, with ejection of an M electron for atomic numbers above 90, and with ejection of electrons lying in states of lower energy, over the whole range of atomic number of interest in this paper. Generally, however, the ejection of an N electron in such a process is very much less probable than that of an M electron, when the energy conditions permit the latter.

When transitions of the Coster–Kronig type are permitted, they will have a predominating influence on the distribution of energy in the L spectrum; the radiation width of the L_1 level will be low compared with the total width of that level, and the excitation of the L_3 level will be increased. The coefficient, A_{13}, therefore, will be large and will be computed. Even when these transitions are energetically impossible, this coefficient, A_{13}, may not vanish, however, because transitions of the type $L_1 \to L_3 N$ can still occur. Even if the probability of such a process is only 10% of that of the Coster–Kronig transition when fully developed, the value of A_{13} could be about 0.2, since the total width of the L_1 level is about 3 v. at tantalum, and 10% of the maximum width of the Coster–Kronig transitions is about 0.6 v. Transitions of this kind should produce satellites of $L\alpha$ and $L\beta_2$ which do not show the 'intensity anomaly'. Such satellites have been studied by Pincherle (30), but their origin is not entirely clear and the quantitative information is not sufficient for an estimate of the width of the L_1 level due to this cause.

Transitions of the type $L_2 \to L_3 N$ must contribute to the width of the L_2 level. These transitions must also be associated with the production of satellites of $L\beta_2$ which do not show an 'intensity anomaly'; here again there is

no evidence to permit a computation of the width due to this process. How-
ever, the extremely low intensities of the satellites of $L\beta_2$ for the atomic
numbers below 68 (cf. Richtmeyer and Kaufman (35)) indicate that the
probabilities of the processes $L_1 \rightarrow L_3N$ and $L_2 \rightarrow L_3N$ are negligible in com-
parison with those of the other Auger processes which can occur.

Transitions of the type $L_1 \rightarrow L_2N$ are energetically possible for most of the
N levels in the heavy elements. They should produce Auger electrons with
less energy than those produced by either of the processes just considered
and should be, therefore, more probable. These transitions contribute to
the excitation of the L_2 level, but the magnitude of the coefficient A_{12} must
be small except possibly at tantalum, because the probability of the process
is certainly very much smaller than that of the Coster–Kronig transitions.

In the absence of quantitative information the coefficients A_{12} and A_{23} will
be assumed to be zero and dropped from Equation (1). This assumption
may be questioned on the grounds that the transition leading to doubly
ionized M levels, or double ionization in the M and the N levels, might be
less likely to occur because the energies of the Auger electrons are greater.
The justification for the assumption can rest only on the results of experiment.
Setting A_{12} and A_{23} equal to zero, Equation (1) reduces to:

$$q_1 = u_1f_1 \; ; \qquad q_2 = u_2f_2 \; ; \qquad q_3 = f_3(u_3 + A_{13}u_1). \qquad (2)$$

A_{13} will be computed on the assumption that the Coster–Kronig process is
the only one which contributes to it, as explained above.

Experimental Fluorescence Yields

Reliable experimental results are available only for the fluorescence yield
of the L_3 levels. Measurements have been made by Küstner and Arends (23)
for elements between tantalum and bismuth, and by Stephenson (38) for lead,
thorium, and uranium. These authors used essentially the same method: a
determination of the amount of the secondary radiation emitted from a target
irradiated with X-rays with a wave length lying between the absorption limits
of the L_2 and L_3 levels. Their results are given in the first and second rows of
Table I, and are plotted in Fig. 2; the agreement between their results is
satisfactory.

Küstner and Arends (23) have also attempted to measure the fluorescence
yields of the L_2 and L_1 levels by decreasing the wave length of a monochromatic
radiation until it lay between the absorption limits of the L_1 and L_2 levels and
just shorter than the latter. The increase in yield of the secondary radiation
was interpreted as being due to the characteristic radiation of the level for
which the wave length of the absorption limit is just above that of the primary
radiation. But above tantalum this interpretation of the results should not
apply to the L_1 level owing to the secondary excitation of the L_3 level. Their
figures for the fluorescence yield of the L_2 level are not subject to this objection,
if the coefficient A_{12} is assumed to be zero; but the results show a decrease with

increasing atomic number which is very difficult to understand since the radiation width must increase rapidly with atomic number and the total width of the L_3 level changes very little.

TABLE I

EXPERIMENTAL VALUES FOR THE FLUORESCENCE YIELD OF THE L_3 LEVEL

z	Ta(73)	W(74)	Ir(77)	Pt(78)	Au (79)	Pb(82)	Bi(83)	Th(90)	U(92)
Küstner & Arends (23)	0.191	0.207	0.244	0.262	0.276	0.337	0.367	—	—
Stephenson (38)	—	—	—	—	—	0.32	—	0.42	0.44
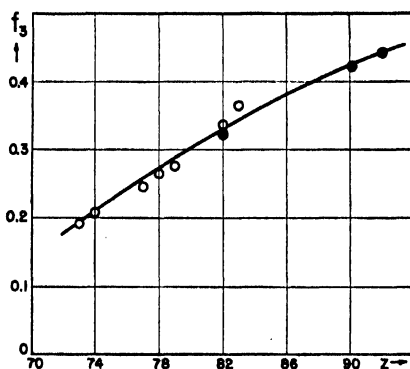
FIG. 2. *The fluorescence yield of the L_3 level as a function of the atomic number. Open circles: according to Küstner and Arends (23); full circles: according to Stephenson (38).*

Radiation Widths and Total Widths

Owing to the absence of experimental data on the fluorescence yields of the L_1 and L_2 levels, these quantities will be deduced by dividing theoretical radiation widths by the experimental values of the total widths. To check the validity of this method of calculation, the calculated values of the fluorescence yield of the L_3 level will be compared with the experimental values. The coefficient A_{13} is given by the ratio of the partial width of the L_1 level due to the Coster–Kronig transitions to the total width of that level. The partial width, in this case, can be deduced from measurements of the line widths. The total widths can be measured directly by studying the shapes of the absorption edges of the three levels. The differences in the widths, however, can be obtained much more accurately by measurement of the widths of the spectrum lines; since the width of a line is equal to the sum of the widths of the initial and final state, the difference in the widths of two lines with the same final state is equal to the difference in the widths of the initial states. When the average of this result is taken for several lines, an accurate value is obtained.

For gold ($Z = 79$), the widths of the three L levels have been measured by Richtmeyer, Barnes, and Ramberg (34) by fitting the constants of a theoretical formula to suit the experimental curve for the shape of the absorption edges. They showed that if the absorption in the edge is due to the ejection of the electron into a region of unoccupied levels in which the distribution in energy is uniform and continuous, the shape of the absorption edge should be given by the formula:

$$\mu(\nu) = c \left[\frac{1}{2} - \frac{1}{\pi} \tan^{-1} \left(\frac{\nu_{E_0} - \nu}{\Gamma/2} \right) \right],$$

where ν_{E_0} is the frequency of ionization of the level of the free atom, ν the frequency considered, c a constant, and Γ is the total width of the level for half-absorption. On the low frequency side the shape of the edge should correspond to that given by this formula; but on the high frequency side, the shape is distorted by the uneven distribution in energy of the states of the free electron in the solid material of the target. This phenomenon is particularly evident in the absorption edge of the L_1 level. Richtmeyer, Barnes and Ramberg considered the measurement of the width of the L_3 level to be the most accurate (4.4 v.). The widths of the remaining levels are calculated from this by using the differences in the widths of the levels obtained from their measurements of the line widths. They found that the width of the L_2 level is less than that of L_3 by 0.7 v. (a result which is confirmed by the measurements of Richtmeyer and Barnes (33) on the widths of the $K\alpha_1$ and $K\alpha_2$ lines of tungsten), and that the width of the L_1 level is greater by 4.3 v. Their final values are, therefore: $L_1 : 8.7$ v.; $L_2 : 3.7$ v.; and $L_3 : 4.4$ v.

The level widths for tungsten and platinum have been measured by Bearden and Snyder (4) and those of tungsten, more recently, by Coster and de Lang (10) by fitting the theoretical curve at the low frequency end to the observed shapes of the absorption edges. The results are summarized in Table II.

TABLE II

TOTAL WIDTHS OF L LEVELS IN VOLTS

C-L: Coster and de Lang, ref. (10); B-S: Bearden and Snyder, ref. (4); R-B-R: Richtmeyer, Barnes, and Ramberg ref. (34)

	Tungsten		Platinum	Gold
	C-L	B-S	B-S	R-B-R
L_1	9.5	4.9 ± 1.0	8.0 ± 1.0	8.7
L_2	—	3.0 ± 0.5	3.5 ± 0.5	3.7
L_3	3.1	3.4 ± 0.5	3.6 ± 0.5	4.4

Coster and de Lang's value for the width of the L_1 level is very discordant; this discrepancy illustrates the difficulty of these measurements, especially those relating to the L_1 level, which, for tungsten, is distorted by the presence of the 'white line' at the higher frequency end of the absorption edge.

The constancy of the widths of the L_2 and L_3 levels between tantalum and bismuth might seem surprising in view of the fact that the radiation widths are increasing rapidly with atomic number. This is explained by the fact that the radiation widths are small in comparison with the total widths, and probably change over this range by only about 0.5 v., which is of the order of the error in the measurements in the total width. The constancy of the total widths of these levels is demonstrated in the measurements of Williams (42) and of Cooper (9).

By plotting the results of Table II for the width of the L_3 levels against the atomic number, a mean value is obtained. For $Z = 76$, the width is 3.6 v.; this value will be used as the basis of further calculations.

Using a nonrelativistic theory, Ramberg and Richtmeyer (31) have calculated the Auger widths and the radiation widths of the levels for gold. For the radiation widths they give the following figures:

$$L_1 = 1.8 \text{ v.;} \qquad L_2 = 2.9 \text{ v.;} \qquad L_3 = 1.8 \text{ v.}$$

If the total width is taken to be 4.0 v. for the L_3 level in gold, the fluorescence yield is about 0.4 for this level, which is too high in comparison with the experimental value—about 0.27. Pincherle (28) has also calculated the radiation and Auger widths on a nonrelativistic basis, and finds 1.6 v. for the width of the L_3 level in gold. However, the nonrelativistic calculations are unsatisfactory. They do not give the correct ratio for the intensities of the $L\beta_3$ and $L\beta_4$ doublet, and in the case of Ramberg and Richtmeyer's work, they predict total widths which are too large (these authors find that the total width of the L_3 level in gold is in excess of 13.7 v.). The width of the K level is also too large; they find 66 v. for the width of this level and point out that the actual width is about 54 v., a value which is obtained by an extrapolation from the experimental width for tungsten by the fourth power of the atomic numbers of these elements (cf. Richtmeyer and Barnes (33)).

The relativistic calculations of Massey and Burhop (26) lead to a lower value for the width of the K level in gold (about 47 v.) nearer the correct figure and also give the correct ratio for the intensities of the $L\beta_3$ and $L\beta_4$ lines.* Their estimates are used for the basis of the calculations of the fluorescence yields in this paper. Since these authors did not calculate the radiation widths of some of the weaker lines, estimated values of the latter are included here in the total radiation width. In Table III, the contribution of the more important lines to the total width is given in terms of percentages, the calculations being made (for L_2 and L_3) on the basis of Jönnson's (22) measurements for tungsten, with the assumption that the relative intensities of the lines originating in one level remain approximately constant over the range of atomic numbers between tantalum and bismuth. For the L_1 radiations, the calculations are based on the measurements of Bötzkes (6).

* *Their predictions for the relative intensities of the Auger electrons ejected in the processes which produce a double ionization in the L levels do not seem to be in agreement with experiment (cf. Ellis (15)).*

Using the values given in Table III, the radiation widths obtained by Massey and Burhop, for gold, are equivalent to:[*]

$$L_1 : 0.70 \text{ v.}; \qquad L_2 : 1.18 \text{ v.}; \qquad L_3 : 0.92 \text{ v.}$$

To obtain the radiation widths for neighboring elements, these figures may be multiplied by the ratio of the fifth power of the atomic numbers, which is approximately the variation with atomic number shown by Massey and Bur-

TABLE III

RELATIVE CONTRIBUTIONS TO THE RADIATION WIDTHS IN PERCENTAGES

L_1		L_2		L_3	
β_3	44	β_1	85	α_1	75
β_4	32	η	2	α_2	9
γ_2	8	γ_1	13	β_6	1
γ_3	13	γ_6	1	β_2	13
γ_4	3			1	3

hop's values for antimony, gold, and uranium. For $Z = 76$, the total width will be 3.6 v. (as discussed above) and the radiation width of the L_3 level will be 0.77 v. The Auger width is equal to the difference—2.8 v. If this width is assumed to be constant, the best value for the total width in gold is 3.7 v., giving a rather low value—0.25—for the fluorescence yield of the L_3 level, but possibly not outside the experimental error of the measurements of Küstner and Arends. The radiation width of this level in uranium is 2.16 v. if calculated from Massey and Burhop's figures and from Allison's (1) value of the intensity of the line $L\beta_2$ relative to that of $L\alpha_1$. Assuming that the Auger width is constant throughout this range of atomic number, at 2.8 v., the fluorescence yield of uranium in the L_3 level is found to be 0.43, which is in agreement with the results of Stephenson (see Fig. 2).

The width of the lines characteristic of the L_1 level as an initial state have been studied in detail by Cooper (9). He measured the widths of the lines $L\beta_4(L_1 \to M_2)$, $L\beta_3(L_1 \to M_3)$, $L\gamma_2(L_1 \to N_2)$ and $L\gamma_3(L_1 \to N_3)$ and showed that they increased continuously from tungsten to thallium, and by the same amount. The variation of these widths with atomic numbers is illustrated in Fig. 3, which is taken from Cooper's results. In this figure, the mean difference of the width of a line for atomic number Z from that of the same line for tantalum is plotted against Z, the ordinate in each case being an average of the differences corresponding to the four lines referred to above. The accuracy of each point is about 0.2 v. The increase in widths at tantalum illustrates the appearance of the Coster–Kronig transitions above this element; at thallium, the probability of the two processes $L_1 \to L_3 M_{4,5}$ was found to

---

[*] *The transition probabilities given by Massey and Burhop are measured in transitions per unit atomic time; it has been assumed in making these calculations that a probability of one in these units is equivalent to a width of 27.4 ev.*

be a maximum (not shown in the figure) by Shrader, according to some unpublished results quoted by Cooper. Shrader found that the intensity of the $L\alpha_1$ satellite relative to the parent line rising with increasing atomic number
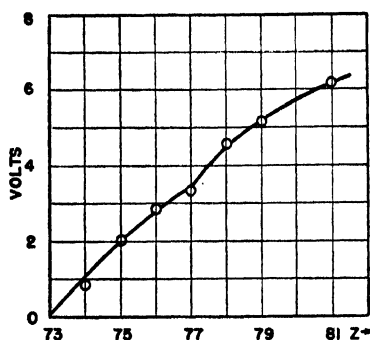
FIG. 3. *The difference between the width of the L_1 level in an element of atomic number Z and the width of the L_1 level in tantalum (Z = 73), after Cooper (9). The difference between the width of a line of the L spectrum for atomic number Z and that of the same line for tantalum is averaged over the lines $L\beta_3$, $L\beta_4$, $L\gamma_2$, and $L\gamma_3$, and is plotted, in volts, against the atomic number.*

from zero at tantalum on account of the $L_1 \rightarrow L_3M_5$ process has a discontinuity at platinum (Z = 78) owing to the onset of the $L_1 \rightarrow L_3M_4$ process, increases to a peak in the region of thallium, and then falls slowly to thorium. The reduction in the intensity of the satellites above the thallium–bismuth region is doubtless due, in part, to the rising radiation width and also to the increasing energy of the Auger electron.

Now the ordinates of Fig. 3 are equal to the partial widths of the L_1 levels due to the Coster–Kronig transitions. Since the experimental results for the total widths of the L_1 levels are unreliable, these widths must be obtained from the constituent parts: the radiation width, the Coster–Kronig width, and a constant width representing the remainder of the nonradiating transitions. The radiation width is obtained from the results of Massey and Burhop for gold with a suitable adjustment for the variation with atomic number; the constant width is obtained from the gold results. It has been shown that the best value for the width of the L_1 level in gold is 8.0 v.; the Coster–Kronig width is 5.1 v., and radiation width is 0.7 v.; the constant width is therefore 2.2 v. The total widths of the L_1 level are listed in the first row of Table IV: the fluorescence yield, f_1, in the second row. It will be seen that the yields are low and roughly constant over a wide range. The low value of this fluorescence yield is consistent, in general, with the low values deduced by Pincherle (29) which are necessary to account qualitatively for the very low intensities of the L_1 radiation which are observed in cathode ray excitation. The values obtained here are lower than that obtained by Küstner and Arends for tantalum (f_1 = 0.28), where their method might be expected to give accurate results.

TABLE IV

FLUORESCENCE YIELDS AND COEFFICIENTS CALCULATED FROM THE THEORETICAL RADIATION
WIDTHS OF MASSEY AND BURHOP AND LEVEL WIDTHS OBTAINED FROM TABLE II

The values in brackets are obtained by interpolation or extrapolation of these
figures

Z	73	75	77	79	81	83	90	92
Γ_1 ,v.	2.8	4.8	6.1	8.0	9.0	(9.2)	(9)	(9)
f_1, %	17	11.0	10.0	9.0	9.0	(10.0)	(15)	(16)
A_{18}, %	0	42	54	65	67	(70)	(60)	(60)
f_2, %	31	33	37	39	43	46	56	59
f_8, %	18	20	23	25	27	30	39	41

The values of the coefficient A_{18} are listed in the third row of the table.
The numerical values for f_2 and f_8 are given in the fourth and fifth rows of the
table. These quantities are equal to the ratios of the radiation widths (cal-
culated from Massey and Burhops figures) to the total widths obtained by
adding the sum of these radiation widths to a constant quantity representing
the nonradiating transitions. The value for this constant quantity is taken
from the figures for gold. The value of f_2 for tantalum is close to that obtained
by Küstner and Arends for this element. It has already been pointed out
that the theoretical figures of Massey and Burhop lead to a value for the
fluorescence yield in gold which is about 10% lower than the experimental
value. It is possible that all these yields are too low by a similar amount,
but rather than make an arbitrary adjustment of the figures in this ratio in
order to bring the fluorescence yield of L_3 into agreement with the experi-
mental value for gold, the theoretical values for the fluorescence yields given
in Table IV will be used in subsequent calculations as they stand.

X-Ray Intensities in Cathode Ray Excitation

A comparison of the intensities of the spectrum lines in cathode ray excita-
tion might be expected to give a check on the ratios of the fluorescence yields
which have been listed in Table IV. However, such a comparison is difficult
to make because the relative excitation of the levels is not known with
certainty. It appears that the greater part of the X-ray emission from thick
targets arises from indirect or fluorescence excitation. The relative excitation
of L radiation by fluorescence and cathode rays in targets of heavy elements
does not seem to have received attention; but the work of Hansen and Stoddard
(18), and of Stoddard (39, 40) on the excitation of the K radiations in copper,
palladium, and in gold, shows that the indirect excitation greatly predominates
in the heavy elements. If, as would appear very likely, this is also the case
for the production of the L radiations, it is difficult to know what values to
assign to the quantities u_1, u_2, and u_3. Further, the experimental results
which are available have been corrected for equal probability of ionization for
each electron in the levels on the assumption that cathode ray excitation only

is effective; even if these corrections are justified they are very dubious, because there in a lack of agreement between the variation in energy of the ionization function, as determined for the K level by Webster, Hansen, and Duveneck (41), and by Clark (7), and the theoretical curves of Rosseland (36), Bethe (5), and others, and because the relative values of the peaks of the ionization functions must be deduced from these theoretical formulae. Finally, the corrections do not allow for the secondary excitation of the L_3 level by the Coster–Kronig process.

A comparison of the intensities of the lines characteristic of the L_1 and L_2 levels might be expected to show the least discordance with experiment because the ionization energies of these levels are the closest together. If u_1 is equated to u_2, the value for the ratio of the intensities of the lines $L\beta_3$ and $L\beta_1$ will be obtained from the formula:

$$I\beta_3/I\beta_1 = \frac{f_1}{f_2} \cdot \frac{\lambda\beta_1}{\lambda\beta_3} \cdot \frac{C\beta_3}{C\beta_1} ,$$

where the λ's are the wave lengths of the lines and $C\beta_3$ and $C\beta_1$ are the fractional radiation probabilities given in Table III. If the excitation of these levels is indirect, in the main, the intensities would be expected to be less than those given by this equation. The wave length of these lines is very nearly equal in the range of atomic number of interest here. Hence,

$$I\beta_3/I\beta_1 = 0.52 \, f_1/f_2 . \tag{3}$$

The ratios of the intensities of $L\beta_3$ to $L\beta_1$ have been measured in some instances by Hicks (19), Jönnson (22), and by Bötzkes (6). Cooper (9) has shown that the intensities of the L_1 lines fall relatively to that of $L\beta_1$ for increasing atomic numbers above tantalum, and has given uncorrected figures for the percentage intensities of $L\beta_3$, $L\beta_4$, $L\gamma_3$, and $L\gamma_2$ with respect to $L\beta_1$. The ratios of the observed intensities of $L\beta_3$ to $L\beta_1$, and $L\gamma_2$ to $L\gamma_1$ are collected in Table V.

TABLE V

EXPERIMENTAL VALUES FOR THE RATIOS OF THE INTENSITIES OF THE LINES $L\beta_3$ TO $L\beta_1$, AND $L\gamma_2$ TO $L\gamma_1$, IN PERCENTAGES

Z	Ta 73	W 74	Re 75	Os 76	Ir 77	Pt 78	Au 79	Tl 81
$L\beta_3$ to $L\beta_1$								
Hicks (19)	13	—	—	—	—	—	—	—
Jönnson (22)	—	16	—	—	—	—	—	—
Bötzkes (6)	12	—	—	—	—	—	—	—
Cooper (9)	18.5	16.2	15.2	13.9	14.2	14.1	13.0	9.4
$L\gamma_2$ to $L\gamma_1$								
Jönnson (22)	—	17	—	—	—	16	—	—
Bötzkes (6)	17	—	—	—	—	—	—	—
Cooper (9)	17.3	14.1	13.3	11.5	12.4	—	10.5	11.0

Substitution of the values for f_1 and f_2 from Table IV into Equation (3) gives ratios for the intensities of the lines $L\beta_2$ to $L\beta_1$ which are in general agreement with those of Table V, except at tantalum where the result is too high. At tantalum the ratio should be 28%, the observed value is about 17%; at Re ($Z = 75$), Equation (3) gives 17% in agreement with Table V; in Au (79), 12%; in Tl (81), 11%, also in general agreement. For the ratios of the γ lines, the ratio of $C\gamma_2$ to $C\gamma_1$ is 0.6, which gives figures about 10% higher than those for the ratios of $L\beta_2$ to $L\beta_1$. A large error at tantalum (73) is to be expected because it is in this element that the calculation of the total width of the L_1 level is the least accurate.

A comparison of the intensities of the lines $L\beta_1$ and $L\alpha_1$ may be made in a similar manner. For cathode ray excitation, the 'corrected' experimental results should be comparable with the values obtained from a formula with u_1 and u_2 proportional to unity, and u_3 proportional to 2. Thus:

$$I\beta_1/I\alpha_1 = \frac{u_2}{u_3 + A_{13}u_1} \cdot f_2/f_3 \cdot \left(\frac{\lambda\alpha_1}{\lambda\beta_1}\right) \cdot C\beta_1/C\alpha_1$$

$$= \frac{1}{2 + A_{13}} \cdot f_2/f_3 \left(\frac{\lambda\alpha_1}{\lambda\beta_1}\right) \cdot C\beta_1/C\alpha_1 \qquad (4)$$

Again, if fluorescence is the predominating mode of excitation, the calculated intensities should be appreciably less than those obtained from this equation, because the fluorescence processes, generally, favor the excitation of the L_3 level relative to that obtained with cathode ray bombardment. Equation (4) does not lead to satisfactory agreement with the experimental determinations. Some experimental values are listed in Table VI.

TABLE VI

EXPERIMENTAL VALUES FOR THE RATIOS OF THE INTENSITIES OF THE LINES $L\beta_1$ AND $L\alpha_1$
CORRECTED ACCORDING TO THE ROSSELAND FUNCTION

Ta			W	Pt
Hicks (19)	Andrew (2)	Bötzkes (6)	Jönnson (22)	Jönnson (22)
0.57	0.72	0.60	0.52	0.52

In the region of atomic number of interest here, the ratio $C\beta_1/C\alpha_1$ is 1.13 and $\lambda\alpha_1/\lambda\beta_1$ is about 1.15. For tantalum, the intensity ratio is found to be 1.1. The most accurate value of the intensity ratio is probably that of Andrew (2), who used an ionization chamber for detection of the radiation. His experimental result, corrected with the Rosseland function, is 0.72, and, corrected with the empirical Webster formula, it is 0.58. The disagreement, in this element, is not due to a lack of consideration of the Coster–Kronig processes: it is probably due to the indirect excitations, which, as pointed out above, favor the excitation of the L_3 level. That the ratios of the fluorescence

yields, f_2 and f_3, are approximately correct, at least for bismuth, is shown in the measurements of the L radiations emitted following the internal conversions produced in the disintegration of ThB, which are described in the following paper.

The Total Fluorescence Yields

(1) *Fluorescence Excitation*

The total fluorescence yield may be defined as the total number of quanta emitted per ionization of the L levels. Remembering that $\Sigma u = 1$, this quantity is given by adding the terms of Equation (2):

$$f_0 = f_1 u_1 + f_2 u_2 + f_3(u_3 + A_{13}u_1). \tag{5}$$

Experimental values for the total fluorescence yield have been given by Lay (25) using fluorescence excitation by the K radiation of molybdenum. In this case the relative excitations of the three L levels may be computed from the magnitudes of the absorption jumps given by Compton and Allison (8). From tungsten to uranium, the appropriate value of u_1 differs little from 0.18, u_2 varies between 0.29 to 0.35, and u_3 between 0.53 to 0.46. The results of the evaluation of Equation (5) are given in Table VII together with

TABLE VII

TOTAL FLUORESCENCE YIELDS WITH FLUORESCENCE EXCITATION
(WITH MOLYBDENUM K RADIATION)

Z	W 74	Os 76	Pt 78	Au 79	Pb 82	Bi 83	U 92
Calculated from Eq. (5) and Table IV	0.23	0.26	0.29	0.29	0.33	0.36	0.47
Lay's results (25)	0.30	0.35	0.35	0.36	0.40	0.40	0.45

the results of Lay. It will be seen that the calculated figures are somewhat lower than the empirical results; since the excitation of the L_3 level is the most important, this lack of agreement is probably due to the low figures for the fluorescence yields, f_3, which have been used (Table IV).

(2) *Internal Conversion in L Levels*

The total fluorescence yields to be expected from conversion in the L levels are given in Table VIII. These have been calculated for $u_1 = 0.90$, $u_2 = 0.09$, and $u_3 = 0.01$, which are approximately in the ratios of the excitations observed by Arnoult (3) for the internal conversion of the 40 kev. transition of ThC–C''. The results are very similar to the figures calculated for fluorescence excitation although the relative excitations are very different.

In the following paper, the results of Table VIII have been compared with the experimental results for the fluorescence yield for L conversions in the disintegration of ThC (for which the product nucleus is thallium) and for

TABLE VIII

TOTAL FLUORESCENCE YIELDS FOR L CONVERSION

	q_1	q_2	q_3	f_0
Ta 73	0.15	0.02	0	0.18
Re 75	0.10	0.03	0.08	0.21
Ir 77	0.095	0.033	0.112	0.24
Au 79	0.081	0.035	0.150	0.27
Tl 81	0.081	0.039	0.165	0.29
Bi 83	0.090	0.041	0.192	0.32
Th 90	0.135	0.050	0.215	0.40
U 92	0.144	0.053	0.225	0.42

RaD (bismuth). The ratio of f_2 to f_3 is estimated from selective absorption measurements on the L radiations emitted following internal conversion in the K levels in bismuth; it is shown that the values used for these quantities are about 10% too low, in general agreement with a remark in a previous paragraph in this paper. This leads to the conclusion that the figures of Table VIII are also too low by about the same amount and for the same reason. Further, the results for RaD indicate that the yield of radiation from the L_3 level given in Table VIII is too low; this would seem to show that the neglect of the coefficient A_{12} is not justified in the case of internal conversion in the L levels where the excitation of the L_1 level greatly exceeds the excitation of the other levels. Taking this into account, the figures for f_0 in the table should be increased by some 25%.

References

1. ALLISON, S. K. Phys. Rev. 32 : 1. 1928.
2. ANDREW, V. J. Phys. Rev. 42 : 591. 1932.
3. ARNOULT, R. Ann. phys. 12 : 240. 1939.
4. BEARDEN, J. A. and SNYDER, T. M. Phys. Rev. 59 : 162. 1941.
5. BETHE, H. A. Ann. Physik, 5 : 325. 1930.
6. BÖTZKES, M. Z. Physik, 89 : 667. 1934.
7. CLARK, J. C. Phys. Rev. 48 : 30. 1935.
8. COMPTON, A. H. and ALLISON, S. K. X-rays in theory and experiment. 2nd ed. D. Van Nostrand Company, Inc., New York. 1935.
9. COOPER, J. M. Phys. Rev. 61 : 234. 1942.
10. COSTER, D. and DE LANG, H. Physica, 13 : 385. 1947.
11. COSTER, D. and LANGEN, K. W. DE. Physica, 3 : 282. 1936.
12. COSTER, D. and KRONIG, R. DE L. Physica, 2 : 13. 1935.
13. COSTER, D., KUIPERS, H. H., and HUIZINGA, W. J. Physica, 2 : 870. 1935.
14. DRUYVESTEYN, M. J. Dissertation, Groningen. 1928.
15. ELLIS, C. D. Proc. Roy. Soc. London, A, 139 : 336. 1933.
16. FRILLEY, M., SURUGUE, J., and TSIEN, S-T. J. phys. radium, 7 : 350. 1946.
17. FRILLEY, M. and TSIEN, S-T. Compt. rend. 220 : 144. 1945.
18. HANSEN, W. W. and STODDARD, K. B. Phys. Rev. 43 : 701. 1933.
19. HICKS, V. Phys. Rev. 36 : 1273. 1930.
20. HIRSH, F. R. Phys. Rev. 50 : 191. 1936.
21. HIRSH, F. R. and RICHTMEYER, F. K. Phys Rev. 44 : 955. 1933.
22. JÖNNSON, A. Z. Physik, 36 : 426. 1926.

23. Küstner, H. and Arends, E.   Ann. Physik, 22 : 443.   1935.
24. Langen, K. W. de.   Physica, 6 : 27.   1939.
25. Lay, H.   Z. Physik, 91 : 533.   1934.
26. Massey, H. W. S. and Burhop, E. H. S.   Proc. Cambridge Phil. Soc. 32 : 451.   1936.
27. Pearsall, A.   Phys. Rev. 46 : 694.   1934.
28. Pincherle, L.   Nuovo cimento, 12 : 81.   1935.
29. Pincherle, L.   Nuovo cimento, 12 : 162.   1935.
30. Pincherle, L.   Phys. Rev. 61 : 225.   1942.
31. Ramberg, E. G. and Richtmeyer, F. K.   Phys. Rev. 51 : 913.   1937.
32. Randall, C. A. and Parratt, C. G.   Phys. Rev. 57 : 786.   1940.
33. Richtmeyer, F. K. and Barnes, S. W.   Phys. Rev. 46 : 352.   1934.
34. Richtmeyer, F. K., Barnes, S. W., and Ramberg, E. G.   Phys. Rev. 46 : 843.   1934.
35. Richtmeyer, F. K. and Kaufman, S.   Phys. Rev. 44 : 605.   1933.
36. Rosseland, S.   Phil. Mag. 45 : 65.   1923.
37. Stahel, E.   Helv. Phys. Acta, 8 : 651.   1935.
38. Stephenson, R. J.   Phys. Rev. 51 : 637.   1937.
39. Stoddard, K. B.   Phys. Rev. 46 : 837.   1934.
40. Stoddard, K. B.   Phys. Rev. 48 : 43.   1935.
41. Webster, D. J., Hansen, W. W., and Duveneck, F. B.   Phys. Rev. 43 : 839.   1933.
42. Williams, J. H.   Phys. Rev. 45 : 71.   1934.

THE EMISSION OF *L* RADIATION IN THE DISINTEGRATION OF ThC AND RaD[1]

By B. B. Kinsey[2]

Abstract

The amount of *L* radiation resulting from the *K* conversion of γ-radiation emitted in the disintegration of ThB has been measured and found to be in general agreement with the calculations of the preceding paper. This amount, which is determined mainly by the fluorescence yield of the L_3 level, confirms the results of Küstner and Arends; selective absorption measurements confirm the calculated value for the ratio of the fluorescence yields of the L_2 and L_3 levels for the product element (bismuth). The yields of *L* radiation resulting from the *L* conversion of the low energy γ-radiation emitted in the disintegrations of ThC and of RaD have been measured and compared. In the first case the yield is too high, and in the second it is too low compared with the calculated values. Selective absorption measurements indicate that the yields of the L_1 and L_2 levels, taken together, are equal to that of the L_3 level. It is shown that the experimental result for ThC can be explained on the assumption that Auger transitions of the type $L_1 \rightarrow L_2N$ play some part in the distribution of energy in the spectrum; the result for RaD, which is consistent with the results of Stahel (1935), indicates that the low energy γ-transitions emitted by that element and converting in the *L* levels are excited in less than 100% of the disintegrations.

Introduction

The object of the measurements described in this paper was to determine the amount of *L* radiation which is emitted following the internal conversion of γ-radiation in the *L* levels in the heavy elements.

The yield of *L* radiation has been calculated in the previous paper where it was shown that a determination of this quantity is of some interest in the case of RaD. Now the determination of the fluorescence yield of *L* radiation from RaD requires both a measurement of the amount of *L* radiation emitted and a knowledge of the number of times the excited state is formed. It will be shown that there is some doubt as to the value for the latter quantity; for this reason, the amount of *L* radiation from RaD cannot be used as a check on the calculations of the fluorescence yield given in the previous paper. Therefore, a measurement has to be made on the yield of *L* radiation from a neighboring element for which the excitation of the γ-transition and the internal conversion coefficient are known with greater precision. There are very few cases among the heavy elements in which the γ-transitions have been studied in sufficient detail for this purpose. The only one suitable is the 40 kev. transition which is excited in the disintegration of ThC, for which the product nucleus, ThC″, is an isotope of thallium. ThC is very easy to prepare as a constituent of the active deposit of thoron and can be obtained as thin layers with very high specific activity. A detailed study has therefore been made of the various *L* radiations emitted by this deposit. A by-product of this

---

[2] *Member of the United Kingdom Staff.*

work has been the measurement of the L radiations emitted following the K conversions produced by the disintegration of ThB, and this work has led to a confirmation of the calculation of some of the fluorescence yields discussed in the preceding paper.

Apparatus

The apparatus used in these measurements is shown in Fig. 1. The radio-active sources were supported on an aluminum slide at the position O in the figure. The radiation was detected by a counter, C, containing a mixture
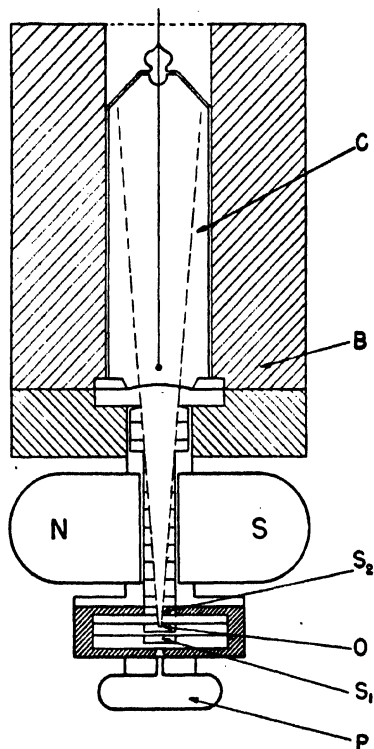
FIG. 1. *Apparatus used for the measurement of the L radiation emitted by the thorium active deposit.*

of argon, xenon, and alcohol. The electrons emitted by the source were prevented from operating the counter by the use of a small permanent magnet NS. That no electrons from the source, or Compton electrons from a filter placed at S_2, produced pulses in the counter, was verified by plotting an absorption curve of the counting rate against the thickness of a cellophane filter. After subtraction of the effect due to the hard radiations, the absorption coefficient was found to be equal to that expected of the L radiations, viz., radiations with a wave length of about one Ångstrom unit.

The beam of radiation was limited by a brass diaphragm, and the channel between the pole faces of the magnet was lined with aluminum and provided with a series of stops to trap the electrons. The radioactive material

was confined to an area bounded by a circle, $\frac{1}{8}$ in. in diameter, so that the diaphragm presented the same solid angle to all points within this circle. The beam of radiation, defined in this manner, passed through the counter from end to end without intersecting the wall of the counter. The counter wire was suspended horizontally with a small glass bead at the end where it faced the source; the area of the bead was insignificant in comparison to that of the section of the cone of radiation at this point. The end of the counter facing the source was closed with a mica window of thickness 9 mgm. per sq. cm. The counter was contained in a thick lead cylinder (B) and the whole apparatus was screened from external radiations by enclosure within thick lead walls.

To facilitate the coincidence experiments with β-particles, the source holder and the slides supporting the filters were enclosed in a steel cylinder which screened the source and its immediate vicinity from the stray magnetic field of the permanent magnet. A small hole in the far end of this steel structure allowed α- or β-particles to pass from the source through a thin window into a counter working either in the proportional region or as a Geiger–Müller counter. When coincidence measurements were made, or when the total L radiations emitted from ThB in equilibrium with its products were measured, care was taken to ensure that the activity was deposited on one side of the supporting foil only, the active surface facing downwards in Fig. 1. In this way, α- or β-particles could pass into the proportional counter at P with very little residual absorption. However, most of the other measurements were made with the active surface facing the xenon-counter; in comparing the results, therefore, a small correction has to be made to allow for the absorption of the radiations in the supporting foils and to account for the slight difference in the geometrical conditions. This correction was usually of the order of 6%.

Preliminary experiments were made with a counter filling consisting of xenon and alcohol in the usual proportions of argon–alcohol fillings. Subsequently, argon was mixed with the xenon to obtain satisfactory counting rate plateaus (7 cm. pressure of argon and 3 cm. of xenon). To ensure that the content of xenon and argon was known with sufficient accuracy, the alcohol and xenon were admitted first and successively frozen into a side tube on the counter with a freezing mixture of solid carbon dioxide and acetone and with liquid air; finally the argon was introduced and the counter sealed off. Filled in this way, and operated continuously day and night, the counter was found to have stable and reproducible characteristics over a period of several months.

Method of Measurement for Thoron Deposits

The active deposit was prepared on thin foils of aluminum and platinum. A few hours after removal from the emanating apparatus, the deposit of ThB is in equilibrium with its daughter products, all of which will then decay with the period of the parent. The number of atoms disintegrating per second can then be calculated for each member of the series in terms of the rate of disintegration of one of them. There will be a strong emission of L radiation

which follows·the K conversion of the γ-rays emitted in the transition ThB–C; another powerful emission will result from L conversion in the α-decay of ThC, and a much weaker one will accompany the K conversion of the γ-radiation emitted from ThC″–D.   The branch of the decay of ThC which produces the nucleus ThC′ will not be expected to produce a measurable amount of L radiation, because the intensity of the γ-radiation emitted in this process is very low and it is only weakly converted.   The general decay scheme of these elements with their periods is shown in Fig. 2.   The total amount of
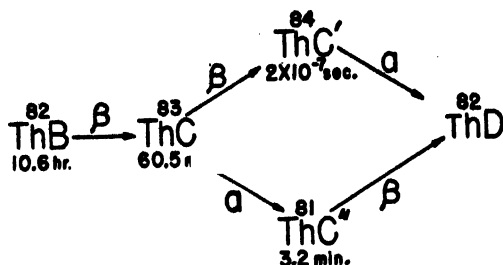
FIG. 2. *Decay scheme for elements of the thorium active deposit.*

L radiation is measured by a determination of the soft radiation emitted by ThB in equilibrium with its products; the amount produced by ThC–C″ and by ThC″–D is obtained by a study of the radiation produced by separated sources of ThC and ThC″.   The difference between the first two results gives a measure of the radiation produced by ThB–C.   In this case, since most of the radiation follows the emission of the K radiation of the product nucleus, viz., ThC, the measurement is in effect a check on the experimental values of the fluorescence yield of the L_3 level of bismuth (ThC) as determined by Küstner and Arends (24).   The measurement of the quantity of the L radiation of ThC–C″ should test the validity of the figures given in the preceding paper for thallium.   Finally, selective absorption measurements will give information on the relative values of the fluorescence yields.

The counting rate of the counter is in three parts, the first due to the hard radiations emitted by the source, the second due to cosmic rays, and the third due to L radiation.   The last is distinguished from the first two by subtracting from the total counting rate the amount which is observed when a filter (containing about 30 mgm. of nickel per sq. cm.) is placed in the position S_2 in Fig. 1. For a source of ThB in equilibrium with its products, the absorption curve of the total radiation in nickel is given in Fig. 3, Curve A.   Curve B (plotted in logarithmic ordinates) shows the result of subtracting the hard component of the radiations.   This soft component, represented by Curve B, has the absorption coefficient corresponding to L radiations.   A nickel filter of 30 mgm. per sq. cm. reduces this radiation to about 3% of its original intensity.

Except for the L radiation emitted by ThC″, which was measured in a separate experiment, the experimentally determined quantities are the ratios of the counting rates due to L radiation to the number of atoms of ThC disintegrating per second.   This ratio is a counting efficiency, which will be called ϵ_1

for a source of Th (B + C) in equilibrium with its products and ϵ_2 for a source of ThC in equilibrium with ThC''. The quantities required are the efficiencies per atom disintegrating per second for each of the constituents of the active
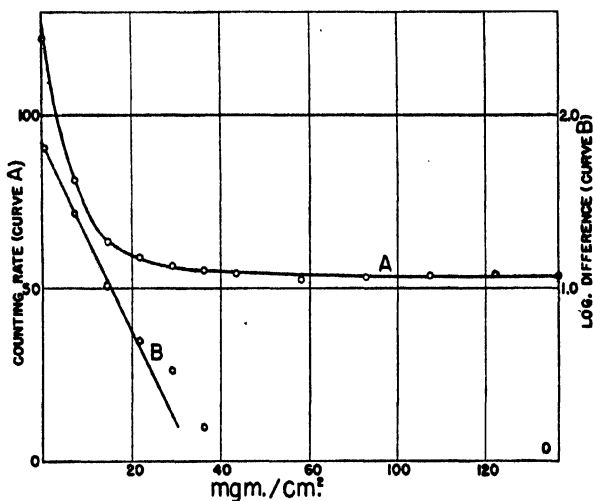
FIG. 3. *The absorption in nickel of the radiation emitted by Th(B + C). Ordinates: Curve A, counting rate, including hard radiations; Curve B, logarithm of the difference between the counting rate and that of the constant ordinate of Curve A.*

sources; these efficiencies will be denoted by ϵ_B, ϵ_C etc. They may be determined for ThB from the measurements of ϵ_1 and ϵ_2 and they will be compared with the calculations after account is taken of the absorption of the radiation in the air, in the mica window of the counter and in the filling gas. Let N_B, N_C, and $N_{C''}$ be the number of atoms of ThB, ThC and ThC'' disintegrating per second. Then, the observed quantities are related to the required quantities by the following equations, if sufficient time* is allowed to elapse after the preparation of the sources to ensure the establishment of a transient equilibrium in each case:—

$$N_C \epsilon_1 = N_B \epsilon_B + N_C \epsilon_C + N_{C''} \epsilon_{C''}$$
$$N_C \epsilon_2 = N_C \epsilon_C + N_{C''} \epsilon_{C''} . \qquad (1)$$

These equations neglect any L radiations emitted in the disintegration ThC–ThC'–ThD; this neglect is justified by coincidence measurements to be described later. The difference between these expressions gives the efficiency for the detection of the radiation emitted by ThB–C:—

$$\epsilon_B = N_C/N_B(\epsilon_1 - \epsilon_2).$$

In transient equilibrium, N_B and N_C are related by the equation:

$$N_C/N_B = \frac{\lambda_C}{\lambda_C - \lambda_B} = 1.11,$$

* *Three or four hours is a sufficient time for ThB and 10 min. for ThC.*

where λ_C and λ_B are the disintegration constants of these atoms ($\lambda_C = 0.69$ hr.$^{-1}$ and $\lambda_B = 0.065$ hr.$^{-1}$). Thus:—

$$\epsilon_B = 1.11(\epsilon_1 - \epsilon_2). \tag{2}$$

The efficiency for ThC is obtained by subtracting from ϵ_2 a quantity proportional to the efficiency for ThC″, which is measured in a separate determination. The fraction of atoms of ThC disintegrating by α-decay is 0.34, so that the relation between the numbers of atoms of ThC″ and ThC disintegrating per second is given by:

$$N_{C''} = 0.34 \, N_C \frac{\lambda_{C''}}{\lambda_{C''} - \lambda_C} = 0.365 \, N_C, \tag{3}$$

the disintegration constant of ThC″ being 13.0 hr.$^{-1}$. Substitution of (3) in (1) gives:—

$$\epsilon_C = \epsilon_2 - 0.365 \, \epsilon_{C''}.$$

There are two methods of measuring the efficiency for ThC which should give the same result. In the first, which will be called the direct method, the strength of the sources was determined in a separate measurement by counting the total number of α-particles collected in a known solid angle; the ratio of the counting rate of L radiation to the strength of the sources, in disintegrations of ThC per unit time, gives the quantities ϵ_1 and ϵ_2. In the second, or coincidence method, coincidences were observed between the α-particles and the pulses in the xenon counter; the ratio of the coincidence counting rate to the counting rate for α-particles gives a measure of the efficiency. The difference in the two coincidence ratios that are measured with and without a nickel filter of 30 mgm. per sq. cm. is the efficiency for detection of L radiation for the transition ThC–C″, viz., ϵ_C*. A similar coincidence method was also used to measure the efficiency for the L radiation of ThB–C; the result is more complicated in its interpretation and will be dealt with later.

Measurements by Direct Methods

(a) The efficiency for ThB–C

The first step in the determination of ϵ_B is the measurement of ϵ_2, the efficiency for detection of the radiation emitted by ThC in equilibrium with its products. In the preliminary measurements, sources of ThC were prepared by deposition on one side of a nickel foil from warm, dilute hydrochloric acid solution. The results for the efficiency of detection of L radiation soon showed a discrepancy when compared with the measurement of the efficiency determined by the coincidence method. This discrepancy was found to be due to the absorption of the L radiation within the nickel foil, and the subsequent reradiation of a considerable fraction of it as the K radiation of nickel, with a wave length of about 1.65 Å. Later, thinner layers of nickel were used, deposited electrolytically on a very thin layer of gold sputtered on aluminum

---

* *The use of the coincidence method is justified by the recoil experiments of Ellis (11), which show that the lifetime of the 40 kev. state is less than 10^{-7} sec.*

foil 2.0 mgm. per sq. cm. in thickness. Finally, pure ThC was prepared by electrolytic deposition on platinum in dilute hydrochloric acid solution using a method described by Hevesey and Paneth (22); the deposit was dissolved in nitric acid, the solution was concentrated by evaporation, and a drop of it was allowed to dry on a thin cellophane foil. This last method gave a result, which, when the contribution of the disintegration ThC″–D was subtracted from it, is consistent with the coincidence measurement of ϵ_C.

The results are collected in Table I, *A*; the observed results are given in the third column; a correcting factor for the nickel *K* radiation is given in the fourth column*, and the corrected result is given in the fifth column. The errors given are the statistical errors involved in the mean of the measurements; they are relatively high because of difficulties in obtaining ThC sources of sufficient strength, and because it was necessary to count for short periods so that the corrections for the decay of the source should not be too large. The purity of the source was tested by allowing it to decay for 24 hr.: the remaining α-activity is due to the generation of ThC by ThB, and is a measure of the ThB content; in practice, the impurity of ThB amounted to less than 1% of the initial ThC content. The initial strength of the source was measured in each case by counting the number of α-particles passing through a hole in a brass plate into a proportional counter filled with argon at low pressure. The dead time of the counters used in these measurements was negligible.

The measurements with sources of Th(B + C) were made with the active surface facing the proportional counter. In this case a small correction for the slightly differing solid angle (2%) and for the absorption in the support of the source is applied before comparing the results with those obtained for ThC. The sources on aluminum foil were prepared by exposing to the emanator a sandwich of two aluminum foils stuck together with grease, dissolving away the grease in ether, and separating the foils. In this way a source was obtained deposited on one side of the foil only. This foil, cut to the right size, was supported on a thin cellophane foil, 3.6 mgm. per sq. cm. in thickness. Other sources were prepared by deposition from the emanation on platinum

---

The correcting factor for the reradiation of the nickel K radiation was calculated in the following manner. Neglecting the absorption of the nickel K radiation in the nickel foil, to a first approximation the fraction of the total number of L quanta absorbed by a foil of thickness m gm. per sq. cm. and mass absorption coefficient, μ/ρ, is readily shown to be:

$$q = \frac{1}{2}\left\{ 1 - \int_0^{\pi/2} e^{-m \cdot \mu/\rho \cdot \tan\theta} \cdot \sin\theta \, d\theta \right\}$$

when the activity is deposited on one side of it only. Of this, a fraction 0.89 is absorbed in the K shell of nickel, the remainder gives rise to the L radiation of nickel, which is strongly absorbed in the air and in the mica covering the window of the counter and is therefore not detected. Of that fraction, the proportion which gives rise to K emission is given by the fluorescence yield for nickel —0.364 according to Arends (2). The transmission of the 1.65 Å radiation through the air between the source and window is 0.89 times that of thallium L radiation, and through the mica window 0.67 times. Further, the nickel radiation is absorbed in the counter to an extent, 2.15 times greater than thallium L radiation. The efficiency of detection, therefore, has been increased by the fraction: $q. \, 0.89 \times 0.364 \times 0.89 \times 0.67 \times 2.15 = 0.42 \, q.$

Therefore, the observed results must be corrected by the factor $1/(1 + 0.42 \, q)$. This correction neglects the absorption of the nickel K radiation in nickel. The error involved in making this approximation is very small.

TABLE I

SUMMARY OF THE RESULTS OF MEASUREMENTS ON THE EFFICIENCY OF DETECTION OF L RADIATION FROM SOURCES OF ThC AND Th(B + C), IN UNITS OF 10^{-5}

Support	Number of measure-ments	Uncorrected	Correction factor	Corrected
A: measurement of ϵ_2				
Nickel, 7.4 mgm./sq. cm.	4	5.00 ± 0.05	0.86	4.30 ± 0.05
" 0.5 " " "	2	4.23 ± 0.10	0.95	4.03 ± 0.10
Cellophane	3	3.85 ± 0.15	—	3.85 ± 0.15
			Mean	4.06 ± 0.10
B: measurement of ϵ_1				
Aluminum and cellophane	4	9.02 ± 0.10	1.06	9.60 ± 0.10
Cellophane	2	9.20 ± 0.10	1.03	9.50 ± 0.10
			Mean	9.55 ± 0.08

with subsequent dissolution in nitric acid concentration, and evaporation on thin cellophane foils of the same thickness. The results are given in Table 1, *B*. The difference between the mean values given in Table I, using Equation (2), gives ϵ_B :

$$\epsilon_B = 6.10 \pm 0.15 \times 10^{-5}.$$

(b) The L radiation emitted by ThC″–D

The L radiation in this case was measured with reference to the emission of hard γ-radiation instead of α-particles as a standard. For this purpose, a Geiger counter was set up near the source, and when encased in a cylinder of lead $\frac{1}{4}$ in. in thickness, the counting rate registered by it is a measure of the content of ThC″. Sources of ThC″ were prepared free from ThB and ThC by recoil from a source of Th(B + C) under reduced pressure. Both counters were operated simultaneously during two equal consecutive periods, long compared with the half-life of ThC″ (3.2 min.). Let c_1 and c_2 be the number of counts registered by the xenon counter in the two periods, and let c_1' and c_2' be the corresponding quantities recorded by the lead-screened counter; then the differences in the ratios $(c_1 - c_2)/(c_1' - c_2')$ measured without and with a nickel filter, after correction for dead time, determines the amount of L radiation in terms of the hard γ-radiation emitted by the source. With a source of ThC, it was sufficient to determine only the differences in the ratios of the counting rates in the two counters, correcting for the background, the dead time, and the decay of the source.

The ratio for ThC″ was found to be one-tenth of that obtained with a source of ThC in equilibrium with its products. The statistical error in this result was about 100%. Since the response of the lead-screened counter was a measure of the activity of ThC″ in the two sources, the contribution to the efficiency ϵ_2 due to ThC″–D must be about 10%. Subtracting 10% from the figure for the mean value of ϵ_2 given in Table I, A, the following value for the efficiency for ThC is obtained:

$$\epsilon_C = (3.7 \pm 0.4) \times 10^{-5}.$$

Taking the ratio of the number of atoms of ThC″ disintegrating per unit time to the number of atoms of ThC disintegrating per unit time as 0.365, the ratio of $\epsilon_{C''}$ to ϵ_C is found to be about 0.3. Thus,

$$\epsilon_{C''} \simeq (1 \pm 1) \times 10^{-5}$$

Coincidence Measurements

For measurements on ThC, a source of Th (B + C) was deposited on one side of a thin layer of aluminum as described in a previous paragraph. The active surface faced a proportional counter, the α-particles passing into it through a thin window; the total stopping power of the air between the window and the source, and the window itself, was equivalent to that of 2.0 cm. of air. That all the α-particles could be detected in the counter without reduction in number by absorption was verified by plotting absorption curves. The pulses produced by the proportional counter were passed into a fast amplifier with a band width of about 2 Mc., the pulses from the xenon counter were also amplified, and both were connected to a mixing unit. The size of the pulses from the xenon counter, and the size of those produced by the fast amplifier for the most energetic α-particles, were each made about 60 v.; these pulses both operated a multivibrator in each channel of the mixing unit, for which the threshold voltage was maintained constant at about 3 v. A minimum delay was therefore ensured between the coincident times of detection in the counters and the instants at which they operated the circuits of the mixing unit. However, the large diameter of the xenon counter might be expected to produce an appreciable delay in that counter.* To determine the minimum resolving time at which the full coincidence counting rate would be expected to be developed, a subsidiary experiment was made to measure the coincidence counting rate between β- and γ-rays from a source of Co^{60} with the aid of another thin walled counter of much smaller dimensions. The coincidence rate in this experiment was found to rise rapidly as resolving times were increased to 1 μsec. and remain constant above this amount. The minimum resolving time used in subsequent work, therefore, was 1 μsec.

* Cf. Hartog, Miller and Verster, ref. (21). The proportional counter was filled with argon with 2% of carbon dioxide.

For coincidence measurements on the L radiation emitted by ThB–C the proportional counter was removed and a Geiger counter with a thin window of about 1.5 cm. air equivalent was used in its place. The source was prepared in the same way as for the measurements with ThC.

Coincidence Measurements with α-Particles

The coincidence measurements with α-particles fall into three categories:

1. The measurement of the efficiency, when both the long and the short range α-particles are recorded, and no filter is used in front of the xenon counter.

2. Coincidence counting with both groups of α-particles with a filter of nickel, 30 mgm. per sq. cm. in thickness, placed between the source and the xenon counter.

3. Coincidence measurements with sufficient absorption in the path of the α-particles, so that those due to ThC–C″, the shorter range group, are completely absorbed, and without a filter before the xenon counter.

The difference between the efficiency as measured by Methods (1) and (2) gives the efficiency for detection of L radiation for ThC–C″, viz., ϵ_C per atom of ThC. Method (3) gives the efficiency for detection of all types of radiation for atoms of ThC disintegrating along the branch ThC–C′–D. If this result is multiplied by 0.65, the fraction of ThC atoms disintegrating in this manner, it should give the same value as Method (2) (provided no L radiation is emitted in this branch), since the hard radiations emitted by ThC–C″ are of very low intensity compared with those emitted by ThC–C′.

Since the coincidence counting rate was very low, a procedure was adopted in which the total number of coincidences was measured in a time comparable with the lifetime of the source (half period, 10.6 hr.). For this purpose the mean value of the background counting rate, due to cosmic rays (q_0) of the xenon counter, was determined before and after a run. The initial counting rate (q_γ) of the xenon counter was determined, together with the initial counting rate (q_α) for the α-particles. If Q_c is the total number of genuine coincidences recorded in the time of duration of the run, t, the efficiency for detection per α-particle is:

$$\epsilon = \frac{Q_c}{q_\alpha} \cdot \frac{\lambda_B}{1 - e^{-\lambda_B \cdot t}}$$

The efficiency of the detection of L radiation is then given by the differences between these expressions obtained with and without a nickel filter. In each case, from the observed number of coincidences (Q_0), the number due to random coincidences must be subtracted. This number is calculated from the resolving time (τ) and the initial counting rates, using the formula:

$$Q_r = \frac{2\tau q_\alpha}{\lambda_B} \cdot [\tfrac{1}{2}q_\gamma(1 - e^{-2\lambda_B \cdot t}) + q_0(1 - e^{-\lambda_B \cdot t})].$$

The statistical error in the measurement of an efficiency contains significantly statistical errors in Q_c and Q_r only, because both the initial counting rates can be determined with high accuracy. It was found that the resolving time, measured with random coincidences, could be trusted to remain constant to about 1% over a period of continuous operation of several weeks, and could be measured to that order of accuracy. The error in ϵ is therefore given by $\sqrt{(Q_0 + Q_r)}/(Q_0 - Q_r)$. The results obtained are plotted in Fig. 4 as a func-
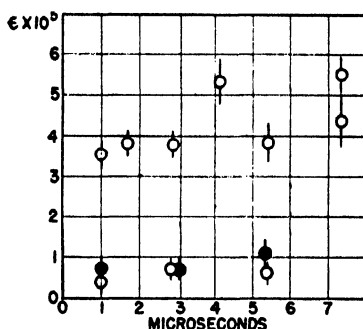
FIG. 4. *The efficiency for the detection of radiation emitted by ThC in units of 10^{-5} plotted against the coincidence resolving time, in microseconds. Open circles: results of Methods (1) and (2). Full circles: Method (3).*

tion of the resolving time. The values obtained at the higher resolving times are very inaccurate, owing to the large correction for random coincidences. At the lower resolving times this correction amounted to about 10%, but at the higher values for the resolving time, the correction could amount to 50% of Q_0.

The mean results of these measurements are given in Table II together with the measurement of ϵ_C obtained by the direct method. It will be seen that the two results agree within the experimental error of 10%. The equality

TABLE II

All coincidence results corrected by 6% to allow for absorption in aluminum and cellophane and for slightly different geometry

Method	Number of measurements	Mean corrected result
(1) No filter, both ThC and ThC′ α-particles	6	4.16 ± 0.2
(2) Ditto, with filter	3	0.52 ± 0.2
(3) No filter, ThC′ α-particles only	3	0.80 ± 0.3
Difference, (1) minus (2)	—	$\epsilon_C = 3.6 \pm 0.3$
By direct method	—	$\epsilon_C = 3.7 \pm 0.4$

of the results obtained by Methods (2) and (3) in the second and third rows of the table shows that no appreciable L radiation is emitted in the ThC–ThC'–ThD branch of the disintegration (in the latter case, the measured efficiency has been multiplied by 0.65).

Coincidence Measurements with β-Particles

The greater part of the L radiation emitted by ThB–C is the result of the secondary process following the emission of K radiation after K conversion. A coincidence measurement of the efficiency for production of this L radiation should serve as a check on the validity of the method as applied to ThC.

Since the greater part of the β-emission from ThB is of low energy, the residual absorption between the source and the interior of the Geiger counter was made as low as possible. The coincidence counting rate depends, then, not only on the coincidences between the L radiation and the β-emission of ThB, but also on the coincidences between the α-particles and the L radiation of ThC–C'' (since the α-particles will also be registered by the counter), on L radiation coincidences with the β-particles emitted by ThC''–D, and on coincidences between the various hard radiations and the α- and β-particles. The efficiency is measured as the ratio of the total number of genuine coincidences to the initial counting rate of the counter, and the portion due to L radiation is measured by the difference between the efficiencies obtained without and with a nickel filter.

Let h_r be the single counting rate in the Geiger counter of particles of type r and if these particles contribute to the L radiation detected in the xenon counter with an efficiency ϵ_r, the total efficiency for L radiation measured by the difference method is given by ϵ_3 :

$$\epsilon_3 = \frac{Q_c}{q_g} \cdot \frac{\lambda_B}{1 - e^{-\lambda_\beta \cdot t}} \cdot \frac{1}{f} = \sum_r (h_r \epsilon_r),$$

where q_g is the initial counting rate in the Geiger counter, f a correction factor of the order of unity to correct for the dead time of that counter, t the duration of the measurements, and the other symbols have their previous significance. If τ_0 is the dead time of the counter, the correction factor f is given by:

$$f = 1 + q_g \tau_0 \left[1 - \frac{1}{2} \left\{ \frac{1 - e^{-2\lambda_\beta \cdot t}}{1 - e^{-\lambda_\beta \cdot t}} \right\} \right].$$

To determine the efficiency for ThB–C, then, the efficiency due to the L radiations of ThC–C'' and ThC''–C must be subtracted from the result for ϵ_3 . After making these corrections, the efficiency due to ThB–C will consist of two terms, one representing the coincidence rate between the L radiation and the nuclear β-particles emitted by ThB, and the other representing the coincidence counting rate which arises from coincidences with the conversion electrons emitted in this transition. If both could be detected without any absorption between the source and the counter, the efficiency for detection.

would be the same in both cases, so that the net efficiency would be just double that detected by the direct method. The absorption, however, reduces the numbers of primary β-particles more rapidly than the conversion electrons owing to the preponderance of low energy β-particles in the former. If ϵ' is the efficiency remaining after subtraction of the irrelevant terms, and if the fractions of the primary and conversion electrons remaining after absorption are y_p and y_e respectively,

$$\epsilon' = \epsilon_B(y_p + y_e).$$

y_e may be computed from the absorption curves given by Eddy (10) for those conversion electrons, and y_p may be calculated from the absorption curve of the β-particles emitted from ThB after subtraction of the contribution of the conversion electrons.

To determine the values of the fractions denoted by h, absorption curves were made for the β-particles emitted by Th(B + C) and ThC. Two such curves are shown in Fig. 5; the ordinate of each curve is equal to the ratio
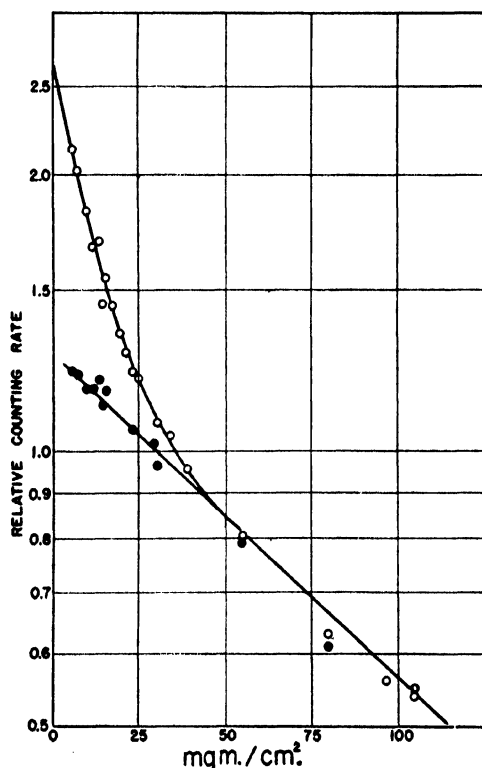
FIG. 5. *Absorption of electrons. Upper curve: from Th(B + C); lower curve: from ThC. The ordinates are the ratio of the number of electrons emitted per unit time to the number of α-particles emitted by the source in the same geometrical conditions. The abscissae are the total amount of absorption in aluminum in the path of the electrons.*

of the number of β-particles to the number of α-particles emitted by each source under the same geometrical conditions. The latter quantity was obtained by removing the absorbing material, lowering the potential on the counter until it operated in the proportional region, and connecting it to an amplifier and discriminator. Both α- and β-particle counts were corrected for the decay of the source and, when the counter was operated in the Geiger region, for the dead time of the counter. The number of primary β-particles from ThC in transient·equilibrium with its products should exceed the number of α-particles emitted by about 2%; it will be seen that the excess is actually about 20%. This is due, no doubt, to scattering at the walls of the hole defining the beam of particles entering the counter. The difference between the two curves represents the number of β-particles due to ThB. It was found very difficult to measure this difference with high accuracy because the curve is very sensitive to the thickness of the aluminum absorbers. Only a few measurements have been made, therefore, in the region of very small absorptions.

The results are collected in Table III. In this table the differences between the efficiencies, without and with a filter, have been corrected by 6% to allow for the absorption in the supporting foil and for the slightly different geometry.

TABLE III

RESULTS OF COINCIDENCE MEASUREMENTS WITH ThB

Efficiencies are given in units of 10^{-5}

Absorption	ϵ_3	h_α	$h_\alpha \epsilon_c$	$h_{c''} \epsilon_{c''}$	h_B	$h_B \epsilon'$	$y_p + y_s$	ϵ_B
5 mgm./cm.²	4.40 ± 0.28	0.32	1.18	0.3	0.30	2.9 ± 0.3	1.7	5.8 ± 1.0
7 "	2.70 ± 0.25	0	0	0.4	0.31	2.3 ± 0.3	1.6	4.8 ± 0.8
13 "	2.91 ± 0.40	0	0	0.4	0.32	2.5 ± 0.3	1.1	7.1 ± 1.1

Mean result $\epsilon_B = 5.9 \pm 0.8$

h_B is the fraction of the counting rate in the Geiger counter due to the electrons from ThB and is obtained from the difference between the two curves; the contribution due to the small amount of L radiation emitted by ThC''–D is roughly estimated from previous information and the fraction of the counting rate due to ThC in equilibrium with its products. The value for y_s is taken from Eddy's measurements, and y_p is estimated by subtracting from the difference curve the number of electrons due to the conversion of the F, E, and H γ-rays, which (in the absence of absorbing material) is taken to be 0.35 electrons per disintegration of ThB. The final result is given in the last column of the table; it is inaccurate because of the large statistical error involved in the measurements, and the difficulty in estimating the fractions denoted by y. It will be seen that the mean result agrees quite well with that obtained by the direct method.

The Counter Efficiency

The experimental efficiencies must now be compared with the calculated values. The first step in this direction is the calculation of the counter efficiencies. Let Ω be the solid angle defined by the brass diaphragm of Fig. 1, z_L the number of L conversions per disintegration. Then if q represents the number of quanta emitted from an L level, E the efficiency with which they are detected in the counter, and R the mean value by which the efficiency is increased by absorption and re-radiation at the end of the counter, the efficiency of detection of L radiation per disintegration is given by:

$$\epsilon = \frac{\Omega}{4\pi} \cdot z_L \cdot \sum_{1,2,3} (qE) \cdot R . \tag{4}$$

The quantities denoted by q have been calculated in the preceding paper (Table VIII). The efficiency E is given by the formula:

$$E = \sum_{\lambda} [C_{\lambda} T_{\lambda} (1 - e^{-k\lambda})] , \tag{5}$$

where C_{λ} is the fraction of the radiation width concerned with the emission of a radiation of wave length λ (Table III of the preceding paper), T_{λ} is the transmission coefficient in the air between the source and counter, the mica window of the counter, and the dead space in the latter before the active region, and k_{λ} is a quantity depending on the absorption within the counter. If d is the effective length of the counter, and if m and μ/ρ are the superficial densities and mass absorption coefficients of the constituent gases, k is given by:

$$k = d \sum (m \cdot \mu/\rho) .$$

The greater part of the absorption in the counter is due to the xenon content. For this element, the following mass absorption coefficient* has been used:

$$\mu/\rho = 103\lambda^{2.73} \text{ sq. cm. per gm.,}$$

where the wave length λ is measured in Ångstrom units. For argon, Colvert's (5) result has been used:

$$\mu/\rho = 33.4\lambda^{2.7} + 0.67\lambda^{0.94} \text{ sq. cm. per gm.}$$

The transmission of the mica window has been calculated from data given by Williams (44).

To measure the effective length of the counter, the counting rate of the counter was plotted against its position (along the axis) when a sheet of hard γ-radiation, defined by a channel in a lead block, was allowed to traverse the counter symmetrically in a plane perpendicular to the axis. The results are shown in Fig. 6. The distance between the positions at which the counting rate is reduced to one-half represents the effective length. The mean result for different fillings was 13.7 cm.

* *This result has been obtained from an extrapolation of the results of Schultz (36) for tellurium and the results of Laubert (26) for tin. The figures obtained are in close agreement, but appreciably higher than the result obtained by White (43), using xenon itself (93 sq. cm. per gm.).*

The absorption of the radiation and its re-radiation in the form of the characteristic X-rays of the material forming the end of the counter produces an increase in the efficiency which is represented by the factor R in Equation (4).
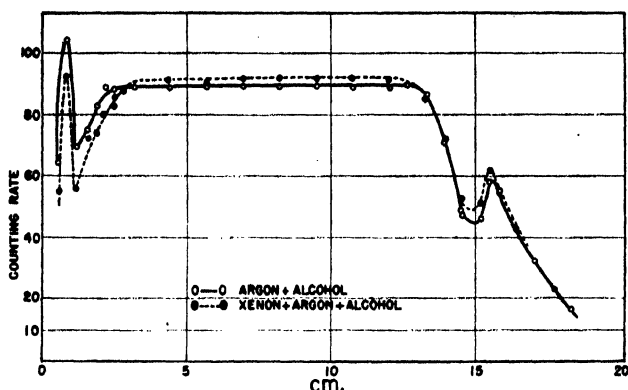
FIG. 6. *Measurement of the effective length of the counter. The ordinates represent the counting rate of the counter; the abscissae, the distance along the axis of the counter in centimeters. The peaks at the end of the curves are due to scattering of γ-radiation into the active region of the counter by the flange supporting the mica window and the junction of the counter wall with the conical endpiece.*

An elementary calculation shows that the effect is only a few per cent in the case of xenon fillings and three or four times larger for a brass-ended counter filled with argon. The result should be negligible with an aluminum endpiece. To test this, the counting rates of L radiation were measured with RaD sources with both brass and aluminum endpieces, and with xenon–argon and with argon fillings. As anticipated, with the argon fillings the counting rates with the brass endpiece were some 10% higher than with the aluminum end. The mean results of several measurements with the different fillings are listed in Table IV, in which H is the counting rate and H/E is the counting rate divided by the efficiency calculated * from Equation (5); a correction of

TABLE IV

COMPARISON OF THE COUNTING RATES OF RaD SOURCES WITH DIFFERENT FILLINGS AND WITH DIFFERENT ENDPIECES

Endpiece	Filling	Source No. 1		Source No. 3	
		H	H/E	H	H/E
Brass	Xe + A	5.70 ± 0.05	20.1	1.57 ± 0.10	5.5
	A	2.58 ± 0.04	20.3	0.67 ± 0.02	4.3
Aluminum	Xe + A	5.97 ± 0.05	21.1	1.43 ± 0.04	5.1
	A	2.35 ± 0.04	20.6	0.55 ± 0.03	4.8

* *This efficiency was calculated on the basis of an energy distribution in the L spectrum obtained in selective absorption measurements described in a later paragraph.*

10% has been applied only in the case of the argon filling and the brass end-piece.   The agreement in the figures for this ratio show that the mass absorption coefficients of xenon and argon which have been used are mutually consistent.   For the xenon fillings, therefore, R is equated to unity.

Calculation of the Efficiency for ThC–C″

The efficiency for the detection of the L converted radiations of this disintegration is given by Equation (4).   The value of z_L, the number of L conversions per disintegration, may be obtained directly from measurements on the electrons ejected from the L levels, or it may be calculated from the excitation of the 40 kev. state, experimental information on the γ-emission from that state, and the fraction of the electrons which are converted in the L levels.

In measurements on the conversion electrons, Gurney (20) found 0.18 L electrons and Arnoult (3) 0.23 L electrons per α-disintegration of ThC. Flammersfeld (14), however, has shown that these figures are too low*; he obtained 0.59 L electrons per disintegration using a special method of preparing the source.   His figure must be corrected for the electrons due to the K conversion of the γ-ray denoted by E by Ellis, which have not been detected separately from the L_1 conversion of the 40 kev. transition of ThC.   This K conversion should amount to about 0.10 electron per α-disintegration of ThC (see Table V).   Flammersfeld's figure for the number of L electrons must therefore be reduced to 0.49 electron per α-disintegration of ThC, and since the efficiencies measured experimentally are reckoned in terms of the total disintegration rate of ThC, z_L becomes 0.17.

Lewis and Bowden (28) found that the 40 kev. state is excited directly in 70% of the α-disintegrations of ThC.   The total excitation of this state, by α-emission from ThC and by γ-ray emission from higher states, probably amounts to about 72%.   If the γ-ray emission** (about $13 \pm 8\%$ per α-disintegration) is subtracted from this figure, the total number of conversion electrons should be about 0.59 ± 0.05 per α-disintegration, which is in agreement with a result obtained by Richardson and Leigh-Smith (35).   Flammersfeld gives 0.82 and Arnoult gives 0.72 for the fraction of these electrons which are converted in the L levels.   These figures include, however, the electrons due to the E γ-ray; for purposes of calculation, the fraction will be assumed to be 0.75, which may be accurate to 5 to 10%. z_L is therefore $0.59 \times 0.35 \times 0.75 = 0.15$ electron per disintegration of ThC.

Both methods of computation of z_L involve errors which are difficult to assess.   Taking the mean of the two, viz., $z_L = 0.16$, the counter efficiencies,

---

This consisted in concentrating a solution of ThB in equilibrium with its products and evaporating a drop of it on to a very thin foil of lacquer.   Previous workers had obtained lower results by using a source deposited directly from the emanation, a procedure which causes some of the ThB atoms to be driven into the surface by α-recoil from ThA.

** *From measurements by the author, hitherto unpublished.*

E, for the radiations of the L_1, L_2, and L_3 levels are respectively 0.270, 0.276, and 0.351. Using the figures for the q's given in the preceding paper, and $\Omega/4\pi = 1.62 \times 10^{-3}$, the efficiency is found to be:

$$\epsilon_C \text{ (from calculation)} = 2.5 \times 10^{-5}$$
$$\epsilon_C \text{ (from observation (Table II))} = 3.7 \times 10^{-5}$$

The experimental result is thus appreciably higher than that calculated. The significance of this will be discussed after the measurements on RaD have been described.

Calculation of the Efficiency for ThB-C

In this case, most of the L radiation follows the K conversion; to a smaller extent L radiation is also produced by L conversion and by Auger transitions between the K and L levels.

The uncorrected results of Duane and Stenstrom (9) correspond to transition probabilities for the emission of the $K\alpha_1$ and $K\alpha_2$ lines in tungsten which are respectively 0.51 and 0.26 of the total radiation probability of the K level. Massey and Burhop's (30) figures give 0.53 and 0.26 for both gold and uranium and these are adopted in the present calculations. If f_K is the fluorescence yield of the K level, the excitation of the L_3 and L_2 levels by K conversion is therefore 0.53 and 0.26 of $z_K f_K$.

The amount of L radiation arising from L conversion is given in Table VIII of the preceding paper.

The Auger electrons arising from transitions from the K level producing ionizations in the L levels were detected by Ellis (12) by a photographic method. His values for the intensities of these electrons is equivalent to about 8.0% of the intensity of the F-line; if the intensity of this line is taken to be 0.28 electron per disintegration, the number of Auger transitions corresponds to 6.6% of the number of times the K level is excited. Flammersfeld's (14) results for this quantity are probably more accurate, and are equivalent to 2.4% of the K excitation. The fluorescence yield, f_K, therefore, must be very near 0.97. The greater part of the remaining 3% lead to double ionizations in the L levels; counting each ionization of the L_1 level as an excitation of the L_3 level, by the Coster-Kronig process, the excitation of the L_3 level by Auger transitions is therefore 3% per K conversion. The ionization of the L_1 level will be taken to be 3% and that of L_2, 1% per K conversion. Thus, the total number of quanta emitted by the three levels per disintegration is given by the equations:

$$Q_1 = 0.09\, z_L + 0.03\, z_K f_1$$
$$Q_2 = 0.04\, z_L + z_K f_2(0.26 f_K + 0.01) \qquad (6)$$
$$Q_3 = 0.19\, z_L + z_K f_3(0.53 f_K + 0.03).$$

The number of conversion electrons which are emitted in the disintegration ThB-C are listed in Table V below, which is compiled from Flammersfeld's

(14) results. The number of K conversion electrons of the E γ-ray is computed from his figure for the number of the L conversions, using his value (5.5) for the ratio of the intensities of the K to the L conversion of the F γ-ray.

TABLE V

CONVERSION OF THE γ-RAYS OF ThB–C, ACCORDING TO FLAMMERSFELD (14), IN ELECTRONS PER DISINTEGRATION OF ThB

γ-ray	z_K	z_L
F	0.284	0.0513
E	(0.035)	0.0063
H	0.011	0.002
D	0.0016	
Total	0.332	0.060

Using the figures given in Table IV of the preceding paper, Equation (6) gives: $Q_1 = 0.007$, $Q_2 = 0.040$, $Q_3 = 0.065$. The counter efficiencies, E, (Equation (5)) for bismuth radiations, were found to be 0.234, 0.246, and 0.327 for the radiations of the L_1, L_2 and L_3 levels respectively. The efficiency for the detection of the L radiation, ϵ_B, is found to be:

From calculation   5.4   ($\times$ 10^{-5})

From direct observation   6.1 $\pm$ 0.2

From coincidence measurements 5.9 $\pm$ 0.8

It will be seen that there is a fair agreement.

Calculation of the Efficiency for ThC''–D

The efficiency for the production of L radiation from ThC''–D may be calculated in a similar manner. In this case the product element, ThD, is an isotope of lead, and in view of the inaccuracy of the measurement of the efficiency it is sufficient to assume that the sensitivity of the counter is the same as for bismuth. The efficiency required is therefore given by the efficiency for ThB–C reduced in the ratio of the numbers of K conversion electrons emitted by the two nuclei. From Flammersfeld's results, the total number of electrons resulting from K conversion attributable to ThC''–D is 0.0228 electron* per disintegration of ThC, when ThC'' is in equilibrium with it. Since the total number of K conversion electrons emitted by ThB–C is 0.33 electron per disintegration of ThB, to a sufficient accuracy,

$$\epsilon_{C''} = \frac{0.0228 \times 5.4 \times 10^{-5}}{0.37 \times 0.33} = 1.0 \times 10^{-5}$$

which is in agreement with the observed efficiency.

* *This quantity is the sum of the numbers of K conversion electrons, per disintegration of ThC, for the γ-rays, G, L, M, P, and X, after a correction has been made for the superposition of the K conversion electrons of the ray M on the L_1 conversion of the ray L.*

Selective Absorption Measurements

The ratio of the number of quanta emitted by the L_1 and L_2 levels (taken together) to the number emitted by the L_3 level can be estimated by the method of selective absorption.   If an absorbing material is used for which the K absorption limit lies at a wave length above those of the lines of the L spectrum to be examined, the absorption will be strong; if below, the absorption will be relatively weak.   When the absorption limit lies in the middle of the L spectrum the intermediate value of the absorption coefficient can be used to measure the relative intensities of the radiations with wave lengths below and above the limit.   Fig. 7 shows the distribution of the lines of the L series for thallium

FIG. 7.   *Distribution in wave length of the lines of the L spectrum of thallium (81) and bismuth (83) with reference to the wave lengths of the absorption limits of selenium and arsenic.*

and bismuth and the position of the K absorption limits of selenium and arsenic. It will be seen that, except for the line $L\beta_2$ and some very weak lines, all the more intense radiations of the L spectrum can be grouped into two categories, the lines originating in the L_3 level with wave lengths above that of the absorption limit and the lines characteristic of the L_1 and L_2 levels with wave lengths less than that limit.   For thallium, arsenic, and for bismuth, both selenium and arsenic are suitable absorbing materials.

Let P be the counting rate, P_0 a constant representing the counting rate in the absence of the absorber, a and $(1-a)$ the proportions of the counting rate (in the absence of absorption) due to the L_1 and L_2 levels and due to the L_3 level, respectively, n the number of absorbing foils, and k a quantity representing the absorption per foil, i.e., the sum of the products of the superficial densities of the constituents with their mass absorption coefficients. Let k' refer to the mean value of this quantity for wave lengths lying below that of the absorption limit, and k'' to wave lengths above the limit.   Then:

$$P/P_0 = ae^{-nk'} + (1 - a)e^{-nk''}$$

and

$$\bar{k} = -\frac{1}{P_0}\left(\frac{dP}{dn}\right)_{n=0} = ak' + (1 - a)k''.$$

The absorbers were made by evaporating selenium *in vacuo* on to thin foils of aluminium (2.0 mgm. per sq. cm.); the arsenic absorbers were prepared by evaporation of arsenious oxide on aluminium foils of the same thickness.

A small correction must be made for the absorption in these foils; if k_0 refers to the absorption in the aluminum of the foil and, in the case of the arsenic foils, to the oxygen in chemical combination with it, the above equation must be replaced by

$$\bar{k} = ak' + (1 - a)k'' + k_0 ,$$

whence

$$a = \frac{\bar{k} - k'' - k_0}{k' - k''} .$$

Since the radiations from L_1 and L_2 are concentrated about the group of lines, $L\beta_3$, $L\beta_2$, $L\beta_1$, and $L\beta_4$, it is sufficient to ignore the γ-group and to use the mean wave length of the β-group of lines to calculate k'. Similarly, k'' is computed for the wave length of the line $L\alpha_1$.

Now the counting rate, a, includes that due to the line $L\beta_2$ which arises from the excitation of the L_3 level, and a correction must be made to allow for the fact that this line lies below the K absorption limit. The radiation width corresponding to this line is about 13% of the total radiation width of the L_3 level. If then, Q_{12} is the number of quanta emitted by both the levels, L_1 and L_2, Q_3 that emitted by the level L_3, the Q's are related to a by the expression:

$$\frac{a}{1 - a} = \frac{Q_{12} + 0.13Q_3}{0.87 \times Q_3} \cdot \frac{\text{Probability of detection of } L_1 \text{ and } L_2 \text{ radiations}}{\text{Probability of detection of } L_3 \text{ radiations}}$$

Selective Absorption Measurements with ThB–C

In this case the admixture of L_1 radiations due to L conversions is very small; the measurement of the ratio of Q_{12} to Q_3 is therefore a check on the ratio of the fluorescence yields f_2 and f_3 which have been calculated in the preceding paper. Since these radiations arise from bismuth, both selenium and arsenic are appropriate absorbing materials. The absorption curves for selenium are given in Fig. 8. *A* is the absorption curve of a source of ThC in equilibrium with its products, the source being deposited in a pure state on a thin film of cellophane with the active surface facing the xenon counter; *B* is the absorption curve of a source of Th(B + C) deposited on a cellophane surface in a similar way. The ordinates of the curves are adjusted so that, in the absence of an absorber, the counting rates are in the ratio of the mean values of ϵ_1 and ϵ_2 which are given in Table I. The difference in the ordinates of these two curves is the absorption for the L radiation due to ThB–C, and is represented by the curve *C* in the figure.

The values for the k's were obtained by an interpolation of the figures given by Schultz (36). With selenium, the mass absorption coefficient is 158 for the β-group of radiations; for $L\alpha_1$, it is 36 sq. cm. per gram; for arsenic, the corresponding figures are 145 and 33 sq. cm. per gram. The results are given in the first two rows of Table VI; both materials give $Q_{12}/Q_3 =$ 0.71. From a previous paragraph, the sum of the number of quanta from L_1

and L_2 is 0.047, and from L_3, 0.065 per disintegration of ThB; the ratio of these two values is 0.73.   This is good agreement and confirms the calculations which have been made for f_2.
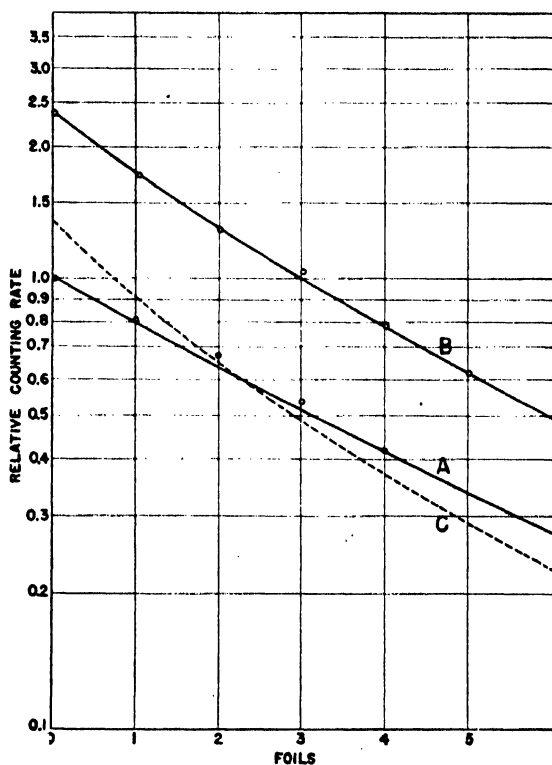

FIG. 8.   *The absorption of L radiation in selenium. Curve A: ThC. Curve B: Th(B + C). The ordinates are chosen so that both sources contain equal numbers of atoms of ThC disintegrating per second.   Curve C is obtained by subtracting Curve A from Curve B.*

TABLE VI

RESULTS OF SELECTIVE ABSORPTION MEASUREMENTS WITH THB AND THC

Absorber	Amount of absorber per foil	$\bar{k}$ per foil	k_0 per foil	a	Q_{12}/Q_2
		For ThB-C			
Se	4.5 mgm./sq.cm.	0.430	0.036	0.42	0.71
As	2.36 mgm./sq.cm. (as metal)	0.231	0.039	0.42	0.71
		For ThC-C''			
As	2.36 mgm./sq.cm.	0.290	0.043	0.48	0.91
As	1.50 mgm./sq.cm.	0.210	0.042	0.54	1.18
				Mean	1.04

Selective Absorption Measurements with ThC–C″

The measurements on the absorption of the L radiation from a source of ThC are given in the lower part of Table VI. Except for a small amount (about 10%) due to the conversions associated with the disintegration of ThC″–D ,this L radiation is due to thallium, and therefore arsenic is the only absorbing material which can give a selective effect. The values of k' and k'' were calculated for the radiations of thallium from an interpolation of Schultz' results. The mean value found for Q_{12}/Q_3 is about unity. The calculated intensities are 0.12 quanta per L conversion from the L_1 and L_2 levels, and 0.165 quanta per L conversion from the L_3 level. This gives $Q_{12}/Q_3 = 0.73$. The discrepancy is appreciable.

The absorption of the ThC radiation in selenium (Fig. 8) gives a mass absorption coefficient of about 36 sq. cm. per gm. which is approximately the value to be expected for the α- and β-groups of radiations for which the wave lengths lie just above that of the K absorption limit of selenium.

The Radiations from RaD

For many years it has been supposed that the emission of a very low energy primary β-particle from RaD leads to the excitation of the RaE nucleus at 47 kev. above its ground state. Recent experiments have shown that all the disintegrations of RaD do not follow this simple procedure and that some serious discrepancies exist. The evidence for this will now be reviewed.

The energy of the secondary electrons from RaD has been measured by Curtiss (7) who showed that the difference between their energies is consistent with the energies of the X-ray levels of RaE, which is an isotope of bismuth. The number of these secondaries per disintegration is still uncertain. Using a cloud chamber method Kikuchi (23) (1927) concluded that the rate of production of the secondaries is slightly less than the disintegration rate of RaD. The accuracy of his figure was limited by special difficulties involved in his cloud chamber technique. The number of secondaries was studied by Stahel (37) in 1931 using a counter method. He obtained 0.83 electron per disintegration; this figure should be an upper limit to the number of secondaries because the effects of scattering and reflection tend to increase it. More recently, very much lower figures for the number of secondaries have been given by Lee and Libby (27) (1939) and by Ouang Te-Tchao and collaborators (31) (1943). In these experiments, the influence of absorption on the number of secondaries is not clear and it is difficult, therefore, to assess the value of the results.

The distribution in energy of the secondaries has been studied in cloud chambers by Feather (13) (1929), Petrová (32) (1929) and by Richardson (33) (1931). The general shape of the energy distribution obtained by these workers is in agreement with that obtained by Curtiss using a β-spectrograph. The energy distribution, however, has been studied by a more accurate method by Richardson and Leigh-Smith (34) (1937) who introduced RaD

into a cloud chamber in vapor form. They were able to identify the electrons due to internal conversion, the Auger electrons, and the primary nuclear electrons of RaD, and showed that 60% of the latter must have a range of less than 0.05 cm. of air at N.T.P. corresponding to an energy of 5 kev. Since only a fraction of the primary β-particles were observable, these authors were unable to measure the relative numbers of conversion electrons to primaries.

According to the measurements of Curtiss, the energy of the γ-ray associated with the disintegration of RaD is 46.7 kev. The absolute intensity of this radiation has been studied by a number of experimenters: by Gray and O'Leary (19) (1929), by Stahel and Sizoo (39) (1930) and by Gray (18) (1932). Recent results are probably more accurate and give three or four quanta emitted per 100 disintegrations of RaD. Von Droste (8) found 3.5%; Bramson (4) 3.1%; Gray (18) 4%; and Stahel (38) (1935) 3.8%. Recently, using the method of crystalline diffraction, Frilley (15) has shown that the 47 kev. radiation is accompanied by weaker radiations with energies at 43, 37, and 32 kev.; the 47 kev. radiation appears to contribute about 80% of the energy of the γ-radiation in this range. Further, using a strong source of RaD, Tsien and Marty (41, 42) have found two softer radiations with energies of 7.3 and 23 kev.

The yield of L radiation from RaD was measured by Stahel (38) in 1935. He found 0.25 L quanta are emitted per disintegration, in approximate agreement with an earlier determination by Gray (18). The spectrum of this radiation was examined by Frilley and Tsien (17) (1945) using a Cauchois spectrograph. These authors concluded that the emission of radiation from the L_1 level relative to that of the L_2 level was less frequent than was to be expected. In another paper, Frilley, Surugue, and Tsien (16) have pointed out that this discrepancy might be due to the presence of Auger transitions of the Coster–Kronig type.

The L Radiations from RaD

It will now be shown that the measurements of Stahel on the L radiation of RaD are not consistent with the assumption that the 47 kev. radiation and the weaker radiations with energies of about 40 kev. are excited in 100% of the disintegrations.

Stahel used his measurement of the L radiation to calculate the conversion coefficient of the 47 kev. radiation. The yield of L radiation is equal to the product of the excitation of the excited state corresponding to that radiation (which he assumed to be 100%) with the fluorescence yield and the fraction of the ejected electrons which are produced by conversion in the L levels. For the fluorescence yield he used Lay's result (25); for the fraction, that of Curtiss (7) (60%). From these figures he concluded that the γ-radiation was 97% converted.

Curtiss's value for the fraction is probably too low, because he used the photographic method of detection which, in this energy range, enhances the effect of the more energetic electrons from the M and N levels. The cloud chamber results of Richardson and Leigh-Smith (34) are free from this objection; they found 0.84 for this fraction with a statistical error of 10%. It has been shown that the fraction appropriate to the 40 kev. transition of ThC–C'' is about 0.75 and there is no theoretical reason to show that this fraction should vary appreciably with atomic number. Using this value, and a total fluorescence yield of 0.47*, the total number of conversions obtained from Stahel's result is 0.71 per disintegration. Now the number of γ-quanta which are capable of converting in the L levels is only 0.04 per disintegration; the rate of production of L converting excited states in RaE is therefore appreciably less than the disintegration rate of RaD. This conclusion is confirmed by the new measurements described below.

Measurements on the L Radiations of RaD

Sources of RaD were prepared from the nitric acid solution of the contents of some old radon tubes. After evaporation and solution in dilute hydrochloric acid, the polonium was first removed by rotation of a silver foil in the solution for 24 hr.; the RaE was then removed by cathodic deposition on platinum, the method of Hevesey and Paneth (22, p. 217); finally, the RaD was removed using a higher current. After solution in nitric acid, the pure RaD was concentrated and allowed to evaporate on two cellophane foils; these sources are called No. 2 and No. 3 in the measurements which follow. The strength of these sources was determined by following the growth of polonium in them, the measurements being made with a proportional counter with a fixed geometry in a manner similar to that used for the measurement of the strength of sources containing ThC. After a time t, the ratio of the number Q_α of α-particles emitted per second by a source of initially pure RaD, to the number Q_D of disintegrations of that source per second, is given to a first approximation by the equation:

$$Q_\alpha/Q_D = 1 - \lambda_D t - \frac{\lambda_E}{\lambda_E - \lambda_{Po}} \cdot e^{-\lambda_{Po} \cdot t} + \frac{\lambda_D}{\lambda_{Po}} (1 - e^{-\lambda_{Po} \cdot t}) + \frac{\lambda_{Po}}{\lambda_E - \lambda_{Po}} \cdot e^{-\lambda_E \cdot t}$$

where the λ's refer to the disintegration constants of RaD, RaE, and Po. With numerical values for these constants, the equation reduces to:

$$Q_\alpha/Q_D = 1.033 - \lambda_D t - 1.069\, e^{-\lambda_{Po} \cdot t} + 0.036\, e^{-\lambda_E t} \qquad (7)$$

The emission of α-particles from the source was followed for a period of about 90 days; the results are plotted in Fig. 9 after subtraction of a small amount representing contamination of the source by polonium not entirely extracted by silver. The amount subtracted was of the form $Ce^{-\lambda_{Po} t}$, the constant C being determined in each case by making the points fit the curve (7).

* *This figure is obtained from the calculated value for bismuth given in Table VIII of the preceding paper, multiplied by the ratio of the experimental and calculated efficiencies for the L radiations of ThC–C''.*

The initial value of this correction was only about 3% of the strength of the RaD sources. The source strengths determined in this way are given in Table VII together with the mean counting rates measured in the counter
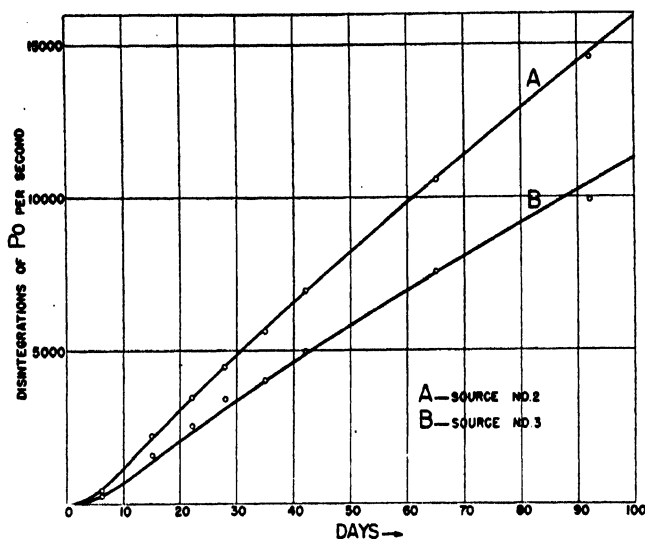

FIG. 9. *Growth of polonium in sources of RaD. Ordinates: number of α-particles emitted per sec., less $Ce^{-\lambda_{Po}t}$, where $C = 1200$ disintegrations per sec. for source No. 2, and $C = 1000$ for source No. 3. Abscissae: time in days after preparation of the sources. Curve A: calculated from Equation (7) to fit points of source No. 2; Curve B: calculated to fit source No. 3.*

filled with the same xenon mixture used in the ThC and ThB measurements. These rates were obtained as the difference between the counting rates measured without and with a filter of nickel, 30 mgm. per sq. cm. in thickness. An absorption curve of the radiation in nickel showed that about 5% of the counting rate without the nickel filter was due to the γ-radiations, and that, with this filter, about 3% of the L radiations is transmitted through it. The counting rates in Table VII have therefore been increased by 3% to account for this effect.

TABLE VII

EFFICIENCIES FOR DETECTION OF L RADIATION FROM RaD

	Source No. 2	Source No. 3
Mean counting rate per sec.	4.38 ± 0.08	3.30 ± 0.10
Disintegrations of RaD per sec.	4.20×10^4	2.97×10^4
Efficiency, ϵ_D	$10.4 \pm 0.2 \times 10^{-5}$	$11.1 \pm 0.3 \times 10^{-5}$
Mean efficiency	$10.7 \pm 0.2 \times 10^{-5}$	

The efficiency was calculated from the figures given in Table VIII of the preceding paper. In this case (bismuth), $q_1 = 0.090$, $q_2 = 0.041$, and $q_3 = 0.192$ quanta per L conversion. Assuming, for the moment, that the total

conversion is 97% of the disintegration rate of RaD, and that the fraction of the conversion electrons ejected from the L levels is 0.75, the comparison of observed and calculated efficiencies is:

<div style="text-align:center">

From calculation: 11.0×10^{-5}

From observation: 10.7×10^{-5}.

</div>

This agreement is accidental because the calculated values of the fluorescence yields are certainly too low.

Selective Absorption Measurements on RaD

Selective absorption measurements have been made on the source No. 2 similar to those made with sources of ThC and Th(B + C). The results are given in Table VIII. By comparison with the results of Table VI it will be seen that the mean results for the ratio Q_{12}/Q_3 are very similar in the two cases and both are greater than the calculated result, which, for bismuth, is 0.68.

<div style="text-align:center">

TABLE VIII

RESULTS OF SELECTIVE ABSORPTION MEASUREMENTS WITH SOURCES OF RaD

</div>

Absorber	Amount of absorber per foil	$\bar{k}$ per foil	k_0 per foil	a	Q_{12}/Q_3
Se	3.6 mgm. per sq. cm.	0.386	0.036	0.50	1.05
As	2.36 mgm. per sq. cm. (as metal)	0.257	0.039	0.51	1.10
				Mean	1.07

Comparison of the Results for ThC and RaD

If the ratio of the number of conversions in the L levels to the total number of conversions is assumed to be the same for ThC and RaD, the ratio of the experimental values for the efficiencies should be nearly equal to the ratio of the total number of conversions, because the counter efficiencies (Equation (5)) are very nearly equal. Using the figures given in the preceding paper, the ratio of the counter efficiency for ThC to RaD is 1.03. Although the calculated efficiencies are too low, this ratio is unlikely to be in error. The total number of conversion electrons is about 0.60 electron per α-disintegration of ThC; assuming, then, that 0.97 conversion electron is produced by RaD per disintegration, the ratio of the efficiencies (ϵ_C/ϵ_D) should be:

<div style="text-align:center">

From calculation   0.23

From experiment   0.35.

</div>

The discrepancy is clearly outside the errors of computation and measurement. It seems certain that the L radiation emitted by ThC, although excessive by comparison with the calculated values, cannot be anomalous;

for if the 40 kev. state could decay in any way other than conversion or γ-emission with the full energy, this process would have been detected in a more complex structure in the groups of α-particles emitted by ThC. The discrepancy can be explained if it is assumed that the γ-rays emitted by RaD are not excited in every disintegration, and this conclusion is in general agreement with the analysis of the measurements of Stahel already discussed.

This explanation, however, leads to serious difficulties, for the deficit in the number of γ-transitions must be made up by β-transitions to the ground state of RaE, and the maximum energy of these β-particles must exceed 47 kev. The continuous spectrum of these β-particles would not have been detected by the earlier observers. In the cloud chamber such β-particles would appear unaccompanied by secondary tracks. If it is assumed that 80% of the disintegrations produce L and M conversion electrons, about 40% of these disintegrations will produce tracks in the cloud chamber which are single or accompanied by a very short range nuclear β-particle corresponding to the normal mode of disintegrations. Half of the observed single tracks, then, should belong to the continuous distribution; the work of Richardson and Leigh-Smith (34) shows no evidence of this.

Discussion of the Fluorescence Yield

The findings of the present measurements will now be reviewed.

(1) The selective absorption measurements in the case of ThB sources show that the fluorescence yields of the L_2 and L_3 levels, viz., f_2 and f_3, calculated in the preceding paper, are in the correct ratio. The measurements on the total yield of radiation show that there is agreement between the experimental and calculated values of these fluorescence yields. The results, however, are consistent with the conclusion of the preceding paper, that the radiation widths calculated from Massey and Burhop's (30) figures are too low by 10%.

(2) The selective absorption measurements on the radiations emitted by ThC and RaD show clearly that these radiations are essentially of the same type. There is no reason to suppose therefore that the energy distribution is anomalous, as has been suggested by Frilley and Tsien (17), unless the anomaly is common to both disintegrations. However, the total yield of the L_1 and L_2 levels, relative to the L_3 level, is greater than anticipated, and the predicted ratio of 2 to 1 for the yields of the L_1 and L_2 levels is not apparent in the intensity measurements of Frilley and Tsien. An elementary calculation on the basis of the intensities given by these authors for the lines $L\beta_4$ and $L\beta_1$ shows that the yields of the L_1 and L_2 levels are approximately equal. This discrepancy cannot be explained in terms of an error in the values for the fluorescence yields which have been used in the calculation, for it has already been shown that the ratio of f_2 to f_3 is correct; and if f_1 were too great, the correction necessary is not substantiated by the X-ray evidence.

(3) An enhancement of the L_2 lines could be obtained if it is assumed that Auger transitions of the type $L_1 \rightarrow L_2N$ occur. The value of the coefficient A_{12} required to make the total yield of the L_1 and L_2 levels together equal to

that of the L_3 level is 0.12 for bismuth and thallium, corresponding to a partial width in the L_1 level of about a volt. These transitions will increase the total fluorescence yield of the L levels by an amount which will give a fair agreement between the calculated and experimental efficiencies of detection for the radiation of ThC although the result for RaD—on the basis of 97% conversion—will be much too great. Taking this effect into account and increasing all the fluorescence yields by 10%, the total fluorescence yield in thallium is increased from 0.29 to 0.36, and in bismuth from 0.32 to 0.41. The comparison of the efficiencies therefore becomes:

	ThC–C″	RaD–E
From calculation	3.2×10^{-5}	14.1×10^{-5}
From observation	$3.7 \pm 0.4 \times 10^{-5}$	$10.7 \pm 0.2 \times 10^{-5}$

L Radiation Accompanying α-Particle Emission

On general theoretical grounds a feeble emission of X-rays might be expected to accompany the production of α-particles. A feeble emission of L radiation associated with the disintegration of polonium has been reported by Curie and Joliot (6); more recently, a strong emission of L radiation associated with the disintegration of U^{234} has been observed by Macklin and Knight (29). The observation of the latter authors is difficult to understand except in so far as it results from internal conversion in an excited state which has hitherto escaped detection. The equipment used in the present work was not very sensitive but sufficient information was obtained to show that for polonium and for ThC′ the emission of L radiation is very weak. A measurement of short duration with a pure polonium source revealed no L radiation; from the statistical errors of the measurement it was concluded that this radiation must be equivalent to less than one quantum emitted per 200 disintegrations, in agreement with the work of Curie and Joliot. The maximum yield of L radiation from ThC′ may be computed from the statistical errors of the coincidence measurements, (2) and (3), of Table II. The efficiency is less than 0.5×10^{-5} per disintegration of ThC′, which is equivalent to less than one quantum per 100 disintegrations.

Acknowledgments

References

1. ALLEN, S. J. M. Phys. Rev. 24 : 1. 1924.
2. ARENDS, E. Ann. Physik, 22 : 281. 1935.
3. ARNOULT, R. Ann. phys. 12 : 240. 1939.
4. BRAMSON, S. Z. Physik, 66 : 721. 1930.
5. COLVERT, W. W. Phys. Rev. 36 : 1619. 1930.

6. CURIE, I. and JOLIOT, F.　J. phys. radium, 2 : 20.　1931.
7. CURTISS, L. F.　Phys. Rev. 27 : 257.　1926.
8. DROSTE, G. VON.　Z. Physik, 84 : 17.　1933.
9. DUANE, W. and STENSTRÖM, W.　Proc. Natl. Acad. Sci. U.S. 6 : 477.　1920.
10. EDDY, C. F.　Proc. Cambridge Phil. Soc. 25 : 50.　1929.
11. ELLIS, C. D.　Proc. Roy. Soc. London, A, 136 : 396.　1933.
12. ELLIS, C. D.　Proc. Roy. Soc. London, A, 139 : 336.　1933.
13. FEATHER, N.　Proc. Cambridge Phil. Soc. 25 : 522.　1929.
14. FLAMMERSFELD, A. F.　Z. Physik, 114 : 227.　1939.
15. FRILLEY, M.　Compt. rend. 218 : 505.　1944.
16. FRILLEY, M., SURUGUE, J., and TSIEN, S.-T.　J. phys. radium, 7 : 350.　1946.
17. FRILLEY, M. and TSIEN, S.-T.　Compt. rend. 220 : 144.　1945.
18. GRAY, J. A.　Nature, 130 : 738.　1932.
19. GRAY, J. A. and O'LEARY, A. J.　Nature, 123 : 568.　1929.
20. GURNEY, R. W.　Proc. Roy. Soc. London, A, 112 : 380.　1926.
21. HARTOG, H. DER, MILLER, F. A., and VERSTER, N. F.　Physica, 13 : 251.　1947.
22. HEVESEY, G. VON, and PANETH, F. A.　A manual of radioactivity.　2nd ed.　Oxford University Press, London, New York, Toronto.　1938.
23. KIKUCHI, S.　Proc. Phys.-Math. Soc. Japan, 4 : 143.　1927.
24. KÜSTNER, H. and ARENDS, E.　Ann. Physik, 22 : 443.　1935.
25. LAY, H.　Z. Physik, 91 : 533.　1934.
26. LAUBERT, S.　Ann. Physik, 40 : 553.　1941.
27. LEE, D. D. and LIBBY, W. F.　Phys. Rev. 55 : 252.　1939.
28. LEWIS, W. B. and BOWDEN, B. V.　Proc. Roy. Soc. London, A, 145 : 235.　1934.
29. MACKLIN, R. L. and KNIGHT, G. B.　Phys. Rev. 72 : 435.　1947.
30. MASSEY, H. W. S. and BURHOP, E. H. S.　Proc. Cambridge Phil. Soc. 32 : 461.　1936.
31. OUANG, T.-T., SURUGUE, J., and TSIEN, S.-T.　Compt. rend. 217 : 535.　1943.
32. PETROVÁ, J.　Z. Physik, 55 : 628.　1929.
33. RICHARDSON, H. O. W.　Proc. Roy. Soc. London, A, 133 : 367.　1931.
34. RICHARDSON, H. O. W. and LEIGH-SMITH, A.　Proc. Roy. Soc. London, A, 160 : 454.　1937.
35. RICHARDSON, H. O. W. and LEIGH-SMITH, A.　Proc. Roy. Soc. London, A, 162 : 391.　1937.
36. SCHULTZ, K.　Ann. Physik, 27 : 1.　1936.
37. STAHEL, E.　Z. Physik, 68 : 1.　1931.
38. STAHEL, E.　Helv. Phys. Acta, 8 : 651.　1935.
39. STAHEL, E. and SIZOO, G. J.　Z. Physik, 66 : 741.　1930.
40. TSIEN, S.-T.　Phys. Rev. 69 : 38.　1946.
41. TSIEN, S.-T. and MARTY, C.　Compt. rend. 220 : 688.　1945.
42. TSIEN, S.-T. and MARTY, C.　Compt. rend. 221 : 177.　1945.
43. WHITE, T. N.　Phys. Rev. 46 : 865.　1934.
44. WILLIAMS, J. H.　Phys. Rev. 44 : 146.　1933.

INDIAN AGRICULTURAL RESEARCH
INSTITUTE LIBRARY, NEW DELHI.

Date of Issue	Date of Issue	Date of Issue
29.7.65		